An evaluation of novel remotely sensed data to improve and verify ocean- atmosphere forecasting.

Charles Galdies

An evaluation of novel remotely sensed data to improve and verify ocean-atmosphere forecasting.

Thesis submitted for the
Degree of Doctor of Philosophy
Department of Geography, University of Durham.

Charles Galdies B.Sc., M.Sc.

November 2005.

ABSTRACT.

The aim of this study is to evaluate the use of novel remote observations and spatial data analysis to improve the skill of an ocean forecasting system for the central Mediterranean Sea. A high-resolution (0.042° by 0.042°) ocean forecasting system was setup consisting of an atmosphere model (NCEP Eta model) that was coupled to an ocean model (Princeton Ocean Model). This coupling consisted of the provision of surface atmospheric fluxes predicted at 3-hourly intervals to drive forward the ocean model. This research study dealt with a variety of aspects to improve this forecasting system using an inter-disciplinary approach.

The main aspect of this thesis is an evaluation of novel, remotely-sensed data acquired by an orbiting passive microwave sensor as a tool to assess and improve ocean forecasting. Thus, SST derived by the Tropical Microwave Imager onboard the TRMM satellite was evaluated for its potential to define one of the lower boundary conditions of the Eta model. The impact was positive, and resulted in an average improvement of the skill of the model to predict lower surface marine winds by approximately 10%. TMI-data proved extremely useful to derive instantaneous turbulent heat fluxes and other surface geophysical fields that were needed to diagnose and fine-tune the skill of the Eta model to forecast these fields. The TMI SST product also proved to be a valuable data source for data assimilation by the ocean model. An optimised data assimilation scheme was derived resulting in a bias of just –0.05 °C after a 15-day model integration run.

This thesis shows how spatial data analysis can provide more detailed information about the high-resolution forecasts and their quality in addition to standard verification tools. Routines that explore the spatial data of the forecasts, observations and their relationship were developed and applied. Geostatistical analysis was used to model the spatial structure of the residual fields of the predictions and observations, and to translate the degree of spatial correlation in numerical and graphical terms.

Key words: ocean-atmospheric modelling, NCEP Eta atmosphere model, Princeton ocean model, remote sensing, Tropical Microwave Image, Sea Surface Temperature, AVHRR calibration, exploratory spatial data analysis, geostatistics, air-sea fluxes, data assimilation, fine-tuning.

Table of contents.

List of tables and illustrations.

Declaration.

The work contained in this thesis is entirely that of the author. Material from the published works of others, which is referred to within this thesis, is credited to the author(s) in question in the text. No part of this work has been submitted for any other degree in this or any other university.

The main body of text (excluding References and Appendices) is approximately 67,430 words in length.

Statement of copyright.

Acknowledgements and dedication.

Special thanks go to my supervisors, Dr. D. N. M. Donoghue and Dr. Y. Zong from the Department of Geography of the University of Durham, for their support throughout the entire study, for reviewing this manuscript and for providing numerous helpful suggestions.

During the research work, I used the computing facilitates at the Euro-Mediterranean Centre on Insular Coastal Dynamics, Malta. Here, I would like to thank the Director of the Centre, Dr A. Micallef, for his encouragement to pursue my studies, and Prof A. Geraci from the University of Catania for his technical support.

I am indebted to Ms S. Music for her technical support in setting up the modelling system, to Dr. S. Nickovic, for his fruitful guidance and discussions of the research plan. Thanks also go to Mr. B. Telenta and Mr G. Pejanovic for their assistance.

Appreciation also goes to Prof. Fedor Mesinger from NOAA/NCEP, who is one of the main developers of the Eta atmosphere model, for the fruitful exchanges of ideas and for his encouragement to carry out a study to diagnose and fine-tune part of the Eta model schemes.

I am grateful to Remote Sensing Systems (www.remss.com), sponsored by the NASA Earth Science REASoN DISCOVER Project, for making available important data used in this work.

Finally, I would like to acknowledge the continuous support and encouragement given to me by my wife Ruth.

I dedicate this work to my beautiful daughter Clara.

List of Acronyms

The acronyms which occur most frequently in this thesis are spelt out below.

ADEOS	Advanced Earth Observation Satellite
AES	Atmospheric Environment Service
ALERMO	Eastern Mediterranean and Aegean basins eddy resolving model
AMSR	Advanced Microwave Sounding Radiometer
AOI	Area Of Interest
AOT	Atmospheric Optical Thickness
AQUA	AQUA Satellite, formerly known as Earth Observation System PM, signifying its afternoon equatorial crossing time
AQUARIUS	NASA satellite mission to measure global Sea Surface Salinity
ATSR	Along Track Scanning Radiometer
AVHRR	Advanced Very High Resolution Radiometer
AWIPS	Advanced Weather Interactive Processing System
BIL	band-interleaved-by-line
CAC	Climate Analysis Centre, Washington DC
CLIVAR	Climate Variability and Predictability Programme
COADS	Comprehensive Ocean-Atmosphere Data Set
CoastWatch	NOAA-wide program comprised of Central Operations and six regional nodes of the United States
COMPASS	Centre for Oceanographic Prediction and Atmospheric Support Services
Coriolis/ WindSat	Wind Satellite measuring ocean surface *wind speed* and *wind direction* using a polarimetric radiometer
CPC	Climate Prediction Centre
CPSST	Cross Product Sea Surface Temperature algorithm
CTD	Conductivity, temperature, depth readers
CYCOFOS	Cyprus Coastal Ocean Forecasting and Observing System
DA	Data Assimilation
DAO	Data Assimilation Office
DECCON	DECompression and CONversion software
DEMETER	Development of a European multi-model ensemble system for seasonal to interannual prediction
DFMR	Department of Fisheries & Marine Research, Cyprus
DMSP	Defense Meteorological Satellite Programme
DREAM	Dust Regional Atmospheric Model
ECMWF	European Centre for Medium-Range Weather Forecasts

ENVISAT	Environment Satellite (ERS follow-on)
ERS	European Remote-Sensing Satellites
ESA/ESRIN	European Space Agency / European Space Research Institute
ESDA	Exploratory Spatial Analysis
Eta	Eta Atmospheric Model
ETS	Equitable Threat Score
EuroGOOS	European association fostering European co-operation on Global Ocean Observing System
FETCH	Flux, Etat de la Mer, et Teledetection en Conditions de fetch[1] variable
FOAM	Forecasting Ocean Assimilation Model
ftp	File transfer protocol
GDAS	Global Data Assimilation Scheme
GEWEX	Global Energy and Water Cycle Experiment
GFDL	Geophysical Fluid Dynamics Laboratory.
GOOS	Global Ocean Observing System
GHRSST-PP	GODAE High Resolution Sea Surface Temperature Pilot Project
GIS	Geographic Information System
GODAE	Global Ocean Data Assimilation Experiment
GOES	Geostationary Operational Environmental Satellite Programme
GOOS	Global Ocean Observing System
GrADS	Grid Analysis and Display System
GRIB	Gridded Binary data
GSFC	Goddard Space Flight Center
HEXOS	Humidity Exchange Over the Oceans
HIRS	High Resolution Infrared Radiation Sounder
HOAPS	Hamburg Ocean Atmosphere Parameters and Fluxes from Satellite Data
IASI	Infrared Atmospheric Sounding Interferometer
ICoD	Euro-Mediterranean on Insular Coastal Dynamics
IMET	Improved Meteorological System
IRS	Indian Remote Sensing Satellite
IOC	Intergovernmental Oceangraphic Commission
IR	InfraRed
JASON	Not an acronym but the name of a joint French/US altimeter mission
LAC	Local Area Coverage
LAM	Local Area Model
LEGOS	Laboratoire d'Etudes en Geophysique et Oceanographie Spatiales
LUT	Look-up table
MCSST	Multi Channel Sea Surface Temperature
MedGOOS	Mediterranean association fostering Mediterranean co-operation on Global Ocean Observing System
MedNet	Mediterranean Network for the provision of

[1] *http://dataserv.cetp.ipsl.fr/FETCH/HTML/INFO_DATA/VAGUES/FETCH_VAGUES.html (accessed on 01.11.04).*

	oceanographic modelling software for the Mediterranean Sea funded by the European Union Marine Science and Technology programme (MAST).
Meso Eta	Mesoscale Eta model
Meteor	Russian Meteorological Satellite
METEOSAT	Meteorological Satellite (European Meteorological Satellite)
METOP	Operational meteorological and climate monitoring mission (European Space Agency)
MFS	Mediterranean Forecasting System
MFSPP	Forecasting System Pilot Project
MOM	Modular Ocean Model
MSE	Mean Square Error
MSG	METEOSAT Second Generation Mission
NASA	National Aeronautics and Space Administration
NCAR	National Center for Atmospheric Research
NCEP	National Centre for Environmental Prediction
NDBC	National Data Buoy Center
NEMOC	Naval European Meteorology and Oceanography Center
NESDIS	NOAA's National Environmental Satellite, Data, and Information Service
NetCDF	network Common Data Form
NGM	Nested Grid Model
Nimbus-7	One of NASA's NIMBUS series of orbiting weather satellites
NLSST	Non-Linear Sea Surface Temperature
NMC	NATIONAL METEOROLOGICAL CENTER
NOAA	National Oceanographic and Atmospheric Administration
NESDIS	NOAA's National Environmental Satellite, Data, and Information Service
NRT	near real-time
NSCAT	NASA Scatterometer (on ADEOS)
NWP	Numerical Weather Prediction
Okean-O	oceanographic research satellite
ODBS	Offshore Data Buoy Center
ODU	Optical Depth Unit
Olwr	Outgoing longwave radiation
ORBVIEW	Series of orbiting satellites developed by ORBIMAGE, carrying the SeaWiFS instrument
SEAWIFS	Sea-viewing Wide Field-of-view Sensor Project
PIRATA	Pilot Research Moored Array in the Tropical Atlantic
POEM	Physical Oceanography of the eastern Mediterranean Project
POES	Polar Orbiting Environmental Satellite
POM	Princeton Ocean Model
RADARSAT	Radar Satellite (Canadian)
RAMSES	Regional earth observation Application for

	Mediterranean Sea Emergency Surveillance
ROFS	Regional Ocean Forecast System
RS	Remote Sensing
RTM	Radiative Transfer Model
SAA	Satellite Active Archive
SAGE	Stratospheric Aerosol and Gas Experiment
SEAFLUX	Ocean Surface Turbulent Flux Project
SeaWinds	Microwave radar designed specifically to measure ocean near-surface wind speed and direction
Secq	is the secant of the satellite zenith angle q of AVHRR sensor
SEVIRI	Spinning Environmental Visible and InfraRed Instrument *(European Space Agency)*
Sich-2	multipurpose Earth remote sensing satellite, an improved version of the Sich 1 built under the National Space Programme of Ukraine
SKIRON	Weather forecasting system developed for the Hellenic Meteorological Service
SMOS	Soil Moisture and Ocean Salinity Mission
SMSST	satellite-measured skin surface temperature
SOC	Southampton Oceanographic Centre
SPM	short-term prediction misfit
SPOT	Systeme Pour l'Observation de la Terre (French Satellite)
SRB	Surface Radiation Budget experiment
SS	Skill Score
SSM/I	Special Sensor Microwave / Imager
SST	Sea Surface Temperature
TAO	Tropical Ocean-Atmosphere
TERRA	TERRA Satellite, formerly known as Earth Observation System AM, signifying its morning equatorial crossing time
ERS-1 and ERS–2;	European Space Agency's European Remote Sensing Satellites
MOS 1/1b	Modular Optoelectronic Scanner (ocean colour sensor on IRS)
TOGA	Tropical Ocean Global Atmosphere Coupled Ocean Atmosphere Response Experiment -
TOMS	Total Ozone Mapping Spectrometer
TOPEX/POSEIDON	Topography Experiment (the US altimeter on T/P)
TRMM	Tropical Rainfall Measurement Mission
UWM	University of Milwaukee - Wisconsin
VOS	Voluntary Observing Ships
WAFS	World Area Forecast System
WCRP	World Climate Research Programme
WGASF	Working Group on Air-Sea Fluxes
WMO	World Meteorological Organisation
WOCE	World Ocean Circulation Experiment
WVSST	Water Vapour Sea Surface Temperature algorithm
XBT	Expendable Bathythermograph

List of Notations

ζ	Dimensionless parameter that partly defines the depth of the viscous sublayer
γ	Transmittance ratio as detected between channel 4 and 5 of NOAA/AVHRR
ρ	density of air (kg m^{-3})
τ	nudging period (hrs)
a_1-a_4; b_1-b_4	NOAA/AVHRR operational SST algorithms coefficients published by NESDIS
10 m	10 meter wind (m s^{-1})
C_{E10m}	Dalton coefficient
C_{H10m}	Stanton coefficient
$C_{i,j}$	Temperature (K) for the radiance value retrieved by NOAA/AVHRR channels i and j
c_p	specific heat of water at constant pressure (J kg^{-1} K^{-1})
$e^*(T_A)$	vapour pressure of the air at a height of 10 m (mb)
e_s	Saturation vapour pressure (kPa)
L	latent heat of vaporisation of water (J kg^{-1})
MS	Match Score
MSE	Mean square error (units are the same as the units of the estimator)
P	atmospheric pressure P at elevation z (kPa)
P_z	pressure at z height (kPa)
q_a	specific humidity at Z height above sea water (kg kg^{-1})
Q_E	latent heat flux (W m^{-2})
Q_H	Sensible heat flux (W m^{-2})
q_s	specific humidity at ocean surface (kg kg^{-1})
r	relative humidity (%)
R_{ij}	ratio of respective atmospheric transmittance between channel 4 and channel 5 of NOAA/AVHRR
Secq	secant of the satellite zenith angle q
SS	Skill score
TBi	Temperature brightness of channel *i* (K)
T_K	absolute temperature (K)
T_{Kv}	temperature of dry air (K) that would have the same density and pressure as the moist air
u_a	10 m wind speed in m s^{-1}
UT	Universal Time (hrs)
W	precipitable water vapour (g cm^{-2})
z_o	Height at which the wind velocity extrapolates to zero on the logarithmic wind profile under neutral conditions

Chapter 1

INTRODUCTION.

1.1. Operational ocean forecasting.

Ocean modelling is a relatively young branch of marine science that has developed during the past two decades to address a wide range of applications (Flemming, 1995). The main thrusts behind the realisation of ocean modelling include:

1. An enhanced skill of ocean numerical models to simulate and predict oceanic features.
2. An acceptable simulation of highly nonlinear dynamical systems.
3. Enhanced computing power that makes feasible more sophisticated computation of numeric simulations of the oceans.

Operational ocean forecasting constitutes one of the most important applications of ocean modelling, and is used to produce predictions of the three-dimensional physical sea state and related marine biochemical components for a certain time period (Nittis *et al.*, 2001). Other uses of ocean modelling include the study of ocean currents, the interaction between the atmosphere and ocean, transport of biogeochemical materials, climate prediction, assimilation of observations to provide dynamically consistent ocean fields, pollution dispersal, fisheries and military applications.

Operational forecasting of the sea state encompasses a technical framework that provides a continuous oceanographic service of significant socio-economic and environmental importance[1]. Strong interest has been expressed in this particular application and, as a

[1] *http://www.bom.gov.au/bmrc/ocean/GODAE/Presentations/godae_sraph/ (accessed on 01.11.04).*

result, the Global Ocean Observing System (GOOS) has been established to promote and coordinate international and national efforts for the development of large-scale and regional ocean observing and forecasting systems (IOC, 1998). The European initiative of GOOS – EuroGOOS[2], has in the past ten years coordinated activities on ocean observation and forecasting to help the advancement of operational oceanography on a European level. Its plan is to introduce six regional projects to establish operational forecasting systems into the regional seas of Europe.

Vigorous oceanographic research in the 1980s, aimed at developing a multiscale Mediterranean circulation model, was accompanied by a new era of numerical prediction in the region. Modelling efforts of the general circulation and data assimilation, coupled with improvements of model dynamics, played a significant role in strengthening ocean modelling in the Mediterranean (Robinson *et al.*, 2001). Through the MedGOOS[3] initiative, the Mediterranean Forecasting System[4] is the latest, region-wide test case that is now providing basin-scale, weekly ocean forecasts (Pinardi and Flemming, 1998).

1.2. High-resolution, small-scale ocean forecasting.

High-resolution ocean forecasting has numerous military and civilian applications. Some of these applications include assimilation and synthesis of global satellite surface data, anti-submarine warfare and surveillance, high resolution ocean forecasting, optimum ship track routing, search and rescue, high resolution boundary conditions for even higher resolution coastal models, pollution and tracer tracking, fisheries, and ocean structure design such as deep-sea oil platforms.

---

[2] *http://www.eurogoos.org/ (accessed on 01.11.04).*
[3] *which is the Mediterranean component of GOOS.*
[4] *http://www.bo.ingv.it/mfstep/ (accessed on 01.11.04).*

These high-resolution models are able to resolve much of the along-isopycnal mixing, due to eddies and important topographic features, than coarse models can. However, the computational cost and manpower requirements create several difficulties. First, experiments with these models cannot be carried out for very long periods, and so their model solutions are not equilibrated and thus not independent of the initial conditions. Second, there are serious difficulties in assessing the scale of variability produced by these models because of a lack of observational data at the appropriate spatial and temporal scales.

1.3. Ways to improve high-resolution ocean forecasting.

1.3.1. Need for fine spatio-temporal surface forcing.

Ocean modelling has to reflect all the processes that determine the properties of the ocean, the distribution of heat and chemicals as well as its motion. Some of these processes initiate at the sea surface and are related to exchanges between the atmosphere and the ocean (Charnock, 1994). An essential component for ocean models in relation to the distribution of ocean currents, salinity and temperature are the air-sea fluxes of momentum, water substance and heat.

Scientific groups within the global climate prediction community, including the World Climate Research Program (WCRP), the Joint Working Group on Air-Sea Fluxes (WGASF), the Global Energy Water Cycle Experiment GEWEX Radiation Panel, and the US Climate Variability and Predictability (CLIVAR) have expressed the need for high-quality spatial and temporal air-sea fluxes (Taylor, 2000). According to SEAFLUX (1999), such a dataset could assist the oceanographic community to address the following tasks:

1. to better understand the transport budget of heat and freshwater in the global ocean;

2. to diagnose the temporal variation of coupled atmosphere-ocean systems and to improve the day-to-day prediction of air-sea energy fluxes and their influence on small-scale ocean surface variability;
3. to provide surface forcing information to help drive ocean models, and
4. to evaluate the accuracy of forecasted air-sea surface fluxes by atmosphere-ocean models.

Points 3 and 4 above are of direct relevance to this study.

The spatial and temporal characteristics of air-sea flux datasets vary according to the application. For many climatological applications relevant to the GEWEX Radiation Panel and the US CLIVAR Committee, a 1° spatial resolution, 3- to 6-hourly time resolution and accuracy of 5 W m^{-2} for individual components of the surface heat budget are required. It is interesting to note that applications requiring fine spatial and temporal air-sea fluxes are expanding rapidly as high-resolution ocean predictive modelling is becoming more feasible due to advances in computer technology. For this reason, the Joint Working group on Air Sea Fluxes (Taylor, 2000) states that "*...for ocean general circulation models, high-resolution forcing fields...3 hourly winds are required to simulate the shear in the mixed layer, and a 50 km resolution is sought for the wind stress curl*".

The three major, often inter-dependent, sources of flux estimates are shipboard, buoy and satellite observations, and numerical atmosphere models.

1.3.1.1. *In situ* observations.

Direct air-sea flux estimates are scarce, especially in the Southern hemisphere. Moreover, these estimates show errors of around 15 to 25 W m^{-2} in the annual mean, depending on the field studied (Gleckler and Weare, 1997) and are organised as monthly means, averaged over

areas of 1.0° by 1.0° or even coarser. Higher quality turbulent flux measurements are available from research ships taken during field experiments, and increasingly from "flux-measuring" buoys. Nevertheless, the amount of data generated is still small.

Alternatively, air-sea fluxes can be measured using bulk flux algorithms produced by correlating *in situ* flux measurements with basic observational values of sea surface temperature, wind, surface air temperature and humidity. A variety of different bulk flux algorithms are used, with most recently developed research-quality algorithms showing fairly good agreement with observations in conditions of moderate wind speed and neutral or unstable conditions (Taylor and Yelland, 2001). However, there are still outstanding issues with bulk algorithms that lead to inaccuracies in the final estimates including conditions of light wind and stable stratification. The influence of sea spray, treatment of sea state, appropriate averaging scales, parameterisation of mesoscale gustiness and behaviour of scalar sublayer transfer also lead to discrepancies (SEAFLUX, 1999).

From such sets of observations, climatological air-sea flux data have been generated and collected as comprehensive datasets such as the Comprehensive Ocean-Atmosphere Data Set - COADS (Woodruff *et al.*, 1987). The most recent global climatologies (monthly 1.0° by 1.0° grid), including a correction from observational biases, have been compiled by da Silva *et al.* (1994a-e) and from Josey *et al.* (1998).

1.3.1.2. Satellite observations.

Most air-sea fluxes are not measured directly from satellite observations, and instead are calculated by including remotely sensed geophysical fields into sophisticated bulk parameterisations. Remote sensing is limited when it comes to the direct measurement of certain basic variables needed for the parameterisation, such as near surface specific humidity and surface air temperature.

This is not so for the direct measurement of wind speed and direction, which are now a recent addition to the global satellite-direct flux database. Wind speed climatologies derived from SSM/I and ERS[5] scatterometer have been available on a weekly basis since July 1991 for the case of ERS data (Bentamy *et al.,* 1997). The combination of several satellite wind products is promising and the recent NSCAT scatterometer has now made the derivation of a global daily wind vector field possible (Barnier, 1998).

Recently, new opportunities are emerging with the possibility of combining information from various sensors. Recent studies to derive turbulent heat fluxes using NOAA AVHRR[6] (to retrieve Sea Surface Temperature - SST) and SSM/I[7] sensors (to estimate surface wind speed and indirect surface air humidity) were successful, with an error of around 30 W m^{-2} on instantaneous fluxes and 15 W m^{-2} for monthly averages (Schulz *et al.,* 1997). Jones *et al.* (1997) describe the estimation of ocean latent heat flux from satellite data using a neural network approach. In spite of recent improvements, there are still significant systematic and random differences between satellite and *in situ* estimations of turbulent air-sea fluxes and these arise primarily from uncertainties in the near-surface moisture field.

Direct satellite estimates of radiative fluxes have also significantly improved in recent years as a result of the Surface Radiation Budget (SRB) experiment (Darnell *et al.*, 1996). The NASA/GEWEX SRB Project has developed a 12-year global dataset of radiative fluxes on 1^{o} by 1^{o} grid. The derived accuracy is estimated to be 10 W m^{-2} for monthly means[8]. Comparisons with other sources indicate that there can be an overestimation by almost 20 W m^{-2} (Barnier, 1998).

---

[5] *European Research Satellite.*
[6] *NOAA Advanced Very High Resolution Radiometer.*
[7] *Special Sensor Microwave Imager.*

1.3.1.3. Numerical modelling.

The availability of forecasted (Telenta *et al.,* 1998) and analyses[9] (Barnier, 1998) flux data produced by atmosphere models are becoming increasingly important for operational ocean forecasting. Numerical Weather Prediction (NWP) models are providing dynamically consistent surface fluxes and basic variables that have global, regular, and dense coverage in space and time. The availability of 3-hourly forecasted momentum fluxes for example, is highly desirable by oceanographers to resolve frictional velocity issues. Requirements for the heat and freshwater fluxes are not as stringent, and 6-hourly to daily values are acceptable (Taylor, 2000). Like other flux products, NWP products have biases that are difficult to evaluate since verification procedures ultimately have to rely on *in situ* and satellite-derived observations.

The best approach in operational, high-resolution ocean-state forecasting is to force the ocean model with short- and medium-term atmospheric forecasts. In this way, fine-detailed and consistent forecasted atmospheric fields and air-sea surface fluxes drive the ocean model in a forecasting mode. This particular setup requires the availability of initial data for both the ocean and atmosphere models on a routine, near real-time (NRT) basis. Primary data sources include satellite measurements as well as "first-guess" fields coming from diverse sources such as global or regional models.

While many operational applications still call for simulated air-sea fluxes with at least medium spatial (1^{o} x 1^{o}) and temporal (daily to monthly mean) resolution, the demand for forecasted, high temporal (3-hourly) and fine spatial (less than 50 km) resolution is increasing rapidly. These requirements can only be met by numerical models having well-developed turbulence schemes which makes them highly

---

[8] *http://www.gewex.org/srb.html (accessed on 01.11.04).*

[9] *Analyses is the resultant output of the process by which an atmosphere model propagates information concerning the state of the atmosphere from data-rich areas to data sparse areas. This output, together with observations and forcing fields, can be used as initial conditions for a forecasting numerical model.*

attractive to oceanographers (Fischer and Flemming, 1999). The derivation of air-sea surface fluxes using atmosphere models is therefore highly relevant for the present study.

1.3.2. Need for improved initial conditions for atmosphere models to derive better air-sea flux products.

One of the usual shortcomings in numerical modelling is the limited accuracy of the initial boundary (i.e. surface and lateral) conditions of the model parameters, which can lead to a systematic error in the forecast.

An important initial condition for any atmosphere model setup, simulating the atmosphere over water surfaces, is the SST (Robinson and Donlon, 2000). Atmospheric numerical forecasters initialise this surface condition using coarse, modelled SST, which for uncoupled, short to medium-range forecasts remains constant throughout the model integration[10]. The coarse nature of the SST fields introduces uncertainties in the lower model layers that affect and deteriorate the simulation of the near-surface atmospheric parameters. It is therefore of significant interest to substitute this initial surface condition with more accurate observational data.

The advantage of using remotely sensed sea surface observations is attributed to their almost continuous data information over the desired geographic area with significant meso-scale resolution. Remotely sensed SST data, for example, give an opportunity to initialise the surface condition of high-resolution atmosphere models on a continuous and quasi-synoptic basis. The assimilation of high-resolution SST data within the prognostic equations of dynamic models, such as atmosphere models, can profoundly influence the accuracy of derived air-sea fluxes (Gill, 1982).

[10] *Such as the case for the SKIRON system: http://www.uga.edu/atsc/mm5/HowToDoRealTimeMM5.pdf (accessed on 01.11.04).*

Meteorological microwave radiometers are now offering an excellent SST product, although at a reduced resolution than that offered by infrared sensors. The Tropical Microwave Imager (TMI) onboard the Tropical Rainfall Measuring Mission (TRMM)[11] satellite is an example of a passive microwave sensor designed to provide quantitative atmospheric and surface information over a wide swath. By measuring the minute amounts of microwave energy emitted by the Earth's atmosphere, passive microwave sensors are able to quantify the water vapour, the cloud liquid water, and the rainfall intensity in the atmosphere, as well as the SST and 10 m wind speeds over the oceans (Wentz and Meissner, 1999).

Three important features make passive microwave sensors ideal for the purpose of model initialisation. These include (1) their ground resolution providing data with 0.25° grids, (2) their wide swath (approximately 1000 km) on the surface, and (3) their ability to derive SST in the presence of cloud cover and aerosols (fig. 1.1). This ability gives these sensors a distinct advantage over infrared radiometers in providing the necessary initial boundary information to atmosphere models. Furthermore, unlike infrared radiometers, microwave sensors are insensitive to atmospheric water vapour (Wentz and Meissner, 1999). The accuracy of SST data derived by the TMI sensor, for example, has a bias of –0.08 °C and a standard deviation of 0.57 °C when compared to TAO[12] and PIRATA[13] buoys, while the AVHRR Pathfinder SST has a bias of 0.02 °C and a standard deviation of 0.53 °C when compared to *in situ* data (Gentemann *et al.,* 2004). A major limitation of microwave sensors are their sensitivity to sea-surface roughness and precipitation. This implies that their data is not reliable in areas exposed to precipitation and extreme wind conditions.

---

[11] *TRMM is an international mission dedicated to measuring tropical and subtropical rainfall and is providing long-term data sets of rainfall and energy budget measurements which will be used to better understand global climate changes and their mechanisms. The orbiting spacecraft was launched in November 1997; http://trmm.gsfc.nasa.gov/homepage.html (accessed on 01.11.04).*

[12] *Tropical Atmosphere Ocean Network/National Data Buoy Center ; see http://www.ifremer.fr/cersat/en/data/colocsb.htm (accessed on 01.11.04).*

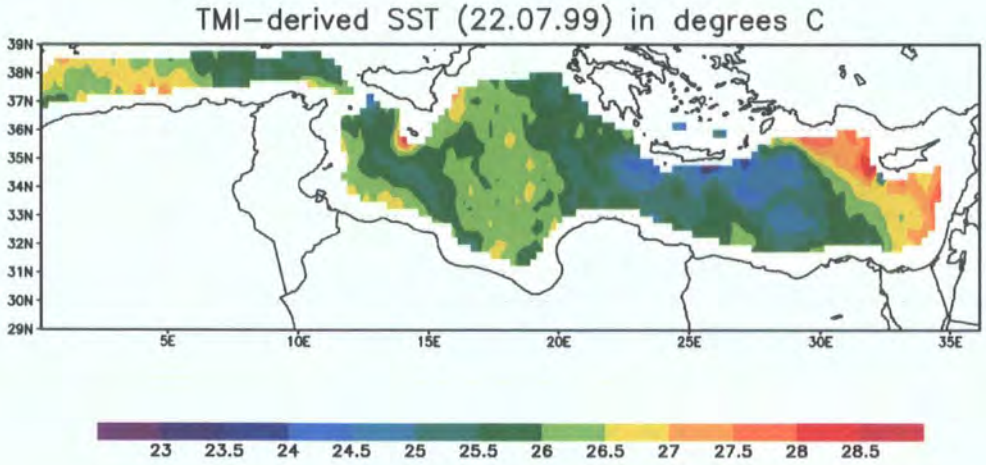

Figure 1.1. Example of microwave-derived SST (in °C) derived from the Tropical Microwave Imager (TMI) at a 0.25° grid resolution. Image covers part of the Mediterranean Sea and detail exhibits mesoscale oceanic features.

Apart from direct observations, predicted fields derived from global atmosphere models can also offer an excellent source of initial conditions for small-scale, high-resolution numerical models. This is a standard feature that is adopted by major forecasting centers where a global and at least one "limited-area" forecasting system are operated, with the latter using the lateral boundary data that is forecasted by the former. The approach is to drive a nested, higher resolution model with boundary conditions derived from a Limited Area Model (LAM) (fig.1.2).

[13] *Pilot Research Moored Array in the Tropical Atlantic;*

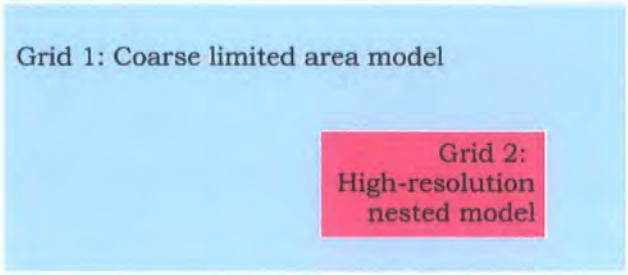

Figure 1.2. High-resolution grid nested in parent grid of the limited area model. The limited area model provides improved initial boundary conditions to the higher resolution nested model.

For example, at the UK Meteorological Office (Staniforth, 2001), model domains of the order of 2000 by 2000 km and even smaller are used. In contrast, the operational Eta limited-area atmosphere model at the National Centre for Environment Prediction (NCEP) is run on a domain greater than 11,500 by 8,500 km. This large-scale domain can serve both to keep contamination at the lateral boundaries (Laprise *et al.*, 2000) far away from the region of interest and to improve large-scale circulation (Mesinger *et al.*, 2002).

There are currently a very small number of research institutions with such a setup in the Mediterranean, such as the Centre for Ocean and Marine Prediction and Atmospheric Services (COMPASS)[14], the ALERMO[15] and CYCOFOS[16] systems. They are all configured to provide high-resolution operational forecasts of air-sea fluxes over selected areas in the Mediterranean Sea. A common approach is to collect "first guess" initial conditions generated externally by a global prediction model with a grid resolution of 1.25° by 1.25° for 10 standard pressure levels. The LAM is then run using these initial conditions to provide the boundary conditions for a nested, higher resolution atmosphere model. In this manner, the best possible temporal and spatial resolution of

http://www.pmel.noaa.gov/pirata/ (accessed on 01.11.04).
[14] *http://www.icod.org.mt/modeling/index.htm (accessed on 01.11.04).*
[15] *http://www.oc.phys.uoa.gr/dok4.htm (accessed on 01.11.04).*

boundary conditions in the area of interest is achieved through model nesting.

1.3.3. Use of data assimilation.

Data assimilation is the incorporation of observations into a mathematical model to improve the initialisation of dynamical models. It is a novel, versatile methodology that makes efficient, accurate and realistic estimation of initial conditions possible, which might not otherwise be feasible or available (Robinson and Lermusiaux, 2001). The initial and boundary conditions necessary for integration of the equations of an ocean model (i.e. velocity components, pressure, density, temperature and salinity) are very often difficult, if not impossible, to measure because of high sampling, technical and resource requirements. Using model numerics, data assimilation adjusts these fields according to their physical relation with the independent observations.

Conventionally, data assimilation consists of schemes that can be performed simultaneously. The specific uses of data assimilation depend upon the quality of datasets and models, and the desired purposes of the field and parameter estimates. Briefly, data assimilation schemes include the following processes:

- *Observation analysis* to (a) interpolate in space and time the observations on a regular network of grid-points and (b) filter out small amplitude random and systematic errors;
- *Dynamical forced adjustment* of the variables by the aid of relationships between different variables utilising cross-correlated observed information, and
- *Normal mode initialisation* of the parameter fields before insertion of the data into numerical forecast models.

[16] *http://www.ucy.ac.cy/cyocean (accessed on 01.11.04).*

One approach among dynamical forced adjustment methods is known as Newtonian relaxation or nudging (Hoke and Anthes, 1976), and is widely applied in regional scale models. It consists of replacing forecast values by observed ones, at all data points. The *a priori* hypothesis is that the observations are exact. The blending estimate is a scalar linear combination of the forecast and data values at all data points, with user assigned weights.

Newtonian relaxation provides field balancing during a full-model pre-forecast integration. This is done by adding the correction terms in the prognostic equations (by means of a nudging coefficient), thus forcing the model fields toward the target analysis as defined by the observations (Robinson and Lermusiaux, 2001). In addition, this dynamic balancing reduces spin-up effects of prognostic fields and consequently would not be distorted during initialisation. The final state is the result of both model adjustment mechanisms as well as the observed information.

1.3.4. Fine-tuning of numerical schemes.

Even if the above features do not introduce limits on the ability to predict the surface atmospheric and ocean-state, numerical forecasting would still be hampered by the imperfect level of the model numerics. Hidden within the numerical terms are representations of physical processes that are too small in scale and sometimes too complex to be completely included in a numerical model (Tribbia, 1997). This encourages modellers to introduce into their physical models statistical empirical relationship or "parameterisation" schemes to describe these processes. These schemes can be further tuned according to the desired model application.

Fine-tuning the numerical scheme responsible for the simulation of air-sea fluxes can strongly enhance the predictive skill of an ocean forecasting system. Because of this coupling between atmosphere and

ocean models, the assessment and improvement of the forecasting quality of air-sea fluxes becomes crucial (Mesinger, 2002, *personal communication*).

1.4. Spatial data analysis in oceanic forecasting.

From the above description, it is evident that the main approach to improve high-resolution ocean forecasting can be condensed into two distinct approaches, namely: (1) provision of accurate initial model conditions coupled with data assimilation techniques, and (2) the fine-tuning of model numerics. The outcome of these approaches in turn necessitates an objective accuracy assessment of the improved forecasting skill.

The role of remote sensing and spatial exploratory techniques embraces the above approaches in their entirety (fig. 1.3). Spatial analysis can be used to explore, visualise and model the relations between the forecasted and true states of the ocean and the atmosphere derived from Earth observations from space, and to assess whether the technical goal has been achieved or not.

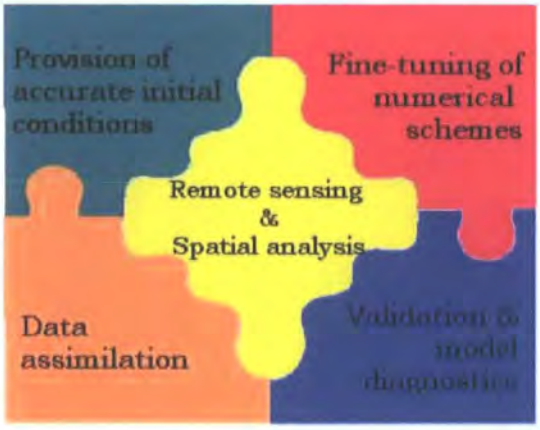

Figure 1.3. The role of remote sensing and spatial analysis is central to the aim and objectives of this study as tools to improve ocean forecasting.

Forecast verification (i.e., the quantitative assessment of forecast quality) is an essential component of any ocean forecasting system. Information concerning the quality of forecasts is needed by end-users to monitor and improve the forecast quality by looking at the *consistency*[17], *quality*[18], and *value*[19] of the model forecasts. However, it is the *forecast quality* that is particularly relevant to forecast verification, which is dependent on a number of attributes, including bias, association, accuracy, skill, resolution and sharpness.

Yet, forecast verification procedures currently in place are quite primitive (from a methodological point of view) and generally fail to meet the fundamental needs of the end users in a satisfactory manner. *Standard* verification methods range from simple "eyeball" verification, dichotomous (yes/no) verification[20], to histogram plotting of the relative frequencies of forecast and observed categories, exploratory plots[21] and summary scores[22] for forecasts of continuous variables. More complex verification methods are used for probabilistic forecasts dedicated to occurrence of particular meteorological/oceanic phenomena.

These traditional procedures translate forecast quality into "scores" by essentially comparing a collection of matching pairs of forecast and collocated observed values. However, these scores represent the accuracy of millions of points and often do not provide sufficient information to assess the performance of forecast models.

On the contrary, *diagnostic* verification methods delve more deeply into the nature of forecast errors. These procedures get away from the pairwise smoothing constraint and tend to identify features and

---

[17] *the degree to which the forecast corresponds to the forecaster's best judgment about the situation.*
[18] *the degree to which the forecast corresponds to what actually happened.*
[19] *the degree to which the forecast helps the decision maker to realise some incremental economic and/or other benefit.*
[20] *using statistical measures such as threat scores.*
[21] *using scatter and box plots.*
[22] *mean error, bias, mean absolute error, root mean square error, correlation coefficient, skill score.*

compare the attributes of these features (e.g. size, shape, magnitude and position) in an overall perspective[23].

Exploratory spatial data analysis is of particular relevance to the validation and diagnosis of numerical models. Techniques such as feature matching, spatial similarity, and autocorrelation studies can be used to analyse the spatial relationship between the model forecasts and collocated observations. These methods, based on image processing and data mining techniques, are able to determine in detail the performance of a given forecasting system by producing similarity or dissimilarity indices that can be easily compared. In spite of their relevance, the use of these procedures in ocean modelling is practically non-existent. A thorough search of the literature on the subject yields very few results, suggesting that the use of exploratory spatial data analysis and geostatistics to assess the performance of ocean-atmosphere models is still in its infancy.

1.5. Definition and scope of the study.

Some research programmes in the Mediterranean, such as COMPASS[24] and ALERMO, have adopted a similar operational framework to that used by the Regional Ocean Forecasting System (ROFS)[25]. ROFS is based on hydrodynamic, three-dimensional ocean circulation model which simulates temperature, salinity, surface elevation, and currents for a region off the U.S. East Coast. The model is driven at the ocean surface boundary by heat, moisture, and momentum fluxes provided by a mesoscale atmospheric forecast model. However, unlike ROFS, the modelling system of COMPASS and ALERMO lacks a scheme that assimilates daily remotely sensed observations for its operational ocean forecasting. This study is intended to supplement the research and development work that is currently being carried out in the

[23] *such as scale decomposition methods and object-oriented methods.*
[24] *http://www.icod.org.mt/modeling/index.htm (accessed on 01.11.04).*
[25] *http://polar.wwb.noaa.gov/cfs/ (accessed on 01.11.04).*

Mediterranean by COMPASS. Because of the ongoing plans to downscale the current operational model setup to coastal areas, fine-tuning of the forecasting system reflecting the new spatial conditions is highly desirable, pushing further the spatial resolution of ocean forecasts to around 4 km and even less. By means of novel, high-resolution earth observation data, these systems can now be driven to produce much more realistic simulations of the atmosphere and oceans.

This study addresses the above plans by setting up and improving an ocean forecasting system to better simulate and forecast the oceanic state at high-resolution over the central Mediterranean.

1.5.1. Physical characteristics of the geographical area.

The geographical domain selected for this study covers part of the Ionian Sea (15.78°E, 33.18°N - 19.18°E, 35.74°N), situated in the eastern part of the Mediterranean Sea. The bathymetry of this study area (fig. 1.4) varies considerably, from the wide Libyan continental shelf (around 500 m) to the basin and troughs of the Central Ionian (around 4000 m) and the complex continental margin off the Greek coast, with its associated islands and canyons.

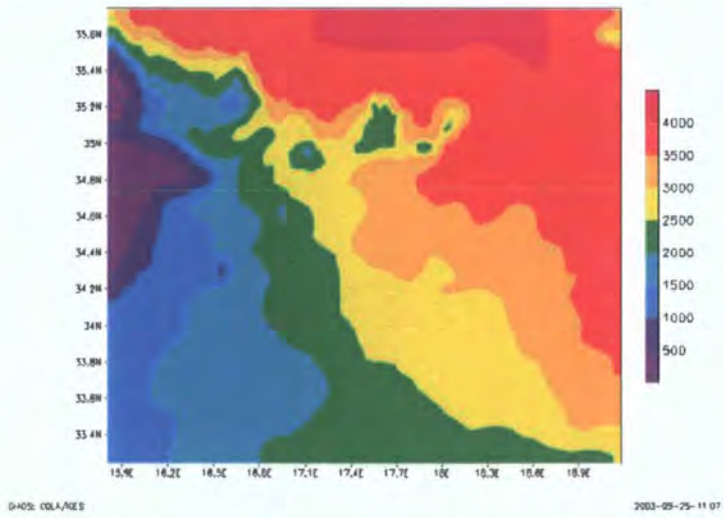

Figure 1.4. Ocean bathymetry over the integration model domain in meters.

This Ionian Sea constitutes a suitable test area for studies related to air-sea interaction where climatic and Atlantic characteristics drive dynamics and dense water formations. The extreme forcings by the local north-westerly winds and by the inflow of cool and less saline Atlantic waters lead to significant air-sea interactions and subbasin scale features (jets and gyres) that eventually affect the basin-wide circulation. Important variabilities exist and include (1) shape, position and strength of permanent subbasin gyres, mesoscale meanders and swirls, (2) meander patterns, bifurcation structure and strength of permanent jets, (3) occurrence of transient and aperiodic eddies, jets and filaments (Robinson et al., 2001). All these factors are often translated in an anti-clockwise gyre in the northern Ionian Sea that flows northern into the Adriatic Sea. In addition, the fast thermohaline circulation of the Ionian Sea interacts with the cooler, less saline Maltese front, causing the front to meander with surface displacements of up to 50 km. This jet of Atlantic Water continues to flow through the central Levantine all the way to the shores of Israel (Robinson *et al.*, 2001).

This thermohaline circulation is coupled to a strong seasonal change signal and it provides a good opportunity to gain experience and knowledge across the range of relevant dynamical issues involved in researching the proposed modelling system. It is interesting to note that this area has been excluded from one of the most significant pilot ocean forecasting projects in the Mediterranean due to some technical limitations [26] and therefore, the choice of this study area becomes even more relevant to the advancement of numerical ocean forecasting in the Mediterranean.

Since this study is focussed on the use of remotely sensed data retrieved by the TMI sensor, the highest latitude of the geographical area does not exceed 40°N (fig. 1.5) because of the low inclination orbit of the satellite.

[26] *the Mediterranean Forecasting System.*

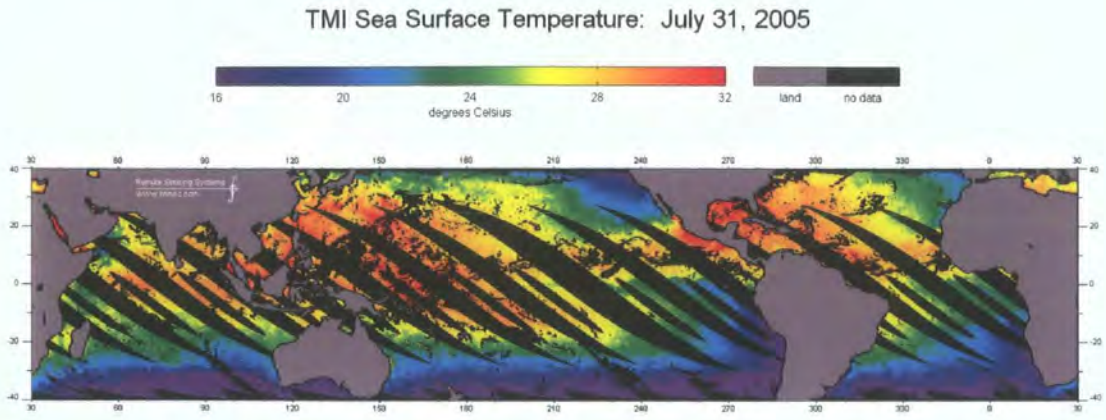

Figure 1.5. Global coverage of the TMI sensor on board the TRMM satellite on July 31, 2005, showing maximum latitude of 40°N in the northern hemisphere.

1.5.2. Period of analysis.

This timing period for this research study is dependent entirely on the availability of an annual set of a complex set of data, in particular, to the availability of a full dataset of atmospheric and ocean model initial and boundary conditions. Other datasets include a suitable annual coverage of remotely sensed data for model validation. The extension of this time frame to more than one year was omitted due to practical reasons related to the substantial amount of model data generated, management, archiving and statistical analysis.

1.5.3. Choice of numerical models.

The basis of the ocean forecasting system used in this study is a high-resolution atmosphere model that is coupled to an ocean model.

The atmosphere model chosen for this study is NCEP's Eta model. It is a limited-area hydrostatic model with a comprehensive physical package and a variety of features in its numerical formulation that makes it unique to operational modeling. Its Arakawa grid computes the momentum field (u-wind and v-wind) on different points than the mass

field (temperature and moisture). Other unique features of the numerics of the model include its step-mountain ('eta') vertical coordinate (Mesinger, 1984); its Arakawa-type horizontal momentum advection scheme (Janjic, 1984), and its algebraic conservation of energy in transformations between the kinetic and potential energy in both space and time differencing (Mesinger, 1984). Within the model's physics package some of the special features are in the modified Betts-Miller convection scheme (Janjic, 1994) and its viscous sub-layer scheme over water surfaces (Janjic, 1996b).

Other reasons for choosing this model include:

- The Eta model code is written in standard FORTRAN (ANSI FORTRAN), and is easy to transfer and install on different computers.
- The model has been used on mainframes produced by all major western manufacturers (e.g. IBM, CDC, DEC, Honywell-Bull, Cray, Convex) as well as on widely used workstations (e.g. Sun, Indigo, Indy, Power Challenge, Indigo2, PC, Cluster parallel computer).
- The model is being upgraded continuously, and special attention is being paid to the improvement of the parameterisation of physical processes. The Abdus Salam Centre for Theoretical Physics in Trieste (Italy), operated jointly by the United Nations and the Italian Government, trains scientists on the use of the Eta model.
- The model is used for both research and operational purposes in more than 20 meteorological institutions throughout the world. In the Mediterranean region it is used for operational weather forecasting (Italy, Turkey and Serbia-Montenegro, Algeria, Greece and Malta). At the NCEP (formerly NMC) Washington, the model has been operational (it is run twice daily) since 1993.

- At ICoD (Malta), where the present research study has been carried out, the Eta model has been operational for eight years, and has been adapted to work on both LINUX and SUN operating systems.

The ocean model chosen for this study is the Princeton Ocean Model (POM)[27]. POM was developed by Blumberg and Mellor in the late 1970s, while others made several subsequent contributions. POM has been extensively used to simulate the circulation of the Mediterranean Sea as described by Zavatarelli and Mellor (1995), Horton *et al.,* (1997), Drakopolous and Lascaratos (1997), and for specific areas such as the Adriatic Sea by Zavatarelli and Pinardi (1995) and the Levantine Sea by Lascaratos and Nittis (1998). Similarly, as in the case of the Eta model, ICoD (Malta) has used the POM model for research and operational forecasting of the Mediterranean Sea since 1994, and therefore the use of this model for the present research was expected. This model has been also adapted to work on SUN and LINUX operating systems.

POM is a hydrodynamic, sigma coordinate, free surface, primitive equation ocean model, which includes a turbulence sub-model. POM has a bottom-following sigma coordinate system in the vertical, a free surface and a split mode time step. The horizontal diffusion terms are evaluated using the Smagorinsky (1963) horizontal diffusion formulation. The vertical mixing coefficients are computed according to the Mellor-Yamada 2.5 turbulence closure scheme (Mellor and Yamada, 1982).

The aim of this thesis is to evaluate the use of novel remote sensing observations and spatial data analysis to improve and assess the skill of this high-resolution ocean forecasting system. It makes use of the above numerical models by coupling them together to produce high spatial (4 km) and temporal (3-hourly) predicted atmospheric and oceanic forecasts. The atmospheric forecasts assist the underlying ocean model

[27] *http://www.aos.princeton.edu/WWWPUBLIC/htdocs.pom/ (accessed on 01.11.04).*

to produce forecasts such as SST, salinity and ocean currents in both the horizontal and vertical dimensions. This "one-way coupling" (fig. 1.6) presents an interesting research alternative to fully coupled ocean-atmosphere forecasting system.

The main objectives of this thesis can be summarised as follows:

- Compilation of a suitable database needed to validate the high-resolution ocean forecasting system.
- Investigating the potential of using novel remotely sensed data to initialise, fine-tune and assimilate the forecasting models.
- Develop, use and assess the effectiveness of exploratory spatial data analysis and geostatistics to verify, diagnose and fine-tune the ocean forecasting system.

Each of these major objectives raises a number of research questions that are analysed in detail in chapter 2.

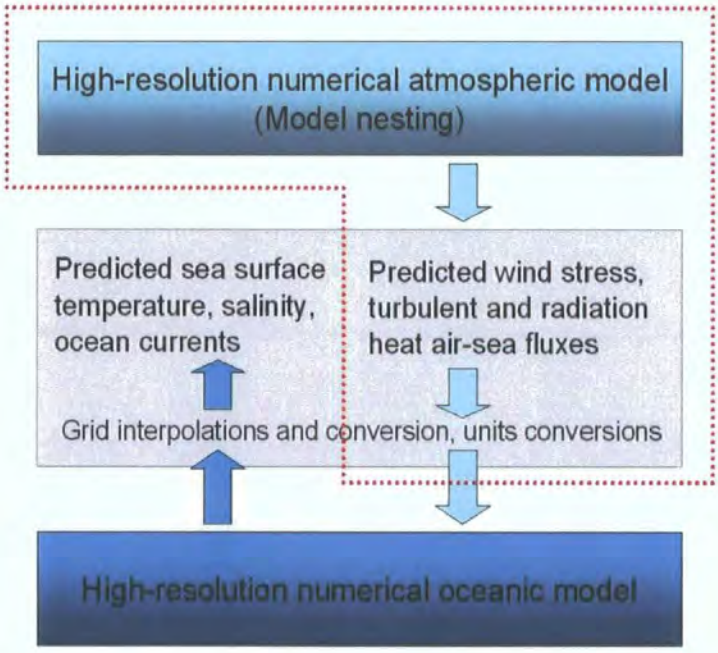

Figure 1.6. Illustration showing a one-way coupled atmosphere-ocean model system. The system uses the predicted, high spatio-temporal air-sea fluxes to force the underlying ocean model to forecast the future oceanic state.

Chapter 2

RESEARCH APPROACH.

2.1. Research goal and objectives.

The overall goal of this research is to evaluate the use of novel remote-sensing observations and spatial data analysis to improve and assess the skill of a high-resolution ocean forecasting system.

The first main aspect of this study is the compilation of a database needed to initialise, assimilate, fine-tune and validate the ocean forecasting system. Remote sensing is here used to obtain repeated and collocated information on atmospheric and oceanic variables derived from microwave and infrared sensors over the area of interest. Important parameters, such as turbulent heat fluxes that cannot be remotely sensed, need to be estimated using bulk parameterisation by merging together data from climatological datasets collecting *in situ* and orbiting sensors.

Another aspect is an investigation of the potential of using novel remotely sensed data to (1) fine-tune the modelling of the 10 m wind speed by the the atmosphere model, and (2) be assimilated by the ocean model including an assessment of whether these actions provide a better high spatio-temporal description of the ocean surface circulation.

The third aspect is to develop and make full use of spatial exploratory data analysis and geostatistics to validate, diagnose and fine-tune the ocean forecasting system. These techniques will provide an insight into the basic strength and weakness of the model performance. Since forecast quality is a crucial determinant for the success of this study, objective verification of the above-mentioned actions is a desirable adjunct to the present objectives.

The following are the main objectives of this study.

2.1.1. Compilation of a database to validate the skill of the ocean forecasting system.

The availability of oceanic and atmospheric data that is collocated with model forecasted data is mandatory for the present research goals. This study therefore addresses the acquisition, processing and archiving of suitable remotely-sensed observations and climatological datasets as an independent data source to validate the skill of the ocean forecasting system.

High-resolution derived products (such as turbulent heat fluxes) can be obtained by fusing together different data types acquired from different sources. Data fusion from different remote sensors is by no means a new development, but in the past, the research has concentrated on the technique of integration through spatial co-registration rather than on methodologies to interpret the combined datasets (Justice *et al.,* 1991). With the availability of multi-temporal, region-specific datasets, this study tries to synergise different data sources over the geographical area of interest. In turn, accuracy assessment of the derived products against independent climatological datasets becomes another aspect of this research.

In some cases, such datasets are provided in an uncalibrated, raw format. This is the case with high resolution, infrared observations of the SST, which this study attempts to calibrate in the absence of collocated *in situ* match-up data. Due to the lack of operational *in situ* data in the area of interest, against which satellite brightness temperature can be linearly correlated, this approach represents the only way to calibrate the high-resolution infrared radiances retrieved from this data-scarce area. The calibrated SST scenes over the same model integration domain can then be used to validate the ocean model's forecasted SST.

The above considerations require the synthesis of an appropriate database that can be used to validate the skill of the forecasting system. As a result, the following research questions are put forward:

- Can passive microwave remote sensing be fused with climatological data to produce quasi-instantaneous, but accurate air-sea fluxes? And if so, can an annual air-sea turbulent flux climatology be generated over the area of interest be generated?

- Is it possible to produce regional-specific, accurate SST maps derived from infrared sensors using appropriate calibration algorithms in the absence of an *in situ* match-up database?

To address these objectives, a number of tasks are performed in Chapter 4 as follows:

1. to acquire, process and reformat multi-annual climatological datasets (surface air temperature and SST, latent and sensible heat flux, and 10 m wind magnitude);

2. to gather a 10-year monthly climatological aerosol optical thickness acquired by NOAA AVHRR;

3. to gather a one-year (1999) monthly climatology database of outgoing longwave radiation as retrieved by NOAA AVHRR;

4. to acquire, process and reformat, a one-year (1999) daily TMI-derived geophysical fields (total precipitable water vapour, cloud liquid water, 10 m wind magnitude, SST and precipitation rate), and

5. to acquire, decode, process and reformat 1.1 km AVHRR (LAC) channel 3, 4 and 5 radiances and collocated NLSST[28] values over a wide oceanic area for a two-year period (1998 – 1999).

The climatological datasets (surface air temperature, SST, latent and sensible heat flux, 10 m wind magnitude and outgoing longwave radiation) will be used to assess the performance of the atmosphere model over a period of one year. The climatological aerosol optical thickness is necessary for the interpretation of infrared radiances acquired by NOAA AVHRR over the area of interest. The microwave-derived remotely sensed parameters are used for a number of tasks, including estimation of instantaneous air-sea fluxes that are collocated with model forecasts, initialisation of the surface boundary condition of the atmosphere model, model fine-tuning and data assimilation by the ocean model.

The brightness temperatures acquired from channels 4 and 5 of the AVHRR sensor are regressed against collocated NLSST values to derive single-line equations for a range of atmospheric conditions defined by the relationship between these channels. In addition to this approach, a number of currently available AVHRR calibration algorithms that do not require a collocated set of *in situ* data will be evaluated. The aim is to use these calibrated AVHRR scenes to assess the forecasting skill of the high-resolution ocean model.

[28] *Non-linear sea surface temperature; obtained using the split-window, non-linear SST calibration algorithm based on the correlation between infrared brightness temperature and collocated, in situ buoy SST.*

2.1.2. Improving the skill of the Eta model to forecast air-sea fluxes.

The use of the Eta model to forecast air-sea fluxes is a recent aspect in its long history of weather forecasting since 1984 (Mesinger, 2002, *personal communication*). It is therefore appropriate to study the model's skill to forecast these fields over a wide range of weather conditions.

An availabile, continuous, high-resolution, remotely-sensed surface field that strongly affects the properties of air-sea fluxes (such as the latent and sensible heat fluxes) is the 10 m wind magnitude. This parameter can be continuously retrieved using microwave radiometry over the Mediterranean Sea and so offers an extremely interesting opportunity to assess and fine-tune the skill of a high-resolution, nested Eta model to predict such a field. These considerations make it possible to explore research questions directed at the improvement of operational forecasting of air-sea fluxes, such as:

- What is the present level of accuracy of the 'standard' Eta model to forecast turbulent and radiative fluxes against remotely-sensed and climatological observations?

- Can the use of remotely sensed, high-resolution 10 m wind magnitude assist in fine-tuning the Mellor-Yamada level 2 scheme[29] of the Eta model that simulates the air-sea fluxes?

and,

- Can exploratory spatial data analysis and geostatistics assist in identifying model performance and in the overall tuning of the sub-model scheme?

[29] *Appendix II*

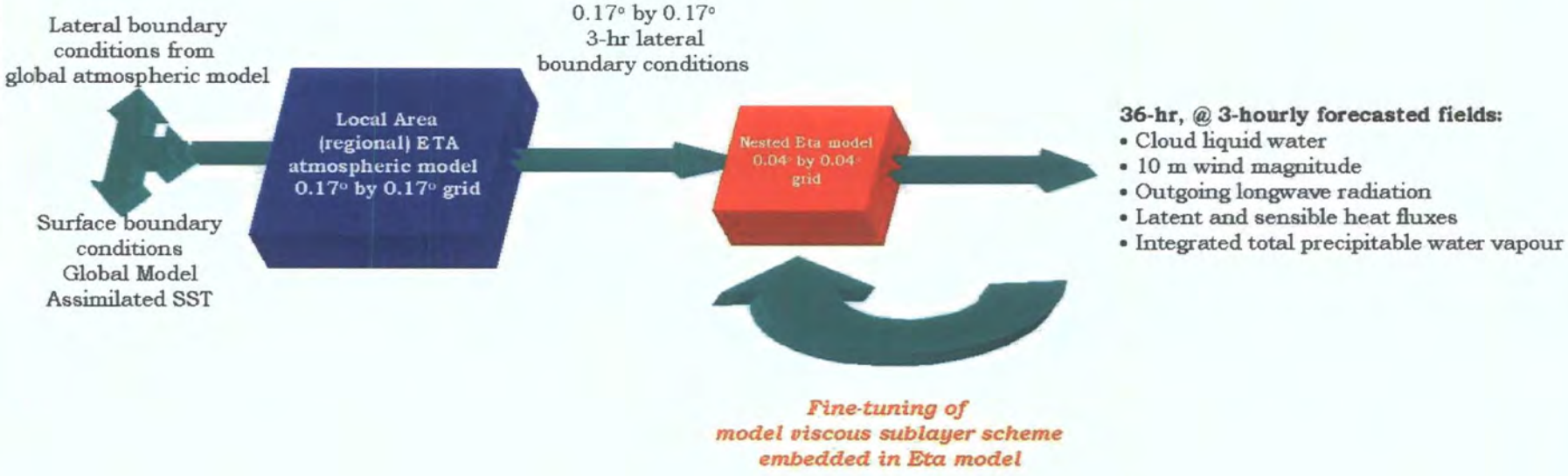

Figure 2.1. Required experimental setup to address the second objective of this study – improving the skill of the atmosphere model to forecast air-sea fluxes.

These issues are explored in chapter 5, for which an experimental setup is required as shown in figure 2.1. A limited area atmosphere model with a horizontal resolution of around 0.17^{o} x 0.17^{o} (entire Mediterranean region) is driven by a 1-year long dataset consisting of lateral and surface boundary conditions forecasted by a global model at 1.25^{o} by 1.25^{o} horizontal resolution. This local area model consists of datasets that are used to drive another Eta model that is nested within the model domain of the LAM. The resolution of the nested atmosphere model is around 0.04^{o} by 0.04^{o} horizontal resolution. The limited-area model provides high mesoscale definition and *quasi*-geostrophic initial conditions for the nested model, which generates short-range forecasted geophysical fields (36-hour) every 3 hours. Only a small part of this data set, specifically addressing air-sea fluxes, will be considered.

The general forecasting skill of the high-resolution Eta model to forecast turbulent and radiative heat fluxes and other basic variables are evaluated against empirical evidence using standard and tailored diagnostic verification methods. The latter include new schemes to measure similarity/dissimilarity and spatial matching using image processing and GIS analysis. Standard geostatistical techniques are also used to discern and compare spatial patterns.

A parallel experiment is set up to fine-tune the Eta's Mellor-Yamada scheme. This is done by running, in parallel, modified numerical codes that predict the 10 m wind magnitude under a range of low to moderate wind magnitude conditions, spanning from 3 to 12 m s^{-1}, during which the numerical scheme is active.

2.1.3. Assessing the impact of using microwave-derived SST to initialise the surface boundary conditions of the atmosphere model.

This is the third objective of this study, namely to assess the improvement, if any, of providing the atmosphere model with more accurate initial surface boundary conditions.

As outlined in the introductory description[30], the use of remotely sensed, high-resolution SST acting as the surface boundary conditions of the Eta model could well improve the forecasting of variables that are highly sensitive to this boundary condition, including air-sea fluxes. This approach raises a number of questions, which the present study attempts to address:

- Can high-resolution SST data retrieved by orbiting microwave sensors be used as the surface boundary condition for the high-resolution Eta atmosphere model to better predict short-range air-sea fluxes?

- Can the direct insertion of SST retrieved by orbiting passive microwave sensors into the Eta model result in a better forecasting skill when compared with the traditional approach that uses instead coarse, modelled-SST fields derived from global models?

To test the above hypotheses, a number of experimental tasks are carried out in chapter 6 as schematised by figure 2.2a. The high resolution Eta model is initialised by daily, 1-year long data-set consisting of lateral boundary conditions predicted from a global model at 00 UT. The SST surface boundary condition at 00 UT is provided from two sources: (1) coarse resolution GDAS global model and (2) from high-resolution, TMI sensor onboard the TRMM satellite. A TMI-derived SST dataset is acquired for an entire year, processed and suitably

[30] *Section 1.3.2.*

formatted to be ingested by the model. A switch is set up to use either one of these sources during model initialisation. In this manner, two parallel sets of forecasted air-sea fluxes are predicted. The *reference set* denotes those fluxes produced when the model is initialised with SST derived from the global model and the *experimental set are those* initialised with remotely-sensed SST.

The high-resolution atmosphere model produces a wide range of short-range, forecasted geophysical fields for 36-hour, every 3 hours. Due to the huge amount of data generated by the full experiment, only the 10 m wind magnitude is used to identify the most effective system. Validation of the two sets of forecasted fields depends on the availability of collocated observations; it makes use of both standard verification methods and diagnostic (exploratory spatial data analysis and geostatistics) measures. The pair of annual sets of predicted air-sea fluxes are later used to drive the ocean model, in a similar parallel experimental mode (see fig. 2.2b) as described in section 2.1.4.

2.1.4. Improving oceanic forcing and prediction.

The fourth objective of this study is to improve the overall skill of the ocean forecasting model using two approaches: (1) provision of accurate air-sea fluxes as upper boundary conditions, and (2) assimilation of remotely sensed SST to dynamically adjust the ocean model fields prior to the actual forecast run.

The provision of a better representation of the air-sea fluxes as developed in section 2.1.3. could lead to a more realistic prediction of the sea-state, such as SST. In addition to this, the fine-tuning of the embedded data assimilation scheme could contribute towards a more accurate, short-range forecasts of the ocean state.

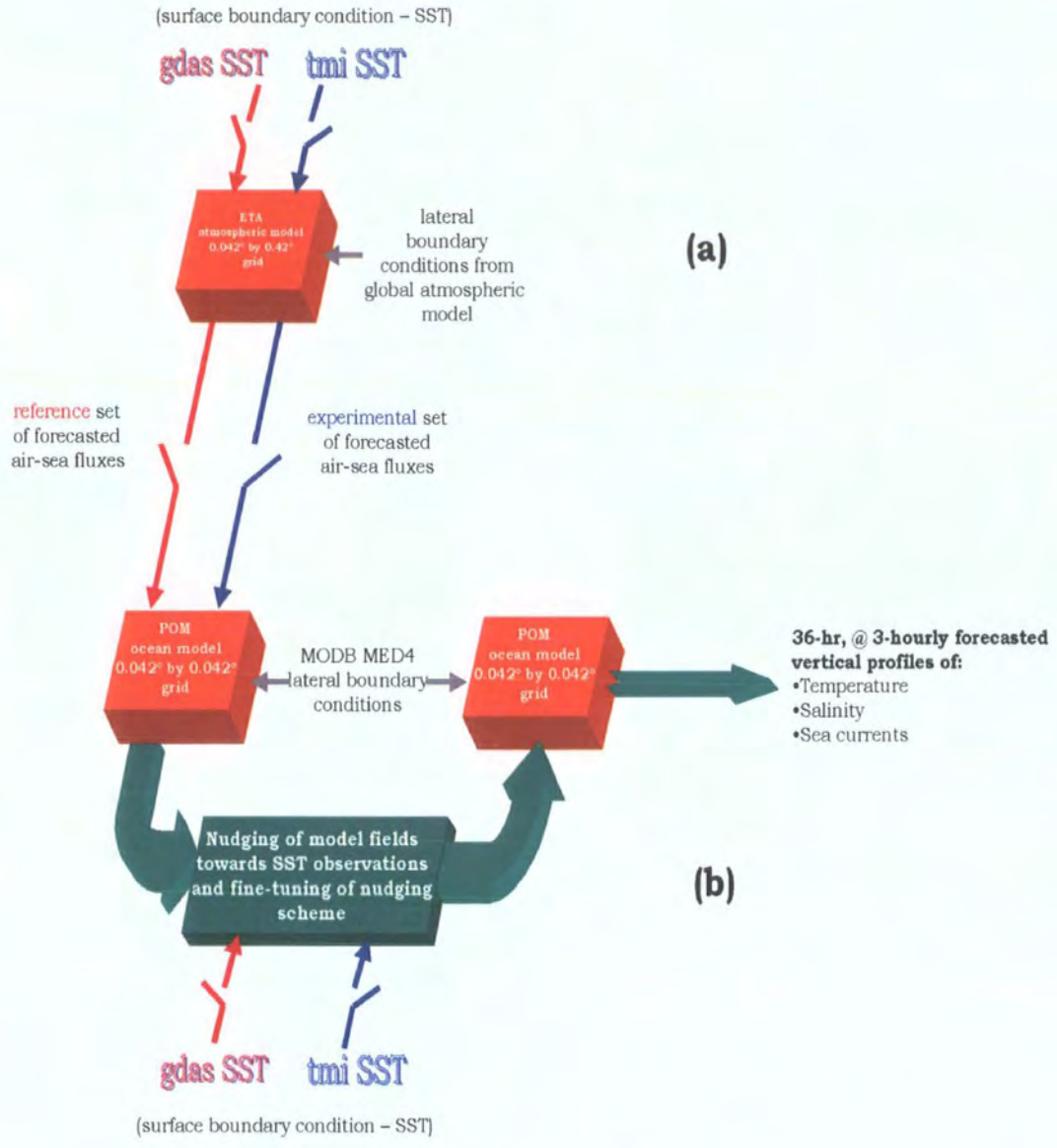

Figure 2.2 a-b. Required experimental setup to address (a) the impacts of using TMI-derived SST to initialise the surface boundary conditions of the atmosphere model (section 2.1.3.), and (b) to improve ocean forcing and prediction (section 2.1.4.).

Newtonian relaxation is a data assimilation scheme that is very appropriate for the present study by providing flexibility in the adjustment and determination of the best values for the coefficients. The value of the nudging coefficient as well as duration of the nudging is critical for the success of this data assimilation scheme. The selection of an optimal value is based on empirical experience and is fine-tuned following an accuracy assessment of the final forecasts against collocated remotely sensed observations.

The above considerations and suggested setup make it possible to explore research questions which will be useful for the improvement of operational ocean forecasting system, such as:

- Can a hydrostatic, Princeton Ocean Model (POM) with a horizontal resolution of 0.042^{o} be efficient in predicting small-scale ocean basin surface features?

- Can near-real time surface boundary conditions, such as microwave-derived SST, together with forecasted 36-hour momentum, turbulent and radiative heat forcing fields be sufficient for the ocean model to accurately predict surface oceanic fields?

- Can Newtonian relaxation (as a data assimilation scheme) of the initial model fields towards remotely sensed SST enhance the accuracy of 24-hour surface ocean forecasts?

The selection of the area of interest is based on the availability of a full data coverage, close to the 00 UT SST dataset derived from the TMI sensor. These research questions are addressed in chapter 7, and require an experimental setup as shown in figure 2.2b. A high-resolution ocean model is setup with an integration domain and horizontal resolution corresponding to the nested Eta model. The ocean model uses the pair of datasets that the atmosphere model generates in section 2.1.3. as its surface boundary conditions as well as the initial

SST condition. Lateral boundary conditions are derived from a climatological database as "first guess" fields.

A switch is set up to use only one source of initial surface conditions at a time. The specific SST data dynamically adjusts the initial oceanic fields towards the SST information in a pre-run mode. Here the data assimilation scheme is fine-tuned to achieve the best adjustment towards SST. Following this stage, the actual model integration is run in forecasting mode.

The assessment of the impact of (1) improved short-range, 36-hour predicted momentum, turbulent and heat flux forcing fields and (2) assimilating TMI-derived SST as compared to the use of modeled SST data, on the overall ocean forecast accuracy is performed. This is done by validating the accuracy of the two sets of forecasted SST against high-resolution 1.1 km SST maps using both basic statistical and image processing analysis (fig. 2.2b).

The main structure and internal linkage of the ocean forecasting system used in this study is illustrated by figure 2.3. A comprehensive list of the entire datasets required for this study, their sources and usage is shown in table 2.1 together with a schematic diagram (fig. 2.4) highlighting the inter-linkages of the acquired and estimated data for forecast verification, fine-tuning, initialisation and data assimilation off the ocean forecasting system.

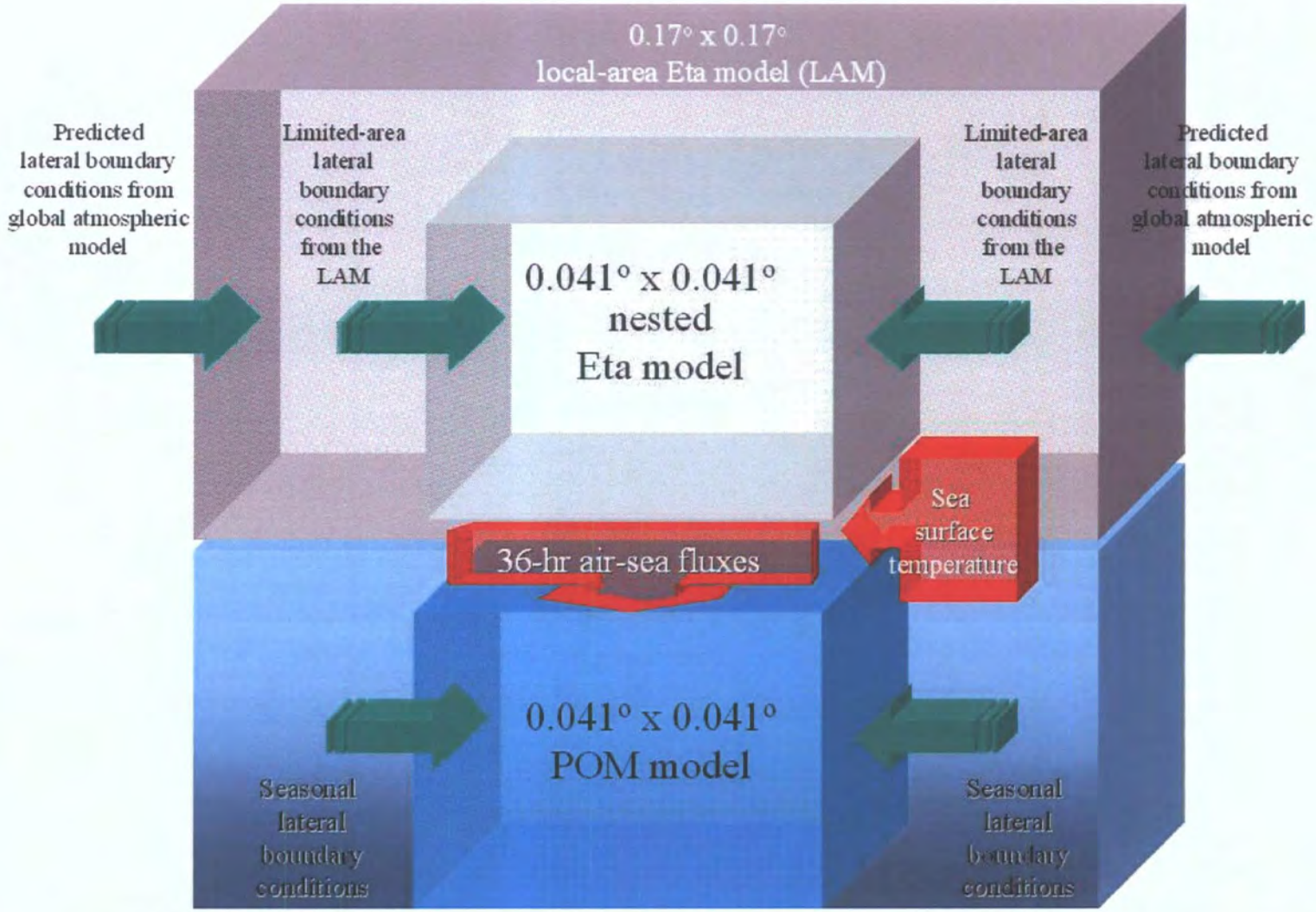

Figure 2.3. An illustration of the main setup and internal linkage of the ocean forecasting system used for this study.

Source	Geophysical field	Use
Advanced Very High Resolution radiometer (AVHRR)	SST	• Validation of ocean model SST forecasts
	Outgoing longwave radiation	• Validation of radiative package of atmosphere model
	Aerosol optical thickness	• Validation of radiative package of atmosphere model • Assisting in the calibration of AVHRR radiances
Total Ozone Mapping Spectrometer (TOMS)	Aerosol Index	• Validity of AVHRR brightness temperature data
Tropical Microwave Imager (TMI)	SST	• Initial surface conditions of atmosphere and ocean models • Use for data assimilation • Reference dataset for the calibration of AVHRR radiances • Validation of ocean model SST forecasts • Derivation of turbulent heat fluxes
	10 m wind magnitude	• Validation and fine-tuning of the turbulent scheme of the atmosphere model • Derivation of turbulent heat fluxes
	Precipitation rate	• Use to flag and null erroneous collocated pixels of other geophysical fields
	Cloud liquid water & Total Precipitable water vapour	• Validation of general performance of the convection schemes of the atmosphere model
Comprehensive Ocean-Atmosphere Data Set (COADS)	2 m air temperature	• Derivation of turbulent heat fluxes • Validation of atmospheric forecasted 2 m air temperature
	SST	• Validation of monthly average TMI-SST
Southampton Oceanic Climatological Atlas (SOC)	10 m wind magnitude	• Validation of monthly average TMI-wind magnitude
	SST	• Validation of monthly average TMI-SST
	Latent & sensible heat flux	• Validation of calculated latent and sensible heat fluxes
CoastWatch Database	NLSST	• Reference dataset for the calibration of AVHRR radiances over CoastWatch region
	Channel 4 & 5 radiances	• Derivation of split-window SST algorithm

Table 2.1. List of data sources required for the verification, fine-tuning and initialisation of the ocean forecasting system.

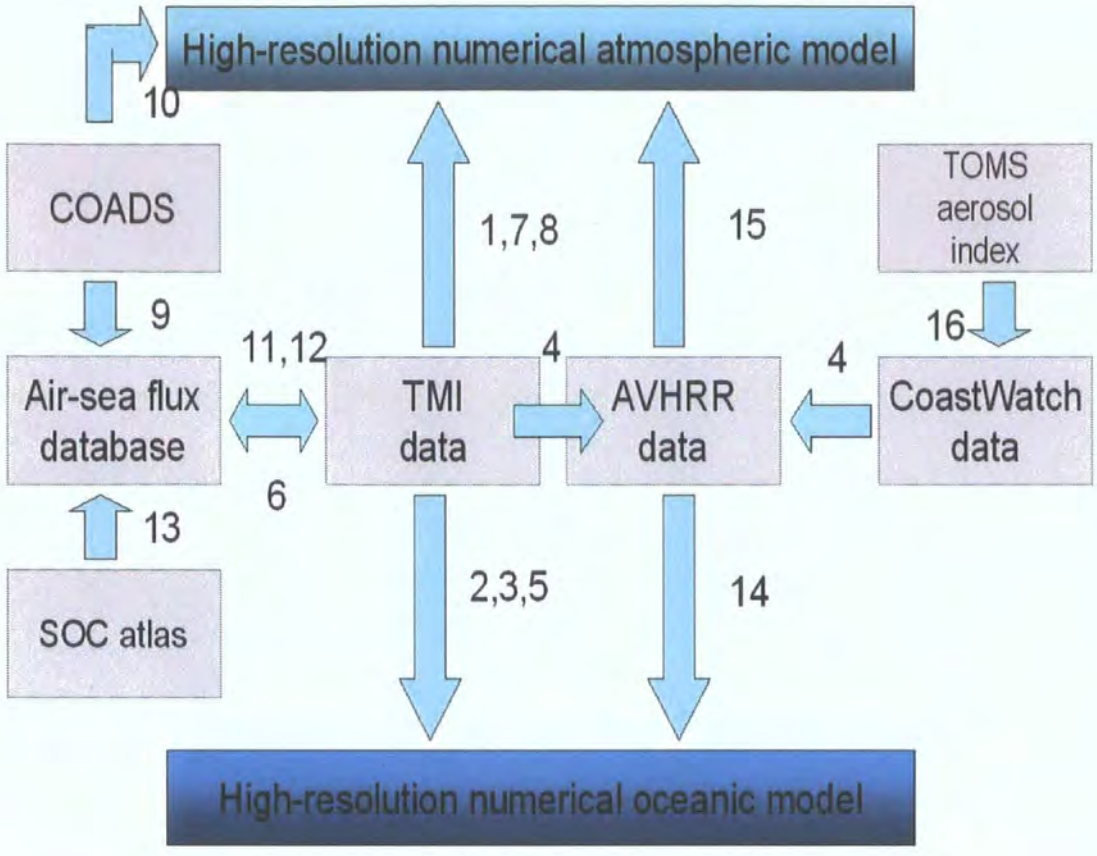

Figure 2.4. Interaction of acquired and derived data for data quality, forecast verification, fine-tuning and validating the ocean forecasting system.

Process number:

1 Provision of initial surface conditions to atmosphere model
2 Provision of initial surface conditions to the ocean model
3 Use for data assimilation
4 Calibration of AVHRR brightness temperature
5 Validation of ocean model SST forecasts
6 Derivation of turbulent fluxes
7 Validation and fine-tuning of the turbulent scheme of the atmosphere model
8 Validation of the general performance of the convection schemes of the atmosphere model
9 Derivation of turbulent heat fluxes
10 Validation of forecasted surface air temperature
11 Validation of monthly average TMI SST data
12 Validation of monthly average TMI wind data
13 Validation of calculated latent and sensible heat fluxes
14 Validation of ocean model SST forecasts
15 Validation of radiative package of the atmosphere model
16 Validity of AVHRR brightness temperature

2.2. Outline of the thesis.

The structure of the thesis follows a logical path addressing the aim and objectives of this study. Chapter 3 gives the background and current scientific challenges upon which the research questions posed by this study are based. Chapters 4, 5, 6 and 7 present the research work on the evaluation of novel remote sensing data to improve high-resolution ocean forecasting.

Thus, chapter 4 addresses the synthesis of a database that is used for the diagnostics, fine-tuning and verification of the atmosphere and ocean models. The required data quality is stringent and should be of high spatio-temporal resolution, often instantaneous geophysical fields are needed to verify single-forecasts of the models. In this chapter, emphasis is given on assessing the accuracy of the constructed database against independent, collocated climatological datasets. Alternative calibration techniques of remotely sensed data are also addressed in view of the lack of *in situ* collocated data over the geographical area of interest.

Chapter 5 addresses the setting-up of the atmospheric modeling system. This work involves the coupling of limited area, atmosphere model within which a high-resolution model is nested. This nesting approach ensures better initial conditions to the high-resolution model to predict a number of relevant geophysical fields over the ocean surface. Research work addresses the current accuracy of the predicted fields and fine-tuning of predicted air-sea fluxes against remotely-sensed observations. The use of novel remotely sensed data and geospatial analysis encompasses this work and prepares the way for further application of these procedures in subsequent chapters.

This nested atmosphere model also forms part of the experimental framework of chapter 6, in which a set of experiments are carried out to improve the prediction of surface fluxes by the provision of a high

resolution, novel SST dataset derived by an orbiting passive microwave sensor. Geostatistical and tailored exploratory spatial data analysis are used to qualify and quantify such an impact.

In chapter 7, a scheme is implemented using the numerics of a high-resolution primitive-equation ocean model to assimilate novel remotely-sensed SST as an alternative to conventional, modelled SST data. The scope is to dynamically adjust the high-resolution predictions towards remotely sensed observations. The validity and sensitivity of the results are checked against the high-resolution information included in the database.

Finally, a general discussion and recommendations for further research follows. The results are summarised and achievements made by this thesis are outlined in relation to work done in the Mediterranean. Recommendations for further research are put forward both to extend this research as well as to further develop the applied novel techniques.

Chapter 3

REVIEW OF PREVIOUS RESEARCH.

3.1. Operational ocean forecasting.

The goal of operational ocean forecasting is to produce predictions of the physical sea-state and other related components for a certain time period. Today, ocean forecasts are an important component in modern-day management of ocean ecosystem in view of anthropogenic stress and the safety and efficiency of marine industries. The benefits of having a continuous forecast of ocean variability at exceptional space-time resolution are numerous.

Operational forecasting had its early successes in meteorology during the seventies. Since then, the daily to weekly meteorological forecast skill has been increased by major Numerical Weather Prediction (NWP) centers around the globe, such as the National Centre for Environmental Prediction (NCEP), the UK Meteorological Office and the European Centre for Medium Range Weather Forecasting (ECMWF).

The development of ocean forecasting has progressed more slowly than its atmospheric counterpart because of the lack of routine and accurate measurements needed to both initialise and validate ocean models. Predictions of the sea-state raise problems similar to those found in atmospheric weather forecasting, since the predictability time scale of the oceanic system is practically set by the accuracy with which the initial condition is known. Due to scarcity of oceanic observations, forecasting of deep ocean currents, for example, are still at the research stage such as the Forecasting Ocean Assimilation Model (FOAM) of the UK Met Office[30].

[30] *http://www.meto.gov.uk/research/ocean/operational/foam/ (accessed on 01.11.04).*

In spite of this limitation, ocean forecasting started as soon as numerical ocean modelling reached sufficient maturity at the beginning of the eighties. Since then, a number of ocean forecasting systems have been developed to forecast specific ocean variables, driven by a demand for monitoring of coastal flooding and ship routing. A good example of a successful operational global system to predict wave and storm-surge forecasting (Komen *et al.,* 1994) is the UK Met Office's FOAM. This model is made feasible by the availability of highly accurate surface wave information, tides and surface atmospheric winds. The UK Met Office has run global and regional wave models for many years to provide forecasts of sea state, as a support to a range of user applications.

3.1.1. Main limitations due to data requirements.

The advent of computers opened up a whole new array of mathematical models aimed at finding a "solution" to complex geophysical processes. However, there is a risk associated with computer simulation done with either grid-point or spectral models (Doswell, 2000), since their solutions are based on a set of approximations (and simplifications). One reason for this approximation is the lack of precise initial information at the start of the numerical integration. The current finite observational system only provides approximate initial conditions, of which details strongly influence a specific final model solution. So far, most of the existing ocean models use the wind stress from the Hellerman and Rosenstein database, COADS data or some local data sets (May, 1982) as a mechanical forcing. In addition, the ocean model's SST and salinity fields are nudged towards climatological datasets such as Levitus'. However, a serious drawback of using climatic (or "fixed") data is that the main variability that they contain is at most seasonal.

The end result is a modelled ocean current that would grossly resemble the present oceanic state, where a "true" equilibrium state can only be achieved after thousands of years of model integration (McWilliams,

1998). As a consequence, it is not feasible at present to integrate a global ocean general circulation model to reach equilibrium with mesoscale (i.e. 50 – 100 km) resolution (McWilliams, 1998). This is the degree of resolution required to assist in the management of the ocean ecosystem.

3.1.2. Short- to medium-range ocean forecasting.

Ocean modellers can shorten the costly model computations required to reach true equilibrium by *forcing* the ocean model using forecasted atmospheric constituents that directly affect it, giving the model the ability to enhance its forecasting skill on a much shorter time scale.

The ocean receives energy through its air-sea interface in the form of kinetic (i.e. the momentum flux) and potential energy (i.e. the turbulent- and radiative heat and freshwater fluxes). The surface winds blow over the ocean and drive not only the clearly visible surface waves, but also the large-scale currents in the upper ocean layer. At the same time, the temperature of the near surface atmosphere will modulate the SST via vertical heat fluxes. The interplay between air temperature, SST and their difference makes up a major part of the global air-sea interaction. As with temperature, salinity variations are primarily determined by air-sea fluxes that can change the buoyancy of the fluid. Evaporation leaves salt behind and increases the salinity of the surface seawater, while precipitation decreases it. Like temperature, salinity has a significant effect on the thermohaline circulation. Because of such dependencies on air-sea fluxes, short- to medium-range ocean forecasting models rely entirely on the provision of an accurate representation of these surface boundary conditions in forecast mode.

Apart from providing valuable initial information, high quality air-sea fluxes together with basic meteorological variables are also needed to assess the model's forecasting skill. Such estimates must be associated with a realistic error assessment and specification of the true resolution

of the data. This quality need also be reflected in the resolution of air-sea fluxes in both temporal and spatial terms. The required spatial resolution very often varies according to the application: from coarse resolution global scale models running over centuries, to eddy resolving models over a few decades. For many global and regional applications in the coming years, monthly means on a 1^{o} by 1^{o} grid are sufficient (Taylor, 2000). However, the number of applications which have finer temporal and spatial requirements is rapidly increasing as ocean model resolution increases with available computer power. The demand for high-resolution momentum fluxes is most pressing, and in order to accurately resolve the wind stress curl (being the primary forcing of ocean gyres) a spatial resolution of at least 50 km is required. Heat fluxes having a similar resolution would allow a good resolution of the gradients across major oceanic currents.

With regards to temporal resolution, Taylor (2000) recommends the use of three-hourly winds as forcing fields for ocean models if short-term fluctuations of the wind stress is to be resolved. In the case of heat fluxes, six hourly to daily values have been recommended.

3.2. Data sources for fluxes and related variables.

The basic set of air-sea fluxes needed to drive ocean forecasting models include the net heat input by solar radiation, the non solar heat flux (the sum of the sensible, latent and infrared heat fluxes), the wind stress vector; the wind stirring, the evaporation rate, the precipitation rate, the river runoff and sea ice-melts (when applicable). Additional required surface variables are the SST, sea surface salinity, ocean albedo, surface wind speed, air temperature and specific humidity at specified height, mean sea level pressure, cloud fraction, sea ice coverage and growth rate. According to the forcing method used, other parameters such as exchange coefficients and all variables entering the determination of the stability of the air column may also be required to calculate air-sea fluxes.

Air-sea fluxes can be estimated either directly or from bulk parameterisation formulae using basic air-sea state variables.

3.2.1. Direct flux observations.

The direct estimation of air-sea fluxes requires dedicated field experiments (Taylor, 2000), and as a consequence has so far led to few estimates of large-scale flux fields. Rather, direct estimation is used to develop, calibrate and verify alternative estimation methods.

Direct flux estimates in the Mediterranean sea are scarce. During March-April 1998, a significant survey was carried out to measure fluxes in a restricted part of the Gulf of Lion (Hauser *et al.*, 2003). As part of the Project "Flux, Etat de la Mer, et Teledetection en Conditions de fetch[31] variable" – FETCH, the survey made comparisons between buoy and ship turbulent fluxes measurements using different approaches.

3.2.2. Parameterisation of fluxes.

Air-sea fluxes can also be estimated using empirical correlations between fluxes and sea- and air-state basic variables. These correlations are called bulk formulae and can be used to determine heat and momentum fluxes from their relationship with basic variables. The same formulae are applicable whether the basic variables have been measured *in situ*, using orbiting sensors or have been calculated by a numerical atmosphere model.

A key issue of this indirect approach is the validity of the parameterisations. The availability of different bulk formulae to estimate specific air-sea fluxes result in different estimations. Taylor (2000) discusses this discrepancy for the parameterisation of

[31] *http://dataserv.cetp.ipsl.fr/FETCH/HTML/INFO_DATA/VAGUES/FETCH_VAGUES.html (accessed on 01.11.04).*

turbulent heat fluxes and found clear differences in the standard deviations of the variability of the heat fluxes derived using a different traditional bulk formulae.

The parameterisation of the turbulent heat fluxes (i.e. the latent and sensible heat fluxes) is based on the relationship between basic meteorological variables such as 10 m wind speed, air and sea surface temperatures and humidity. Despite years of research, uncertainty still exists as to the behaviour of these bulk formulae at wind speeds exceeding 10 m s^{-1} (Taylor, 2000).

The coefficients used by bulk formulae include the drag coefficient value for the calculation of wind stress (Large and Pond, 1981, 1982; or Smith, 1980, 1988), and the Stanton and Dalton coefficients C_{H10m} and C_{E10m} for the calculation of the sensible and latent heat flux respectively. The right value for these coefficients is still debatable; for example, a constant Dalton number of 1.32 ± 0.07 was recommended on the basis of several turbulence-based datasets where the highest wind speed is 4 m s^{-1}. Smith (1989) suggests a constant "consensus" value (10^3 C_{E10m} = 1.2 ± 0.1) for winds between 4 and 14 m s^{-1}. The Humidity Exchange Over the Sea (HEXOS) experiment results (DeCosmo *et al.*, 1996) suggest a near constant value with (10^3 C_{E10m} = 1.12 ± 0.24) for winds up to 18 m s^{-1}.

Parameterisation formulae that are currently used to obtain the radiative heat fluxes are considered to be relatively crude, relying on the estimate of cloud cover to characterise the effects of cloud on the fluxes. Satellite based estimates use measurements of the top-of-the atmosphere radiation, and Radiative Transfer Models (RTMs) to estimate the surface value. Atmospheric models use simplified RTM schemes for computational efficiency. However, at present the limiting factor in most models is the representation of clouds and their radiative effects, where low level stratiform clouds are often poorly modelled (Taylor, 2000).

3.2.2.1. Improved parameterisation using new bulk formulae.

The limited accuracy of the parameterised fluxes becomes unacceptable for the study of the coupling behaviour of the ocean and atmosphere. Along with improved instruments and further experimental studies, new bulk formulae aimed at incorporating better physical descriptions of the transfer process have been developed.

These improved bulk formulae differ from the traditional approach in several ways. Typically, the momentum roughness length z_0, (the height at which the wind velocity extrapolates to zero on the logarithmic wind profile under neutral conditions), is obtained from a formula that takes sea state into account. The roughness lengths for temperature and humidity are in turn calculated from z_0 by considering the transfer of heat through the interfacial boundary layers. Generally, the flow over the ocean is smooth for a 10 m wind speed below about 2 m s^{-1} and fully rough above 8 m s^{-1}; between these limits there is a transition regime.

Liu *et al.* (1979) propose the "surface renewal theory" by including the interfacial sublayer at the air-sea interface. In this interfacial layer, of the order 1 mm thick, molecular diffusion plays a significant role in the transport. Across this interfacial layer, small eddies of air transfer heat randomly and intermittently between the "bulk" turbulent fluid and the surface itself which therefore warms or cools by conduction from the eddies. This model approach provides an improved method to account for physical conditions that are known to affect the air-sea exchanges by the inclusion of the effect of stability and interfacial conditions in bulk parameterisation.

The application of traditional bulk formulae has led to a much-improved space and time data coverage when compared to the much limited coverage provided by direct flux measurements. This is further

supported by the fact that the determination of basic variables is generally more accurate than the determination of the fluxes themselves.

3.2.2.2. Sources of basic geophysical variables for bulk formulae.

Main sources for *operational*[32] sea-state variables include (1) *in situ* measurements from buoys and ships, (2) from remote sensing, and (3) from numerical weather prediction.

(i) *In situ* operational measurements.

Operational *in situ* measurement of basic variables is done by Voluntary Observing Ships (VOS), ocean weather ships and buoys. The quality of these measurements has changed throughout the years as improvements have been made to the instrumentation. This is the case for the measurement of SST and wind (Folland and Parker, 1995).

VOS have offered routine meteorological and sea surface parameters for decades (CLIVAR, 1996). Sub-surface temperature profiles are obtained by means of expendable bathythermographs on board commercial vessels. However, the sampling limitations of ship data are obvious when compared with the flux coverage generated by Numerical Weather Prediction (NWP) models (White and da Silva, 1999). VOS measurements are ideal in generating climatological monthly means, which have been found to be well correlated with fluxes generated by NWP models over most of the global oceans.

For the purpose of operational ocean forecasting, such variables need to be supplied from the areas of interest in a quasi-real time, consistent mode. For this reason, buoy measurements become the only effective sources but their cost is prohibitively high for deployment in large numbers. Most buoy arrays are located near coasts such as the NDBC

and AES buoys off North America, and the ODBS off Japan (Taylor 2000). Although primarily established for weather forecasting and nowcasting purposes, these buoys have also been used for calibration of remotely sensed data from satellites, such as SST (Reynolds and Marisco, 1993), altimeter wind speeds and wave heights (Gower, 1996), scatterometer wind data (Geshelin and Dobson, 1997) and passive microwave winds (Wentz, 1997). Currently, there is no Mediterranean-wide operational buoy network, but one such localised network exists in the Aegean coastal areas. Moored buoys deployed near coasts are of limited value for ocean model initialisation because of the characteristically high SST gradients commonly found in such areas.

Operational buoy arrays have also been deployed in the open sea such as the Tropical Ocean-Global Atmosphere (TOGA) array (McPhaden *et al.,* 1998). However, global coverage of the oceans is still not feasible given the resources required (McPhaden *et al.,* 1998). "Flux buoys" which measure all the variables required to estimate the heat, momentum and radiative fluxes have recently been developed by the National Science Foundation as part of the World Ocean Circulation Experiment (WOCE) resulting in the improved IMET system (Weller and Taylor, 1998). Such buoys are more expensive than conventional ones, but the deployment of a good number of these buoys is being favourably considered by the GOOS programme[33].

Drifting buoys provide marine data away from shipping lanes and are used for adjusting the meteorological and oceanic satellite calibration. The accuracy of buoy data varies, but is usually better than ± 0.5 °C, and is significantly better than ship data (Reynolds, 1999).

(ii) Remotely sensed measurements.

---

[32] *That is instantaneous collection for model analyses, initialisation and model diagnostics/verification.*

[33] *http://www.gosic.org/goos/Ocean_climate_observations.htm (accessed on 01.11.04).*

Satellite remote sensing provides the most practical means to provide such datasets. Basic air-sea state variables are being made available by a number of orbiting satellites, including the:

- NOAA series of polar-orbiting satellites;
- The Defense Meteorological Satellite Program (DMSP);
- Geostationary meteorological satellites operated by NOAA (GOES), Japan (GMS) and Eumetsat's METEOSAT;
- The European Space Agency's ENVISAT;
- RADARSAT-2;
- TOPEX/POSEIDON;
- JASON-1;
- Coriolis/WindSat
- SAGE III/Meteor-3M satellite mission is a joint partnership between NASA and the Russian Aviation and Space Agency (RASA);
- ORBVIEW 2 / SEAWIFS;
- Nimbus-7, Earth Radiation Budget Instruments;
- TRMM, AQUA and TERRA satellites;
- Earth Radiation Budget Satellites, Earth Radiation budget experiment;
- Indian Research Satellites IRS;
- Sich-2/Okean-O oceanographic research satellite;
- The European Space Agency's past ERS-1 and ERS–2;
- The Japanese Advanced Earth Observing Systems, such as MOS 1/1b (1987-1996; still ongoing), and
- SeaWinds on ADEOS-2.

In general, each orbiting sensor has its own strengths and weaknesses regarding the volume sampled, frequency of measurement, the parameter measured, spatial coverage, instrument accuracy and external (non-meteorological) influences on the measurements. The most important criterion for flux determination is the required consistency of flux and/or meteorological basic variable data over time.

The following is a description of the remotely sensed geophysical variables that are relevant for the present study.

(i) Sea surface temperature.

Accurate global retrievals of SST from AVHRR have been available on an operational basis since 1981 (Reynolds, 1999). Walton *et al.* (1998) reviewed the accuracy of the various algorithms used to retrieve SST from AVHRR. Their results showed that the root mean square (RMS) accuracy, when compared to drifting buoys, has improved from 0.8 °C in 1989 to 0.5 °C in 1998 with a bias between —0.2°C to +0.4 °C. They also showed that the sensor calibration is susceptible to changes in atmospheric transmission effects due to changes in aerosol loading of volcanic and aeolian origin. However, the main source of error for the AVHRR is the instrument calibration accuracy, thus requiring continuous quality control assessment against drifting buoys.

A similar, but overall better performance infrared radiometer, is the Along Track Scanning Radiometer (ATSR). Barton *et al.* (1995) described the validation of the ATSR sensor on board research vessels, quoting an absolute accuracy of 0.1 °C, and the SST measurement as close to 0.2 °C in accuracy after correction for reflected sky radiation and surface emissivity. It has been suggested that the ATSR may be used both as a source of SST data and as a source of calibration data for the wider swath AVHRR instrument. ATSR has improved sensor stability and built-in calibration systems, but is also prone to interference coming from cloudy pixels. Another limitation is its 500 km wide swath.

It has long been recognised that passive microwave radiometry offers a solution to the above-mentioned cloud and aerosol contamination problems. This is because at frequencies below 12 GHz, the surface electromagnetic radiation is proportional to the SST and since microwaves can penetrate clouds with little attenuation, a clear view of the sea surface under all weather condition except rain can be obtained.

Remotely sensed SST using passive microwave radiometry is also made available by orbiting satellites such as the TRMM spacecraft. It carries the TMI sensor that has a full suite of microwave channels ranging from 10.7 GHz to 85 GHz, with a swath width of 760 km, and pixel resolution ranging from 6 to 50 km. TMI is the first in a series of satellite microwave radiometers that measures SST under nearly all weather conditions. Wentz *et al.* (2000) describe the accuracy of the TMI-retrieved SST, showing an RMS difference between the daily averaged buoy and satellite SSTs ranging from 0.5 to 0.7 ^{o}C. The presence of precipitation and high wind speeds negatively affect the accuracy of passive microwave radiometry and becomes inadequate under such situations.

(ii) Humidity.

Various kinds of satellite observations are providing information about moisture fields like clouds, precipitation and water vapour. One of the most widely used rainfall estimation techniques is the GOES Precipitation Index based on the work of Richards and Arkin (1981). This estimate has the advantage of having a high horizontal resolution of about 8 km in mid-latitudes with a temporal resolution of about 30 minutes.

Humidity data from the Special Sensor Microwave Imager (SSM/I) have a spatial resolution ranging from 12.5 to 25 km and temporal resolution of twice a day. Their combination with the visible and infrared database retrieved by Geostationary Operational Environmental Satellite (GOES) provides a better representation of hydrometeorological variables (Manobianco *et al.,* 1994). Wentz and Spencer (1998) propose an efficient method for the physical retrieval of precipitation rates from SSM/I, described as a unified ocean parameter retrieval algorithm that also diagnoses total integrated water vapour, cloud water and wind

speed. The RMS difference between the SSM/I water vapour retrieval and radiosondes is about 5 mm for rain rates from 1 to 15 mm h^{-1}.

Jones *et al.* (1999) used a neural network algorithm to obtain monthly averages of humidity. Input to this algorithm were the integrated precipitable water vapour and SST extracted from the Surface Marine data provided by da Silva *et al.* (1994a-e) and the monthly averages of SSM/I brightness temperatures on a 1° by 1° grid. The global RMS error stated was 0.77 g kg^{-1} with smaller errors in the North Atlantic and in the North Pacific (0.6 g kg^{-1}) and larger errors in the southern Indian, Pacific and Atlantic Oceans (1.2 g kg^{-1}) reflecting the small observation density in the da Silva dataset for these regions. Comparison of these methods to independent *in situ* measurements is however needed to evaluate this method more carefully.

(iii) Marine winds.

Satellite instruments capable of measuring wind speed and direction include scatterometers, altimeters and passive microwave radiometers.

Wind vector estimates from scatterometers are based on empirical relationships relating back-scattered energy to wind speed at 10m under neutral conditions. Scatterometer data are now available from numerous sources, each using different model functions. The accuracy of scatterometery is relatively excellent compared to errors for winds from VOS. Validation of the European Remote Sensing Satellite (ERS) scatterometer wind retrievals for example, shows a systematic underestimation of nearly 0.75 m s^{-1} and an RMS error of around 1.3 m s^{-1} (Graber *et al.*, 1996).

The Wentz (1997) all weather algorithm is a physical approach to retrieve wind speed from passive microwave sensors measurements in rain free situations, with an error of 0.5 m s^{-1} against collocated *in situ* data.

(iv) Surface air temperature.

Currently, there are no means to estimate the surface air temperature from satellite measurements, but indirect methods have been developed. A very simple method is to assume slightly unstable conditions at any location at any time and set $T_a=T_s-1$, where T_a is the surface air temperature and T_s is the SST (Schulz *et al.*, 1997). The results of Wells and King-Hele (1990) show that most of the observed air-sea temperature differences in the tropical oceans are of the order of 1°C. However, if instead of the assumed unstable conditions, stable conditions occur, the error in surface air temperature estimation could lead to an underestimation of the exchange coefficient for latent heat flux (using bulk parameterisation) by around 50% (Schulz *et al.*, 1997). Another simple method is to compute T_a from the retrieved air specific humidity assuming a constant relative humidity of around 80% (Liu, 1988) or using a climatological relative humidity. However, this might be too rough an estimate to derive the sensible heat flux using bulk parameterisation.

Alternatively, surface air temperature can be measured using the empirical relationship between the total precipitable water obtained from SSMI/I measurements, the near-surface humidity (Liu, 1986), and AVHRR multi-channel SST. Using this approach, the estimated root mean square error of satellite-derived air temperature is around 0.53 to 0.56 °C when compared to TOGA TAO buoys (Jones *et al.*, 2003).

Jones *et al.* (1999) described a method to derive monthly means of T_a from SSM/I measurements of total precipitable water and SST analysis from NCEP using neural network techniques. The network was trained with data extracted from the Surface Marine Data provided by da Silva *et al.* (1994a-e).

(v) Longwave radiation.

Global measurements of the outgoing longwave radiation (olwr) at the top of the atmosphere is one of the longest series of data retrieved by the 10-12 μm infrared channels onboard the NOAA operational satellites (Ohring *et al.,* 1984). However, this dataset has not been widely accepted because its estimation is based on theoretical calculations rather than direct measurements. It has been noted that this estimation technique is prone to systematic errors of the order of 20 W m^{-2} or larger in geographical regions characterised by stable temperature and moisture profiles over extended time periods (Ellingson *et al.*, 1989a; Gruber *et al.,* 1994). Oh (1998) attributes this inaccuracy to the geographically restricted air temperature profile on which the algorithm has been trained and tuned, and as a consequence systematically displays low values in subtropical high-pressure regions (such as the Mediterranean basin), and high values over daytime desert regions. Ellingson *et al.* (1989b) proposes an olwr estimation technique based on radiance measurements from the High Resolution Infrared Sounder (HIRS). This technique gives much smaller RMS errors when compared to the AVHRR technique, presumably because it uses more spectral information than the AVHRR.

(vi) Salinity.

Observation of ocean salinity from space has been identified as a high priority for the Global Ocean Data Assimilation Experiment (GODAE) requirements. Despite its importance, such observations are not yet in operation (Taylor, 2000). Yueh *et al.* (2001) describe how microwave remote sensing can be used to derive global maps of surface salinity with acceptable precision, but which still represents a challenge to be implemented.

An interesting mission is the European Space Agency's Soil Moisture and Ocean Salinity (SMOS) mission, scheduled for launch in early

2006. SMOS will be able to observe ocean salinity with an accuracy of 0.1 psu every 10 days at 200 km spatial resolution (Berger *et al.,* 2002). AQUARIUS is another mission that is being developed by NASA which focuses on the provision of global sea surface salinity maps to resolve missing physical processes that link the water cycle, the climate, and the ocean.

3.2.3. Climatological datasets.

The most extensive historical compendium of basic variables and related fluxes is the Comprehensive Ocean-Atmosphere Data Set (COADS) which, besides having individual observations, also contains monthly summaries (Woodruff *et al.,* 1998). This dataset[34] also includes sets of COADS-derived fluxes (da Silva *et al.,* 1994a-e).

Another useful climatological reference is the Southampton Oceanography Centre surface flux climatology directory (Version 1.1), which contains climatological monthly mean values of air-sea fluxes on a global grid in netCDF format. The fields have been derived from the COADS1a (1980-93) dataset enhanced with additional metadata from the WMO47 list of ships (WMO, 1993).

The Global Precipitation Climatology Project (Huffman *et al.,* 1997) offers global maps of long-term mean values of flux data collected by *in situ* and satellite observations. Output from numerical weather models has also been merged with the data as part of data assimilation processes.

Another climatological database, with a resolution of 2.5° by 2.5° in latitude and longitude, covering a 17-year period from 1979 to 1995 is the CPC Merged Analysis of Precipitation (Xie and Arkin, 1997). This database consists of monthly precipitation in addition to a variety of satellite sensor measurements, gauge observations and model

[34] *http://www.cdc.noaa.gov/coads/coads1a.html (accessed on 01.11.04).*

reanalysis conducted by National Centers for Environmental Prediction (NCEP) in collaboration with the National Center for Atmospheric Research (NCAR).

3.2.4. Modelled NWP datasets.

Three major weather and climate centers are involved in producing atmospheric reanalysis on the global scale. These are the Goddard Space Flight Center (GSFC), the Data Assimilation Office (DAO), NCEP in collaboration with NCAR and the European Center for Medium Range Weather Forecasts (ECMWF).

NWP models serve users interested in many different phenomena and different forecast lengths. In operational ocean forecasting, the interest lies in making available continuous, fine spatio-temporal, short- and medium-range forecasts of near surface parameters and fluxes that can be used as both initial and driving fields for ocean forecasting models (Taylor, 2000).

The most recent atmospheric models are now very comprehensive and contain sophisticated physical parameterisations to predict a large number of processes in the atmosphere, such as the exchange of radiation at the Earth's surface (Pan, 1999), and air-sea energy fluxes. In addition, they also include advanced data assimilation schemes used to provide an optimal initial atmospheric state on the basis of previous forecasts and real-time (*in situ* and satellite sensor) observations. It has been claimed that when coupled to data assimilation schemes, numerical weather prediction models can provide realistic forecasts of the air-sea fluxes with an unprecedented temporal and spatial coverage of the entire global ocean surface (Atlas *et al.*, 1996).

There are many advantages when using these numerical atmospheric models to determine air-sea fluxes, the major one being their improved schemes to calculate the transfer coefficients during the estimation of

the surface fluxes. Their surface parameterisation schemes have been modelled on the current knowledge of the characteristics of the lowest layer of air near the sea surface. The high vertical resolution offered by these atmospheric models, for example, permit the application of the Liu *et al.* (1979) surface renewal model based. Unlike bulk formulae with constant transfer coefficients, these models are able to include the effects of stability and interfacial conditions that are applicable in approximately stationary and horizontally homogeneous moderate wind speeds.

3.2.4.1. NCEP's Eta model.

The Eta model is an operational limited area model with a variety of unique features in its numerical formulation. One such feature is the viscous sublayer model (Janjic, 1994) that is able to sufficiently resolve and improve on the transfer coefficients for the estimation of air-sea fluxes. Other unique features include its algebraic conservation of energy in transformations between the kinetic and potential energy in both space and time differencing (Mesinger, 1984, Janjic *et al.,* 1995), and numerical treatment of lateral boundary conditions (Mesinger, 1977). Special features of the model's comprehensive physical package include its modified Betts-Miller convection scheme (Janjic, 1994) and Fritsch-Kain scheme (Mesinger *et al.,* 2002); its Mellor-Yamada level 2.5 turbulence closure (Janjic, 1996a) and its prognostic cloud water/ice scheme (Zhao and Carr, 1997).

The Eta atmosphere model was originally designed using primitive equations based on the hydrostatic approximation. It was used in an operational way in June 1993 as the short-range North American forecast model at the NCEP (then known as the National Meteorological Center). The decision to use this model was based upon extensive experimental evidence obtained for validation during the initial stages of development (Mesinger *et al.,* 1988). At that time, the horizontal grid spacing was 80 km and it had 17 layers in the vertical. The model has

been implemented in three geographical regions: North America, Europe and the tropical regions of Australia. In 2000, a new non-hydrostatic Eta version was released for the NWP community (Mesinger, 2002). Consequently, the model can now be applied for high resolution, small-scale atmospheric prediction of around 1 km or even less.

Substantial testing, tuning and further development of the model has been carried out by NCEP. The model has also been implemented in the tropics, over Europe and the Mediterranean basin, as well as in many other geographical areas all over the world using varying resolutions and integration domain sizes. An interesting feature of the model is that little re-tuning is needed when horizontal resolution is changed. Table 3.1. shows the application of the Eta model by some Mediterranean research and weather forecasting agencies. One successful application in this region is its use as part of an oil spill early warning system in the Mediterranean (RAMSES project) with a 4 km grid spacing[35].

A review of the results of numerical experiments (Black and Janjic, 1988; Mesinger *et al.,* 1988; Mesinger and Black, 1989; Black and Mesinger, 1989; Lazic and Telenta, 1988; Lazic, 1990) suggests that the Eta model is competitive with other sophisticated regional models using similar resolutions, and requiring about the same computational effort. Moreover, these experiments document the ability of this model to improve predictions when the grid resolution is increased. At the same time, the flexibility of the parameterisations allow further tuning and refinements. The Eta model was tested by Papadopoulos *et al.* (1997) to assess the surface and radiation parameterisation schemes for different model grid resolutions, which was found to be dependent on high resolution permanent and semi-permanent datasets. A major improvement was the revised Betts-Miller scheme over the oceans and a new flexible viscous sublayer scheme, in addition to improving the Mellor-Yamada level 2 and level 2.5. (Janjic, 1994). Recent updates include the revised land-surface physics and updated cloud package (in

[35] *http://ramses.esrin.esa.it/ (accessed on 01.11.04).*

2002) and the inclusion and updating of the Kain-Fritsch scheme (in 2003).

Programmes/ Agencies	NWP model	Domain size	Sources
SKIRON	Eta NCEP, MM5	Mediterranean and a nested model	University of Athens http://forecast.uoa.gr/
RAMSES	Eta NCEP	Mediterranean and nested models over small areas	ICoD; ESA/ESRIN; SPOT Image http://ramses.esrin.esa.it
CYCOFOS	Eta NCEP	Mediterranean and a nested model	Oceanography Center, DFMR, Nicosia, Cyprus http://www.ucy.ac.cy/cyocean/New/index.php
DREAM	Eta NCEP	Mediterranean and nested models over small areas	ICOD http://www.icod.org.mt/modeling/index.htm
REAL TIME WEATHER PREDICTION SYSTEM, TEL AVIV UNIVERSITY	Eta NCEP	Mediterranean	Tel Aviv University http://earth.nasa.proj.ac.il/dust/current/dust.html

Table 3.1. Application of the Eta model by Mediterranean research and weather forecasting agencies.

Additional packages that are applicable to the air-sea surface fluxes include the Geophysical Fluid Dynamics Laboratory (GFDL) radiation scheme that simulates the radiative atmospheric effects, which include interactive random overlap cloud effects. This scheme is relatively efficient because it uses extensively, pre-calculated values of various parameters (look-up tables) with no effect on accuracy. The model contains the entire column of climatological and seasonally varying ozone and CO_2 along with the appropriate absorption coefficients. This is being currently updated by a real-time ozone reanalysis derived from NCEP (Nickovic 2000, *personal communication*). Recent changes were also made to the scheme reflecting a more precise estimation for the total energy entering the atmosphere in order to simulate the aerosol effects.

Studied phenomena produced by the Eta model (Pielke, 2001) include the forecasting performance of quantitative precipitation, moisture transport impacts and basin/sub-basin budgets, land surface phenomena, in particular vegetation and soil moisture/water transport impacts, the effect of topography on the choice of the vertical coordinate, tropical cyclones and other studies. However, no studies have addressed the accuracy of its modelled air-sea fluxes (Mesinger, 2002 *personal communication*).

3.3. Technical approaches in operational ocean forecasting.

3.3.1. Coupling of atmosphere and ocean models.

Forcing an ocean model with climatological air-sea flux estimates often results in an unrealistic prediction of ocean surface fields, such as the SST. For example, the attempt of Rosati and Miyakoda (1988) to drive an upper ocean global model with specified climatological wind-stress and heat flux showed that the predicted SST could be significantly different from the climatological SST used in the calculation of the flux. In their analysis, they question the utility of such climatological forcing. In addition, the absence of any interaction between their ocean model and the atmosphere also accounted for the drift of the model SST.

A solution to minimise these errors lies in coupling ocean and atmosphere models together. This necessitates the use of forecasting atmosphere models that generate oceanic surface fluxes to drive the ocean model underneath. This setup is termed as "one-way atmosphere-ocean coupling" and can be further elaborated by using the oceanic model's parameterisation schemes to adjust some of the driving forces that have been generated by the atmosphere model. This is termed "two-way atmosphere-ocean coupling" or "full coupling".

A surface flux-type thermal boundary condition allowing for a one-way coupling of an ocean model to a prescribed atmosphere was first proposed by Haney (1971). However, in spite of 30 years research, it is only recently that some progress has been made in this field. Barnier *et al.* (1996) still express the need to understand the dynamics that drive the general circulation of the ocean by investigating the response of ocean models under the action of a prescribed atmosphere. Holland and Bryan (1994) for example, emphasised the difficulty of parameterising oceanic fluxes and in turn adjusting the resulting heat flux through evaporation.

Recently, the European Union has funded project DEMETER for ECMWF to introduce global coupled ocean-atmosphere models[36]. The coupling has had a beneficial impact on the Center's short and medium range forecasts and development is still ongoing[37].

An excellent example of a one-way coupled system is the Regional Ocean Forecasting System (ROFS, Ver. 3.6)[38]. This system is based on a hydrodynamic ocean circulation model developed jointly by the National Weather Service's Environmental Modelling Center, the National Ocean Service's Coast Survey Development Lab, Princeton University and the US Navy. This three-dimensional model produces 24-hour simulation of temperature, salinity, surface elevation and current for a region off the East Coast of the United States. The model is driven at the ocean surface boundary by heat, moisture and momentum fluxes provided by NCEP's Eta atmospheric forecast model. The ocean model is driven along its open boundaries by climatological estimates of temperature, salinity and transport. The spatial resolution of the model varies from approximately 20 km offshore to about 10 km inshore.

---

[36] *http://www.ecmwf.int/research/demeter/general/index.html (accessed on 01.11.04).*
[37] *http://www.ecmwf.int/about/special_projects/bengtsson_ocean-atmosph-num.expt/(accessed on 01.11.04).*
[38] *http://polar.wwb.noaa.gov/cofs/Description.html (accessed on 01.11.04).*

3.3.2. Development of local area, high resolution coupled model systems.

The continuous progress in computer science and technology is strongly reducing the computational burden of coupled model systems (Warner and Seaman, 1990). The way forward was demonstrated during 1991 by the European Center for Medium Range Weather Forecasts (ECMWF), when it improved its nominal 1.125° by 1.125° horizontal resolution model over 19 pressure levels of 1987 to the 60 km resolution over 31 levels. This improvement allowed a much better representation of orographic and related processes during model simulation.

Small-scale forecasting systems working with grid spacing as small as 5 km horizontal resolution are much dependent on initial information at mesoscale level as to maintain both a high forecasting skill and to allow the boundary layer to evolve more realistically. However, the limited availability of atmospheric data, necessary to initialise and update the atmospheric component of the forecasting system, seems to remain the main obstacle that prevents an increase in the grid resolution in operational models. Recently, measures have been taken in this direction to start implementing Local Area Models (LAMs). These models are usually nested inside regional or global forecasting models that provide the initial and the predicted boundary conditions for their nested LAMs (Buzzi *et al.*, 1994; Paccagnella *et al.*, 1994).

The existence of a global and of at least one regional, or "limited-area" forecasting system is now a current feature in all operational weather and oceanic research centers. Yet, the purpose of using a LAM output can be radically different (Mesinger *et al.*, 2002). For example, LAMs can serve both to keep contamination at the lateral boundaries as far away from the region of interest as possible (Laprise *et al.*, 2000); and to improve prediction of large-scale motion (Mesinger *et al.*, 2002).

3.3.3. Temporal and spatial resolution of ocean variability.

An ocean model with the necessary spatio-temporal resolution can help oceanographers understand this spectrum of variability. However, the space/time spectra of ocean variability are, in general, poorly known at present. The oceanic response to the short temporal atmospheric variability for example, is not well documented, but it is common knowledge that the diurnal cycle and several-day variability associated with synoptic weather systems are considered to be the major sources of short time scale variability in the upper ocean (Schott and Leaman, 1991).

Basin-scale SST variability, for example, very much depends on the scale at which it is observed and/or forecasted (Price *et al.*, 1986). It may have spatial scales set by the atmosphere alone or by a combination of atmospheric and oceanic processes. Vertical advection, can also give rise to small-scale variability with longer persistence times than the variability associated with similar scales in the atmosphere.

The vertical resolution can also pose problems in the model's representation of the boundary layer. Since the model treats the fluid within each layer as a homogeneous parcel, the degree of resolution determines the effect which physical processes may have on the model parameterisations and ultimately on the final representation of the boundary layer. In general, the greater the number of layers defining the boundary layer, the closer to reality the representation is likely to be.

To date, there are remarkably few published studies on the influence of varying the resolution of ocean models on the accuracy of predicted fields (McWilliams, 1998). Studies show that a horizontal grid spacing of more than 50 km is enough for the simulation of water mass distribution, but a resolution of up to at least 10 km becomes mandatory to simulate mesoscale eddies and intense, narrow currents

credibly (i.e. with qualitative similarity to observations). Recently, the US Naval Research Laboratory has embarked on a project to provide accurate, very high resolution, 4-dimensional descriptions of the coastal ocean environment at horizontal resolutions of 10 m to 1 km, vertical resolutions of around 1 m, and temporal scales of hours to days[39].

At present, eddy-resolving ocean models can only be used for intervals as long as decades and domains as large as basins, whereas coarse-resolution models are suitable for centennial and millennial fluctuations and the approach to equilibrium in global domains. Although growing computer power will narrow this division, it will take at least a decade, and perhaps much longer, before eddy-resolving models will have a greater role in large-area ocean forecasting (McWilliams, 1998).

Again, a major drawback in the use of small-scale ocean models is the lack of high frequency spatial and temporal observations needed to verify predicted features at even up to 4 times a day. Such a frequency of observations is only obtained from a restricted number of locations around the globe. This is certainly not the case for the Mediterranean area.

3.3.4. Approaches in model verification.

Forecast verification is an essential component of any ocean forecasting system, since it is the process by which the degree of correspondence between forecasts and observations is assessed (Murphy and Daan, 1985). It establishes the credibility of forecasting systems, which in turn is increasingly required in an era when programme benefits must be demonstrated. Brown *et al.* (2002) argued that the science of verification is undergoing major changes and development, as standard methods have been found not to meet the needs associated with high-resolution gridded forecasts.

[39] *http://www7320.nrlssc.navy.mil/html/vhr4d/ (accessed on 01.11.04).*

In practice, traditional forecast verification has generally consisted of (i) calculating quantitative measures of one or two aspects of forecasting performance such as bias, accuracy or skill and (ii) drawing conclusions regarding absolute and/or relative performance on the basis of numerical values of these measures (Murphy, 1997).

The main element that defines which forecast fields or specific numerical schemes can be verified rests on the availability and type of collocated observations. The availability of raster-based remotely sensed observations partly satisfies this criterion, making comparisons of data sets of particular geophysical parameters relatively easy (Murphy and Winkler, 1987).

The evaluation of model accuracy has traditionally been subjective, with the forecaster using the experience to develop opinions about the model's accuracy. This can be done via simple visual comparisons of graphical plots representing the model output and observations. However, these comparisons can be misleading since they often contain personal biases and impressions, and as models become more complex and change more frequently, a more objective means of evaluating model performance is required. As a result, model accuracy assessment tools have evolved to provide an objective measure of model skill that can be used by forecasters. The end product is an objective summary of model accuracy and/or related errors that include both systematic and random ones.

The objective assessment of model accuracy is always constrained by the limited representation of the model forecasts in relation to the corresponding atmospheric and oceanic truth. Specifically, model forecasts represent both fluids as a discrete array of area-averaged values as opposed to the continuous fields found in the real world, which in turn are weakly represented by satellite sensors and/or *in situ* observations or analyses. No matter how sophisticated these

observations and forecasts become, they will never represent the true fields perfectly.

3.3.4.1. Statistical measures and model assessment tools.

Different statistical measures can be used in model verification by assessing the degree of fit between the model output and empirical data, the most common ones being the root mean square error, the mean absolute error and standard deviation (Alvera-Azcarate *et al.*, 2004). Additional statistical measures are used by weather forecasters to assess the spatial accuracy of their forecasts, including threat score, equitable threat score, correlation and anomaly correlation (Glahn *et al.*, 1991). These measures are devised to assess the spatial occurrence of precipitation against observations derived from rain gauge stations.

Graphical tools are used to assist forecasters to plot, visualise, analyse and interpret forecasted data. These tools consist of computer software ranging from freeware distributions based on UNIX/LINUX environments, such as the Graphical Display Analysis Systems[40] to well-established commercial GIS products. As Tufte (1983) points out, graphics gather their power from content and interpretation beyond the immediate display of numbers. Data plotting can work as an error detection method by amplifying deviations from an expected pattern. However, references to the use of GIS display and analysis in the field of oceanic forecasting are almost non-existent.

3.3.4.2. Exploratory spatial data analysis.

The above-mentioned statistical measures are limited in their ability to assess spatial similarity between forecasts and observations in an objective way. This is because common descriptive statistics and histograms are unable to capture spatial relationships and tend to

[40] *http://grads.iges.org/grads/head.html#SOFT (accessed on 01.11.04).*

simplify forecasts that have a large amount of spatial detail that needs verification.

According to Brown *et al.* (2002), high-resolution models need to be given a proper evaluation that measures their operational capabilities. It may be necessary to rely more on diagnostic measures such as entity-based techniques, pattern recognition and other scientific techniques, which are more appropriate for finer scales. The latest approaches in exploratory spatial data analysis and GIS analysis can be an extremely useful to assess the temporal and spatial accuracy of model forecasting systems. Understanding the variation of spatial scales as an index of forecasting performance presents a challenging and unexplored field in ocean forecasting. More specifically, the use of Exploratory Spatial Data Analysis (ESDA) can describe and visualise spatial distributions, identify atypical locations (spatial outliers), discover patterns of spatial association (spatial clusters), entity classification using pattern matching (Brown *et al.,* 2002) to evaluate the displacement between forecast and observed entities and to decompose the error into various components (e.g., displacement, pattern, volume); and suggest different spatial regimes and other forms of spatial instability (Anselin, 1999) in the output fields of atmosphere and ocean models. The bottom-line approach to be mimicked *objectively* is visual verification, which is able to consider all of the attributes of interest, but unfortunately is labour intensive and subjective. These new methods (e.g., event- or object-based approaches) can provide a more complete picture of forecast performance.

Techniques that can evaluate the spatial similarity between forecasts and collocated observations can be a very useful for the forecast verification. Holt *et al.* (1998) define spatial similarity as "*the spatial matching and ranking according to a specific context and scale*". It is governed by context (function, use, goal), scale (coarse or fine level), repository (the application, local domain, site and data specific), techniques (the available technology for searching, retrieving and

recognising data) and measure and ranking systems. Here, the degree of match is the score between the forecast (source) and the observation (target), where both can be a pixel, region or coverage. The principles that govern spatial similarity are not just the attributes but also the relationships between two phenomena. By further developing and applying the much-needed tool of spatial similarity in oceanic forecasting, this approach can serve as an organising and exploratory tool. Here, spatial phenomena are classified and clustered, relationships identified and generalisations made from previous experiences or knowledge.

3.3.4.2. Geostatistics.

Apart from map drawing/overlaying and doing statistical and GIS operations on the spatial information, ESDA requires a third component: statistical analysis to compute spatial models. Spatial modelling of observations (often in the form of raster information), and the continuous, and highly resolved model output fields can be done using variogram modelling. Since Curran (1988) introduced the application of geostatistics techniques in a remote sensing context, the variogram is now widely adopted for modelling the spatial variation for remote sensing applications, such as soil mapping (Dubayah *et al.*, 1997), biomass estimation (Atkinson and Curran, 1995), and landscape pattern (Turner *et al.*, 1991). According to Treitz (2001), variogram analysis offers the advantage of relating some key descriptors to the spatial characteristics of the maps or their residuals. Understanding the spatial characteristic of maps or residuals constitutes the first step in a geostatistical study, which is usually followed by structural analysis (determining the spatial correlation or continuity of the data) and interpolation (kriging or simulations to predict values at unsampled locations). For the purpose of model verification, empirical studies of the semi-variogram plots of residuals is often sufficient to analyse the variability between forecasts and observations. The shape of a semi-variogram, for example, may be fitted with a model, of which the range

and sill are two parameters that describe the spatial variation. The range generally indicates the extent to which values sampled from spatial process are similar. The height of sill relates to the spatial variability of images. Variography is another method used to analyse spatial variability by improving the visibility of spatial structures on variograms of both raw and transformed data.

Exploratory spatial data analysis is still an unexplored branch of applied statistics for the ocean forecasting community. This is clearly the case for the Mediterranean Forecasting System (MFS) where the impact of data assimilation techniques and the use of real-time observations is being assessed using standard verification measures common to the NWP community. These measures include short-term prediction misfit (SPM), RMS difference from the reference runs as a function of time and from verification data sets. Model errors will be tackled using an Ensemble Kalman Filter[41].

3.4. State of ocean forecasting in the Mediterranean.

Over the past few decades, the Mediterranean basin has been identified as a suitable test area for the understanding of processes associated with the ocean general circulation. A review of the relevance of the Mediterranean physical oceanography in a global context is given by the Physical Oceanography of the Eastern Mediterranean (POEM) Group (POEM, 1992). These studies have shown that the circulation of the Mediterranean is composed of many subbasin-scale features which may be relatively permanent, recurrent, or intermittent (Robinson *et al.*, 1991; Millot, 1991). The formation mechanisms for these features are complex and can generally be assigned to surface wind stress, surface thermohaline fluxes and accompanying water mass formations, inflow/outflow through the Strait of Gibraltar, and bathymetric control. The surface wind stress is also subject to orographic control and is

[41] *http://www.cineca.it/mfspp/workpackages/des_wp4.html (accessed on 01.11.04).*

strongly modified near the coasts, in straits and near the higher and larger islands. Korres *et al.* (1997) observed that intense atmospheric variability over the Mediterranean at seasonal and interannual time scales makes the heat and momentum budget at the air-sea interface strongly interannual.

3.4.1. Type of ocean forecasting models.

A good number of general circulation ocean models have been used to study and simulate the circulation of the Mediterranean Sea. Out of these, the two most popular and widely used models are the Mediterranean Modular Ocean Model and the Princeton Ocean Model.

3.4.1.1. The Geophysical Fluid Dynamics Laboratory - Modular Ocean Model (GFDL-MOM).

The GFDL-MOM was developed by Pacanowski *et al.* (1990). It is a three-dimension primitive equation model that has been used extensively by Korres *et al.* (1997) to simulate oceanic circulation in the Mediterranean using a 9-year NCEP monthly mean atmospheric analysis fields to drive the model for a hindcast period between 1980-1988. Detailed analysis of various experiments performed can be found in Pinardi *et al.* (1997).

Pinardi *et al.* (1997) used a basic formulation of the GFDL-MOM with a 0.25^{o} by 0.25^{o} horizontal resolution and 31 levels in the vertical dimension. The model dynamics were nudged against climatological datasets of temperature and salinity. The driving surface forces for the ocean model were monthly mean atmospheric parameters, retrieved from NCEP analyses and monthly mean cloud cover from COADS. The model was initialised with additional climatological data coming from the comprehensive historical data set (Brasseur *et al.*, 1996) collected for the Mediterranean and integrated over an 11-year period.

Raicich (2004) also used MOM with a higher, 0.125° by 0.125° horizontal grid spacing and 31 vertical levels and forced by ECMWF 6-hr operational analysis to simulate temperature and salinity variability in the Mediterranean Sea.

3.4.1.2. The Princeton Ocean Model (POM).

This model was developed in the late 1970's by Blumberg and Mellor, while several subsequent contributions were made by others. The model has been applied to several coastal (Orlic *et al.*, 2004) and estuarine regions as well as to open oceans, and sometimes used with an embedded ecosystem model structure embedded within the ocean model (Chai *et al.*, 1999).

POM is a three-dimensional hydrodynamic, primitive equation ocean model, which includes a turbulence sub-model. It uses curvilinear coordinates in the horizontal dimension, while in the vertical dimension a terrain following σ-coordinate system is used. Parallel to the integration of the 3-D equations, a set of depth integrated 2-D equations are solved in order to calculate the free surface variations. Temperature, salinity, velocity and surface elevation are the prognostic variables. The horizontal diffusion terms are evaluated using the Smagorinsky (1963) horizontal diffusion formulation. The vertical mixing that this submodel parameterises allows for the formation of a fairly realistic, seasonally varying, mixed layer and can, in principle, model the formation of relatively saline intermediate water by the thermohaline fluxes[42].

Working at fine model domains, POM is able to reproduce eddy dynamics that play a major role on the circulation field especially in the synoptic time scale. The prognostic variables are the sea level elevation, the three components of velocity, temperature and salinity, turbulent kinetic energy and turbulence macroscale. The last two parameters are

part of the turbulence closure scheme that provides realistic parameterisation of vertical mixing (Mellor and Yamada, 1982).

Zavatarelli and Mellor (1995), Horton *et al.* (1997), Drakopolous and Lascaratos (1997), Brenner and Rosentraub (2004) are among those who have used POM to understand the Mediterranean Sea general circulation and its sub-basins. Zavatarelli and Pinardi (1995) used POM to simulate the ocean circulation in the Adriatic Sea, while Lascaratos and Nittis (1998) and Brenner and Rosentraub (2004) concentrated on simulating the circulation of the Levantine Sea, Aegean and part of the Ionian basins. The latter's computational grid had a horizontal grid spacing of around 5 km and covered the entire area of Levantine Sea. Surface forcing consisted of monthly mean climatological wind stress, atmospheric pressure and heat fluxes based on the 15-year ECMWF reanalysis. Lateral boundary conditions at the open boundaries were specified from the eighth year of a climatological simulation with the MFSPP full Mediterranean model.

The POM model is now an integral part of the forecasting systems of the RAMSES, COMPASS[43], CYCOFOS and POSEIDON. Its integration grid spacing ranges from 0.25° by 0.25° to 0.02° by 0.02° in the horizontal dimension. The model is being currently combined with biological models in the Gulf of Trieste (Adriatic Sea) as part of the MFS initiative[44].

3.4.2. Operational ocean forecasting systems.

In the Mediterranean, a small number of research and development centers perform one-way forcing of ocean models to produce and disseminate daily ocean forecasts. Operational programmes such as SKIRON/POSEIDON of the Marine Research Center of Greece and the COMPASS of the Euro-Mediterranean Centre on Insular Coastal

---

[42] *Detailed technical information on POM is available at http://www.aos.princeton.edu/WWWPUBLIC/htdocs.pom (accessed on 01.11.04).*
[43] *http://www.icod.org.mt/modeling/index.htm (accessed on 01.11.04).*

Dynamics each have a one-way coupled, atmosphere-ocean modelling system configured to provide high-resolution air-sea surface flux forecasts over predefined regions in the Mediterranean basin. In order to achieve the best possible temporal resolution in the area of interest, the systems usually apply two different forcing model configurations. The first simulation is performed by a regional atmosphere model run at coarse horizontal resolution (such as 0.25° by 0.25°) and using boundary conditions from a global model (Nittis *et al.*, 2001). Its better-resolved "regional" forecast is then used to provide the initial and boundary conditions for the finer nested atmosphere model (such as 0.10° by 0.10° in horizontal resolution) situated well within the regional integration domain.

The operational ocean forecasting provided by RAMSES incorporates an operational forecasting oil slick forecasting system based on COMPASS' one-way coupled regional (0.25° by 0.25° grid) and nested (0.042° by 0.042° grid) atmosphere-ocean model system that provide 5-day, high resolution meteorological and marine forecasts of predefined areas to predict the movement of potential oil slicks. The RAMSES consortium partners involved are ESA/ESRIN, SPOT Image and ICoD.

The Mediterranean Forecasting System (MFS) is also currently providing, on an operational basis, weekly forecasts of surface currents, sea surface temperature and salinity[45].

Ongoing development of the operational ocean forecasting at ICoD (through Project COMPASS) include the improvement of its atmospheric model by using (1) input data containing ozone fields up to 10 kPa, (2) new cloud physics scheme, (3) the full coupling of an aerosol atmosphere model as to better resolve attenuation of radiation due to aerosols, and (4) full two-way coupling with ocean model (Nickovic, *personal communication, 2002*).

[44] *http://www.bo.ingv.it/adricosm/bullettin.html (accessed on 01.11.04).*

Products tailored for ocean forecasters can also be obtained from major European weather agencies such as MeteoFrance[46] and ECMWF. However, their forecasting system can be considered as a "closed" system, which delivers products according to defined, customer-oriented requirements.

3.5. Challenges in ocean forecasting in the Mediterranean.

3.5.1. Major technological and information gaps.

One of the main challenges in the region is the provision of useful operational forecasts addressing socio-economic and environmental needs[47]. In this respect, one of the main tasks of EuroGOOS is to speed up the process of validating forecasting models and to transfer them to operational agencies. Once there, efforts are needed to engineer the modelling procedures into a robust, operational form that can cope with the data flow and delivery. However, there are many problems still to be solved, especially in the area of data assimilation.

The overall strategic objective of the EuroGOOS that deals with numerical ocean forecasting is:

> *"To develop, test, implement and upgrade the most efficient numerical models for those marine variables and parameters which are of highest priority for users of operational forecasts; to identify and compare the best modelling systems for different variables, regions, and scales; to develop the most efficient data assimilation methods for operational ocean modelling and forecasting".*
>
> (EuroGOOS, 2004)

[45] *http://www.bo.ingv.it/mfstep/ (accessed on 01.11.04).*
[46] *http://www.meteo.fr/e_index.html (accessed on 01.11.04).*
[47] *http://www.eurogoos.org/index.php (accessed on 01.11.04).*

One of its medium-term objectives is to:

> *"Implement operational models in ... the Mediterranean ... predicting hydrodynamic parameters, chlorophyll, nutrients, water quality, primary productivity, suspended sediment load, coastal sediment transport, and coastal erosion".*
>
> (EuroGOOS, 2004)

In 2002, EuroGOOS identified nine main priorities (EuroGOOS, 2003) including (1) the advancement and implementation of a marine monitoring and forecasting system, (2) the establishment of operational forecasting suite, (3) the implementation of regional systems based on local and regional user requirements, and (4) the technical development for marine monitoring, forecasting, nowcasting and hindcasting. These priorities are based on the results of the most complete survey and analysis so far conducted by EuroGOOS of the full-range of potential customers and their preferences for marine operational data (Fisher and Flemming, 1999). The aim of the EuroGOOS Requirements Survey (ERS) was to identify the classes of applications and uses for operational data on the marine environment, to identify what products and ocean-state variables are required, and to define the accuracy, resolution, space and time scales and forecast periods of these products.

The survey showed that there were not more than 20 physical parameters which are most frequently required by users of operational data. Out of these, wind, waves, tides, meteorological forcing of the sea surface, storm surges, currents, temperature and salinity are being requested. There are urgent requirements for biological and sedimentological parameters which cannot yet be reliably modelled in an operational mode.

One important result is that 53% of all respondents requested variables connected to the sea surface. Out of this proportion, surface current

velocity and direction top the list, followed by other surface variables, such as SST, wind stress, sea surface salinity, etc. Respondents also assigned a specific spatial resolution for each variable chosen. Figure 3.1 shows a high preference for a spatial resolution of 1 km for many different variables. Regarding temporal resolution, figure 3.2 shows that almost half of the cases chose a temporal resolution in the dimension of 6 hours to 1 day for many surface fields variables (6 out of a total list of 15 variables).

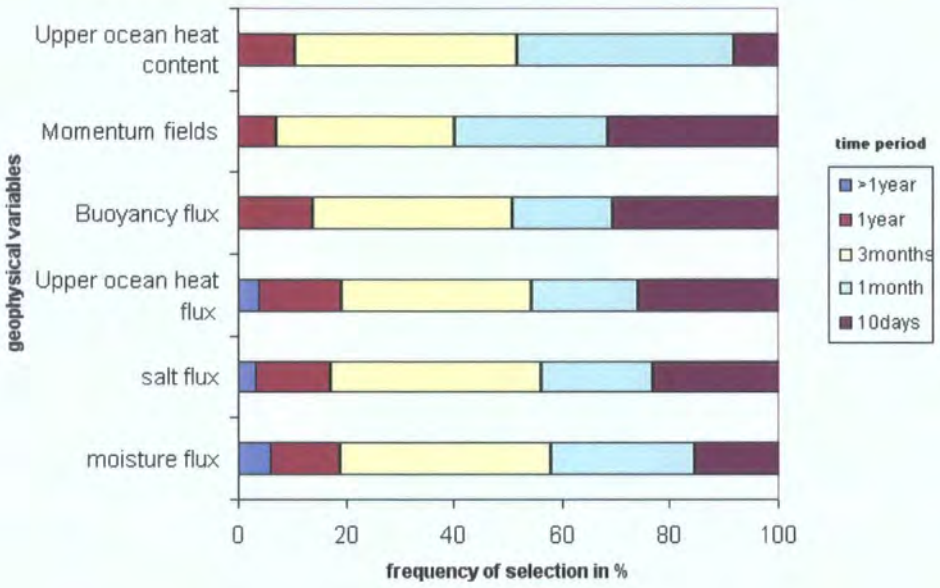

Figure 3.1. The required spatial resolution for some important oceanic surface variables (frequency of selection in % of requests of that variable). Variables requested on a varying spatial resolution, ranging from 1000 km, 500 km, 100 km, 10 km, 0.5 km to <0.5 km. (Source: Fischer and Flemming, 1999).

Concerning forecasted periods and accuracy for surface field variables, most respondents requested ranges between 10 days to 20 years with a preference for shorter periods (fig. 3.3). Around 40% of the respondents selected the 1% accuracy level. Of particular relevance are the accuracies quoted for variables pertaining to the upper ocean layer.

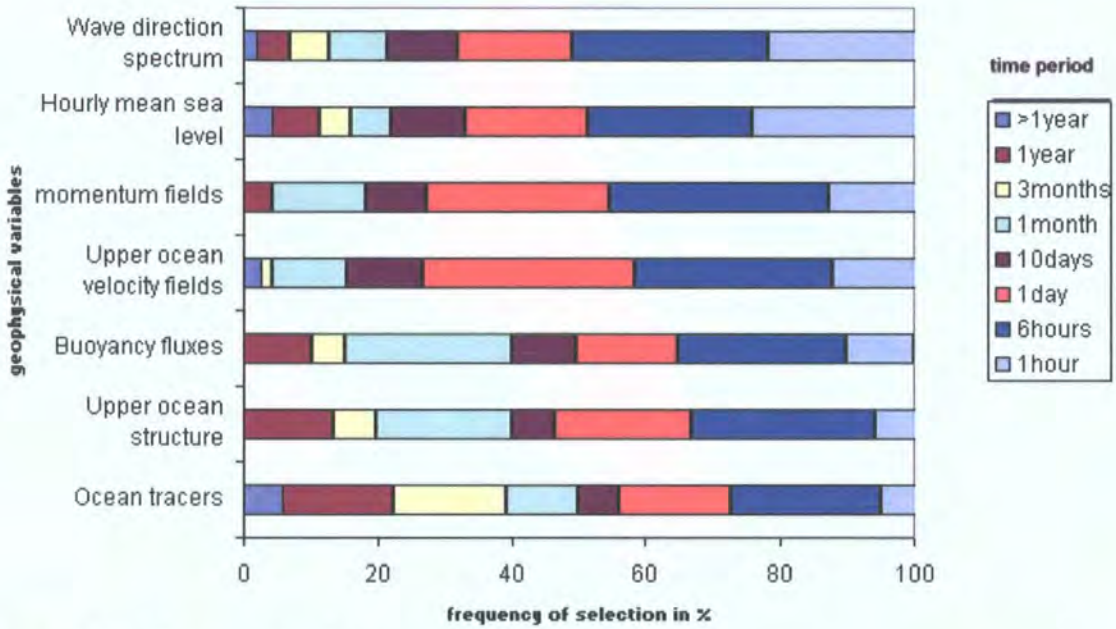

Figure 3.2. The required temporal resolution for some important oceanic surface variables (frequency of selection in % of requests of that variable). Variables requested on a variable resolution, ranging from >1 year down to 1 hour. (Source: Fischer and Flemming, 1999).

The EuroGOOS Requirements Survey therefore exposes a primary economic demand from main European marine activities for improved operational marine data. Based on the main findings from this survey, together with the specific technological and information gaps in the Mediterranean, the component of GOOS for the Mediterranean - MedGOOS, has launched the setting up of the Mediterranean Forecasting System (MFS) in collaboration with Mediterranean coastal states. This initiative is driven by the *"strong public demand for improved management of water quality in the sea"* (Pinardi and Flemming, 1998). As a result the MFS is directly involving a large

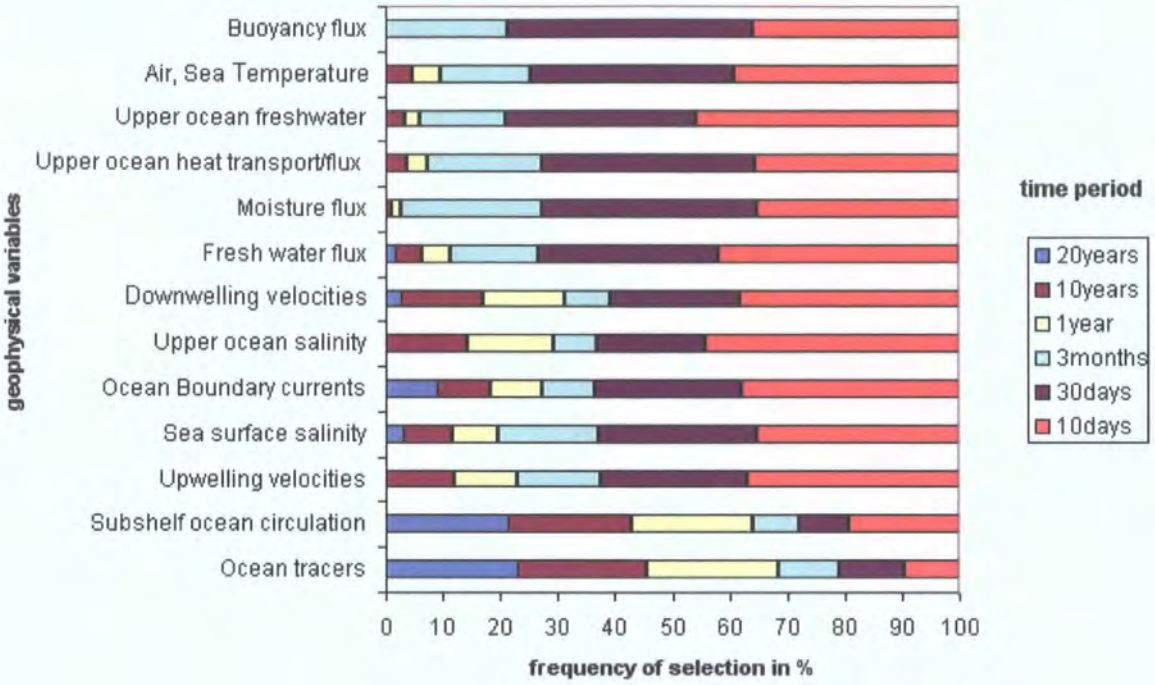

Figure 3.3. Requested forecast period for some important oceanic surface variables (frequency of selection in % of requests of that variable). Variables requested on forecast period ranging from 20 years, 10 years, 1 year, 3 months, 30 days to 10 days. (Source: Fischer and Flemming, 1999).

number of Mediterranean countries with an exchange of expertise. A main objective within MFS is "*capacity building of local centers to model the shelf areas with state of the art hydrodynamic modelling*" (Pinardi and Flemming, 1998). One major approach to address such a challenge is the:

> *"construction of a basin wide ocean circulation nowcast/forecast model and associated data assimilation of the Mediterranean Sea...capable of predicting the currents on the time scales of few weeks to months together with nested regional/coastal/shelf models".*

Another approach is the

> *"construction of coupled atmosphere-ocean regional model over the Mediterranean area. Techniques for coupling with extended range atmospheric simulations should be assessed".*

3.5.2. Model initialisation and data assimilation using accurate, real-time observations.

In ocean forecasting, the goal of data assimilation is to obtain the best possible initial estimate of the changing ocean. This has much in common with modern numerical weather forecasting, but because observations are much sparser in the ocean and the memory of the ocean is much longer than that of the atmosphere, challenges for data assimilation and prediction tend to be substantially greater that those in the atmosphere. These challenges encompass a rich variety of problems including computing and networking, accuracy analysis of observations, numerical formulation of partial differential equations, statistical analyses and descriptions of the atmosphere and ocean, and the interpretation of ocean data. This is particularly true for the Mediterranean area, where operational forecasting is still in its infancy.

During the last decade, a number of investigations gave rise to a more accurate initialisation and assimilation of atmosphere and ocean models using real-time remotely sensed data. Met-ocean parameters such as TMI-derived latent heat (performed by the ECMWF), marine winds (Krasnopolsky and Gemmill, 2001), satellite altimeter data (Gavart *et al.,* 1999) and moisture fields (such as integrated water vapour) retrieved from microwave sensors (Kuo *et al.,* 1993) have been assimilated into mesoscale numerical atmosphere and ocean models.

The MFS initiative is also addressing this challenge by encouraging the setting-up and testing of near-real time acquisition and processing of remote sensing data serving as prototypes for future implementation of

operational ocean forecasting. It recommends the use of near-real time remote sensing, such as altimetry, SST and ocean colour data since these provide unique data sets for the setting up of such a system. One of the main objectives of MFS is the development of an SST product that is operationally retrieved from the AVHRR sensor on NOAA satellites.

The Ocean Circulation and Prediction Team at LEGOS[48], Toulouse, has been developing data assimilation methods and conducting data assimilation experiments in the Mediterranean in order to study and help predict the large scales and the mesoscale circulation in the region. Observations such as altimeter and temperature profiles are being assimilated. Three different assimilation algorithms have been developed and tested (1) a reduced-order sequential optimal interpolation scheme, (2) an adaptive filter scheme, and (3) an ensemble forecasting scheme based on the Monte-Carlo method (De Mey and Benkiran, 2002).

3.5.3. Assimilation of SST in ocean forecasting models.

Ocean surface temperature is one of the most significant boundary conditions for the general circulation of the atmosphere. The ocean exchanges vast amounts of heat and energy with the atmosphere and these air-sea interactions have a profound influence on the Earth's weather and climate patterns. SST is also very sensitive to changes in the ocean circulation.

The surface temperature is also considered an important prognostic ocean model field and an ocean model output of primary interest. For these reasons, data assimilation schemes that blend SST observations with ocean model dynamics have become well established (Bell *et al.*, 2000). In the case of short-range oceanic forecasts, the initial surface boundary condition can be provided from timely remotely-sensed SST, which is kept constant throughout the forecasting period. However, the

[48] *http://www.obs-mip.fr/omp/umr5566/english/index.htm (accessed on 01.11.04).*

assumption that the observed SST field does not change significantly with time is not a reasonable one for medium- to long-range forecasts.

There are two main sources of SST for data assimilation. The first being historical climatological monthly mean analyses such as the CAC analysis (Climate Analysis Centre, Washington DC) as used by Castellari *et al.* (1998) to assimilate SST in an ocean circulation model. This source was obtained from a combination of ship opportunities and satellite data (Reynolds, 1982) and is available in two datasets: one for the period 1970-1981 on a 2° by 2° grid, the other for the period 1982-1988 on a 1° by 1° grid.

The other source is real-time, remotely sensed SST. Horton *et al.* (1997), for example, assimilated night-time 8 km MCSST by nudging the dynamic model fields in an optimal interpolation based analysis. The accuracy of SST was then stated as being 0.7-0.8 °C. Assimilation of SST derived using a multi-channel sea surface temperature (MCSST) algorithm was done at constant depth levels by redefining the temperature and interpolating the appropriate model variable from the ocean model's sigma levels to levels of constant depth. Once the assimilation is performed the new values are interpolated back to the depth of the original sigma coordinates. During the assimilation period the original model values were replaced by the modified ones at the surface, by using the model's embedded surface mixed-layer, and propagated down to the base of the mixed layer. The assimilation of MCSST for high resolution ocean forecasting presents an interesting challenge in order to adapt and optimise this method.

The MFS project is currently studying the impact of assimilating near real-time SST. Daily AVHRR NOAA-14 night data over the western Mediterranean Sea are being acquired and computed weekly (median value) with a resolution of about 2 km, and then averaged with a resolution of 0.125°. Over the eastern part of the sea, AVHRR NOAA-15 night and morning data are acquired and a daily average is computed

with a resolution of 0.125°[49]. After the two main datasets are normalised, an entire SST dataset is produced every week and a weekly mean calculated using data from the previous week. SST is interpolated over the whole Mediterranean Sea on the model grid of 0.125° by 0.125° using objective interpolation.

No research is being carried in the Mediterranean addressing the potential of using microwave-derived SST as (1) a source of initial surface boundary conditions for, and (2) to dynamically adjust the fields of small-scale, high-resolution ocean and atmosphere models. The availability of such data provides an opportunity to study the impact of assimilating this dataset on the model predictions of ocean forecasting systems.

3.5.4. Optimising remotely sensed SST observations for oceanic forecasting.

In the last decade there has been an advance in obtaining more precise measurements of remotely sensed SST, fundamentally because of its great importance in detecting climatic changes (Hamad *et al.*, 2004) and operational oceanic forecasting (D'Ortenzio *et al.*, 2000).

However, research is still underway to develop efficient and accurate techniques to accurately measure SST from space. This is mainly driven by the high accuracy that is required by researchers studying climate change and ocean circulation. The stated accuracy of SST for climatic studies, for example, has been reported to be 0.3 K (Barton *et al.*, 1989).

(i) SST measurement at infrared wavelengths.

The retrieval of SST from Earth-orbiting infrared radiometers is the technique of marine remote sensing which has had the widest impact on oceanographic science (Barton, 1995). InfraRed (IR) sensors such as

[49] *http://www.cls.fr/html/oceano/projets/mfspp/processing_en.html (accessed on*

AVHRR, on polar orbiting and geo-stationary meteorological satellites have provided routine observations of SST for over two decades. AVHRR has proved to be extremely useful in support of meso-scale to basin-scale ocean studies. Among the reasons for this include the good correlation with *in situ* data, high resolution and the wide network of data retrieval and distribution.

Various SST retrieval techniques have been proposed. The easiest way to accurately retrieve SST from the sensor radiances is by processing the data at the different sensor wavelengths. In a review of techniques, Barton (1995) showed how this differential absorption is exploited by SST algorithms for thermal IR radiometers. There are three classes of SST algorithms using thermal infrared data: (1) the most extensively used "split-window" algorithm (McMillan and Crosby, 1984) which uses the AVHRR wavelength of channel 4 (with a wavelength at 10.3-11.3 μm) as the lowest order estimate of SST and the difference channel 4 minus channel 5 (with a wavelength at 11.5-12.5 μm) brightness temperatures to correct for the atmosphere; (2) the "dual-window" algorithm, which uses the channel 4 brightness temperature and the difference of channel 3 (with a wavelength at 3.55-3.93 μm) minus channel 4 brightness temperatures to correct for the atmosphere, and (3) the "triple-window" algorithm, using the channel 4 brightness and the difference of channel 3 minus channel 5 brightness temperatures to correct for the atmosphere.

The MCSST was NOAA/NESDIS's first operational procedure since the early 1980's when data from the AVHRR were first available (McClain *et al.,* 1985; McMillan and Crosby, 1984). This most widely used (McClain, 1981) and globally routine (McClain *et al.,* 1985) solution is obtained from a set of linear equations under the assumption that the channel atmospheric or brightness temperatures are equal. The relationship between the split-window value and the actual SST is derived by regression against a global set of *in situ* SST data.

01.11.04).

Minnet (1991) showed that the accuracy of MCSST is around ± 0.3 K for dry atmospheres and ± 1.0 K for moist atmospheres. The errors are due, in part, to satellite calibration and precision, variations in surface emissivity (for which the sea is assumed to have an emissivity value of 1.0), and the linear assumption of the split-window technique. However, a number of shortcomings have been documented that limit the accuracy of the MCSST algorithm. These are primarily:

(a) Least-squares fit of "skin" radiances to 'bulk' SST measurements.

The linear regression coefficients used for the MCSST algorithm are derived from a least squares fit of radiance data with *in situ* SST data from ships and drifting buoys. Ship SST values, however, were found to have large biases due to the heat in the engine rooms where the temperatures were recorded. In an effort to achieve consistency, the comparisons with the *in situ* data were restricted to the use of data from drifting buoys only (Strong and McClain, 1984).

In the case of buoys, SST measurement do not take place within the thin radiative 'skin' of the ocean that is viewed by the infrared radiometers from space (Grassl, 1976; Schluessel *et al.,* 1990). Instead SST values are read from 0.5 m to a few metres below the surface of the ocean – referred to as 'bulk' SST. The difference between the 'bulk' and 'skin' temperatures is evident, arising from the varying interactions between the air and sea interface (Robinson *et al.,* 1984). MCSST neglects the difference between this bulk and skin SST. The skin SST is preferred estimate for the calculation of air-sea fluxes (Schulz *et al.,* 1997).

(b) Use of global data sets to derive algorithm coefficients.

NOAA's split-window coefficients are derived from a global data set match-up of buoy-derived SST (McClain *et al.,* 1985). The use of

extracted correlation coefficients therefore has to be taken with caution when used to retrieve regional (such as Mediterranean) SST data, especially under regionally-specific climatic conditions (Coll *et al.*, 1994; Shenoi, 1999). When analysed, Llewellyn-Jones *et al.* (1984) found deviations of 0.4 K when the coefficients extracted from a global match-up datasets were applied to a mid-latitude data set. The author concluded that the use of global linear algorithms for regional SST retrieval is not recommendable, because a certain degradation of the results is expected in small areas, where the coefficients may be inadequate and inaccurate. This applies particularly to ocean regions where there is a lack of *in situ* data sets at adequate resolution and frequency against which IR brightness temperature data is regressed. This is the case for regions such as the central Mediterranean Sea where only historical climatological datasets exist, and where buoy stations are absent.

(c Use of a 'first guess' state of atmosphere

The MCSST algorithm assumes a 'first guess' of the state of the atmosphere for which the SST retrievals will be accurate. In this case, the atmosphere has a typical vertical arrangement of water vapour and temperature. All algorithms will give good SST estimates as long as the atmospheric state is equivalent to their first guess[50]. The improvements and success of a global algorithm would then depend on how best it can represent the 'average state' of the atmosphere and how much variance it can tolerate. Deviations from this first guess could then give errors in the estimation of SST (Barton, 1995).

In areas like the Mediterranean, the atmosphere comes under the influence of seasonal winds and its atmosphere is often highly stratified in the lowest few kilometers from the surface. Hence, the atmospheric state is most likely to be different from the 'first guess atmosphere' and is likely to result in errors in SSTs retrieved using global algorithms.

Water vapour is a good example of an atmospheric component that is not evenly distributed on a regional or global scale. The total water vapour content in the vertical column, i.e. the precipitable water W, may change from 0.5 g cm^{-2} for high latitudes to about 6 g cm^{-2} for the equatorial regions (Arbelo and Herrera, 1995).

Ways to refine "split-window" algorithms have been explored by different researchers. A good number of alternative algorithms have been proposed in the last decade or so (a review is found in Prata *et al.*, 1995) that provide a correction for the above discrepancies. Recent work (Harris and Mason, 1992; Sobrino *et al.*, 1993; Ulivieri *et al.*, 1994; Yu and Barton, 1994; Francois and Ottle, 1996) showed that surface temperature retrievals may be significantly improved by incorporating additional information in the algorithm reflecting realistic regional atmospheric and oceanic conditions. Improved algorithms include the *satellite-measured 'skin' SST* (or satellite-measured surface "skin" temperature, (SMSST) routine (Schluessel *et al.*, 1987), a *water vapour sea surface temperature* (WVSST) routine (Emery *et al.*, 1994), a non-linear 'split-window' algorithm (NLSST) and a cross-product sea surface temperature algorithm (CPSST) derived by Walton *et al.* (1998). The NLSST algorithm is now the one being used operationally by NOAA. The AVHRR Oceans CoastWatch[51] and Pathfinder SST[52] algorithms, for example, are based on the NLSST algorithm.

Both NLSST and MCSST operational algorithms compute their coefficients by comparisons with selected buoy SST data. Thus they still represent a mix between the radiative 'skin' temperature sensed by the IR satellite sensor and the 'bulk' temperature measured by buoys. As a result the NOAA algorithms are 'tuned' to convert the satellite 'skin' SST observations into estimates of buoy 'bulk' SST. In this case, the selected

---

[50] *http://www.rsmas.miami.edu/groups/rrsl/pathfinder/Algorithm/algo_index.html (accessed on 01.11.04).*
[51] *http://coastwatch.noaa.gov (accessed on 01.11.04).*
[52] *http://www.rsmas.miami.edu/groups/rrsl/pathfinder/Algorithm/algo_index.html (accessed on 01.11.04).*

coefficients reduce the root mean square differences between the satellite brightness temperatures and the coincident buoy SST values. On global scales, the algorithms perform with a scatter of about 0.7 ^{o}C and a mean bias of about ± 0.1 - 0.3 ^{o}C. However, this does not guarantee that the algorithms will provide a uniform performance everywhere; on regional scales, the error usually exceeds these limits. Again, the use of a global set of coefficients, which may be good for one geographical area or one season can give poor performance for other areas or other seasons.

(ii) Alternative approaches to traditional SST retrieval algorithms from IR radiometers.

As Hagan (1989) points out, the theoretical relation of radiative transfer equation with the split-window method shows that the ratio of spatial variation in channel 4 and channel 5 brightness temperatures, R_{54} could be a useful parameter to reduce the errors in SST retrieval. This ratio has not been used in previous SST satellite measurement research except by Harris and Mason (1992) who used this ratio to modify the MCSST coefficients. It can be treated as an independent measurement because it is a spatial statistical value proportional to the ratio of the atmospheric transmittance in the two channels. It only requires the brightness temperatures as single-pixel measurements which represent the initial surface radiance as well as atmospheric absorption.

Under this concept an SST retrieval method was developed by Yu and Barton (1994) with a similar form to the linear (MCSST) and non-linear (CPSST) algorithms, but where the coefficients are not obtained by regression with *in situ* data. Yu and Barton (1994) claimed that the method has the main advantage of saving a large amount of manpower and material resources of collecting *in situ* data. In addition, they showed that this method could give better measurements than the MCSST products. However, they pointed out that further development

is required before a fully operational system uses this approach to retrieve SST in areas lacking a match-up database.

A second approach is the use of a split-window algorithm having coefficients that are optimised for the Mediterranean region. The optimised algorithm, such as that derived from the CMS Lannion data set[53] (Coll *et al.,* 1994), can be used to derive regional-specific SST.

A third approach is to perform regression analysis between IR channels centered at 11 and 12 μm and the atmospheric profiles generated by a radiative transfer model. The coefficient of the SST algorithm can then be determined synthetically. An alternative approach can be taken by using, instead of a model, the differential absorption of the two split-window channels 4 and 5 due to water vapour (Mathew *et al.,* 2001). In this case, the corresponding difference in brightness temperature will give a signature of the atmospheric water vapour profile. With the availability of calibrated temperature brightness from channels 4 and 5 and collocated SST estimation, the coefficients can be derived empirically at the pixel level. This approach therefore offers the advantage of deriving more accurate regression models based on regional-specific atmospheric profiles.

(iii) Other factors to be considered during SST retrieval.

Of particular concern to the AVHRR-user community are the radiative effects of high levels of tropospheric turbidity as would happen when Saharan dust cloud is in residence over the north tropical Atlantic and central Mediterranean (e.g. Rao, 1992). Dust clouds originating from Sahara desert are a prominent feature of the climate of the desert and its bordering regions (fig. 3.4). The main reason for this concern is the error introduced in the retrieved SSTs by the absorption and emission of IR radiation by atmospheric aerosols (Kaufman *et al.,* 1997); in addition the enhanced diffused reflection of solar radiation by aerosols

causes rejection of valid data during daytime by mimicking clouds in the cloud-screening tests used in the retrievals.

This lowering of retrieved SST on line-of-sight aerosol optical thickness as small as 0.1 to 0.5 μm was confirmed by May *et al.* (1992). They based their analysis on near-simultaneous buoy measurements of SST and retrieval of SST and aerosol optical thickness from AVHRR measurements in the presence of the Saharan dust cloud.

Figure 3.4. A common significant dust event over the central Mediterranean Sea (source: NOAA Operational Significant Event Imagery).

Using model simulations, Takayama and Takashima (1986) observed that as their model atmosphere changed from 'clear' (surface meteorological range 23 km) to 'hazy' (surface meteorological range 5km), the depression of AVHRR channel 4 radiance from the prescribed value was enhanced by 0.2 °C due to the increase in atmospheric

[53] *The CMS-Lannion, France, data set has been collected over the North Atlantic Ocean and the Mediterranean Sea.*

turbidity. Similarly, Barton *et al.* (1989) suggest that under 'clear' conditions (surface meteorological range: 23 km), maritime aerosols could contribute approximately 0.2 ^{o}C to the depression of channel 3 radiance.

To understand the impact of aerosols, information on their variation and the spatial distribution is required, often expressed by the optical thickness or mass concentration. At least information should be available on the presence of aerosols when infrared radiances are being used to derive SST. Additional information on the degree of aerosol absorption, scattering properties, vertical profiles, size distributions, and compositions can assist image processors to calibrate with more certainty AVHRR radiances. However, infrared radiance data during extreme events should be discarded and instead, alternative sensors that are insensitive to atmospheric aerosols should be used.

(iv) SST measurement at microwave wavelengths.

Data from satellite-borne microwave radiometers have become extremely useful and important for studying the modelling and forecasting skills of ocean and atmosphere models. Their capability to simultaneously measure ocean surface wind speed, SST, sea ice cover, and vertical profiles of air-temperature and atmospheric water (vapour, liquid and ice) makes microwave radiometers unique tools for such research purposes.

The most important feature that makes microwave radiometry so attractive is that SST can be measured through clouds, which are nearly transparent at 10.7 GHz. This is a distinct advantage over the traditional infrared SST observations that require a cloud- and dust aerosol free field of view. Ocean areas with persistent cloud coverage can now be viewed on a daily basis. Furthermore, microwave retrievals are not affected by aerosols and are insensitive to atmospheric water vapour. However, microwave retrievals are sensitive to sea-surface

roughness and raindrops of diameter larger than cloud droplets, and as a result, SST retrievals are not reliable when rain is present. When rain is detected at 37 GHz, the SST retrieval is discarded.

Retrieval of SST from the microwave radiances requires that the influence of atmospheric attenuation and sea surface roughness be removed from the observations. A physically based retrieval algorithm is used to remove these effects. When rain is not present, the attenuation is very small at 10.7 GHz, with 97% of the sea surface radiation reaching the top of the atmosphere. Using the higher frequency channels (19 to 37 GHz), the algorithm precisely estimates the 3% attenuation due to oxygen, water vapour and clouds. The polarisation ratio (horizontal versus vertical) of the measurements is used to estimate sea surface roughness.

(a) The Tropical Microwave Imager (TMI).

In November 1997, the TRMM[54] spacecraft was launched. One of the payloads was the TMI sensor having a full suite of channels ranging from 10.7 GHz to 85 GHz and represents the first satellite sensor that is capable of accurately measuring SST through clouds. The capability of measuring SST through clouds has long been a goal of microwave radiometery. A global SST product unaffected by clouds and aerosols would be of great benefit to both the scientific and commercial communities.

TRMM has yielded significant scientific research data over the last seven years to users around the globe, offering a global dataset consisting of SST, surface wind speeds derived using two different radiometer channels, atmospheric water vapour, liquid cloud water and precipitation rates. TRMM data has aided NOAA, other government agencies, and other users in their operational work of monitoring and predicting rainfall and storms, as well as in storm research. In spite of

its original 3-year lifetime, NASA has recently announced that it will extend its operations until at least 2010.

The design of TMI is based on the highly successful SSM/I, which measures the intensity of radiation at five separate frequencies 10.7, 19.4, 21.3, 37 and 85.5 GHz. The frequencies are similar to those of the SSM/I, except that TMI has the additional 10.7 GHz channel that is able to penetrate non-raining clouds with little attenuation, giving a clear view of the sea surface under all weather conditions except rain. At this frequency, atmospheric aerosols have no effect, making it possible to produce a very reliable SST time series for climate studies. The other main improvement of TMI over SSM/I is its ground resolution as a result of its lower orbiting altitude of 350 km compared to 860 km of the SSM/I. TMI has a 780 km-wide swath on the surface. The higher resolution of TMI, as well as the additional information supplied by the precipitation radar further helped the development of algorithms.

The empirical retrieval algorithms are derived from a high-quality data set that collocates the satellite brightness temperatures with buoy- and/or radiosonde-measured geophysical variables in time and space. The physically based algorithms use a large amount of such empirical data for parameterisations (Wentz, 1997) in order to represent a wide range of global meteorological events. High wind speed events have been fairly rare in most match-up data sets because wind speeds of gale force (>17 m s^{-1}) or greater at a given time cover no more that 5% of the global ocean surface.

Gentemann *et al.* (2004) showed that the accuracy of SST data derived by the TMI sensor has a bias of –0.07 °C and standard deviation of 0.57 °C when compared to *in situ* buoys. Because the brightness temperature may be influenced as much by temperature effects on the emissivity as by the variation of black body radiation with temperature, the relationship between SST and brightness temperature is non-linear,

[54] *TRMM is a joint programme between NASA and the National Space Development*

and frequency-dependent. For surface roughness and atmospheric effects to be removed, sophisticated algorithms are essential for accurate retrieval of SST.

Previous microwave radiometers were either too poorly calibrated or operated at too high of a frequency to provide a reliable estimate of SST. In spite of its coarse resolution compared to IR-derived SST, the results for the TMI SST retrievals are quite impressive and have led to improved analyses in a number of important scientific areas, including ocean modelling. In fact, its original three-year long mission has been extended by an indefinite number of years until is expected to hit the minimum fuel threshold for controlled re-entry. This extension is based on the popularity of the TRMM sensors with weather forecasters. A major step forward was made in 2002 with the launch of the AQUA[55] satellite (sibling of TERRA) on 4 May 2002. An Advanced Microwave Scanning Radiometer (AMSR), having an additional 6.9 GHz channel that will enhance SST retrieval, was launched on board the AQUA satellite. In 2005, the Conical Microwave Imager Sounder will be a primary sensor flying on the National Polar Orbiting Environmental Satellite System. Built on the success of the SSM/I and TMI satellites, this sounder shall be able to measure the global SST field to an accuracy of about 0.2°C at a spatio-temporal resolution of 50 km in 3 days (Wentz *et al.*, 2000).

Thanks to the recent suite of orbiting passive microwave sensors, the availability of a continuous provision of global SST data can be instrumental to test the following research challenges:

1. provision of initial surface boundary conditions for local area atmosphere and ocean models.
2. nudging of dynamic ocean model fields towards SST fields prior to ocean forecasting.

Agency of Japan (NASDA). http://trmm.gsfc.nasa.gov/ (accessed on 01.11.04).

[55] *http://aqua.nasa.gov/ (accessed on 01.11.04).*

3. derivation of air-sea fluxes from bulk formulae in combination with other basic variables that are simultaneously derived using the same sensor (including 10 m wind speed and humidity profiles).

3.5.5. Remote sensing to fine-tune and verify ocean forecasting systems.

The design and fine-tuning of physical numerical packages for the accurate prediction of air-sea fluxes is crucial for the reliability of ocean forecasting system. Although these parameterised processes occur at small scales, they depend on, and in turn affect, the larger scale fields and processes that are explicitly resolved by a numerical model. The details of the parameterisations have a profound effect on the model forecast, especially at longer time scales, and are therefore the subject of very intense ongoing research.

Studies addressing the forecasting quality of air-sea fluxes by numerical weather prediction models (Dekic *et al.,* 1997) as well as the impact which model resolution has on the resulting forecast quality (Mesinger 2002, *personal communication*) are scarce. Not all NWP models are optimised to produce fluxes and the achieved space/time resolution is not optimal because their parameterisation formulae used are not adequate. Operational NWP groups very often focus on forecast performance that is related to atmospheric fields, and operational changes in physical parameterisations are often made to improve observable atmospheric fields of importance to weather forecasters. Their effect on the surface fluxes is not always as carefully assessed, partly because of a lack of confidence in independent estimates of the surface fluxes. At NCEP, for example, a change in the operational analysis/forecast system, while beneficial in many respects, can lead to a lack of lower boundary forecasting skill in certain areas (Siefridt *et al.,* 1999). Complaints from meteo-marine forecasters then usually lead to adjustments in the parameterisation schemes of sensible and latent heat.

A major hurdle in the fine-tuning and verification of small-scale forecasts is the lack of high frequency spatio-temporal sampling at up to 4 times a day. Operational meteorological satellites can now offer high-resolution and accurate real time data. With a swath width of about 1400 km, orbiting microwave sensors are providing almost global, high resolution coverage on a daily basis of geophysical parameters notably, ocean surface wind speed, ice features, cloud liquid water, integrated water vapour, precipitation over land and water, snow cover and sea surface temperature. A single scatterometer of the ERS-AMI design for example, provides over 90% coverage of the ocean within 96 hrs and with high enough resolution to detect mesoscale variability of the wind (Zecchetto and Cappa, 2001). A single scatterometer of the NSCAT design provides coverage over 90% of the ocean within 48 hrs. The newer SeaWinds design provides over 90% coverage within 24 hrs. Ocean surface wind speed data are having the most direct use in marine weather analysis and weather forecasting. Wind magnitude data derived by the tropical microwave imager are very accurate[56] with an RMS difference between the sensor and *in situ* buoys of 0.84 m s^{-1}.

This availability of global ocean data will allow objective fine-tuning and validation of numeric parameterisation schemes. Ocean surface wind speed data, for example, is suitable to fine-tune the model prediction of air-sea fluxes as well as to generate air-sea fluxes using bulk parameterisation. Fine-tuning of other schemes is also possible, such as the cumulus parameterisation schemes contained in the latest generations of numerical atmosphere models (Gemmill and Krasnopolsky, 1998) and to improve storm track and hurricane prediction (Brown *et al.*, 2002).

No studies to fine-tune the prediction of air-sea fluxes generated by the Eta atmosphere model have been yet been undertaken by operational forecasting centres in the Mediterranean.

[56] *http://www.ssmi.com/tmi/tmi_validation.html#wind (accessed on 01.11.04).*

3.5.6. Improving model diagnostic verification for ocean forecasting.

Standard verification methods for spatial forecasts can only provide limited information about the quality of these forecasts, especially for the case of fine-scale models and forecasts. New object- or field-based approaches show promise for providing information that is more useful to the ocean forecasting community.

The recent rapid growth in geographic information science has created new opportunities to use geometric concepts to explore the performance of ocean forecasting systems. The use of spatial representation in ocean forecasting by looking for new ways to enlarge its scope and potential is challenging. Such diagnostic procedures are able to detect temporal errors that may originate from "out-of-phase" initial model boundary conditions and model numerics. These errors can be easily confounded with other errors, especially systematic ones, when standard verification procedures are instead used. On the other hand, diagnostic verification is able to characterise such errors from a spatial perspective. So far, diagnostic verification has been poorly applied for the improvement of ocean forecasting systems.

Spatial exploratory data considerations such as (1) the degree of spatial relation or similarity between forecasts and observations (Holt and Benwell, 1997) at different scales (Savitsky and Anselin, 1997); (2) analysis of error propagation techniques (Hunter *et al.,* 1999) and related reliable estimates that can guide forecasters; (3) detection of patterns in spatial data and understanding of underlying processes (Longley and Batty, 1996), and (4) spatio-temporal correlation for multidimensional data (Varma, 1999), are new and exciting challenges to diagnose ocean forecasting systems. Further development of these approaches should be pursued (Brown *et al.*, 2002).

Ocean forecasting generates demands that can justify the use of exploratory spatial data analysis with standard commercial applications. Diagnostic verification tools for ocean forecasting that take into account spatial data analysis could include:

- the development of spatial similarity indices and texture recognition techniques to better analyse the relationship between forecasted and collocated observations,
- improved spatial visualisation and correlative method for oceanic surface features, and,
- improved analysis of spatio-temporal relations as produced by ocean forecasting systems.

3.6. Summary.

The goal of operational ocean forecasting is to provide prediction of the physical sea-state and other related components for a certain time period. The benefits of having continuous forecasting of ocean variability at unprecedented space-time resolution are numerous.

In spite of opening up a whole new array of mathematical approaches to find a "solution" to complex geophysical fields, numerical models still limit their output to either grid points or spectral basis. Another limitation is the impact of imprecise information that defines the initial conditions of numerical models. This chapter showed how very often, existing numerical ocean models use climatological data to mechanically force and nudge their numerical fields to produce daily forecasts. A serious drawback here is that climatological data does not contain any daily variability.

An important research challenge highlighted by this chapter was the much-needed progress in the field of model initialisation using accurate, real-time observations. The primary constraint includes a

number of technological problems connected with the scarcity of oceanic observations as well as to computational and numerical limitations. Remote sensing is depicted as being a primary contributor to data assimilation and initialisation of atmosphere and ocean models, with particular reference to research in the Mediterranean. Research gaps exist on the potential use of microwave-derived SST both as a source of initial conditions and to dynamically adjust the fields of small-scale, high-resolution ocean and atmosphere models.

This chapter discussed the research work related to the forcing of ocean models by forecasted atmospheric constituents, which gives them the ability to enhance the overall forecasting skill over a short time scale. The evolution of the oceanic variability depends on air-sea fluxes and thus, short- to medium-range ocean forecasting tends to greatly benefit by the provision of accurate fluxes that define the model's surface boundary conditions. Apart from providing valuable initial information, high quality air-sea fluxes together with basic meteorological variables can also be used to assess the model's forecasting skill.

The basic set of air-sea fluxes as well as other surface variables required for operational ocean forecasting were described in some detail. Air-sea fluxes can be measured *in situ* or from bulk parameterisation formulae using basic air-sea state variables. Another, much used source is from climatological datasets. This chapter described the pros and cons of acquiring air-sea flux data by direct observation and through parameterisation. In the latter case, the acquisition of accurate basic variables is mandatory where the main sources for operational[57] sea-state basic variables include *in situ* measurements from buoys and ships, from remote sensing and from numerical weather prediction. Emphasis was made on the role of remote sensing and numerical weather prediction in providing instantaneous and forecasted geophysical variables respectively. The

[57] *Instantaneous collection for data assimilation, initialisation and model verification.*

advantages and disadvantages of the three acquisition techniques were discussed.

Unlike bulk formulae, with constant transfer coefficients, numerical weather prediction models are able to include the effects of stability and interfacial conditions, which in addition to their high vertical resolution, make them excellent sources for air-sea flux datasets. Research shows that the Eta atmosphere model is a good example of a modern numerical atmosphere model that is able to simulate and predict weather phenomena even at mesoscale and microscale level. It is well tested and tuned at varying resolutions and integration domain sizes over most of the globe, including the Mediterranean. The chapter gives an appraisal of its major schemes, pointing out that very few studies have yet addressed the accuracy of its simulated air-sea fluxes, and the need therefore, to pursue such a line of research.

The technical approaches in operational forecasting were also presented in view of their relevance to the present study. The technical implications and advantages of coupling together atmosphere and ocean models were discussed, and the drawbacks when using climatological datasets to force ocean models. Research also shows how model coupling can also cater for local-area, high-resolution forecasts by using a model nesting concept.

Studies show that the spatio-temporal resolution of the variability of oceanic features dictates an appropriate model resolution for their simulation. There have been few studies, however, on the influence of ocean model resolution on the accuracy of predicted fields. This chapter identified a major limitation to fully use small-scale ocean models due to the lack of high spatio-temporal observations needed to verify model predictions.

This chapter highlighted the importance of diagnostic verification in order to assess the quality of forecasted data and stresses the

importance of objective evaluation. It shows how model verification tools have evolved to provide an objective measure of model skill. Currently, statistical measures and graphical tools used in model verification are simple and do not make use of GIS display and analysis. This chapter stressed the advantages of using exploratory spatial data analysis to assess the temporal and spatial accuracy of model forecasting systems. This included techniques such as the analysis of spatial similarity between forecasted and collocated observations and related geostatistics. Based on the current research, this chapter suggested ways to improve diagnostic verification for ocean forecasting and identifies an increasing need for more analysis that is exploratory, coupled with the use of Earth observation data. New research challenges to use descriptive and spatial exploratory analysis were identified. Such research has the potential to generate new analytical methods embedded in commercial applications. This review listed down potentially novel verification tools for ocean forecasting that are based on spatial data analysis, some of which will be used in subsequent chapters of this thesis.

The current technical challenges in the field of ocean forecasting in the Mediterranean were also mentioned, with an emphasis on major technological and information gaps. This chapter described the current state of ocean forecasting in the Mediterranean, with particular reference to the type of operational forecasting systems used in the region. Results were presented defining the requirements identified by the ocean forecasting community and end-users of forecasted products.

Finally, this chapter showed how remote sensing can be an extremely useful tool to fine-tune the numerical prediction of air-sea fluxes. Studies that verify the skill of the Eta model to forecast air-sea fluxes are scarce if non-existent. This chapter provided a review of the strength and weakness of using high resolution SST derived from infrared sensors to verify ocean forecasts. Alternative data calibration approaches to retrieve SST from AVHRR were discussed, with the scope

of using them to calibrate scenes from geographical areas that lack operational, *in situ* data against which infrared radiances are regressed and calibrated.

Chapter 4

COMPILATION OF A DATABASE TO VALIDATE THE OCEAN FORECASTING SYSTEM.

4.1. Construction of a high-resolution database.

Thanks to the rapid development of information-processing technology, numerical modelling of the ocean and atmosphere is becoming more powerful and sophisticated, and can now simulate phenomena from the micro to the planetary scales. At the same time, such numerical modelling requires a comprehensive set of collocated data that is required for its validation.

Remote sensing is especially suited to derive such datasets. While *in situ* measurements are limited to data at one or a few points in time, remote sensing allows the collection of information of extensive vertical and horizontal domains without disturbing the medium being observed. On the negative side, remote sensing techniques cannot always provide precise measurements of the desired meteorological and oceanic variables. This is the case with some important hydro-meteorological data, and this limitation is still preventing the use of remote sensing in this area of research. This inability is made up for using other alternatives, such as the use of numerical models and bulk parameterisation to fuse data coming from different sources and derive unknown derivatives.

4.2. Required geophysical elements.

The objectives set by the present study require a set of collocated, independent observations to complement the task of validating the high

spatio-temporal resolution forecasts. This database must provide suitable temporal and geographical information of the oceanic and atmospheric variability against which the models' accuracy can be assessed objectively.

Due to the fact that no instantaneous, high-resolution air-sea fluxes over the Ionian basin are available for this study, this database has to contain enough information as to generate additional products, including air-sea fluxes. By inserting basic geophysical fields such as highly resolved collocated wind magnitude and sea surface temperature into bulk formulae, instantaneous air-sea fluxes can be derived and used to assess the skill of the ocean forecasting system.

Since the objective verification of the present forecasting system lies on the accuracy of this database, it also becomes pertinent to test the accuracy of the derived database. Independent collocated datasets can be derived from climatological datasets and used for this purpose.

The required geophysical elements for this database[61] are the following:

(i) Sea surface temperature.

High spatio-temporal sea surface temperature data are a key variable needed for the present study to parameterise turbulent heat fluxes as well as to validate the high-resolution SST forecasts produced by the ocean model.

For this work, optical- and microwave-derived SST data will be used separately and jointly, each source with its own strengths and weaknesses. Whereas high resolution infrared-derived SST is highly valuable to validate high-resolution SST forecasts, it poses extensive calibration requirements. The lack of collocated *in situ* SST over the area of interest implies that alternative algorithms need to be adopted

[61] *Table 2.1 lists the use of these geophysical elements for this research study.*

and used in this study. Microwave-derived SST is provided in calibrated form by data dissemination centers. However, it can never reach the same spatial scale as infrared-derived SST.

Monthly climatological SST is used to assess the accuracy of the remotely sensed counterpart and to identify anomalies during the study period.

(ii) Oceanic winds.

Apart from validating forecasted oceanic winds, this geophysical field is required to estimate turbulent air-sea fluxes. Wind speed fields can be acquired instantaneously from orbiting passive microwave sensors and are provided in calibrated form by data dissemination centers.

(iii) Surface air temperature.

This parameter is required to calculate the turbulent heat fluxes using bulk parameterisation formulae and to validate the skill of the atmosphere model to forecast this geophysical field.

As described in section 3.2.2.2., the acquisition of instantaneous air temperature poses technical problems. This study will continue on the work conducted by Schulz *et al.* (1997) by refining it to reflect the real climatology of the geographical area under study.

(iv) Humidity profiles.

Parameters such as precipitation rates, the vertically integrated humidity values of cloud liquid water and precipitable water vapour provide useful information on the presence of air masses that are closely related to synoptic scale features[62]. These profiles are used to

[62] *Liquid water, for example, resides in clouds and is directly related to regions of precipitation and to active weather systems such as precipitation, storms and fronts (McMurdie & Katsaros, 1996). A large amount of liquid water is generally associated*

validate collocated convective processes forecasted by the atmosphere model and to understand the climatology of the area of interest.

The availability of high-resolution, spatio-temporal humidity profiles also assists in the interpretation of other data residing in the database, including microwave-derived data, and the differential absorption and calibration of infrared radiances of the sea surface in the 10 μm to 12.5 μm of the electromagnetic spectrum.

(v) Outgoing longwave radiation.

This parameter is required to assess the accuracy of the radiation package of the atmosphere model. This scheme is computationally-expensive and is important in the determination of the radiative heat fluxes.

Section 3.2.2.2. describes the sourcing of this parameter as well as the strength and weakness of acquisition by remote sensing. Its derivation is still at the experimental stage (WCRP/GEWEX, 1996) and more work is needed before reliable estimates of the longwave radiation can be made available by orbiting satellites (WCRP/GEWEX, 1996).

(vi) Turbulent heat fluxes.

Collocated, high spatio-temporal resolution flux data over the area of interest are used to validate the same fields forecasted by the atmosphere model. This high-resolution flux data is estimated by inserting the basic met-ocean variables collected in the database from various sources, into bulk formulae. To ensure an objective and sound verification of the performance of the atmosphere model, these high-

---

with strong convective activity (cumulus clouds) and turbulent surface weather conditions, whereas small amounts of liquid water are associated with near neutral or stable regions (such as stratiform clouds) and constant or steady surface weather conditions.

resolution flux products are, in turn, verified against an independent set of collocated climatological data.

(vii) Aerosol optical thickness.

This information is useful to assess the clarity of the atmosphere over the area of interest. As described in section 3.5.4., these data are used to validate model-related performance to forecast the radiative heat flux. In addition, this data are used to validate the suitability of infrared-derived SST during episodes of high dust occurrence in the atmosphere.

4.3. Methodology.

4.3.1. Collection of relevant met-ocean datasets and derived geophysical fields.

4.3.1.1. Instantaneous 10 m wind magnitude, SST and hydro-meteorological fields.

The Tropical Microwave Imager (TMI) is a well-calibrated sensor and contains suitable frequency channels for the retrieval of these fields. Each daily global coverage of the sea surface is organised into seven ascending and descending datasets as follows:

- Time of data retrieval
- sea surface temperature
- 10 m surface wind speed using 11 GHz
- 10 m surface wind speed using 37 GHz
- integrated precipitable water vapour
- cloud liquid water
- precipitation rate

(i) Data retrieval.

Daily TMI data covering a full year period (January-December 1999) was retrieved by ftp from http://www.ssmi.com. TMI data is provided as binary data and cover a global region extending from 40°S to 40°N. Each daily data file consisted of fourteen 0.25° x 0.25° grid (1440, 320) byte maps.

(ii) Data decoding, processing and formatting.

Two fortran codes were written to decode, process and format the TMI data. The first was the *tmi2monthly.f* script[63] which read, processed and re-formatted the binary daily TMI into Grid Analysis and Display System (GrADS)-format monthly set of sequential daily ascending and descending data.

Since precipitation induces error in the retrieval of the geophysical parameters by the TMI sensor (Gentemann *et al.,* 2004), rain pixels were used to mask off same-area pixels from the other collocated ascending and descending geophysical field maps. Since valid geophysical data lay between 0 and 250, pixels were scaled according to the calibration information supplied with the data as to obtain meaningful geophysical fields.

GrADS-formatted TMI monthly datasets using *TMI2monthly.f* were visualised to note orbit time and the integrity of the fields over the area corresponding to the high-resolution domain of the ocean forecasting system. This enabled the assignment and temporal collocation of the various remotely-sensed fields to similar field elements that were predicted by the models.

All fields were arranged into gridded ascii XYZ format. Following the generation of *TM2"mon"cent.gdat* files (where *mon* is the month), a set of

[63] *Appendix I; Section I.1.1.*

gridded ascii XYZ files were produced for all geophysical parameters retrieved from ascending and descending orbits.

4.3.1.2. Instantaneous very high-resolution SST fields.

This section refers to the calibration of raw AVHRR data in the absence of collocated *in situ* SST data. In this study, a restricted choice of calibration algorithms were considered and evaluated in view of the constraints presented during this study as described in section 3.5.4.

For this reason, a database was required consisting of high-resolution, uncalibrated infrared radiances and a collocated SST map. The NOAA CoastWatch database presents an ideal medium that provides (1) 'raw' 1.1 km AVHRR temperature brightness data from channels 3, 4 and 5 data and (2) collocated NLSST pixels. This database was extensively used to compare and derive an optimal calibration algorithm to be applied over the central Mediterranean.

Figure 4.1 shows a general experimental scheme to assess the suitability of potential algorithms. Acquisition of suitable data is described below. The data consists of infrared radiances from AVHRR channels 3, 4 and 5 together with SST maps derived using the non-linear SST calibration algorithm. The suitability of calibration algorithms shown in figure 4.1. is assessed using the final correlation between the calibrated results and the NLSST maps.

4.3.1.2.1. Data acquisition and archiving.

The following data was acquired and archived:

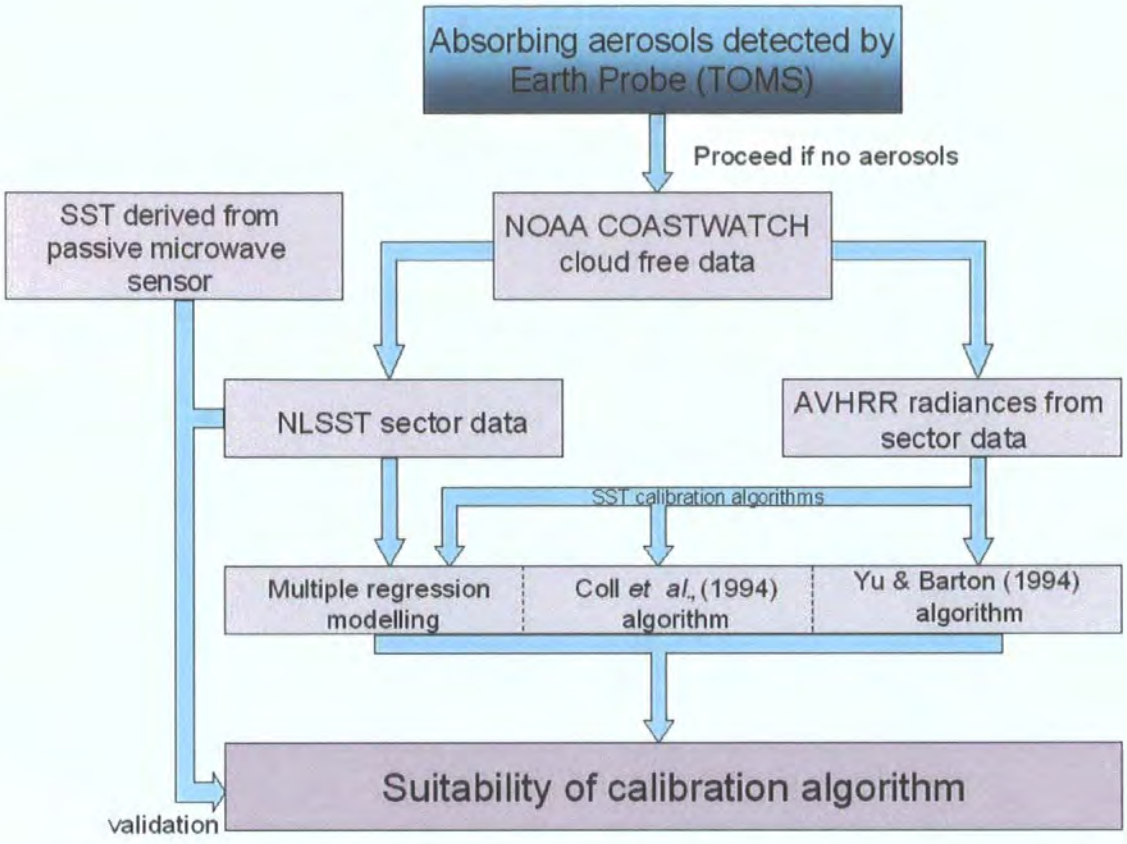

Figure 4.1. Experimental scheme to derive a suitable SST calibration algorithm based on CoastWatch data.

(i) Absorbing aerosols over the Atlantic Ocean.

Daily data acquired by the Total Ozone Mapping Spectrometer (TOMS) satellite was retrieved by ftp[64]. The daily maps showed the absorbing aerosols over the Atlantic Ocean, which included the south and east coast of the United States (inset in fig. 4.3). Days having traces of absorbing aerosols were noted.

[64] *http://coastwatch.noaa.gov/ (accessed on 01.11.04).*

(ii) The CoastWatch database.

CoastWatch data covering a period of two years (1998-1999) were retrieved from the NOAA CoastWatch Active Access System[65] for the South East Coast Node in the United States. This region has been selected in view of the full availability of data, including *in situ* buoy data (NODC) and GOES datasets.

The area of interest extends from (32°N, 73°W) to (37°N, 79°W). The oceanic area was subdivided into sectors to facilitate data handling and processing (fig. 4.2).

The CoastWatch database provides NLSST and MCSST products, in addition to raw AVHRR data. According to the technical documentation provided by NESDIS[66], the split-window algorithms used by CoastWatch are as follows:

$$NLSST = a_1(T_4)+a_2(T_4-T_5)(MCSST)+a_3(T_4-T_5)(secq-a)-a_4 \quad (3.1)$$

$$MCSST=b_1(T_4)+b_2(T_4-T_5)+b_3(T_4-T_5)(secq-1)-b_4 \quad (3.2)$$

where T_4 and T_5 are the AVHRR 11 μm and 12 μm channel temperatures in Kelvin; Secq is the secant of the satellite zenith angle q; NLSST and MCSST are the non-linear and linear multi-channel SST respectively, in degrees Celsius; a_1-a_4 and b_1-b_4 are constant coefficients.

[65] *http://coastwatch.noaa.gov/cw_form_cwf.html (accessed on 01.11.04).*
[66] *http://coastwatch.noaa.gov/poes_sst_algorithms.html (accessed on 01.11.04).*

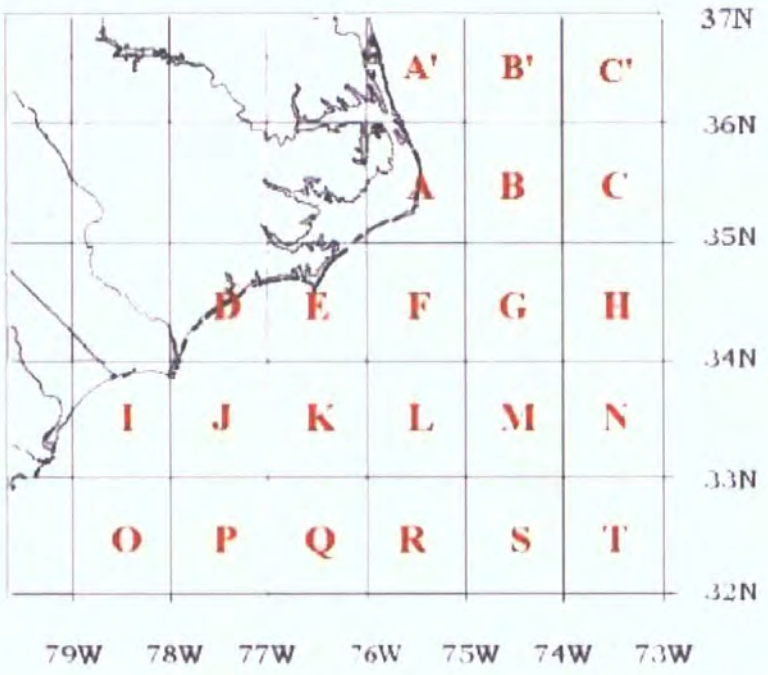

Figure 4.2 showing the South East Coast as one of the nodes of CoastWatch. The area was subdivided into sectors for the purpose of the present investigation.

Figure 4.3 shows an example of the extraction of AVHRR- and related data (NLSST and collocated infrared radiances) from a sector that is free from aerosols and clouds.

During the entire two-year period, a total of 286 sectors were found suitable (table 4.1), for which the above data was extracted and archived.

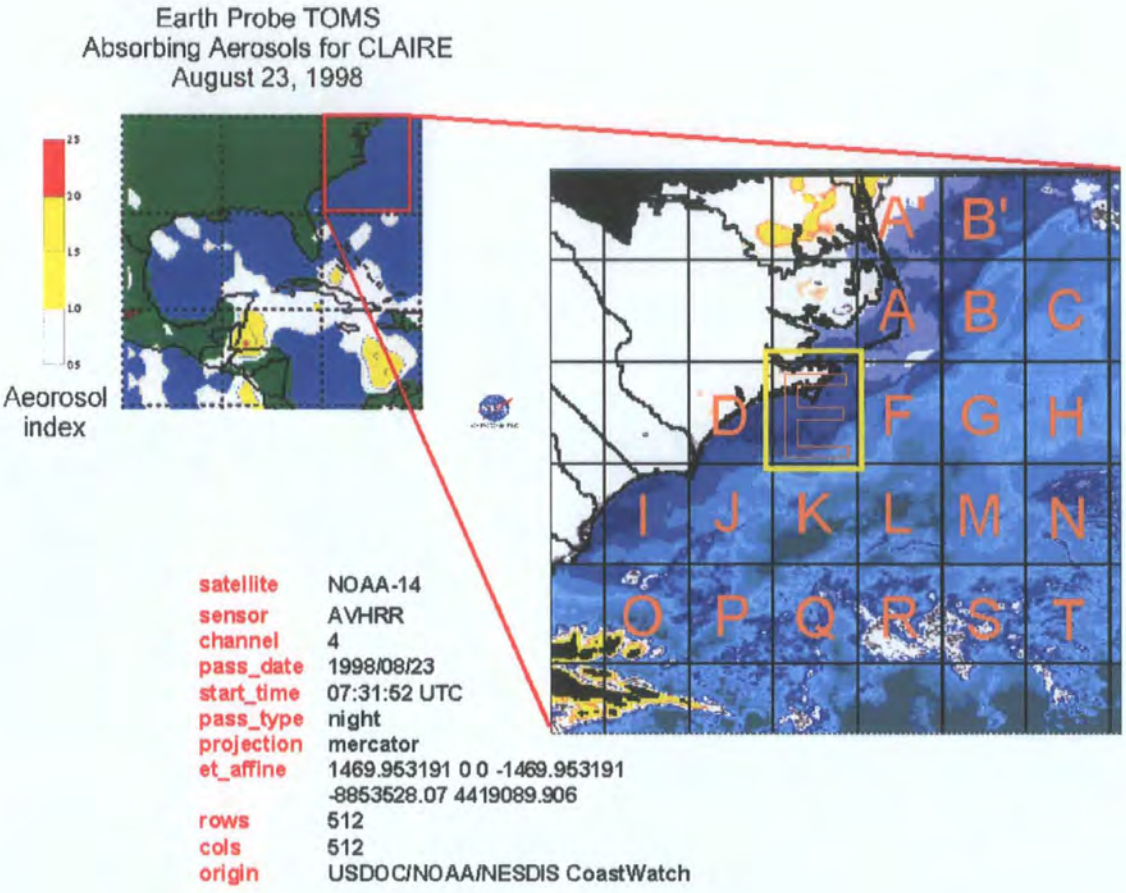

Figure 4.3. The northwestern coast of the US and its segmentation. Selection of valid channel 4 and 5 brightness temperatures (1.1 by 1.1 km pixel resolution) from individual sectors depended on the absence of clouds (using channel 1 CoastWatch data) and absorbing aerosols as detected by TOMS data.

Date	Image ID	SECTOR																							
		A'	B'	C'	A	B	C	D	E	F	G	H	I	J	K	L	M	N	O	P	Q	R	S	T
1998																								
Feb_18	908																							
Feb_18	910																							
Feb_18	922																							
Feb_19	008																							
Feb_19	012																							
Feb_20	123																							
Feb_20	207																							
Feb_20	211																							
Feb_20	222																							
Feb_21	207																							
Feb_21	211																							
Feb_21	222																							
Feb_25	608																							
Feb_25	611																							
Mar_14	307																							
Mar_15	408																							
Apr_13	308																							
May_16	607																							
Jun_03	407																							
Aug_23	507																							
Sep_05	808																							
Nov_28	208																							
1999																								
Jan_19	1908																							
Mar_17	600																							
Mar_17	607																							
Mar_23	208																							
Mar_29	808																							
Mar_30	900																							
Apr_14	400																							
Nov_07	100																							
Nov_07	108																							

Table 4.1. Cloud- and aerosol-free, valid geographical sectors (shaded in gray) from the South East coast area of the US. Visible and IR data from these sectors were retrieved during 1998 and 1999.

4.3.1.2.2. Assessing the applicability of the Yu & Barton (1994) SST calibration algorithm.

The mathematical formalism for this algorithm has been developed by Yu and Barton (1994), hereinafter referred to as YB94. The SST retrieval algorithm is equivalent to:

$$T_s = T_j + \frac{C_i}{C_i - R_{ij}C_j}\,(T_i - T_j) \tag{4.1}$$

where T_i is channel 4 brightness temperature, T_j is channel 5 brightness temperature and

$$\gamma = \frac{C_i}{C_i - R_{ij}C_j} \tag{4.2}$$

The coefficient γ is a temperature dependent variable. The ratio of the spatial variation of the brightness temperature in one channel to that in another channel, R_{ij}, is proportional to the ratio of their respective atmospheric transmittance. This ratio is used to determine the theoretical coefficient. In order to minimise these effects, a statistical method was used to determine the ratio as suggested by YB94. The general approach was as follows:

$$\frac{\Delta T_5}{\Delta T_4} = \sum_{s}^{n*n}\left(\frac{T_5(n) - \bar{T_5}}{T_4(n) - \bar{T_4}}\right) / N \tag{4.3}$$

where n*n is the matrix number and S is $[\frac{D}{2} \le |T_4(n) - \overline{T_4}| \le 2D]$. D is the dispersion of each valid pixel value of the 11 μm image from the mean radiance value of the entire sector, and N is the number of valid pixels. This selection ensures that the ratio does not include those cases where $T_4(n)$-$\overline{T_4}$ is close to zero.

Coastwatch data with extension *.lc3, *.lc4, *.lc5 and *.ls7 was retrieved and archived according to date. The software DECCON Version 1.0 (DECompression and CONversion of NESDIS CoastWatch Imagery Files) was provided by CoastWatch[67] and downloaded. The software was installed and used to decompress, navigate, convert and correct the above file extensions to the following configuration:

- Raw binary.
- Degrees Celsius.
- 0 to 31.7 range for channels 3, 4 and 5.
- 0 to 31.7 range for NLSST.
- Image overlay.
- 255 background colours.
- Graphics embedded.

Using ERMAPPER image processing software (version 5.5), the uncompressed binary data from each full scene as per ID was imported into 4 layers consisting of superimposed channel data and NLSST and saved as a multi-layer *.ers file. The entire geographical area was then displayed and data from each 1° by 1° sectors were extracted according to the annotated map shown in figure 4.2. Land pixels were masked using a formula that was applicable to all 4 layers by assigning a null value to the range of land pixel values measured. Individual channel layers and the NLSST layer of sectors with no cloud cover were then saved as individual *.ers files into separate folders with a 74 by 91 pixel matrix.

Cloud- and aerosol-free same-sector layers (table 4.1) were exported as ascii BIL files and imported into statistics software where every sectored 1° by 1° data (AVHRR temperature brightness information and NLSST) was re-scaled, using coefficients published by CoastWatch, as follows:

[67] *http://coastwatch.noaa.gov/cw_software.html (accessed on 01.11.04).*

If *ith* TB_j is null then null

else

$TB_{j(i)} = (0.124 + 273.16)$

$NLSST = NLSST_C * 0.124$

where TB_j is the brightness temperature from channels 3, 4 and 5, and $NLSST_C$ is the values of NLSST included in the raw CoastWatch datasets.

Following re-scaling, pixels that failed through a simple ratio test, a gross cloud check, night-time medium/high level cloud test, and a fog/low stratus test as described by Kriebel (1996) were nulled. Next, the difference between the individual brightness temperature pixels of channels 4 and 5 and the mean value derived for that entire sector $[T_i(n)-\bar{T}_i]$ was calculated. The dispersion was calculated for the total sectoral data for channels 4 and 5. The differences between valid *ith* TB_4 and TB_5, TB_4 and NLSST were calculated and the sectoral average noted.

Each sector dataset was further filtered by assigning null values to individual brightness temperature pixels from channels 4 and 5 showing greater than the given dispersion range. The number of valid and nulled pixels were noted. The ratio of individual channel 5 $[T_i(n)-\bar{T}_i]$ to channel 4 $[T_i(n)-\bar{T}_i]$ pixel values was calculated and noted.

The values C_4 and C_5 were then calculated according to the following relation (e.g. in the case of NOAA-14):

$$C_4 = (1.438833*929.3323/(TB_{4(i)} * TB_{4(i)}))*$$
$$(EXP(1.438833*929.3323/ TB_{4(i)})/$$
$$(EXP(1.438833*929.3323/ TB_{4(i)})-1))-(2/ TB_{4(i)}))$$

$$C_5 = (1.438833*835.1647/(TB_{4(i)} * TB_{5(i)}))*$$
$$(EXP(1.438833*835.1647/ TB_{5(i)})/$$
$$(EXP(1.438833*835.1647/ TB_{5(i)})-1))-(2/ TB_{5(i)}))$$

The averages for C_4 and C_5 for each sector were noted. The value for γ was calculated for each individual *ith* pixel according to:

If *ith* variance is null then null
else
$\gamma = C_{4(i)}/(C_{4(i)} - \text{ratio} * C_{5(i)})$

The average sectoral γ was also noted. The final SST was then derived using the following relation:

If $TB_{4(i)}$ is null then null
else
$SST=(-10.6 + 11.27 * \text{ratio}) + TB_{5(i)} + (\gamma * (TB_{4(i)} - TB_{5(i)}) - 273.16)$

where the first term in brackets expresses one of the split-window terms as formulated by YB94. The average, minimum, maximum, standard deviation and skewness of the range of SST derived from each sector were calculated and noted. The difference between the *ith* NLSST and the theoretically derived *ith* SST was also calculated and the sectoral average was calculated to note accuracy.

The following relationships were investigated:

1. derivation of SST using YB94 vs NLSST.
2. derivation of SST and NLSST vs the difference between these two values.

3. Statistical relationship between derived R_{54} ratios and γ values, with NLSST.

To test the validity of this regional algorithm, valid gridded XYZ ascii brightness temperature data collected as described in section 4.3.1.2.5. were converted to StatGraphics format and calibrated using the SST equation above. sea were calibrated. Valid gridded XYZ ascii brightness temperature data collected from suitable AVHRR scenes over the central Mediterranean were calibrated as described in section 4.3.1.2.5. using the YB94 algorithm. The resulting SST was then statistically compared with collocated TMI-derived SST scenes using basic statistical measures.

4.3.1.2.3. Derivation of multiple regression models based on the split window method.

The technique developed here is based on the relationship between the ratio of the variations of the satellite brightness temperatures derived from AVHRR channels 4 and 5.

From section 4.3.1.2.2., a look-up-table was produced giving the mean difference between $[TB_4\text{-}TB_5]$, the slope $[\Delta TB_4/\Delta TB_5]$, the NLSST and the total number of AVHRR pixels analysed.

Since the range of mean values for $[TB_4\text{-}TB_5]$ and the slope $[\Delta TB_4/\Delta TB_5]$ contain information about the instantaneous atmospheric water vapour profiles, data rows having the same slope values were grouped together and archived. From such groups, a list of multiple regression models were produced using StatGraphics Plus Version 3.0, each tagged to a specific value of $[TB_4\text{-}TB_5]$ and the corresponding $[\Delta TB_4/\Delta TB_5]$.

To test the applicability of this approach over the central Mediterranean region, valid gridded XYZ ascii brightness temperature data were converted to StatGraphics format and calibrated using equation 4.4

above. Suitable channel 4 and 5 brightness temperatures were derived as described in section 4.3.1.2.2. analysed, and their profile in terms of [TB_4-TB_5] and [$\Delta TB_4/\Delta TB_5$] was extracted. According to the resulting profile extracted from the data acquired in section 4.3.1.2.5., the relevant SST multiple regression model was selected. These data were statistically compared with collocated TMI-derived SST scenes using basic statistical measures.

4.3.1.2.4. Use of the Coll *et al.* (1994) "regional" split-window algorithm.

The applicability of the linear mid-latitude algorithm derived by Coll *et al.* (1994) using the French CMS-Lannion dataset was assessed. This dataset is composed of 348 points partly collected over the Mediterranean Sea (Antoine *et al.,* 1992). The optimised split-window algorithm for this data is:

$$SST = TB_4 + 2.13*(TB_4-TB_5) + 0.18 \qquad (4.4)$$

To test the validity of this regional algorithm, valid gridded XYZ ascii brightness temperature data collected as described in section 4.3.1.2.5. were converted to StatGraphics format and calibrated using equation 4.4 above. The resulting SST was then statistically compared with collocated TMI-derived SST scenes using basic statistical measures.

4.3.1.2.5. Calibration of high-resolution, infrared radiances acquired over the ocean model domain.

Local Area Coverage (LAC) 1.1 km AVHRR imagery for the period July 20th 1999 to August 7th 1999 containing 16-bit channels 3, 4 and 5 radiance data were retrieved from NOAA's Satellite Active Archive (SAA)[68] and archived. Raw (uncalibrated) infrared radiances from

[68] *http://www.saa.noaa.gov (accessed on 01.11.04).*

swaths covering the spatial domain of the ocean forecasting system: (15.78°E, 33.18°N) to (19.18°E, 35.74°N) were extracted and archived.

ERDAS Imagine V8.4 Professional was used to import, calibrate and process individual data. By using the Import/Export option (Type: NOAA AVHRR) files were imported from the archive using the following rectification settings:

- Panoramic Distortion Correction applied.
- Write Transform to Image.

and radiometric and scan angle[69] settings:

- Radiometric Calibration applied.
- Sun Angle Correction applied[70].

The Import options were the following:

- Output data compression: none.
- Unsigned 16-bit; Block Size: 64.
- Select Layers: 1-3.
- Creation of Pyramid Layers enabled.

The entire archive was imported and checked. Scenes showing extensive contamination by cloud and dust were discarded (table 4.2).

The rectangle properties of the area of interest (AOI) were defined using the Viewer option and saved as domain.aoi. The full AVHRR scene was resampled to within the AOI boundaries to derive a new output

---

[69] *Radiometric corrections allowed calibration constants and sun angle data present in the AVHRR data to be applied to the data. The constants (slope and intercept) and sun angle data convert the raw pixel values to energy measured by the sensor in units of milliwatts per square meter per steradian per centimeter in Bands 3, 4, and 5, and further into brightness temperature.*

[70] *This allows a basic correction (1 / cosine({sun angle})) to be applied to the pixel values.*

consisted of separate channel 3, 4 and 5 brightness temperature data having an unsigned 16-bit format. Data was instead exported in Surfer binary grid (*.grd), imported using ERMapper V5.5 and exported in gridded XYZ ascii.

Using the above three algorithms (i.e. YB94, multiple regression models, and Coll94), infrared radiances of the sea surface were calibrated and their accuracy assessed. The final 1.1 km by 1.1 km SST maps were used to validate the SST forecasts produced by the ocean model.

Image	Sat/Orbit no.	Date	Time (UT)	Data Integrity over domain
N14/NSS.LHRR.NJD99201.S1415.E1427.B234	LAC/23466	Jul 20 1999	13:15:55	no contamination
N14/NSS.LHRR.NJD99202.S1404.E1415.B234	LAC/23480	Jul 21 1999	13:04:29	no contamination
N14/NSS.LHRR.NJD99203.S1353.E1404.B234	LAC/23494	Jul 22 1999	12:53:00	no contamination; presence of dust aerosols over Gulf of Gabbes moving eastwards
N14/NSS.LHRR.NJD99204.S1352.E1352.B235	LAC/23508	Jul 23 1999	12:41:33	no contamination; presence of dust aerosols
N14/NSS.LHRR.NJD99205.S1330.E1341.B235	LAC/23522	Jul 24 1999	12:30:10	presence of dust aerosols and cloud coverage
N14/NSS.LHRR.NJD99206.S1318.E1330.B235	LAC/23536	Jul 25 1999	12:18:40	presence of extensive dust aerosols and cloud coverage
N14/NSS.LHRR.NJD99207.S1307.E1318.B235	LAC/23550	Jul 26 1999	12:07:25	presence of dust aerosols and cloud coverage
N14/NSS.LHRR.NJD99208.S1255.E1307.B235	LAC/23564	Jul 27 1999	11:55:58	presence of dust aerosols and extensive cloud coverage
N14/NSS.LHRR.NJD99209.S1244.E1255.B235	LAC/23578	Jul 28 1999	11:42:22	presence of extensive cloud coverage
N14/NSS.LHRR.NJD99210.S1455.E1426.B235	LAC/23593	Jul 29 1999	13:15:11	presence of extensive cloud coverage
N14/NSS.LHRR.NJD99211.S1403.E1414.B236	LAC/23607	Jul 30 1999	13:03:29	presence dust aerosols and clouds
N14/NSS.LHRR.NJD99212.S1352.E1403.B236	LAC/23621	Jul 31 1999	12:52:09	presence of cloud coverage
N14/NSS.LHRR.NJD99213.S1340.E1352.B236	LAC/23635	Aug 01 1999	12:40:35	presence of dust aerosols and cloud coverage
N14/NSS.LHRR.NJD99214.S1329.E1340.B236	LAC/23649	Aug 02 1999	12:29:07	presence of dust aerosols and extensive cloud coverage
N14/NSS.LHRR.NJD99216.S1306.E1317.B236	LAC/23677	Aug 04 1999	12:06:16	presence of cloud coverage
N14/NSS.LHRR.NJD99217.S1254.E1306.B236	LAC/23691	Aug 05 1999	12:54:53	presence of extensive cloud coverage
N14/NSS.LHRR.NJD99218.S1243.E1254.B237	LAC/23705	Aug 06 1999	11:43:31	extensive cloud coverage; partial satellite coverage over area of interest
N14/NSS.LHRR.NJD99219.S1229.E1236.B237	LAC/23719	Aug 07 1999	11:29:04	no satellite coverage over area of interest

Table 4.2. Details of individual AVHRR LAC scenes, including data integrity, collected over the central Mediterranean during the period 20 July – 7 August 1999. Source: Satellite Active Archive – NESDIS.

4.3.1.3. Outgoing longwave radiation.

Monthly values of total, day and night outgoing longwave radiation over the area of interest were retrieved by ftp from the SAA archive. The source of this 1999 climatological data is from the NOAA Pathfinder Programme. The resolution of each pixel within the subset is equivalent to 1° by 1° latitude – longitude. From this data the monthly mean outgoing longwave radiation was derived.

4.3.1.4. Aerosol optical thickness.

Monthly datasets consisting of aerosol optical thickness covering a ten-year period between 1990 and 2000 were downloaded from the SAA archive in ascii format. This dataset consisted of physical information derived from the Pathfinder dataset. Datasets relevant to the area of interest with a nominal grid resolution of 2.5° by 2.5° latitude-longitude, were downloaded and archived. From this data, a ten-year average monthly aerosol optical thickness was derived over the area of interest.

4.3.1.5. Climatological fields.

Monthly climatological fields over the Mediterranean region were derived from two sources:

(a) Naval European Meteorology and Oceanography Centre (NEMOC) in Rota, Spain[71]

The original source for this data is the Comprehensive Ocean and Atmosphere Data Set (COADS). The data has been smoothed into sparse regions for continuity using a bicubic interpolation method.

---

[71] *https://www.nemoc.navy.mil/data/unclass/static/climo/med/ (accessed on 01.11.04).*

Air and sea surface temperature were extracted from the original data and geo-rectified using ERMapper. The exact geographical area corresponding to the area of interest was specified and monthly air- and sea surface temperature sets were geo-linked, and individually saved in *.ers format. Using the look-up-table provided, pixels within the subset were converted into Kelvin.

Calibrated raster files of air and sea surface temperature were then overlaid to derive the monthly mean difference. The final map was converted into ascii BIL format for subsequent statistical analysis.

(b) Southampton Oceanography Centre (SOC) Ocean – Atmosphere Heat, Momentum and Freshwater Flux Atlas.

The Southampton Oceanography Centre (SOC) Ocean – Atmosphere Heat, Momentum and Freshwater Flux Atlas was used to derive relevant datasets of marine meteorological reports spanning the period 1980 – 1993.

This Atlas[72], comprising of air-sea fluxes and meteorological data was extracted in ascii form. Monthly values of SST, surface air temperature, latent and sensible heat fluxes were extracted in ascii format with 9 fields to a line. Each line has flux estimates for a 1° by 1° cell centered on the longitude, latitude values specified in the first two columns; land is indicated by –999. The grid runs from (84.5°S, 179.5°W) to (84.5°N, 179.5°E) so there are 61,200 cells in total. The fields used are longitude, latitude, wind speed (m s^{-1}), 10 m air temperature (°C), 10 m stability dependent specific humidity (g kg^{-1}), sea surface temperature (°C), and relative humidity. These were extracted separately from the original file format in ascii xyz and imported into ERMapper. The values falling within the area of interest (15.78°E, 33.18°N) to (19.18°E, 35.74°N) were extracted, gridded, contoured mapped and summary statistics were

[72] *http://www.soc.soton.ac.uk/JRD/MET/fluxclimatology.html (accessed on 01.11.04).*

calculated to note the maximum, minimum, mean and standard deviation of each respective field for every season.

4.3.1.6. Derivation of instantaneous turbulent heat fluxes.

The bulk aerodynamic method with stability dependent bulk transfer coefficients as described by Liu *et al.* (1979) was used to generate instantaneous air-sea fluxes. The basic parameters required were air temperature, SST and 10 m wind magnitude. The SST and wind speed were obtained from instantaneous, collocated retrievals from the TMI sensor.

(a) *Semi*-instantaneous air temperature.

The monthly average sea – air temperature difference over the area of interest was calculated as follows, which is a modification of the method used by Schulz *et al.* (1997), in order to obtain a more realistic estimate (see section 3.2.2.2.):

$$T_{DIFF} = [T_{sCOADS} - T_{aCOADS}] \quad (4.5)$$

where T_{DIFF} is the monthly difference between the average SST and air temperature values derived from COADS data over the area of interest[73]. By including the monthly term from the remotely-sensed SST, a *semi*-instantaneous air temperature was obtained accordingly:

$$T_a = [T_{sTMI} - T_{DIFF}] \quad (4.6)$$

(b) Sensible heat flux.

Using the bulk parameterisation, the sensible heat flux is estimated with transfer coefficients that relate the flux to variables measured, i.e.

[73] *derived in section 4.3.1.5.*

$$Q_H = \rho c_p C_H u_a (T_s - T_a) \quad (4.7)$$

where Q_H is the sensible heat flux; C_H is the Stanton number (=0.00125 as provided by Liu *et al.* (1979) for moderate wind speed, slightly unstable conditions); T_S is the SST in K; T_A is the air temperature in K (calculated using equation 4.8); ρ is the density of air (=1.2256 kg m^{-3}); c_p is the specific heat of water at constant pressure (=1010 J kg^{-1} K^{-1}); and u_a is the 10 m wind speed in m s^{-1}.

(c) Latent heat flux.

The bulk formula that parameterises the flux mainly as a function of near-surface wind speed, air humidity and sea surface temperature was used to derive the latent heat flux as follows:

$$Q_E = \rho L C_E u_a (q_s - q_a) \quad (4.8)$$

where Q_E is the latent heat flux; C_E is the Dalton number; q_s and q_a are the specific humidity at ocean surface at Z height above sea water; ρ is the density of air (=1.2256 kg m^{-3}); u_a is the 10 m wind speed in m s^{-1} and L is the latent heat of vaporisation of water. C_E is the Dalton number equivalent to 0.00125 (Liu *et al.,* 1979).

Gill (1982) defines L by the equation

$$L(T_A) = 2.5008 \times 10^6 - 2.3 \times 10^3 T_A \quad (4.9)$$

q_S is the saturation specific humidity at T_S

$$q_S = \frac{0.622e^*(T_S)}{P_S - 0.378e^*(T_S)} \quad (4.10)$$

q_A is specific humidity at T_A

$$q_a = \frac{0.622re^*(T_A)}{P_Z - 0.378e^*(T_A)} \tag{4.11}$$

$e^*(T_A)$ is the vapour pressure (mb) of the air at a height of 10m and P_z is the pressure at z height. $e^*(T_A)$ is obtained from the specification of T_A and relative humidity, r (Brutsaert, 1982). Oberhuber (1988) used

$$e^*(T_x) = 6.11 \times 10^{(Tx-273.16)/(Tx-35.86)*7.5} \tag{4.12}$$

for saturation vapour pressure, where T_x is the air surface temperature.

The value of relative humidity is equal to the ratio:

$$r = \frac{e_A}{e_S} \tag{4.13}$$

where e_A and e_S are the actual vapour pressure and saturation vapour pressure at sea surface respectively.

According to Smith *et al.* (1991), e_A is calculated from the equation

$$e_A = \left(1 - \frac{T_K}{T_{KV}}\right)\frac{P}{0.378} \tag{4.14}$$

where T_K is the absolute temperature (=273.16 + T_A) and T_{Kv} is the virtual temperature[74]. For average conditions (i.e. e_A in the range of 1-5 kPa and P between 80-100 kPa), T_{Kv} can be approximated as

$$T_{Kv} \approx 1.01(T_A + 273) \tag{4.15}$$

---

[74] *The virtual temperature is the temperature of dry air that would have the same density and pressure as the moist air.*

The atmospheric pressure P at elevation z (kPa) can be calculated according to Burman *et al.* (1987) as

$$P = 101.3\left(\frac{293 - 0.0065z}{293}\right)^{5.26} \qquad (4.16)$$

assuming that $P_0 = 101.3$ kPa at $z_0 = 0$, and $T_{K0} = 293$ K for T = 20 °C.

The saturation vapour pressure was calculated as a function of temperature using a variation of the integrated form of the Clausius-Clapeyron equation (see AWIPS technical documentation[75]). An additional linear term is added to this value in order to give a better fit to the measured relationship of saturation vapour pressure and temperature in the Smithsonian Meteorological Tables. The equation for calculating saturation vapour pressure is:

$$e_s = \exp\left(26.66082 - 0.009138T - \frac{6106.396}{T}\right) \qquad (4.17)$$

where T is the temperature. The saturation vapour pressure formula is accurate to one part in a thousand over the range from –25 °C to 35 °C.

4.3.2. Accuracy of the derived database.

A multi-sample comparison analysis was performed to statistically compare the derived database with independent data derived from the Southampton Oceanography Centre (SOC) Ocean – Atmosphere Heat, Momentum and Freshwater Flux Atlas.

---

[75] *http://www.meted.ucar.edu/awips/validate/dewpnt.htm (accessed on 01.11.04).*

Summary statistics were calculated by comparing the average 1999 monthly values of the two databases. Statistics included data count, average, standard deviation, mean difference and mean error.

4.3.3. The database format.

The data was arranged into two main groups as shown in table 4.3. The first set of data consists of instantaneous fields that are co-temporal with the models' predicted fields. Validation of single forecast days for verification rested on the time of acquisition of the instantaneous variables/derived products over the area of interest.

The second set of data consisted of monthly climatological means of the relevant geophysical fields.

Group 1
Instantaneous, high-resolution fields collocated with individual model forecast fields
Precipitation rate
Absorbing aerosols
10 m wind magnitude
Sea surface temperature
Cloud liquid water vapour
Integrated precipitable water vapour
Turbulent heat fluxes (latent & sensible heat)
Group 2
Climatological, coarse, monthly means over the area of interest
Aerosol optical thickness
Outgoing long wave radiation
Air temperature, Sea Surface Temperature

Table 4.3. The two groups of datasets that constituted the current database.

4.4. Results and discussion.

4.4.1. The quality of the database.

A systematic monthly comparison was done on the instantaneous acquired/derived fields against the global SOC climatology data (fig. 4.4) to quantify the accuracy of the database[76]. It is important to note that the SOC atlas covers only monthly average fluxes at a horizontal resolution of 1° by 1°, against the 0.25° by 0.25° resolution of the acquired instantaneous parameters (10 m wind magnitude, SST, surface air temperature, total precipitable water vapour and cloud liquid water).

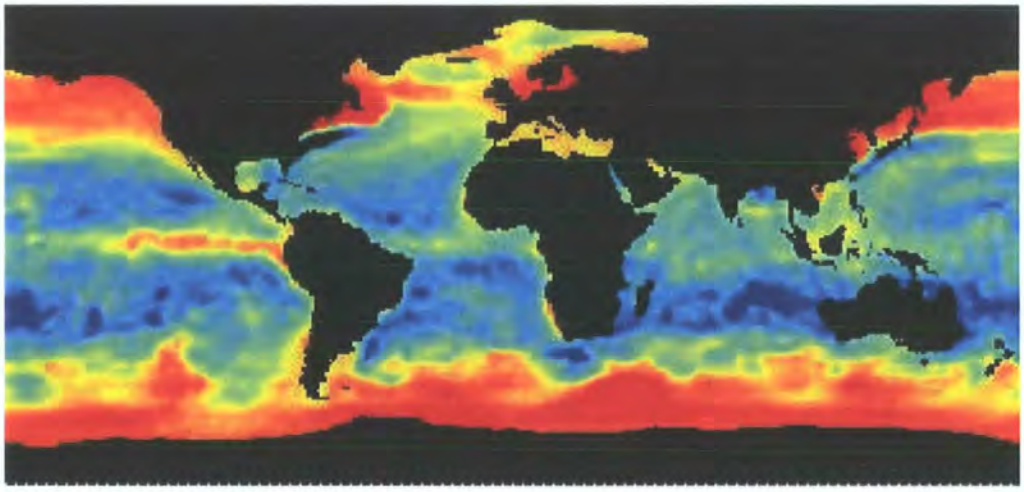

Figure 4.4. Global distribution of latent heat flux during the month of April (mean: 10.77 W m^{-2}; standard deviation: 5.54 W m^{-2}; Source: SOC Ocean-Atmosphere Heat, Momentum and Freshwater Flux Atlas).

The SOC climatology was developed by the Hadley Centre (UK Meteorological Office) and detailed information about the accuracy of this dataset is provided by Josey *et al.* (1999). Josey (2001) and Josey *et al.* (2002) verified the SOC wind stress and surface heat flux

[76] *Full statistical data are shown in Appendix V.*

climatology against NCEP/NCAR, ECMWF, UWM/COADS, moored buoys and against the Hellerman and Rosenstein datasets, concluding that it is a valuable wind climatology dataset that can be used in contemporary hydrographic and modelling studies.

Figures 4.5 and 4.6 are examples of rasterised monthly datasets derived from the SOC and the instantaneous database over the area of interest. The most noticeable feature is the higher mesoscale definition of the basic variables and estimated air-sea fluxes, since these are based on the TMI sensor's resolution of 0.25° compared with a 1.0° resolution of the climatological database. However, both sets of data show broad spatial similarities.

SOC Ocean-Atmosphere Heat, Momentum and Freshwater Flux Atlas

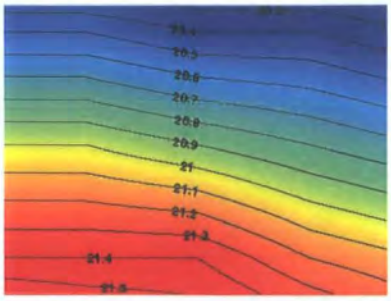

Sea surface temperature (°C)

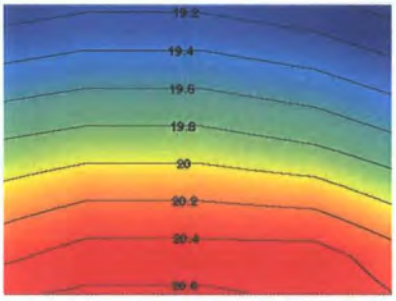

Surface air temperature (°C)

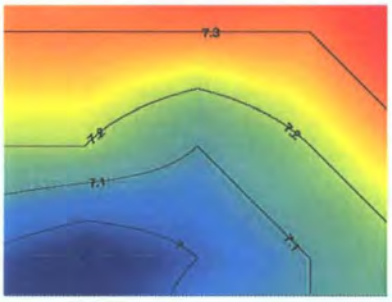

10 m wind magnitude (m s^{-1})

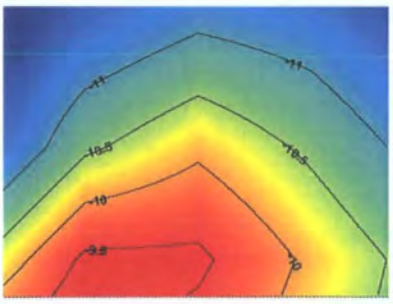

Sensible heat flux (W m^{-2})

Database of instantaneous basic fields and fluxes

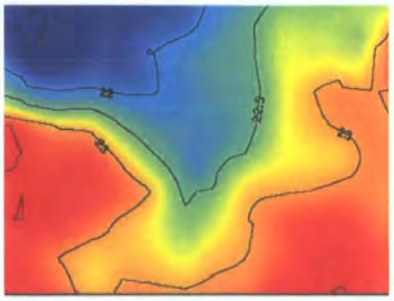

Sea surface temperature (°C)

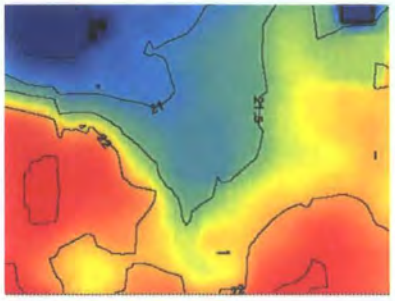

Surface air temperature (°C)

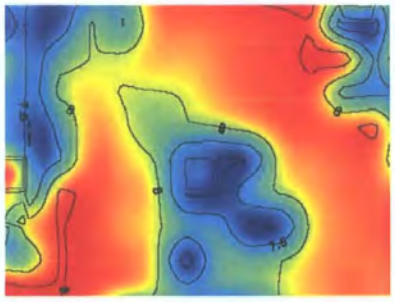

10 m wind magnitude (m s^{-1})

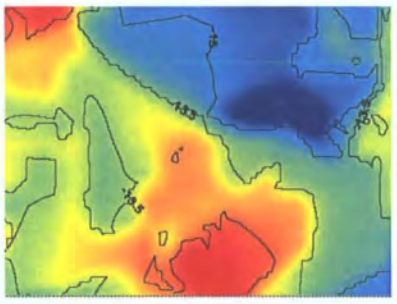

Sensible heat flux (W m^{-2})

Figure 4.5. Example of monthly averages derived from the SOC Atlas (left) and constructed database (right) during the month of November 1999. Data covers the area of interest (15.78°E, 33.18°N) to (19.18°N, 35.74°N). Temporal range of monthly mean of the acquired, instantaneous fields: 12-23 UT.

SOC Ocean-Atmosphere Heat, Momentum and Freshwater Flux Atlas

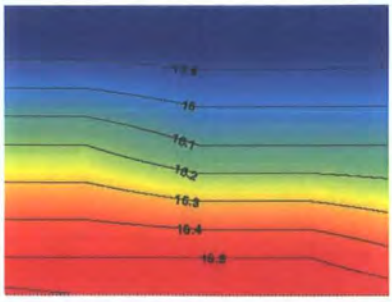

Sea surface temperature (°C)

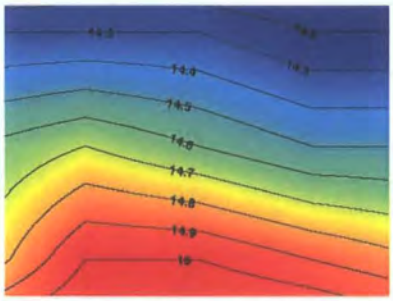

Surface air temperature (°C)

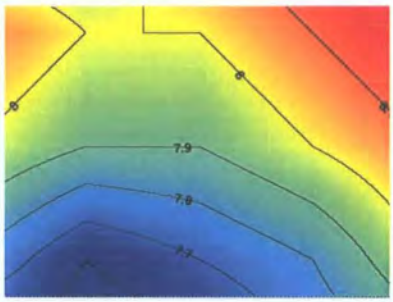

10 m wind magnitude (m s^{-1})

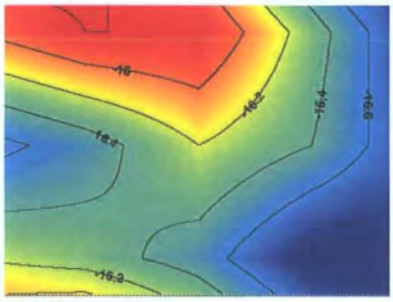

Sensible heat flux (W m^{-2})

Database of instantaneous basic fields and fluxes

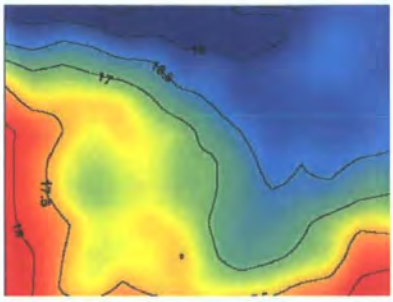

Sea surface temperature (°C)

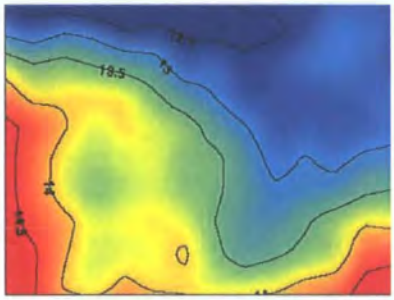

Surface air temperature (°C)

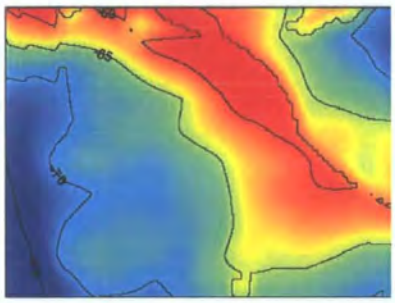

10 m wind magnitude (m s^{-1})

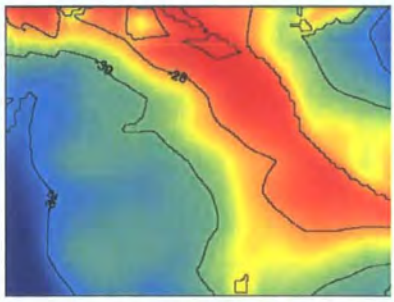

Sensible heat flux (W m^{-2})

Figure 4.6. Example of monthly averages derived from the SOC Atlas (left) and constructed database (right) during the month of January 1999. Data covers the area of interest (15.78°E, 33.18°N) to (19.18°C, 35.74°N). Temporal range of monthly mean of the acquired, instantaneous fields: 03-09 UT.

4.4.1.1. Surface wind magnitude.

The average monthly 10 m wind magnitude derived by remote sensing is in good agreement with the average SOC climatology data (figs. 4.7 and 4.8) over the Ionian basin, with a mean bias of 1.2 m s^{-1} (fig. 4.9). The monthly trend for the remotely sensed fields concurs with the description provided by Castellari *et al.* (1998), with a wind field maximum in winter due to strong mistral winds (December – February).

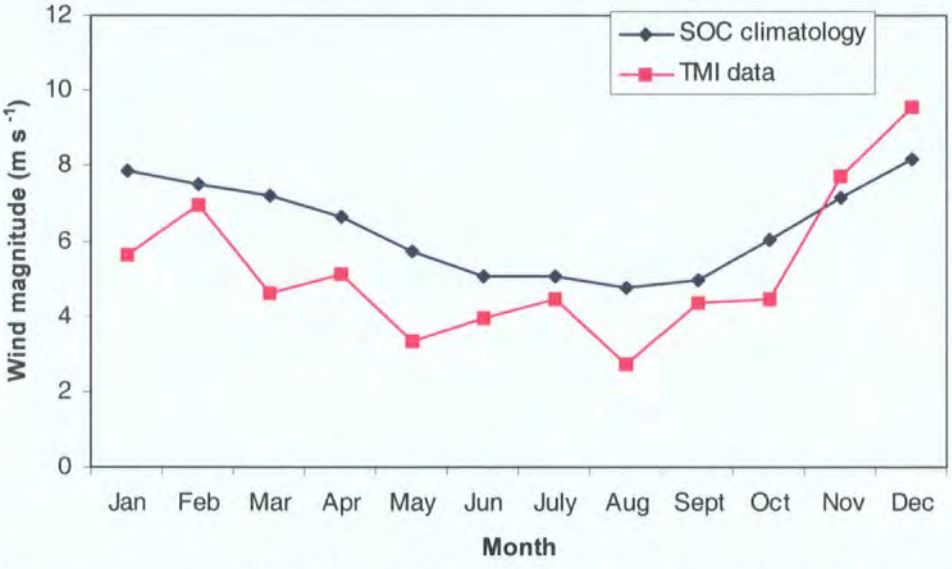

Figure 4.7. Average 10 m wind magnitude (m s^{-1}) over the area of interest for 1999. The monthly data derived from SOC data shows a generally higher magnitude than the data acquired by the tropical microwave imager.

The smaller fluctuation of the SOC climatology data is attributed to its larger database, smoothed out by data collected over a 13-year period. On the other hand, the TMI data reflects the monthly trend for data collected only during 1999, and each monthly value is based on a varying number of observation dates depending on the availability of satellite overpass.

The monthly average and standard deviation of the remotely-sensed wind magnitude during the study period is shown in figure 4.8. It shows a normal annual trend, with minima during the month of August

and maxima during December. The variability of basin average wind speed amplitudes is larger in winter than in summer due to strong northerly Mistral component, as has been observed by Castellari *et al.*, 1998, and this gives rise to increased variability of the field over the Ionian basin.

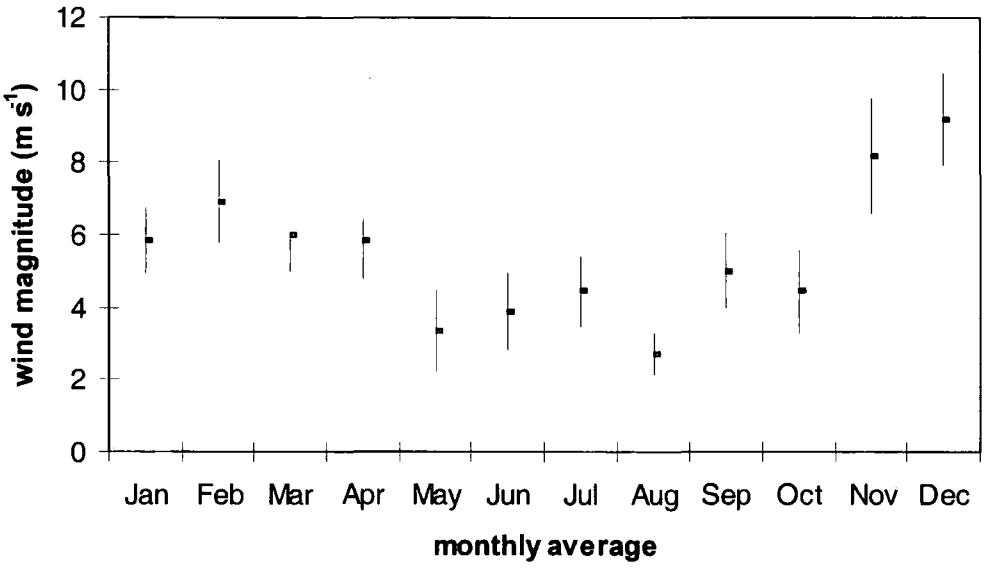

Figure 4.8. Annual trend of the mean and standard deviation of the remotely sensed wind magnitude (m s^{-1}) acquired during 1999 over the area of interest.

A close inspection of figure 4.9 shows a constant bias of around 1.5 m s^{-1} against COADS data during the first 6 months (January to June), which then decreases during the remaining 6 months (July to December). The increased magnitude of the remotely sensed wind data during the latter half of the year may indicate an irregular trend that occurred in the region during 1999 as compared to the monthly average 10-year climatology. This trend will be eventually reflected in the estimated set of instantaneous sensible and latent heat fluxes, since their estimation is directly proportional to the wind speed retrieved by the TMI sensor.

As far as the published global accuracy of the TMI-derived wind data is concerned, the published RMS is 0.84 m s^{-1} when the retrievals were

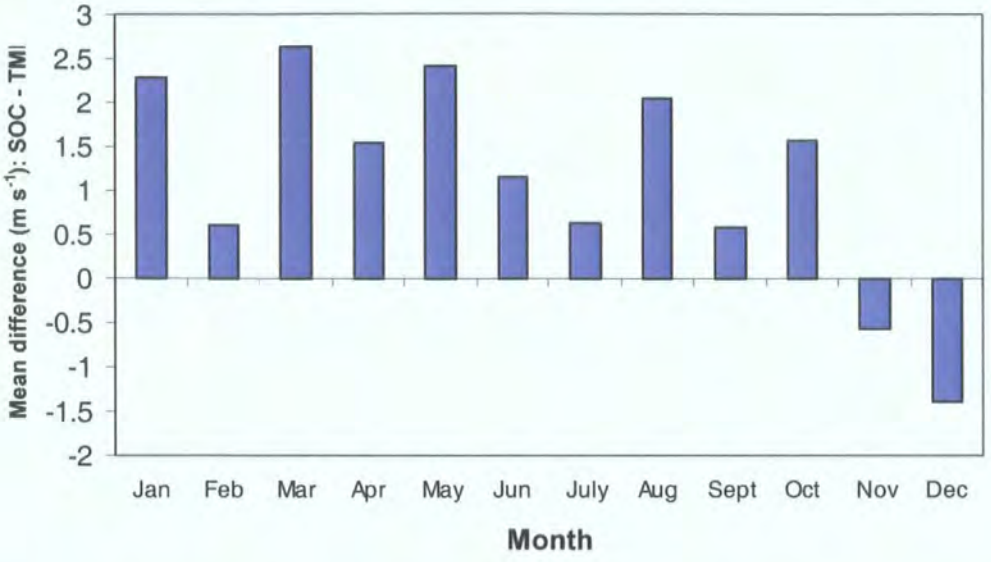

Figure 4.9. Average mean difference between SOC- and TMI-wind magnitude (m s^{-1}) derived during 1999 over the area of interest. A decreasing bias is noticeable during the high wind speed months.

compared with around 20,000 collocated buoys globally during the period 1998-2000[77]. Meissner *et al.* (2001) noted that within the northern latitudinal band (30°N to 80°N), the high wind speeds exhibited during winter lead to strong biases in the calibration procedure. This is close to the tendency of the bias between the TMI-retrieved and the SOC wind speeds seen during November - December.

Due to their accuracy and high resolution, the use of remotely-sensed wind data to calculate the instantaneous turbulent heat fluxes presents a better alternative than when using global modelled data. Castellari *et al.* (1998) observed that global modelled data very often drift from climatological datasets (such as the Hellerman and Rosenstein datasets) and May (1986) climatological data sets) resulting in an over-estimation of the dominant westerly component of the wind stress over the Mediterranean basin.

[77] *http://www.ssmi.com/tmi/tmi_validation.html#wind (accessed on 01.11.04).*

4.4.1.2. Air-sea temperature difference.

The monthly average air-sea temperature difference over the area of interest is shown in figure 4.10. The mean annual value is –0.61 °C with a standard deviation of 0.82 °C, a minimum of –1.6 °C during winter and a maximum of 0.8 °C during summer.

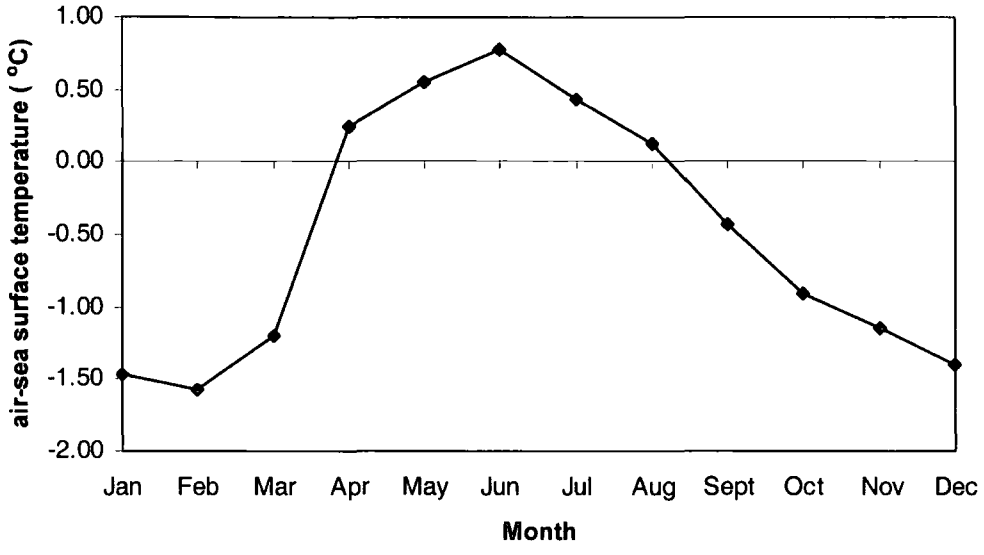

Figure 4.10. Annual trend of the air-sea temperature difference (in °C) during 1999 over the area of interest.

The monthly values of surface air surface derived from COADS and SOC climatology are very similar (fig. 4.11), with the COADS data showing a slightly higher average temperature profile than the SOC and semi-instantaneous measurements. The profile derived using the semi-instantaneous approach described in section 4.3.1.6. shows a close agreement to both climatological profiles. It has an annual mean air temperature of 20.8 °C and a standard deviation of ± 5.0 °C. The annual average difference between this and the two climatological datasets (i.e. SOC and COADS) is + 1.7 °C and + 0.9 °C, respectively. This makes it closer to the COADS multi-annual climatological dataset.

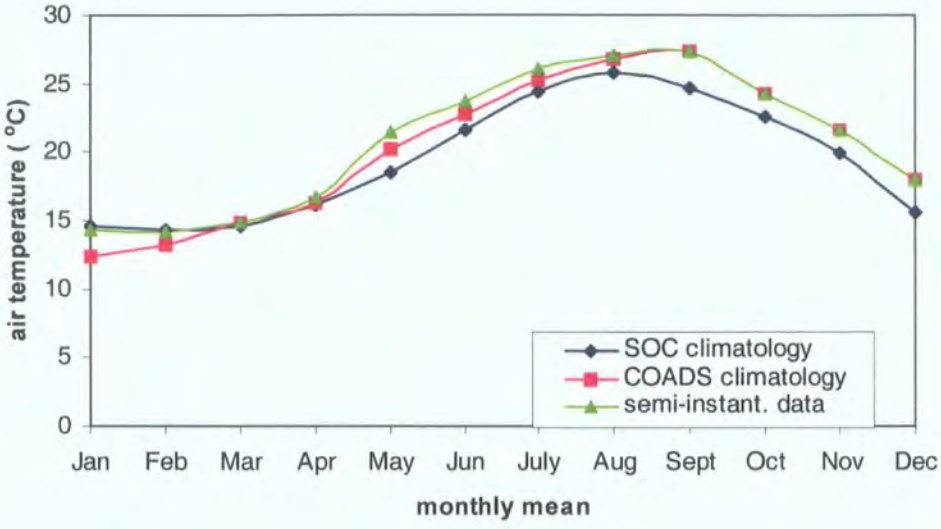

Figure 4.11. Domain average trend of surface air surface temperature (°C). The quasi-instantaneous data shows a close agreement with the two, multi-annual climatological profiles.

The measurement of air temperature from remote sensing continues to be problematic and more research is required (GEWEX, 1999). The approach used by this study to the calculation of air surface temperature (section 4.3.1.6.) represents a viable alternative that is more sophisticated than that followed by Schluessel *et al.* (1995) and Schulz *et al.* (1997). These investigators derived the annual profile of the air temperature over the sea by subtracting the SST with a constant surface air temperature value throughout the year. Castellari *et al.* (1998) slightly improved this treatment by further defining this relationship and giving two distinct values for winter and summer.

A limitation in the present derivation of the air temperature is that no correction is given for the diurnal variation, which may lead to surface temperature that may range by 1.2 °C (Webster *et al.*, 1996). Table 4.4 shows the monthly average time of the TRMM satellite overpass in 1999 during which instantaneous geophysical fields were collected and archived. Some anomalies can arise when these fields are averaged out

on a monthly basis since this step lacks data normalisation to account for diurnal variation. This can contribute to the monthly variability shown by the semi-instantaneous air-temperature data.

Month	Average time of satellite overpass (UT)
Jan	04.00
Feb	22.50
Mar	22.75
Apr	24.00
May	19.80
Jun	10.90
Jul	02.00
Aug	18.75
Sep	21.90
Oct	04.00
Nov	17.36
Dec	22.50

Table 4.4. The average time of TRMM satellite overpass during 1999 during which instantaneous geophysical fields were collected and archived.

4.4.1.3. Sea surface temperature.

Results show a good agreement between the annual trends of the remotely sensed (mean: 21.3 °C; standard deviation: ± 4.6 °C) and climatological data (mean: 20.2 °C; standard deviation: ± 4.1 °C) as shown in figure 4.12. The mean overall difference from SOC data is 1.1 °C (fig. 4.13).

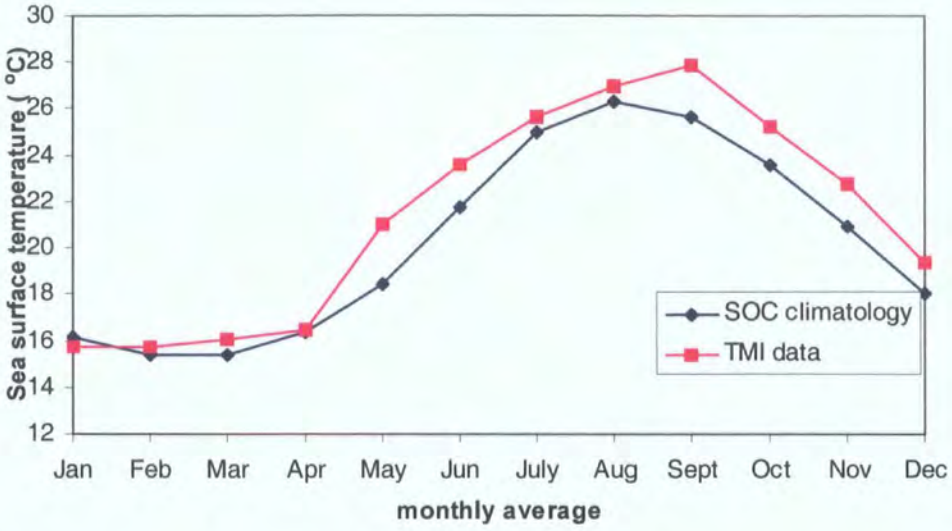

Figure 4.12. Annual trends of the SST data (in °C) from the two data sources for 1999 over the area of interest.

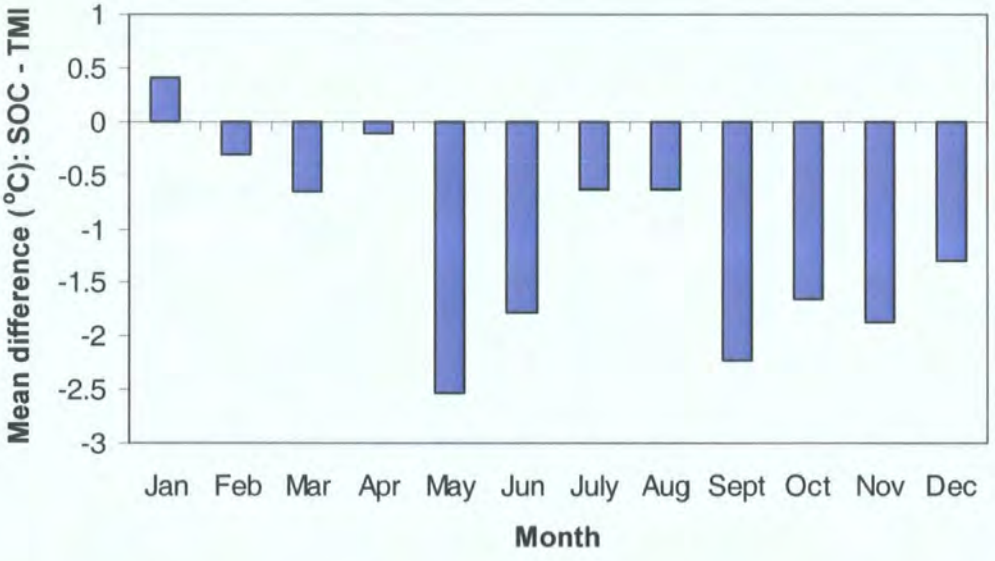

Figure 4.13. Annual trend of the monthly difference (in °C) between the two datasets (SST_{SOC} minus SST_{TMI}) during 1999.

This observed bias is partly attributed to the fact that unlike SOC data, the remotely-sensed SST is a skin-SST, measured within a thin water layer (~500 μm) at the air-sea interface where conductive and diffusive heat transfer processes dominate. A strong temperature gradient is characteristically maintained in this thin layer sustained by the magnitude and direction of the ocean-atmosphere heat flux. Concerning

the accuracy of TMI-derived SST, data comparison made during December 1997 to June 1999 with over 9000 TMI to TAO/NDBC buoy collocations showed an averaged difference of around 0.15 ^{o}C[78]. The causes for this error include the accuracy of satellite retrievals, the spatio-temporal mismatch between the buoy point observation and the satellite footprint, and the difference between the ocean skin temperature and the bulk temperature measured at the buoys at 1 to 1.5 m depth.

4.4.1.4. Ocean surface heat flux.

As mentioned in section 3.2.2., the use of bulk formulae presents a good alternative to the sparse distribution of direct flux measurements. This approximation can be calculated using basic variables that can be collected *in situ* or by remote sensing. Since there is no *in situ* data available over the Ionian basin during the study period, and since climatological data only provide coarse monthly averages, this study utilised instantaneous fields acquired by the orbiting microwave sensor over the area of interest to estimate the instantaneous air-sea fluxes.

The estimated sensible heat flux database is in good agreement with the average SOC climatology data derived over the Ionian basin. Both datasets exhibit the same temporal trend with the least flux transfer from the air to the sea occurring during the warm months. Strong winds and greater air-sea temperature difference drive a larger negative flux during the colder months as shown in figure 4.14. The monthly mean variability of the calculated dataset is shown in figure 4.15.

[78] *http://www.ssmi.com/tmi/tmi_validation.html#sst*

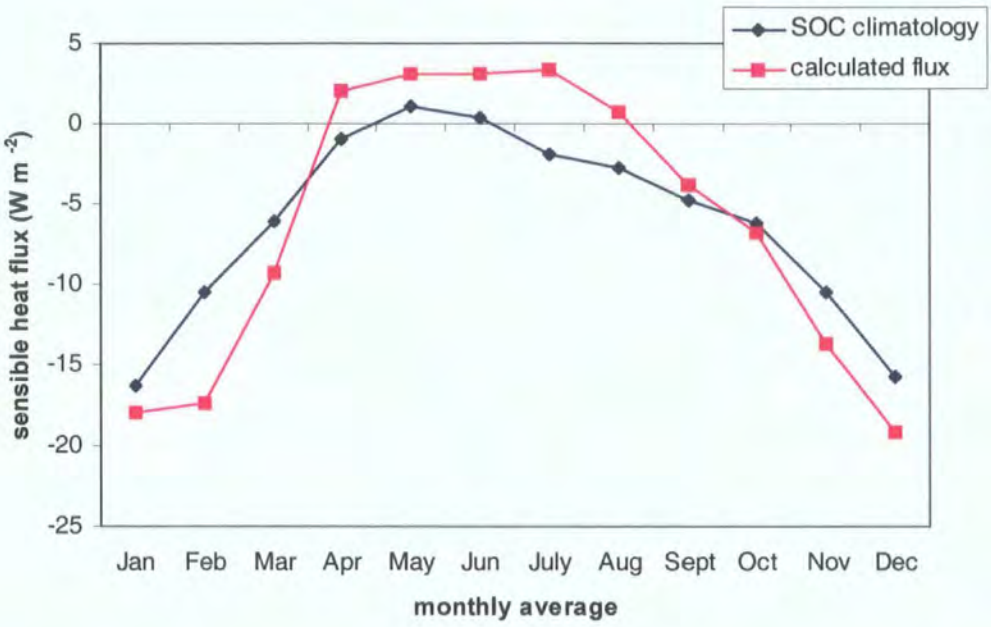

Figure 4.14. Comparison between the monthly means of the estimated heat flux data and SOC climatology (in W m^{-2}) over the area of interest.

The Mediterranean Sea is characterised by a sensible heat flux that shows a strong inter-annual variability with maxima during January and December, attributed to strong Mistral and lowest air temperature in the same period (Castellari *et al.*, 1998). Minimal downward flux for the entire Mediterranean basin occur around July and is related to the maximum in air temperature. The results from this study show an annual average value for the calculated sensible heat flux of -5.9 ± 8.5 W m^{-2} compared to an annual average value of -6.2 ± 5.9 W m^{-2} given by the SOC data over the same area of interest. The mean annual difference is -0.3 W m^{-2}, which is considered to be a very good estimate against the climatology data (fig. 4.16). The constantly low variability during the summer months is particularly striking (fig. 4.15).

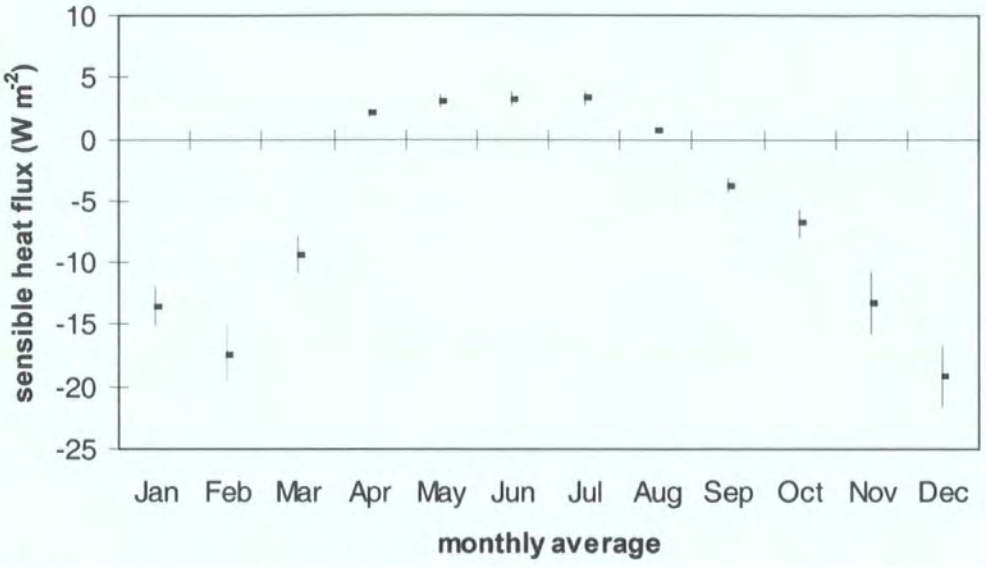

Figure 4.15. Annual trend of the parameterised, monthly mean sensible heat flux (W m^{-2}) over the area of interest.

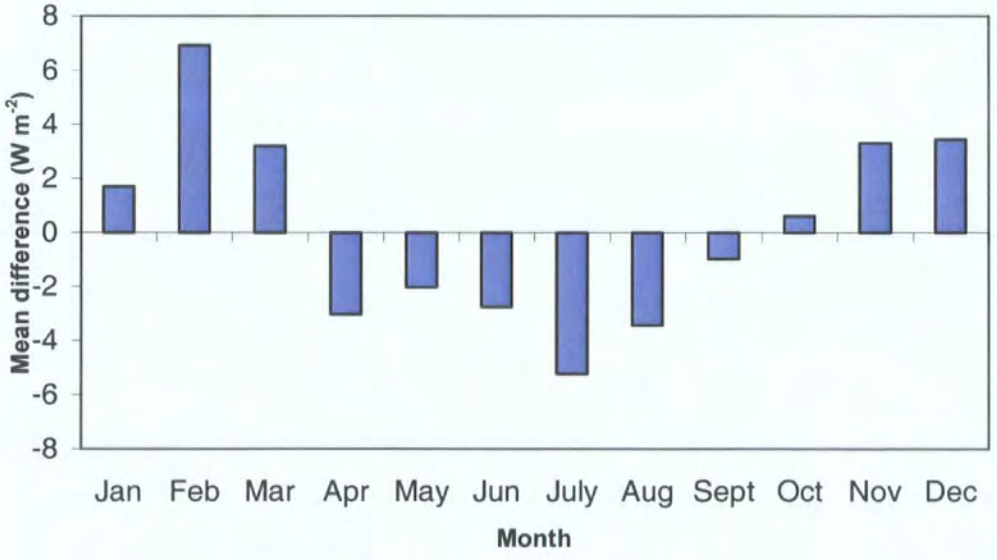

Figure 4.16. Annual average difference between SOC data and the parameterised dataset (W m^{-2}) over the area of interest.

The pattern of the latent heat flux is primarily determined by a combination of the wind speed and the humidity difference between the air and the sea. The comparison between the estimated monthly flux data and the SOC Atlas is shown in figure 4.17. The two datasets follow the same annual trend, with the SOC data showing a generally stronger loss except from April till June. The strongest losses, in the order of –125 W m^{-2}, occur during the colder months, when the difference between the two interfaces becomes prominent. Over the entire period, the monthly variability of the calculated heat flux follows that shown by the annual trend of the wind speed as retrieved by TMI sensor. This is because the bulk parameterisation of the latent heat flux strongly depends on the input of the wind speed into the bulk formula. The overall trend of the calculated dataset is more or less constant (fig. 4.18) with the highest values observed during November and December as in the case of the sensible heat flux.

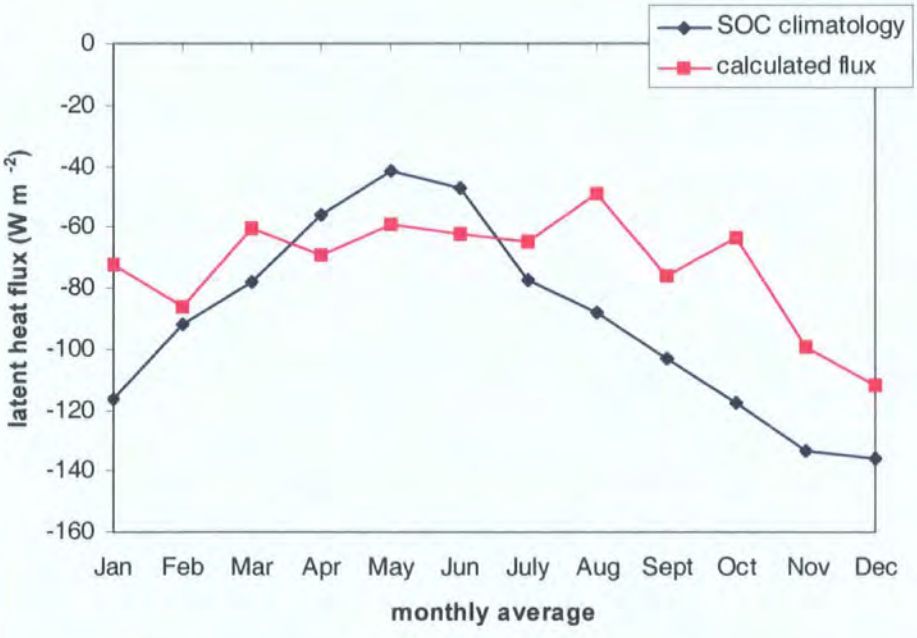

Figure 4.17. Comparison of the monthly average latent heat flux (W m^{-2}) between the estimated dataset and SOC climatology over the area of interest.

Looking at figure 4.19, the bias [LH_{SOC} minus $LH_{ESTIMATED}$] is maximum during October by around -55 W m^{-2}. The annual mean difference is –18.8 W m^{-2}. Interestingly, studies carried out by Castellari *et al.* (1998)

show that the latent heat flux reaches a maximum in January (with a value of around −280 W m^{-2}) and a minimum in August (around −22 W m^{-2}). An annual average of around −124 W m^{-2} is observed for the whole Mediterranean. The estimated latent heat flux shows a similar highest minima during August of around −40 W m^{-2} and a maxima in December of around −110 W m^{-2}. The discrepancy from both the observed interannual Mediterranean-wide climatology and SOC data can be attributed to some local, climatic anomalies that occurred during the latter part of the study period (1999), such as deviations in the 10 m wind magnitude from normal climatology. This variation (see section 4.4.1.1.) is able to trigger a larger rate of evaporation flux from the sea into the atmosphere. This can explain the positive trend of the latent heat flux during the latter half of the year when compared to the averaged climatology over the same area.

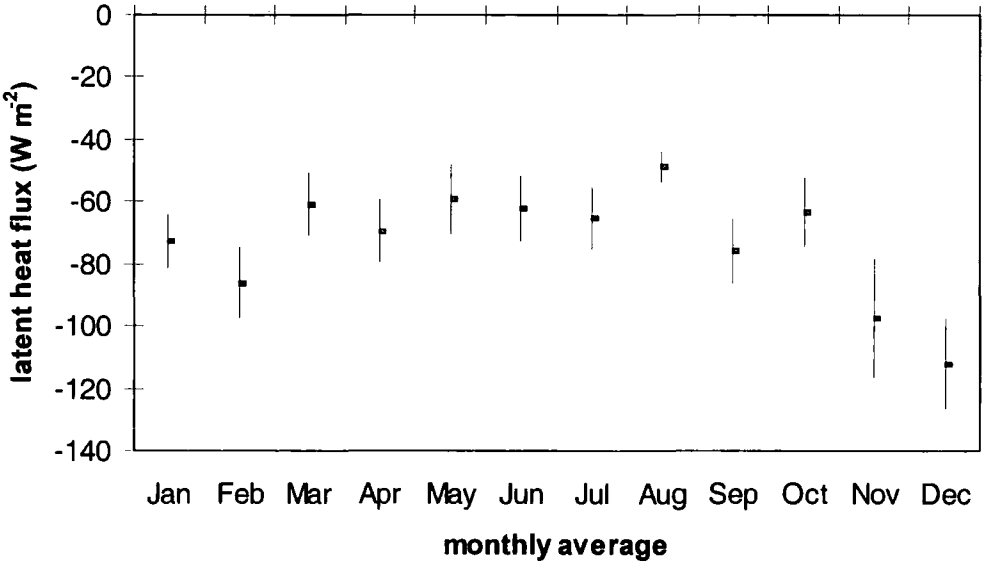

Figure 4.18. Average monthly variability of the calculated latent heat flux (W m^{-2}) during 1999 over the area of interest.

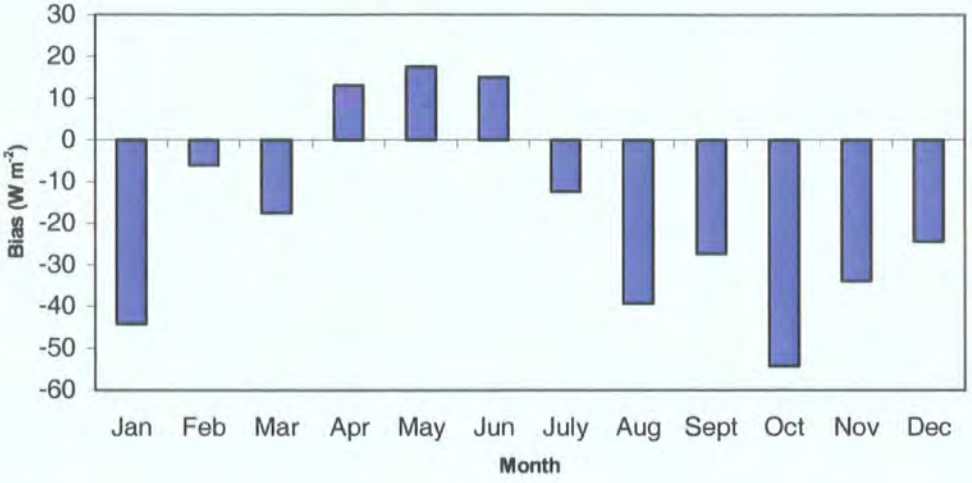

Figure 4.19. Average mean difference of the latent heat flux between the SOC data and the estimated database (W m^{-2}) during 1999 over the area of interest.

The turbulent and radiative heat fluxes constitute together the total exchange of heat flux at the sea surface. The exchange of heat and moisture across the air-sea interface, particularly that driven by the latent heat flux, is able to exert a strong influence on the atmospheric and oceanic circulation.

The estimation of the *instantaneous* turbulent heat flux database using remotely-sensed data derived from passive microwave sensor enabled an all-weather parameterisation of the turbulent heat fluxes except for pixels contaminated by precipitation. Moreover, errors due to sensor variability and co-temporality were removed because the variables used were all derived from the same sensor retrieved at the same time with the exception of the air surface temperature. This method presents a much better approach to derive a high-resolution, instantaneous heat flux fields at four times more than the resolution of other databases, such as the Hamburg Ocean Atmosphere Parameters and Fluxes from Satellite Data (HOAPS) database[79].

[79] *http://www.hoaps.zmaw.de/ (accessed on 01.11.04).*

Similar approaches to estimate the turbulent heat fluxes using basic fields derived from remote sensing were also used by a number of investigators. Schulz *et al.* (1997) measured latent heat flux at the air-sea interface using weekly AVHRR-derived SST and SSM/I-derived near surface wind speed. The boundary layer water vapour content was retrieved from SSM/I measurements with an accuracy of 0.06 g cm^{-2} from which the near-surface humidity was derived. Their method revealed a standard error of approximately 30 W m^{-2} in comparison with scarce data from merchant ships. However, problems are inherent in this method because of the use of AVHRR MCSST, since this SST source is inaccurate in the presence of atmospheric aerosols and clouds (Reynolds, 1993). ATSR 2 - derived SST has also been used by Xue *et al.* (1997) to derive sensible heat flux using bulk formulae.

The method used in this study uses *sub-skin* SST (at around 500 μm depth at the water side of the air-sea interface where conductive and diffusive heat transfer processes dominate) temperature layer where molecular and viscous heat transfer processes begin to dominate (Donlon *et al.,* 2002). The use of this *sub-skin* SST therefore ensures a better derivation of the turbulent heat fluxes than other remotely-sensed SST that is calibrated against bulk SST (i.e. buoy data). Therefore, the present comparison with climatological atlases may be prone to have differences since these atlases have been derived using partly, the bulk-SST as one of the variables in the bulk parameterisation (GEWEX, 1999).

The lengthy approach used in this study to determine the near surface air humidity stems from the lack of remotely-sensed humidity data at the sea surface. To remedy this information gap, Liu and Niiler (1984) and Liu (1986, 1988) used the atmospheric water vapour column content or the total precipitable water vapour as an approximation for monthly mean values of surface humidity. However, Taylor (1982) expresses his doubts on the use of the total precipitable water as a good predictor for the surface humidity stating that the correlation between

the two is not high enough. This is contested by Schulz *et al.* (1993) who have observed a good linear fit of 0.98 between the two parameters. Following this research path, Schluessel *et al.* (1995) have slightly improved this indirect method and managed to reduce the systematic error. Jones *et al.* (1997) have defined a new sophisticated method to derive specific humidity and air temperature from satellite data using a neural network approach.

The theoretical approach used in the present study is an alternative to this lack of humidity data. Thus, an approximation in the calculation of the latent heat flux was made for the determination of the actual vapour pressure at sea surface (see equation. 4.14), which requires information on the virtual temperature. This parameter was approximated (see equation 4.15) by considering average conditions.

The air temperature over the sea surface, for which no instantaneous values are available from the area of interest during 1999, was calculated by studying the monthly climatological difference between the air and the sea temperature from the collocated COADS database. This mean monthly air-sea temperature difference was then deducted or added to (depending on the month) the instantaneous TMI-derived SST. In this manner, the inclusion of climatological, average information in the bulk formulae was thus minimised, and provided a *semi*-instantaneous value for the air temperature.

The values of the Stanton and Dalton numbers were the same as those used by Liu *et al.* (1979). They were chosen on the basis that they give good results for moderate wind speeds and slightly unstable conditions as is the case for the climatology of the Ionian basin. Little research has been done on the behaviour of these coefficients when wind speeds become stronger than 12 m s^{-1} (Taylor, 2000).

4.4.1.5. Outgoing longwave radiation.

The annual variation in the outgoing longwave flux over the area of interest is relatively small, ranging from 230 to 288 W m^{-2} (fig. 4.20). This trend reflects the balance between the air and the sea-air temperature difference, cloud cover and amount of water vapour. The average value is close to that described by Charnock (1994) for the zonal average at this latitude.

The determination of longwave radiation from satellite data involves taking measurements at the top of the atmosphere and accounting for the effects of the atmosphere using a radiative transfer model. The obvious problem is how to account for the effects of clouds, especially since the surface radiative flux is dependent on the height of the lowest cloud, a quantity that is not easily determined by satellite. According to Darnell *et al.* (1996), the monthly mean bias for remotely sensed average data validated over a three-year period against collocated, *in situ* measurements is about 5 W m^{-2} with an RMS difference of 24 W m^{-2}.

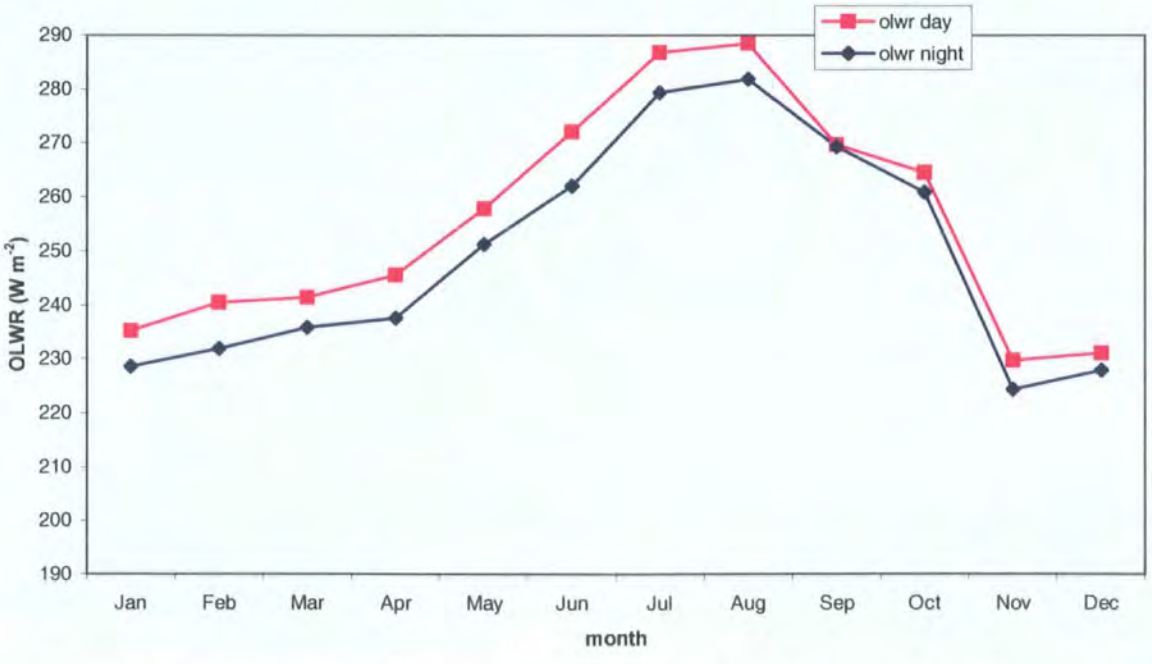

Figure 4.20. The monthly outgoing longwave radiation (W m^{-2}) retrieved from NOAA AVHRR over the area of interest.

The derivation of the outgoing longwave radiation remains experimental and more work is needed before reliable estimates can be obtained from satellites (WCRP/GEWEX, 1996). A new, improved formula for determining the outgoing flux at the ocean surface at mid-high latitudes has recently been published by Josey *et al.* (2003), which was embedded in a stochastic atmosphere model.

4.4.1.6. Aerosol optical thickness.

Figure 4.21 shows the monthly variability of the aerosol optical thickness (AOT) over the area of interest based on a 10-year climatology. Aerosol optical thickness peaks during the months of June to August. Minimal values occur in December, during which a value of around 50 ODU is observed. The monthly spatial variability is shown in the raster maps (fig. 4.22 a-l).

The monthly AOT maps, which are good indicators to quantify the dust aerosol radiative forcing, show that atmospheric dust aerosols are a prominent feature of the climate of the area of interest. This arises from the close proximity to the northern African coastline, making the area susceptible for this kind of atmospheric contamination. D'Almeida (1986) states that tens of millions of tons of terrigenous mineral particles per year are exported from the Saharan region to nearby regions and are likely to modify the radiative energy pattern in the atmosphere (Legrand *et al.,* 1992). Atmospheric dust has been described as having a screening effect, thus modifying the upward transfer of radiance emitted by the sea through the dust layer, when the sea and dust have appreciable different temperatures.

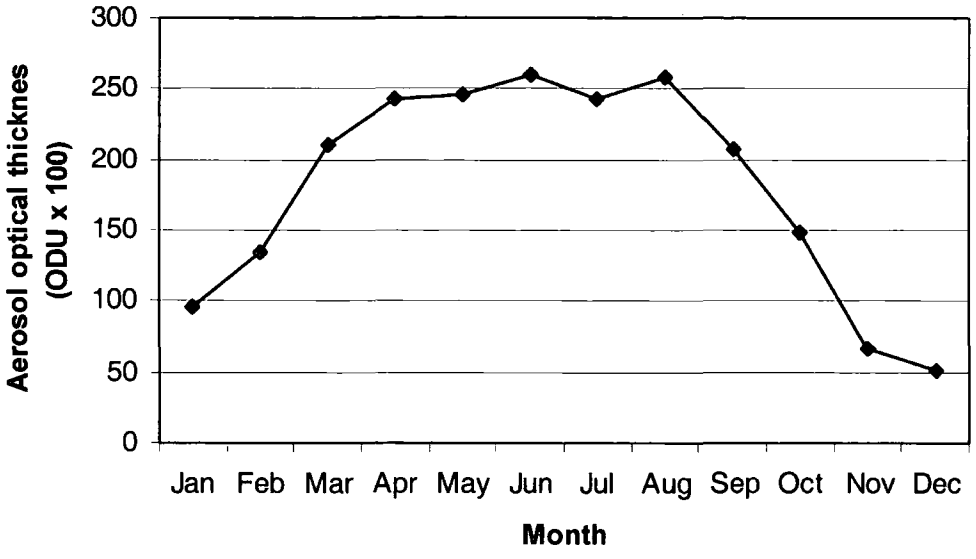

Figure 4.21. The average monthly variability of the Aerosol optical thickness (in Optical Depth Units x 100) over the area of interest.

Apart from the climatological dust load information over the Ionian basin, this dataset is also useful to interpret the accuracy of the radiative heat fluxes, such as OLWR and infrared radiances of the sea surface as measured from the top of the atmosphere. It is well known that atmospheric dust particles affect the upwelling infrared radiances by absorption and scattering in the short-wave regime and by absorption and emission in the long-wave radiation regime. This information is required to assess the calibration of infrared scenes retrieved during July – August (see section 4.4.3.), which happens to correspond to the highest climatological AOT values over the geographical area (fig. 4.22 a-l). What is striking about this information is that this two month period is characterised by a persistent incidence of high aerosol content that is consistently confined over restricted geographical areas, such as the area under study, as seen in figs. 4.22 f, g and h.

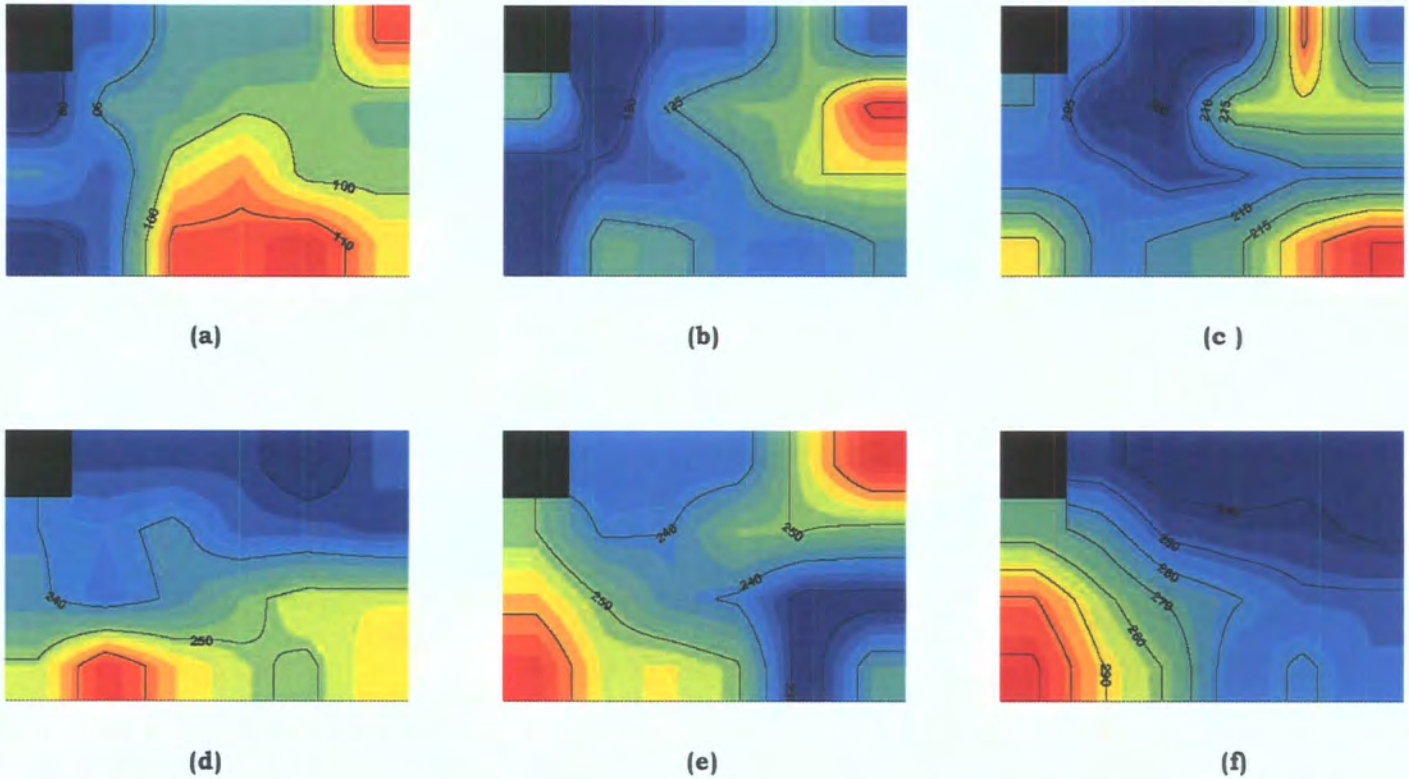

Figure 4.22 a – f. The 10-year monthly averages of the Aerosol Optical Thickness over the area of interest: (15.78°E, 33.18°N) to (19.18°E, 35.74°N). The data was retrieved from NOAA AVHHR and represent raster maps 1° by 1° latitude – longitude for the months of (a) January, (b) February, (c) March, (d) April, (e) May, and (f) June. Values are in Optical Depth Units (x100). Black pixels are due to land masking.

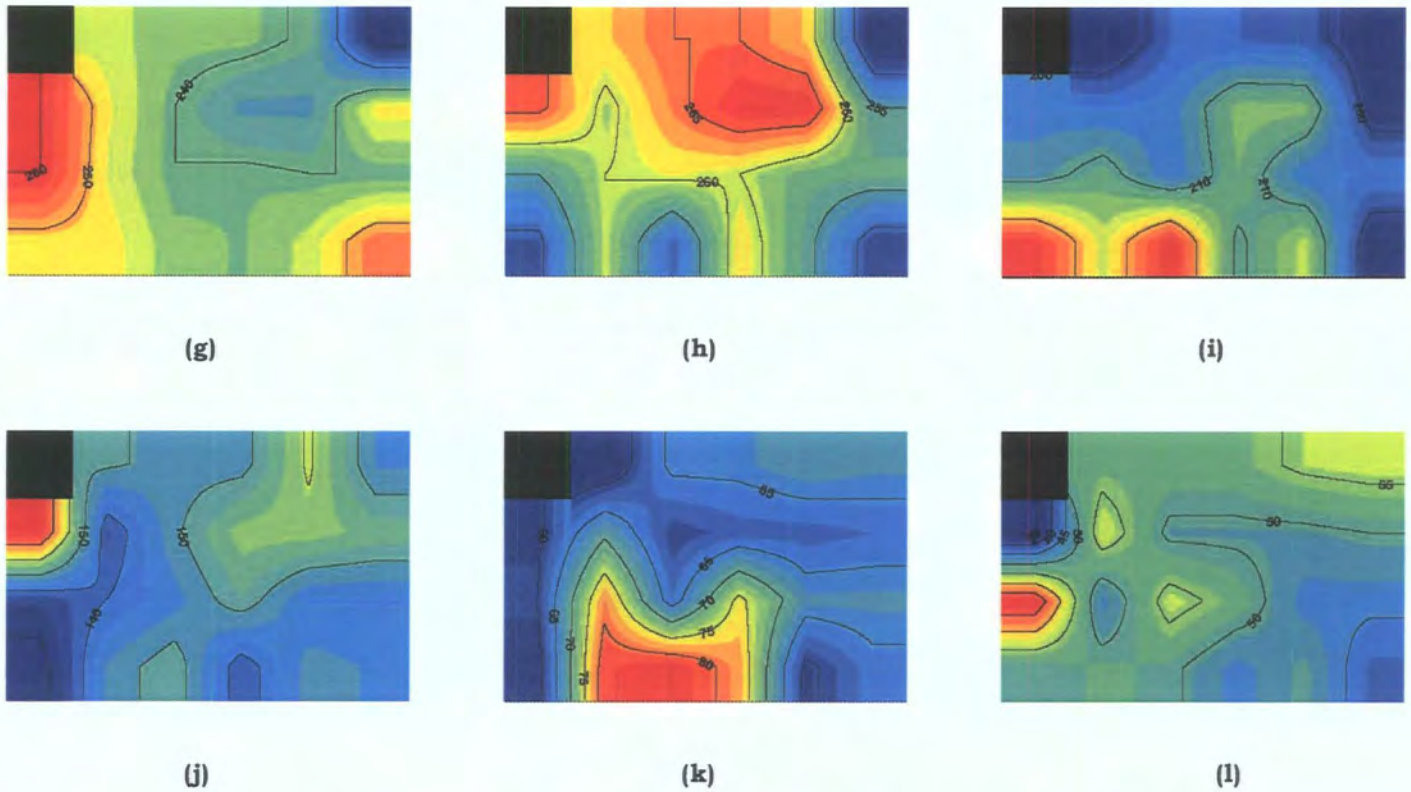

Figure 4.22 g – l. The 10-year monthly averages of the Aerosol Optical Thickness over the area of interest: (15.78°E, 33.18°N) to (19.18°E, 35.74°N). The data was retrieved from NOAA AVHHR and represent raster maps 1° by 1° latitude – longitude for the months of (g) July, (h) August, (i) September, (j) October, (k) November and (l) December Values are in Optical Depth Units (x100). Black pixels are due to land masking.

4.4.2. Calibration of high resolution, infrared radiances.

This section presents the analysis of the three algorithms that were studied and adapted for the central Mediterranean, where no operational *in situ* data is collected. Infrared radiance data of the sea surface over part of the Ionian basin were collected for a continuous, 16-day period in view of their use to validate the accuracy of predicted SST by the ocean forecasting system as presented in chapter 7.

4.4.2.1. The YB94 algorithm.

The gamma factor provided an indication of the efficacy of the YB94 algorithm. The gamma value having the least error obtained by Yu and Barton (1994) ranges from 4.75 and 4.82, with a bias of 0.01 K and standard deviation of 0.12 K when compared to the MCSST algorithm. This is in close agreement with the gamma value retrieved over the CoastWatch area as shown in figure 4.23. From this relation, the best gamma value was extracted that gave the least bias from the NLSST algorithm.

These results also show that the relationship between the ratio R_{54} and the slope $\Delta TB_4/\Delta TB_5$ (ratio of the atmospheric transmittance), which constituted some of the studied parameters (see table V.7 a-i), is negative (fig. 4.24). The good linear relationship between the two parameters is reflected by a correlation coefficient of 0.7.

The efficiency of the YB94 algorithm is shown by the good correlation with the NLSST algorithm, giving a coefficient of 0.82 and strong linear function passing from the origin (fig. 4.25). A closer inspection of the relationship between the YB94-derived SST and deviation from collocated NLSST values (fig. 4.26) indicates that for a typical summer SST over the Ionian basin (in the region of 22 °C to 28 °C), the algorithm's performance underestimates the SST by an average of

–0.5 °C to –0.7 °C respectively (fig. 4.26). This deviation occurs when the gamma value ranges between 3.8 and 4.3 (fig. 4.23).

Another useful indicator of the performance of the YB94 algorithm is the relationship between gamma and the water vapour profile using the equation derived by Ottle *et al.* (1997). This relationship shows that an optimal gamma value is derived when the atmospheric water vapour profile is around 2 g cm^{-2} (fig. 4.27). The inverted exponential profile shown in figure 4.30 indicates that a water vapour profile higher than 2 g cm^{-2} can deteriorate the performance of the YB94 algorithm by deriving a less than optimal value for gamma. This is not so when the water vapour value is less than 2 g cm^{-2}: the change in gamma value becomes even greater for small reductions in the atmospheric water vapour profile. According to these results, therefore, gamma is negatively correlated with the amount of atmospheric water vapour. The significance of this relationship becomes even more important when the YB94 algorithm is used in geographical regions characterised by higher water vapour profiles, such as the central Mediterranean.

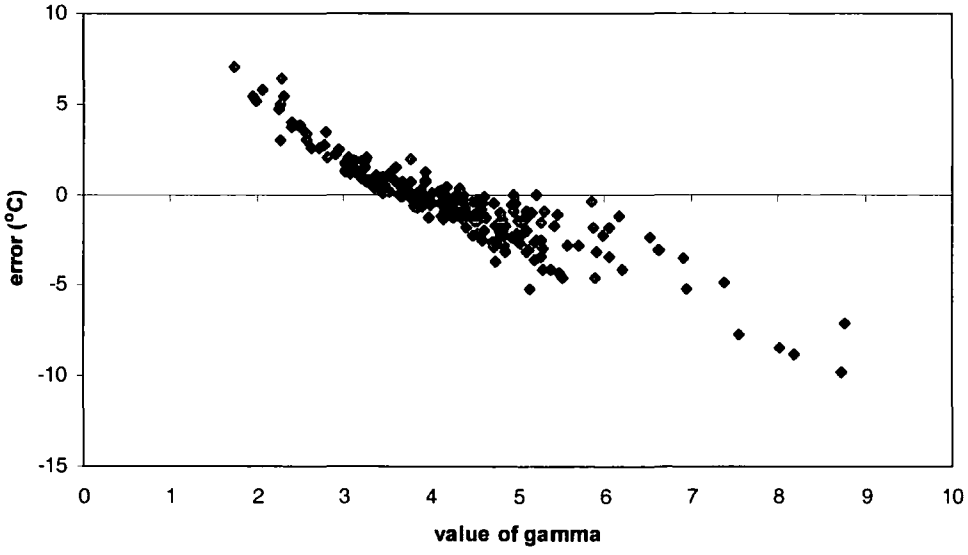

Figure 4.23. Relationship between the gamma value and [SST_{NLSST} minus SST_{YB94}] value (denoted as error in °C) derived from AVHRR scenes over the CoastWatch area during 1998-1999.

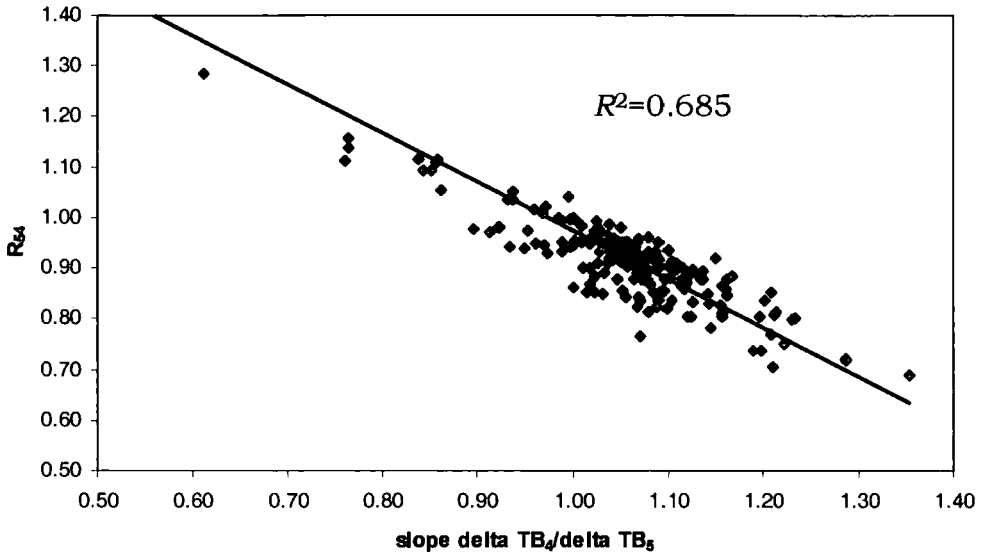

Figure 4.24. Relationship between the R_{54} ratio versus the ratio ΔTB4:ΔTB5 derived from AVHRR scenes from the CoastWatch area during 1998-1999.

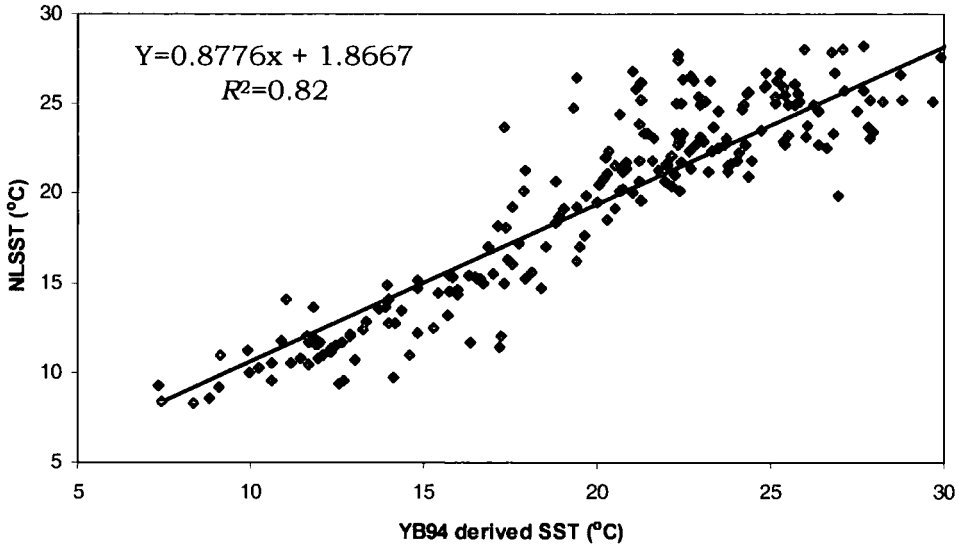

Figure 4.25. Relationship between the YB94-derived SST (°C) and collocated NLSST (°C) derived from the CoastWatch area during 1998-1999.

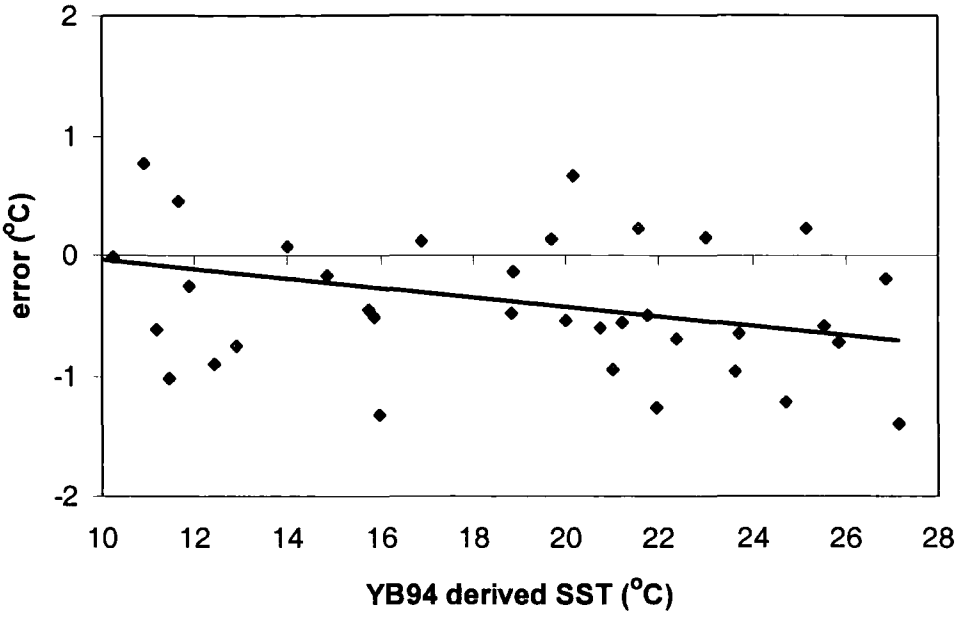

Figure 4.26. Relationship between the YB94 derived SST in °C and [SST_{NLSST} minus SST_{YB94}] difference (in °C) derived from the CoastWatch area during 1998-1999.

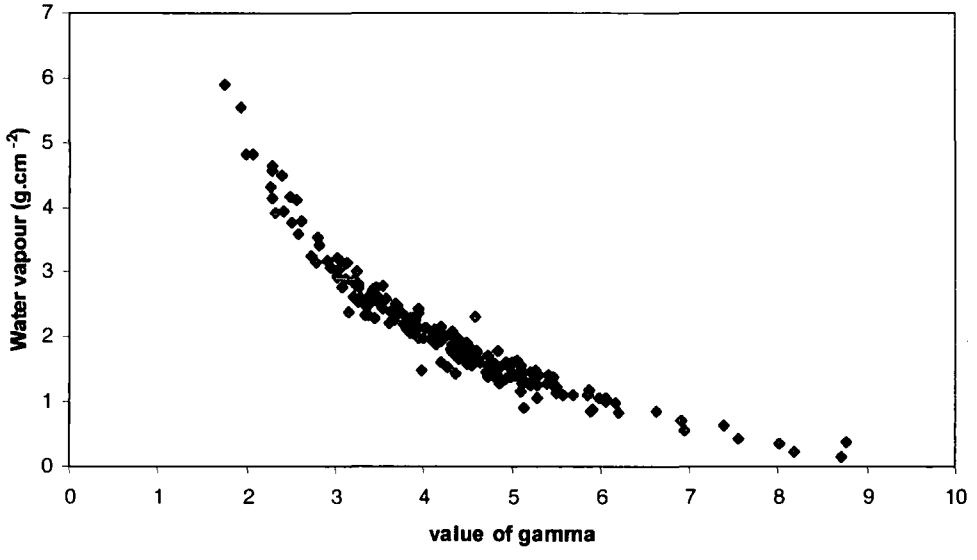

Figure 4.27. Relationship between the gamma value and collocated total atmospheric water vapour profile derived from the CoastWatch area during 1998-1999.

The CoastWatch area was used to test the validity of the YB94 algorithm before applying this calibration procedure for the Mediterranean region.

Figures 4.28a and 4.28b show examples of brightness temperature data derived from AVHRR channels 4 and 5 respectively on 23rd August 1998 over sector E (fig. 4.3). The key features noted between the YB94-retrieved SST data (fig. c) and the NLSST map (fig. d) are (1) the similar statistical results of the area of interest, showing an overall differences as low as 0.2 °C, and (2) the similar final spatial distribution of the thermal signature.

The results presented in table V.7 a-I support the use of the YB94 algorithm. This conclusion rests on the assumption that the collocated NLSST is accurate and reliable enough to serve as a substitute to *in situ* match-up data. The use of the NLSST source is supported by the studies of Li *et al.* (2001) who observed a maximum error of 0.14 °C against *in situ* data[80] for the NLSST algorithm.

The use of an *in situ* match-up data instead of NLSST would have presented a number of technical problems. These include (1) lack of operational buoys in open seas; (2) inherent biases related to *in situ* measurement[81] (3) the different scale of satellite (1.1 km) against buoy measurement (point data).

[80] *The satellite sensor SST and buoy SST pairs were matched-up only if they were coincident within 25 km and 4 hours.*
[81] *Section 3.5.4.*

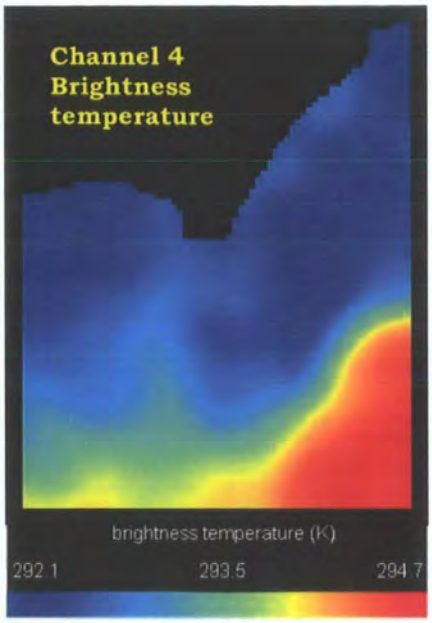

min. mean max.

(a)

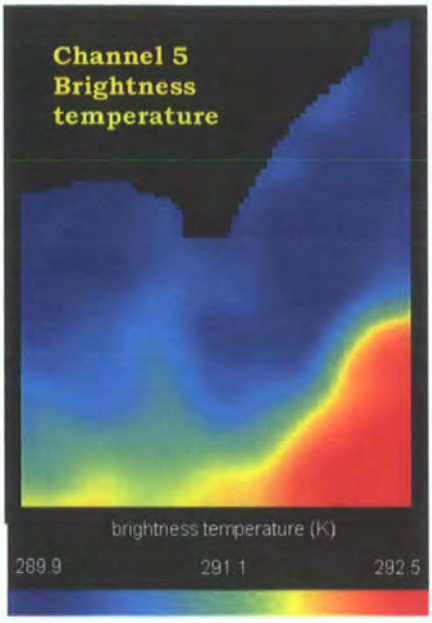

min. mean max.

(b)

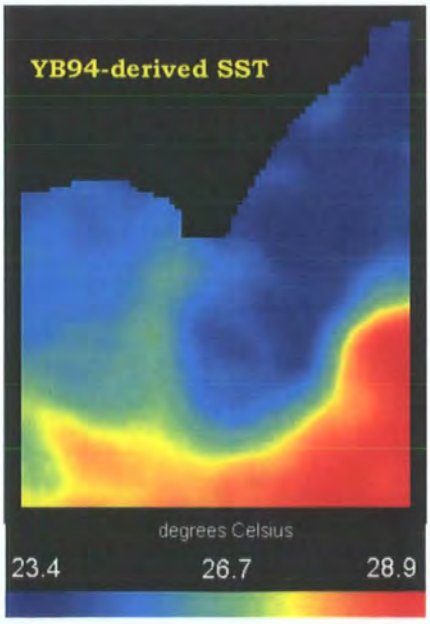

min. mean max.

(c)

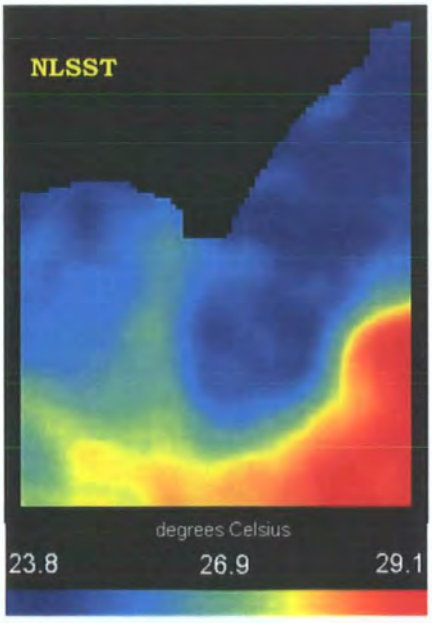

min. mean max.

(d)

Figures 4.28 a - d. Brightness temperature data (in Kelvin) derived from (a) channel 4 and (b) channel 5 on 23rd August 1998 over sector E (see fig. 4.3: 77°W-76°W; 34°N-35°N). The YB94-retrieved SST raster data (c) shows similar SST scale (in °C) and pattern as the NLSST map (d).

4.4.2.2. Linear regression modelling using the split-window technique.

The split-window technique has proved to be the most useful atmospheric correction method for SST derived by infrared sensors (Arbelo *et al.*, 2000). This technique uses two different channels within the 10.5 - 12.5 μm window, which are affected by different absorption due to the wavelength dependence at water vapour continuum (McMillin, 1975).

To overcome the limitations mentioned in section 3.5.4., this study attempted to derive a range of split-window coefficients each reflecting particular vertical atmospheric water vapour profiles as defined by the slope $[TB_4/TB_5]$, ranging from 1.01 to 0.86.

The equations presented in tables 4.7a-b are models derived from the multiple regression between NLSST, TB_4, and the difference between TB_4 and TB_5. The dependent variable (NLSST) is linearly correlated to the independent ones (TB_4 and TB_4-TB_5) throughout the analysis, with strong R^2 and mostly similar partial regression coefficients for each of the independent variables over the entire range of slope $[\Delta TB_4/\Delta TB_5]$ values. In his review on SST algorithms retrieved by infrared sensors, Barton (1995) referred to the same split window formalism where the partial regression coefficient related to TB_4 is close to unity. As is the case in table 4.7 a-b, this value of coefficient implies that at the lowest order, the sea surface temperature equals the measured brightness temperature. The other coefficient related to the differential absorption between channels 4 and 5 (or the slope $[\Delta TB_4/\Delta TB_5]$) is equivalent to the transmittance through the atmosphere from the surface to the satellite and is dependent on both the mass absorption coefficient of the atmospheric absorbers and the path length (Barton, 1995). The dependence of this coefficient on the temporal structure of the atmospheric vertical profile always induces a degree of variability, as shown in the present results.

Month-Day	Image ID	Coast-Watch Sector	No. of pixels	Group	Regression model	Atmospheric transmittance	R-squared (adjusted for d.f.) %	Mean Absolute residual Error	No. of studentized residuals >2.0
03-15	408	A	2286	1	NLSST = 21.05 + 0.94*TB_4 - 0.65*TB_4-TB_5	[$\Delta TB_4/\Delta TB_5$] = 1.01	99.03	0.34	645
05-16	607	M	6460	1					
05-16	607	Q	202	2	NLSST = -12.42 + 1.05* TB_4 + 1.36*TB_4-TB_5	[$\Delta TB_4/\Delta TB_5$] = 0.98	99.92	0.09	80
03-15	408	F	6735	2					
11-28	208	L	1195	2					
03-14	307	B'	4599	3	NLSST = -3.09 + 1.01*TB_4 + 1.69*TB_4-TB_5	[$\Delta TB_4/\Delta TB_5$] = 0.97	99.96	0.12	244
09-05	N/a	P	1064	3					
11-28	208	C	205	3					
04-13	308	A'	5317	4	NLSST = -25.57 + 1.10*TB_4 - 0.83*TB_4-TB_5	[$\Delta TB_4/\Delta TB_5$] = 0.96	93.96	0.29	735
04-13	308	B'	5940	5	NLSST = -10.22 + 1.04*TB_4 + 1.14*TB_4-TB_5	[$\Delta TB_4/\Delta TB_5$] = 0.95	99.90	0.12	892
04-13	308	C'	4972	5					
11-28	208	C'	1756	5					
03-15	408	J	5072	6	NLSST = 3.61 + 0.99*TB_4 + 1.56*TB_4-TB_5	[$\Delta TB_4/\Delta TB_5$] = 0.94	99.76	0.16	999
03-15	408	K	792	6					
04-13	308	B	4512	6					
04-13	308	J	6469	6					
05-16	607	B'	6365	6					
05-16	607	G	894	6					

Table 4.7a. Look up table containing the suite of single line equations valid for different atmospheric states as defined by their slopes ranging from 1.1 to 0.94. The regression analysis was done over a two-year period over the CoastWatch area. Regression models are statistically significant at the 1% level (P-value <0.01).

Month	Image ID	Coast-Watch Sector	No. of pixels	Group	Regression model	Atmospheric transmittance	R-squared (adjusted for d.f.) %	Mean Absolute Error	No. of studentized residuals >2.0
04-13	308	K	6282	7	NLSST = -17.22 + 1.06*TB_4 + 1.53*TB_4-TB_5	[$\Delta TB_4/\Delta TB_5$] = 0.93	99.81	0.11	477
11-28	208	B	1277	7					
11-28	208	M	965	7					
04-13	308	A	3559	8	NLSST = -16.00 + 1.06*TB_4 + 0.87*TB_4-TB_5	[$\Delta TB_4/\Delta TB_5$] = 0.92	99.25	0.25	1123
05-16	607	N	6599	8					
06-03	407	A'	5533	8					
06-03	407	K	1957	8					
11-28	208	J	5274	8					
11-28	208	K	2849	8					
11-28	208	O	1987	8					
05-16	607	F	1499	9	NLSST = -2.22 + 1.01* TB_4+ 1.85*TB_4-TB_5	[$\Delta TB_4/\Delta TB_5$] = 0.91	99.70	0.11	281
06-03	407	B'	4009	9					
03-15	408	P	402	10	NLSST = 12.71 + 0.96*TB_4+ 1.87*TB_4-TB_5	[$\Delta TB_4/\Delta TB_5$] = 0.90	98.93	0.14	707
06-03	407	A	5417	10					
06-03	407	B	1420	10					
11-28	208	N	4655	10					
11-28	208	P	321	10					
03-15	408	O	3757	11	NLSST = -9.20 + 1.03*TB_4 + 1.56*TB_4-TB_5	[$\Delta TB_4/\Delta TB_5$] = 0.89	99.73	0.12	437
05-16	607	C	636	11					
05-16	607	C'	5460	11					
03-15	408	I	4389	12	NLSST = -21.93 + 1.08*TB_4 + 0.04*TB_4-TB_5	[$\Delta TB_4/\Delta TB_5$] = 0.87	99.39	0.25	432
05-16	607	R	2707	12					
05-16	607	B	3113	13	NLSST = -10.88 + 1.04*TB_4 + 1.14*TB_4-TB_5	[$\Delta TB_4/\Delta TB_5$] = 0.86	99.62	0.09	117

Table 4.7b. Look up table containing the suite of single line equations valid for different atmospheric states as defined by their slopes ranging from 0.93 to 0.86. The regression analysis was done over a two-year period over the CoastWatch area. Regression models are statistically significant at the 1% level (P-value <0.01).

Coll *et al.* (1994) associated the constant (i.e. - intercept) of the split window algorithm to the emissivity effect and Barton (1995) showed that it can range from 28 to −17 for a total of 21 algorithms used to retrieve SST through subtropical atmospheres. This is also the case for the resulting models, where each regression equation refers to particular atmospheric vertical profiles as detected by the two infrared channels.

Table 4.7 a-b also gives an indication of the magnitude of the residuals for each group of slopes (mean absolute residual error and number of Studentized residuals). Further analysis of these residuals may stabilise even further the regression models. The presence of undetected, contaminated pixels due to fog, as well as the inherent inaccuracies of the dependent variable (NLSST), may be giving rise to such instability. Uncertainties do however exist in these measurements, which include the accuracy of the original NLSST dataset, the contamination of unresolved cloud and aerosols and errors in the satellite calibration.

The dependency and sensitivity of $[\Delta TB_4/\Delta TB_5]$ on the atmospheric transmittance shows that it is not proper to use globally-retrieved coefficients from NESDIS to correct regional SST imagery with enough accuracy. This was also expressed by Sobrino *et al.* (1993) following their observations on the impact of the atmospheric transmittance and total water vapour content on SST retrieval from AVHRR.

Although the approach used is similar in concept to that developed by Sobrino *et al.* (1993), it is technically different and more simple. In their work, they have simulated channels 4 and 5 of AVHRR/2 of NOAA-11 using a radiative transfer model with a range of atmospheric conditions and surface temperature that reflected a worldwide variability. The present study uses instead the empirical knowledge derived from the NOAA AVHRR readings from channels 4 and 5 and collocated NLSST pixels to derive the algorithms. Indeed, the slope $\Delta TB_4/\Delta TB_5$ was

calculated for each collocated pair of pixels (a total of 203,010 pixels) and the resulting mean slope for each sector was categorised to represent the water vapour profile of different atmospheric states during the 2-year study period. This grouping was necessary to average out the errors inherent in this method, which may originate from the inaccuracy of the original NLSST dataset embedded in any split-window algorithm (an average of ± 0.14 °C against *in situ* data – [Li *et al.*, 2001]), the contamination of unresolved cloud and aerosols, and errors in the sensor calibration. Similar errors are also encountered when such line algorithms are derived by regressing brightness temperature from channels 4 and 5 against *in situ*, collocated data.

The approach used in this study provides a powerful tool by providing appropriate split-window coefficients that best match the atmospheric composition present when individual AVHRR scenes are acquired over any area of interest. In this manner a suite of single line equations suitable for different atmospheric states are produced as suggested by Steyn-Ross *et al.* (1999). The modelling of the atmospheric composition over a two-year period provides to the present study a statistically robust approach to calibrate AVHRR scenes over a range of atmospheric profiles without the need of collocated *in situ* SST data. The total number of pixels analysed to generate these linear equation is shown in tables 4.7a-b.

These single-line equations can be fine-tuned and be made geographic-specific by further sub-grouping relevant pixel ratios extracted from additional scenes of geographical areas under investigation. In this manner, a finer range of slope variation can be defined from relevant imagery.

The accuracy of this algorithm is tested against an independent set of SST data and results are described in section 4.4.3.

4.4.3. Calibration of AVHRR scenes over the Ionian basin.

The performance of the three algorithms - the YB94, the multiple regression model (in the form of a look-up-table - LUT) and Coll94 algorithms were assessed for suitable NOAA AVHRR images acquired between 20th July and 7th August 1999 over the Ionian basin. This time frame was determined by the ocean forecasting system used in this study[82].

It proved very difficult to obtain valid AVHRR scenes over the area of interest during the 16-day time-frame, resulting in only 5 suitable AVHRR overpasses (table 4.2). The remaining swaths where strongly affected by cloud cover and dust aerosols due to an episode of dust uptake from the Sahara desert that started on 22nd of July and reached the area of interest on the 26th of July 1999 (information derived from an independent run of a dust model[83]). Table 4.8 gives a summary of the performance of the calibration algorithms for the valid AVHRR scenes. The use of AVHRR data to validate oceanic forecasts is always problematic. Lermusiaux and Robinson (2001) encountered the same problem when trying to verify their 16-day model integration run, for which only four AVHRR scenes were found to be suitable for comparison.

The accuracy assessment is not based on a collocated set of *in situ* match-up data; instead, it is based on an independent set of collocated SST derived from the TMI sensor. The assessment was based on the average difference of collocated [$SST_{algorihtm}$ minus SST_{TMI}]. Sobrino *et al.* (1993) used a similar approach to assess the accuracy of their results by comparing their algorithms to an independent set of CPSST and MCSST data.

---

[82] *See section 7.1. for justification of the selected time frame.*
[83] *See Appendix III for an overview of this simulation.*

Despite the lack of *in situ* data, and the use of a small number of suitable AVHRR imagery, this study provided some interesting results. On the whole, both the regression modelling and Coll94 algorithm gave

Date	algorithm	SST Field (°C)				remarks
		mean	maximum	minimum	Standard deviation	
20-Jul-99	YB94	34.80	39.87	31.03	1.43	R_{54}=1.02; γ=7.12
	Coll94	27.25	30.74	25.56	0.78	
	LUT	27.02	30.38	25.39	0.75	$\Delta TB_4/\Delta TB_5$ =1.1; group 2
	TMI	26.23	27.10	24.82	0.44	
		mean	max	min	stdev	
21-Jul-99	YB94	31.59	>40.00	26.39	3.88	R_{54}=1.94; γ=1.16
	Coll94	27.17	30.08	25.82	0.49	
	LUT	25.55	27.25	24.23	0.30	$\Delta TB_4/\Delta TB_5$ =0.8; group 22
	TMI	25.92	26.40	24.92	0.25	
		mean	max	min	stdev	
22-Jul-99	YB94	31.91	>40.00	26.09	2.91	R_{54}=1.80; γ=1.98
	Coll94	26.90	28.23	25.42	0.33	
	LUT	26.99	28.37	25.56	0.35	$\Delta TB_4/\Delta TB_5$ =0.7; group 23
	TMI	26.20	26.85	25.52	0.30	
		mean	max	min	stdev	
01-Aug-99	YB94	28.66	36.04	26.77	0.78	R_{54}=0.83; γ=3.40
	Coll94	29.51	31.0	27.61	0.67	
	LUT	28.43	29.72	26.72	0.61	$\Delta TB_4/\Delta TB_5$ =1.1; group 2
	TMI	27.29	28.92	26.43	0.52	

Table 4.8. Performance of the three algorithms (YB94, the multiple regression models look-up-table – LUT, and Coll94) for valid AVHRR scenes over the area of interest.

a very close estimate of SST that are consistent with the SST_{TMI}, but at a much finer resolution. Results indicate that for the selected AVHRR imagery, the appropriate model extracted from the look up table fares better than the Coll94 algorithm. The use of both algorithms is encouraging, with the regression modelling approach offering a wider range of possible single-line equations depending on particular atmospheric conditions, whereas the regional one (i.e. Coll94) is not flexible at all. As discussed in chapter 3, a degree of inherent difference between these two algorithms and the TMI-derived data is always

expected due to the fact that their accuracy is based on the bulk SST sampled by buoys (in the case of NLSST) and ships (in the case of Coll94). On the other hand, TMI-retreived SST is the 1 mm thick *sub-skin* SST.

The Coll94 and LUT display a similar amount of small standard deviation, indicating a certain degree of robustness. Table 4.8 indicates that regression modelling constitutes the most appropriate approach for estimating SST from valid AVHRR data, with the COLL94 ranking second. This similarity gives some confidence in using the look-up-table approach for the calibration of AVHRR imagery.

Antoine *et al.* (1992) gives an error estimate of 0.75 K for the Coll94 algorithm, which can be improved by taking into account scan angle effects. Agreeing with Minnett (1990), Coll *et al.* (1994) observed that no significant increase in accuracy was achieved when allowance for seasonal variation is inserted in the algorithm. This algorithm shows a systematic underestimation of about 0.5 K for low values of TB_4-TB_5 (< 0.5 K), while an overestimation tendency happens when the difference is between 0.7 to 2.5. Greater differences result in gross under-estimation.

The results clearly show that the YB94 algorithm does not perform well for the imagery derived over the area of interest. Contrary to those obtained when operated over the CoastWatch area, the efficacy of the YB94 algorithm was seen to deteriorate when it was applied for the Mediterranean region. This could be due to a number of factors. In the case of the CoastWatch data, the values of R_{54} range from 0.8 to 0.95. The Mediterranean scenes gave a value of R_{54}, which in most cases, was above unity. This indicates that the derivation of the ratio was below optimal, in spite of using an improved statistical approach to determine R_{54} as suggested by Yu and Barton (1994). Here a test window of 61 by 82 cloud-free pixels was selected instead of the smaller 50 by 50 pixels window used by these authors.

Whereas the slope [$\Delta TB_4/\Delta TB_5$] derived from the Mediterranean AVHRR scenes was within range of the linear regression models, giving realistic SST fields, the corresponding gamma values were found to be beyond the range of accuracy[84] previously noted over the CoastWatch area. The gamma value is 3.40, which according to figure 4.23 should give an over-estimation of around +1 ^oC. This is roughly the same error observed when the SST field over the central Mediterranean is compared to collocated TMI-derived SST fields.

What could be the cause of such a deterioration of the YB94 algorithm? The main factor which affects the accuracy of the R_{54} and ultimately that of the gamma value, is the dispersion threshold used in the algorithm. The same threshold relationship is used with CoastWatch data, but this time the threshold reflected a higher variation that could be possibly attributed to the varying attenuation caused by the high atmospheric water vapour present over the central Mediterranean throughout the study period. Walton *et al.* (1998) demonstrated that this variability not only affects the magnitude of the gamma parameter, but also its functional dependence upon the channel temperature difference.

It is interesting to note that the trend of the TMI-derived integrated precipitable water vapour over the area of interest during the period of 20th July to 7th August 1999 (fig. 4.30) increased from 2.2 to around 3.0 g cm^{-2}.

[84] *Except for the case of August 1st.*

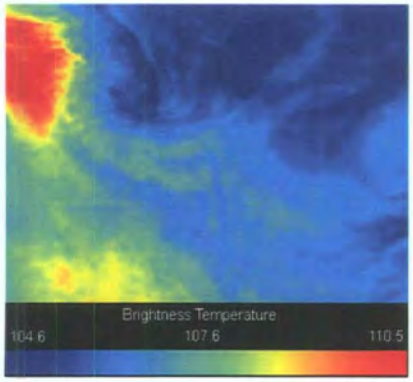

(a)

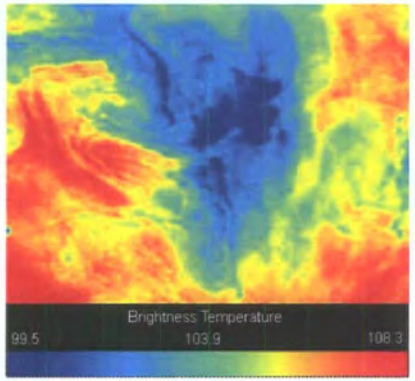

(b)

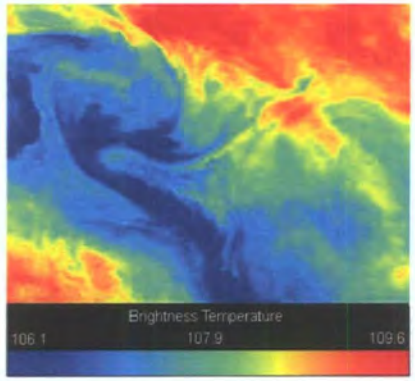

(c)

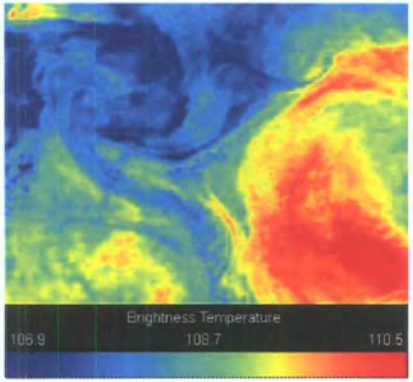

(d)

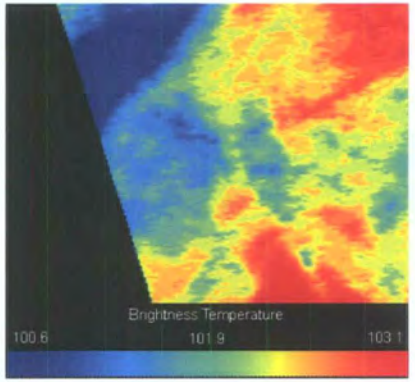

(e)

Figures 4.29 a-e. The presence of a mesoscale gyre as seen from the brightness temperature derived from AVHRR scenes (in K) acquired on (a) 20.07.99 (b) 21.07.99 (c) 22.07.99 (d) 23.07.99 and (e) 06.08.99, over the Ionian basin: 15.94°E-18.27°E;33.39°N - 35.56°N.

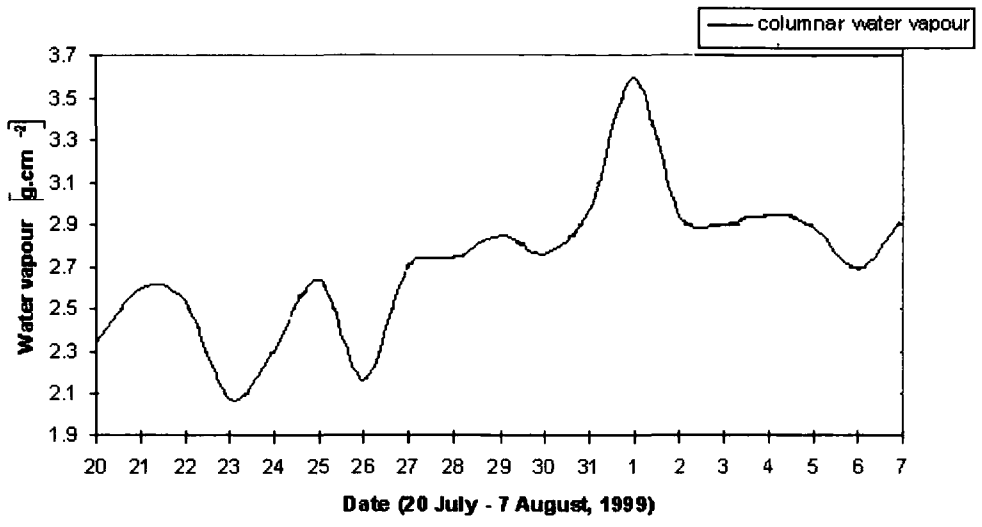

Figure 4.30. TMI-derived daily integrated precipitable water vapour (g cm^{-2}) over the area of interest during the period 20 July to 7 August 1999.

The optimal gamma value over the CoastWatch area was found to be around 3.5 to 4.0, giving a corresponding atmospheric water vapour as calculated by the equation given by Ottle *et al.* (1997) of around 2.0 g cm^{-2} and even less – a value that is exceeded during the time frame over the Ionian basin. The 3-D profile of the precipitable water vapour (fig. 4.31) cannot be considered as homogeneous over the area of interest and is attributed to the particular climatological conditions over the central Mediterranean. This heterogeneity can adversely influence the retrieval of proper R_{54} and gamma values, which according to Barton (1995) leads to a failure of the algorithm.

A potential contaminant for all three algorithms is the unresolved cloud pixels in the analysis. Walton *et al.* (1998) for example, refers to the need of filtering cloud contaminated pixels to improve the accuracy of the YB94. Cloud detection within the area of interest was based on the amount of spectral information given for each pixel and a combination of spectral channels (near-infrared and thermal infrared) was used in this study as described by Kriebel (1996). This was done by applying a set of threshold tests to each pixel to determine the amount of cloud

contained within it. A simple ratio test was also applied to filter out contaminated radiances as detected by channels 4 and 5. Pixels were set to a null value if the ratio of collocated radiance channel 4 and 5 exceed 0.5. A gross cloud check was also used, which is a thermal infrared threshold test using the brightness temperature calculated from channel 5 as a check on cloud contamination. Over the sea, the selection of the appropriate threshold temperature was easy to find, and valid channel 5 pixels had to exceed the threshold of 288.16 K. Other cloud filtering tests - the Thin Cirrus Test and Fog/Stratus Test (Kriebel, 1996) – were also used. This makes use of the temperature difference between calibrated channels 3, 4 and 5. The temperature difference was used to detect most types of clouds including semi-transparent cirrus ones because of the different emissivities of cloud at the two wavelengths. The thresholds were set according to Kriebel (1996); however, the author states that these thresholds do vary for particular regions and seasons.

There is still considerable room for improvement of these algorithms, particularly in assessing the confidence of the two most successful algorithms: the Coll94 and LUT approach. To do this, multi-year AVHRR passes over the area of interest need to be calculated, calibrated and compared with independent data.

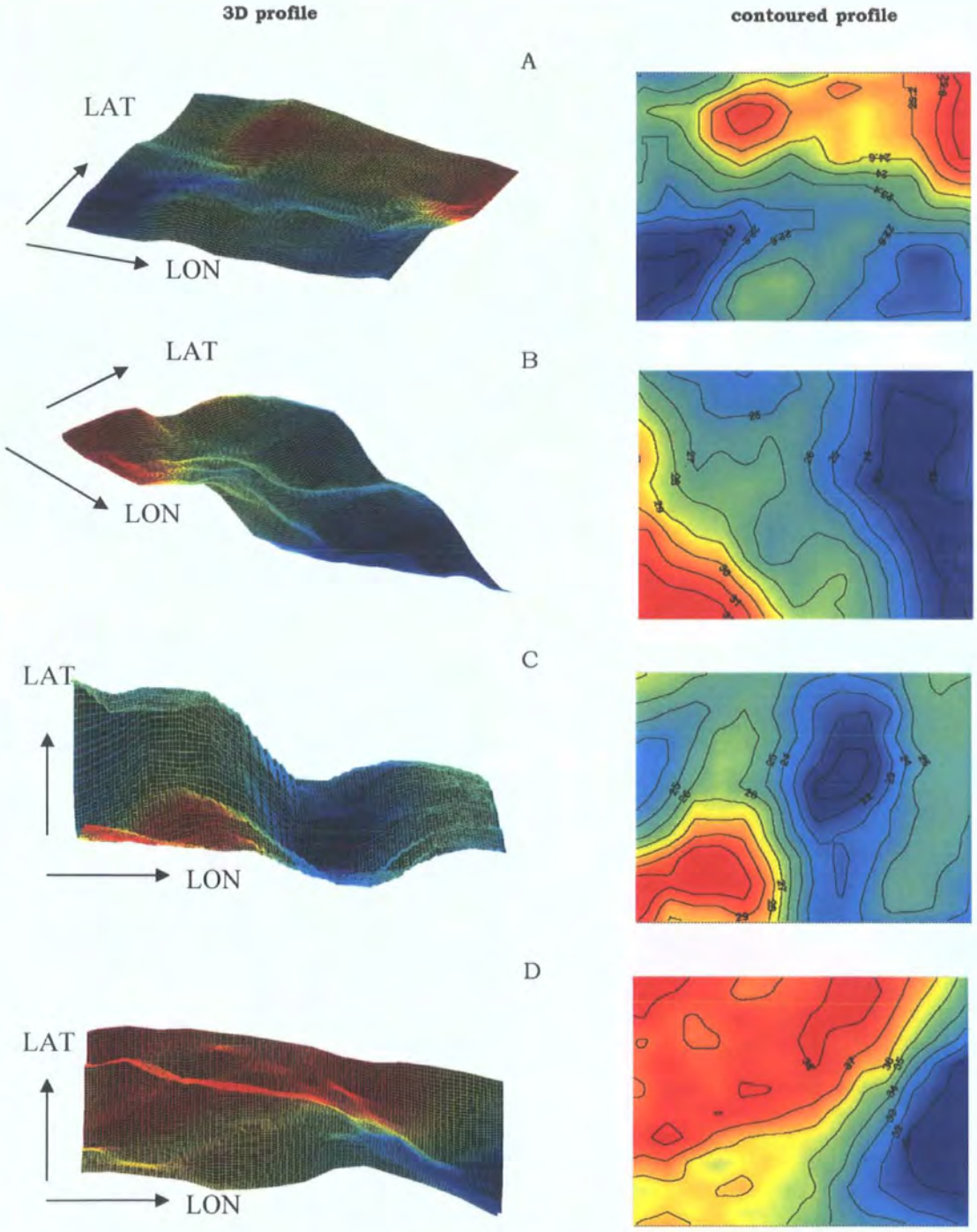

Figure 4.31. The variability of the total precipitable water vapour profile (in g cm^{-2} x 10) over the area of interest (LAT: 33.24^{o} – 35.74^{o}N; LON: 15.74^{o} – 19.17^{o}E) as retrieved by the TMI sensor on (A) 20th July 1999 at 3:48 UT (B) 21st July 1999 at 5:41 UT (C) 22nd July 1999 at 4:46 UT and (D) 01st August 1999 at 23:12 UT.

4.5. Summary.

This chapter described the work carried out to construct and assess the accuracy of a database of observations. The aim of this work was to have available an independent set of collocated data with which to validate and improve the ocean forecasting system. The database not only provided climatological information on relevant geophysical parameters over the area of interest, but also high-resolution, instantaneous parameters of the surface and vertical climatology of atmospheric variables that have been calculated from basic variables derived by different remote sensing platforms.

The accuracy of this database is deemed important for the validation of the ocean forecasting system. The database was thoroughly evaluated against sets of independent climatological data as discussed in section 4.4.1. The calculation of instantaneous turbulent air-sea heat fluxes from and orbiting passive microwave sensor was outlined in section 4.4.1.4.

With regard to the accuracy of the database, the 10 m wind speed data showed a mean annual speed of 5.22 ± 1.96 m s^{-1}, giving a bias of just 1.2 m s^{-1} against SOC data. There was also good agreement between the annual trends of the SST profiles derived from the two datasets, where the remotely sensed data showed an annual average value of 21.3 ± 4.6 °C compared to an annual average of 20.2 ± 4.1 °C derived from the SOC Atlas. The mean annual bias between the remotely-sensed SST and SOC data over the area of interest was 1.1 °C. The semi-instantaneous surface air temperature dataset was also close to that provided by the SOC data, with an annual average value of 20.8 ± 5.0 °C with a mean bias of + 1.7 °C and + 0.9 °C against the SOC and COADS climatologies respectively.

The estimated instantaneous sensible heat flux data gave an annual average value of –5.9 ± 8.5 W m^{-2} which agreed well with the annual

average value of –6.2 ± 5.9 W m^{-2} provided by the SOC Atlas. The estimated annual average latent heat flux was –73.0 ± 18.13 W m^{-2} compared to –90.77 ± 32.03 W m^{-2} given by the SOC dataset. The mean annual bias was –18.8 W m^{-2} indicating an under-estimated annual value.

The accuracy of the other datasets, such as the integrated precipitable water vapour, cloud liquid water, aerosol optical thickness and outgoing longwave radiation, was not assessed simply because of the lack of alternative data. These values were obtained by remote sensing; the humidity profiles are obtained by passive microwave remote sensing at a high spatial (0.25°) and temporal (less than 24 hrs) resolution. The other two are multi-annual climatological datasets with a coarse spatial (1° by 1°) and temporal (monthly) resolution.

Section 4.4.2. discussed the results following the calibration of AVHRR radiance scenes acquired over the Ionian basin without the use of collocated *in situ* SST data. These calibrated high-resolution scenes will be used to verify the high-resolution forecasts of the ocean model (Chapter 7). The accuracy of different algorithms was assessed, as was their applicability over the Mediterranean. A novel aspect of this study was the derivation of a look-up table that consisted of single line equations. Each of these equations can be used in the future for specific atmospheric conditions with particular water vapour profiles. This approach proved to be an efficient way to calibrate AVHRR scenes over the central Mediterranean and thus verify the 24-hr SST forecasts generated by the high-resolution ocean model.

The next chapter describes the setting-up of an atmospheric modelling system over the Mediterranean Sea with particular emphasis over the Ionian basin. Using this database, work is carried out to assess its predictive accuracy and to fine-tune a prominent numerical scheme to enhance its skill to predict the atmospheric fluxes over the ocean surface.

Chapter 5

ASSESSING AND IMPROVING THE SKILL OF THE ETA MODEL TO FORECAST AIR-SEA FLUXES.

5.1. Introduction.

Numerical Weather Prediction (NWP) models serve many users interested in many weather phenomena at different timescales. In operational ocean forecasting the interest of NWP lies in making available continuos, fine spatio-temporal forecasts of near surface parameters and fluxes (Taylor, 2000) as initial and driving fields for ocean models. In this manner, the forecasted atmospheric fields can reduce the time scale required for ocean models to attain *quasi*-geostrophic conditions in their simulation and to reach a forecasted sea-state that is close to observations[86].

There are many advantages in using modern numerical atmosphere models to determine air-sea fluxes, the major one being their improved schemes to calculate the transfer coefficients during the estimation of the surface fluxes. Their surface parameterisation schemes have been modelled on the current knowledge of the characteristics of the lowest layer of air near the sea surface. The high vertical resolution offered by these atmosphere models, for example, permit the application of the Liu *et al.* (1979) surface renewal model based on the well-established Monin-Obukhov similarity theory (Monin and Obukhov, 1954). Unlike bulk formulae with constant transfer coefficients, these models are able to include the effects of stability and interfacial conditions that are applicable in approximately stationary and horizontally homogeneous moderate winds.

[86] *Section 3.1.2.*

5.1.1. NCEP's Eta model.

The Eta model is an operational atmosphere model with a variety of unique features in its numerical formulation[87]. The latest public version of the Eta model, known as "Workstation Eta" is now a complete, full physics system, and is easy to setup and configure. The code is considered very efficient, and is approximately 25-33% faster than MM5 on 2 CPU, with a 90% performance gain going from 1 to 2 CPU's. It has a non-hydrostatic option switch and can be operative in both Eta and sigma coordinate options. It also supports shared multi-processor platforms. Because of its non-hydrostatic feature, the model can now be applied for high resolution, small-scale atmospheric prediction of around 1 km or even less. The model is fully supported by the National Weather Service of the US and has been distributed to around 60 national weather forecasting offices nationally.

5.1.2. Aim of the study.

At the time of writing, verification of the "viscous sublayer" scheme embedded in a nested, high-resolution Eta model has not been done by other investigators, and so there is no quantitative knowledge of the skill of the Eta model to predict air-sea fluxes (Mesinger, 2002, *personal communication*). A literature search carried out in 2005 to check if there has been any progress did not result in any substantial study in this regard.

The primary aim of this chapter is to provide quantitative information on the overall skill of the Eta model to forecast air-sea fluxes and related surface fields. The observed skill of the Eta viscous sublayer is fine-tuned to further improve its predictability. Comparative verification measures are applied to determine the quality of forecasts and their relative accuracy with collocated observation(s). This approach condenses the large amount of data generated from the single forecast

[87] *Section 3.2.4.1.*

experiments into a summary representation of the most important variations of the predicted data. These measures include mean, standard deviation, bias error and mean square error. This chapter also uses concepts of exploratory spatial data analysis to be able to identify spatial error drifts and graphically identify the impact of fine-tuning a numerical scheme. For this purpose, a routine is designed to assess the spatial similarity of predicted field with collocated rasterised observations.

5.2. Methodology.

5.2.1. Setup and running the local area, and nested Eta atmosphere models.

A Pentium MMX configured with 800MHz and 64MB of RAM was used for the two versions of the Eta model working on a LINUX system with gnu C and fortran 77 compilers. This computer was connected to a local area network with ample space for archiving the data on hard disks and external storage material. Each model consisted of appropriate folders containing fortran 77 source codes and related executable files that (1) decoded binary data coming from World Area Forecast System (WAFS), Global Data Assimilation (GDAS) System, land cover, and topography data and convert it according to model coordinate system; (2) constituted the numerical schemes of the model; and (3) calculate the output of all relevant forecasted fields and their conversion into standard coordinates for displaying. Csh shell scripts unified the operation of all these three main groups of codes, as identified by a secondary file specifying the location of data files.

The modelling process was divided into three stages: pre-processing, processing and post-processing. The pre-processing phase used routines that generated the needed fields from databases. This was done by interpolating external data sets to the Eta grid, and generated

data sets for 3-D initialisation of the atmosphere model. Model pre-processing is described in detail Appendix II, section II.3.1. Two atmosphere models were setup: (1) a limited-area, Mediterranean-wide model and (2) a model nested within the regional one, located over the Ionian basin. Model preprocessing starts with the definition of the model boundaries, horizontal and vertical resolutions and model time step, followed by the preparation of constant input data such as topography and land cover data. The lateral (WAFS) and surface (SST) boundary conditions are then decoded and used by the regional Eta model to initialise its boundary conditions. Full details of the constitution of these datasets and the way how they are used by the model are provided in Appendix II.3.1.3. The spatial domains of the local area (regional) and the nested model are shown in figure 5.1. Examples of model-generated lateral boundary conditions generated by the WAFS and reformatted in GrADS format are shown in figures 5.2 and 5.3.

The processing phase involved the numerical calculation of the future state of the atmosphere using the numerical schemes embedded in the model for a number of pre-defined time steps that eventually lead to a short-range atmospheric forecast. This phase is described in Appendix II, section II.3.2. The daily integration of the local area (regional) Eta model generated mesoscale, 3-hourly lateral boundary conditions for a 36-hour forecast. These were used to initialised the lateral boundary conditions of the nested Eta model.

In post-processing, computations were made to the raw model output to transform it to a format readily usable by forecasters. Diagnostics and meteorological parameters were derived from the forecast variables. In addition, model variables were interpolated vertically to surfaces used by forecasters (isobaric, isentropic, and constant altitude) and interpolated horizontally to output grids. Contour plots were also made.

The post-processing stage is described in Appendix II section II.3.3. This stage consisted of the generation of predicted air-sea surface fluxes by the nested Eta model as the new surface boundary conditions to drive the ocean model[88]. These consisted of 36-hour, 3-hourly forecasts of the latent and sensible heat fluxes, outgoing and incoming long- and short-wave radiation, u- and v-component of momentum flux, moisture heat flux, surface air temperature and surface pressure. The final, high resolution forecasts were converted in gridded standard format for subsequent model verification against collocated observations.

[88] *see Chapter 7*

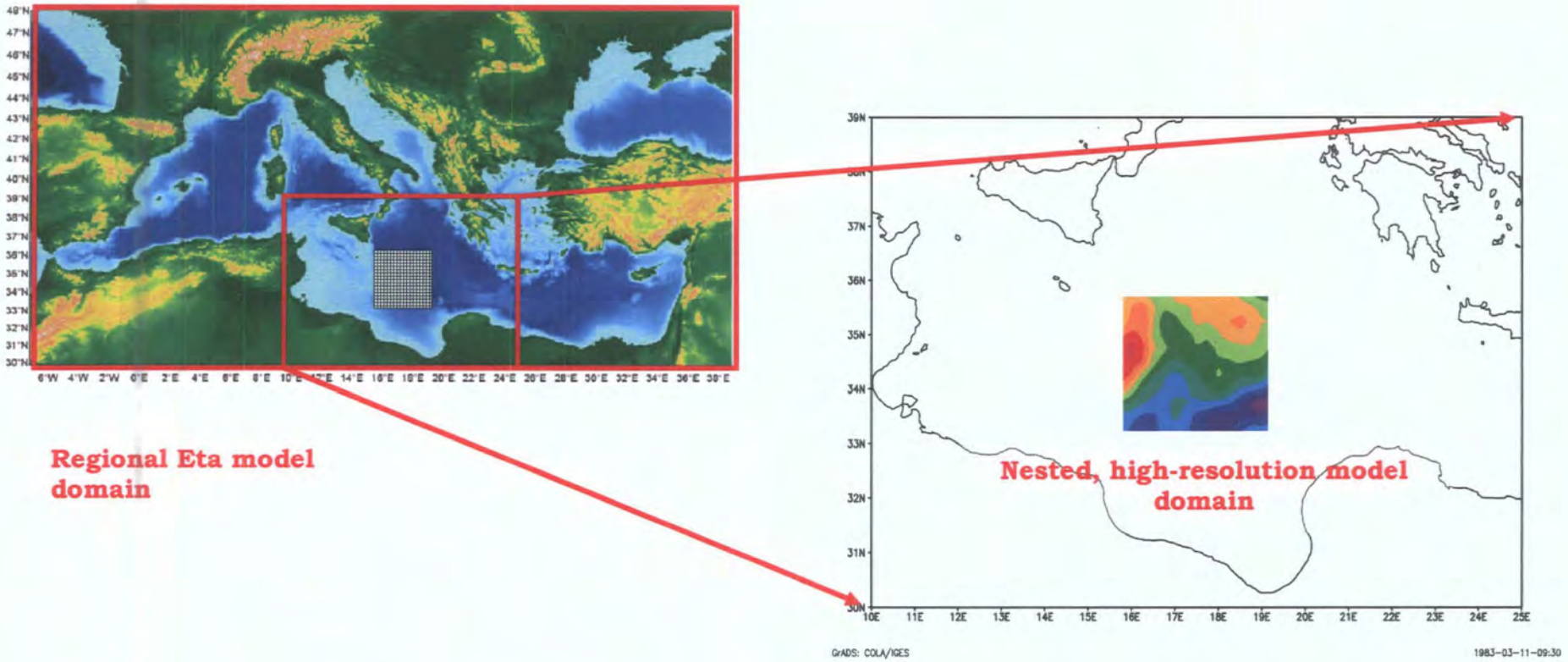

Figure 5.1. Domains of the limited area, Mediterranean-wide Eta model (LAT: 29.00° – 47.50°N; LON: -10.00°W – 42.00°E). Nested within its integration domain is the high-resolution Eta model (LAT: 33.24° – 35.74°N; LON: 15.74° – 19.17°E).

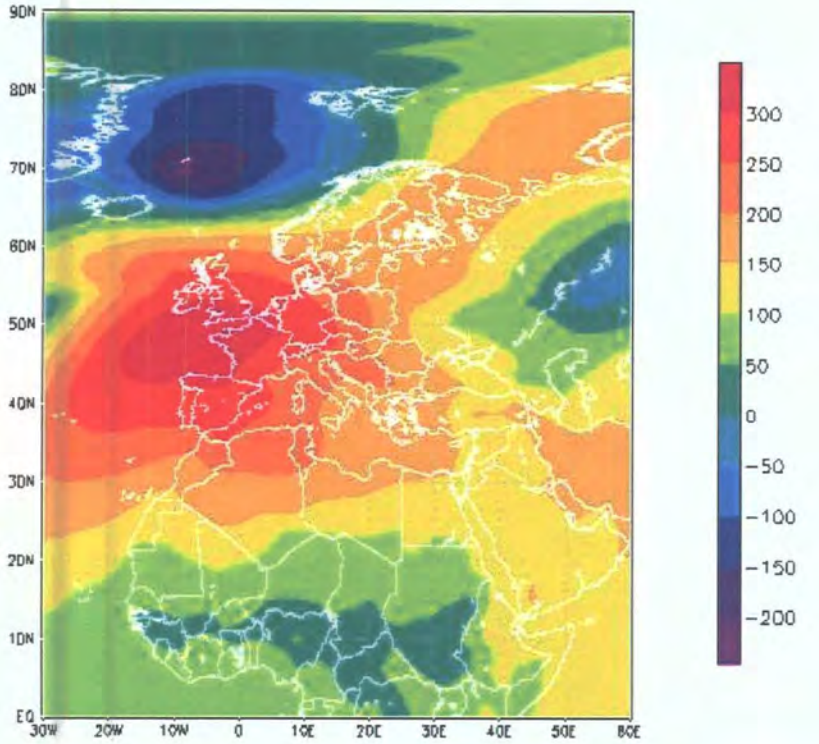

Figure 5.2 Graphical display of initial WAFS lateral boundary conditions (octant grid 37) for 2nd Feb 1999 at 1800 hrs UT. Data relates to geopotential height in mb at z=1000.

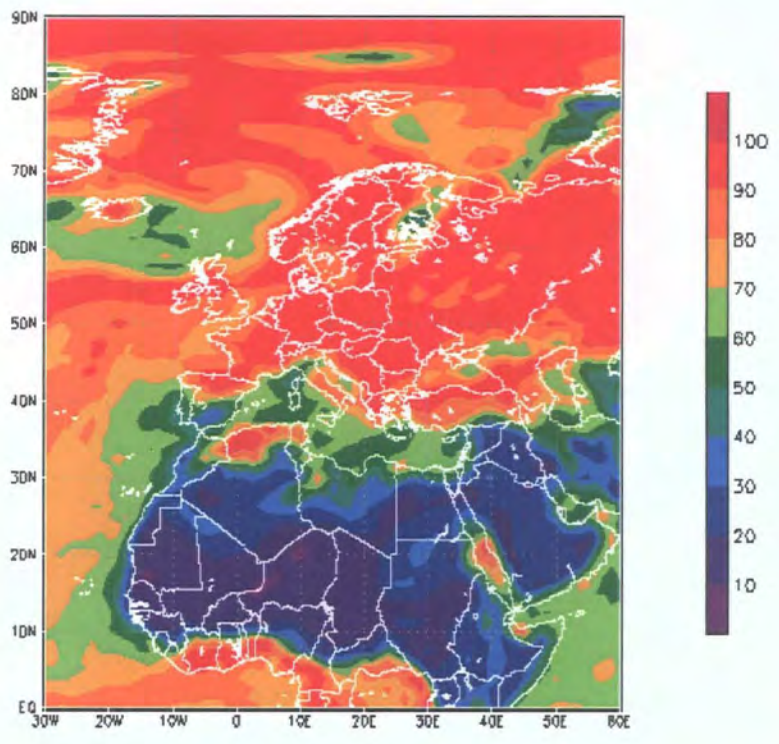

Figure 5.3 Graphical display of the initial WAFS lateral boundary conditions (octant grid 37) for 2nd Feb 1999 at 1800 hrs UT. Data relates to relative humidity in % at z=1000.

These three stages were run using an automated script as shown in Appendix II (section II.3.4.) following the process shown in figure 5.4. By defining a series of dates using the "foreach" command, dates and integration times and folder names for the output files were created automatically. WAFS- and GDAS-derived lateral and surface boundary conditions in GRIB format were first copied from the central archive to a specific folder from which they were subsequently called and converted to GrADS format using *grb2grads.f*[89] routine. This stage gave the facility to display the initial data. Conversion into Eta transformed coordinates followed using *grads2anec.f* routine. The sst routine (see *sst.F* [90]) converted the SST from GrADS format into a binary file was used by the model to initialise its surface boundary field.

The subsequent processing prepared the boundary conditions over the domain area of the regional model run, including the preparation of seasonal/monthly initial conditions for the aerosols, ozone, radiation, etc., using the GFDL package.

Following the processing stage, the routine *outnest.f* converted the 3-hourly output data into standard latitude and longitude coordinate files and wrote the transformed data into GrADS format to be graphically displayed. This routine also prepared prognostic 3-hourly fields that were used as the new mesoscale lateral boundary conditions for the nested model (fig. 5.5).

[89] *Appendix II; Section II.2.1.*
[90] *Appendix II; Section II.2.3.*

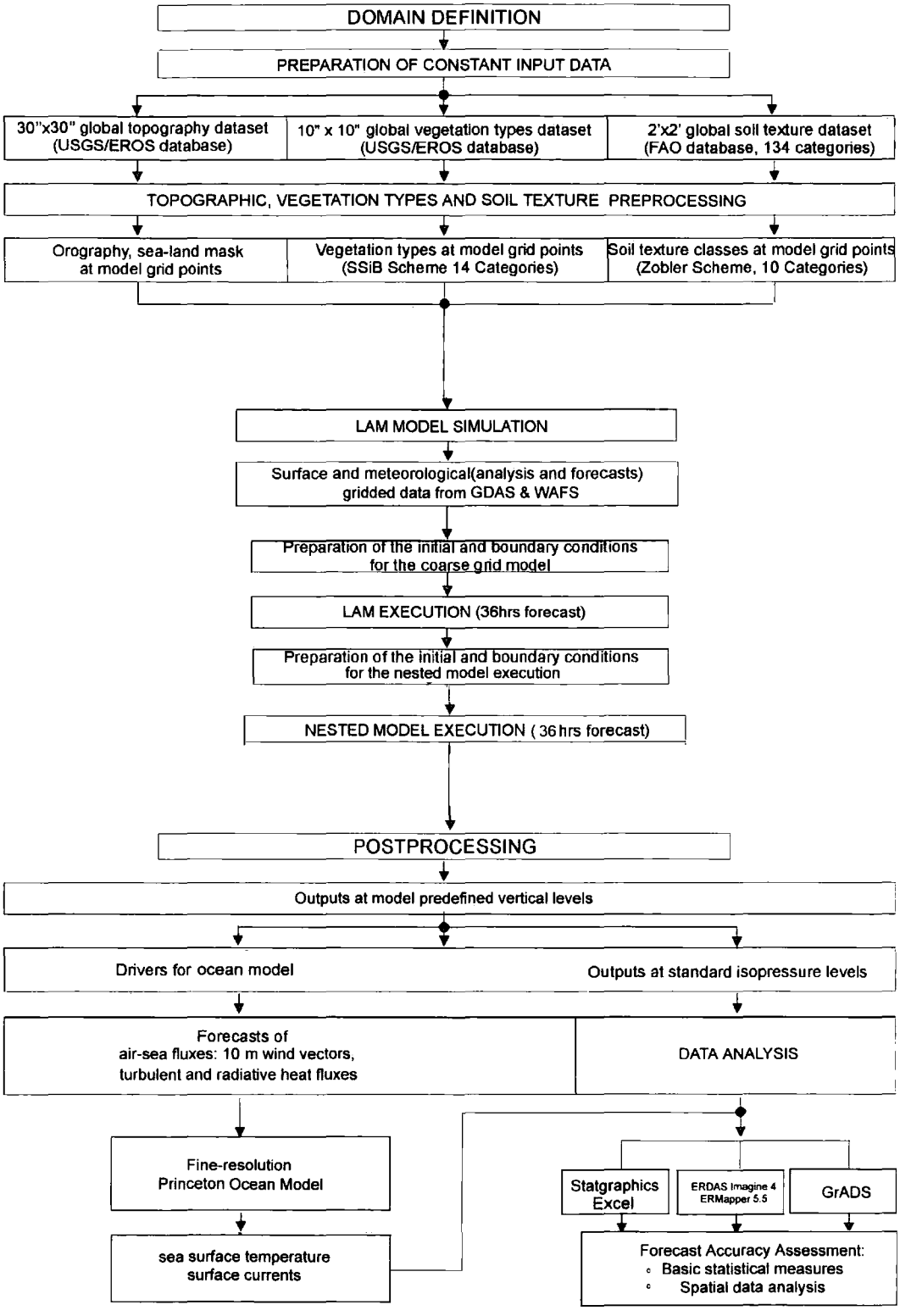

Figure 5.4. Flowchart and interaction between the various stages of the two Eta models and input of forecasted air-sea surface flux fields into the ocean model. The Data Analysis component used image processing, GIS and statistical software for model diagnostics. (LAM= Limited Area Model).

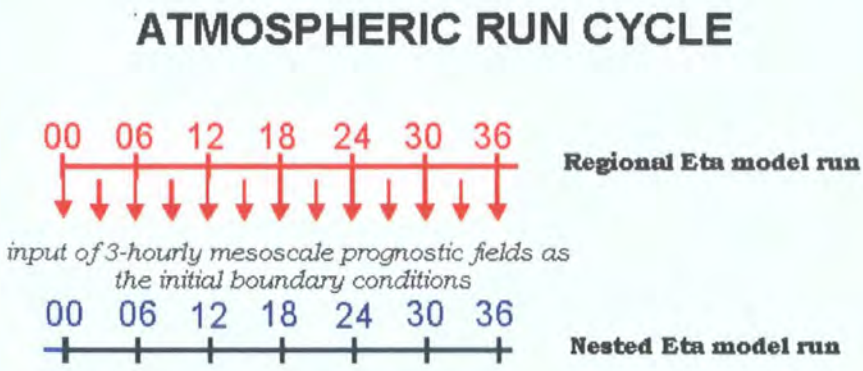

Figure 5.5 Use of 3-hourly predicted mesoscale fields generated by the limited area model to intialise the lateral boundary conditions of the nested, high-resolution Eta model.

A second script file was run for the nested Eta model with the horizontal resolution of 0.041666° and utilising 24 standard pressure levels (1000, 980, 960, 940, 920, 900, 870, 850, 820, 770, 730, 700, 650, 600, 550, 500, 450, 400, 350, 300, 250, 200, 150 and 100 hPa). Model integration followed exactly the same pre-processing, processing and post-processing stages of the limited area model, except that 3-hourly mesoscale lateral boundary conditions produced by the local area model were instead used to initialise the nested model. The subsequent pre-, processing and post-processing stages were identical to those of the regional model. Automated archiving of data was done according to the integration date and time.

5.2.2. Validated atmospheric parameters.

5.2.2.1. 10 m wind magnitude.

Forecasted wind magnitude was calculated as the resultant of the 10 m wind vectors in the x(u) and y(v) dimension, or

$$U_{10}(m\ s^{-1}) = \sqrt{(u_{10}^2+v_{10}^2)}$$

where u_{10} and v_{10} are the 10 m wind components. Pixel to pixel validation of Eta-generated 10 m wind magnitude fields was performed against collocated TMI-derived 10m wind magnitude fields[91]. Data was filtered as to exclude contamination due to low variable winds (< 3 m s^{-1}) and high winds (> 12 m s^{-1}).

5.2.2.2. Turbulent heat fluxes.

SST and wind magnitude fields extracted from the TMI sensor were used to calculate the sensible and latent heat fluxes. Values of 10 m wind magnitude in the region of < 3 m s^{-1} and > 12 m s^{-1} were not used in the calculation of the heat fluxes.

Pixel-to-pixel validation of Eta-generated sensible and latent heat fluxes was done against collocated flux fields derived from the database[92].

5.2.2.3. Radiative heat flux.

The outgoing longwave radiation (OLWR) is the only radiative heat flux parameter used to assess the radiative package of the Eta model as compared to the monthly average observation collected by NOAA pathfinder during 1999[93].

Validation of Eta-generated outgoing longwave radiation was performed using statistical software by comparing mean values against monthly fields derived from the database.

5.2.2.4. Columnar cloud liquid water.

This parameter is related to the degree of condensation of atmospheric water vapour. The integrated cloud liquid water is an important

[91] *Section 4.3.1.1.*
[92] *Section 4.3.1.6.*
[93] *Section 4.3.1.3.*

parameter for determining both the initiation and amount of precipitation from cloud systems. Pixel-to-pixel comparison between Eta forecasted integrated cloud liquid water and remotely sensed observations[94] gave an indication of the accuracy of the model's convection parameterisation scheme to predict such events.

5.2.2.5. Total columnar precipitable water vapour.

The accurate prediction of this parameter by atmosphere models can be highly beneficial for both the oceanographic and atmospheric community. This parameter indicates the amount of water vapour in the column and is a function of the atmospheric temperature profile. Sinks of this water vapour are clouds or condensation on surfaces.

Pixel-to-pixel validation of Eta-generated total precipitable water vapour against similar collocated fields (derived from the database) was performed using statistical software.

5.2.2.6. Near surface air temperature.

Validation of Eta-generated 2 m air temperature was done using statistical software by comparing predicted mean monthly values against collocated fields extracted from the database[95].

5.3. Fine-tuning of the Eta model viscous sublayer depth.

The viscous sublayer model embedded in the Eta model is a sophisticated scheme that calculates amongst other fluxes, the 10 m wind. The research questions presented in section 2.1.2. require an experimental setup that performs a number of Eta model simulations over water surface as to fine-tune equations 5.15[96]. This is based upon

---

[94] *Section 4.3.1.1.*
[95] *Section 4.3.1.6.*
[96] *Appendix II; Section II.1*

verification of forecasts against the 10 m wind magnitude observations derived from the database.

A schematic diagram of the experiment is shown in figure 5.6. The fine-tuning is focused on the scheme embedded in the nested Eta model. High-resolution model runs were repeated using a value for the parameter that defines the depth of the viscous sublayer, ζ, of 0.20, 0.35, 0.70 and 0.80.

A substantial number of forecasted output fields generated by the parallel experimental runs were validated against satellite observations. The total number of single-forecast verification analyses (see table 5.1 a-b), amount to 524. The selection of these single-forecast dates were defined by:

1. the availability and integrity of initial surface and lateral boundary conditions, and,
2. the availability and integrity of collocated observation data.

The scalar and spatial accuracy of the 4 sets of forecasted 10 m wind speed was assessed on the basis of objective correspondence between forecasts and collocated 10 m remotely sensed observations.

Statistical measures including bias and root mean square error were used[97]. The sets of single forecasted dates validated against remotely sensed wind speed observations were grouped together according to the average Eta-model predicted wind speed as follows: 3.0 - 3.9 m s^{-1}; 4.0 - 4.9 m s^{-1}; 5.0 - 5.9 m s^{-1}; 6.0 - 6.9 m s^{-1}, and 7.0 - 11.0 m s^{-1}. For each category, the respective RMSE values for the 4 sets of data were normalised and plotted against increasing wind speed.

Exploratory spatial data analyses was also applied[98].

---

[97] *Section 5.4.*

[98] *Section 5.4.3.*

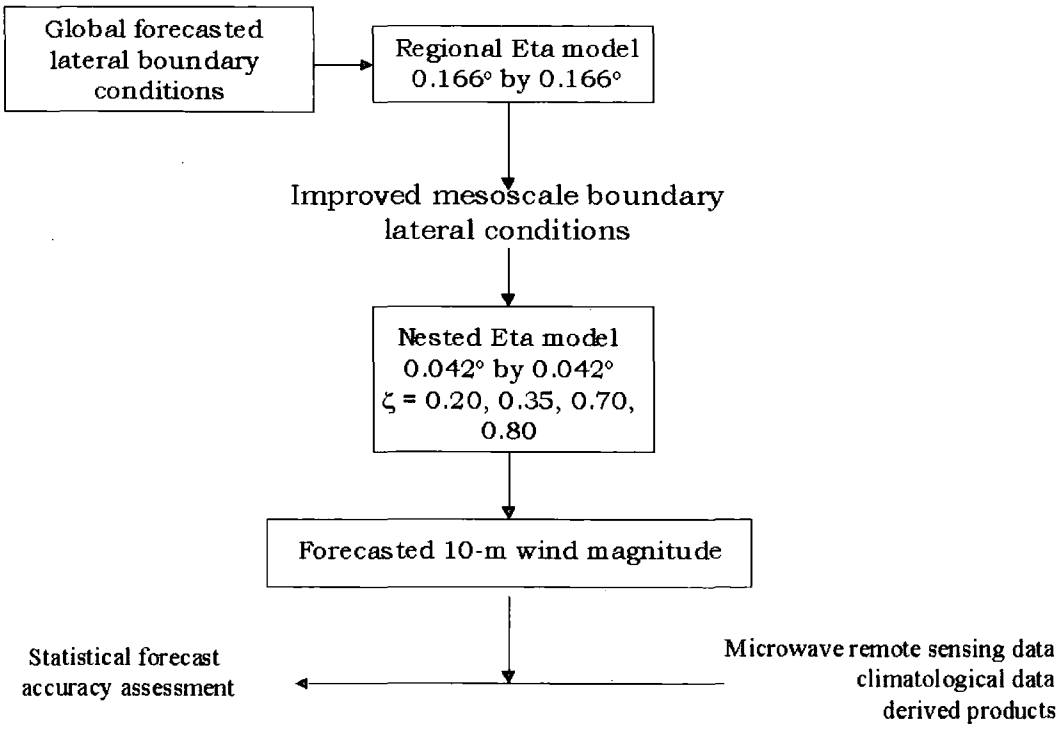

Figure 5.6 Schematic diagram of the experiment to fine-tune the Eta viscous sublayer. The nested model was run four times, each run using a different ζ value embedded in the viscous sublayer scheme. Subsequent model verification is described in section 5.4.

5.4. Model output accuracy assessment.

The accuracy of the forecasting system was assessed on the basis of the objective correspondence between the forecasts and collocated data extracted from the database[99] (Glahn *et al.*, 1991; Murphy, 1997).

The database used in the verification processes had a space-time correspondence with all forecasts validated at the pixel level (tables 5.1 a - b). Two classes of statistical verification methods were applied: (1) the basic forecast distributions and their summary measures, (2)

[99] *Section 4.3.1.*

Month: JANUARY								
Dates	9	10	11	12	15	17	28	29
TMI pass close to 3 hr interval over 33.5°N/17.5°E	✔	✔	✔	✔	✔	✔	✔	✔
Valid TMI data to calculate heat fluxes	✔	✔	✔	✔	✔	✔	✔	✔
Ascending or Descending	D	A D	A	A	D	A	A	A

Month: February										
Dates	2	6	7	8	13	16	25	26	27	28
TMI pass close to 3 hr interval over 33.5°N/17.5°E	✔	✔	✔	✔	✔	✔	✔	✔	✔	✔
Valid TMI data to calculate heat fluxes	✔	✔	✔	✔	✔	✔	✔	✔	✔	✔
Ascending or Descending	D	D	D	D	D	A	D	A	A	A

Month: March										
Dates	2	3	9	10	13	20	21	22	26	28
TMI pass close to 3 hr interval over 33.5°N/17.5°E	✔	✔	✔	✔	✔	✔	✔	✔	✔	✔
Valid TMI data to calculate heat fluxes	✔	✔	✔	✔	✔	✔	✔	✔	✔	✔
Ascending or Descending	D	D	A D	D	D	D	D	A	D	A

Month: April													
Dates	1	2	6	7	8	9	12	13	14	20	23	25	26
TMI pass close to 3 hr interval over 33.5°N/17.5°E	✔	✔	✔	✔	✔	✔	✔	✔	✔	✔	✔	✔	✔
Valid TMI data to calculate heat fluxes	✔	✔	✔	✔	✔	✔	✔	✔	✔	✔	✔	✔	✔
Ascending or Descending	A D	A	D	D	A	A	D	A D	A	A	D	A	D

Month: May					
Dates	1	7	16	18	29
TMI pass close to 3 hr interval over 33.5°N/17.5°E	✔	✔	✔	✔	✔
Valid TMI data to calculate heat fluxes	✔	✔	✔	✔	✔
Ascending or Descending	A	A	D	A	D

Month: June																
Dates	2	4	9	10	12	13	14	15	16	17	18	19	21	22	26	27
TMI pass close to 3 hr interval over 33.5°N/17.5°E	✔	✔	✔	✔	✔	✔	✔	✔	✔	✔	✔	✔	✔	✔	✔	✔
Valid TMI data to calculate heat fluxes	✔	✔	✔	✔	✔	✔	✔	✔	✔	✔	✔	✔	✔	✔	✔	✔
Ascending or Descending	A	A	A	D	D	A	A	D	A D	A	A	A	A	D	A	D

Month: July																
Dates	1	2	4	8	9	10	13	14	15	16	20	21	22	25	26	27
TMI pass close to 3 hr interval over 33.5°N/17.5°E	✔	✔	✔	✔	✔	✔	✔	✔	✔	✔	✔	✔	✔	✔	✔	✔
Valid TMI data to calculate heat fluxes	✔	✔	✔	✔	✔	✔	✔	✔	✔	✔	✔	✔	✔	✔	✔	✔
Ascending or Descending	D	D	A	D	A	A	D	A D	A	A	D	A	A	A	D	D

Month: August										
Dates	01	02	07	08	09	12	14	20	22	26
TMI pass close to 3 hr interval over 33.5°N/17.5°E	✔	✔	✔	✔	✔	✔	✔	✔	✔	✔
Valid TMI data to calculate heat fluxes	✔	✔	✔	✔	✔	✔	✔	✔	✔	✔
Ascending or Descending	A	A	A D	D	D	A D	D	A	D	A

Table 5.1a. Single forecast verification matrix for the nested model runs during 1999. Validation depends on the availability of collocated observations/derived products. When available, forecasts at 12, 15, 18, 21, 24, 27, 30 and 33 hrs from the start of the model run were validated against objective data.

Month: September										
Dates	05	06	07	09	11	17	20	21	22	23
TMI pass close to 3 hr interval over 33.5°N/17.5°E	✔	✔	✔	✔	✔	✔	✔	✔	✔	✔
Valid TMI data to calculate heat fluxes	✔	✔	✔	✔	✔	✔	✔	✔	✔	✔
Ascending or Descending	A	A	A	D	A	A	D	D	A	A

Month: October									
Dates	14	15	16	17	20	21	26	27	31
TMI pass close to 3 hr interval over 33.5°N/17.5°E	✔	✔	✔	✔	✔	✔	✔	✔	✔
Valid TMI data to calculate heat fluxes	✔	✔	✔	✔	✔	✔	✔	✔	✔
Ascending or Descending	A D	D	A	A	D	A	D	D	D

Month: November														
Dates	06	07	08	09	11	12	13	15	17	18	19	23	24	25
TMI pass close to 3 hr interval over 33.5°N/17.5°E	✔	✔	✔	✔	✔	✔	✔	✔	✔	✔	✔	✔	✔	✔
Valid TMI data to calculate heat fluxes	✔	✔	✔	✔	✔	✔	✔	✔	✔	✔	✔	✔	✔	✔
Ascending or Descending	D	D	A	A	D	D	A	A	D	D	A	D	D	A

Month: December										
Dates	05	08	11	12	13	17	18	19	24	25
TMI pass close to 3 hr interval over 33.5°N/17.5°E	✔	✔	✔	✔	✔	✔	✔	✔	✔	✔
Valid TMI data to calculate heat fluxes	✔	✔	✔	✔	✔	✔	✔	✔	✔	✔
Ascending or Descending	D	A	A	D	A	D	A	A	A	A

Table 5.1b. Single forecast verification matrix for the nested model runs during 1999. Validation depends on the availability of collocated observations/derived products. When available, forecasts at 12, 15, 18, 21, 24, 27, 30 and 33hrs from the start of the model run were validated against objective data.

performance measures of the forecasts and their decompositions. This was done in order to describe the characteristics of the forecasts, the corresponding observations, and the relationship between the forecasts and observations.

5.4.1. Basic forecast distributions and their summary measures.

A multi-sample comparison analysis was performed to compare the sets of data (i.e. model forecasts and observations). Summary statistics were collected to display statistical information about the center, spread, and shape of the data. The data count, the average, covariance, standard deviation, correlation, mean difference and mean error were calculated.

5.4.2. Performance measures of the forecasts.

A number of different characteristics of forecasting performance were identified which represented various aspects of the quality of the forecasts. In addition to the basic characteristics, other features of interest were studied involving the marginal distributions of the forecasts and observations. Statistical analysis was performed on a pixel-to-pixel basis. These measures were the following:

Bias: This is a simple difference of forecast (f) minus observation (o) and equals the error between scalar quantities

$$\overline{b} = \frac{1}{N}\sum_{i=1}^{N} f_i - o_i$$

which can be arithmetically averaged in area and time. The difference (error) field provides a quick look at model's forecast performance or bias. Bias or tendency was measured to identify magnitude of systematic tendencies to under- or over-forecast a particular variable with forecasting time.

Forecast accuracy: This referred to the accuracy of the model forecasts.

RMSE: The Root Mean Square Error is defined as the positive square root of the mean square error

$$\text{RMSE} = \left(\left(\frac{1}{N} \right) \Sigma_f \Sigma_x \, p(f, x)(f - x)^2 \right)^{1/2}$$

RMSE depends on the range of atmospheric variability and on the atmospheric flow. It typically increases with forecast time since the predictive skill of the model drifts away with time. It provided a useable

statistic to verify model forecasts and is applicable to a large number of analysis and forecast elements and model types.

5.4.3. Spatial data analysis.

Spatial analysis was performed (1) to analyse the relationship between Eta forecasted fields and observations, (2) to identify spatial properties of and (3) to understand the inter-relationship between surface fields.

5.4.3.1. Spatial similarity and feature matching analysis.

Similar approaches to spatial problems have been used. Jones and Roydhouse (1994), for example, examined weather patterns and Holt and Benwell (1999) modelled the natural forest environment. Their studies support the use of spatial similarity to answer questions concerning the presence of similar, user-defined spatial phenomena within different subsets. The concept of spatial similarity analysis developed by Cobb *et al.* (1998) was formalised in this study. This consisted of the combination of fields and their associated inherent knowledge as to determine the position of similar clusters between observed and Eta forecasted fields. Each feature is considered as a set of attribute-value pairs and from this representation, a degree of matching similarity was determined.

A windows-based ERMAPPER 5.5 algorithm with raster display features was written to recode the raster information between observed and predicted fields into a set of normalised class values that assisted the calculation of spatial similarity. By using proximity analysis, the observation field was assigned as a reference while the forecasted field as the source to measure degree of similarity. These two recoded fields were then overlayed and the difference between the coinciding classes was related to the similarity between them. An ISOCLASS, unsupervised classification processed the resulting raster field and generated a classified map consisting of a single band, byte raster dataset, with

each data point holding an integer value that corresponded to the class number (or degree of similarity) for that point. The ERMAPPER algorithm also defined results to be displayed as a look-up-table indicating the degree of spatial similarity through a matching and two-way ranking measure (fig. 5.7).

The analysed predicted and observed fields were consistent with the model grid resolution. The result was the synthesis of a map indicating the levels of similarity based on constraints as defined by the algorithm.

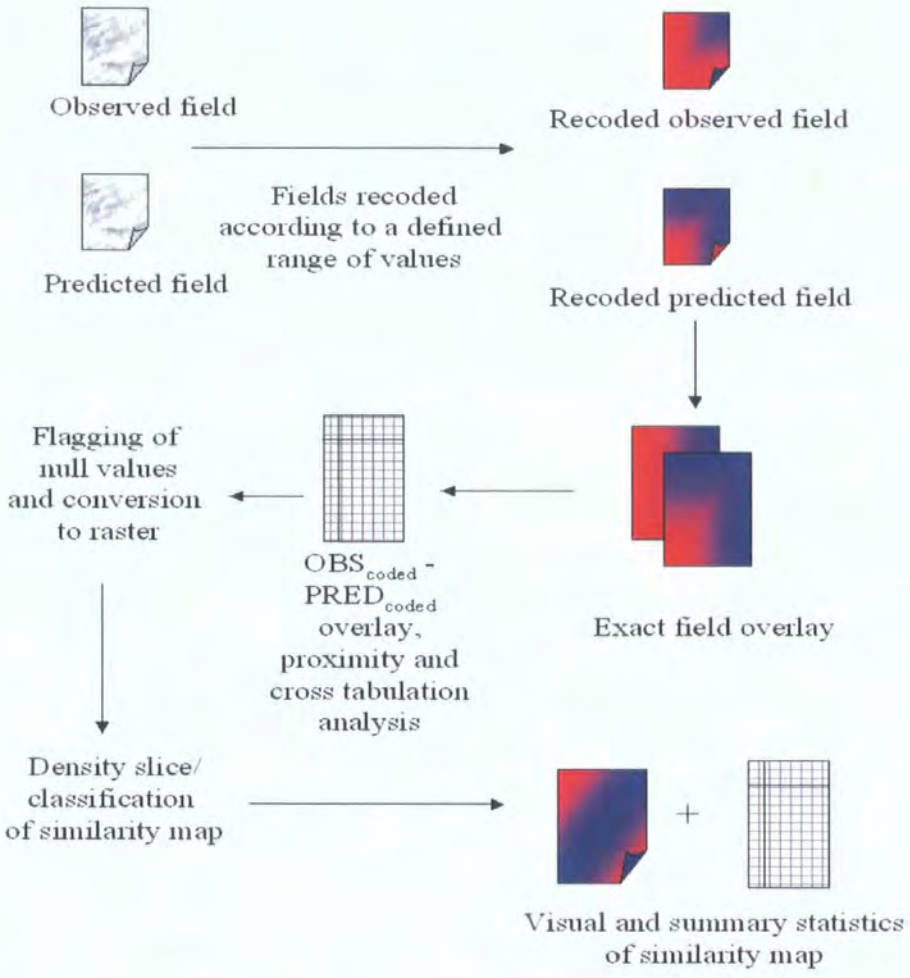

Figure 5.7. Flowchart of the spatial similarity analysis between predicted and observed field and derivation of interrelationship between surface fields.

5.5. Results and discussion.

5.5.1. The experimental approach.

The following points were considered in the setting up of the atmospheric modelling system:

1. ***software and operating systems:*** The Eta model code is written in fortran and c language, and has been ported and tested on different machines, including HP, SGI, DEC, IBM and LINUX workstations. LINUX is growing in popularity; it is freely available and its compatibility with personal computers as well as free source compilers such as Fortran 77 that run on LINUX operating system made it an ideal choice for the present study. The formatting of forecast data in gridded ascii provided flexibility for further analysis using different operating systems such as Windows platform, on which statistical and GIS-related analysis together with the required image processing was performed.

2. ***domain size:*** the choice of the domain size impacted on the model execution time, the influence of the boundary conditions, development of computational grid-scale forcing and forecasting skill and value. The choice of the domain size for the limited area model domain (0.17°) rested on the balance between the provision of coarse, modelled lateral boundary conditions from the global model (1.25° resolution) and the requirements of the nested model running at 0.042° resolution. The small-scale nested domain is still at the research phase for NWP in the Mediterranean, and so is considered as a challenge for the present study. This high-resolution model provided forecasted data at unprecedented temporal and spatial scales. In addition to the actual forecasts *per se*, these products were used to force an underlying ocean model running at 0.042° resolution – a scale that also sets an

experimental limit for sub-basin ocean forecasting in the Mediterranean.

3. ***model nesting***: The scope of model nesting is to ensure the provision of much better resolved and more balanced initial fields than if the nested model was directly initialised by the WAFS dataset. As explained in Appendix II.2, the LAM was first used to prepare 3-hourly forecasts of the main prognostic variables which were consecutively used to initialise the boundary conditions of the nested model. This was done in two steps; first, sets of 3-hourly forecasts were produced after the region-wide model was run for each designated date throughout 1999. Second, the region-wide forecasts were made available as boundary conditions of the nested, high resolution model[100], to produce, in turn, high resolution, 3-hourly forecasts over the Ionian sea. To this affect, changes were made to the pre-processing (e.g. model ingestion of initial data; model integration domain, horizontal resolution) and post-processing phases (e.g. calculation of the air-sea fluxes and extraction of forecasted data for model validation) of the model. The processing phase of the two models was exactly the same.

   As well illustrated by Mesinger (1977), the limited area model helps the performance of the nested model by allowing it to develop small scale motion, consistent with the local area model. However, dynamical inconsistencies can still arise based on different vertical resolutions between the two models. Weather features can be affected by "refraction" and "redirection" processes of atmospheric waves when they are introduced at the nested model's lateral boundaries, causing drifts even at the initialisation phase. Such fields may include precipitation, temperature, vertical motion, etc. This is also relevant when the regional model is initialised with the boundary conditions supplied by the global model.

[100] *A description of this process is given in Appendix II.2.5*

4. ***model execution time***: The total integration period was designed to produce short-range, 36-hourly forecasts with a high temporal resolution (3 hours). It is well known that the downward trend in the forecasting skill of any atmosphere model originates from the chaotic nature of the real atmosphere. Far from providing accurate, high-resolution forecasts, the only useful long-range prediction will consist of just the larger scales of predicted motion. At the other end of the forecasting spectrum, the skill of atmosphere models tend to deteriorate only slowly in the early, short-range part of the forecast owing both to their good representation of larger scales which parallels the 'perfect' solution as well as accurate initial conditions.

   In addition to their higher skill, short-range forecasts are highly sensitive to any fine-tuning adjustments made to the model's algorithms. The present approach proved to be very convenient, since it restricts the generation of large amounts of data requiring analyses and validation. The assumption is that ultimately the improved skill will be propagated forward in time to the benefit of the final accuracy of the longer, medium-range forecasts.

   Another reason for the choice of a short integration time is that the accuracy of highly variable parameters, such as turbulent heat fluxes, can only be captured using a short-range predictive mode. Moreover, the present model system uses a constant SST throughout its integration time as its lower surface boundary condition[101]. It is well understood that SST has a diurnal cycle of as much as 3 ^{o}C in near-calm conditions and if not reflected in the model, this variation can cause the models to underestimate daytime ocean-surface evaporation.

[101] *This is similar to all NCEP NWP models. These models prescribe that the SST remain fixed (i.e. retain their initial value) throughout the forecast period.*

5. **phenomena of interest**: the list of fields that can be predicted by the Eta model is wide ranging. The objectives of this study restricted this list to a number of geophysical fields that enabled the analysis and fine-tuning the skill of the current Eta model to enhance its predictability of air-sea fluxes.

6. **displaying and conversion of initial and forecasted data**: a prerequisite of the forecasting system was an interactive desktop tool for easy access, processing and visualization of 4-dimensional gridded, initial and forecasted binary data. The grids were of variable resolution and analysis of fields required a variety of graphical techniques, including smoothed contours, shaded contours, streamlines, wind vectors, grid boxes and shaded grid. Their output into image formats was also required. The Graphical Analysis and Display System (GrADS) proved very useful for such purposes, where the displaying and processing were executed using FORTRAN-like expressions at the command line. GrADS was run in batch mode, and the scripting language facilitated its use to perform long overnight batch jobs. This software is available for free and versions are available for both LINUX and Windows operating systems.

   However, GrADS falls short from being able to analyse the model data from a GIS point of view. ERMapper was used as a GIS program for the visualization, processing and enhancement of the geographic data. Using this software, model forecasts and collocated observations were loaded into different layers, superimposed and processed for comparative and spatial analysis. ERMapper also provided GIS tools for contouring and vector overlay. Its data export facility was conveniently used to convert the raster data into gridded xyz format that was later analysed by statistical packages such as Microsoft Excel (for basic statistical analysis) and StatGraphics (for multiple regression model analysis).

5.5.2. The forecasts.

Figures 5.8 to 5.14 represent a case study of the short-range, main geophysical fields predicted by the limited area model and high-resolution nested Eta models on the 2nd February 1999 at 2100 UT. Figure 5.12 gives an indication of the enhanced small-scale information of the 10 m wind speed forecasted by the nested Eta model. This is also the case for the sensible and latent heat flux maps in figures 5.13 and 5.14.

5.5.3. A climatological analysis of the model accuracy.

A summary of the analysis (forecasted versus observations and derived products) for the period January 1999 – December 1999 is given in this section[102]. A total of 131 single forecasts were analysed throughout this period. This is considered to be a good analytical sample and is comparable to similar verification studies of the Eta model. In this section, reference is principally made to a small number of measures, namely average, standard deviation, bias and RMSE that assist the comparison between forecasted fields and climatological datasets, and hence, its accuracy. This section is not intended to analyse in detail the climatological behaviour of the various geophysical fields, rather it is aimed at testing the accuracy of the forecasts against collocate observations. The general climatic tendencies of these fields are been described in chapter 4.

[102] *Full statistical results are shown in Appendix VI.*

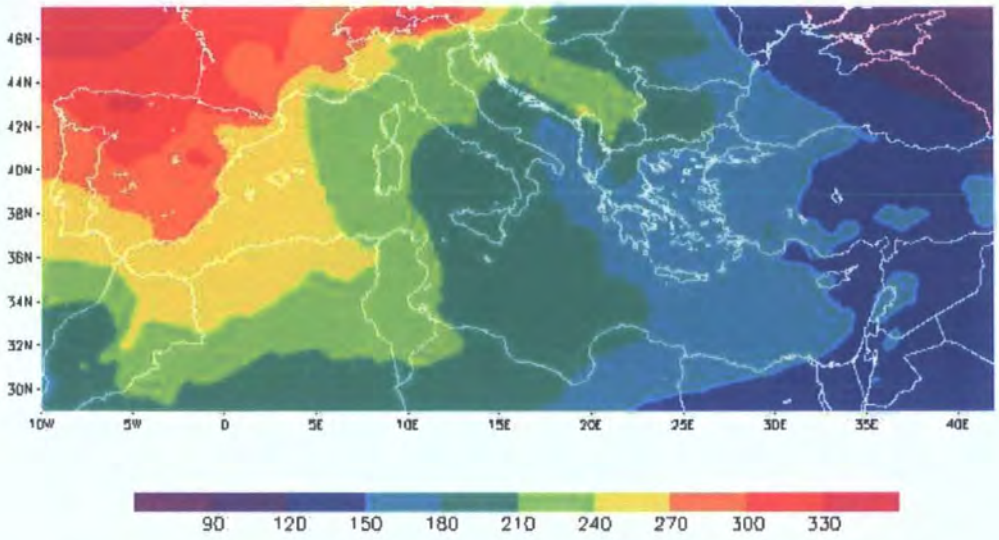

Figure 5.8. Predicted geopotential field at 1000 mb on 2nd Feb 1999 at 2100 UT. Initial conditions were derived from WAFS global model. Notice improved spatial resolution of fields after model integration at 0.17° horizontal resolution compared to fig. 5.2.

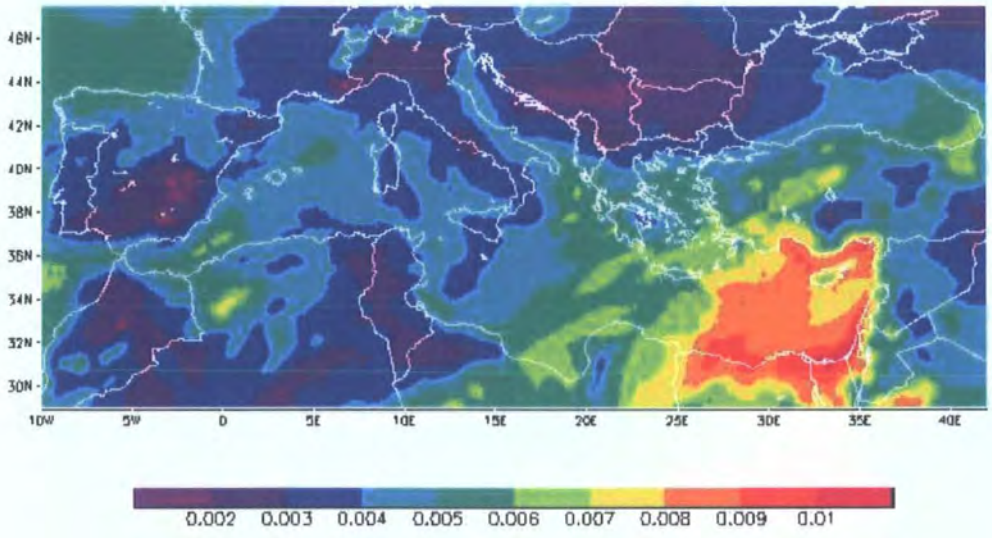

Figure 5.9. Predicted specific humidity field at 1000 mb in kg kg^{-1} on 2nd Feb 1999 at 2100 UT. Initial conditions were derived from WAFS global model. Notice improved definition of fields after model integration at 0.17° horizontal resolution compared to fig. 5.3.

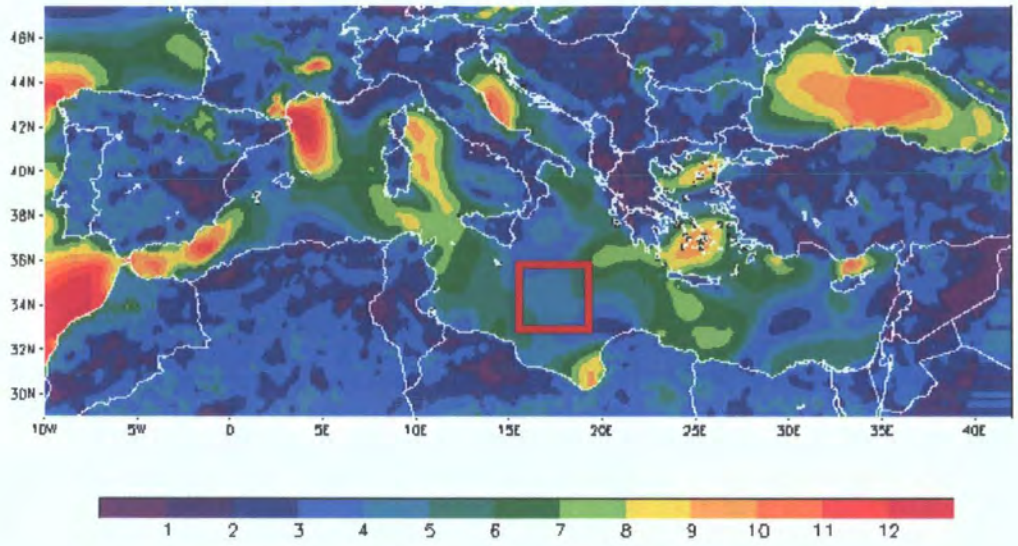

Figure 5.10. Predicted 10 m wind field (in m s^{-1}) at 1000 mb on 2nd Feb 1999 at 2100 UT. Initial conditions were derived from WAFS global model. Notice mesoscale definition of fields after model integration at 0.17° horizontal resolution. Red box marks the model integration domain of the nested Eta model.

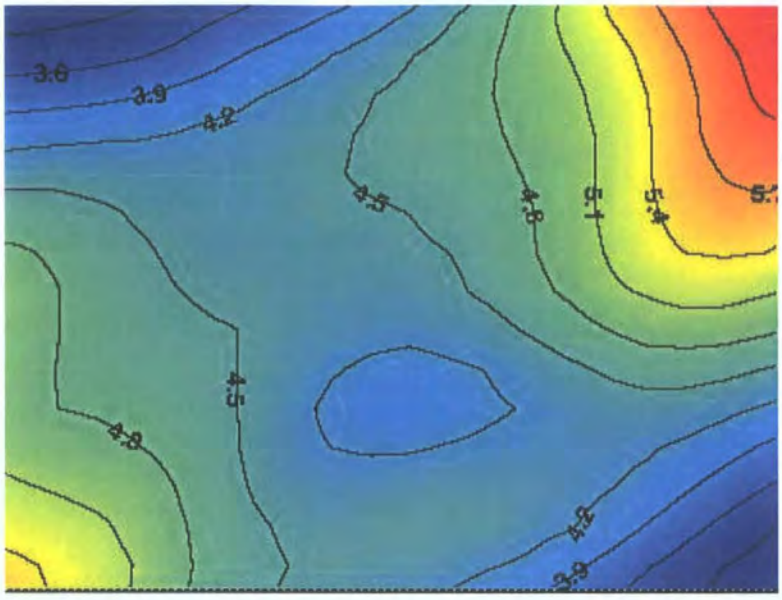

Figure 5.11. Predicted, contoured 10 m wind magnitude field (in m s^{-1}) on 2nd Feb 1999 at 2100 UT extracted from inset box (in red) shown in fig 5.10. Coordinates are: LAT: 33.24° – 35.74°N; LON: 15.74° – 19.17°E. Initial boundary conditions for the local area Eta model are derived from WAFS global model.

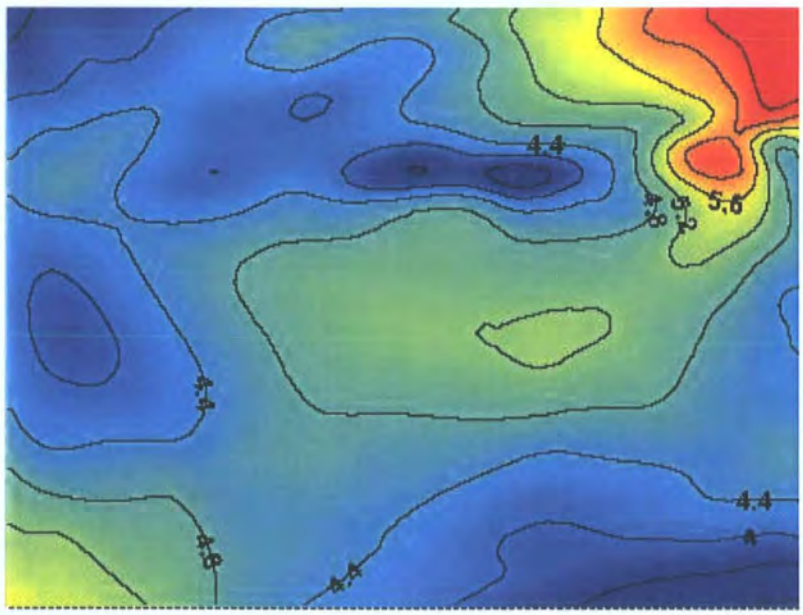

Figure 5.12. Predicted, contoured 10 m wind magnitude field (in m s^{-1}) on 2nd Feb 1999 at 2100 UT derived from the high-resolution, nested model with a horizontal resolution of 0.04°. Coordinates are: LAT: 33.24° – 35.74°N; LON: 15.74° – 19.17°E. Initial conditions were derived from the boundary conditions provided by the limited area model.

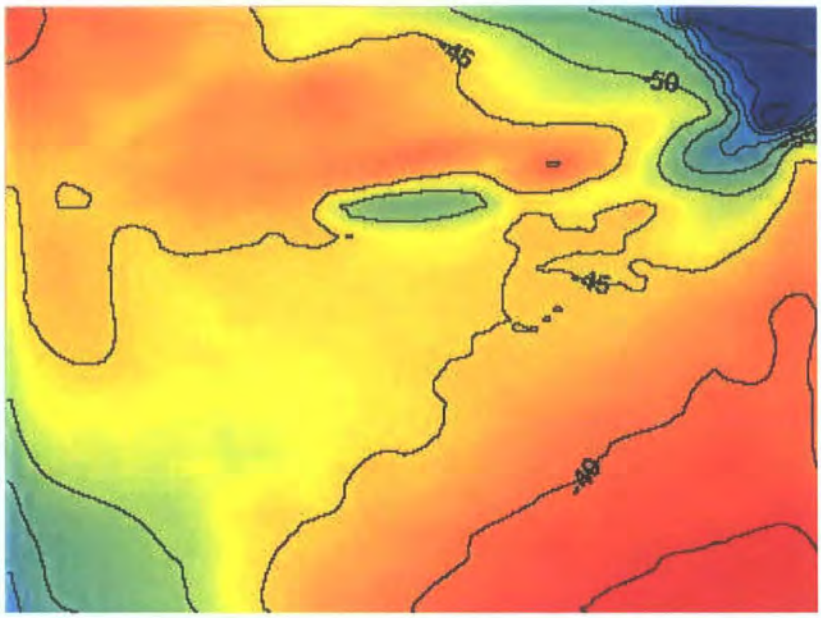

Figure 5.13. Predicted sensible heat flux (in W m^{-2}) on 2nd Feb 1999 at 2100UT. This field was derived from the nested model with a horizontal resolution of 0.04°. Coordinates are: LAT: 33.24° – 35.74°N; LON: 15.74° – 19.17°E. Initial conditions were derived from the boundary conditions provided by the limited area model.

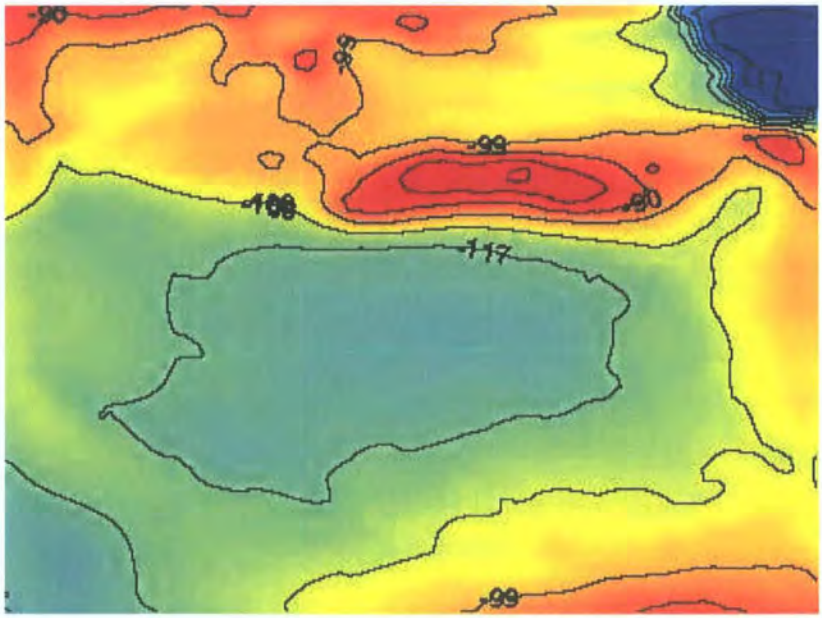

Figure 5.14 Predicted latent heat flux (in W m^{-2}) on 2nd Feb 1999 at 2100UT. This field was derived from the nested model with a horizontal resolution of 0.04°. Coordinates are: LAT: 33.24° – 35.74°N; LON: 15.74° – 19.17°E. Initial conditions were derived from the boundary conditions provided by the limited area model.

5.5.3.1. Integrated precipitable water vapour.

The predicted monthly average integrated precipitable water vapour over the integration domain was 2.06 ± 0.14 g cm^{-2} compared to the observed value of 2.11 ± 0.18 g cm^{-2}. Results show a balanced mean error in the Eta prediction, with an under-forecasting phase during the high levels of spring and summer followed by an over-forecasting trend during autumn and winter (fig. 5.15). The mean bias shown by the Eta model is around –0.05 g cm^{-2}, which is considered to be small.

The mean error and RMSE show an over-forecasting trend that reaches its peak in July, after which it decreases to minimal levels (figs. 5.16 and 5.17). Another interesting aspect is the increasing RMSE drift between 12 hrs to 33 hrs (fig. 5.18). The low trend value observed at 24 hours is probably due to small sample analysed, thus giving an unrealistic RMSE value. Fields that are forecasted before 12 hours were discarded since these may contain unbalanced geostrophic fields due to 'spin-off' effects following initialisation at 00 UT.

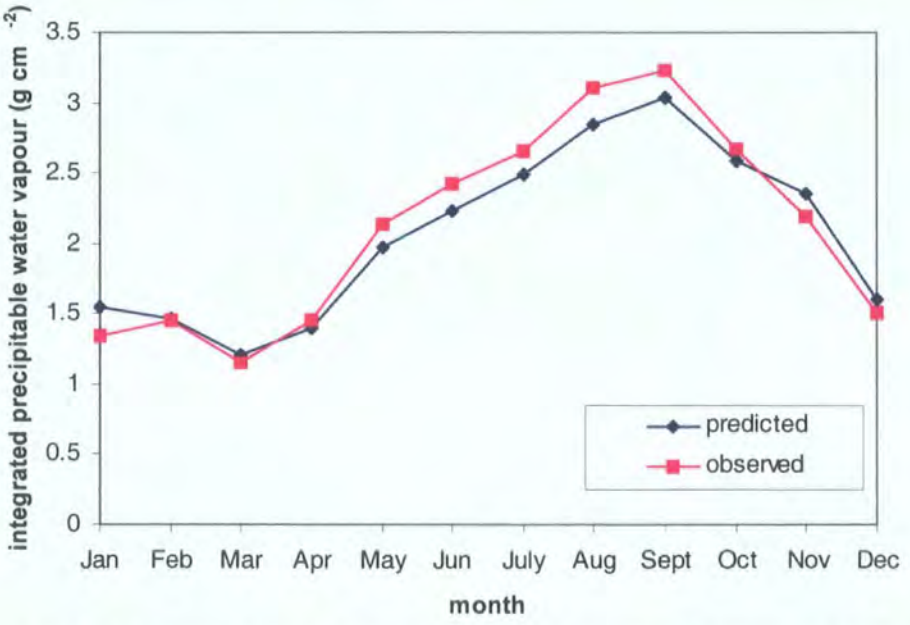

Figure 5.15. Temporal trend of the predicted monthly average Eta and TMI-derived integrated precipitable water vapour (g cm^{-2}).

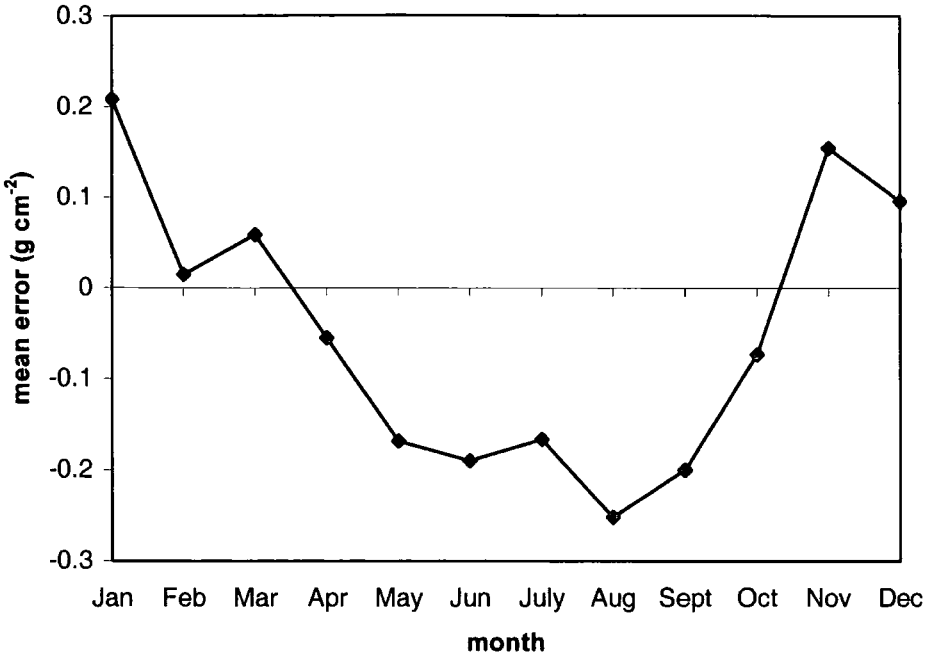

Figure 5.16. Mean error of Eta forecasted integrated precipitable water vapour from the observed field (in g cm^{-2}).

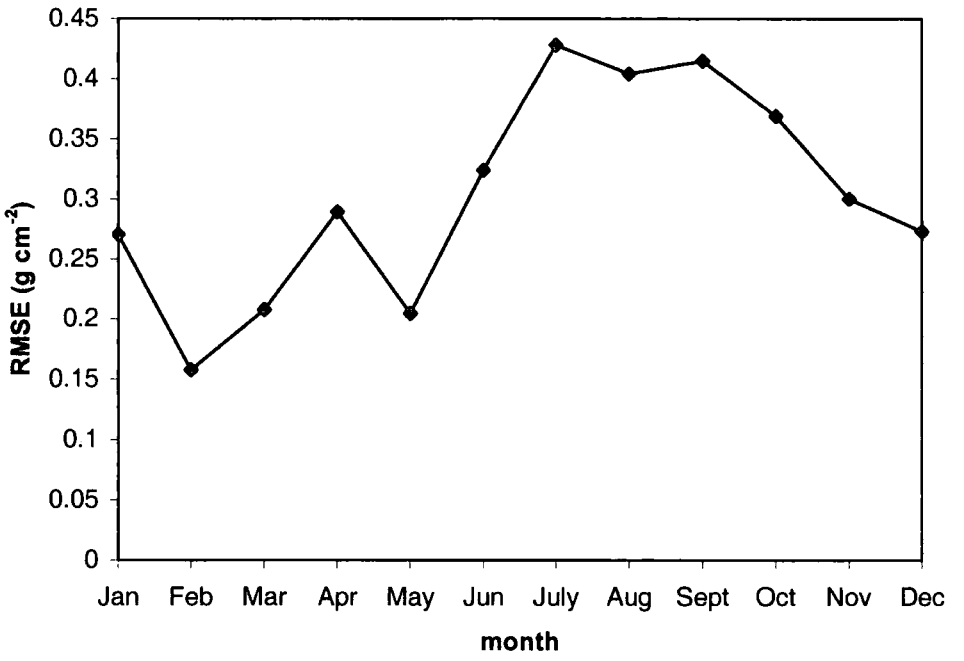

Figure 5.17. Monthly average RMSE between the Eta-forecasted and TMI-derived integrated precipitable water vapour (in g cm^{-2}).

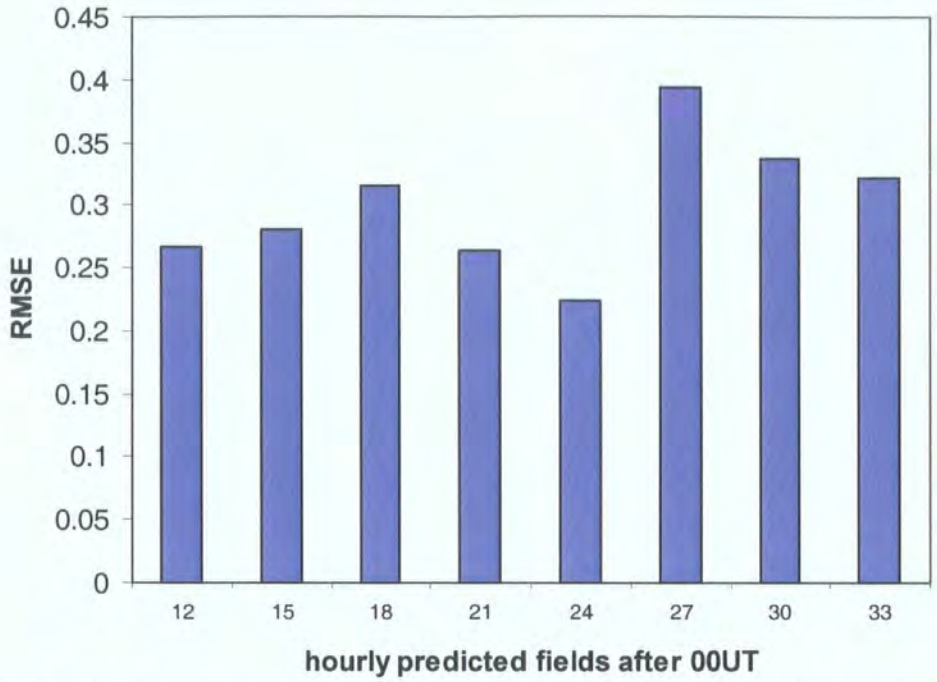

Figure 5.18. Temporal forecasting trend of integrated water vapour when the RMSE values of single-forecasts were grouped according to time of statistical comparison.

5.5.3.2. Integrated cloud liquid water vapour.

The predicted annual integrated cloud liquid water was 0.06 ± 0.07 mm compared to an observed value of 0.03 ± 0.01 mm. An increasing trend of the Eta model to over-forecast this parameter during the colder months is seen in figure 5.19, which is confirmed by a higher RMSE during the same months (fig. 5.20). This indicates a small degree of inaccuracy of Eta to closely predict cloud liquid water during this time. This parameter, which is the amount of liquid water per unit volume of air, varies greatly from cloud to cloud and for an average typical cloud, it may vary from 0.05 to 3 mm. More studies are required to identify the reasons for this inaccuracy and to further fine-tune the physical package that calculates the hydro-meteorological variables. In spite of the improvements made to the Eta model in 1996 to the cloud prediction scheme, more work is needed in this respect, especially

concerning fine-mesh atmospheric prediction. TMI-derived cloud liquid water can greatly assist in the fine-tuning of this numerical scheme.

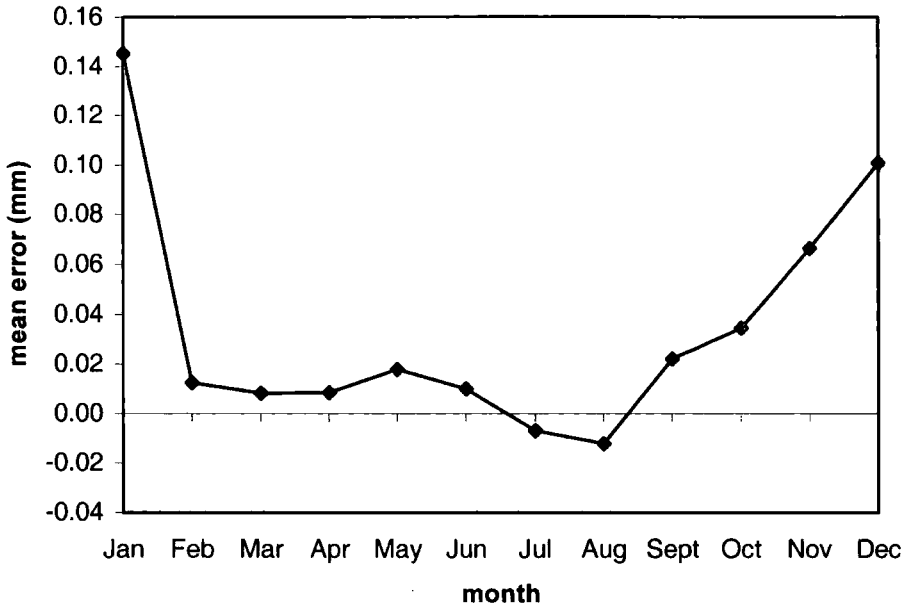

Figure 5.19. Mean error between the Eta and TMI-derived integrated cloud liquid water (mm).

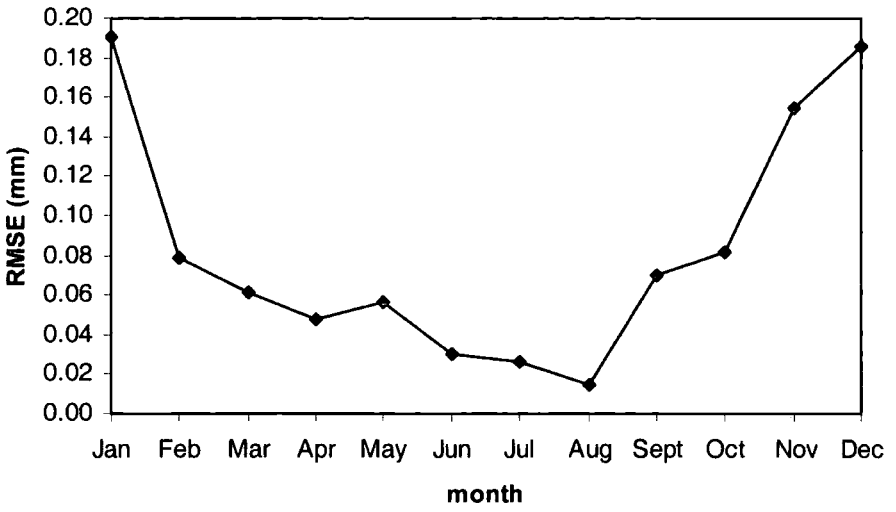

Figure 5.20. RMSE between the Eta forecasted- and TMI-derived integrated cloud liquid water (mm).

5.5.3.3. Outgoing longwave radiation.

The annual trend of the Eta-predicted radiative flux is very close to the observations. However, results show that the model tends to over-forecast this parameter by an annual value of around 174 W m^{-2} (fig. 5.21). Even if the stated systematic error of the observations is included (a maximum of 40 W m^{-2})[103], these results still point to the model's poor performance.

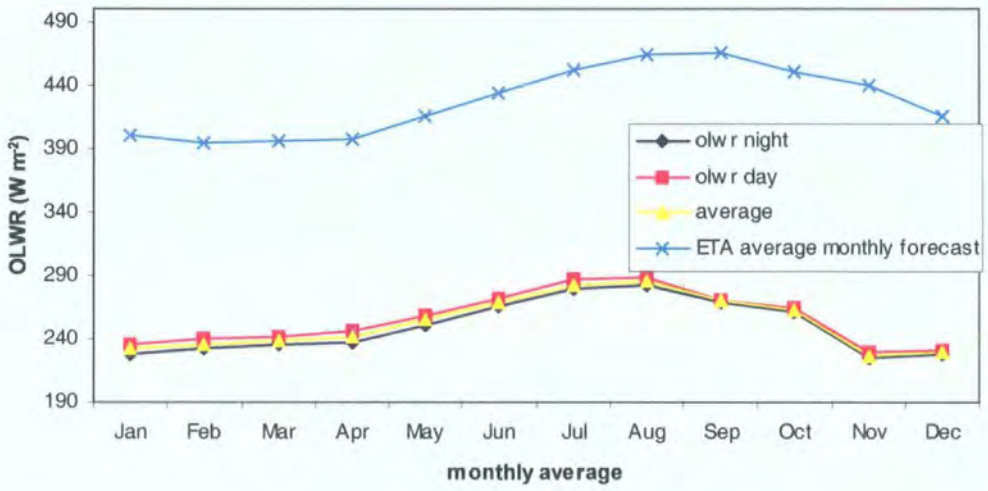

Figure 5.21. Trend of average Eta forecasted- and NOAA Pathfinder derived- outgoing long wave radiation over the Ionian basin during 1999. (NOAA POES: Polar Orbiting Environmental Satellite).

In spite of the recent improvement made to the radiative physical package of the Eta model, a number of approximations are still embedded that limits the prediction of the radiative fluxes (Nickovic, 2002, *personal communication*).

One important aspect of the radiation package is the exclusion of the impact of dust aerosols from this scheme. The presence of dust is very significant especially in areas close to potential sources such as the Sahara desert. The lack of dust transport schemes and their radiative

[103] *Section 4.4.1.5.*

effects on the overall total heat flux tends to over-estimate fluxes such as the outgoing longwave radiation by not taking into account the resultant longwave attenuation by dust.

As shown by the annual dust profile in figures 4.22 a - l, the annual AOT over the area of interest ranges between 50 to 270 (ODU x100). This thickness, which is principally caused by stratospheric dust particles, should lead to a diminution in the outgoing longwave radiation due to longwave absorption and scattering. This lack of physical treatment of the modelled radiation explains the overall higher predicted value for this parameter.

Apart from the lack of radiative forcing due to dust, the radiative package also lacks a fine database of important variable atmospheric components (such as CO_2 and O_3) as well as terrestrial components (soil type, albedo function, etc). This can therefore limit a realistic simulation of the radiative processes and their interaction with other model components.

Papadopolous *et al.* (1997) describe sensitivity studies of the radiation parameterisation schemes of the Eta model. They noticed that over land, an improved description of the underlying surface improves significantly the model performance. In the case of water surface, there is little description that is required to characterise it; however, the vertical description becomes extremely important. The Eta radiation package searches its internal database, such as CO_2 and O_3, to characterise its vertical profile. The presence of the various phases of cloud water, including clouds become also a determining factor in the proper forecasting of the radiation fluxes. This study gives a good indication of the Eta's skill to predict these hydrometeorological parameters.

To date, there is no study available in the literature on the performance of the radiation parameterisation scheme of the Eta model over the

oceans. Papadopolous *et al.* (1997) have tested the Eta scheme but over land surfaces using different model resolution grids.

Another possible source of error is the prescribed SST throughout the model integration. By keeping the SST constant, the small changes that can in reality affect the atmosphere over the course of the numerical forecast are blocked. This restriction on the surface energy budget can also be an important factor that leads to model errors in the calculation and prediction of the radiative fluxes.

5.5.3.4. Surface wind magnitude.

A predicted annual 10 m speed magnitude over the area of interest is 6.1 ± 1.9 m s^{-1} as compared to 5.3 ± 2.0 m s^{-1} given by remotely sensed observations. Figure 5.22 shows that both profiles follow closely the same trend, with prevalent low wind speeds during summer and stronger ones during winter. The variability shown by the the temporal trend in RMSE also follows the same pattern (fig. 5.23). Considering the error inherent in the TMI sensor's measurement of wind (± 1.0 m s^{-1} against buoy data; —1.2 m s^{-1} against SOC data)[104], an annual RMSE of 1.48 m s^{-1} and mean bias of 0.76 indicates a high Eta model skill. This value is lower than that obtained by a similar high-resolution (0.1° by 0.1° domain) Eta model working over the Aegean basin (Nittis *et al.*, 2001).

[104] *Section 4.4.1.1.*

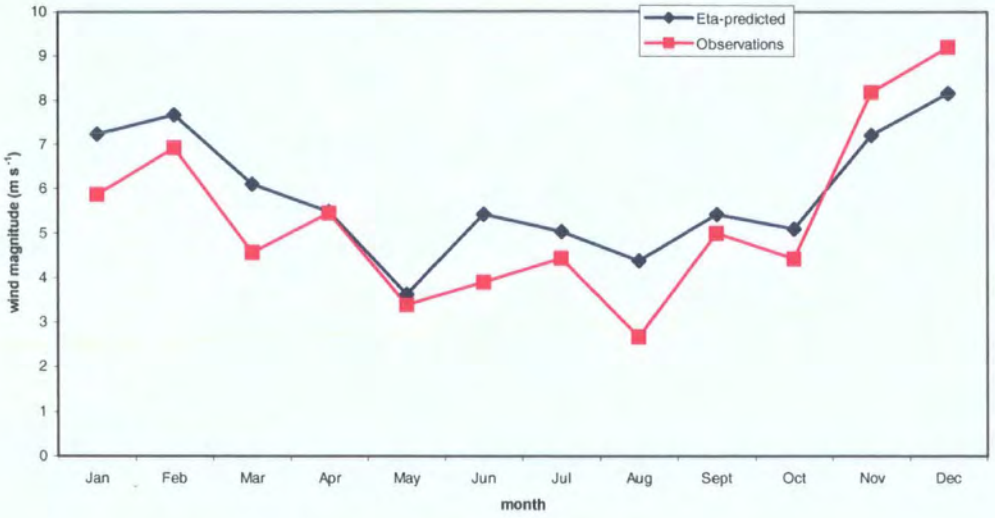

Figure 5.22. Temporal trend of average Eta forecasted- and TMI-derived 10 m wind magnitude (m s^{-1}).

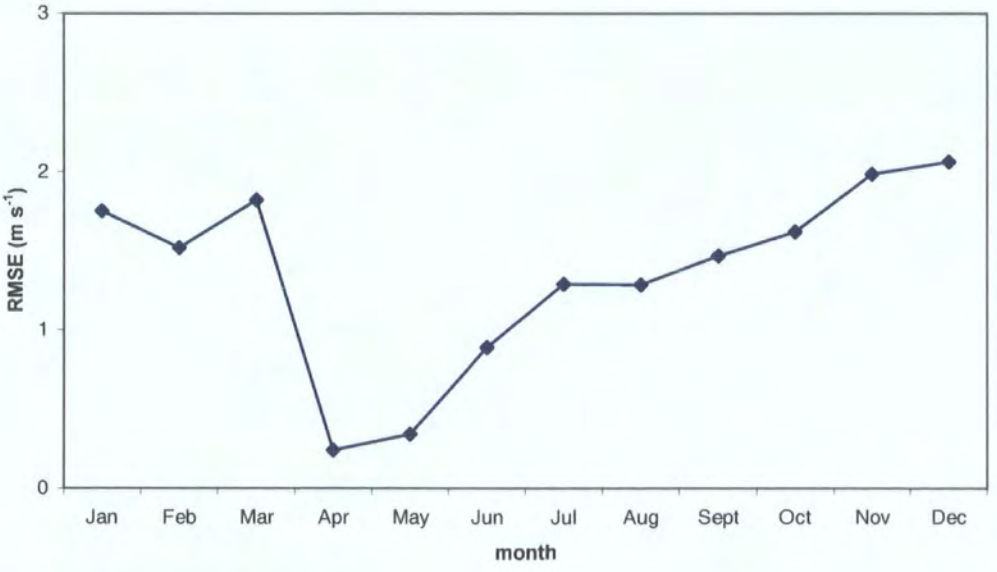

Figure 5.23. RMSE between the Eta forecasted- and TMI- derived 10 m wind magnitude (m s^{-1}).

5.5.3.5. Surface air temperature.

The forecasted 2 m surface air temperature shows an annual value of 20.9 ± 5.3 ºC compared to the *quasi*-instantaneous estimation of 20.8 ± 5.0 ºC (fig. 5.24). Therefore, results show a close agreement between the two sets of data. The mean annual bias is only 0.15 ºC, indicating a slight over-estimation from the database (fig. 5.25), particularly during May and August. The high-resolution Eta model used by Nittis *et al.* (2001) also shows a slight over-estimation over *in situ* buoy measurements.

In the case of May, the monthly average is based on a small number of samples and is not representative of the climatic trend for this month. This is not the case for the August peak, which may indicate an anomaly from the climatological mean, on which the database[105] is partly based.

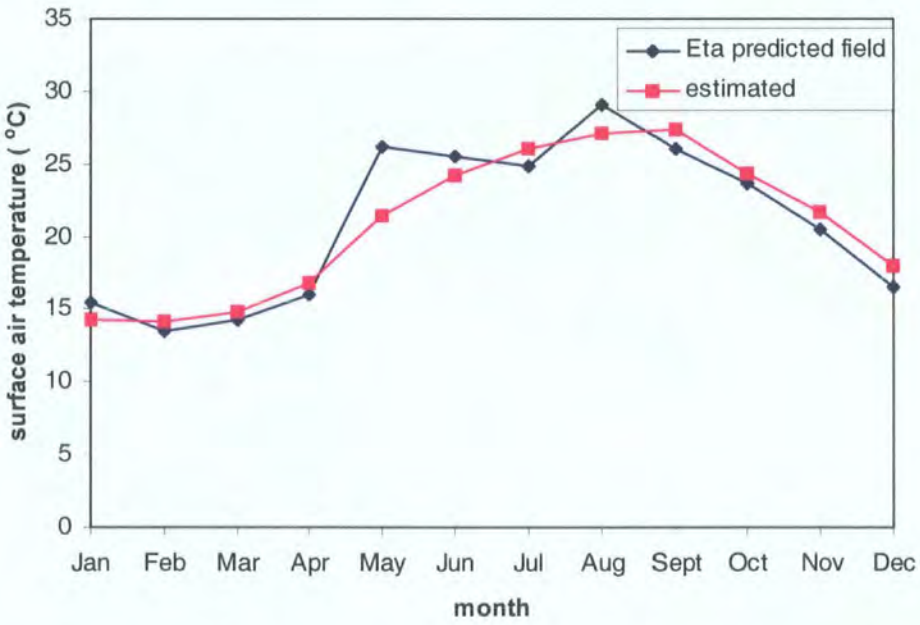

Figure 5.24. Annual trend of Eta- forecasted 2 m air temperature and quasi-instantaneous derivation of air temperature (ºC).

[105] *Section 4.4.1.2.*

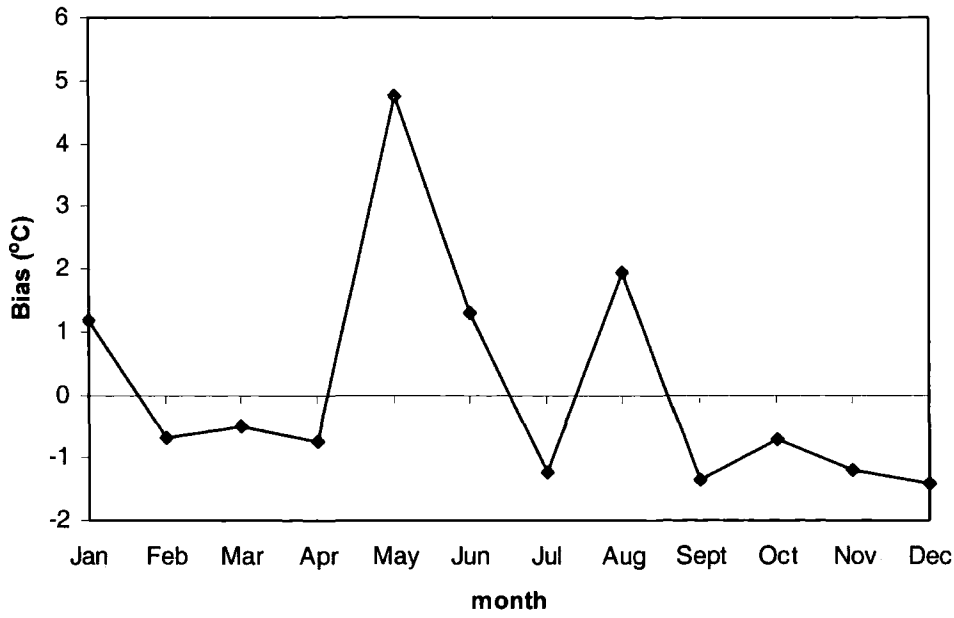

Fig. 5.25. Over-forecasting of the Eta-predicted fields when compared to the SOC climatology over the area of interest. This trend is not as significant when predicted fields are compared with the quasi-instantaneous (estimated) fields derived from the database.

5.5.3.6. Sensible heat flux.

Results show an annual mean predicted sensible heat flux of −15.3 ± 5.1 W m^{-2} compared to an observed mean of −5.9 ± 1.2 W m^{-2}. A strong seasonality trend was observed with minima occurring during winter (January and December) and maxima during summer (fig. 5.26).

The deviation of the forecasted field from the TMI-derived heat flux is evident by the mean error between the two fields (fig. 5.27). The over-forecasting trend of the Eta model starts to increase from July to reach a maximum in December. This general seasonal variability follows that of the wind magnitude; the low wind magnitude values during summer forces close to positive values of sensible heat flux. This is clearly shown by the scatterplot between the predicted Eta- sensible heat flux and 10 m wind magnitude (fig. 5.28).

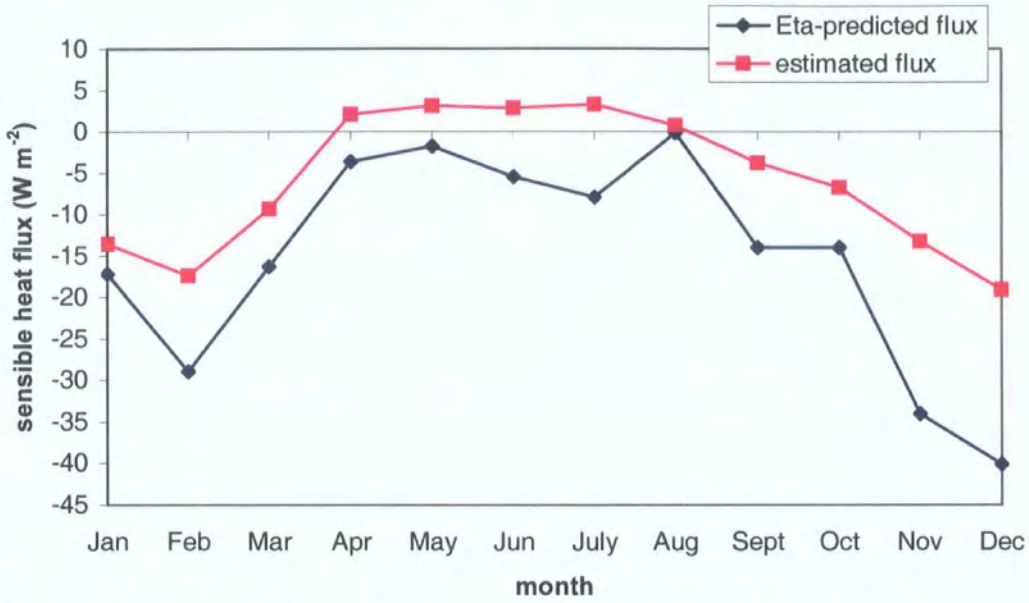

Figure 5.26. Temporal annual trend of predicted and estimated sensible heat flux (W m^{-2}).

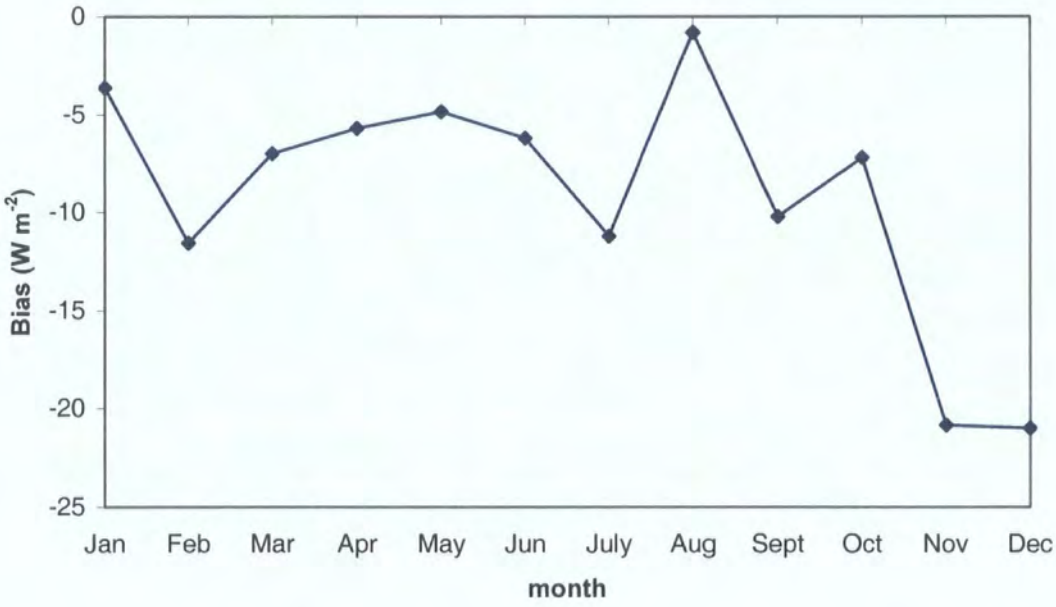

Figure 5.27. Temporal mean bias between the Eta-predicted and estimated sensible heat flux (W m^{-2}).

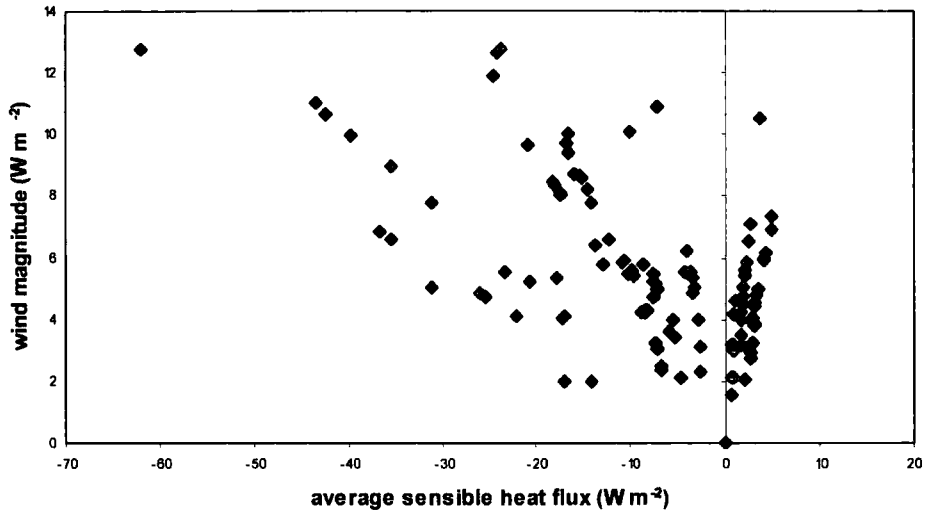

Figure 5.28. Relation between estimated sensible heat flux (W m^{-2}) and 10 m wind magnitude (m s^{-1}) over the area of interest.

As expected, the monthly mean RMSE trend between the predicted and observed fluxes increases during the same period of time (i.e. July-December). The pattern of the overall RMSE (with an annual mean of 14.5 W m^{-2}) also shows a low RMSE during the summer which increases during the winter (fig. 5.29). This is similar to the overall RMSE pattern obtained when observed and predicted wind magnitude fields are compared (fig. 5.23).

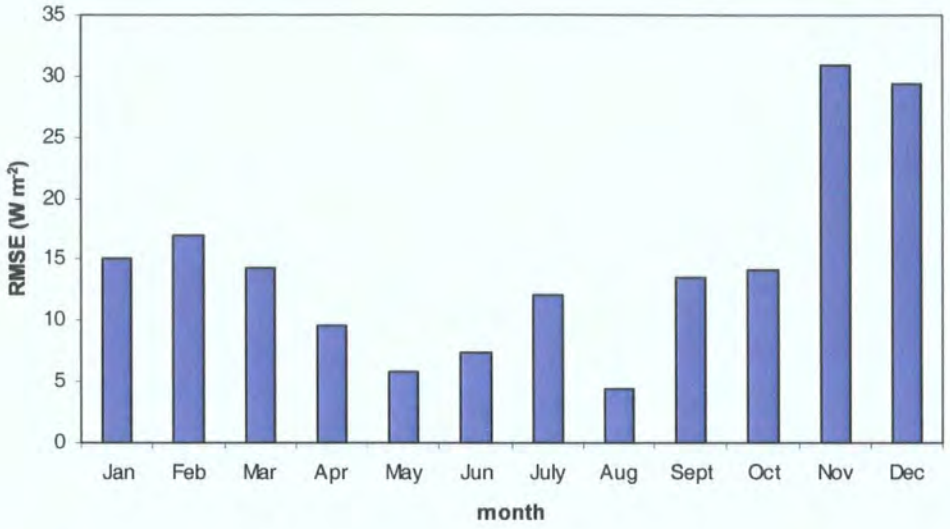

Figure 5.29. Monthly average RMSE between the Eta-predicted and estimated sensible heat flux (W m^{-2}).

5.5.3.7. Latent heat flux.

The predicted mean annual value of the latent heat flux is –89.5 ± 19.07 W m^{-2} as compared to an observed value of –72.4 ± 11.0 W m^{-2} (fig. 5.30). The annual trends of the mean error (fig. 5.31) and RMSE (fig. 5.32) are similar to the ones shown for the sensible heat flux. These results point to an over-forecasting tendency by the model for the latent heat flux from June onwards, with a parallel decrease in its performance as deduced from the RMSE (fig. 5.33.).

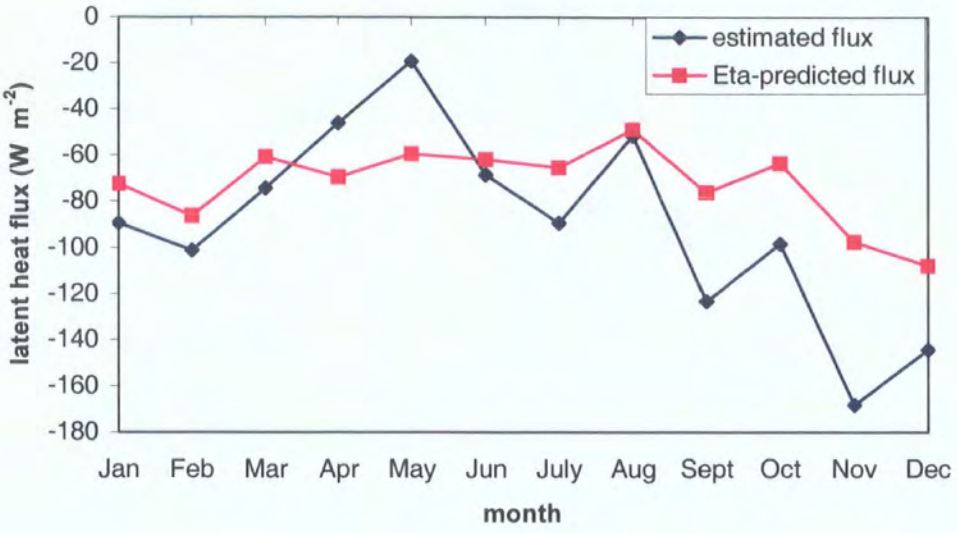

Figure 5.30. Temporal variation between Eta-predicted and estimated latent heat flux (W m^{-2}).

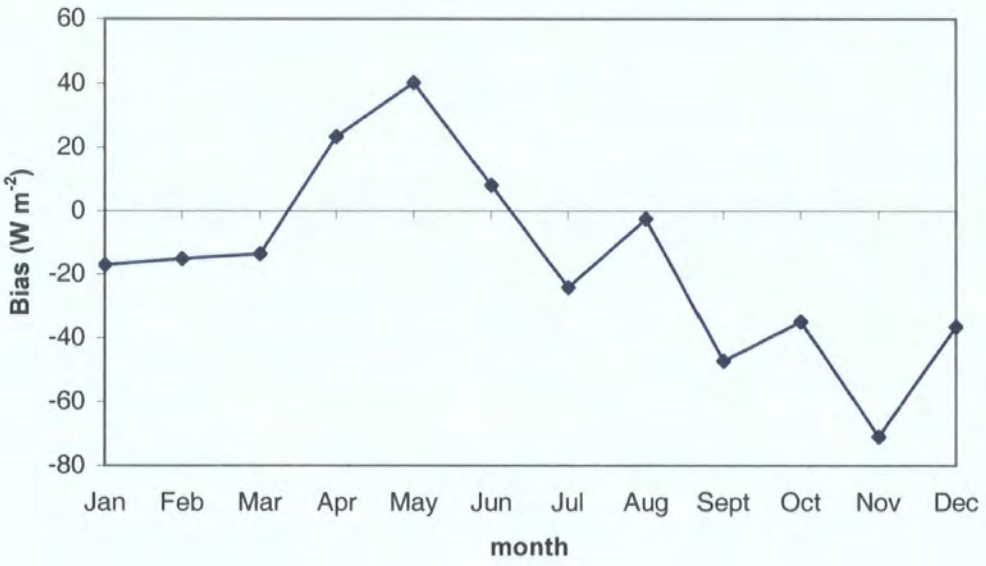

Figure 5.31. Temporal variation of mean monthly error between Eta-predicted and estimated latent heat flux (W m^{-2}).

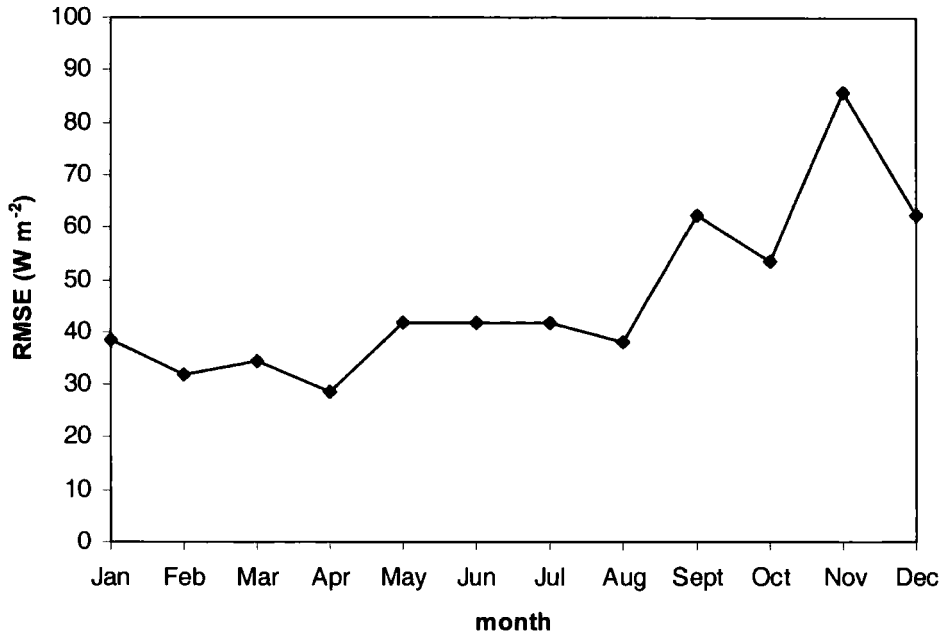

Figure 5.32. RMSE between Eta-predicted and estimated latent heat flux ($W\ m^{-2}$).

5.5.4. Overview of the predictive skill of the nested Eta atmosphere model.

The identification of the Eta's strengths and weaknesses helps to better interpret its output and adjust model biases. This information becomes extremely useful for the overall assessment of the predictive skill of the ocean forecasting system. In the case of the nested Eta model used in this study, the identified biases may be partially removed, but may not be entirely corrected or eliminated. Inherent in these biases are also errors originating from the collocated database. Model biases can be further analysed using exploratory spatial data analysis to identify model error drifts.

A general observation on the overall, climatological performance of the Eta nested model can still be made. Relative to the observations and derived products, the Eta model is accurate enough to predict surface air temperature and integrated precipitable water vapour. The model is also able to predict latent heat and sensible heat fluxes, the latter to a slightly lesser extent. Beljaars (2001) shows how very often the errors in air-sea flux prediction are mainly due to systematic biases in the near surface humidity and temperature and less to the air-sea transfer formulation itself.

The same results show that the Eta radiation package is limited in its ability to forecast the outgoing longwave radiation. NCEP states that the overall clear-sky radiation calculations of the Eta are accurate to within 5%, at least when compared to detailed "line-by-line" radiation calculations[106]. This numerical package is highly depended on the accuracy of simulated cloud content, for which this study identified a slight over-forecasting of integrated cloud liquid water vapour, which is a good indicator of the vertical profile of the cloud content. NCEP however comments that the linkage between the simulated cloud content and radiation is rather crude, and may result in errors. Additionally, the horizontal and vertical errors in cloud location may also have a significant impact on the longwave radiation and associated heating and cooling rates at the model surface and upper layers.

The nested Eta model used by this study contained limited information concerning the diurnal heating cycle and its influence on temperature, moisture, and wind fields. The sea surface temperature was supplied as fixed, initial information that did not change during the model's integration period, therefore providing no information on the diurnal heating.

The skill of the Eta model to forecast 10 m wind magnitude deserves special attention since this variable significantly influences the prediction of the air-sea fluxes. Section 5.5.5 details the fine-tuning of

[106] *http://www.meted.ucar.edu/nwp/pcu2/etarad1.htm (accessed on 01.11.04).*

the Eta viscous sublayer scheme that assists the parameterisation of air-sea transfer of fluxes, including momentum fluxes.

Atmospheric modellers tend to stay away from presenting a list of biases for models that are evolving continuously. Very often, only generic presentations of the model's ability to forecast major events is provided to the public, while detailed analysis is left for internal assessment and model improvement. Detailed model verification information is never issued by the major ocean and weather forecasting systems working in the Mediterranean, such as SKIRON. ECMWF issues only generic data either seasonal or yearly for major variables, such as geopotential over large areas. The Mediterranean Forecasting System is still at the initial stages of verifying the various air-sea surface flux packages that can be used for its basin-scale ocean models. An inter-comparison study between the present results and other similar forecasting systems was therefore impossible.

The single forecast performance results presented by this study provide distinctive information on the performance of the Eta model to forecast especially air-sea surface fluxes and related geophysical fields over the ocean surface. The numerical schemes validated by this study are the same as those found in the model version released at the end of 2002. This implies that the present results can be used to understand and fine-tune such schemes.

5.5.5. Fine-tuning the Eta model viscous sublayer depth.

Section 5.5.5. describes the results related to the fine-tuning of the Eta viscous sublayer scheme. The air-sea transfer formulation in the Eta model consists of three elements: (i) roughness length formulations for momentum, heat and moisture, (ii) Monin-Obukhov similarity functions to account for stability effects and (iii) a boundary layer similarity based gustiness parameterisation[107]. The fine-tuning of the formulation of the

[107] *Appendix II; Section II.1*

viscous sublayer depth can result in a more accurate air-sea transfer including the prediction of momentum fluxes at the ocean surface. Here, the sublayer depth is studied and refined according to specific wind categories that would lead to different air-sea transfer conditions within the viscous sublayer scheme. It is important to note that the distributed version of the Eta model is provided with a single value for the viscous sublayer depth. The relation between the normalised RMSE and the respective wind speed magnitude are shown in figures 5.33 a to d. The entire experimental data is tables VI.8 a-b as shown in Appendix VI.

Figures 5.33 a to b show the normalised indices obtained for the four sets of ζ values plotted against increasing wind speed ranging from (a) 3.0 to 3.9 m s^{-1}, and (b) 4.0 to 4.9 m s^{-1}. These results show that a value of ζ = 0.7 gives the lowest RMSE for a low wind speed regime calculated by the model (3.0 - 4.0 m s^{-1}), which is seen to slightly deteriorate with increasing wind speed. The next best value for ζ is 0.8. The most accurate prediction for the viscous sublayer model under a wind speed regime that ranges from 4.0 – 5.0 m s^{-1} is provided by ζ = 0.2. The next best values are 0.35 and 0.7 in decreasing order respectively.

Figure 5.33 c indicates that a ζ value of 0.2 continues to give consistently low RMSE when the model wind speed ranges from 6.1 – 6.9 m s^{-1}. Figure 5.35 d shows that the optimal ζ value for the highest wind speed regime is 0.8.

Figure 5.33 d points to an interesting aspect of the viscous sublayer model. The drop in the normalised index for all four ζ values suggest an inability of ζ to be effective. At wind speeds higher than 8.0 m s^{-1}, the viscous sublayer model is likely to become ineffective and the other scheme – the turbulent model scheme of Mellor-Yamada becomes active due to the turbulent processes occurring at these higher wind speeds. The common tapering of the normalised RMSE to the lowest levels at

the higher wind speed spectrum indicates that the entire range of wind speed used in this experiment addresses the full functionality of the viscous sublayer model.

These results are condensed in figure 5.34 which provides an overall relation between the normalised RMSE and calculated wind speed for the four values of ζ. Whereas a ζ value of 0.2 gives the best overall result when the model wind speed ranges between 4.4 and 8.1 m s^{-1}, the lowest wind speed regime seems to be best predicted when ζ equals to 0.7. At the highest range of wind speed (i.e. > 8.1 m s^{-1}), a value of 0.8 provides an overall better performance of the viscous sublayer model to predict the model's lowest surface wind speed.

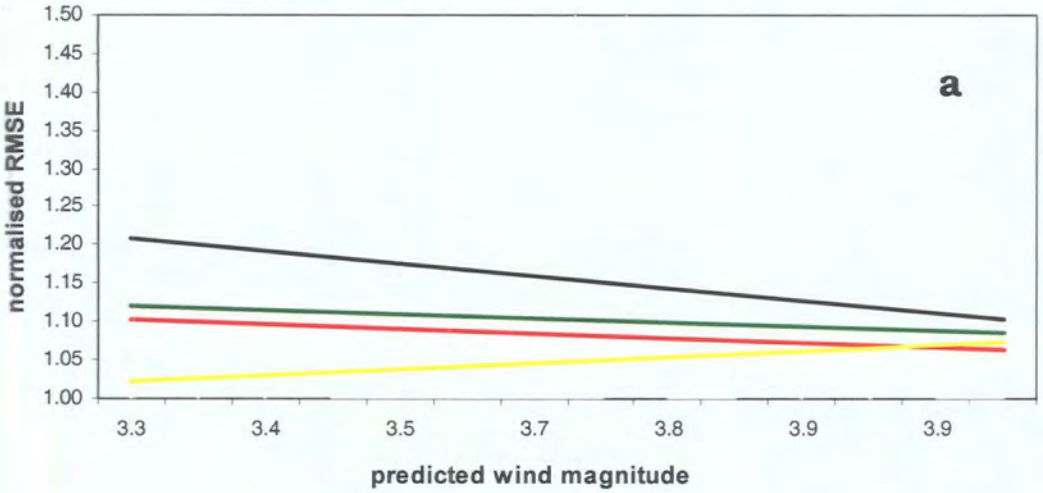

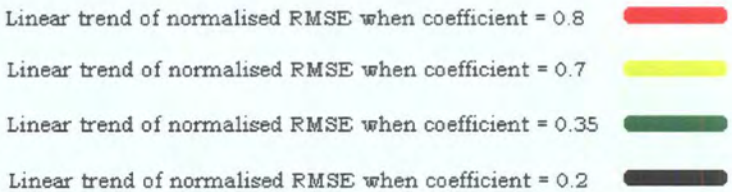

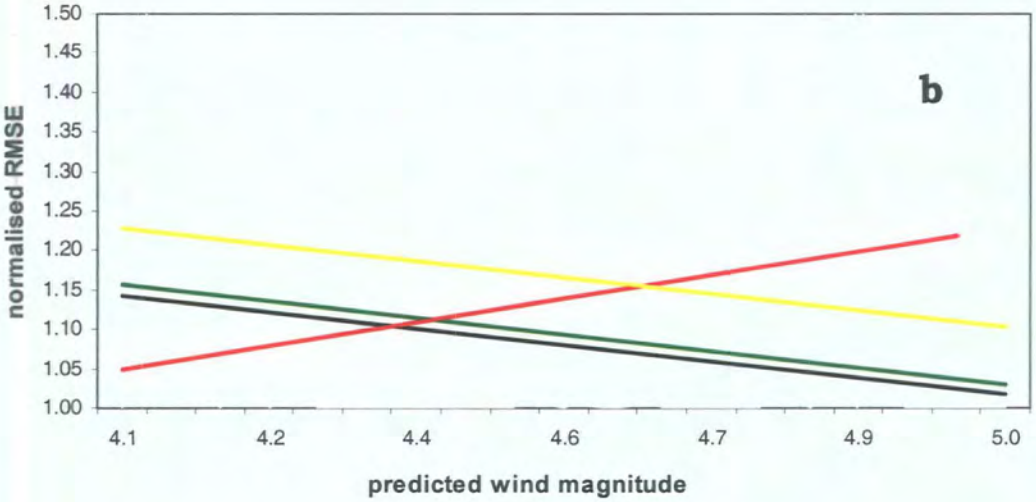

Figures 5.33 a – b. Linear trends of normalised RMSE (m s^{-1}) obtained for the four sets of ζ values plotted against increasing wind speed, ranging from (a) 3.0 to 3.9 m s^{-1}, and (b) 4.0 to 4.9 m s^{-1}.

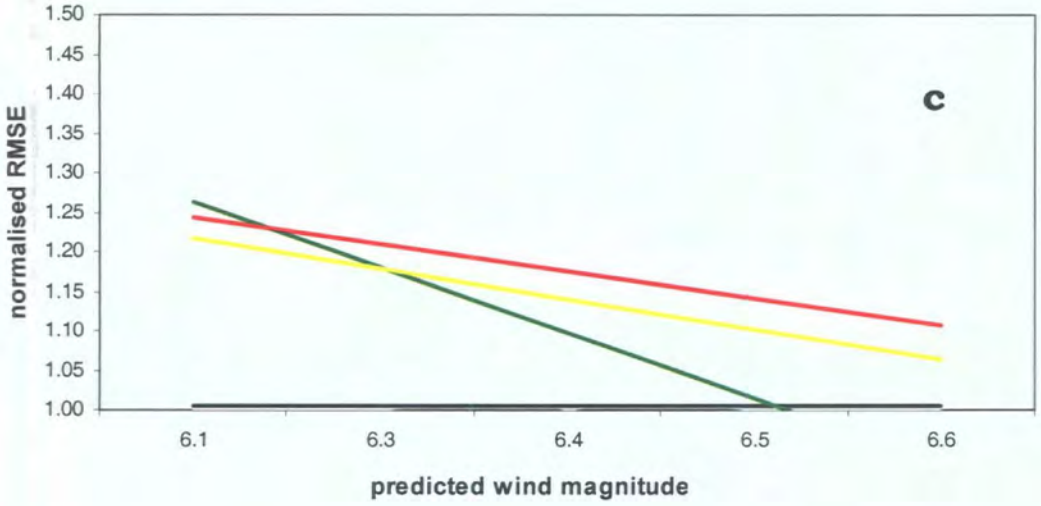

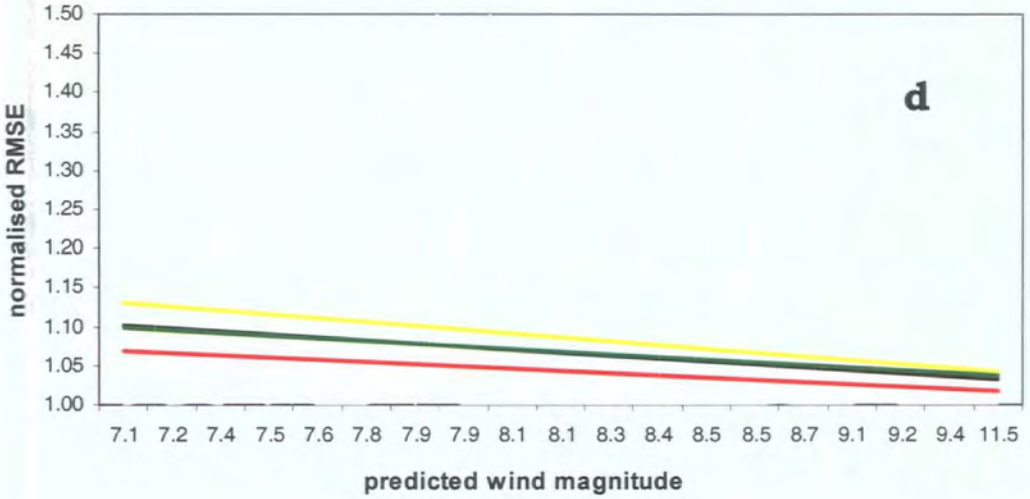

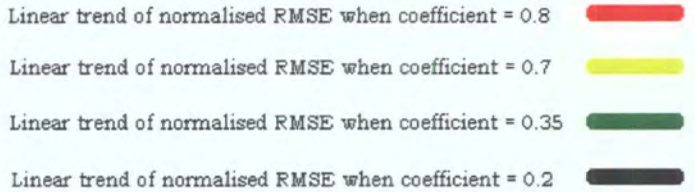

Figures 5.33 c – d. Linear trends of normalised RMSE (m s^{-1}) obtained for the four sets of ζ values plotted against increasing wind speed, ranging from (a) 6.1 to 6.9 m s^{-1}, and (b) 7.0 to 11.0 m s^{-1}.

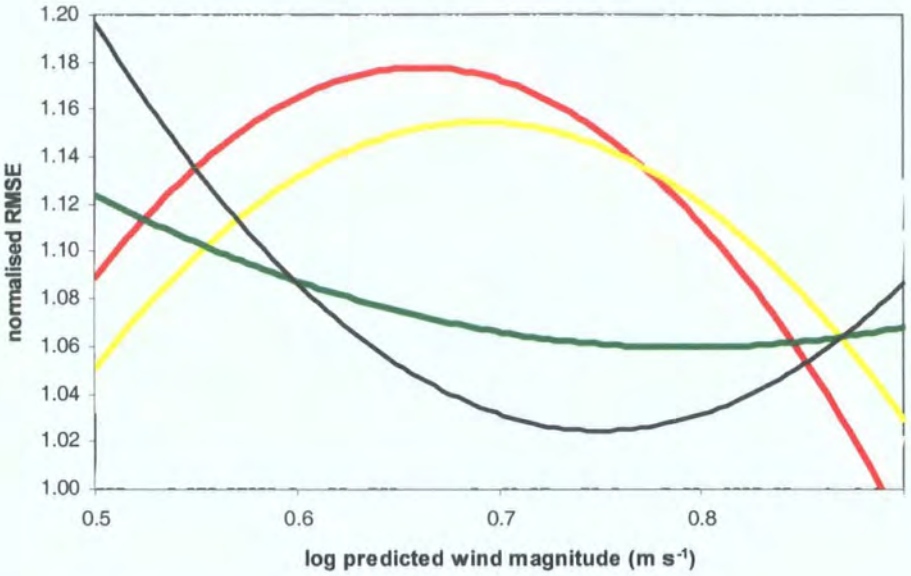

Figure 5.34. Trends of normalised RMSE plotted against the predicted 10 m wind magnitude (m s^{-1}).

ζ = 0.80
ζ = 0.70
ζ = 0.35
ζ = 0.20

Table 5.2 summarises the optimisation of the viscous sublayer depth according to the 10 m wind speed as modeled by Eta. The observed relation between ζ and the wind speed can be embedded in the viscous sublayer scheme of the Eta model. A code can then be used to dynamically tune the scheme according to evolving surface wind conditions that are being simulated by the model.

Predicted 10 m wind speed regime (m s^{-1})	Optimal value of ζ
3.0 – 3.9	0.70
4.0 – 6.9	0.20
7.0 – 12.0	0.80

Table 5.2. Optimal ζ values for different 10 m wind speed regimes. The value of ζ can be dynamically adjusted according to modality of the predicted wind speed regime.

5.5.6. Exploratory spatial data analysis.

The impact of fine-tuning the viscous sublayer on the final quality of the 10 m wind speed forecasts was assessed spatially. This was done using GIS and spatial overlaying of the 10 m wind forecasts with collocated observations and subsequent analysis of their similarity. Spatial analysis was able to identify the resulting relationship of class attributes as well as model drift errors.

5.5.6.1. Spatial similarity and feature matching analysis.

Because of the extensive nature of this spatial analysis, five case studies are presented that best describe the results of the fine-tuning of the model scheme at different wind speed regimes.

(i) Single-forecast spatial similarity analysis for 2nd July at 1500 UT.

Figures 5.35 a to c represent an analysis of the spatial similarity between forecasted and observed fields. Black pixels represent nulled pixels that are below 3.0 m s^{-1}. The average forecasted wind speed for this case study was an average of 3.3 m s^{-1}. These maps show that the number of valid pixels is higher when the value of ζ is 0.7.

In addition, figure 5.35b shows that a ζ value of 0.7 results in a higher degree of similarity between the predictions and observations than does figure 5.35a. A closer inspection of the contoured TMI-observed wind field (fig. 5.35c) suggests that pixel categories attributed to a wind speed range of 3.0 to 5.0 m s^{-1} are being more efficiently predicted when the viscous scheme used a ζ value of 0.7. Spatial similarity analysis therefore supports the results obtained by the standard verification.

(ii) Single-forecast spatial similarity analysis for 2nd August at 2100 UT.

For this case study, the average forecasted wind field is 4.1 m s^{-1}. Spatial similarity analysis shows that a ζ value of 0.7 is also optimal, and this ζ value leads to a larger number of valid pixels.

What is more important is that a ζ value of 0.7 gives a larger portion of pixel classes that are most similar to observations. The contoured TMI-observed wind field (fig. 5.36c) again suggests that the choice of this value leads to better prediction when the predicted wind speed regime is between 3.0 to 5.0 m s^{-1}. These results further support the use of ζ = 0.7 for low wind speed regimes.

(iii) Single-forecast spatial similarity analysis for 12th July at 3300 hrs *(i.e. at 13.07.99 @ 0900 UT).*

The benefit of using a ζ value of 0.2 for higher wind speeds (an average of 5.4 m s^{-1}) is shown by this case study. Both spatial similarity maps (figs. 5.37a and 5.37b) have similar valid pixels indicating close complimentary; however, a ζ value of 0.7 gives a larger area of 'least similar' pixels, especially in categories that are attributed to wind speeds that are greater than 5.0 m s^{-1}. This is easily observed when the spatial similarity maps are compared to the contoured TMI-derived wind field (fig. 5.37c). This technique gives results that complement the standard verification measures.

(iv) Single-forecast spatial similarity analysis for 10th January at 3000 UT *(i.e. at 11.01.99 at 0600 UT).*

This is the best case study showing the most significant fine-tuning of the viscous sublayer scheme. When the average predicted wind speed is 8.0 m s^{-1}, the use of a ζ value of 0.8 is accompanied by a high degree of similarity between the resulting forecasts and collocated observations (fig. 5.38d). What is also noticeable is that identical similarity maps are obtained when the ζ value equals 0.2, 0.35 and 0.7, indicating again[108], the ineffectiveness of using these values for this range of wind speed.

(v) Single-forecast spatial similarity analysis for 09th November at 1800 UT.

Both figures 5.39a and 5.39b show similar spatial patterns. However, a ζ value of 0.2 clearly gives a larger proportion of 'most similar' pixel classes. In this case, spatial similarity analysis suggests that the use of a ζ value 0.7 leads to a model error drift, especially when strong gradients of wind speed categories between 7.5 and 9.5 m s^{-1} are present. On the contrary, these gradients are better resolved and predicted when the ζ value is 0.2. These results again complement the ones obtained in section 5.5.4.

The design and use of a spatial similarity procedure therefore proved extremely useful to identify spatial attributes that assessed the fine-tuning of the viscous sublayer model of the Eta model. The routine that defined the spatial exploratory procedure[109] proved to be sensitive enough for the present objectives, i.e. to identify the relationship of class attributes between the optimally forecasted and observed wind fields, as well as exposing model drift error. This assessment enabled the fine-tuning of the viscous sublayer depth ζ.

---

[108] *As in section 5.5.4.*
[109] *Section 5.4.3.1.*

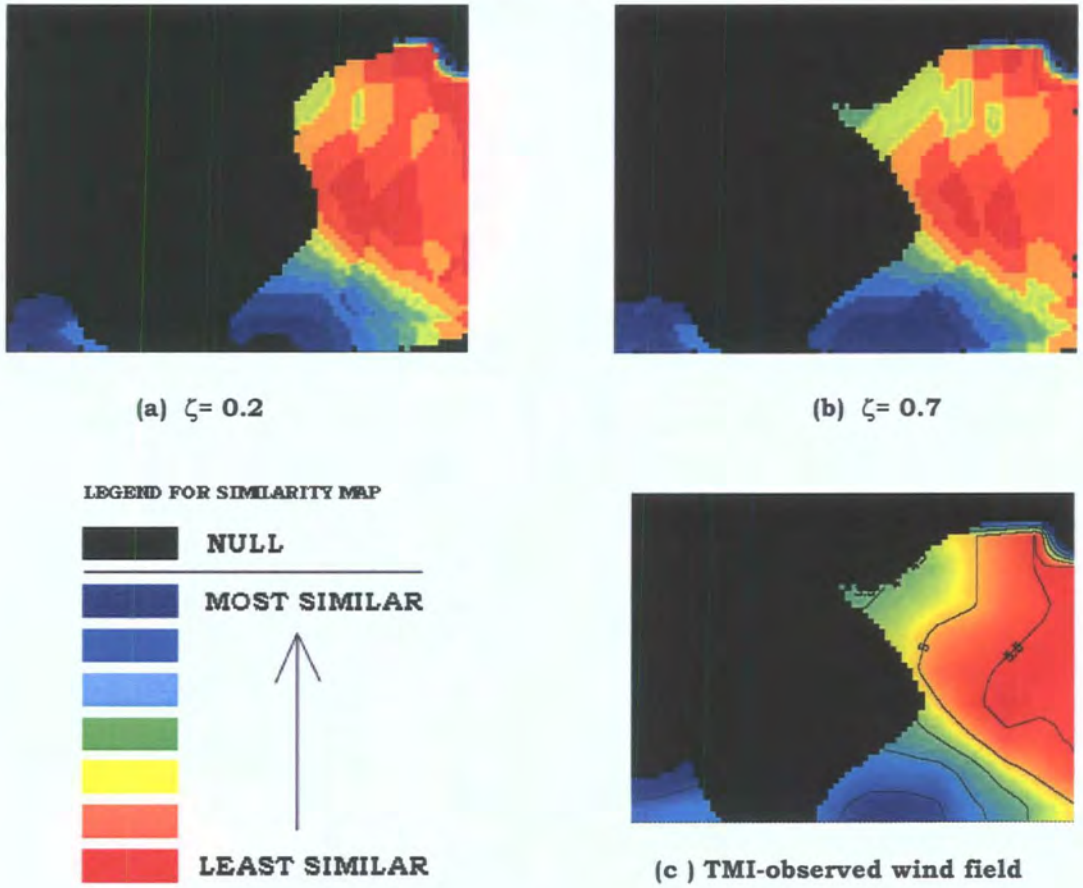

Figure. 5.35. Spatial similarity analysis between collocated, filtered Eta 15-hr forecasted wind fields and observed, filtered 10 m wind magnitude field on the 2nd of July 1999. The observed, contoured 10 m wind magnitude field is shown for reference. The average forecasted wind field regime is 3.3 m s^{-1}. The black area represents nulled pixels that are below 3.0 m s^{-1}.

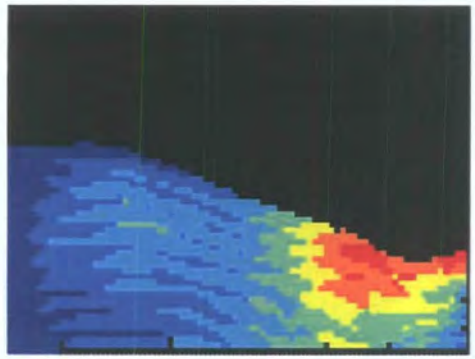

(a) ζ= 0.2

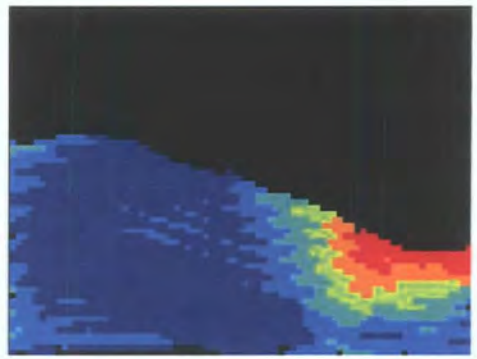

(b) ζ= 0.7

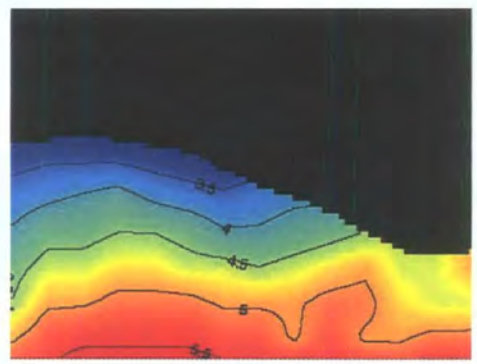

(c) TMI-observed wind field

Figure 5.36. Spatial similarity analysis between collocated, filtered Eta 21-hr forecasted wind fields and observed, filtered 10 m wind magnitude field on the 2nd of August 1999. The observed, contoured 10 m wind magnitude field is shown for reference. The average forecasted wind field regime is 4.1 m s^{-1}.

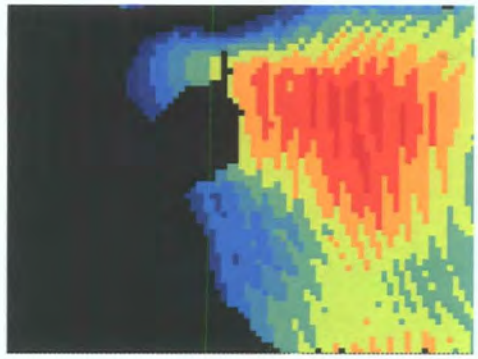

(a) ζ= 0.2

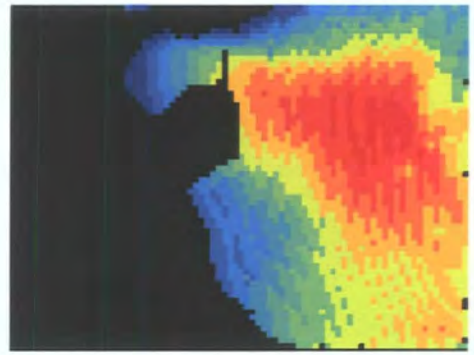

(b) ζ= 0.7

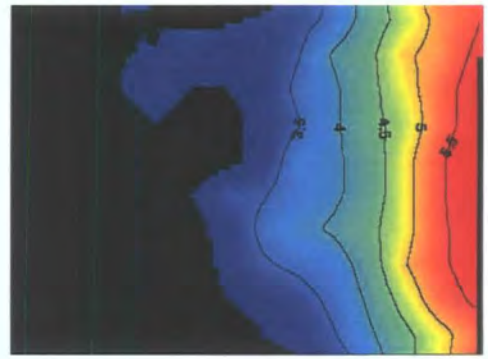

(c) TMI-observed wind field

Figure 5.37. Spatial similarity analysis between collocated, filtered Eta 33-hr forecasted wind fields and observed, filtered 10 m wind magnitude field on the 12th July 1999. The observed, contoured 10 m wind magnitude field is shown for reference. The average forecasted wind field regime is 5.4 m s^{-1}.

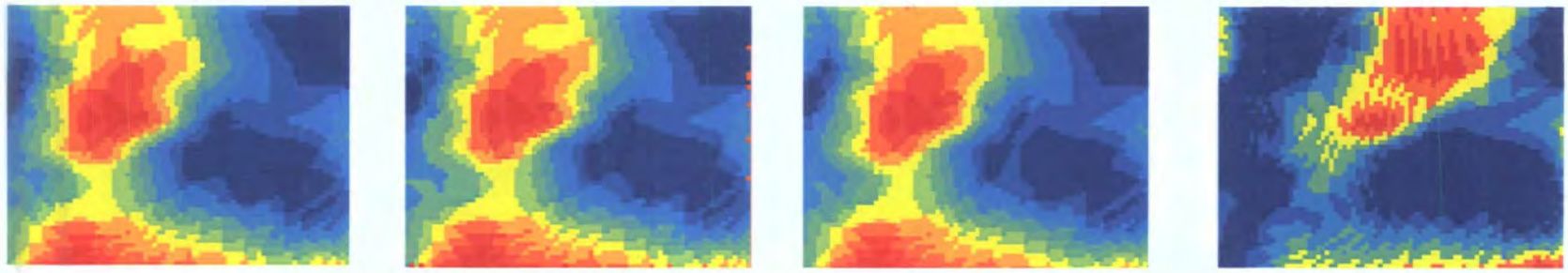

(a) ζ= 0.2 (b) ζ= 0.35 (c) ζ= 0.70 (d) ζ= 0.8

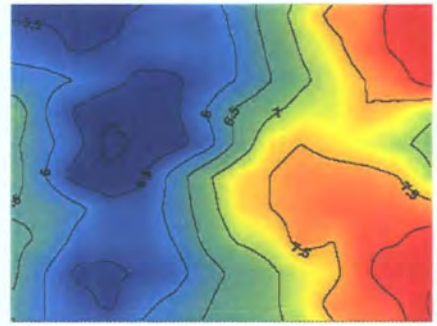

(e) TMI-observed wind field

Figure 5.38. Spatial similarity analysis between collocated, filtered Eta 30-hr forecasted wind fields and observed, filtered 10 m wind magnitude field on the 10th January 1999. The observed, contoured 10 m wind magnitude field is shown for reference. The average forecasted wind field regime is 7.9 m s^{-1}.

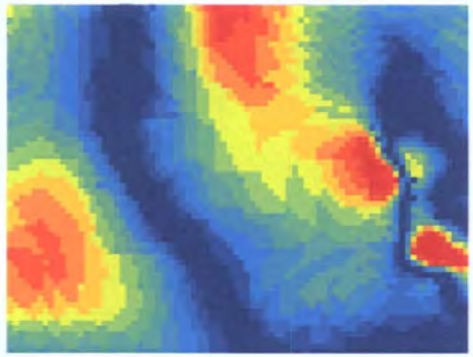

(a) ζ= 0.2

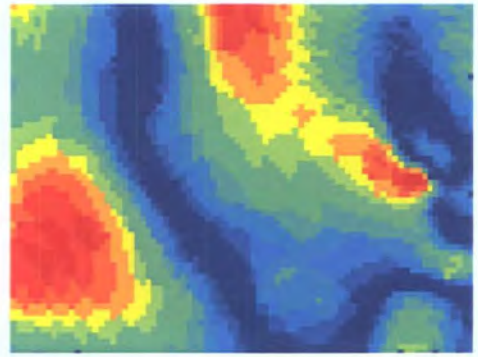

(b) ζ= 0.7

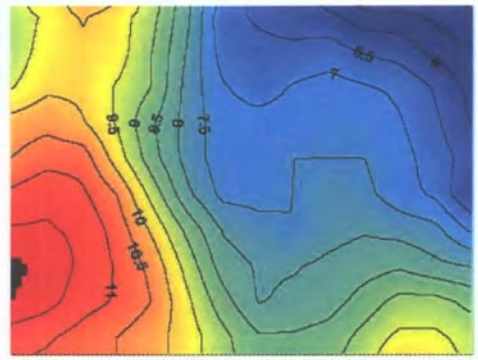

(c) TMI-observed wind field

Figure 5.39. Spatial similarity analysis between collocated, filtered Eta 18-hr forecasted wind fields and observed, filtered 10 m wind magnitude field on the 9th November 1999. The observed, contoured 10 m wind magnitude field is shown for reference. The average forecasted wind field regime is 8.7 m s^{-1}.

Exploratory spatial data analysis demonstrated that it complements the standard verification procedures used to validate the performance of the scheme. However, spatial analysis, in particular spatial similarity, enabled the identification of model error drifts and the characterisation of spatial improvements following adjustment of the viscous sublayer depth. Beljaars (2001) show how further tuning of this scheme can be brought about by including ocean skin temperature effects (warm layer and cool skin), and the effect of salinity on the saturation water vapour pressure at the ocean surface.

5.6. Summary.

This chapter provided a detailed study on the predictive skill of the Eta model to provide suitable met-ocean parameters over a wide range of climatic regimes. Section 5.2.1. described the setup and initialisation of the limited area model using boundary conditions derived from a global model. This section described how these fields were smoothed, balanced and improved as the initial boundary conditions for the nested atmosphere model.

By means of the high-resolution database developed in chapter 4, the research questions put forward in section 2.1.2. were addressed. The level of scalar and spatial accuracy of the nested, high resolution Eta model was identified using a novel objective approach as described in section 5.4.3.

Section 5.5.3. discussed the current forecasting skill of the Eta model to predict air-sea fluxes and related basic variables. The annual forecasting trends of the Eta model were also discussed. Compared to collocated observations taken from the database, the Eta model showed a very good skill to predict the integrated precipitable water vapour (mean bias of -0.05 g cm^{-2}), surface wind magnitude (mean bias of 0.78 m s^{-1}), surface air temperature (mean bias of 0.15 ^{o}C), latent heat

flux (mean bias of −17.1 W m^{-2}) and sensible heat flux (mean bias of −9.2 W m^{-2}). Eta model produced a bias of 174.4 W m^{-2} when its predicted outgoing longwave radiation was compared to satellite estimations.

Apart from summarising the general forecasting skill of the Eta model, this chapter demonstrated the efficacy of remote sensing to assess and rate the performance of the modelling system used in the present study.

Section 5.5.4. discussed the fine-tuning of the Mellor-Yamada turbulence closure scheme. The results of this experiment and suggestions for their operational have been discussed. A novel, exploratory spatial similarity analysis was presented and used to explore the spatial accuracy of this modularity as described in section 5.5.5.

The next chapter addresses the impact of initialising this nested atmosphere model with high-resolution SST data derived by and orbiting passive microwave sensor. Special emphasis is given to the use of exploratory and geostatistical analysis to study the resulting impact on the accuracy of the model predictions.

Chapter 6

IMPACT OF USING MICROWAVE-DERIVED SEA SURFACE TEMPERATURE TO INITIALISE THE LOWER BOUNDARY CONDITION OF THE ETA MODEL.

6.1. Introduction.

The sea surface temperature (SST) plays a crucial role in the coupling of the atmosphere and ocean (Tsintikidis & Zhang, 1998). It is a controlling factor in the exchange of heat and moisture (evaporation), thus determining the marine boundary layer stability. The sea surface temperature also interacts with the atmosphere leading to convective processes that in turn affect the thermohaline conditions of the oceans (Tsintikidis & Zhang, 1998).

In numerical weather prediction, this surface variable plays a crucial component in deriving a true representation of the surface processes at the marine boundary layer of numerical models. Hence, an unrealistic representation of the ocean surface leads to errors in the model forecast, in particular to fine-resolution numerical modelling[110]. The need for improved representation of the actual SST conditions is extremely important and becomes therefore mandatory.

6.2. The experiment.

This chapter presents an evaluation of novel remotely-sensed datasets used to initialise and hopefully improve the ocean forecasting system.

---

110 *http://www.met.tamu.edu/personnel/faculty/fzhang/ATMO689/Lecture19/Lecture19.doc (accessed on 01.11.04).*

The aim is to test the suitability of data from orbiting Tropical Microwave Imager (TMI) to improve the forecast of air-sea fluxes that are used to force the underlying ocean model. The impact of using this alternative source of SST is assessed on the basis of the skill of the model to forecast near surface geophysical parameters that are sensitive to the prescribed initial conditions. Any improvement in forecasting capability would very much benefit application in areas such as oil spill warning systems (e.g. RAMSES), and for warning of extreme events in the Mediterranean region (e.g. COMPASS).

The study area covers an open ocean domain over the Ionian basin (fig. 5.2). Two parallel and identical numerical atmosphere models are used to produce a series of forecasts. The lower surface boundary condition of one of the models is initialised using remotely sensed SST retrieved by the TMI sensor during the period January to December 1999. The initialisation of the atmosphere model using TMI data was denoted as '*experimental*' and compared with a 'twin' setup using SST data derived from the Global Data Assimilation System of the National Centre for Environment Prediction (NCEP) in Washington. The latter dataset is routinely used by operational NWP agencies to initialise their local area atmosphere models to produce daily atmospheric forecasts[111].

The Eta model used is the nested high-resolution version described in section 5.2.1. The experimental work was carried out during the first quarter of 2000 as soon as a full-year, global, high-resolution SST data derived from the orbiting microwave sensor was available for public use. During 1999, the TMI sensor was the only orbiting instrument able to retrieve SST data using passive microwave radiometry. Other geophysical fields were simultaneously collected from the same sensor, including 10 m wind magnitude to assess the forecasting quality of the experimental setup.

[111] *e.g. by the Euro-Mediterranean Centre in Insular Coastal Dynamics and by the RAMSES oil spill modelling system.*

The field of view of the TMI sensor is limited to around 40°S and 40°N, since a low inclination orbit was chosen for the satellite to provide continuous monitoring of tropical latitudes. In this context, the geographical coverage of the TMI data also defined the local area domain over the central Mediterranean, which did not exceed 40°N in latitude (fig. 6.1).

A schematic diagram of the experimental procedure is shown in figure 6.2. The main experimental point is the "switching" of SST sources used to initialise the same atmosphere model. The intialisation of the lower boundary conditions is the only variable used in the experiment while all other parameters remain constant. This includes the definition of the lateral boundary conditions of the model.

6.3. New approaches in model validation.

Model verification measures are applied to determine the quality of forecasts and their relative accuracy with collocated observation(s). For the present objectives, it is convenient to divide model diagnosis into two main areas: *descriptive* and *inferential* statistics. Descriptive statistics relate to the statistical summaries of the forecasted and remotely-sensed data. This approach condenses the large amount of data that is generated from the experiment into an appropriate summary representation of the most important variations of the predicted data. These measures include mean, standard deviation, bias error and mean square error.

Inferential statistics consists of methods and procedures used to draw conclusions regarding the underlying processes and quality of the generated results. Aspatial methods are used to quantify the *skill score* of each model system to forecast the geophysical field. Most current statistical tools used to assess the skill of NWP models use classical aspatial methods. A classical example is the approach taken by the

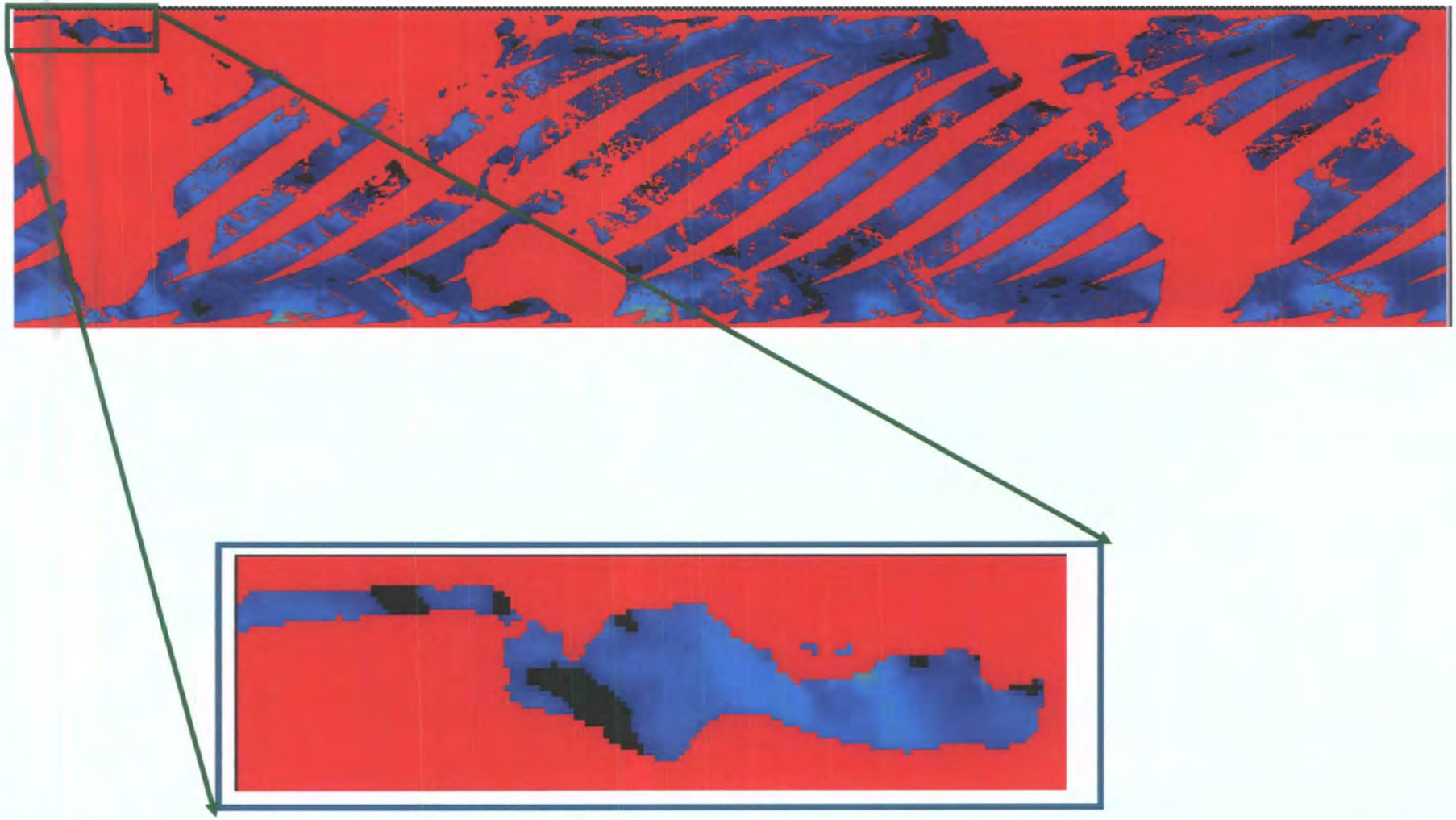

Figure 6.1. An example of a global wind magnitude profile derived by the TMI sensor onboard the Tropical Microwave Mission (TRMM) satellite during its ascending path on July 22, 1999. The inset represents the geophysical field over the Mediterranean area, not exceeding 40°N.

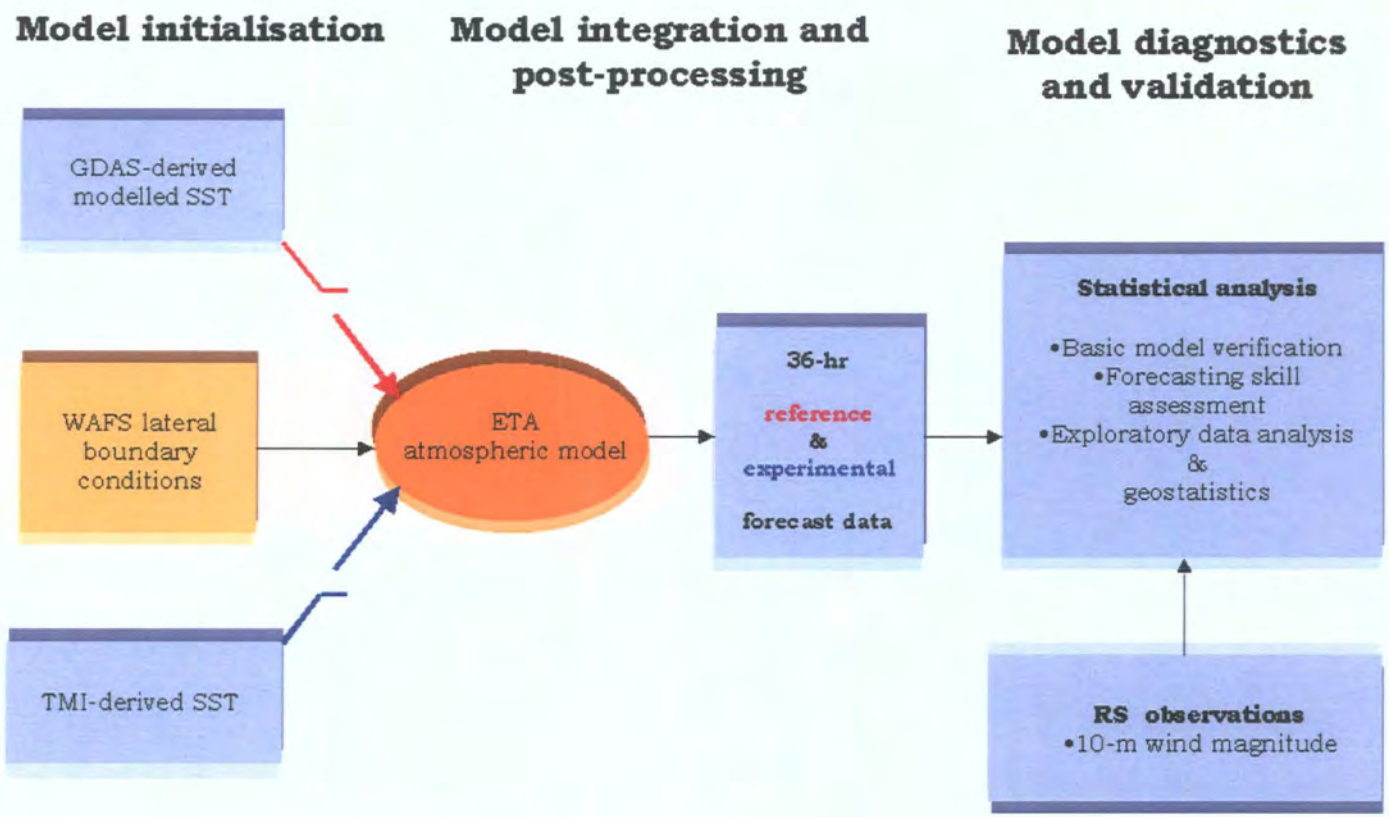

Figure 6.2. Schematic diagram of the experimental procedure to assess the impact when TMI-derived remotely-sensed (RS) SST that is used to initialise the surface boundary condition of the high-resolution atmosphere model.

NOAA Forecast System Laboratory to validate their AWIPS forecast preparation system.

This chapter attempts to approach model validation from a new angle by using the concepts of exploratory spatial data analysis and geo-statistics. This approach is somewhat unique to numerical weather prediction community, since exploratory spatial data analysis is much more familiar to geologists and soil scientists than to meteorologists. In doing so, the present study used special techniques to detect and assess spatial patterns and their modelling based on the data attributes.

To address these novel approaches in numerical weather prediction, a *match score analysis* is here developed to assess the impact, in spatial terms, of introducing a better representation of the SST on the modelling system. Apart from impact assessment, additional spatial techniques are applied to better understand the strengths and weaknesses of the atmosphere model. These include a measure of *spatial similarity* to highlight the spatial accuracy of the forecasts, and *semi-variance* and *variographic analysis* to denote the spatial structure or 'signature' of forecasted and observed fields, as well as the variability of the two set of forecasts. *Variography* is used to understand the spatial structure of the forecasted variables and to explore the scaling properties of the modelling system. This *surface analysis* is applied to understand the spatial relationship between the fields predicted by the *reference* and *experimental* model systems and collocated, remotely sensed observations. The method provided a quantitative measure that indicates how well the pairs of spatial data sets compare with observations

6.4. Methodology.

6.4.1. Remotely sensed SST and wind magnitude.

The process of retrieving and formatting the SST and 10 m wind magnitude data from the TMI sensor onboard the Tropical Rainfall Microwave Mission (TRMM) Satellite is described in section 4.3.1.1.

The TMI daily dataset were studied to note orbit time and the integrity of the SST data field over the area corresponding to the high-resolution Eta domain. This enabled the selection of the appropriate sets of SST data to initialise the Eta model at 00 UTC.

The source code used to organise and format these data is *TMI2monthlyORB.f* by specifying 00 (i.e. ascending) or 12 (i.e. descending):

```
TMI2monthlyORB  19990722TM 0
```

For example, in the script file below:

```
foreach dd (  22 23 24 25 26 27 28 29 30 31)
cp bdat/July/199907"$dd"TM.GZ  .
gzip -d 199907"$dd"TM.GZ  .
TMI2monthlyORB  199907"$dd"TM 0
rm -f 199907"$dd"TM
end
```

only geophysical parameters from the ascending orbits are selected, decoded, processed and sequentially written in GrADS format. The resulting *tm2JULcentORB.gdat* was read using the *tm2JULcentORB.ctl*[112].

[112] *Appendix I; Section I.1.1.*

6.4.2. Quality control.

Special attention has been given to the quality control and model initialisation aspects that allow a strict quality control of the data. This check ensures the insertion of good quality initial SST fields in the numerical model (tables 6.1 a-c). This included:

1. time of retrieval ± 3 hours from 00hrs UT initialisation time.
2. no data gaps due to precipitation.
3. wind speeds over model domain higher than 2 m s^{-1} but not exceeding 12 m s^{-1}.
4. spatial auto-correlation (Moran's Index *I*) of SST raster fields exceeding 0.76.
5. full-data integrity over the area of interest in the Ionian basin.

6.4.3. Initialisation of the lower surface boundary condition of the Eta model.

Details concerning data analysis and selection of valid dates for model initialisation using TMI-derived SST are given in tables 6.1 a - c. The selection of dates for which the model was initialised with this SST data also depended on the availability of both GDAS-derived SST (i.e. the data source for the *reference* setup) and WAFS lateral boundary conditions. Selection also rested on the availability of 10 m wind magnitude observations which ideally had to coincide with the 21st -, 24th -, or 27th-hour forecasted fields, since this interval represents sufficient enough time for the atmosphere model to remove any "spin-up" effect originating from the start of the model integration run.

The experimental work consisted of a parallel series of high resolution, hind-cast model simulations. The *reference* model setup used GDAS-SST model analyses as the initial lower surface boundary data at 00 UT (see fig. 6.3. for an example of a GDAS-derived SST field) together with WAFS data as the initial lateral atmospheric boundary conditions at

Month: JANUARY Dates	18	19	20	21	22	23	24	25	26	27	28	30
SST swath close to 00± 3hrs UT over domain	✔	✔	✔	✔	✔	✔	✔	✔	✔	✔	✔	✔
TMI SST with no rain pixels	✔	✔			✔		✔					
TMI data for model verification	✔	✔	✔	✔	✔	✔	✔	✔		✔		
Availability of GDAS-SST data*	✔			✔	✔	✔	✔	✔	✔	✔	✔	✔
Availability of lateral boundary conditions[f]	✔			✔	✔	✔	✔	✔	✔	✔	✔	✔
Valid TMI SST to initialise lower boundary	✔				✔		✔					

MONTH: FEBRUARY Dates	2	4	5	17	24	25	26	27
SST swath close to 00± 3hrs UT over domain	✔	✔	✔	✔	✔	✔	✔	✔
TMI SST with no rain pixels	✔	✔	✔	✔	✔	✔	✔	✔
TMI data for model verification	✔	✔	✔	✔		✔	✔	
Availability of GDAS-SST data*			✔	✔	✔	✔	✔	✔
Availability of lateral boundary conditions[f]	✔	✔	✔	✔	✔	✔	✔	✔
Valid TMI SST to initialise lower boundary								

MONTH: MARCH Dates	5	6	7	8	9	10	11	12	14
SST swath close to 00± 3hrs UT over domain	✔	✔	✔	✔	✔	✔	✔	✔	✔
TMI SST with no rain pixels	✔	✔	✔	✔	✔	✔	✔	✔	✔
TMI data for model verification	✔	✔	✔	✔		✔	✔		✔
Availability of GDAS-SST data*			✔	✔	✔	✔	✔	✔	✔
Availability of lateral boundary conditions[f]			✔	✔	✔	✔	✔	✔	✔
Valid TMI SST to initialise lower boundary			✔	✔		✔	✔		✔

MONTH: APRIL Dates	21	22	23	25	26	27	28	30
SST swath close to 00± 3hrs UT over domain	✔	✔	✔	✔	✔	✔	✔	✔
TMI SST with no rain pixels	✔	✔	✔	✔	✔	✔	✔	✔
TMI data for model verification	✔	✔	✔	✔	✔	✔	✔	✔
Availability of GDAS-SST data*	✔	✔	✔	✔	✔	✔	✔	
Availability of lateral boundary conditions[f]	✔	✔	✔		✔	✔	✔	✔
Valid TMI SST to initialise lower boundary	✔	✔	✔		✔	✔	✔	

Table 6.1 a. Use of valid TMI-derived SST data for numerical model initialisation from January - April 1999. The choice of forecasting dates depended on criteria listed in sequential order.

[f]Lateral boundary conditions produced by WAFS consists of 6-hourly modelled data. Data unavailability was due to connectivity problems with WAFS server.

**GDAS-SST data consists of 00hrs modelled surface boundary conditions for the atmosphere model. Data unavailability was due to connectivity problems with GDAS server.*

Month: MAY Dates	2	3	4	5	6	15	16	17	18
SST swath close to 00± 3hrs UT over domain	✔	✔	✔	✔	✔	✔	✔	✔	✔
TMI SST with no rain pixels	✔	✔	✔		✔				
TMI data for model verification	✔	✔	✔	✔	✔	✔	✔	✔	✔
Availability of GDAS-SST data*		✔	✔	✔	✔	✔	✔	✔	✔
Availability of lateral boundary conditions[f]	✔	✔		✔	✔	✔	✔	✔	✔
Valid TMI SST to initialise lower boundary		✔			✔				
Valid TMI SST to initialise lower boundary									

Month: JULY Dates	22	23	24	25	26	27	28	29	30	31
SST swath close to 00± 3hrs UT over domain	✔	✔	✔	✔	✔	✔	✔	✔	✔	✔
TMI SST with no rain pixels	✔	✔	✔	✔	✔	✔	✔	✔	✔	✔
TMI data for model verification	✔	✔	✔	✔	✔	✔	✔	✔	✔	✔
Availability of GDAS-SST data*	✔	✔	✔	✔	✔	✔	✔	✔	✔	✔
Availability of lateral boundary conditions[f]	✔	✔	✔	✔	✔	✔	✔	✔	✔	✔
Valid TMI SST to initialise lower boundary	✔	✔	✔	✔	✔	✔	✔	✔	✔	✔

Month: AUGUST Dates	1	2	3	4	5	6
SST swath close to 00± 3hrs UT over domain	✔	✔	✔	✔	✔	✔
TMI SST with no rain pixels	✔	✔	✔	✔	✔	✔
TMI data for model verification	✔	✔	✔	✔	✔	✔
Availability of GDAS-SST data*	✔	✔	✔	✔	✔	✔
Availability of lateral boundary conditions[f]	✔	✔	✔	✔	✔	✔
Valid TMI SST to initialise lower boundary	✔	✔	✔	✔	✔	✔

Month: SEPTEMBER Dates	9	11	12	13	14	16	17	18	19	20	21
SST swath close to 00± 3hrs UT over domain	✔	✔	✔	✔	✔	✔	✔	✔	✔	✔	✔
TMI SST with no rain pixels					✔	✔		✔		✔	✔
TMI data for model verification	✔	✔	✔	✔	✔	✔	✔	✔	✔	✔	✔
Availability of GDAS-SST data*	✔	✔	✔	✔		✔	✔	✔	✔	✔	✔
Availability of lateral boundary conditions[f]	✔	✔	✔	✔		✔	✔	✔	✔	✔	✔
Valid TMI SST to initialise lower boundary						✔		✔		✔	✔

Table 6.1 b. Use of valid TMI-derived SST data for numerical model initialisation from May - September 1999. The choice of forecasting dates depended on criteria listed in sequential order.

[f]Lateral boundary conditions produced by WAFS consists of 6-hourly modelled data. Data unavailability was due to connectivity problems with WAFS server.

**GDAS-SST data consists of 00hrs modelled surface boundary conditions for the atmosphere model. Data unavailability was due to connectivity problems with GDAS server.*

Month: OCTOBER Dates	22	23	24	26	27	28	29	30	31
SST swath close to 00± 3hrs UT over domain	✔	✔	✔	✔	✔	✔	✔	✔	✔
TMI SST with no rain pixels	✔	✔	✔	✔		✔	✔	✔	✔
TMI data for model verification	✔	✔	✔	✔		✔	✔	✔	✔
Availability of GDAS-SST data*	✔	✔	✔	✔	✔	✔	✔		
Availability of lateral boundary conditions[f]	✔	✔	✔	✔	✔	✔	✔	✔	✔
Valid TMI SST to initialise lower boundary	✔	✔	✔	✔		✔	✔		

Month: NOVEMBER Dates	1	2	3	4	5
SST swath close to 00± 3hrs UT over domain	✔	✔	✔	✔	✔
TMI SST with no rain pixels	✔	✔	✔	✔	✔
TMI data for model verification	✔	✔	✔	✔	✔
Availability of GDAS-SST data*			✔	✔	
Availability of lateral boundary conditions[f]	✔	✔			✔
Valid TMI SST to initialise lower boundary					

Month: DECEMBER Dates	9	10	12	13	14	15	16	17	18	19	20	21	22
SST swath close to 00± 3hrs UT over domain	✔	✔	✔	✔	✔	✔	✔	✔	✔	✔	✔	✔	✔
TMI SST with no rain pixels	✔			✔	✔	✔	✔	✔	✔	✔	✔		
TMI data for model verification	✔	✔	✔	✔	✔	✔	✔	✔	✔	✔	✔	✔	✔
Availability of GDAS-SST data*	✔	✔	✔	✔	✔	✔	✔	✔	✔	✔	✔	✔	✔
Availability of lateral boundary conditions[f]	✔	✔	✔	✔	✔	✔	✔	✔		✔	✔	✔	✔
Valid TMI SST to initialise lower boundary	✔			✔	✔	✔	✔	✔		✔	✔		

Table 6.1 c. Use of valid TMI-derived SST data for numerical model initialisation from October - December 1999. The choice of forecasting dates depended on criteria listed in sequential order.

[f]Lateral boundary conditions produced by WAFS consists of 6-hourly modelled data. Data unavailability was due to connectivity problems with WAFS server.

**GDAS-SST data consists of 00hrs modelled surface boundary conditions for the atmosphere model. Data unavailability was due to connectivity problems with GDAS server.*

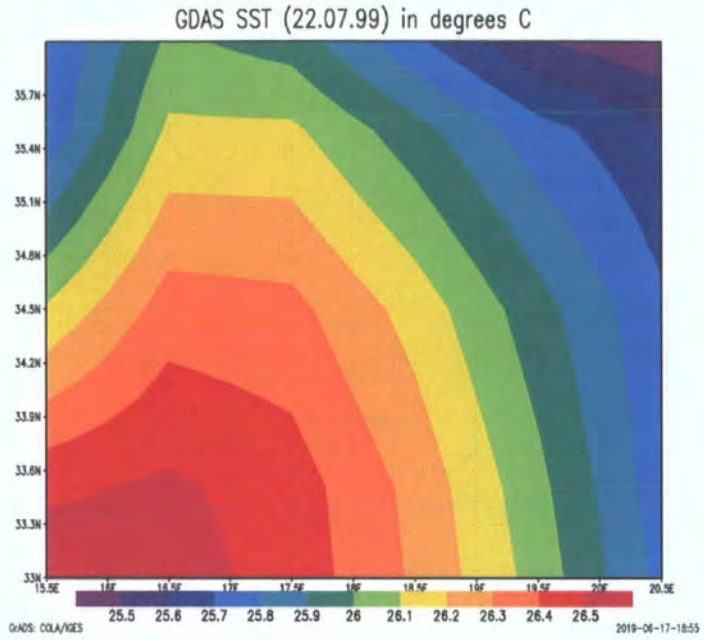

Figure 6.3. GDAS-derived modelled SST data in °C (originally 1° by 1° horizontal grid resolution) for 22nd July 1999 at 00 UT over the model integration domain. The data is interpolated onto 0.042° grid.

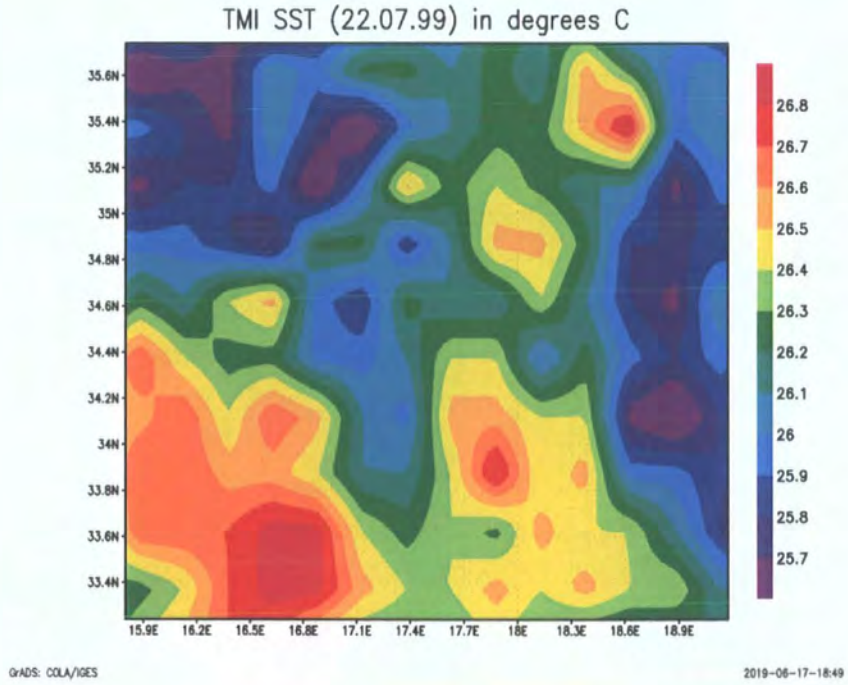

Figure 6.4. TMI-derived SST data in °C (originally 0.25° by 0.25° horizontal grid resolution) for 22nd July 1999 at 2.85 UT over the model integration domain. The data is interpolated onto 0.042° grid.

00 UT respectively and constant input data[113]. The model output was referred to as the "*Reference forecast*".

An identical *experimental* model setup was set up with exactly the same numerics as the *reference* model but using, instead of GDAS-SST data, the denser grid of SST observations collected by the TMI sensor (see fig. 6.4. for an example of a TMI-derived SST field). The model output was referred to as the "*Experimental forecast*".

The switching between the two sources of SST data was done by making available and accessing the appropriate temporal SST dataset, using *sst.f* whereby it calls TMI-SST according to user-defined date (datetohr) from the '*tm2JULcentORB.gdat*' data file. The subroutine RGRADS

```
call RGRADS (id7, 1, 999,  0, IME, JME, 1, 0., WW , NLRET)
```

browses the '*tm2JULcentORB.gdat*' file until it finds the SST field with the specific code of 999 and defines the SST value as WW. The script then re-interpolates the 0.25° by 0.25° latitude-longitude grid SST onto the respective Eta model domain resolution. In this experiment, the switching between the two SST sources was the only difference made to the entire model processing as described in section 5.2.1.

6.4.4. Generation of high-resolution, forecasted air-sea fluxes.

In total, 92 forecast runs were processed[114], each taking around 6 hours to complete. The 36-hr forecasted air-sea surface fluxes for both the reference and experimental models were produced using fortran code fluxes.f [115] and visualised[116]. These fluxes were then extracted into gridded ascii XYZ format using fortran code grads2xyz.f[117], for further analysis 6.4.5. Model validation.

---

[113] *Section 5.2.1.*
[114] *Section 5.2.1.*
[115] *Appendix II; Section II.2.7.*
[116] *Section 5.2.1.*
[117] *Appendix II; Section II.2.2.*

6.4.5. Model validation.

6.4.5.1. Basic statistical distributions and summary measures.

The mean bias showed how much, on average, the forecasts differ from the observations. The standard deviation is a measure of scatter in the results; it is zero when the bias is non-zero, if all the forecasted values are the same.

6.4.5.2. Model performance measures.

The Mean Square Error combines the effects of bias and scatter; it would be equal to the bias if the standard deviation were zero.

A skill score (SS) was used to reflect the average accuracy of the *experimental* forecasts in the sample relative to that produced by the *reference* setup (Murphy, 1997). SS was based on the mean square error, defined as:

$$SS = 1 - (MSE_{exp} / MSE_{ref})$$

where MSE_{exp} is the mean square error of the *experimental* forecasts and MSE_{ref} is that of the *reference* forecasts.

6.4.5.3. Spatial Exploratory Data Analysis.

ESDA was performed using three independent approaches to analyse the performance of the competing models in spatial terms. These were (1) Spatial Match Score Analysis, (2) Spatial similarity and feature matching analysis and (3) Residual semi-variogram analysis.

6.4.5.3.1. Spatial Match Score Analysis.

A spatial measurement was developed to assess any improvement in the spatial accuracy of the *experimental* over the *reference* model forecasts. This procedure highlighted (in graphic form) the exact geographical placement of the forecasted and observed collocated and *quasi* co-temporal 10 m wind magnitude.

This is a measure of the correct placement and timing of a forecast for a particular event (Glahn *et al.*, 1991). A match in terms of the exact overlap between forecast (f) and observation (o) for an occurrence is represented as a hit (h). Statistical match score compares the number of correct placed forecasted pixels to the total area where the event was observed. Match score is calculated according to:

$$\text{Match Score} = h/(f + o - h)$$

MS values ranged from 0.0 to 1.0, where a score of 1 represents a perfect match with the observations and a score of 0 indicates no skill. To facilitate calculation of the score, discrete parameter values in both forecasted and observed fields were categorised, and the resulting classes matched for exact overlap.

The calculation of the spatial match score consisted of a sequential series of GIS-analysis procedures on a grid cell or raster approach. This approach was useful for a number of reasons, such as (1) continuous nature of the real (i.e. floating point) data in space (2) easy integration of digital remotely sensed imagery with the numerical model output of the two forecasting systems and (3) each information type can be stored as a separate data layer for eventual spatial statistical analyses. The analysis was as follows:

1. Three datasets (in ascii XYZ real values) from each single forecast date were prepared equivalent to the *Reference, Experimental* and co-located observations. These were imported into ERMapper[118] using ASCII BIL option with a 61 by 82 grid.

2. Each dataset was filtered and **recoded** according to predefined 10 m wind magnitude intervals as shown in table 6.2.

Class number	10 m wind magnitude interval
1	2.0 – 3.0
2	3.1 – 4.0
3	4.1 – 5.0
4	5.1 – 6.0
5	6.1 – 7.0
6	7.1 – 8.0
7	8.1 – 9.0
8	9.1 – 10.0
9	10.1 – 11.0
10	11.1 – 12.0

Table 6.2. Recoding of wind magnitude intervals from 2 to 10 m s^{-1}.

3. Following step (2), each dataset was saved as "classified".

4. Both the classified r*eference* and e*xperimental* raster sets were **overlayed** over collocated observations and a new dataset was created consisting of two **overlayed** sets: e*xperimental* plus observation and r*eference* plus observation.

5. Each overlayed dataset was then **cross-tabulated** and **colour indexed** according to the function seen below:

[118] *http://www.ermapper.com/ (accessed on 01.11.04).*

if (INPUT1 = 1) and i2=1 then 250 else
if (INPUT1 = 2) and i2=2 then 240 else
if (INPUT1 = 3) and i2=3 then 230 else
if (INPUT1 = 4) and i2=4 then 220 else
if (INPUT1 = 5) and i2=5 then 210 else
if (INPUT1 = 6) and i2=6 then 200 else
if (INPUT1 = 7) and i2=7 then 190 else
if (INPUT1 = 8) and i2=8 then 180 else
if (INPUT1 = 9) and i2=8 then 170 else
if (INPUT1 = 10) and i2=8 then 160 else null

No weighting was given to any class.

6. The resulting two datasets were saved as "combined & classified". Area statistics were calculated for each dataset to extract **union (pixel) scoring.**

7. Match Score was calculated and tabulated.

6.4.5.3.2. Spatial similarity and feature matching analysis.

Spatial similarity was performed to analyse the spatial relationship between the two sets of forecasts and observations. This study uses the same algorithm as described in section 5.4.3.1. This consisted of the combination of fields and their associated inherent knowledge to determine the position of similar clusters between the pair of forecasted fields and the collocated observations.

6.4.5.4.3. Residual semi-variogram analysis.

Semi-variance analysis was performed on raster maps produced from the residuals between the forecasted 10 m wind magnitude fields (originating from the *reference* and *experimental* setup) and collocated observations. Residual maps were generated by subtracting the

individual forecasted ascii datasets from co-temporal observations (archived in ascii xyz). This dataset was imported into ERMapper format for 3-dimensional analysis.

GS+ was used for variogram modelling of these residuals[119]. GS+ is a geostatistical programme that measures and illustrates spatial relationships in geo-referenced data. It analyses spatial data for autocorrelation and then uses this information to make optimal, statistically rigorous maps of the area sampled. GS+ provides three types of spatial autocorrelation analysis. The one used for the present study is the semi-variance analysis, which produced a variogram and five types of variogram models.

The individual geo-referenced residual datasets were imported as text files in GS+ to perform semi-variogram analysis at the full resolution of the residual map. Five types of isotropic models were produced for each residual map, each of which described according to three parameters, namely *Nugget Variance* – the y-intercept of the model, *Sill* – the model asymptote and *Range* – the distance over which spatial dependence is apparent. The *Range* parameter was used to define the best-fit line and the best model fit was selected. The ranges of models considered were spherical, exponential, linear, linear to sill and Gaussian. In addition to the three model parameters nugget, sill, and range, the software provided statistics to aid the interpretation of model output. An important statistic was the Reduced Sums of Squares, which provided an exact measure of how well the model fits the variogram data; the lower the reduced sums of squares, the better the model fits.

These semi-variograms translated the texture information according to the idealised relationships (see fig. 6.5) in the form N (nugget variance), C (sill minus the nugget), R (range) and h (distance).

---

[119] *GS+ (ver. 1989-1999): geostatistics for the environmental sciences is produced by Gamma Design; www.gammadesign.com (accessed on 01.11.04).*

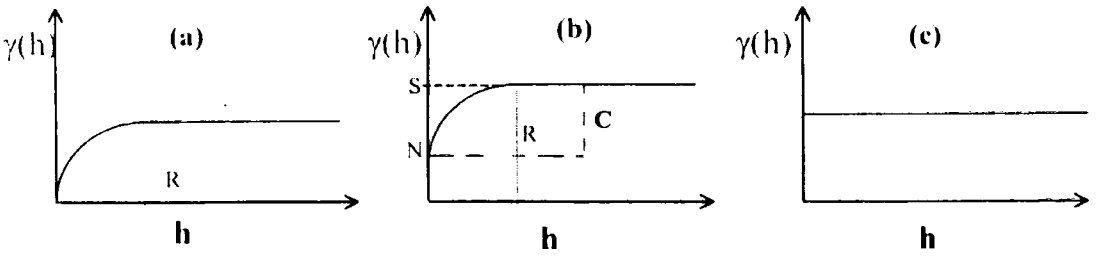

Figure 6.5 Semi-variograms through the origin (a) with nugget effect (b), and with no spatial autocorrelation (c).

C – spatial independent structural variance. It is given by sill minus nugget variance;

h- lag – distance and direction in 2 or more directions between pairs

S – sill – maximum level of γ(h)

R – range – lag value at which γ(h) no longer increases

N- nugget variance – value resulted by backwards extrapolation of the 2 first semi-variance values.

Analyses proceeded with the calculation of the anisotropic semi-variance surface or variogram map for each residual dataset. This map provided a visual picture of semi-variance in every compass direction as to find the most appropriate principal axis that defines the anisotropic variogram model. The center of the map corresponds to the origin of the variogram g(h) = 0 for every direction.

6.5. Results and Discussion.

6.5.1. Relationship between the two annual SST data sets.

As illustrated by figures 6.3 and 6.4, the TMI-derived SST map exhibits considerable mesoscale information. During model integration, this fine detail is interpreted by the model as its initial lower boundary conditions and used to compute the lower geophysical fields in particular.

In spite of the difference in the spatial information, the relationship between the datasets is very linear throughout the year, with a high

coefficient of 0.98. This relation is valid for the entire climatological range of SST over the central Mediterranean (fig. 6.6).

A closer inspection at this relationship shows that TMI-derived SST data tends to be higher by not more than 0.5 K when the temperature ranges between 289 K (15.8 °C) and 299 K (25.8 °C). Above 299 K, the variation becomes very close to zero and the tendency is reversed at higher temperatures as shown by the linear trend in figure 6.7. Considering the high accuracy of TMI-derived SST (with a bias of just —0.07 °C) against *in situ* data[120], the same can be said of the GDAS-derived SST. A higher correlation would have probably been found if the TMI-SST was retrieved at exactly 00 UT. As detailed in section 6.4.2. above, TMI-SST data was valid if its orbital coverage resided within ± 3 hours from 00 UT.

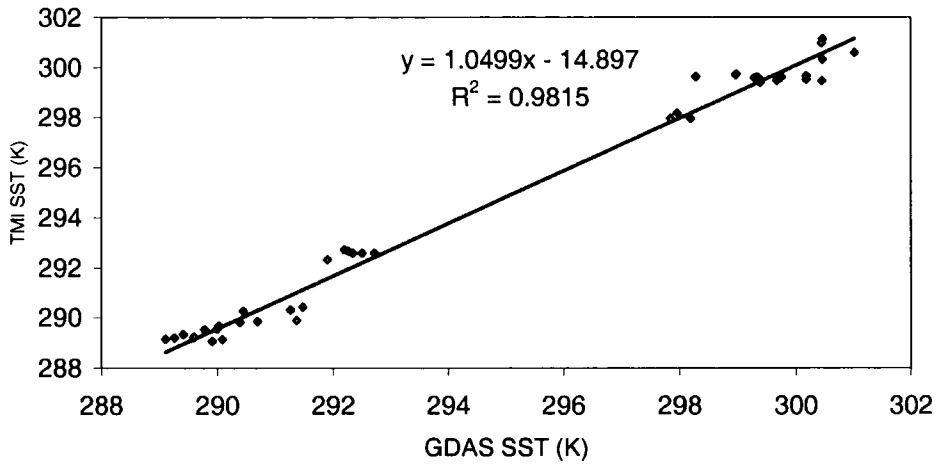

Figure 6.6. Scatterplot of collocated TMI- vs GDAS-derived SST (in Kelvin). Each point represents the average SST value of 5002 raster points representing a complete surface field over the integration domain of the local area model.

[120] *Section 3.5.4.1.2.*

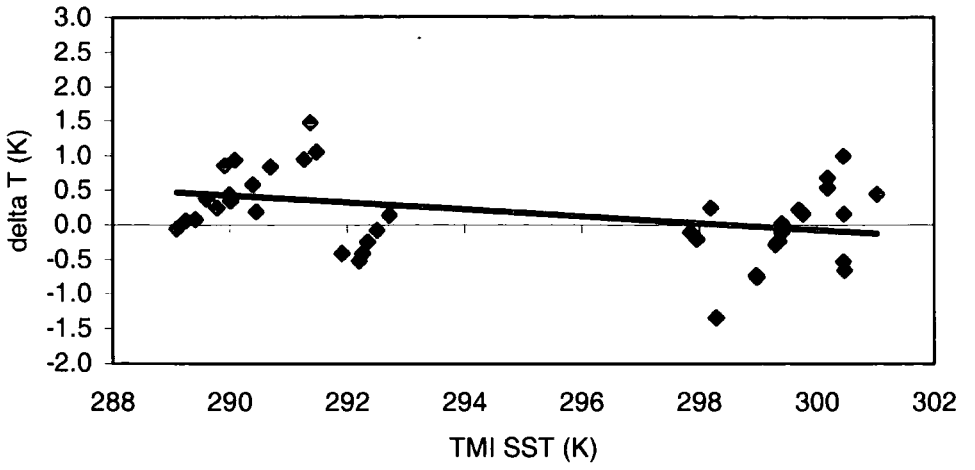

Figure 6.7. Residual plot tendency of TMI- minus GDAS-derived SST (in Kelvin) against TMI-derived SST (in Kelvin). Each point represents the average SST value of 5002 raster points representing a complete surface field over the integration domain of the local area model.

6.5.2. The numerical experiments.

The statistical measures shown under this section were generated by co-temporal comparisons between the forecasts generated by the two model systems and observations. This kind of "single-forecast" analysis is ideal to address both (1) the accuracy of model initialisation of both forecasting systems as well as (2) the resulting forecast performance.

Some examples of the forecasted geophysical fields derived by the *reference* and *experimental* setup are shown in figures 6.8 and 6.9. The most significant observations derived from these two sets of output is that the different initial SST lower boundary conditions lead to different outputs. This shows the influence of SST on the prediction of these fields. This difference is particularly striking for the surface geophysical fields. The spatial pattern of the two sets of the lower atmospheric fields are different, especially for the 2 m air temperature and total heat flux.

Figures 6.10 a-b show the 10 m wind magnitude and total precipitable water vapour as derived by the TMI-sensor on July 28th at 0200 UT. The

10 m wind magnitude field shows the presence of two main fields of high (maximum: 7 m s^{-1}) and low intensity (minimum: 1.5 m s^{-1}) separated by an intermediate field of with a constant gradient from the lower to the higher intensity. This simple spatial arrangement is closer to that predicted by the *experimental* setup in comparison to the field obtained by the *reference* setup (fig. 6.8). The latter also shows two main fields (maximum: 7 m s^{-1}; minimum: 1.5 m s^{-1}) but with the lower intensity area containing a significantly large, isolated higher-intensity cell (approximately at 16.2°E; 37.4°N in fig. 6.8). This is not the case for the same field produced by the *experimental* setup.

The observed integrated precipitable water vapour consists of two main areas containing an average precipitable water vapour of 26.5 mm, and connected together by a gradient of 25 mm. A slightly lower intensity field of around 24 mm separates these two fields on each side of the entire model domain on the north and south. The two model output fields shown in figure 6.9 show two main, higher intensity fields of around 28 mm. However, the field produced by the *reference* setup shows a higher overall intensity, and the output showed a bias toward the higher intensity field. The two fields are joined together by the 25.5 mm field. The same field predicted by the experimental setup, on the other hand, shows an overall field that is more shifted towards the observation, with two main higher intensity fields, separated by a green field corresponding to 24 mm. A minimum of 20.5 mm is shown by the field starting at the bottom right of the area which extends more towards the centre than what is produced by the *reference* setup.

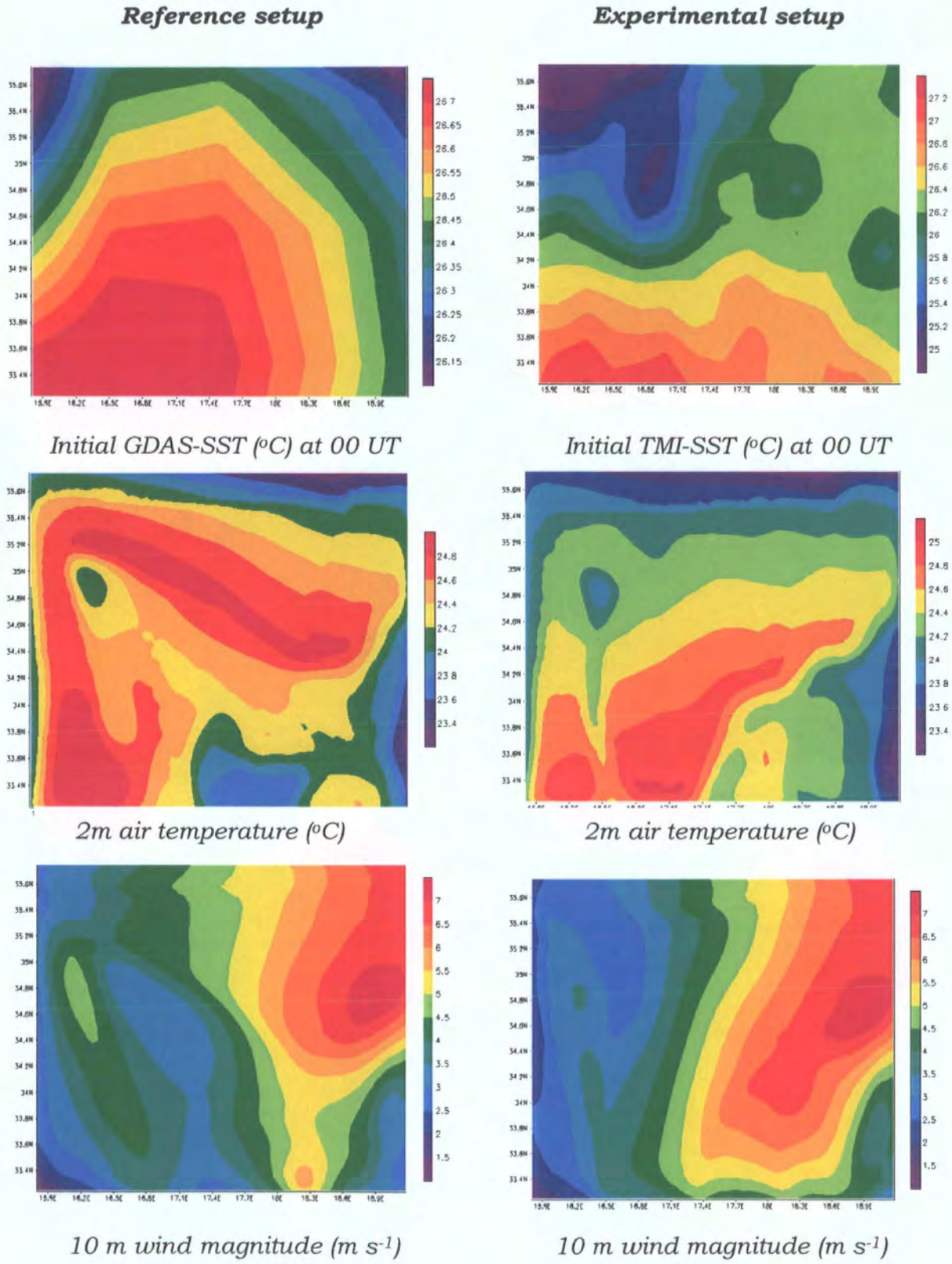

Figure 6.8. Example of fields produced by the Reference (left) and Experimental (right) setup, initialised by the GDAS-SST and TMI-SST respectively. The predicted geophysical fields correspond to the 27th hour fields starting on 27 Jul 1999, 00 UT.

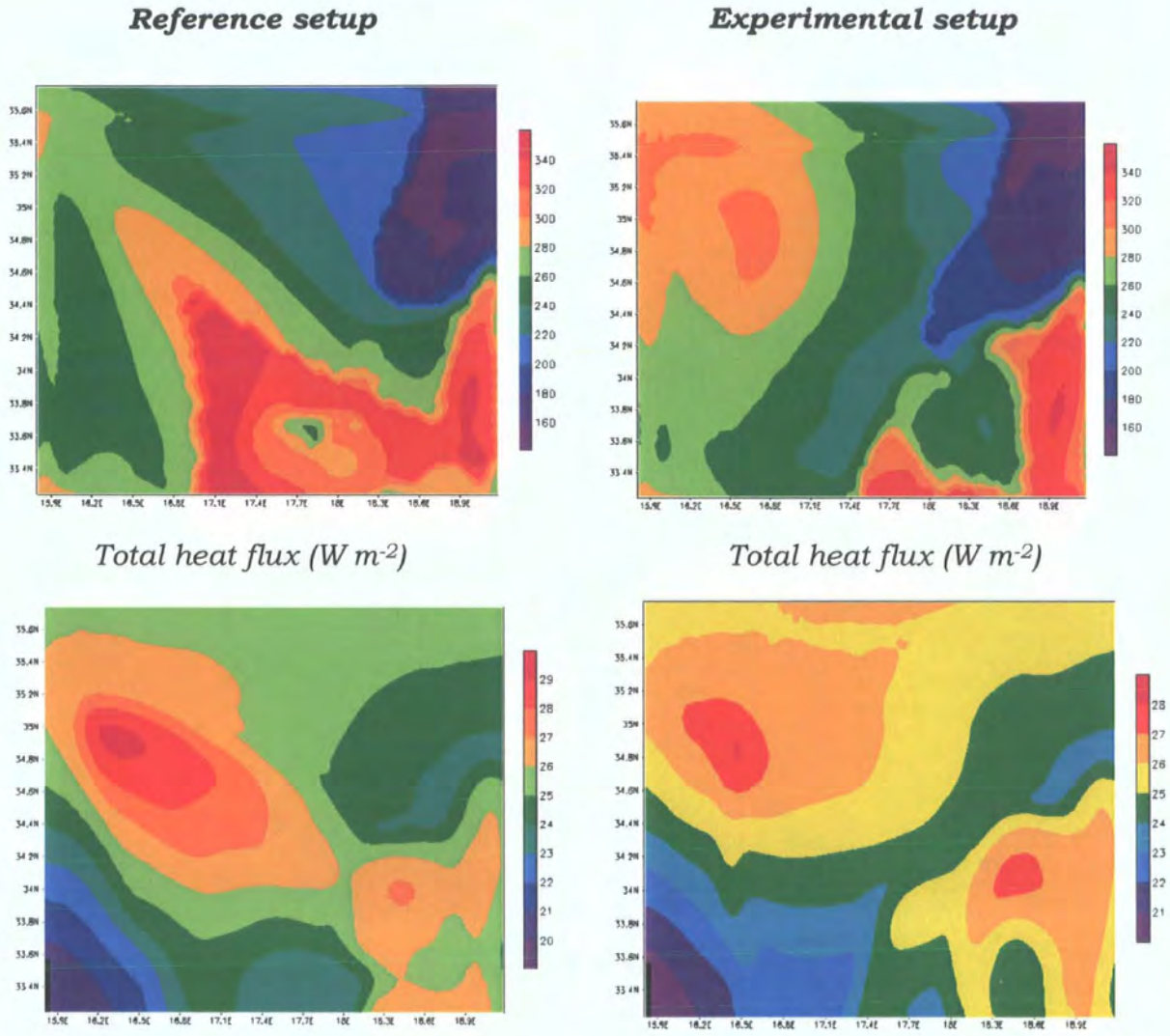

Figure 6.9. Example of fields produced by the Reference (left) and Experimental (right) setup, initialised by the GDAS-SST and TMI-SST respectively. The predicted geophysical fields correspond to the 27th hour fields starting on 27 Jul 1999, 00 UT.

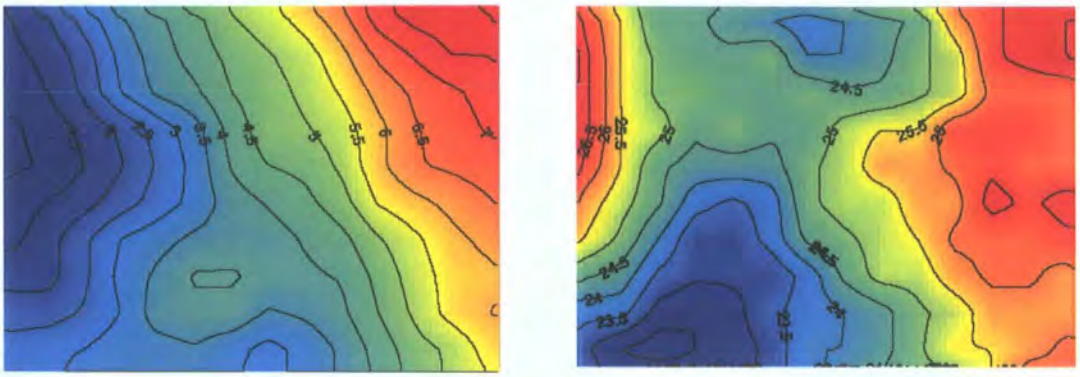

(a) **(b)**

Figure 6.10. TMI-derived (a) 10 m wind magnitude (m s^{-1}), and (b) total precipitable water vapour (in g cm^{-2} x 10^{-1}), on the 28th July at 0200 UT.

A look at the basic statistical measures of the two forecasting systems in relation to observations (table 6.3) shows that both systems produce very similar 10 m wind magnitude fields. These statistics summarise the overall quality of the forecasts against the observations. The standard deviation measures the random model forecast error for each case study, while the bias is a measure of fit of the model to the real atmospheric state by measuring the correspondence between the average forecast and the average observed value of the predictand. Bias, as shown in table 6.3, gives an estimate of the systematic model forecast error.

The small difference between model-generated fields and observations is indicative of a high accuracy of both systems to predict the surface wind speed at forecasting steps ranging between the 21st and 27th hour after model initialisation. However, closer inspection at the relative biases of the two model setup shows that the *experimental* setup outperforms the r*eference* one throughout the year without any seasonal trend. Although a trend has been identified in the difference between GDAS- and TMI-derived SST (fig. 6.7), it seems that the model is not sensitive to this change.

It is also important to note that wind magnitude forecasts were verified only when the wind speed observations, valid at the time of the forecast, was greater than or equal to 2 m s^{-1}. This prevented wind magnitude forecasts associated with light and variable winds from degrading verification scores. The same approach is taken by major numerical weather prediction centers such as NOAA for its NGM-based model output statistics wind guidance over the US territory[121].

[121] *http://www.nws.noaa.gov/om/tpb/akwind.htm (accessed on 01.11.04).*

Month	Verification time	Wind speed range (m s^{-1})	Average		Standard deviation		Bias	
			REF	EXP	REF	EXP	REF	EXP
January	**18:27_19(D)**	3 to 10	8.12	8.14	0.44	0.42	-0.69	-0.68
	22:27_23(D)	2 to 10	4.46	4.51	1.13	1.12	-0.20	-0.15
	24:24_25(D)	2 to 10	5.21	5.13	1.02	0.99	0.30	0.23
March	**07:24_08(A)**	3 to 10	5.21	5.24	1.07	1.15	-1.01	-0.97
	08:27_09(D)	4 to 10	5.33	5.34	0.73	0.72	0.70	0.71
	10:24_11(D)	4 to 10	5.32	5.36	0.75	0.72	0.88	0.93
	11:24_12(D)	3 to 10	4.45	4.44	0.95	0.91	-0.04	-0.05
	14:21_14(A)	3 to 10	5.59	5.69	1.27	1.28	1.03	1.14
	17:21_17(D)	3 to 10	5.39	5.62	1.31	1.33	-0.53	-0.31
April	**21:24_22(A)**	3 to 10	6.09	6.18	1.17	1.20	0.43	0.51
	22:27_23(D)	3 to 10	6.50	6.02	2.16	2.18	1.73	1.25
	23:27_24(D)	2 to 10	4.07	3.84	1.35	1.26	0.55	0.33
	26:24_27(D)	2 to 10	3.39	3.38	0.82	0.81	0.57	0.56
	27:24_28(D)	2 to 10	6.27	6.32	0.97	0.99	1.77	1.81
	28:21_28(A)	2 to 10	5.33	5.76	1.81	1.67	-0.03	0.39
May	**03:21_03(D)**	3 to 12	8.65	8.74	2.52	2.43	-3.20	-3.11
July	**22:27_23(A)**	3 to 10	3.48	3.51	0.36	0.35	0.00	0.03
	23:27_24(D)	3 to 10	4.48	4.23	0.84	0.97	0.30	0.05
	24:27_25(D)	3 to 10	5.76	5.33	1.39	1.19	0.71	0.28
	25:24_26(A)	4 to 10	6.24	6.31	1.31	1.34	1.44	1.50
	26:27_27(D)	3 to 10	5.36	5.39	0.73	0.81	-1.75	-1.72
	27:27_28(D)	4 to 10	5.26	5.62	0.94	0.92	-0.29	0.07
	28:27_29(D)	4 to 10	4.39	4.41	0.26	0.30	0.14	0.15
	29:24_30(D)	4 to 10	7.20	6.93	0.44	0.40	1.04	0.77
	30:24_31(D)	4 to 10	6.81	6.72	0.67	0.63	1.26	1.17
	31:24_31(A)	3 to 10	3.41	3.44	0.42	0.41	-0.22	-0.19
August	**01:21_01(A)**	4 to 10	5.39	5.35	1.01	1.00	0.50	0.46
	02:21_02(D)	3 to 10	4.48	4.49	0.87	0.95	0.09	0.11
	03:21_03(D)	3 to 10	4.51	4.58	0.89	0.93	0.05	0.12
	04:21_04(D)	4 to 10	5.34	5.34	0.72	0.73	0.76	0.75
	05:21_05(D)	3 to 10	4.53	4.54	0.73	0.74	0.42	0.43
	06:18_06(A)	2 to 10	3.11	3.13	0.58	0.55	0.44	0.47
September	**16:21_17(A)**	4 to 10	6.80	6.71	0.98	0.91	0.60	0.51
	18:21_18(A)	4 to 10	4.97	4.71	0.43	0.37	-0.91	-1.17
	20:21_20(D)	3 to 10	9.44	9.38	0.39	0.39	0.81	0.75
	21:21_21(D)	3 to 10	5.61	5.78	1.27	1.43	0.55	0.73
October	**22:27_23(A)**	4 to 10	4.35	4.34	0.26	0.26	-1.63	-1.64
	23:27_24(A)	4 to 10	4.97	5.01	0.52	0.57	-1.08	-1.04
	28:27_29(D)	3 to 10	8.73	8.80	0.79	0.82	0.40	0.47
	29:27_30(D)	4 to 10	5.67	5.64	1.16	1.10	0.68	0.65
December	**13:21_13(A)**	3 to 12	9.66	9.61	0.64	0.59	-1.28	-1.32
	14:21_14(A)	3 to 10	7.06	7.09	1.06	1.06	-1.32	-1.29
	15:24_15(A)	3 to 14	10.36	10.44	0.68	0.69	-0.41	-0.33
	16:21_16(A)	3 to 12	8.44	8.42	1.31	1.37	-0.92	-0.94
	17:21_18(A)	3 to 12	6.14	6.23	1.01	1.04	-2.28	-2.19
	19:21_19(A)	3 to 12	7.26	7.43	0.87	0.88	-2.37	-2.20

Table 6.3. Basic comparative statistics of 10 m wind magnitude (m s^{-1}) forecasts with observations. The date format is: model DAY NUMBER : FORECASTED HOUR _ satellite DAY NUMBER (DESCENDING or ASCENDING orbital swath). REF: reference model wind magnitude forecast; EXP: experimental model wind magnitude forecast).

6.5.3. Performance measures.

The mean square error (MSE) is the average squared difference between collocated pairs of forecasts and observations. For this reason, large discrepancies between forecasts and observations give large positive values. This performance measure gives a clear picture of the performance between the two model setup, showing an overall improvement when TMI-derived SST is used to initialise the lower boundary conditions at the start of the model run (table 6.4). Normalisation of the MSE shows a clear improvement reached by the experimental over the reference setup by an average of 10% in the forecast accuracy of the 10 m wind magnitude (fig. 6.11).

The use of average skill scores for the entire annual analysis give a weak picture of this improvement, and can not be considered as a good index to detect such improvement. Results show that highest scores are observed during the spring and summer seasons, although this period shows the greatest variability in terms of standard errors. Lesser variability accompanied by lower skill scores occurs during the colder months, when the wind magnitude is more intense.

Month	Verification time	Wind speed range (m s^{-1})	MSE		SKILL SCORE
			REF	EXP	
January	**18:27_19(D)**	3 to 10	1.08	1.04	0.04
	22:27_23(D)	2 to 10	1.93	1.81	0.06
	24:24_25(D)	2 to 10	2.01	1.64	0.18
March	**07:24_08(A)**	3 to 10	4.49	4.63	-0.03
	08:27_09(D)	4 to 10	2.39	2.37	0.01
	10:24_11(D)	4 to 10	3.13	3.14	0.00
	11:24_12(D)	3 to 10	0.70	0.61	0.13
	14:21_14(A)	3 to 10	1.45	1.78	-0.23
	17:21_17(D)	3 to 10	5.58	4.80	0.14
April	**21:24_22(A)**	3 to 10	2.20	2.16	0.02
	22:27_23(D)	3 to 10	10.67	8.32	0.22
	23:27_24(D)	2 to 10	2.91	3.15	-0.08
	26:24_27(D)	2 to 10	1.66	1.62	0.02
	27:24_28(D)	2 to 10	3.76	3.87	-0.03
	28:21_28(A)	2 to 10	2.01	1.33	0.33
May	**03:21_03(D)**	3 to 12	0.39	0.30	0.24
July	**22:27_23(A)**	3 to 10	0.27	0.29	-0.10
	23:27_24(D)	3 to 10	1.48	0.74	0.50
	24:27_25(D)	3 to 10	1.43	0.51	0.64
	25:24_26(A)	4 to 10	2.07	2.26	-0.09
	26:27_27(D)	3 to 10	5.23	5.30	-0.01
	27:27_28(D)	4 to 10	0.85	1.14	-0.34
	28:27_29(D)	4 to 10	0.44	0.26	0.40
	29:24_30(D)	4 to 10	1.51	0.94	0.38
	30:24_31(D)	4 to 10	2.70	2.36	0.13
	31:24_31(A)	3 to 10	1.46	1.33	0.08
August	**01:21_01(A)**	4 to 10	0.49	0.52	-0.06
	02:21_02(D)	3 to 10	0.27	0.24	0.11
	03:21_03(D)	3 to 10	0.51	0.65	-0.29
	04:21_04(D)	4 to 10	1.35	1.35	0.01
	05:21_05(D)	3 to 10	0.94	0.91	0.03
	06:18_06(A)	2 to 10	0.78	0.65	0.17
September	**16:21_17(A)**	4 to 10	1.91	1.56	0.18
	18:21_18(A)	4 to 10	3.39	3.09	0.09
	20:21_20(D)	3 to 10	1.77	1.54	0.13
	21:21_21(D)	3 to 10	2.64	2.76	-0.04
October	**22:27_23(A)**	4 to 10	7.24	6.60	0.09
	23:27_24(A)	4 to 10	1.40	1.42	-0.01
	28:27_29(D)	3 to 10	0.78	0.81	-0.04
	29:27_30(D)	4 to 10	2.21	2.12	0.04
December	**13:21_13(A)**	3 to 12	4.30	4.34	-0.01
	14:21_14(A)	3 to 10	2.70	2.53	0.06
	15:24_15(A)	3 to 14	0.52	0.45	0.14
	16:21_16(A)	3 to 12	1.09	1.19	-0.09
	17:21_18(A)	3 to 12	13.10	13.12	0.00
	19:21_19(A)	3 to 12	5.91	5.10	0.14

Table 6.4 Model performance measures in terms of MSE of 10 m wind magnitude (m s^{-1}) forecasts for both reference and experimental model outputs. The verification time format is: model DAY NUMBER : FORECASTED HOUR _ satellite DAY NUMBER (DESCENDING or ASCENDING orbital swath). REF: reference model wind magnitude forecast; EXP: experimental model wind magnitude forecast).

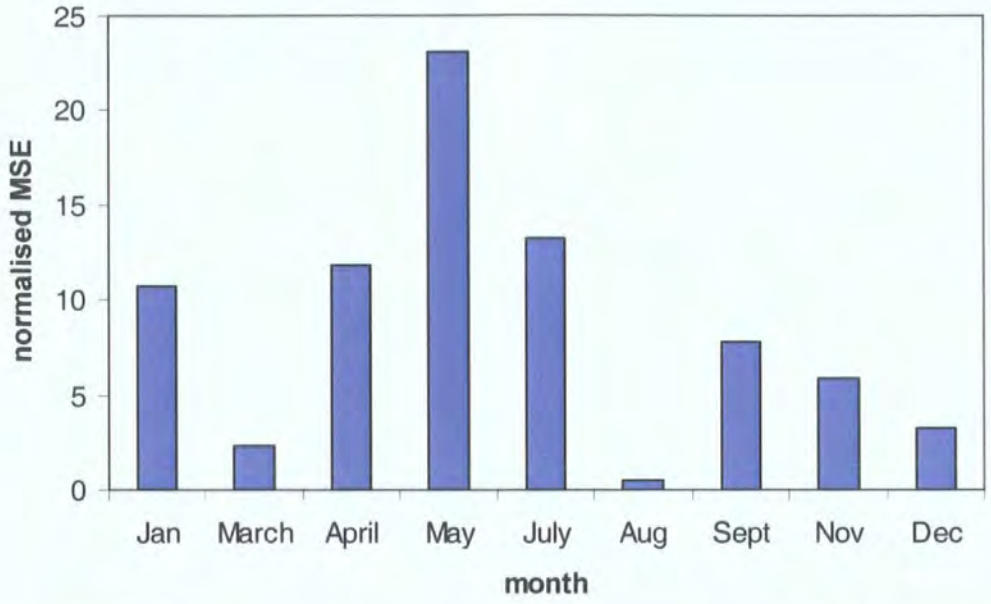

Figure 6.11. Percentage improvement of the experimental relative to the reference setup in terms of improved prediction for the entire annual analysis, based on the MSE.

The choice of single dates for verification throughout the entire analysis corresponded to the availability of observations to both initialise and validate the *experimental* model setup. Lack of matching observations to verify the forecasts during February and June led to the omission of these two months in the analysis. As for those months that were analysed, the single-date verification does not reflect the average behaviour of the model for the entire month and therefore the verification tends to become more sensitive to model errors with respect to the general monthly weather systems. Since the availability of appropriate observations was very much restricted in space and time, intensive model performance analysis such as model error drift with time, were impossible to study.

6.5.4. Exploratory spatial data analysis.

The GIS-based spatial analysis is used to assemble, process and display the spatial relationship between the forecasts produced by the two model setup and remotely-sensed fields. This whole analysis was possible using a range of software functionality ranging, amongst others, 2D and 3D geo-statistical mapping and image processing.

6.5.4.1. Match score analysis.

This spatial method is derived from a well-used scalar approach by meteorologists (Glahn *et al.,* 1991). Generally referred to as "Precipitation Scores", this method is used as a guide to assess the overall Eta performance and in deciding on model changes (Fritsch *et al.,* 1998).

The higher average match score given by the *experimental* setup (table 6.5) is indicative of a better spatial forecasting skill of the wind magnitude intervals selected for the analysis. The improved match score shown by the *experimental* setup provides evidence of the superiority of this modelling setup over the other.

In the present study, match score analysis measures the spatial model forecast accuracy (correct timing and placement) of predicted categories of the wind field against similar observed categories. The exact placement of individual categories belonging to a particular class of wind magnitude value is treated as a complete hit. Obviously, the grouping of pixels from the entire forecasted field is an approach that degrades the forecasted information into a set of wind fields isotherms. However, in the case of numerical model verification, the absolute verification of pixel-to-pixel placement between the forecasted and observed field is unrealistic due to inaccuracies of both the predictand and observation. Rather, the assessment of model performance is

always based on the improved forecasting of categorical classes that are spatio-temporally correct with independent observations.

Similar categorisation is followed by NWP modellers when assessing the scoring of their models against rainfall data, by classifying their predicted fields according to the precipitation intensity as: rain/no-rain, light rain, moderate rain and heavy rain. The resolution of such a categorization would of course depend on the type and spatial resolution of the predictand. For the present study, the generation of high resolution predicted wind magnitude fields made possible a highly sensitive analysis at 1 m s^{-1} resolution. This can be considered an achievement in the area of high-resolution model verification.

Categorising any predicted field into separate classes can offer advantages to the modeller by providing information on the weakness of the numerical model to predict the correct placement of such classes. A case in point is the prediction of weak, variable wind that is below 3 m s^{-1}, which is considered to be a characteristic value over the areas of interest during the summer months. Changing class categories will not affect the analysis as long as the observations are degraded into the same intervals.

Apart from hits, this approach can be further elaborated to generate contingency tables of misses and false 'alarms'. Hypothesis testing can also be included. For example, if attempting to test the hypothesis that the mean error of the two forecasting system for a particular single-forecast verification are identical, under the null hypothesis the samples from the two populations should be interchangeable. Random groupings may then be repeatedly selected with replacement from the pooled samples to build a distribution of error differences consistent with the null hypothesis. The observed difference is then compared to this.

Spatial overlay is also used to stack the selected geo-referenced layers, in the form of maps, so that questions concerning the degree of matching (figs. 6.12 a-b) of the two systems with the observations are asked. Here spatial overlays are used to model this arithmetic relationship. New map layers are built as a result of the operators used.

A limitation in the present study is the restricted availability of valid observations, which varied from one month to another. The sample statistic for the case of May, for example, shows an extremely efficient *Experimental* setup over the *Reference* one; however this is based on only one sample statistic because of the lack of suitable observation data. On the other hand, the match score statistic for the month of July is supported by a much larger number of case studies. Ideally, match score statistics are to be derived for each day of the month for a number of years in order to assess the intra- and inter-annual variability of providing remotely-sensed microwave lower surface boundary conditions as opposed to the initialisation data used for the *reference* setup. In this way, there would be no bias for particular months of the year that may show a higher degree of variability over other, much calmer periods. However, due to the extensive analysis required, the present analysis was restricted to a period of one year.

For the above reasons, formal hypothesis testing of the competing forecast models has been left out. However, from a semi-quantitative point of view, match score analysis does show that in spatial terms, the *Experimental* setup fares better than the r*eference* one.

Month	Verification time	Reference setup				Experimental setup			
		F	H	O	MS	F	H	O	MS
Jan	18:27_19(D)	4836	675	4081	0.082	4843	669	4081	0.081
	22:27_23(D)	4147	1266	4385	0.174	3987	1089	4385	0.150
	24:24_25(D)	4809	1059	4742	0.125	4825	1184	4742	0.141
Mar	07:24_08(A)	4713	628	4934	0.070	4697	698	4934	0.078
	08:27_09(D)	3911	0	1189	0.000	3971	0	1189	0.000
	10:24_11(D)	4300	0	1006	0.000	4300	0	1006	0.000
	11:24_12(D)	3539	1152	3385	0.200	3606	1231	3385	0.214
	14:21_14(A)	4080	1402	4356	0.199	4182	1189	4356	0.162
	17:21_17(D)	4004	498	3901	0.067	4168	493	3901	0.065
Apr	21:24_22(A)	4332	1514	4927	0.195	4352	1342	4927	0.169
	22:27_23(D)	2652	128	4587	0.018	2878	106	4587	0.014
	23:27_24(D)	4301	1019	4148	0.137	4286	1008	4148	0.136
	26:24_27(D)	3446	194	1441	0.041	3442	185	1441	0.039
	27:24_28(D)	4816	61	4613	0.007	4816	31	4613	0.003
	28:21_28(A)	4790	1914	4772	0.250	4800	1358	4772	0.165
May	03:21_03(D)	4218	0	325	0.000	4086	0	325	0.000
Jul	22:27_23(D)	4537	2680	3605	0.491	4254	2549	3605	0.480
	23:27_24(D)	4587	146	1780	0.023	3354	444	1780	0.095
	24:27_25(D)	4780	1048	4299	0.130	4335	2112	4299	0.324
	25:24_26(A)	4677	1391	4863	0.171	4486	1238	4863	0.153
	26:27_27(D)	4386	45	4589	0.005	4112	44	4589	0.005
	27:27_28(D)	2963	1005	2362	0.233	2981	728	2362	0.158
	28:27_29(D)	105	92	330	0.268	123	104	330	0.298
	29:24_30(D)	4961	924	4834	0.104	4974	1935	4834	0.246
	30:24_31(D)	4785	462	4972	0.050	4942	516	4972	0.055
	31:21_31(A)	1306	890	3376	0.235	1507	1119	3376	0.297
Aug	01:21_01(A)	2245	1115	2562	0.302	2254	1127	2562	0.306
	02:21_02(D)	2614	1811	3201	0.452	2776	1822	3201	0.439
	03:21_03(D)	3502	1469	3326	0.274	3863	1411	3326	0.244
	04:21_04(D)	1621	251	1305	0.094	1718	324	1305	0.120
	05:21_05(D)	2951	749	2125	0.173	3063	752	2125	0.170
	06:18_06(A)	3644	711	2438	0.132	3812	848	2438	0.157
Sept	16:21_17(A)	4542	1373	4974	0.169	4564	1387	4974	0.170
	18:21_18(A)	3556	1079	4683	0.151	3902	844	4683	0.109
	20:21_20(D)	2539	248	4184	0.038	2049	530	4184	0.093
	21:21_21(D)	4192	725	3487	0.104	4160	664	3487	0.095
Oct	22:27_23(A)	1117	240	3276	0.058	1981	288	3276	0.058
	23:27_24(A)	4559	823	2962	0.123	4582	768	2962	0.113
	28:27_29(D)	4523	1975	4922	0.264	4531	1996	4922	0.268
	29:27_30(D)	3980	529	1778	0.101	4070	459	1778	0.085
Dec	13:21_13(A)	3606	37	311	0.010	3813	38	311	0.009
	14:21_14(A)	4803	294	4428	0.033	4814	310	4428	0.035
	15:24_15(A)	1581	775	1156	0.395	1544	825	1156	0.440
	16:21_16(A)	4468	1018	3104	0.155	4352	876	3104	0.133
	17:21_18(A)	4427	751	3891	0.099	4371	764	3891	0.102
	19:21_19(A)	4815	0	3158	0.000	4807	32	3158	0.004
				Mean	0.139			Mean	0.145
				Min	0.000			Min	0.000
				Max	0.491			Max	0.480
				Skew	1.095			Skew	1.063

Table 6.5. Raster-based, arithmetic matching between the forecasted and observed wind magnitude maps. F: forecast; H: Hit; O: Observation; MS: Match Score. The verification time format is: model DAY NUMBER : FORECASTED HOUR _ satellite DAY NUMBER (DESCENDING or ASCENDING orbital swath).

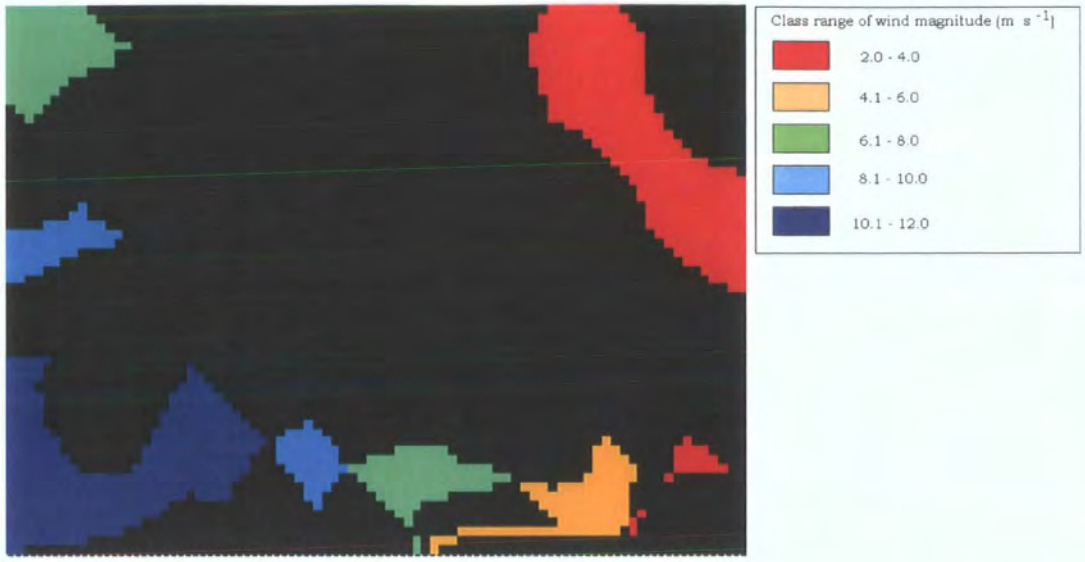

(a)

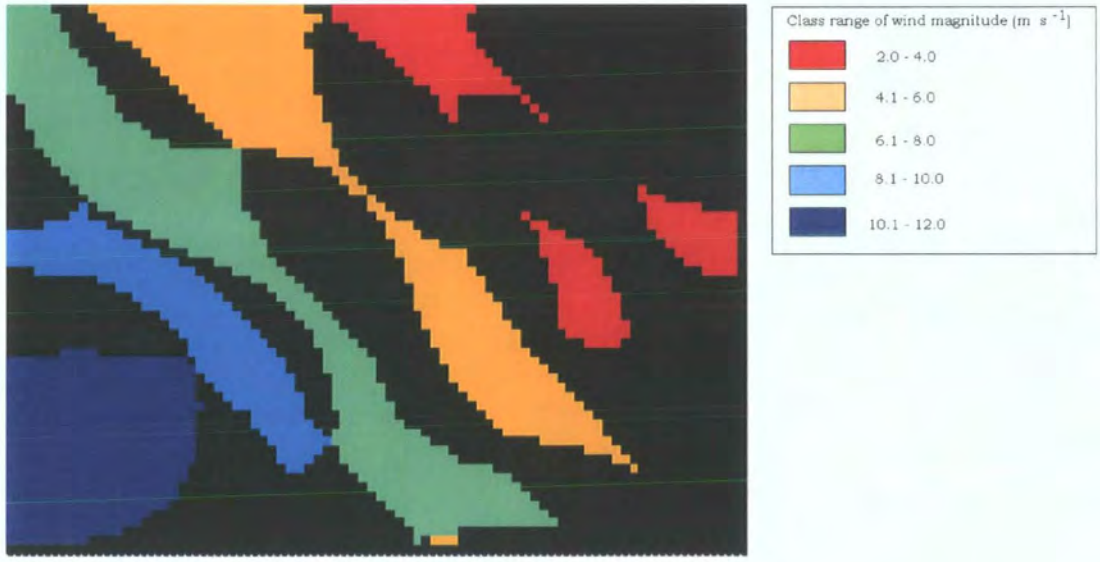

(b)

Figures 6.12 a - b. Overlapping pixels between (a) reference (MS=0.130) and (b) experimental (MS=0.324) model output of 10 m wind magnitude field against observations respectively for July 25th at 3 hrs (see table 5.4.). Nulled, black pixels indicate no overlap. The different colours are classed values (in m s-1) wind fields.

6.5.4.2. Spatial similarity.

As in section 5.5.5., the Spatial Similarity index is used to assess the degree of shared attributes between the two model systems and the remotely-sensed observations. In order to best illustrate the spatial analysis, four case studies are presented that best describe the results covering a representative range of wind regimes over the area of interest.

6.5.4.2.1. Case study 1: 22nd January 1999.

The first case study analyses a wind speed regime that is typical for January. Figure 6.13e shows relatively moderate winds reaching a maximum of 6.5 m s^{-1} within the area of interest. A more or less constant gradient is observed starting with moderate wind gradients of about 7 m s^{-1} to very light wind conditions towards the East, reaching a minimum of 2 m s^{-1}. Black areas represent nulled pixels that are below 2.0 m s^{-1}. Small circular contours with central black pixels coincide with precipitation and are therefore nulled.

A close inspection of the similarity maps) shows that the *experimental* (fig. 6.13b) setup gives an overall higher similarity index than the reference setup (fig. 6.13a).

The individual forecasted wind fields show that the wind gradients generated by the *experimental* setup (fig. 6.13d) are closer in pattern to the observed wind fields than the *reference* ones. This is especially true for the wind magnitude range of 4.5 to 5.0 m s^{-1}, which bulges out towards the north in the *reference* forecast as opposed to a calmer condition given by both the *experimental* forecast and observation.

Minor dissimilarity between the *reference* setup and observations is also shown by the low intensity wind fields of around 2.4 m s^{-1}. The patterns

of such fields produced by the *reference* setup do not agree with those observed, unlike the fields produced by the *experimental* one.

The contoured predicted fields show an overall higher wind magnitude than the observed field, which is in line with the slight over-forecasting skill of the nested Eta model as seen in section 5.5.3.4.

6.5.4.2.2. Case study 2: 24th January 1999.

The closer similarity obtained by the *experimental* setup in figure 6.15b is again demonstrated. Dissimilarity of the *reference* forecast (fig. 6.15a) is mainly concentrated in the lower middle part of the map which is caused by the higher wind magnitude located in this area as observed in the wind magnitude field area of figure 6.14c. Its value of 5.5 m s^{-1} is higher than the wind intensity over the same area in figure 6.14d. However, one should note a similar wind magnitude pattern produced by both the *reference* and *experimental* setup.

The relatively higher wind magnitude field situated at the lower, right portion of figure 6.14c, showing a northward protrusion, also causes dissimilarity. The same pattern is observed in figure 6.14d but in this case the pattern of the *experimental* forecast is closer to the collocated observed field.

6.5.4.2.3. Case study 3: 22nd April 1999.

In this case study, similarity mapping indicates that the *experimental* setup can also provide a better representation of the lower magnitude fields in the region of 3.0 to 3.5 m s^{-1} (fig. 6.15b). This is represented by the larger area of the *island* in the middle left portion of the map. The rest of the map shows a more or less similar degree of predictability (in terms of both field pattern and values) when compared to the observed field.

6.5.4.2.4. Case study 4: 15th December 1999.

The similarity maps obtained for this forecast date again provide important information that is otherwise difficult to detect in the individual (predicted and observed) wind field maps.

A close inspection of the similarity maps (figs. 6.16a) suggests that the *experimental* setup (fig. 6.16b) is able to better predict wind fields patterns in the region of 10.0 to 11.0 m s^{-1}. This is shown by the areas of higher similarity in the lower central and upper right portions of similarity map 6.16b. These predicted high intensity wind magnitude field shown in figure 6.16d is being restricted to the right portion of the area, giving a pattern that is closer to the observation. On the other hand, the high intensity wind field produced by the *reference* setup is more shifted towards the centre. This again shows that the *experimental* setup shows a better performance even with high intensity winds. It also shows that the use of the TMI-derived SST to initialise the Eta surface boundary condition also leads to an overall improvement in the spatial forecast of the 10 m wind fields.

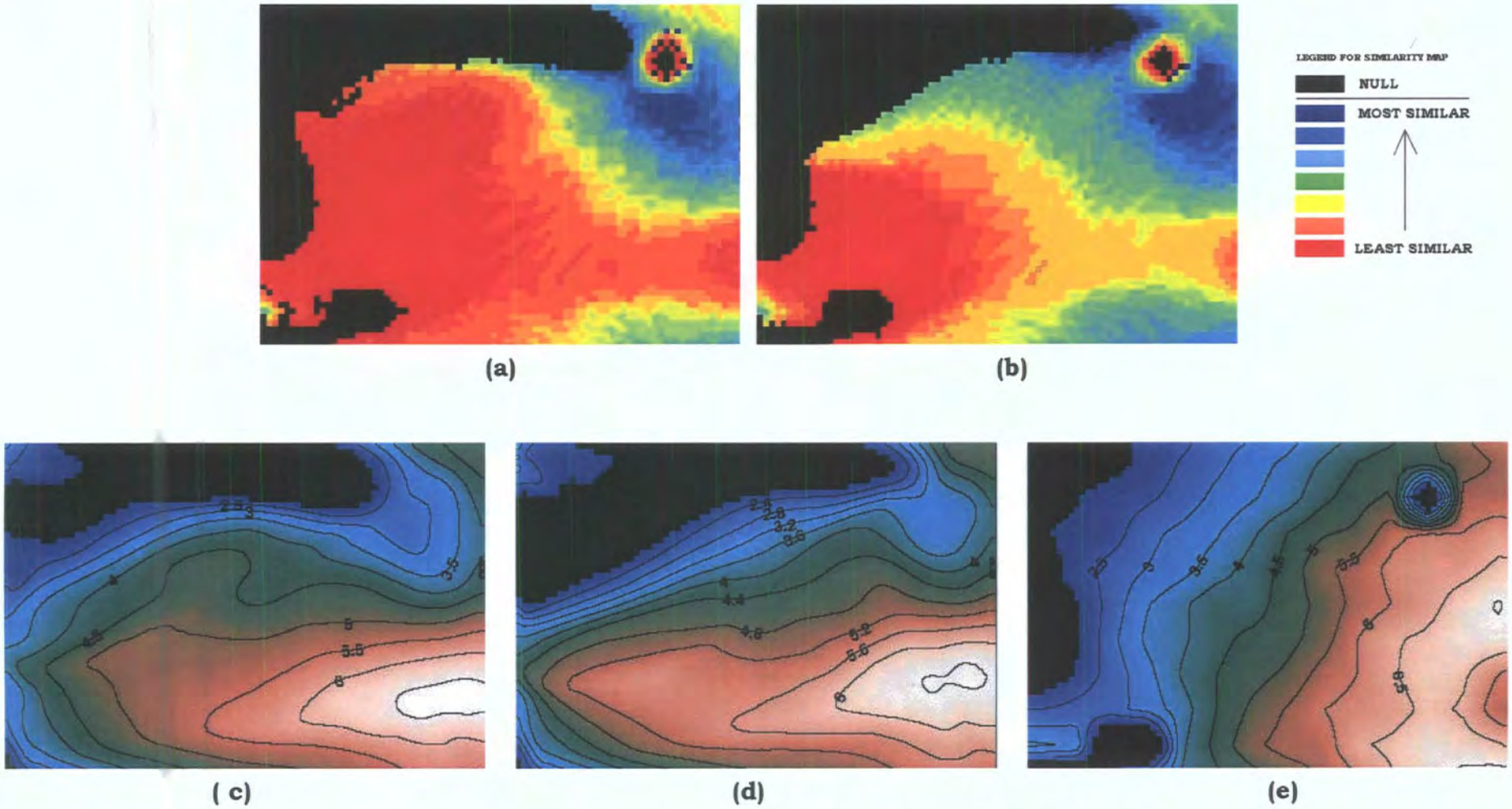

Figures 6.13 a-e. Case study 1: January 22nd 1999: (a) similarity map between predicted surface wind speed by the reference system and observations; (b) similarity map between predicted surface wind speed by the experimental system and observations; (c) predicted wind speed (in m s^{-1}) by the reference system; (d) predicted wind speed (in m s^{-1}) by the experimental system; (e) observed wind speed (in m s^{-1}) by the tropical microwave imager on 23rd January at.02:08 UT. Black pixels represent nulled pixels that are below 2.0 m s^{-1}. Small circular contours with central black pixels coincide with precipitation and are nulled.

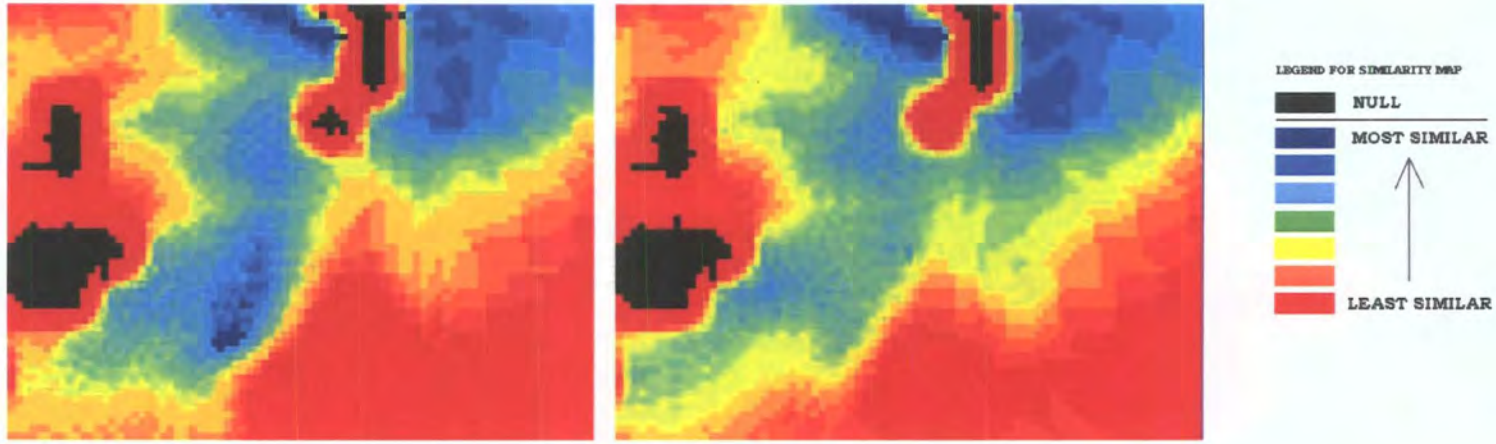

(a) (b)

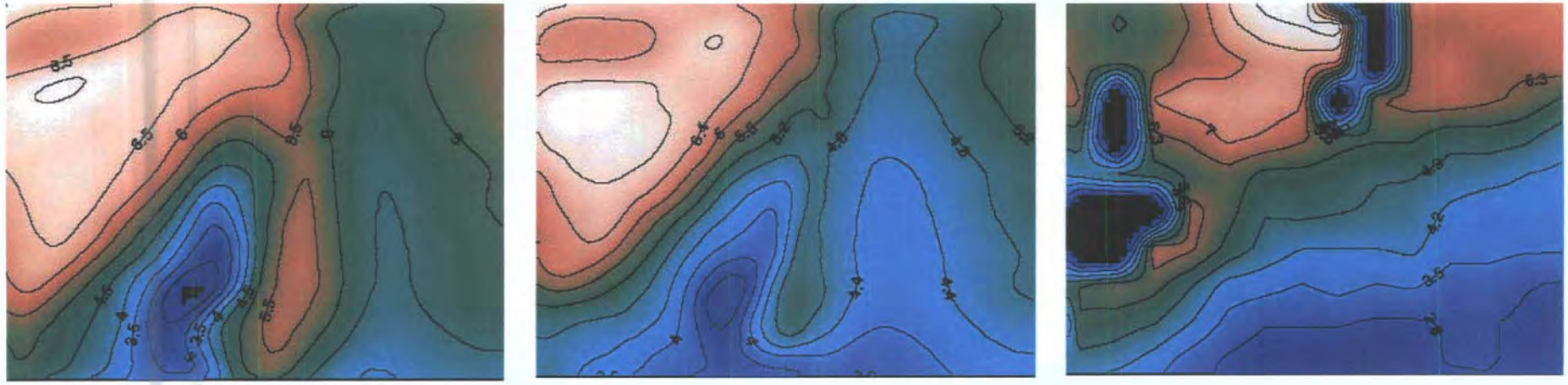

(c) (d) (e)

Figures 6.14 a-e. Case study 2: January 24th1999: (a) similarity map between predicted surface wind speed by the reference system and observations; (b) similarity map between predicted surface wind speed by the experimental system and observations; (c) predicted wind speed (in m s^{-1}) by the reference system; (d) predicted wind speed (in m s^{-1}) by the experimental system; (e) observed wind speed (in m s^{-1}) by the tropical microwave imager on 25th January at.01:12 UT. Black pixels represent nulled pixels that are below 2.0 m s^{-1}. Small circular contours with central black pixels coincide with precipitation and are nulled.

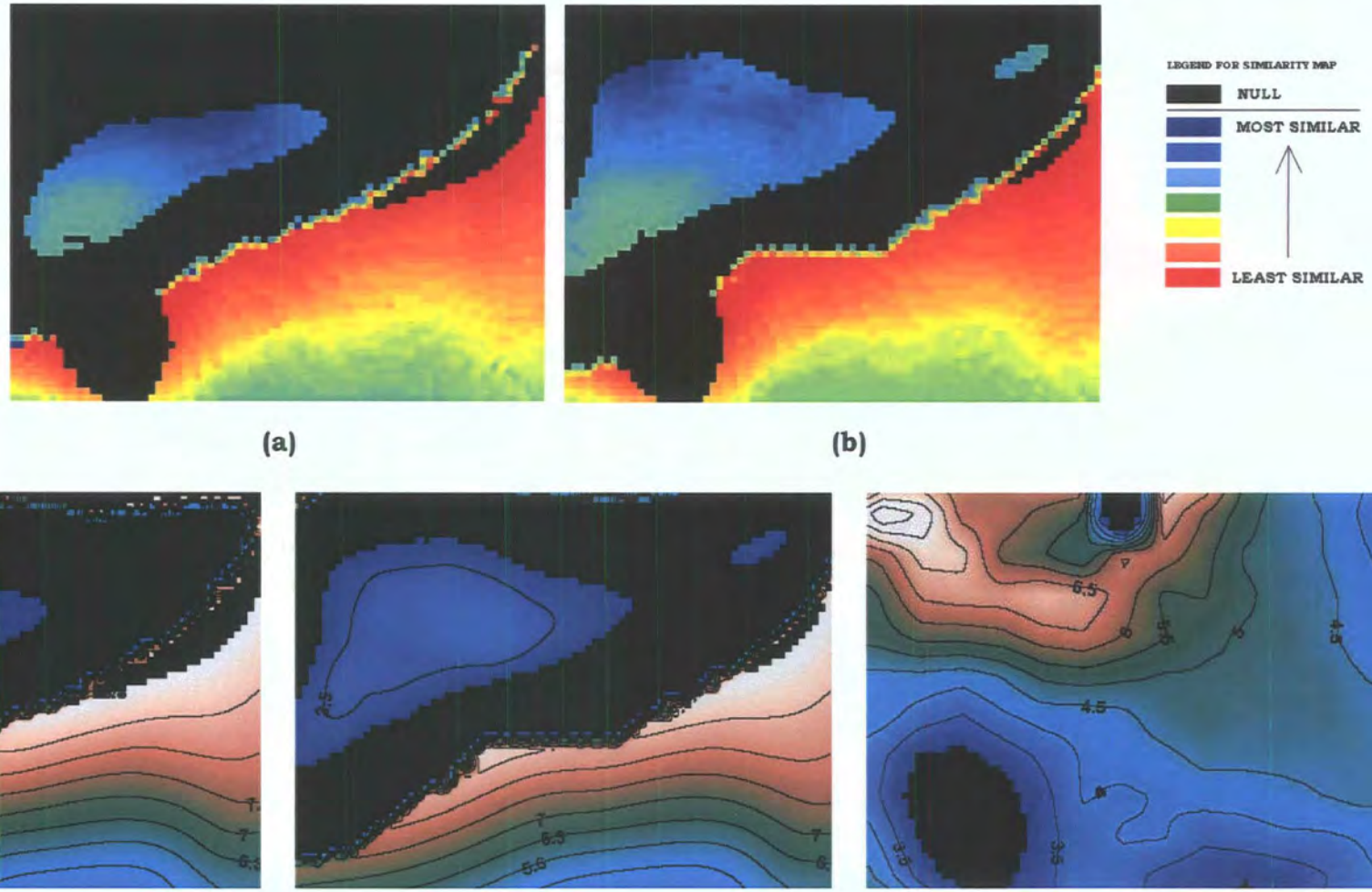

Figures 6.15 a-e. Case study 3: April 22nd 1999: (a) similarity map between predicted surface wind speed by the reference system and observations; (b) similarity map between predicted surface wind speed by the experimental system and observations; (c) predicted wind speed (in m s^{-1}) by the reference system; (d) predicted wind speed (in m s^{-1}) by the experimental system; (e) observed wind speed (in m s^{-1}) by the tropical microwave imager on 23rd April at 03:25 UT. Black pixels represent nulled pixels that are below 2.0 m s^{-1}. Small circular contours with central black pixels coincide with precipitation and are nulled.

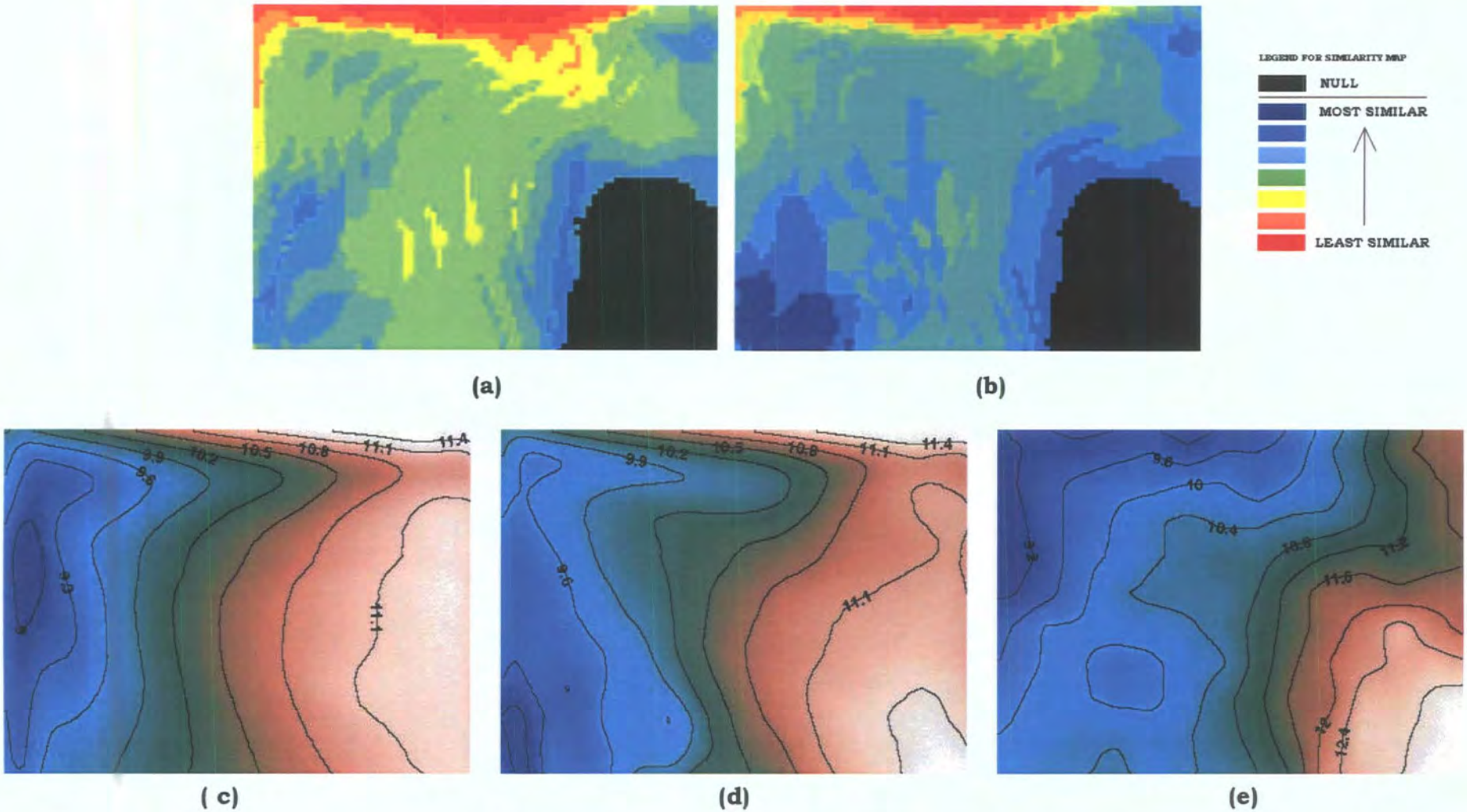

Figures 6.16 a-e. Case study 4: December 15th 1999: (a) similarity map between predicted surface wind speed by the reference system and observations; (b) similarity map between predicted surface wind speed by the experimental system and observations; (c) predicted wind speed (in m s^{-1}) by the reference system; (d) predicted wind speed (in m s^{-1}) by the experimental system; (e) observed wind speed (in m s^{-1}) by the tropical microwave imager on 15th December at 22:50 UT. Black pixels represent nulled pixels that are below 2.0 m s^{-1}. Small circular contours with central black pixels coincide with precipitation and are nulled.

Spatial similarity of individual classes of wind magnitude, rather than the individual pixel values, proved to be a more convenient and realistic way of assessing the tendency of the spatio-temporal attributes of the predicted fields. These results bring out the usefulness of relational spatial similarity rather than the total scalar comparison between the two datasets for ocean forecasting systems.

A big benefit of using the spatial similarity technique is the ease with which the user can define particular adjustments. The system allows results to be displayed that indicate the degree of similarity through a matching and ranking measure. This facility allows the user to search for a set of textural and spatial parameters to derive the similarity between the background information and the new parameters entered into the analysis. This study shows how similarity assessment can be a useful concept for retrieving and analysing spatial information as it may help numerical modelers describe and explore their forecasts, their immediate environment and relationships to observations.

6.5.4.3. Geostatistical analysis.

In this study, geostatistics complemented the application of the other statistical measures so far discussed. The motive behind using geostatistical analysis is to model the spatial structure of the residual fields of the predictions and observations and translate the degree of spatial correlation between these two datasets in numerical and graphical terms. In doing so, residual variography provides an analysis of the spatial variation on the differences between the model output and collocated observations. The sensitivity of this tool focuses on the variation between the competing models with collocated observations.

Figures 6.17 and 6.18 provide an example of residual maps consisting of the differences between the forecasted 10 m wind magnitude (m s^{-1}) generated by the *reference* and *experimental* models, and collocated observations derived from the Tropical Microwave Imager on July 25

and September 20 1999. Only those residual pixel groups ranging from –0.5 to 0.5 are shown in colour; the remaining gradients are shown by means of contours. A greater range of pixels showing minimal difference occurs in figures (b). Areas shown in white correspond to nulled filtered pixels due to either low variable, or high wind speeds.

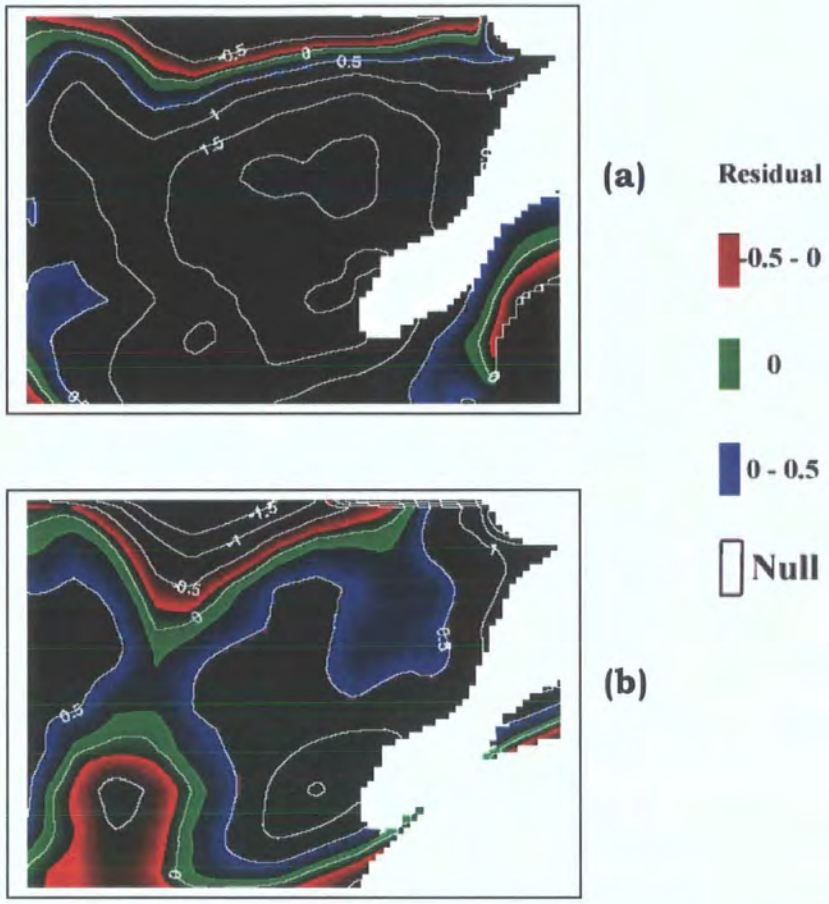

Figures 6.17 a – b. The residual map of the differences between the 10 m wind magnitude (m s^{-1}) forecasted by the (a) reference setup and (b) experimental setup, and collocated observations derived from the Tropical Microwave Imager on July 25 at 2400 UT (or July 26th at 00 UT).

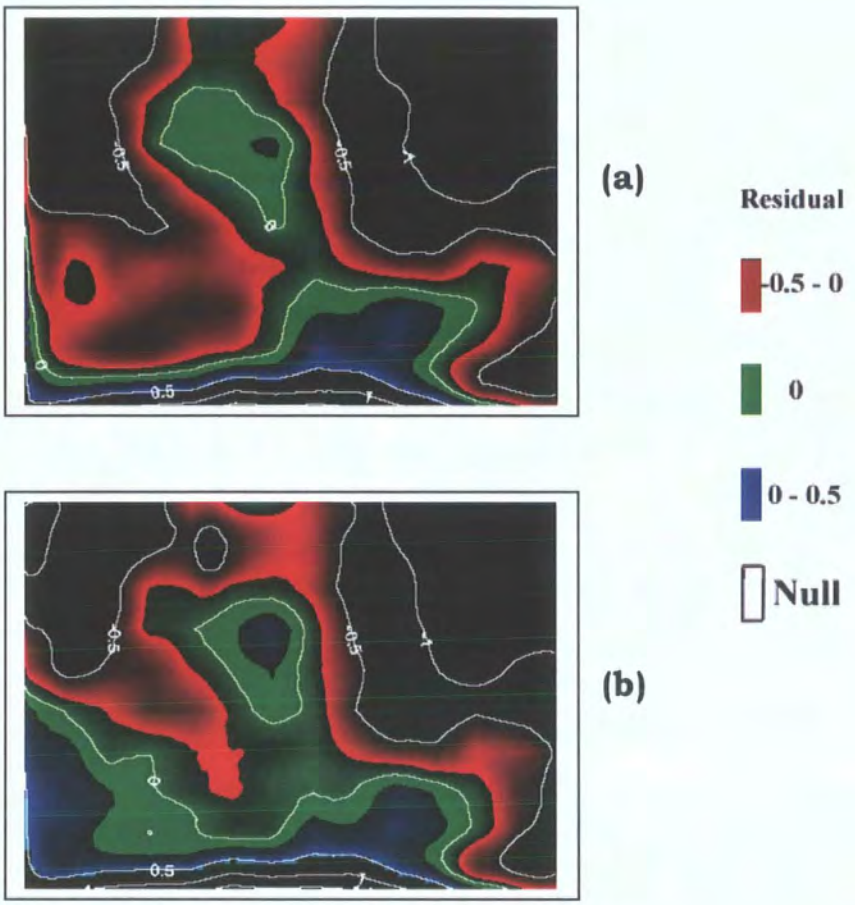

Figures 6.18 a – b showing the residual map of the differences between the 10 m wind magnitude (m s^{-1}) forecasted by the (a) reference setup and (b) experimental setup, and collocated observations derived from the Tropical Microwave Imager on December 15 at 2400 UT.

For comparative purposes, only those residual pixels having a value ranging from –0.5 to 0.5 are shown in colour. The remaining pixels are shown in black with contoured gradients. Areas shown in white correspond to nulled filtered pixels due to either low variable, or high wind speeds[122].

The residual spatial structure between the two sets of data (i.e. forecast and observation) were modelled on the basis of autocorrelation. Pixel values corresponding to the matrix of the geophysical field (in this case the 10 m wind magnitude) that have similar spatial attributes are considered more similar than pixel values further apart. This was used to model the structure of the residual data, i.e. its variability as a function of space by means of variography. The semi-variograms displayed the relation between the semi-variance and the spatial separation (lag distances), and is a quantitative descriptive statistic that can be graphically represented in a manner which characterises the spatial continuity (i.e. roughness) of the residual data sets.

Figure 6.19a – b is an example of the semi-variograms of the residuals obtained between (a) the *reference* prediction and observation, and (b) the *experimental* prediction and observation for April 28th 1999 at 2100 UT. What is easily noticeable is a classic gaussian model fit for both isotropic semi-variograms as well as a lower semi-variance for case (b).

[122] *See section 6.4.2.*

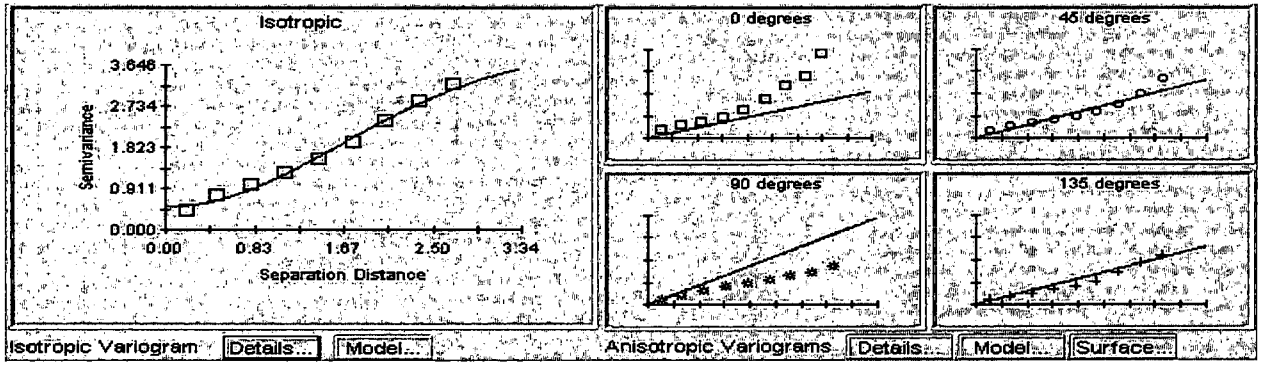

(a)

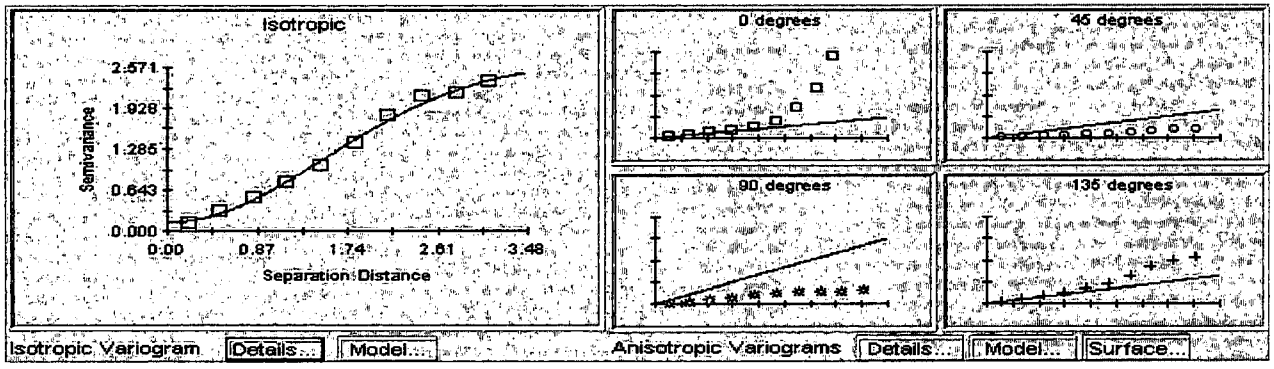

(b)

Figure 6.20 a - b. Semi-variograms of the residuals obtained between (a) the reference prediction and (b) experimental prediction, with observations retrieved on April 28th 1999 at 2100 UT. The best value for the reduced sums of squares defined the gaussian model as the best fit for the isotropic semi-variograms. Note the different slope, accompanied by lower values for the nugget and sill for the residual semi-variogram shown in (b). Variograms indicate the presence of anisotropy in both residuals.

Table 6.5 shows the results of the semi-variograms for all the residuals studied. In almost all cases, results show that the gaussian model exhibited the best overall fit for the isotropic semi-variogram plots derived for the entire residual dataset. The gaussian model is formulated as:

$$\gamma(h) = N + C[1-\exp(-3(h/R)^2)]$$

where N is the nugget, C is the sill minus the nugget, R is related to the range, and h the distance. The use of this linear model through the entire analysis ensured a common qualitative and quantitative analysis for the datasets. The following general observations can be made:

1. The gaussian mode has behaviour similar to a parabola near the origin and is indicative of an extremely continuous process.

2. The linear behaviour at small lag distances suggests that as the lag and semi-variance values increase, the variogram of the *experimental* forecasts approaches the sill asymptotically, suggesting the incorporation of the gaussian model into the theoretical variogram model.

3. These gaussian variograms suggest that in the most significant portion of the semi-variogram model, a single, long-range process dominates. This preference towards the gaussian behaviour was probably due to the way the particular geophysical field behaves, giving a general smooth description of wind field gradients.

4. The semi-variogram models exhibit a strong spatial dependence with very limited random variation. In most cases, the value for the nugget is always low except on few occasions when 'extreme events' occurred, such as extensive precipitation or during strong wind events (e.g. January 24th, March 17th, and December 13th). The presence of random variability included in the numerical forecasts is

therefore extremely low and that most of the variation observed can be attributed to the nature of the geophysical data.

5. The tabulated results (table 6.6) show that out of a total of 46 residual analysis, there were 26 occurrences where the *experimental* model achieves a lower sill than the other competing residuals. The differences in the range also provides an indication of the degree of correlation between the data points, which is positively shifted towards the *experimental* model. Results also show a close relationship between the semi-variogram analysis and the standard verification procedure using skill score. This tests both the sensitivity and complimentarity of geostatistics to assess the spatial relationship of model predictions.

Geostatistical analysis provided this study with additional structural information on the behaviour of the two competing models. The results for the anisotropic semi-variogram analysis, for example, very often indicated the existence of directional trends. The cause of anisotropy may be due to the prevailing variability in the 10 m wind direction over the area of interest, and if so, this could mean that the residuals show a certain degree of dependence on the climatology of the area.

6.5.4.3.1. Spatial variography.

A representation in 2D and 3D space of the behaviour of the variogram was made by drawing a map of the iso-variogram lines as a function of the vector *h*. This was also an excellent way to check for anisotropy by means of a contour plot of semi-variogram values by direction.

The majority of the case studies showed that the iso-variogram lines were approximated by minor ellipses defined along a set of perpendicular main axes of anisotropy. This indicates a small degree of directional drift in the residual wind magnitude, possibly brought about by systematic weaknesses of both forecasting systems to predict the 10

m wind magnitude over the ocean. The cause of this may be due to the model's predictive skill to forecast better categories of wind scales as was highlighted by the spatial similarity analysis when the viscous sublayer model scheme was fine-tuned for events when strong surface winds are prevalent. Similar characterisation is required. The spatial similarity analysis for January 22nd (section 6.5.4.2.1.) and December 15th (section 6.5.4.2.4.) for example, revealed a better prediction of stronger wind field gradients by the experimental model. On the other hand, dissimilarity is observed when wind fields tend to get weaker as supported by the collocated surface wind field maps.

Month	Verification time	Reference				Experimental				Skill
		Model	Sill	Range	Nugget	Model	Sill	Range	Nugget	score
Jan	18:27_19(D)	gau	1.36	2.99	0.19	gau	1.25	2.67	0.16	0.04
	22:27_23(D)	gau	5.23	4.34	0.11	gau	5.23	4.34	0.11	0.06
	24:24_25(D)	gau	2.12	1.09	0.31	gau	1.90	1.47	0.35	0.18
Mar	07:24_08(A)	gau	1.90	1.47	0.35	gau	6.51	2.90	0.01	-0.03
	08:27_09(D)	gau	0.06	1.16	0.004	gau	0.06	1.15	0.006	0.01
	10:24_11(D)	gau	0.13	0.93	0.0001	gau	0.13	0.94	0.0001	0.00
	11:24_12(D)	gau	2	3.8	0.03	gau	2.13	4.25	0.011	0.13
	14:21_14(A)	gau	0.55	1.52	0.001	gau	0.59	1.61	0.001	-0.23
	17:21_17(D)	gau	6.19	3.96	1.38	gau	4.13	2.31	1.05	0.14
Apr	21:24_22(A)	gau	2.34	3.51	0.19	gau	2.35	3.38	0.17	0.02
	22:27_23(D)	gau	8.62	1.61	0.01	gau	12.4	2.20	0.01	0.22
	23:27_24(D)	gau	3.02	1.88	0.13	gau	3.36	1.71	0.48	-0.08
	26:24_27(D)	gau	0.42	1.50	0.001	gau	0.38	1.50	0.001	0.02
	27:24_28(D)	gau	0.35	4.42	0.07	gau	0.20	2.18	0.04	-0.03
	28:21_28(A)	gau	4.00	3.99	0.49	gau	2.68	3.71	0.14	0.33
May	03:21_03(D)	gau	1.60	2.0	0.09	gau	0.23	0.24	0.02	0.24
Jul	22:27_23(D)	gau	0.27	1.35	0.03	gau	0.26	1.26	0.02	-0.10
	23:27_24(D)	gau	0.99	5.53	0.06	gau	0.17	0.61	0.0001	0.50
	24:27_25(D)	gau	0.66	1.10	0.02	gau	0.45	1.21	0.03	0.64
	25:24_26(A)	gau	3.33	3.58	0.16	gau	5.13	4.28	0.06	-0.09
	26:27_27(D)	gau	0.82	1.16	0.14	gau	0.64	1.05	0.15	-0.01
	27:27_28(D)	gau	0.56	1.04	0.16	gau	1.33	1.21	0.001	-0.34
	28:27_29(D)	gau	0.06	0.20	0.00	gau	0.06	0.17	0.00	0.40
	29:24_30(D)	gau	2.13	6.7	0.06	gau	1.39	7.00	0.13	0.38
	30:24_31(D)	gau	1.81	2.58	0.05	gau	1.67	2.66	0.05	0.13
	31:21_31(A)	gau	2.03	4.57	0.001	gau	1.49	5.11	0.08	0.08
Aug	01:21_01(A)	gau	0.47	1.35	0.001	gau	0.51	1.42	0.001	-0.06
	02:21_02(D)	gau	0.32	4.26	0.05	gau	0.25	1.64	0.01	0.11
	03:21_03(D)	gau	0.77	1.95	0.001	gau	1.13	2.44	0.005	-0.29
	04:21_04(D)	gau	0.59	2.97	0.02	gau	1.08	3.12	0.001	0.01
	05:21_05(D)	gau	0.83	2.36	0.03	gau	0.65	2.08	0.02	0.03
	06:18_06(A)	gau	0.64	3.30	0.05	gau	0.34	1.91	0.04	0.17
Sept	16:21_17(A)	gau	1.73	2.17	0.07	gau	1.53	2.27	0.06	0.18
	18:21_18(A)	gau	1.78	2.17	0.13	gau	1.53	1.71	0.04	0.09
	20:21_20(D)	gau	2.01	7.01	0.06	gau	0.47	1.17	0.001	0.13
	21:21_21(D)	gau	3.56	3.6	0.07	gau	4.07	3.85	0.03	-0.04
Oct	22:27_23(A)	gau	0.88	1.4	0.008	gau	4.03	3.03	0.01	0.09
	23:27_24(A)	gau	1.03	1.76	0.001	gau	0.91	1.68	0.008	-0.01
	28:27_29(D)	gau	0.60	1.73	0.005	gau	0.54	1.64	0.011	-0.04
	29:27_30(D)	gau	1.87	1.67	0.001	gau	1.44	1.61	0.001	0.04
Dec	13:21_13(A)	gau	2.59	0.62	0.34	gau	2.56	0.61	0.28	-0.01
	14:21_14(A)	gau	0.75	2.33	0.03	gau	0.66	2.35	0.03	0.06
	15:24_15(A)	gau	0.83	3.95	0.06	gau	0.63	2.80	0.05	0.14
	16:21_16(A)	gau	0.35	0.03	1.57	gau	0.46	1.86	0.04	-0.09
	17:21_18(A)	gau	21.0	4.75	0.01	gau	32.0	4.68	0.01	0.00
	19:21_19(A)	gau	0.67	4.02	0.07	gau	0.54	3.43	0.05	0.14

Table 6.6. Model fit for isotropic semi-variograms of the residuals from January through December. These were best described by the Gaussian (gau) model. An additional column shows the skill score derived following the verification of each single forecast as described in section 6.5.3.

Residual analysis however, proved to be quite insensitive to catch the above-mentioned subtleties, which were easy to capture using spatial match scoring and similarity. A case in point is the single forecast analysis for December 15th. Figures 6.20a – b are 2-D representations of the semi-variograms obtained from the residuals of December 15th. Visual inspection of the two spatial variograms indicate no significant differences and both reveal least semi-variance in the 45° direction. A similar relationship was observed for January 22nd, January 24th, and April 22nd.

No quantitative analysis of the degree of geometric anisotropy was performed since this was beyond the scope of this study. The same holds for the characterisation of the anisotropy in terms of its dependence on lag distances.

This approach has never been applied to verify improvements made on numerical atmosphere models. On the other hand, geostatistics is a fairly common approach to study and derive the distribution, spatial patterns and texture analysis of natural phenomena ranging form insect population (Liebhold *et al.,* 1996), ozone (Liu and Rossini, 1997), forests (Treitz, 2001), mineral resources (e.g. Reis *et al.,* 2003), remotely sensed images (Atkinson and Lewis, 2000; Curran, 1988), down to microbial patterns (Franklin and Mills, 2003). S. Amaral[123] applied variogram analyses to identify best filtering methods to filter RADARSAT images to evaluate resulting spatial variability which was otherwise not visually distinguishable. It is interesting to note that analysis of residual variograms has been done by Holdaway (1996) for the modelling and interpolation of monthly temperature and Aranuvachapun and Maskell (1997) to study temperature frontal fields.

[123] *http://www.dpi.inpe.br/~silvana/PAPER/amaral-ger97.pdf (accessed on 01.11.04).*

(a)

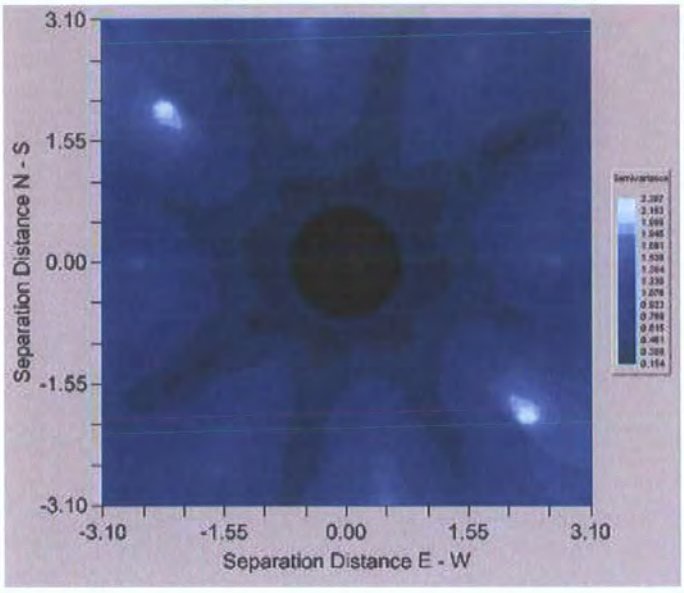

Figure 6.20a. 2-D representation of the semi-variogram obtained from the residual of reference forecast and observed wind fields on December 15th at 00 UT, revealing least semi-variance in the 45° direction.

(b)

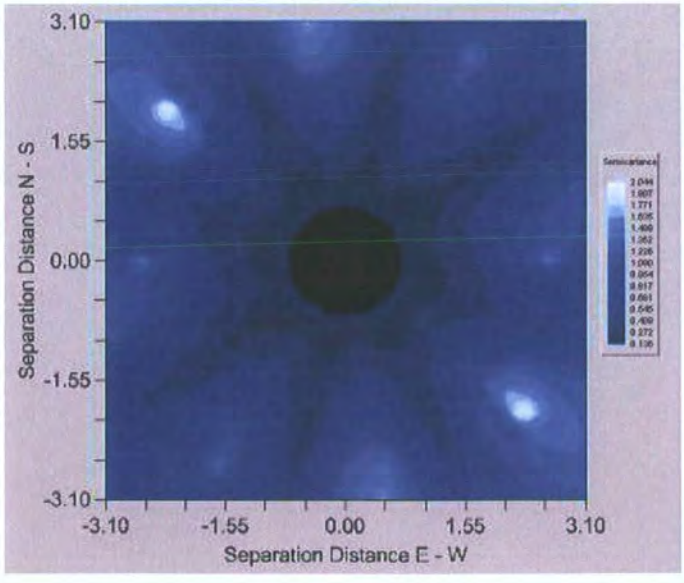

Figure 6.20b. 2-D representation of the semi-variogram obtained from the residual of experimental forecast and observed wind fields on December 15th at 00 UT, revealing least semi-variance in the 45° direction.

6.5.5. Limitations of the verification analysis.

The objective assessment of model accuracy is constrained by the limitations of the model forecasts and by the limited representation of the true atmospheric state. Specifically, model forecasts represent the atmosphere as a discrete array of area-averaged values as opposed to the continuous fields found in real situations. On the other hand, the true atmospheric state against which forecasts are being compared is represented by empirical observations of the atmosphere. Similarly, no matter how sophisticated these observations are, they too will never describe the three dimensional complexity of the atmosphere perfectly.

Since the model output is depicted by values at discrete grid points that represent a gridded average rather than a value at a specific forecast point, care was taken when comparing forecasts against observations that originally had dissimilar area-averaged data (i.e. different grids). Care was taken to carefully interpolate the observations onto an 0.042^{o} by 0.042^{o} grid that exactly matched the model output fields. The post-processing grid was the same as the domain grid of the numerical model and so there was no degradation in the model's computation resolution. If this was not the case, then this would have led to incorrect interpretation of the total forecast performance, especially for low-level parameters, such as the 10 m wind magnitude above sea level.

Observation grid points that potentially contain inaccurate data due to the presence of precipitation or characterised by extreme wind conditions were flagged as null. However, calibration of neighbouring valid, rain-free pixels was still affected by rainy pixels and so a certain degree of error is introduced in rain-contaminated scenes. This inaccuracy may have impacted on the final accuracy of the verification analysis, resulting in localised inconsistencies.

Overall, this study has successfully demonstrated the application of spatial statistical methods to verify the output of weather forecasting

models. The geostatistical analysis of residuals was used as a convenient tool to assess the improved skill of the atmosphere model that was initialised using realistic surface boundary conditions (i.e. remotely-sensed SST). This method complemented the results obtained by both standard statistical routines (average, standard deviation, bias, means square error and skill score) and the exploratory spatial data analysis (Match score analysis and spatial similarity), in that the use of microwave-derived SST as the initial surface boundary condition for the Eta model leads to an overall improved skill.

6.6. Summary.

The work described in this chapter addressed the two main research questions as defined in section 2.1.3. It showed how SST derived from the tropical microwave imager (TMI) using passive microwave technology can be used to define the surface boundary condition for a high-resolution model.

Section 6.5.3. described the analysis of the impact of introducing high-resolution SST conditions into the model as compared to a reference, method. The impact on the predicted surface wind magnitude at 10 m above sea level was used as the key index to evaluate model performance. The range of statistical measures described show an overall improvement of 10% when TMI-derived SST was used to initialise the lower boundary conditions at the start of the model run. Section 6.5.4. described the use of spatial exploratory analysis and geo-statistical methods to identify and study the model's spatial performance. The use of spatial data analysis with image processing and GIS analysis showed an enhanced spatial similarity between the experimental forecasts and collocated observations, especially for specific magnitudes of the surface winds. This was demonstrated in sections 6.5.4.1. and 6.5.4.2. by means of the spatial match score and spatial similarity indices developed by this study. The advantage of using this new remotely-sensed product was presented and discussed.

The use of geo-statistical methods to quantify the spatial variation of the residual component between the forecasts and observations was described in section 6.5.4.3. Semi-variogram analysis identified closer spatial correspondence between the experimental forecasts and observations, characterised by a gaussian relationship and low nugget variance. Variography proved inadequate to catch spatial subtleties which were otherwise easily captured using spatial match scoring and similarity.

From a semi-quantitative point of view, exploratory spatial data analysis showed that the *experimental* model fares better than the *reference* one. It can therefore be concluded that the use of remotely-sensed SST to initialise the lower boundary conditions of a high-resolution Eta model can favourably improve the accuracy of short-range, 10 m wind magnitude forecasts. Clearly, more developmental work is needed if hypothesis testing and more complex or computationally expensive tests are required.

This work is closely linked with the next chapter in which the improved set of air-sea fluxes are used to initialise the surface boundary conditions of the high-resolution ocean model. Moreover, the evaluation of TMI-derived SST to improve the forecasting skill of the ocean model is assessed on the basis of improved initialisation and data assimilation schemes. The high-resolution SST observations are used to adjust the ocean model fields towards observations.

Chapter 7

IMPROVING THE FORCING AND PREDICTION OF THE OCEAN MODEL.

7.1. Introduction.

The progress of ocean modelling is still hindered by a number of constraints. Chassignet *et al.* (2004) identifies these as being due to the dynamical approximations of the fundamental fluid mechanics, the parameterisation of essential processes that occur at high spatial and temporal scales, the boundary and initial conditions and the domain geometry.

One of the constraints that affects eddy-resolving, high-resolution ocean models is the availability of atmospheric forcing to drive ocean models. Theoretical progress over the past years significantly enhanced the understanding of the dependence of the thermohaline circulation to the parameterisation of the air-sea interaction, in particular that of air-sea exchanges of heat. Consequently, this has created a demand for simple yet accurate parameterisations of air-sea fluxes to satisfy the need for ocean model studies.

Scientific progress in ocean data assimilation is still at an early stage of development, but its eventual success will be important to the ocean modelling community in general. According to the World Ocean Circulation Experiment (WOCE)[124], technical gaps still exist in data assimilation, including lack of skill in the underlying model (arising from both poor initial data and dynamical deficiencies), poor knowledge of the statistics of forcing errors and parameterisation errors, lack of model grid resolution and lack of manpower.

[124] *http://sam.ucsd.edu/smwg/smwg_assimilation.html#v1 (accessed 01.11.04).*

Another important constraint is the objective verification of ocean models. This issue already poses a difficulty for coarse resolution models, which are usually compared to hydrographic estimates of a mean state of the ocean. The validation problem is far more significant (mainly at mid and high latitudes) even for seasonal temporal scales of variability because of the lack of appropriate data. The problem is especially severe for eddy-resolving models because of a lack of appropriate data with high enough spatio-temporal variability.

Free surface, sigma coordinate ocean models, such as POM, are now being used for a variety of applications, ranging from small-scale process studies and coastal and estuarine modelling and prediction to basin-scale ocean circulation and climate change modelling (Ezer, 2000). POM was selected by the MedNet[125] project as one of the main ocean circulation models to be used for the study of the Mediterranean Sea[126]. A study is therefore appropriate both to evaluate its sensitivity as well as to enhance its predictive capability.

In this study, POM is used to forecast the ocean circulation over part of the Ionian basin, situated in the central Mediterranean Sea. The numerous ocean-atmospheric processes that are active in this region provide a unique opportunity for observational and modelling studies (Robinson *et al.,* 2001). The model domain corresponds exactly to that of the nested Eta model, with the intent of assessing the impact of the improved high-resolution air-sea flux products on the forcing of the ocean model. The selection of this test area is made on the basis of the availability of a full fifteen-day, close to the daily initialisation time of the POM model (i.e.- 00 UT) SST dataset derived from the TMI sensor that is used for both model initialisation and data assimilation.

Another part of this study attempts to improve the prediction of the POM model using data assimilation. Experiments are performed on a

---

[125] *MedNET was a project to provide oceanographic modelling software for the Mediterranean Sea funded by the European Union Marine Science and Technology programme (MAST).*

comparative basis, assimilating SST derived from (1) GDAS modelled data and (2) the TMI-sensor. The resulting model output is compared with collocated observations. The scope of these experiments is to assess the effectiveness of assimilating passive microwave remote sensing to improve high resolution ocean forecasting. These experiments also evaluate the benefit of optimising a Newtonian nudging scheme as an efficient data assimilation scheme for POM.

The work related to the calibration of NOAA AVHRR imagery, as developed in chapter 4, is here used to analyse the spatial accuracy of the forecasted model fields. The aim is to test the robustness of the improved ocean forecasting system at fine horizontal scales. The geographical scope of this study addresses some of the technical gaps presently faced by the Mediterranean Forecasting System, whose forecasting boundaries are almost entirely outside this region (fig. 7.1).

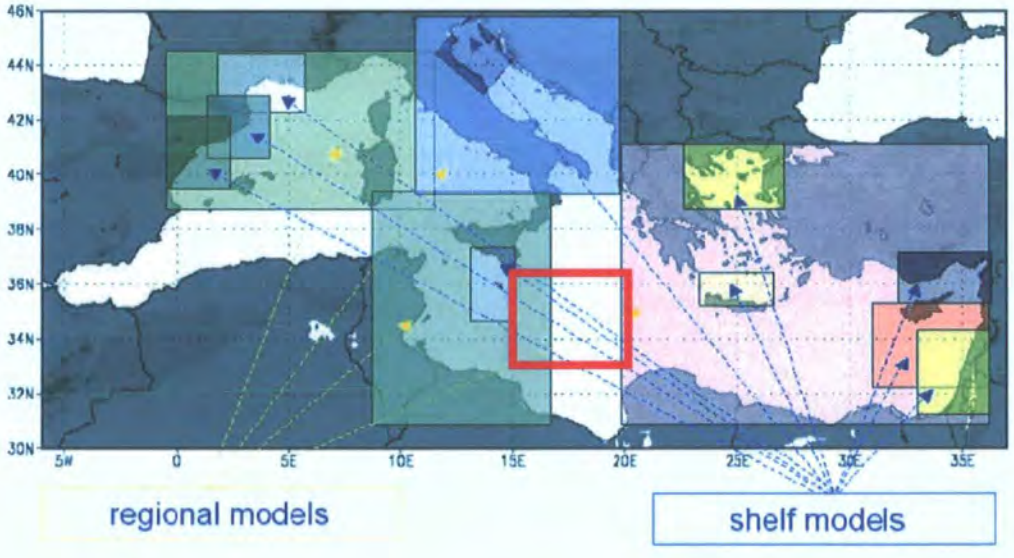

Figure 7.1. Geographical coverage of the modelling of the Mediterranean Forecasting System at the regional and shelf scale. Note the lack of coverage over the central Ionian basin denoted by the red box, which corresponds to the integration domain of the high resolution forecasting used in this study (with courtesy of the Mediterranean Forecasting System).

[126] *http://www.met.ed.ac.uk/mednet/overview.html (accessed on 01.11.04).*

7.2. Methodology.

7.2.1. Setup and running the POM model.

A Pentium MMX configured with 800MHz and 64MB of RAM was used for the POM model working on LINUX system with C and Fortran 77 compilers. The use of the model was simpler than the Eta atmosphere model, and consisted of folders containing Fortran 77 source codes and related executable files that (1) decoded the binary data constituting the lateral boundary conditions obtained from the seasonal Mediterranean Ocean Database (MODB), surface boundary conditions (SST and air-sea heat fluxes), and bottom topography, and convert it according to model σ-coordinate system; (2) constituted the numerical schemes of the model (POM97_oper.f), and (3) calculated the output of all relevant forecasted fields and their conversion into standard levels for displaying. Csh shell scripts unified the operation of all these three main groups of codes. The modelling process was divided into three stages: pre-processing, processing and post-processing. The logic of this setup is similar to that of the atmosphere model.

Pre-processing is described in Appendix IV, section IV.3.1. It consisted of model domain definition, preparation of lateral and surface boundary conditions, data decoding, formatting and data interpolation.

The processing stage is described in Appendix IV, section IV.3.2. The daily integration of the high-resolution POM model generated mesoscale, 3-hourly 3-D oceanic forecasts for a 24-hour forecast. Model processing consisted of two steps: (1) a pre-forecast run that adjusted the model fields towards the SST conditions, and (2) a forecast run using SST to initialise the adjusted model fields at the surface.

The post-processing stage is described in Appendix IV, section IV.3.3. This stage consisted of the generation of predicted oceanic fields. It also generated gridded forecasted variables in ascii xyz format for

subsequent standard and diagnostic model verification against the collocated, 1.1 km pixel resolution SST observations.

These three stages were run using an automated script as shown in Appendix IV, section IV.3.4. By defining a series of dates using the "foreach" command, dates and integration times and folder names for the output files were created automatically. MODB-derived lateral boundary conditions in binary format were first copied from the central archive to a specific folder from which they were subsequently called and converted to GrADS format. This stage gave the facility to display the initial data. Conversion into POM sigma coordinates followed using the *grid.oper* routine. The surface boundary conditions generated by the nested Eta model were ingested and interpolated onto the model's domain to initialise its surface boundary field. Figure 7.2. shows the interaction between the nested Eta model and the ocean model. A routine was called to read the SST information in GrADS format and initialise the surface boundary condition of POM. Automated archiving of data was done according to the integration date and time.

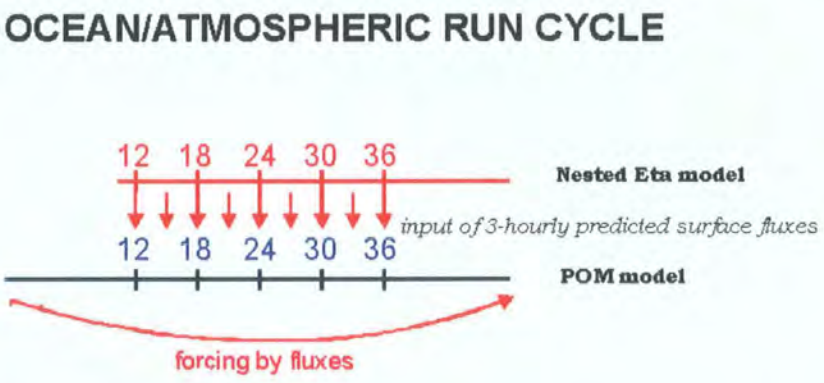

Figure 7.2. Input of 3-hourly atmospheric surface flux fields into POM as its surface boundary conditions.

7.2.2. Impact of using the improved set of surface forcing conditions.

The two high spatio-temporal air-sea flux datasets produced by the Eta model for the period 22nd July – 5th August 1999 were used to analyse their value as surface drivers for the ocean model. Two parallel hind cast experiments were carried out for this period using these two datasets separately (fig. 7.3). The ocean model was initialised starting on the 22nd July 1999 using the M-RESTART file produced by the hind cast sequence of simulations between 1st – 21st July 1999 (fig. 7.4).

The flowchart represented by figure 7.5 shows the setup of the POM model when lateral and surface boundary conditions are supplied to the model, followed by field adjustment and proper forecast runs to produce 3-hourly forecasted ocean fields.

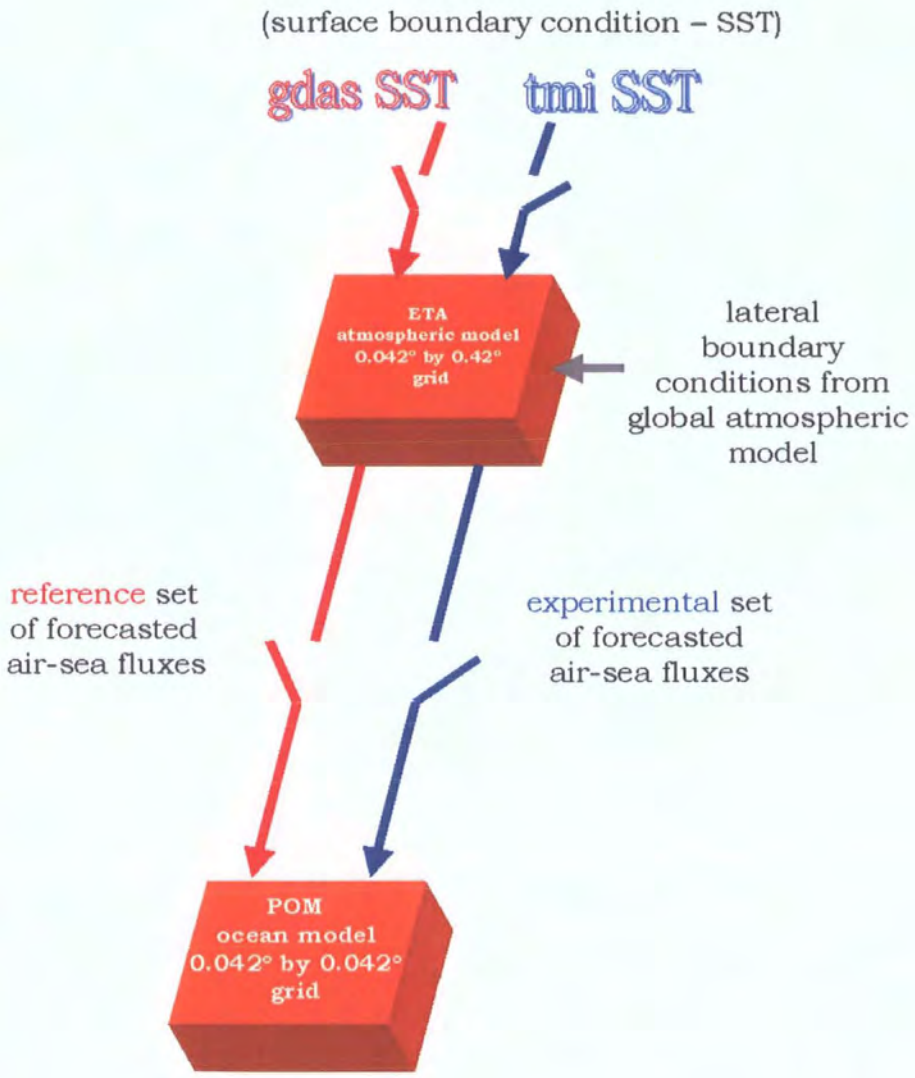

Figure 7.3. The two air-sea flux datasets produced in section 6.4.4. were separately used to initialise the surface boundary conditions of the ocean model. A comparative analysis of the final oceanic forecasts was then performed.

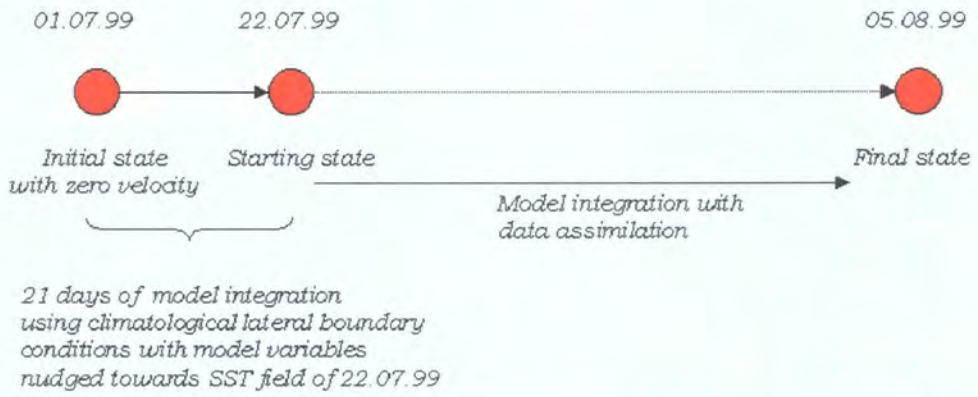

Figure 7.4. Scheme representing the entire model integration process.

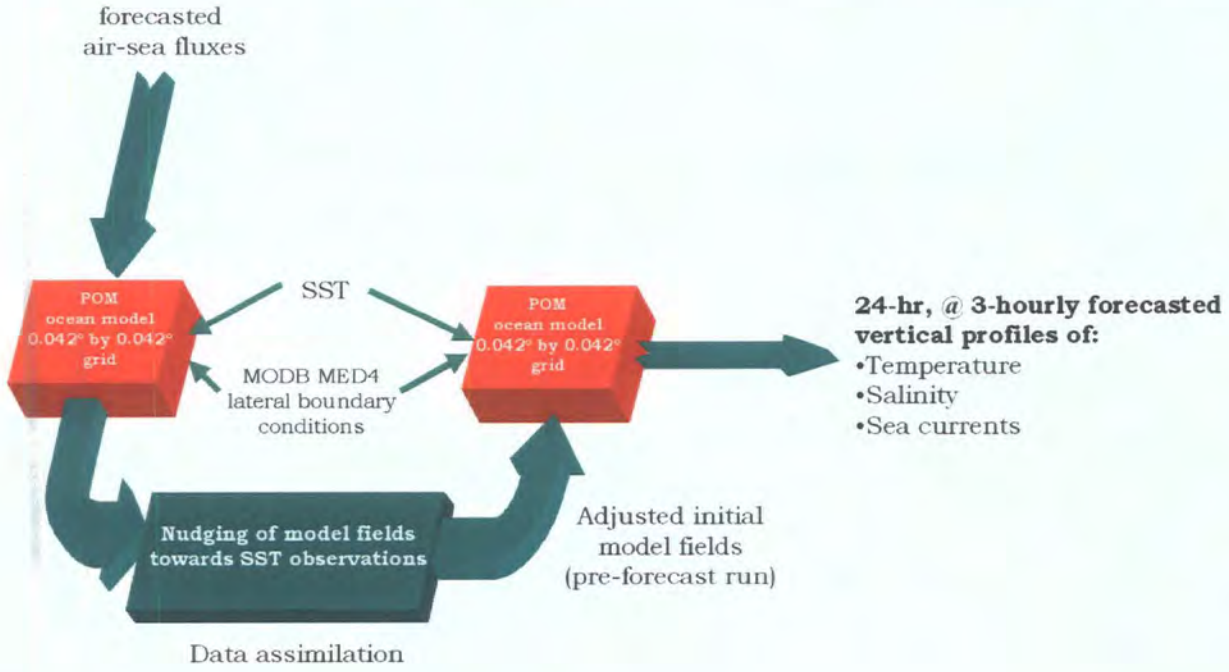

Figure 7.5. Using the POM numerical package, the initial model fields supplied by the lateral and surface boundary conditions were adjusted towards the observed SST data in a pre-forecast run.

Following this adjustment, the proper forecast run was activated to produce 3-hourly forecasted ocean fields for 24 hours. The 24th hour fields provided the initial conditions for the next model run.

7.2.3. Fine-tuning of the data assimilation scheme.

In order to identify the best nudging conditions[127] of the ocean model, three nudging schemes were tested for each of the 2 parallel runs described above.

The pre-forecast, data assimilation runs started from the initial, 3-hourly ocean fields previously forecasted by the ocean model on day (n-1) (included in the M_RESTRT data). The model fields were then "relaxed" towards the SST target field by using the prognostic equation with the correction term of the form:

$$\frac{\partial q^{\text{model}}}{\partial t} + A_q + K_q(q_n^{\text{model}} - q_n^{\text{observations}}) = 0 \qquad (7.1)$$

where q^{model} is the model variable; $q^{observation}$ is the target analysis; A_q is one of the model terms in the dynamical equations such as advection and diffusion and K_q is the relaxation coefficient. The time level t, is the value at which model predictions and observation are made.

Equation 7.1 represents the difference between the model solution and the corresponding observation. The subscript n indicates the time level at which model predictions and observations are made. The tendency of the model prognostic variable ∂q^{model} provides the q_n^{model} at the next time level (n+1). The equation is modified by introducing the relaxation term K_q $(q^{model} - q^{observation})$ that nudges the predicted variable q^{model} to the observed value on the relaxation time scale. K_q, the relaxation function (in x,y,z,t), which in this study is kept constant throughout the pre-forecast run. The role of transferring the assimilated information in the vertical and horizontal is performed by the model itself in a pre-forecast run, acting as a dynamical interpolator/extrapolator.

Three data assimilation (DA) experiments were performed:

[127] *Appendix IV; Section IV.3.2.*

1. To assess the effectiveness of data assimilation, model processing was run with no DA scheme;

2. To assess the effectiveness of varying the time period during which the model fields are dynamically nudged towards the SST observations, the model was run with an active DA scheme (scheme 1 in table 7.2). Three nudging periods (or relaxation time scale) were tested: 06, 12 and 24 hours, and

3. To assess the effectiveness of (1) varying the nudging period and (2) including a second forcing, nudging coefficient, to dynamically nudge the model fields towards the SST observations, model processing was run *with* an active DA scheme (scheme 2 in table 7.2). Four nudging coefficients were tested $5x10^{-3}$, $5x10^{-4}$, $5x10^{-5}$ and $5x10^{-6}$ for each of three nudging periods.

The pre-, processing and post-processing stages of the experimental setup were the same as described in sections 7.2.2. and 7.2.3. above as follows:

1. Use of two sets of surface forcing conditions, and
2. Fine-tuning of the nudging period and coefficient for data assimilation.

Sections 7.2.2. and 7.2.3. were carried out in tandem.

DA scheme					
No scheme	No nudging				
1	Fields nudged for a period τ towards observed SST	τ= 06 hrs	τ= 12 hrs	τ= 24 hrs	
2	Fields nudged for a period τ towards observed SST + use of a nudging coefficient	τ= 06, 12, 24 hrs 5×10^{-3}	τ= 06, 12, 24 hrs 5×10^{-4}	τ= 06, 12, 24 hrs 5×10^{-5}	τ= 06, 12, 24 hrs 5×10^{-6}

Table 7.2. Three experiments were performed to assess the effectiveness of the model's data assimilation scheme and its optimisation.

7.2.4. Model validation and diagnostics.

The forecasting performance[128] of the ocean model was analysed using basic statistical performance measures such as mean, standard deviation, bias and RMSE.

7.2.4.1. Spatial analysis of small-scale surface oceanic features.

Surface analysis was performed to outline and compare forecasted fields with high-resolution information of the ocean surface derived by remote sensing.

[128] *Section 5.4.2.*

7.3. Results and discussion.

7.3.1. Effectiveness of data assimilation on the forecasting quality of the ocean model.

The direct insertion method (i.e. Newtonian relaxation scheme) used in this study consisted of nudging forecast values at all data points towards the observed data, which are assumed to be exact. The blending estimate is a scalar linear combination, with an assigned weight (τ and coefficients, separately and in tandem), of the forecast and data values at all model grid points. The coefficients used in the relaxation scheme were related to dynamical scales and *a priori* estimates of model and data errors used to assimilate GDAS-SST into the ocean model (Telenta, 1999, *personal communication*).

7.3.1.1. No data assimilation scheme.

Figure 7.6. shows the results when the ocean model did not use a data assimilation scheme[129]. The increasing RMSE index, based on the comparison between the forecasted SST field and collocated SST derived by the passive microwave sensor, reached a plateau after the 11th day of integration, to give a more or less stable RMSE of 3^{o}C.

A lower RMSE is obtained when the experimental air-sea fluxes are used to initialise the model throughout the experimental run relative o the other system. An increased standard error with time is shown by the bias index (fig. 7.7) for both runs. A maximum under-forecasted SST value of more than 3^{o}C is reached after the full model integration run (fig. 7.7).

[129] *Statistical results are shown in Appendix VII.*

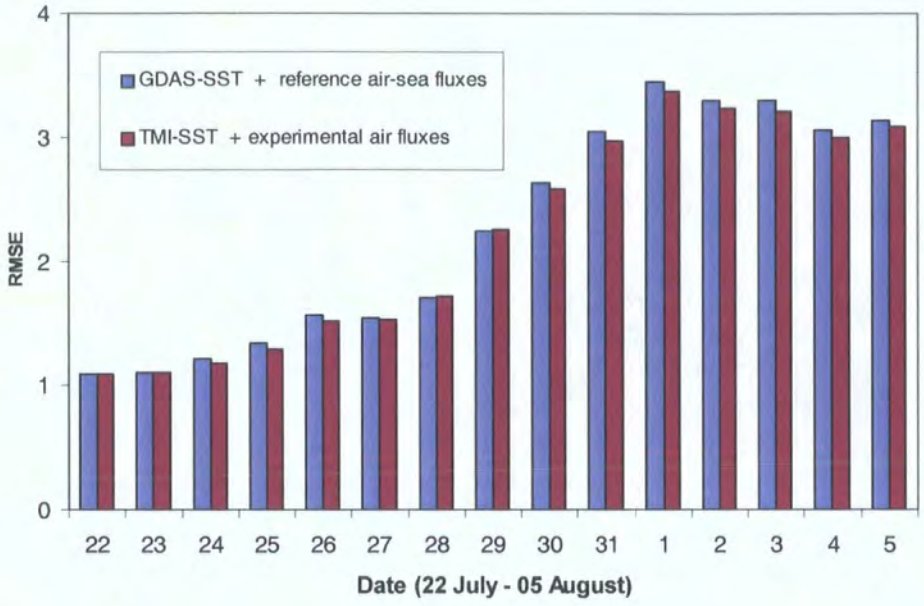

Figure 7.6. RMSE trend between 24-hr predicted SST and TMI-derived SST for the entire period of model integration, with no active data assimilation scheme.

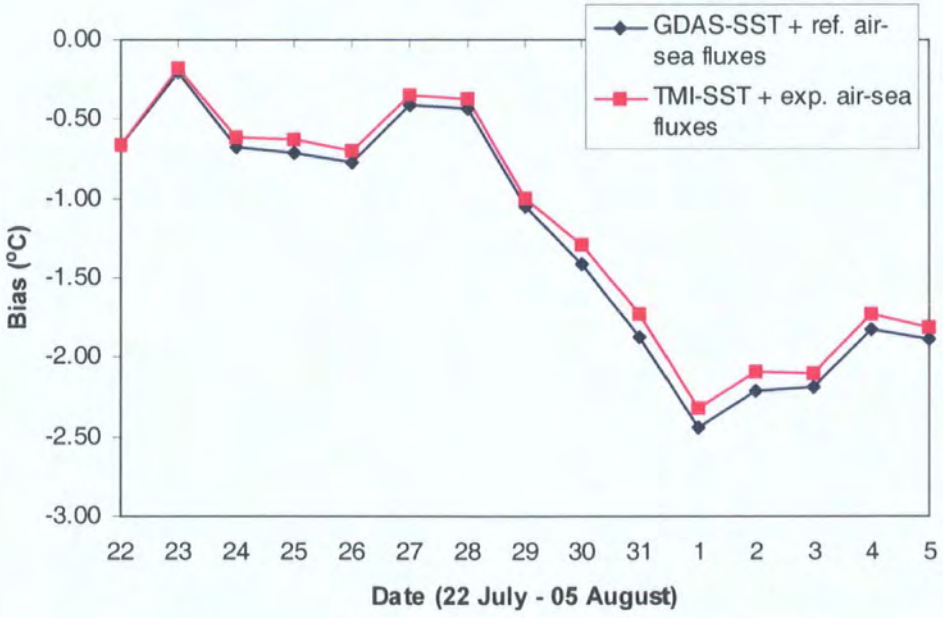

Figure 7.7. Bias trend between 24-hr predicted SST and collocated observed SST throughout the 15-day model integration of POM with no data assimilation.

The results show the importance of data assimilation, the absence of which leads to a significant model error drift and propagation of misfits in the forecasted SST.

7.3.1.2. Newtonian relaxation towards SST with varying nudging periods (scheme 1).

The use of both the experimental and reference datasets lead to a consistent decrease in the bias value with time (figs. 7.8 a-c) with the former giving a lower overall bias and amplitude[130]. This result is consistent throughout the entire run. Minimal bias is achieved after 24 hrs of pre-forecast nudging.

Horton *et al.* (1997) applied a similar DA scheme for their ocean forecasting system by nudging their model towards interpolation based analysis (Daley, 1991) of AVHRR MCSST. The new SST values were assimilated by the model using a nudging period of only 4 hrs. According to Horton *et al.* (1997) a low value of the nudging period was chosen so as to minimise model instability resulting from the sudden insertion of new temperature values. In contrast, these results show that only by increasing the nudging period to 24hrs can the best 24-hr predicted SST field be achieved.

[130] *Statistical results are shown in Appendix VII.*

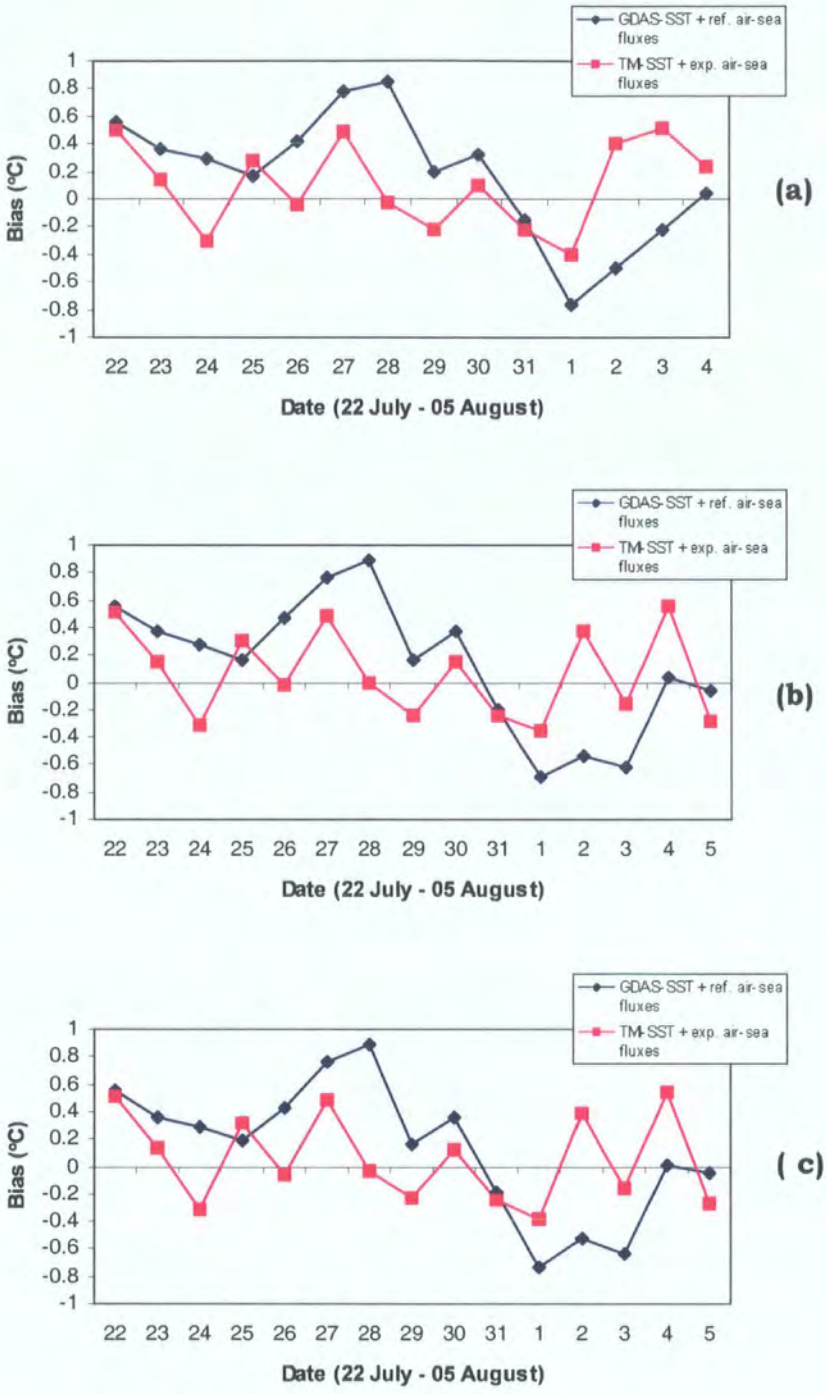

Fig 7.8 a-c. Bias trend between the SST forecasts produced by the two competing models using different initial surface boundary conditions with different nudging periods as follows: (a) 06 hrs, (b) 12 hrs, (c) 24 hrs.

7.3.1.3. Newtonian relaxation towards SST with variable nudging periods and coefficients (scheme 2).

Results are presented in figures 7.9 a-l in the form of linear trends of the resulting biases between the 24-hr forecasted SST fields against collocated observations. What is most apparent in these series of graphs is the smaller, and more stable bias of the forecasting system using TMI-SST and the experimental air sea fluxes as the initial surface conditions for the full model integration run. This pattern holds for all the different nudging periods and coefficients except when the value of the coefficient is $5x10^{-6}$. In both cases, the bias tendency is always negative, implying the presence of model error drift with time, showing a slope that that is much less pronounced by the experimental system than the reference one[131]. However, the different tendencies of the slopes produced by both sets of air-sea fluxes indicates that the two sets of initial conditions lead to two different sets of SST predictions. The small amplitude and stable tendency produced by the experimental set of air sea fluxes suggests a more stable setting.

The overall result show that the best tuning for the data assimilation scheme occurs when the nudging period is set to 24 hrs and the value of the coefficient is 5×10^{-3}. A similar pattern is observed when the value of the coefficient is changed to $5x10^{-4}$ (fig. 7.9 d-f). A different pattern in the bias trend is observed when the value of the nudging coefficient is changed to $5x10^{-5}$, in particular when the nudging period is set to be 06 and 12 hrs (figs. 7.9 g-h). However, this trend is improved when the nudging period is extended to 24 hrs, suggesting that with a weaker coefficient of $5x10^{-5}$, effective data assimilation can only be achieved if the nudging period is increased to a maximum of 24 hours. A nudging coefficient of $5x10^{-6}$ is too weak to adjust the ocean fields towards the observations (figs. 7.9 j-l). The duration of the nudging

[131] *Statistical results are shown in Appendix VII.*

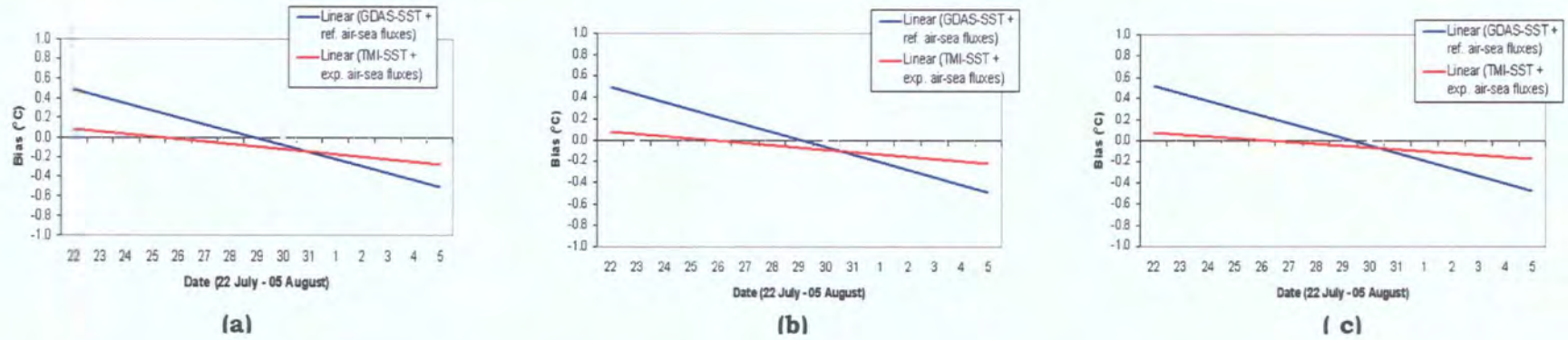

Fig 7.9 a-c. Bias trend between the SST forecasts produced by the two competing models with different initial surface boundary conditions using a nudging coefficient of $5x10^{-3}$ and different nudging periods as follows: (a) 06 hrs, (b) 12 hrs, (c) 24 hrs.

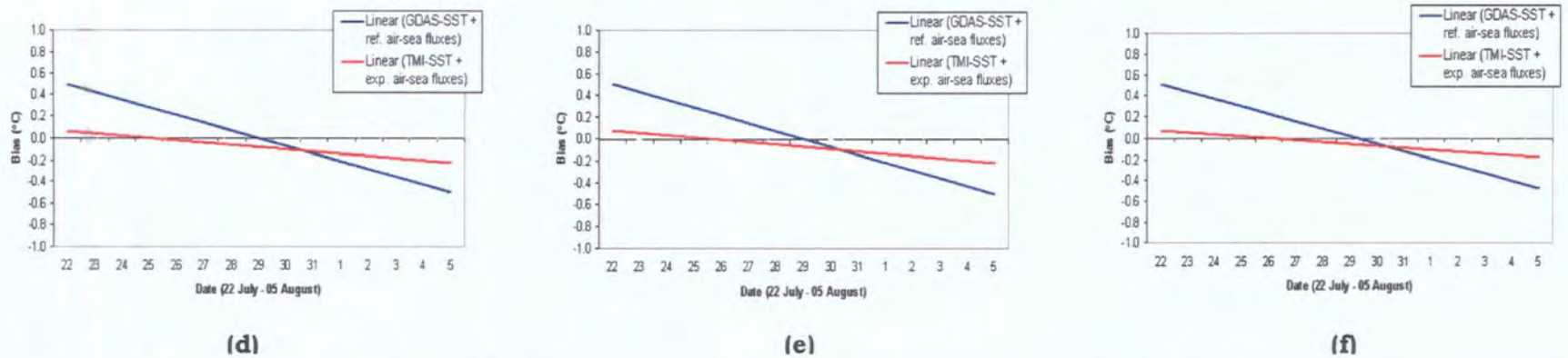

Fig 7.9 d-f. Bias trend between the SST forecasts produced by the two competing models with different initial surface boundary conditions using a nudging coefficient of $5x10^{-4}$ and different nudging periods as follows: (a) 06 hrs, (b) 12 hrs, (c) 24 hrs.

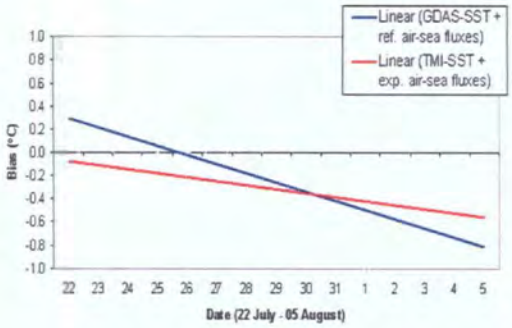

(g)

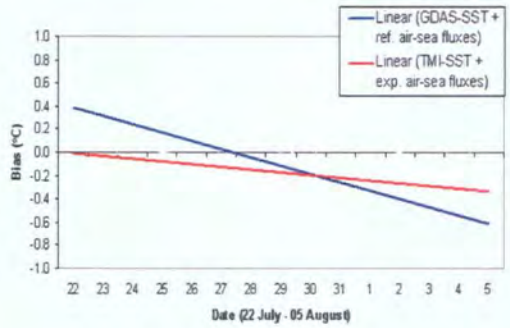

(h)

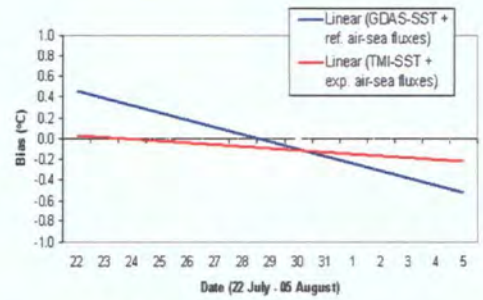

(i)

Fig 7.9 g-i. Bias trend between the SST forecasts produced by the two competing models with different initial surface boundary conditions using a nudging coefficient of $5x10^{-5}$ and different nudging periods as follows: (a) 06 hrs, (b) 12 hrs, (c) 24 hrs.

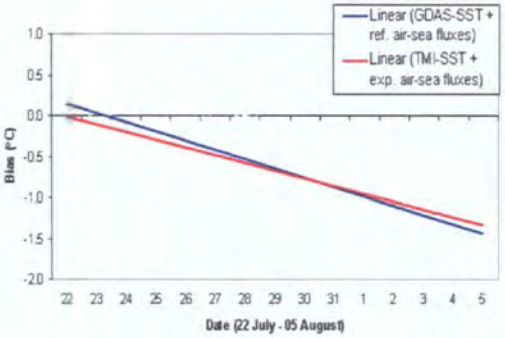

(j)

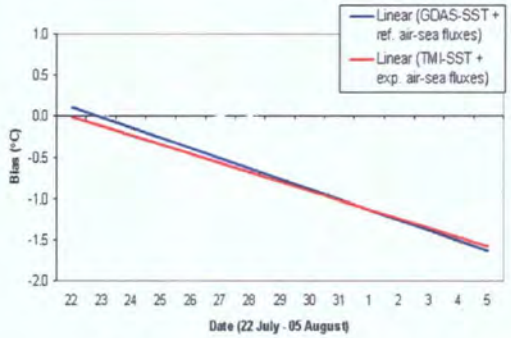

(k)

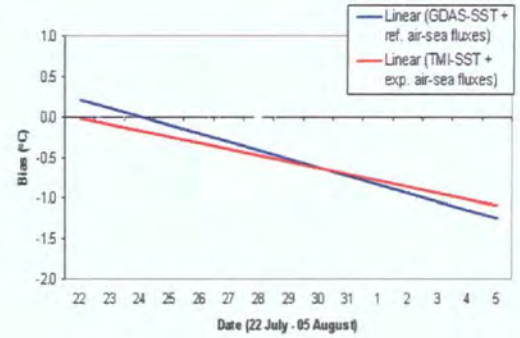

(l)

Fig 7.9 j-l. Bias trend between the SST forecasts produced by the two competing models with different initial surface boundary conditions using a nudging coefficient of $5x10^{-6}$ and different nudging periods as follows: (a) 06 hrs, (b) 12 hrs, (c) 24 hrs.

period is also insufficient for such a weak adjustment. The end result is a final 15-day prediction of an SST field with an overall bias of around 1 °C when a nudging period of 24 hrs is used.

Despite the small period of evaluation, some general remarks can be made. What is evident from this study is that an active data assimilation scheme tends to dampen the fluctuating bias tendency rapidly. The fluctuation in the bias trend is caused by the model's attempt to equilibrate the model dynamics towards the prognostic SST values. However, its degree of damping is seen to be dependent on the two factors that regulate the extent of this fluctuation: the relaxation time $\frac{\partial q^{model}}{\partial t}$ and nudging coefficient K_q.

Following the adjustment of the data assimilation scheme, it can be concluded that the best overall setup is the DA scheme 1 using a nudging period of 24 hrs but without including a nudging coefficient. With this setting, the mean bias over the entire 15-day model integration is only –0.05 °C. The second best option is achieved when a nudging coefficient of $5x10^{-4}$ is used with a 12-hr nudging period. With such a setting, this scheme gives the highest correlation between the model's 24-hr predicted SST field and collocated observations, with a mean bias of –0.07 °C.

In both cases, better results are produced when the experimental air-sea fluxes are used as the surface boundary conditions of the ocean model. The less accurate result achieved when the reference initial dataset was used may be attributed to its poorer spatial information (attributed to GDAS-SST) as well as less realistic reference set of air-sea flux values generated by the Eta model. In spite of this difference, both datasets lead to a better model performance than other ocean forecasting systems in the region. Nittis *et al.* (2001) for example, obtained a bias of 0.1 to 0.8 °C when their 24-hour POM-forecasted SST was compared to collocated *in situ* buoy measurements.

The difference exhibited by means of the standard verification is however very small. Having a high-resolution forecasting system that is able to provide a final bias of –0.05 °C after 15-days of integration is still a very commendable one. If one were to extrapolate the forecasting trend of the ocean model, a highly accurate forecast would, in the end be achieved. But the most important factor in high-resolution forecasts is not the scalar accuracy but the spatial accuracy, for which modelers and end-users show a keener interest. Spatial analysis of the final SST forecast, in fact do expose a marked difference between these two schemes (section 7.3.4.).

The improved one-way atmosphere-ocean coupling offers distinct advantages over current basin-wide forecasting systems and is a novel aspect for operational forecasting for the Ionian region. For example, forecasting models working in the Mediterranean utilise bulk formulae to compute the surface boundary conditions of the ocean models (Lascaratos and Nittis, 1998). Atmospheric variables, such as wind field, air temperature and relative humidity are derived from coarse, monthly averages of 12-hr NCEP analyses for the period 1980-1988. Similarly, using the POM model, Horton *et al.* (1997) forecasted the Mediterranean circulation using wind stress and air-sea fluxes derived from NORAPS fields available at 12-hr intervals. The horizontal resolution of these fields was 45 km and the air-sea fluxes were calculated from these fields using bulk formulae. The systems also use weak relaxation to climatological temperature to prevent climatic-model drifts. Onken *et al.* (2003), for example, used 6-hourly momentum fluxes provided by ECMWF to force their high resolution model over the Straits of Sicily.

Castellari *et al.* (1998) go even as far as assimilating monthly mean SST derived from global models (such as from the Climate Analysis Centre, Washington DC). These authors comment on their limited information provided by their initial fields and suggest the need to setup an operational high-resolution, nested atmosphere model from which to derive the required initial conditions more accurately.

One drawback in the present chapter is the short initialisation time of the ocean model that starts with zero velocity. Ideally, this should start a number of years before the actual experiment to allow the model to achieve *quasi*-geostrophy[132] (in reality geostrophic conditions can only be achieved after a couple of thousand years of model integration and is not feasible for this kind of study).

It is interesting to note that the Mediterranean Forecasting System lacks an operational system whereby high-resolution, real-time atmospheric forcing is fully used to drive its full complement of regional- and shelf-ocean models. Comparative studies are still pending to analyse the impact of using different sources of atmospheric fluxes extracted either directly from its Mediterranean-wide atmosphere model or alternatively, by parameterisation using basic forecasted geophysical variables[133].

The Cyprus Coastal Ocean Model[134] (Zodiatis *et al.*, 2002 a,b,c) is a version of the POM that is being used to provide high resolution ocean forecasts around Cyprus and the Levantine Basin for the Mediterranean Forecasting System. Unlike the present model setup, the Cypriot ocean model is forced using 6-hourly ECMWF atmospheric analysis and forecast provided by Meteo-France at a much coarser resolution (0.5° by 0.5° latitude x longitude). These forecasts consist of air and dew point temperature, mean sea level pressure, clouds and 10 m winds. Air-sea fluxes are parameterised using climatological data (Zodiatis, 2003). Taking into account the modelling of the air-sea fluxes by the sophisticated numerical scheme embedded in the Eta model[135], their

---

[132] *Wu and Haines (1996) ran a version of POM for 100 years as to reach a well-maintained statistically steady thermohaline and equilibrated system at all model levels in the water column, along with budgets of heat and freshwater and their seasonal variabilities.*

[133] *http://forecast.uoa.gr/mfstep/mfstep_6.htm (accessed on 01.11.04).*

[134] *of the Oceanography Centre, Department of Fisheries & Marine Research, Nicosia, Cyprus; http://www.ucy.ac.cy/cyocean/ (accessed on 01.11.04).*

[135] *Appendix II; Section II.1.*

higher spatio-temporal resolution and accuracy[136], the forecasting system setup for the present study presents much greater potential.

7.3.4. Spatial analysis of the forecasted fields.

The validation of the high-resolution forecasts required the availability of comparable observations that capture the small-scale variability of the ocean-state during the integration period of the ocean model.[137]. This section presents the validation of the ability of POM to correctly represent ocean variability over fine spatial scales.

An example of some of the datasets used to initialise, assimilate and verify the predicted oceanic fields is given in figures 7.10a-d. Starting with the calibrated AVHRR data[138], scenes retrieved on the 22nd and 23rd July 1999 show very interesting thermal patterns. These very high-resolution datasets (1.1 km pixel resolution)[139] were an optimal source for comparative analysis of the spatial accuracy of the forecasted SST fields (~ 4 km grid spacing).

The SST derived from the NOAA AVHRR infrared sensor during these two days reveals a surface variability that can be associated with major oceanic currents in the Ionian basin (figs 7.11 a-b and 7.12 a-b). Associated with these ocean fronts are features such as filaments and jets with scales of tens of km down to 5 km similar to the ones described by Gascard (1978). Figure 7.11a shows a calibrated image retrieved by the NOAA AVHRR sensor on the 22nd of July 1999, exhibiting an interesting thermal feature that is evolving in the area of interest. This feature forms part of the transient but recurrent gyre

---

[136] *Section 5.5.3.*
[137] *see Chapter 4.*
[138] *Section 4.4.3.*

[139] *The acquisition and calibration relevant AVHRR scenes over the ocean model domain is provided in section 4.3.1.2.5.*

(a)

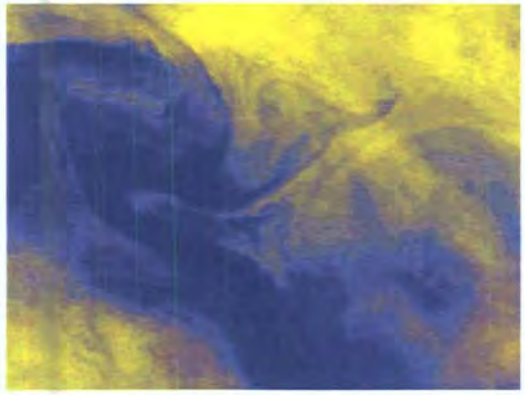

Calibrated
NOAA-14 AVHRR
Subset:
15.94°E - 18.27°E
33.39°N - 35.56°N

22.07.99 at 12:53 UT
Min. Temp: 25.48°C
Max. Temp: 28.45°C
Mean Temp: 26.92°C
Std. Dev.: 0.38

(b)

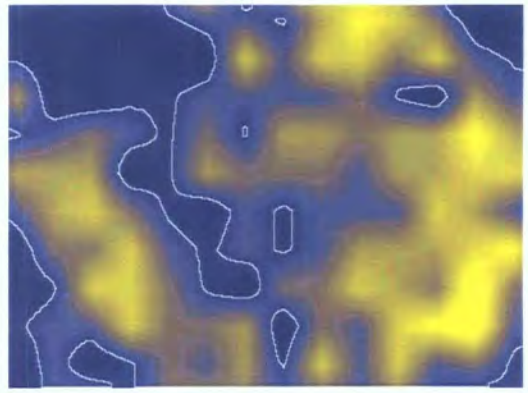

Calibrated
TMI SST data
Subset:
15.94°E - 18.27°E
33.39°N - 35.56°N

22.07.99 at 02:48 UT
Min. Temp: 25.65°C
Max. Temp: 26.84°C
Mean Temp: 26.20°C
Std. Dev.: 0.22

(c)

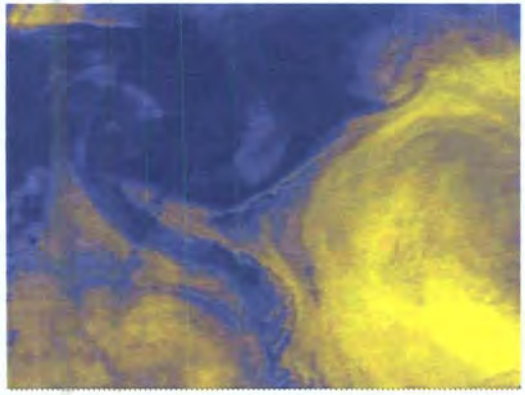

Calibrated
NOAA –14 AVHRR
Subset:
15.94°E - 18.27°E
33.39°N - 35.56°N

23.07.99 at 12:41 UT
Min. Temp: 25.38°C
Max. Temp: 27.77°C
Mean Temp: 26.56°C
Std. Dev.: 0.31

(d)

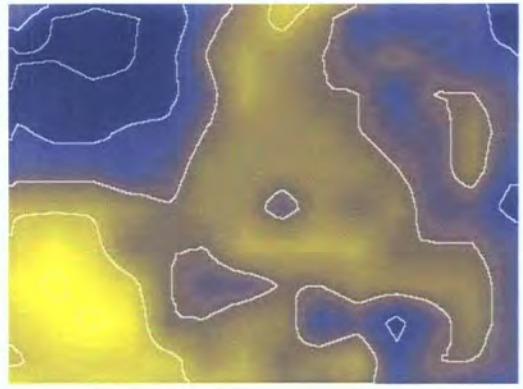

Calibrated
TMI SST data
Subset:
15.94°E - 18.27°E
33.39°N - 35.56°N

23.07.99 at 02:23 UT
Min. Temp: 25.37°C
Max. Temp: 27.00°C
Mean Temp: 26.25°C
Std. Dev.: 0.31

Figures 7.10a-d. An overview of some datasets used to initialise, nudge, and verify the predicted oceanic fields. The thermal profiles (a) and (c) were retrieved by the NOAA AVHRR sensor on the 22nd and 23rd July 1999. (Blue denotes colder and yellow denotes warmer surface water). The thermal profiles (b) and (d) were retrieved by the passive microwave TMI sensor. In spite of the coarser detail identified by the TMI sensor, the thermal signature is still evident (aided by contours), including major filaments originating from the cold core.

Figure 7.11 (a) Composite consisting of radiances derived from NOAA AVHRR channels 1, 4 and 5 showing basin-wide circulation in the Ionian region, and (b) Composite consisting of radiances derived from NOAA AVHRR channels 1, 3 and 4 showing evidence of atmospheric aerosols originating from north Africa. Images retrieved on 22 July 1999 at 12:53 UT (scale 1 cm:130 km)

Figure 7.12 (a) Composite consisting of radiances derived from NOAA AVHRR channels 1, 4 and 5 showing evolution of the surface thermal signature in the Ionian basin, and (b) Composite consisting of radiances derived from NOAA AVHRR channels 1, 3 and 4 showing increasing aeolian dust uptake that is migrating towards the area of interest. Images retrieved on 23 July 1999 at 12:41 UT (scale: 1 cm:130 km).

described by Robinson and Golnaraghi (1994), having considerable fine detail of the intense curling and filamentous jets extruding from the main path of the cold water inflow that is migrating to the north-western part of the integration domain.

In the Ionian basin, this Atlantic Water has an intense looping northward which tends to decrease in amplitude during winter (Robinson *et al.*, 1991). Tziperman and Malanotte-Rizzoli (1991), using a climatological data set, concluded that the path of the mid-Atlantic water upon entering the Ionian Sea tends to be northward during the summer and southward during the remainder of the year. This western Ionian cyclone is a recurrent feature of the Ionian circulation. During the summer period it appears to be more restricted to the west due to the development of an anticyclonic pattern in the eastern Ionian area (Horton *et al.*, 1997).

The dust plume shown in figure 7.13 was observed to be an evolving feature that would ultimately affect the integrity of subsequent AVHRR scenes over the area of interest. The maps represent the predicted dust load over the model integration period during 23 July 1999[140]. The corresponding dust load predicted at 1500 UT, for example, is closely related to the dust plume made visible by the AVHRR, that from Libyan-Tunisian region in North Africa. Subsequent forecasts of this dust plume shows that the amount of dust load increased and affects the entire area of interest. This corresponded with the lack of suitable AVHRR scenes from the 24 July until 7 August 1999.

[140] *A full description of the atmospheric dust model used for this study is given in Appendix III.*

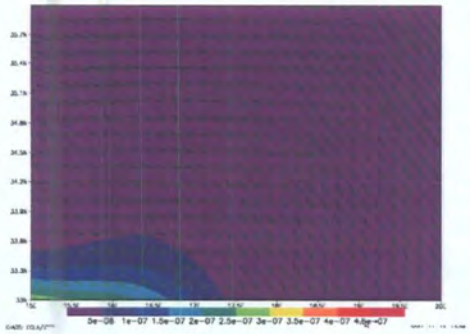

0300 UT

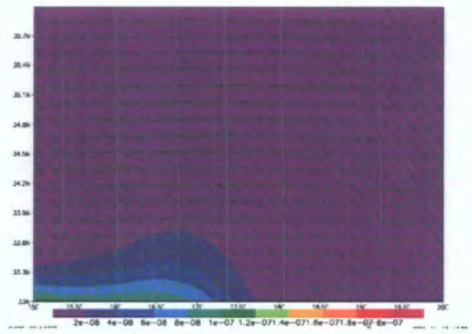

0600 UT

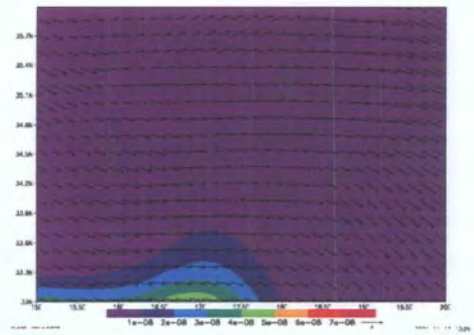

0900 UT

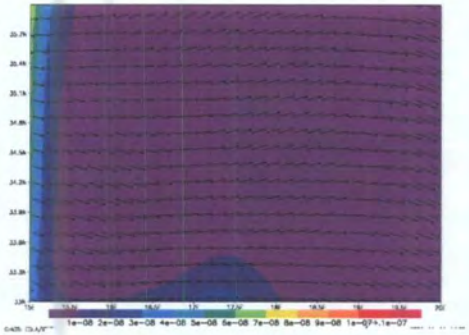

1200 UT

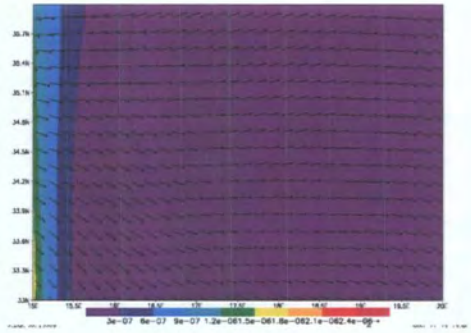

1500 UT

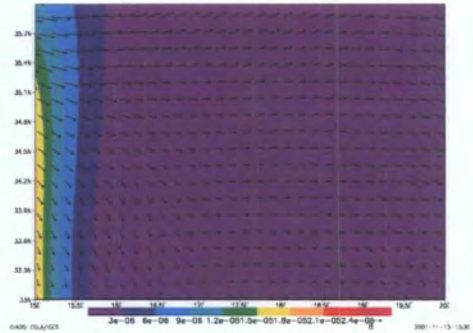

1800 UT

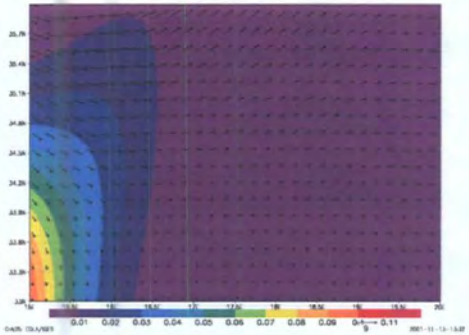

2100 UT

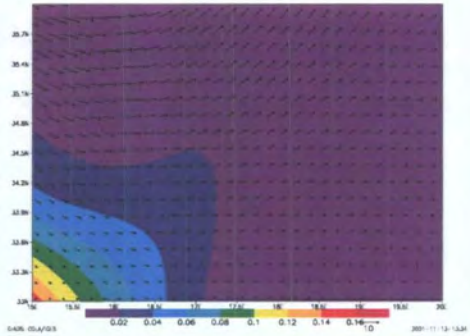

2400 UT

Figure 7.13. Forecasted integrated dust load (g m^{-2}) over the area of interest. Dust originating from the Saharan region is predicted to move eastwards every 3 hours starting from 0300 UT on the 23 July 1999. Superimposed is the resultant wind direction and strength.

Figure 7.11b shows an SST map derived by the lower-resolution TMI sensor some ten hours earlier than the same-day AVHRR image (fig.7.11a). In spite of its coarser detail, the fine thermal signature is still very evident, including major filaments originating from the cold core. Recognition of the main thermal feature is aided by contour lines to delineate the major gradients of the SST profile. The spatial offset of the surface feature is probably explained by the 11-hour difference between the TMI and AVHRR swaths.

Similarly, figures 7.11c and d compliment each other both quantitatively and qualitatively. The eddy's slight decrease in intensity from the 22nd to the 23rd of July is also detectable by the TMI sensor. Figures 7.11a-d suggests that this gyre is evolving and moving north-westerly.

The modelled data generated by this study shows that this thermal pattern is set by a balance of atmospheric[141] and oceanic dynamic processes[142], including wind-driven momentum (fig. 7.14), atmospheric heating and cooling (fig. 7.14), and horizontal and vertical advection in the ocean (figs. 7.15 and 7.16). The connection between the predicted 10 m wind magnitude on the 23rd of July and the surface temperature field are somewhat striking. Because of their duration, strength and orientation, the corresponding winds have a tendency to strengthen both the structure and migration of the thermal feature (fig. 7.11). A closer inspection of figure 7.14 shows that the surface wind is slower over the cooler parts of the water surface, and speeds up over warmer water. The divergence of the wind stress field is shown to increase with the gradient of the temperature field and the coupling is strongest when the wind blows at right angles to the isotherms. Studies over the North Atlantic sea show a coupling between the sea surface temperature and atmospheric forcing, which tend to reinforce each other to create anomalous conditions. The mechanisms thought to be responsible for this behaviour are the surface wind drift, wind mixing and the

[141] *provided by the high resolution, nested Eta model.*

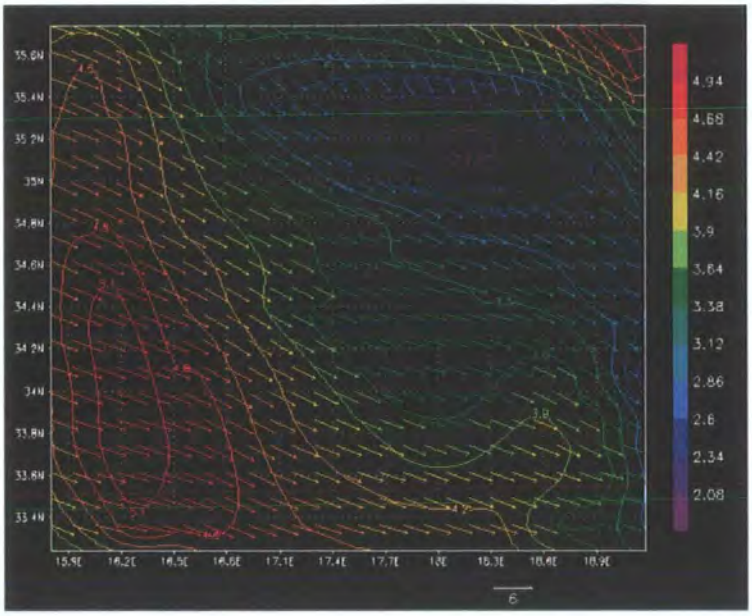

Figure 7.14. 36-hour forecast of the 10 m wind magnitude (m s^{-1}) predicted by the nested Eta atmosphere model starting at 22.07.99 00 UT (equivalent to 23.07.99 at 1200 UT). A stronger wind magnitude is evident on the western and northern borders, which is reinforcing the observed anticyclonic pattern of the collocated SST map retrieved by NOAA AVHRR. (Scale arrow is 6 m s^{-1}).

interchange of heat between the ocean and the atmosphere. Correlation studies conducted by Day (2000) show that such coupling between wind and changes in SST can occur over very short time periods, such as three days.

The close similarity between the SST maps derived from the two orbiting sensors demonstrate the potential of using the all-weather TMI-derived SST to initialise the boundary conditions of the ocean model and to dynamically adjust the model fields. The continuous availability of TMI-retrieved SST during the model integration period also facilitated the analysis of the forecasting skill of the ocean model to forecast SST fields (around 4 km grid spacing) in the absence of *in situ* data from the area of interest[143].

[142] *provided by the high resolution POM.*

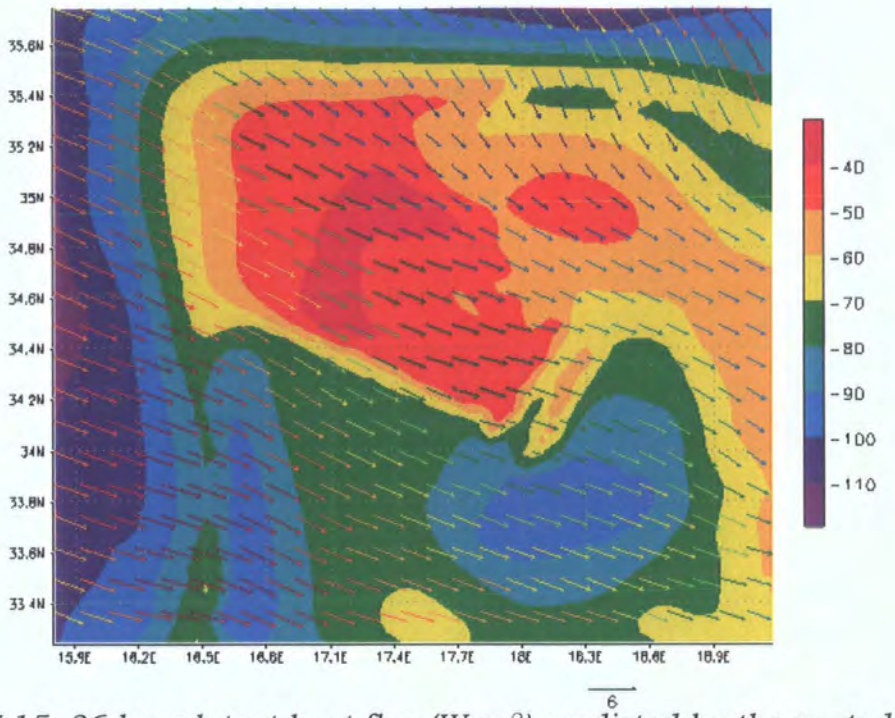

Figure 7.15. 36-hour latent heat flux (W m^{-2}) predicted by the nested Eta atmosphere model starting at 22.07.99 00 UT (equivalent to 23.07.99 at 1200 UT). The central, low flux pattern is related to the calmer, region corresponding to the anticyclonic gyre as retrieved by the NOAA AVHRR sensor. (Scale arrow is 6 m s^{-1}).

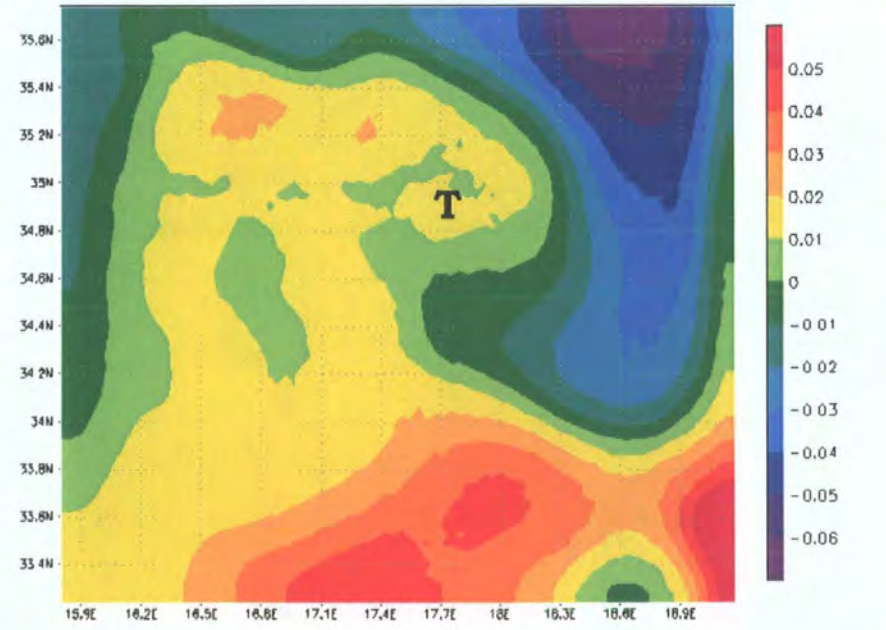

Figure 7.16. 12-hour forecast of the sea surface elevation (m) predicted by the ocean model (using DA scheme 1; τ=24 hours; experimental air-sea fluxes) starting at 22.07.99 00 UT. Central thermal feature is characterised by a stable, slightly elevated sea surface. Central tongue feature (T) is characterised by the higher wind magnitude moving westwards into the gyre.

---

[143] *Section 7.3.1.*

Figures 7.17 illustrates the observed and predicted 24-hour SST field respectively within the area of interest following the initialisation of the ocean model on the 22nd July. The 24-hour forecasted SST field, which is equivalent to 23rd July at 1200 UT is shown (fig. 7.17b). Main features can be noticed that are complimentary to the thermal pattern defined by the microwave SST retrieved on 23rd of July at 02:23 UT that was used to initialise the model run, but with a higher structural definition than the TMI SST field. This high definition closely matches the AVHRR image shown in figure 7.17a. Features such as the cool vortex A, the cool filament at B, the warmer pool C and the sharp temperature gradient at E, are easily traceable. Model data (figs. 7.18 and 7.19) indicates that the direction and magnitude of the predicted ocean surface currents are strongly linked to this vortex, showing minimal translational energy within the cooler pools that form the interior of the anti-cyclonic eddy. Moreover, results show that these small-scale features are coupled to mesoscale atmospheric forcing as noted in figure 7.14. The highly resolved, surface currents predicted by the ocean model give further support to the ability of the ocean model to resolve oceanic circulation at a very high resolution.

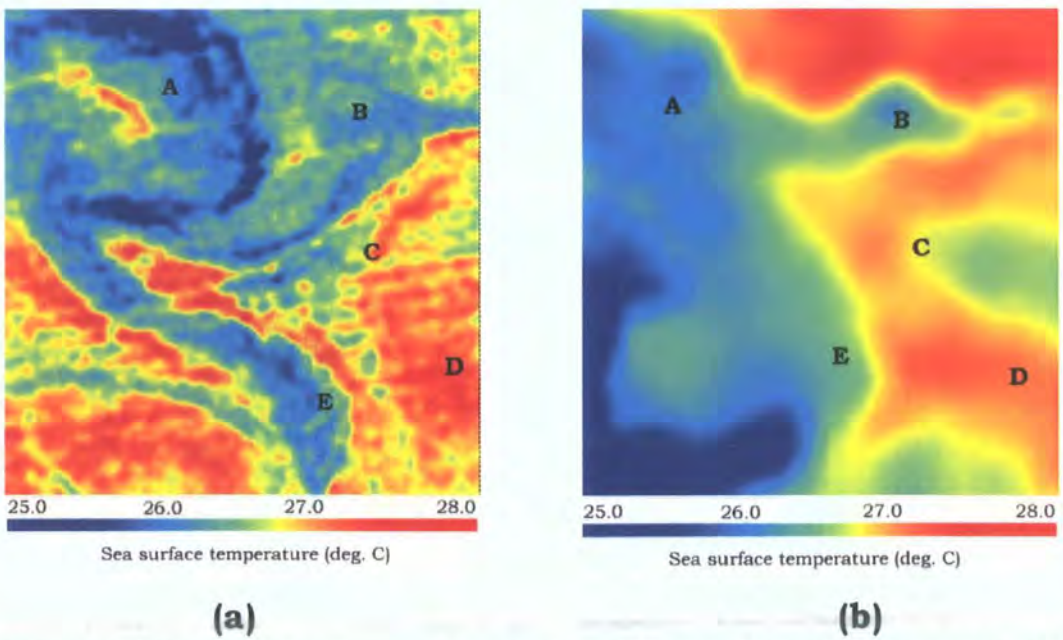

Figure 7.17 a - b. SST features as retrieved by (a) AVHRR on the 23rd July 1999 at 12:41 UT (mean: 26.6 °C; standard deviation: 0.31 °C) and (b) contoured, 36-hour predicted SST field (mean: 26.8 °C; standard deviation: 0.31 °C) (using DA scheme 1; τ=24 hours; driven by the experimental air-sea fluxes) on 22nd July 1999 (equivalent to 23rd July at 1200 UT). A=cool vortex; B=cool filament; C=warmer pool; D & E=sharp temperature gradient.

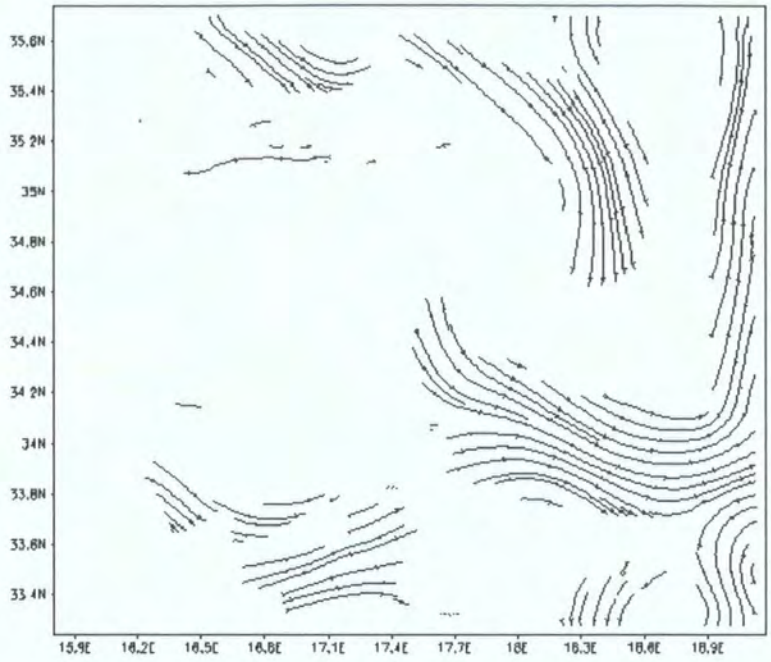

Figure 7.18. Streamlined surface ocean currents as predicted at the 36th hour from the start of the model integration on the 22nd of July 1999 at 00 UT. TMI-SST was assimilated using scheme 1 with τ = 24 hrs.

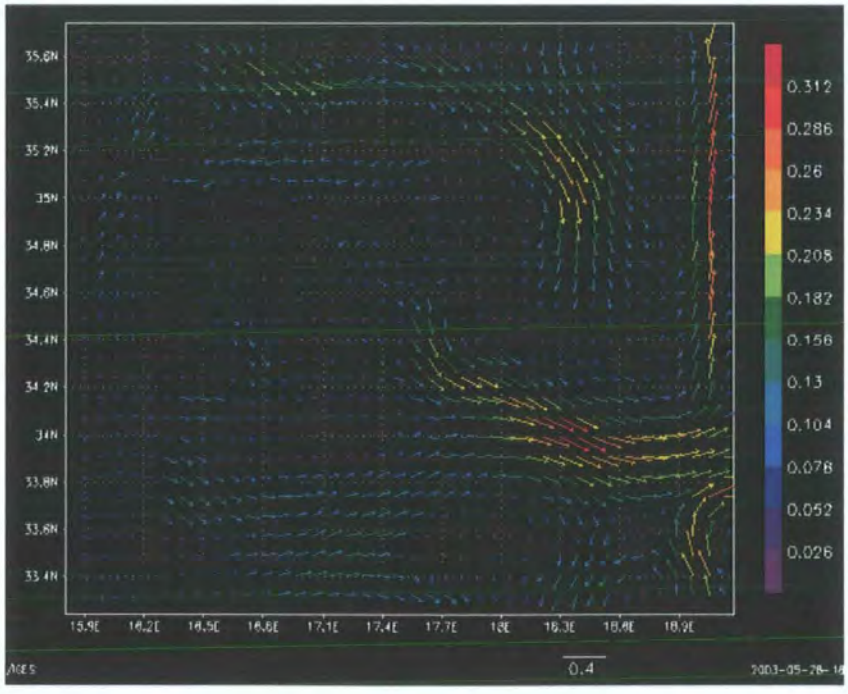

Figure 7.19. Direction and magnitude (cm s^{-1}) of the surface ocean currents as predicted at the 36th hour from the start of the model integration on the 22nd of August 1999 at 00 UT. TMI-SST was assimilated using scheme 1 with a τ = 24 hrs. (Scale arrow is 0.4 cm s^{-1}).

7.3.5. Spatial analysis of the final forecasted SST field.

This section focuses on the spatial accuracy of the surface temperature fields predicted at the end of the 15-day forecast run. This analysis is based on SST observations available from passive microwave remote sensing. No profiles were studied in the vertical dimension because data was lacking[144]. The availability of vertical profiles of temperature and salinity would have assisted the analysis of the error projection in the vertical dimension. It would also have been useful to assess how the data assimilation affects the dynamics of the underlying variables, with a resultant effect on the surface temperature.

The top SST map in figure 7.20 represents the final SST field used to nudge the model fields starting on 05.08.99 at 1200 UT. This field was retrieved on 04.08.99 at 21.7 UT by the TMI sensor. The 00 UT predicted SST field using the experimental air-sea flux dataset and assimilating TMI-derived SST using schemes 1 and 2 are shown on the lower left and right of figure 7.20 respectively. To better resolve the predicted spatial structure, a 5x5 edge preserving smoothing kernel plus an additional low-pass 5x5 kernel were used to enhance the forecasted thermal pattern.

The lower central image represents the SST retrieved by the TMI sensor on 06.08.99 at 2100 UT. A cold tongue is evident, which is also seen in the forecasted fields; however, DA scheme 1 produces a much more defined feature than scheme 2. The forecasted cold feature is seen to be located further south; this offset may be due to a three-hour difference between the forecasted and remotely sensed field.

The histogram maps of the final forecasted SST are shown in figure 7.21. The frequency plot of DA scheme 1 is evidently more focused around a narrow temperature range than the one obtained by DA

[144] *The XBT CTD access server of the Mediterranean Forecasting System starts from the month of September 1999 for a selected number of sampling stations in the Ionian*

scheme 2. This is in line with the spatial texture of the final forecasted SST fields.

The unfiltered forecasted SST maps produced using DA scheme 2 show enhanced "noise" patterns with a consequential loss of a well-defined, final SST map. This behaviour by the model suggests that this scheme propagates errors within the model dynamics leading to model fields that are not equilibrated at the grid-point scale, giving rise to grid-scale high and low values of SST within the overall field. Such noise is not so evident in the forecasted fields produced by the DA scheme 1, where major SST fronts are more compact, easily recognisable and comparable to the observed SST field. This correspondence is also supported by the scalar validation given in section 7.3.1.

---

basin. http://vosdata.santateresa.enea.it:54321/mfs/xcsa/response.php (accessed on 01.11.04).

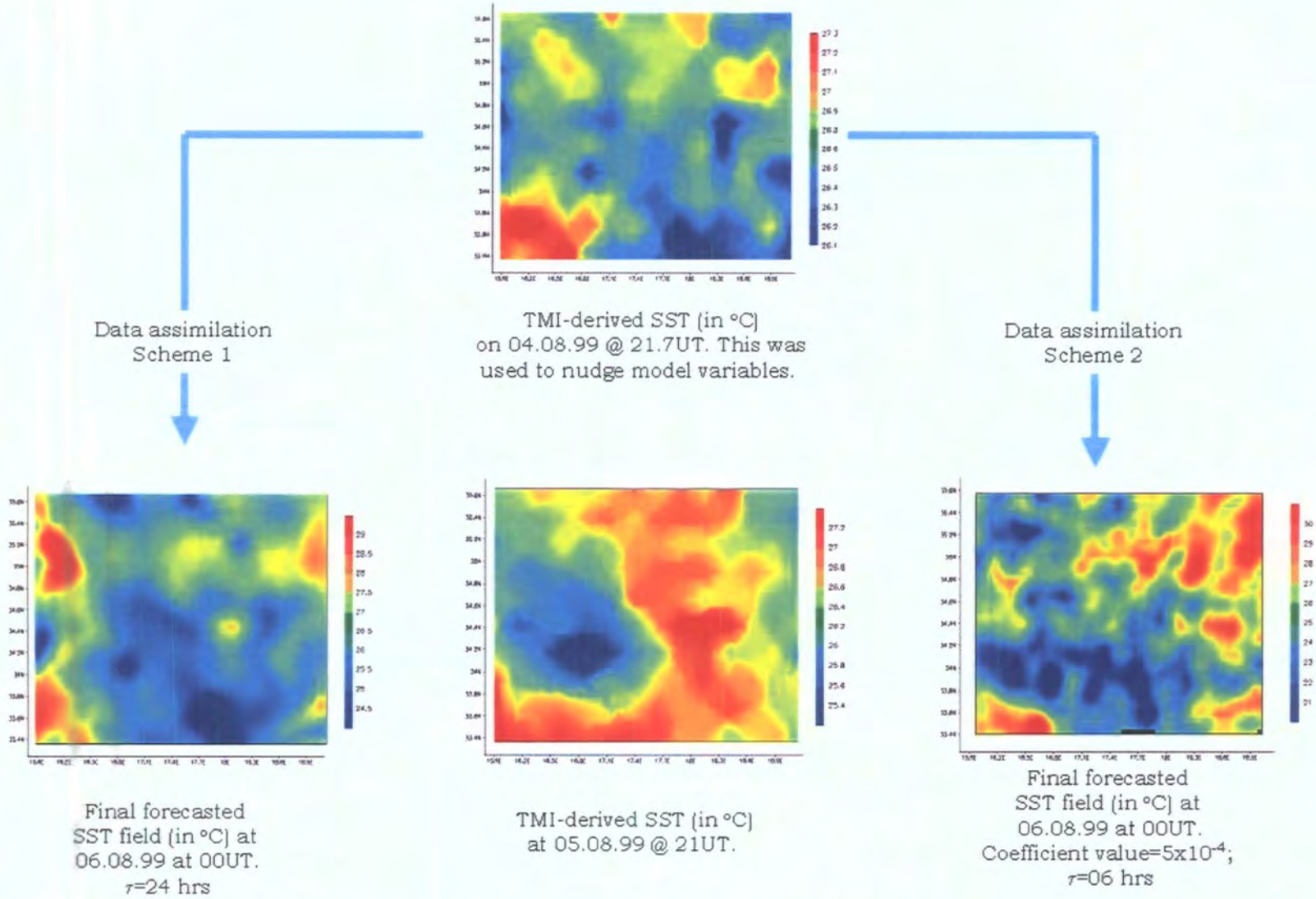

Figure 7.20. Model predicted SST on 6th August at 00 UT using the optimal settings identified for DA schemes 1 and 2 using TMI-derived SST and the experimental set of air-sea fluxes to drive the ocean model.

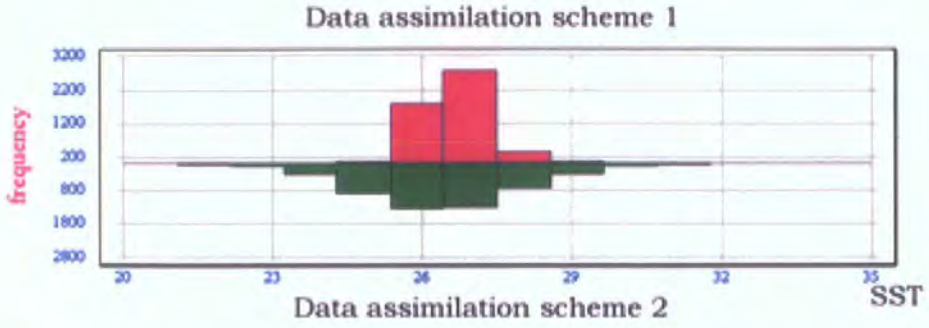

Figure 7.21. Histogram plot of the final forecasted SST maps (in °C) generated by (a) data assimilation scheme 1 using a nudging period τ equal to 24 hours and (b) data assimilation scheme 2 using a coefficient of $5x10^{-4}$. These forecasts were equivalent to 06.08.99 at 00 UT.

The same result is observed when the surface vorticity fields are analysed. Surface vorticity is a good indicator of the stability of the surface fields of the ocean model. In fact, less noise is evident in the surface vorticity field predicted by the DA scheme 1 (fig. 7.22) when compared to that produced using DA scheme 2 (fig. 7.23).

The final forecasted SST maps when DA schemes 1 and 2 are applied using the reference air-sea flux dataset and assimilating GDAS-derived SST are shown in figure 7.24. In this case, the only difference from figure 7.20 is the substitution of the lower left and right SST maps produced by the parallel setup using the *reference* set of air-sea fluxes. The lack of mesoscale information provided by the SST data as well as the inaccuracy of the reference air-sea flux dataset that forced the ocean model is evident from the spatial inaccuracy of the final forecasted SST. The forecasted SST map using DA scheme 2 is increasingly granular, making comparison very difficult.

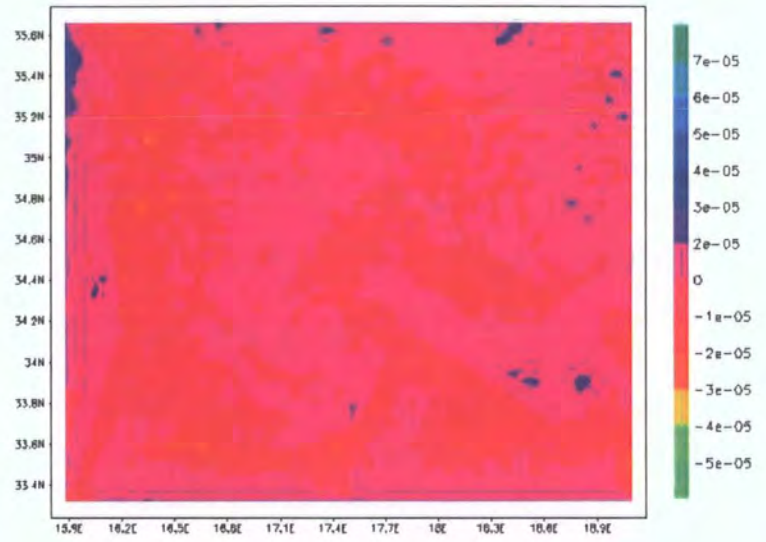

Figure 7.22. Vorticity (m^{-1} s^{-1}) on 06.08.99 at 00 UT as predicted by the ocean model forced by the experimental set of air-sea fluxes and using data assimilation scheme 1 (τ= 24 hours).

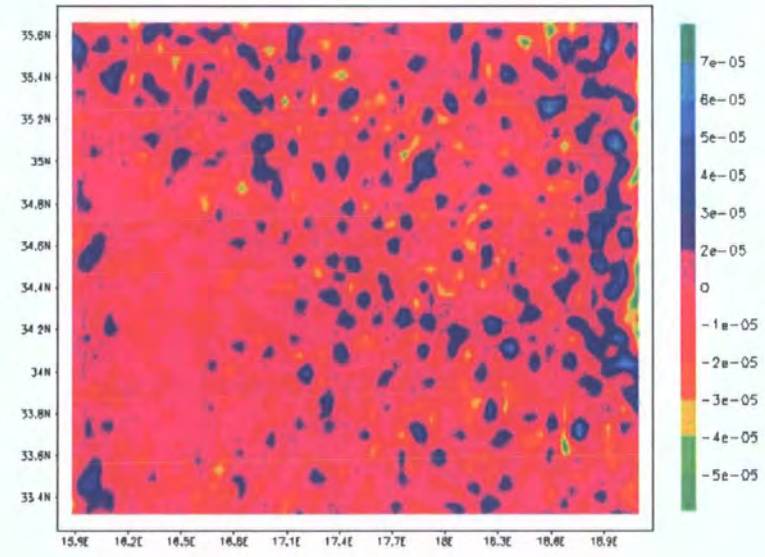

Figure 7.23. Vorticity (m^{-1} s^{-1}) on 06.08.99 at 00 UT as predicted by the ocean model forced by the experimental set of air-sea fluxes and using data assimilation scheme 2 (τ = 06 hrs; nudging coefficient = $5x10^{-3}$).

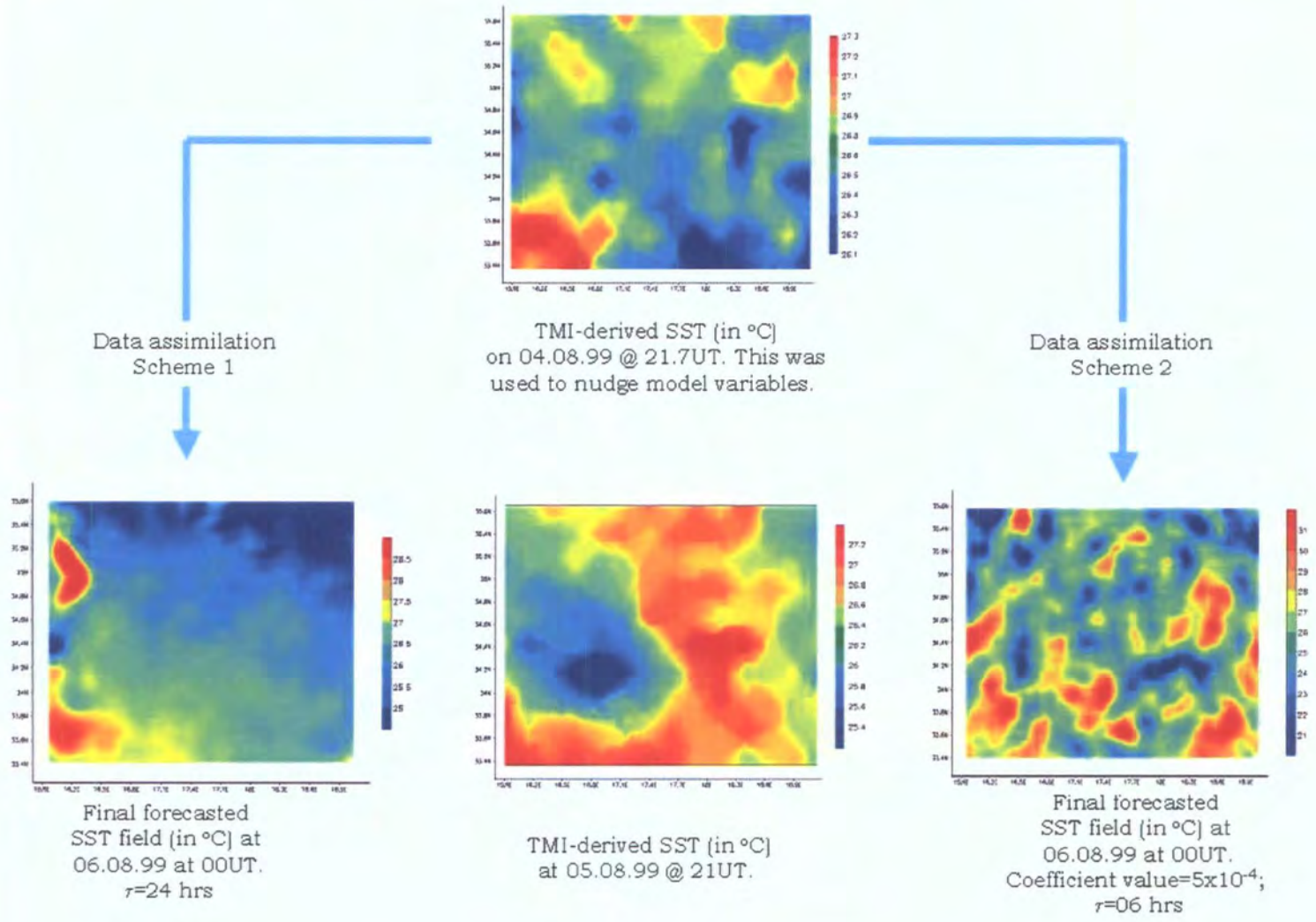

Figure 7.24. Model predicted SST on 6th August at 00 UT using the optimal settings identified for DA schemes 1 and 2 using GDAS-derived SST and the reference set of air-sea fluxes to drive the ocean model.

7.3.6. Limitations of the verification analysis.

It should be noted that the initial remotely-sensed SST fields used for assimilation throughout the entire 15-day period had an orbital time of ± 3 hours close to 00 UT. Errors arising from this lack of co-temporality with the initialisation time at 12 UT need therefore be taken into account. This also stands for the validation of the model predicted SST fields, which were out of phase with the TMI data by a maximum of ± 3 hours. No additional, collocated SST observations were available and therefore this error cannot be quantified. Henceforth, the present performance measures are based on a general, relative bias and RMSE rather than on the absolute value of the forecasts. Similar problems in data assimilation and model verification are always expressed, such as the case of Gavart *et al.* (1999) TOPEX/POSEIDON data assimilation for ocean modelling and verification purposes.

Another limitation of this study is the short, 15-day model integration period. This limit was defined by the availability of integral TMI orbital swaths over the area of interest, which was needed to continuously initialise the surface boundary conditions of the POM model. It is interesting to note that similar, short-scale studies are not uncommon in the case of ocean modelling studies. Onken *et al.* (2003) for example, studied the synoptic circulation and transport in the Tunisia-Sardinia-Sicily region using a model initialisation period of 12 days.

7.4. Summary.

The chapter implemented novel satellite SST assimilation into a high-resolution primitive-equation ocean model and verified the forecasted output. The aim was to achieve an improved dynamical tool capable of simulating the surface ocean processes linked to the air-sea interactions at sub-mesoscale level.

Section 7.2.1. described the setting-up of a high-resolution ocean model over the Ionian basin to provide short-range forecasts of the ocean state. The initialisation of this model using the high-resolution spatio-temporal air-sea fluxes generated by the nested atmosphere model was described in section 6.4.4.

In addition to these forcing fields, an assimilation scheme using TMI-derived SST data was optimised to improve the forecasting skill of the ocean model. Section 7.3. described the results of this optimisation following validation against a set of high-resolution AVHRR dataset.

This entire work was performed over a 15-day model integration window. Section 7.2.3.1. detailed how the ocean model was initialised with zero velocity on July 1st with a climatological mass field. Following this date, the ocean model was driven by the predicted, same-day air-sea fluxes, SST and lateral boundary conditions derived from the previous run. This daily model integration was repeated for 15 days up to 5th August. Section 7.2.5.1. described how the final daily 24-hour predicted ocean fields are generated.

The first data assimilation scheme described in section 7.3.2. presented the most accurate predictions of SST. In this case, the best nudging period for this scheme was found to be 24 hours. With this setting, the mean bias over the entire 15-day model integration was only –0.05 ^{o}C. Section 7.3.3. showed how the inclusion of an additional coefficient in the equation lead to strong nudging towards the initial observations. The optimal nudging coefficient was found to be $5x10^{-4}$ for 12 hours, giving a mean bias of –0.07 ^{o}C. For both data assimilation schemes, model integrations that were initialised using TMI-derived SST and the experimental air-sea fluxes produced a better prediction than the competing traditional system. This demonstrated the potential of using passive microwave remote sensing to improve the ocean forecasting system.

The data assimilation results showed that Newtonian relaxation can provide a better estimate of the ocean state than if assimilation is excluded from the model simulation. This study ensured that the model used for the assimilation was of sufficiently high resolution and accuracy to prevent aliasing the assimilation result towards a model state that is wrong. Model error estimation was based on statistical comparison with observations.

Sections 7.3.4. and 7.3.5. described how AVHRR SST data was used to provide a reliable description of mesoscale gyres in the area under study. The high-resolution sea surface thermal signature observed by AVHRR confirmed the ability of the improved ocean model to predict sub-basin surface circulation. These sections also demonstrated the high complementarity of infrared and passive microwave satellite sensors to provide information on SST thermodynamics over the Ionian basin. The applicability of using the calibration algorithm for validation purposes as developed in chapter 4 was also demonstrated.

Chapter 8

GENERAL DISCUSSION.

8.1. Introduction.

The research presented by this inter-disciplinary study dealt with a variety of aspects that seek to evaluate the use of novel remote observations and spatial data analysis to improve and assess the skill of an ocean forecasting system for the central Mediterranean Sea. The technical details and experimental approaches varied somewhat from one study to another and were presented in separate chapters. In this chapter, the main conclusions that can be drawn from the preceding chapters will be integrated and summarised.

The purposes of this study will be revisited and briefly checked against the research presented. Finally some directions for future research are given.

8.2. Aims of the study.

Chapter 2 presented several key aims which are discussed below:

8.2.1. Identification of research gaps, technical challenges, and optimisation of approaches addressing a wide variety of aims in numerical ocean forecasting research.

The main requisites and existing technical gaps in the field of numerical oceanic and atmospheric prediction have been identified based on a thorough literature search, particularly as they apply to the Mediterranean region. From this information, a range of optimisation approaches were formulated. Chapter 3 consisted of a review of present

research encompassing the current challenges in numerical weather and oceanic prediction, ranging from the main data requisites that drive forward, stabilize and diagnose these models, to the methodological approaches in objective model verification. The chapter introduced some criteria on the best approach to calibrate AVHRR data in the absence of collocated *in situ* match up SST data. These criteria were subsequently formulated in chapter 4 to produce a set of multiple regression algorithms that were optimised for the central Mediterranean region. The potential use of exploratory spatial data analysis to assist in diagnostic verification of the ocean forecasting models was also introduced in chapter 3. Such analysis was subsequently formulated, used and evaluated in chapters 5, 6 and 7.

8.2.2. Compilation of a database to validate the skill of the ocean forecasting system.

Chapter 4 described the construction of a database that consists of a high-resolution time-series of observations acquired by passive microwave remote sensing. The database was central to the process of verifiying the predictions made by the ocean forecasting system in an objective way. This contrasts strongly with other forecasting systems in the Mediterranean region which often give a higher priority to technical improvements, such as data initialisation and assimilation activities, rather than to model verification.

From the basic, remotely sensed variables archived in this database, the latent and sensible heat fluxes were calculated using bulk parameterisation. The criteria discussed in chapter 3 for the calculation of the turbulent heat fluxes, such as the use of suitable coefficients and approximations, were formulated in chapter 4. This study presents a substantive improvement in the methodology used to derive high-resolution, instantaneous air-sea flux products from novel remotely sensed variables such as sea surface temperature and 10 m wind magnitude. These data represent an improved source of information

against which high-resolution model forecasts were verified. This is in stark contrast to the use of coarser, monthly climatological values used by many other forecasting systems worldwide.

The criterion presented in chapter 3 for the calculation of the surface air temperature was formulated and applied in chapter 4, which took into account the monthly variability derived from climatological data of the area under study. This method represented another methodological improvement over current approaches to derive this value for the parameterisation of the turbulent air-sea fluxes as described in section 4.4.1.2.

The approach taken in processing and parameterising these data produced a unique, detailed database of the climatology of the area under study at exceptional spatial and temporal resolution. These datasets were used in chapters 5, 6 and 7 to verify the skill of the Eta and POM models to predict 10 m wind magnitude, cloud liquid water, precipitable water vapour, surface air temperature, turbulent air-sea heat fluxes (the sensible and latent heat fluxes), radiative air-sea heat flux (outgoing longwave radiation), and sea surface temperature. This database contained additional climatological information, which included a 10-year record of climatological aerosol optical thickness, absorbing aerosols and precipitation rates. The principles of verifying such databases introduced in chapter 3 were addressed by verifying the present database against the Southampton Oceanographic Centre Air-Sea Flux Atlas and the Comprehensive Ocean Atmosphere Data Set. The high accuracy and benefits of the present database were presented in detail in chapter 4.

The inclusion of sea surface temperature data in this database was given particular emphasis. Microwave remote sensing provided an all-weather data availability over the central Mediterranean and was able to show extensive mesoscale features. The strength of thermal infrared remote sensing to validate the high-resolution ocean model, was applied

by this study, taking into account the constraints presented by calibration algorithms, in particular by those applied in the absence of collocated, *in situ* data. Tailored algorithms were derived to calibrate radiance scenes acquired over the central Mediterranean Sea (chapter 4) and used to evaluate the improvements in model skill (chapter 7). Special care was taken for the detection, simulation and potential impact of atmospheric dust on the final SST product. Climatological information came from a 10-year long measurements of the aerosol optical thickness, which provided a statistically robust pattern of the aerosol content over the area of interest. In chapter 7, the dust plume which originated from North Africa on the 20th of July was modelled to delineate the extent of the resulting impact on the thermal radiances retrieved by the AVHRR. In this manner, this study presented an inter-disciplinary approach to evaluate and calibrate AVHRR data for the purpose of model verification.

8.2.3. Improving the skill of the Eta model to forecast air-sea fluxes.

One of the main achievements of this thesis is the accuracy assessment of the forecasting skill of a nested, high-resolution Eta atmosphere model against novel remote sensing observations and their derivatives, with special reference to the predictability of surface fluxes over the ocean. The air-sea fluxes are a direct measure of the physical interaction between the atmosphere and ocean and are well-suited to diagnose the model's parameterisations of the boundary layer, radiation and cloudiness. Validation and improvement of these data, especially the wind stress, form an essential part of the process for the coupling of the atmosphere and ocean models (chapter 7). The results presented by this study can be used to further fine-tune the post-processing of the Eta model as to provide more accurate short- to medium-range, high-resolution forecasts. The forecasting tendencies of the Eta model were quantified using standard statistical measures and their decompositions.

The high accuracy of the monthly predictions of the 10 m wind magnitude and surface air temperature data, was followed by that of the hydro-meteorological variables in decreasing order. The RMSE values obtained for the predicted surface wind magnitude were better than those obtained by the Eta-32 mesoscale version published by NCEP[145], the latter showing an average RMSE value of 3.0 m s^{-1} for the 12-hourly predicted wind field on the 28th October 2004. The present results, however, show a significant over-forecasting trend for the predicted outgoing longwave radiation and a correction to Eta's GFDL radiation package that takes into account a realistic aerosol database for the central Mediterranean is a strong recommendation of this study. This is in line with the recent plans to improve the Eta forecast system at NCEP, by including modifications in the cloud microphysics and the use of a new radiation package for Eta (Ferrier *et al.*, 2003).

Chapter 5 also evaluated the use of novel remotely sensed data to fine-tune the viscous sublayer depth, which is a determinant value in the forecasting of the air-sea fluxes under viscous conditions. This study proposes to dynamically adjust the sublayer depth value according to the prevailing surface wind conditions modelled by the Eta model. This approach presented an improved method to fine-tune a numerical scheme of an atmosphere model, based on an objective verification against high spatio-temporal observations derived by an orbiting passive microwave sensor.

As in any scientific experiment, forecast verification is an essential component of numerical modeling to assess the success, or otherwise, of the improvement made to the system. In this study, forecast verification was used to address three important reasons, namely (1) the monitoring of the forecast quality of the full climatic range over the area of interest, (2) the assessment of the improvement of the forecast quality

---

145 *http://www.atmos.washington.edu/~bnewkirk/new_webpage/plot12/STATSBETA.txt (accessed on 01.11.04).*

following fine-tuning, initialisation and data assimilation experiments, and (3) the comparison of the forecasting quality of competing forecasting systems. In this context, the verification of predicted, continuous variables was done to see how the values of the forecasts differ from the values of the observations. For such an assessment, standard verification methods were used such as scatterplots, mean error, bias, root mean square, and skill score.

Diagnostic verification methods were also used in this study. These methods are more complex than the standard ones. Their development is still in its infancy, and therefore, is a research area where new methods can be promoted. Thus, the criteria introduced in chapter 3 on the potential use of exploratory spatial data analysis for diagnostic verification were formulated and evaluated in chapters 5 and 6. Three routines that assisted in the interpretation of the skill of the Eta model in spatial terms were performed to understand the inter-relationship between predicted and observed surface fields.

Match score analysis, being the first of the three exploratory spatial data analysis, has been here developed on the basis of the threat score methodology (Glahn *et al.,* 1991; Goeber and Milton, 2002) used by atmospheric modellers to assess the correct placement and timing of particular, forecasted categories. The present study re-formulated this approach by giving it a fully spatial perspective using GIS and image classification. This spatial match score analysis thus measured the accuracy of the forecast in spatial terms, of whether the event from a category was forecasted or not and whether it was observed or not. Most of the research done on model verification uses the threat score method to analyse and compare the ability of different atmosphere models to accurately locate precipitation events above a certain threshold (Mesinger, 1996). So far, this adaptation of the threat score analysis has never been applied to assess the ability of the Eta model to accurately forecast surface events over oceanic surfaces.

Spatial match score, however, only provides an absolute relation between the predictions and observation on the basis of the exact placing and timing of the event under investigation. The second diagnostic verification method, termed spatial similarity, provided a value-added spatial representation that was indexed according to the degree of similarity. This approach was selected because it takes into account the inherent errors in model verification, namely the limited spatial representativeness and accuracy of the highly variable measurements (such as surface winds over the oceans), thus providing a more realistic assessment of the skill of the Eta model in spatial terms. In addition, spatial similarity assisted model verification by employing a similarity measure that was able to separate out feature clusters. By finding image categories, the similarity index was able to (1) calculate which categories are close to each other in space, and (2) explain why two representations of image segments were similar in the context of numerical predictability. In a nutshell, the focus of the spatial similarity routine was both on how the overall prediction is similar to the observation, and equally on how each of their subparts are similar. A thorough literature search on the subject matter shows a complete lack of this approach in atmospheric modelling. Spatial similarity has been used to measure similarity between remotely sensed images for pattern recognition (Jain and Hoffmann, 1988), and to retrieve images from image databases using query-by-sketch operations (Agouris *et al.*, 1997).

The use of geostatistics constituted the third approach to evaluate the predictive skill of the Eta model. This was done in the context of understanding the impact, on spatial terms, of improving the initial surface boundary conditions of the atmosphere model, as described in chapter 6 (see section 8.2.4. below).

The development of analytical routines to assess the skill of the Eta model in spatial terms was another substantive achievement of this

study. Chapter 5 evaluated how this analysis can be instrumental to identify model errors in a spatial context.

8.2.4. Assessing the impact of using microwave-derived SST to initialise the surface boundary conditions of the atmosphere model.

The optimisation criterion identified in section 2.1.3. for the improvement of the surface boundary description of the Eta model was formulated and tested in chapter 6. In this context, the use of a novel SST dataset derived by the Tropical Microwave Imager was evaluated against a conventional method, using model-analysed SST dataset. While keeping all conditions the same, the remotely sensed product led to a yearly average of around 10% improvement in the prediction of the 10 m wind speed. This improvement was another methodological achievement of this study. Thiebaux *et al.* (2001) described a similar approach to initialise the NCEP Weather Analysis and Forecasting suite of models by using 50 km SST derived from the most recent 24-hours of *in situ* and satellite-derived surface temperature data. This approach was implemented on 30 January 2001, and now provides the sea surface temperature fields for the Meso Eta Model, formerly provided by the NESDIS 50 km satellite-only sea surface temperature analysis. They report that this new SST analysis provides a more accurate lower temperature boundary over water for the Eta and this has improved the marine boundary layer evolution. However no objective statistical analysis has been reported by the group.

Throughout chapter 6, the diagnostic verification routines developed were applied to evaluate the spatial context of the improved model predictions. Both the spatial match score (that measures the precise spatial hit of wind speed categories) and the spatial similarity index, highlighted the superiority of the microwave data to initialise the surface boundary condition of the Eta model. Case studies covering the

main climatic regimes of the area of interest were discussed in this study.

A novelty in the field of atmosphere model verification is the use of semi-variance analysis to model the spatial structure of the residual fields between predictions and observations, and to translate the degree of spatial correlation in numerical and graphical form. This approach supported the results shown by the standard and diagnostic verification, providing further evidence of the improved correspondence between the *experimental* forecasts and collocated observations. Geostatistics described a prevalent gaussian model for the residuals for both the *reference* and *experimental* setup that were characterised by low noise, and having mild degree of anisotropy in the 45° direction. However, variography proved to be a less sensitive tool than the spatial match score for the purpose of identifying the degree of spatial correspondence.

In summary, the *experimental* model setup performed better than the conventional, *reference* one both in quantitative and spatial terms. The extent of the improvement was consistent throughout the study period and it is evident that the mesoscale spatial information offered by the novel remotely sensed dataset is the main cause for such an improvement. Chapter 6 discusses the major constraints of the verification analysis which was based on a single-verification date approach. The choice of specific dates throughout the entire annual analysis depended on the availability of observations to both initialise and validate the two competing models.

8.2.5. Improving oceanic forcing and prediction.

The final goal of this study was presented in chapter 7. The improvements achieved by the previous chapters were ultimately transferred to the ocean model in the form of improved surface boundary conditions to initialise the 15-day ocean model run. The

benefit of having these improved conditions was evaluated by comparing ocean model predictions against a similar model setup that was initialised by the conditions provided by the reference model described in chapter 6. The improved surface boundary conditions resulting from the fine-tuning of the Eta model, coupled to its initialisation using remotely-sensed data acquired by the Tropical Microwave Imager is a novel achievement both for the technical progress of the POM model as well as for its application in the Mediterranean region.

Another technical achievement shown by this study was the successful assimilation of microwave-derived SST into the ocean model. The goals identified in section 2.1.4. were formulated and tested out in chapter 7. This resulted in the optimisation of a data assimilation scheme able to achieve a final forecast for the sea surface temperature that was accurate in both quantitative as well as in spatial terms. The mean bias over the entire 15-day model integration accounted to only –0.05 °C. These results show an improvement over other ocean forecasting systems in the region (e.g. Nittis *et al.*, 2001) that show a bias of 0.1 to 0.8 °C when the 24-hour POM-forecasted SST is compared to collocated *in situ* buoy measurements.

The creators of POM attempted to measure the benefits of assimilating AVHRR-SST into POM (Ezer and Mellor, 1997), but their validation methods was based simply on the visual observation of the predicted Gulf Stream against observations. Assimilation of SST also led to an effective error reduction in the upper layers of the ocean model (above 100m). The authors recommend the combined use of sea surface temperature and sea surface height (obtained by orbiting altimeters) to improve the model skill at lower depths.

The sub-mesoscale spatial information provided by the remotely-sensed, high-resolution thermal ocean maps was equally well-simulated as a result of the most efficient data assimilation scheme identified by this study. The predicted information on the surface water circulation

produced by the present study was much more detailed than that obtained by Horton *et al.* (1997) using a ten-day POM integration over the Ionian basin.

The resulting setup of the improved, high-resolution, ocean forecasting system is illustrated in figure 8.1. The data derived by the orbiting microwave sensor onboard the TRMM satellite is central to (1) the provision of initial SST data for both the atmosphere and ocean model, and (2) model verification. The optimal adjustment of the viscous sublayer depth plays an important role in the provision of accurate surface fluxes, whilst the use a 24-hour nudging period to assimilate SST in POM adjusts the model fields towards the remote sensing observations.

8.3. Future research directions.

The purpose of this section is to address a number of possible research directions that might follow on from this study.

8.3.1. Fine-tuning the multiple regression models for AVHRR calibration.

The look-up table shown in section 4.4.2.2. can be further fine-tuned to reflect the atmospheric variability of the central Mediterranean. This can be done by collocating accurate SST data (derived by *in situ* buoys[146], onboard measurements, or microwave remote sensing) with thermal radiance scenes acquired over the area. An ideal dataset is the World Ocean Atlas from which historical *in situ* data for the Mediterranean region can be extracted and collocated with archived infrared radiances acquired by AVHRR.

[146] *for which a correction would be needed to convert the bulk-SST into a skin-SST.*

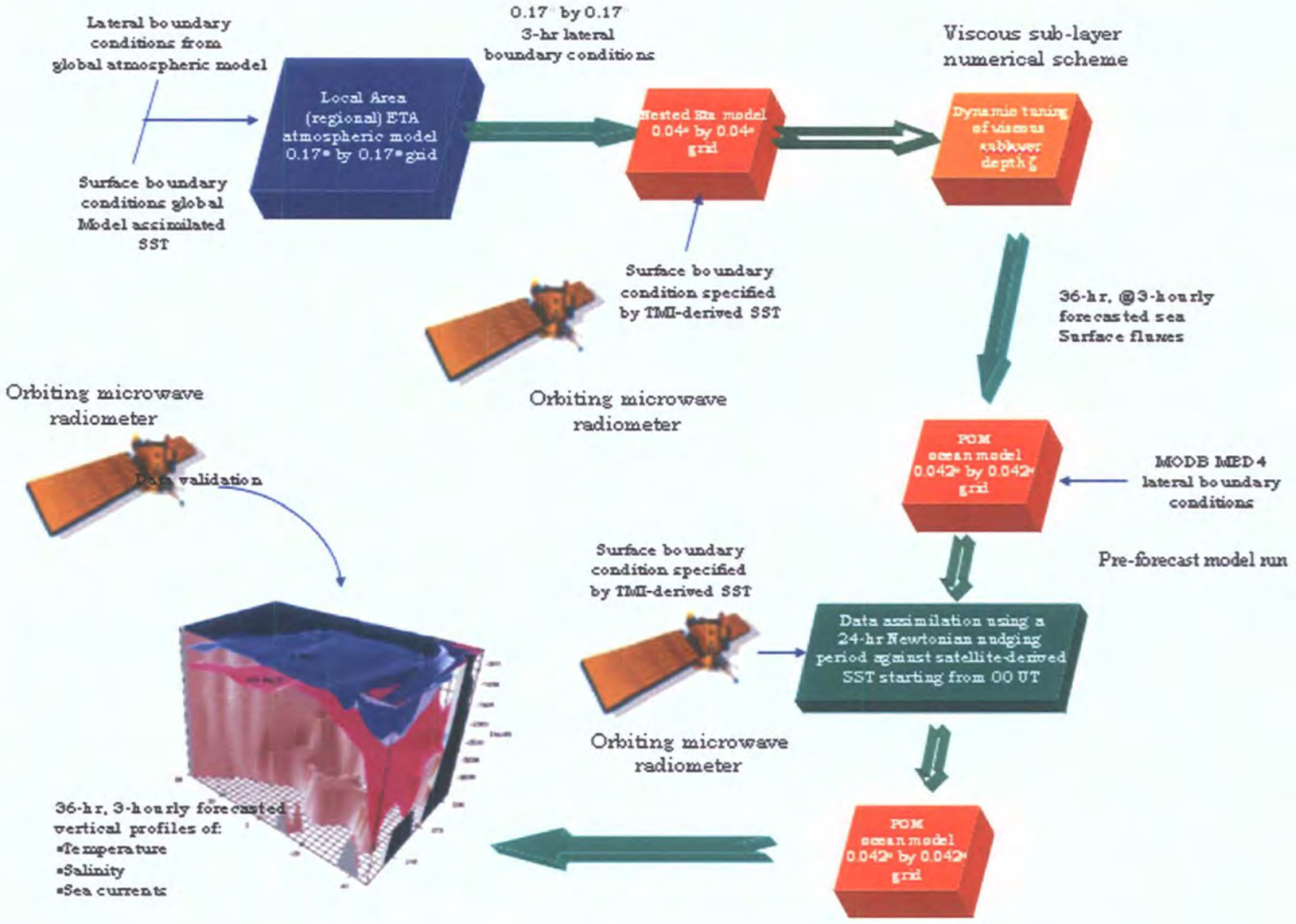

Figure 8.1. Scheme representing the main improvements of the high-resolution, ocean forecasting system for the central Mediterranean resulting from the present study.

8.3.2. Need for new generation of satellite SST.

This thesis points towards the need for a new generation of satellite SST product based on merged multi-sensor array that can simultaneously derive infrared and microwave SST. The challenge is to develop a new generation of SST data products that capitalise on the exceptional benefits of synergistic use of both infrared and microwave sensors to determine SST, as demonstrated by this thesis. Apart from highlighting the systematic differences between the two data sets that, in part is due to the operation of the sensor (i.e. skin and subskin), the all-weather microwave sensor can provide a source of calibration for the finer spatial resolution infrared sensor (e.g. fig. 8.2). Merging these data can also lead to the understanding of the diurnal dependence of the bulk, subskin and skin SST that is required for the initialisation of numerical weather prediction models.

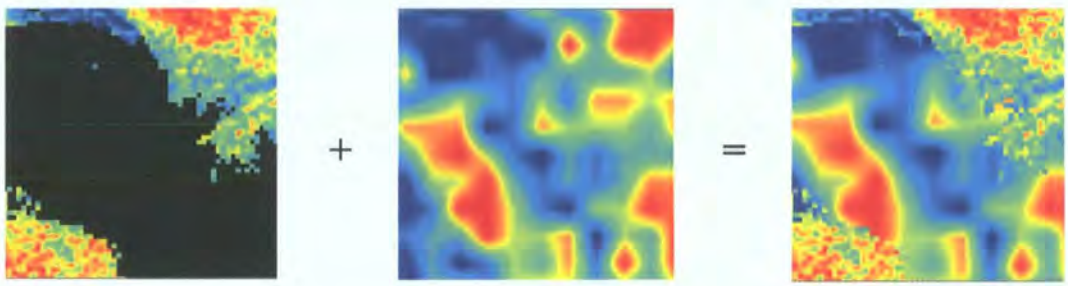

Figure 8.2a-c. A simple example illustrating the benefits of fusing (a) a high-resolution SST map retrieved by the Advanced Very High Resolution Radiometer containing data gaps (due to aerosols or cloud contamination), with (b) an all-weather, lower resolution SST map retrieved by the Tropical Microwave Imager. Using data interpolation techniques, the final, high-resolution field can be used for data assimilation, model initialisation and/or model verification purposes.

The future of microwave-derived SST, with its provision of accurate, all-weather global coverage would soon be complimented by a wider research on its applicability. This thesis can be viewed as one of the

first research efforts that utilises this data source to improve the predictive capability of ocean forecasting systems. Apart from the orbiting TRMM satellite, the recently launched AMSR series of instruments on AQUA (launched May 2003) and ADEOS-II (launched December 2003) are now providing even more accurate retrievals of sea surface temperature data. This availability is leading to the generation of fused SST products as part of the GODAE High-Resolution SST Pilot Project (GHRSST-PP), consisting of twice-daily, global SST fields originally derived from the TMI and AMSR-E orbiting sensors[147]. Near future sources of accurate SST data will include the Spinning Enhanced Visible and Infrared Imager (SEVIRI) and the Infrared Atmospheric Sounding Interferometer (IASI) instruments on the MSG and METOP missions respectively.

The proposed synergy will be very challenging given the number and diversity of inputs. As argued by Merchant (2003), the provision of a merged final product with optimal quality requires various strategies addressing the issues of retrieval and inter-calibration, scale, timing and location of observation, data interpolation and fusion.

8.3.3. Need for more observations for model initialisation and verification.

This thesis would have greatly benefited if an enhanced frequency of observations were available for model initialisation and verification. The global microwave-derived SST is now much more extensive thanks to the recent launching of the AQUA and ADEOS-II satellites, making this data more feasible to use for daily initialisation of atmosphere and ocean models. An enhanced sampling rate would further support model verification, and plans are already available for the launching of a cluster of orbiting small radiometer satellites flown in constellation configuration to provide the necessary diurnal sampling needed to force and verify meteorological models (Kummerow *et al.*, 2000). In particular,

[147] *http://www.remss.com/conf/gentemann/Blended%20SST3.doc (accessed on*

the availability of air-sea fluxes at high spatio-temporal resolution can be instrumental to fine-tune their simulation and prediction by atmosphere models. At the same time, observational uncertainty still limits the precise measurement of the forecast quality; ideally observational uncertainty should be taken into account in verification studies, but this objective is very difficult to actually accomplish and should be a subject of future research.

This study recommends that it is necessary to verify high-resolution forecasts using remotely sensed data and to develop in the future, ocean forecasting models that are able to represent their forecasts in the same way as the observations, including scaling and data formatting. It also recommends that a more refined approach is used when comparing forecasts and observations that have different spatial scales. Translating them both to the same scale is not always the best approach. One possibility would be to "ramp down" the scales to allow comparison. Other approaches for moving between scales – such as wavelet transforms – might be more appropriate than simple interpolation to produce finer observation grids. However, this area still requires further research and testing.

8.3.4. Impact of model resolution.

Further studies on the impact of increasing the model resolution on its predictive quality are needed. Preliminary results of this study showed that the 10 m wind magnitude forecasted by a nested, high-resolution (0.042° by 0.042°) Eta model shows a reduction in the RMSE compared to the same model working at 0.17° by 0.17° (fig. 8.3). Moreover, these results suggest that the higher accuracy may be coming from improved boundary conditions of the nested Eta model, which better define the conditions during the first 12 hours of model integration run. This study recommends further research to examine the sensitivity of a high-resolution Eta model to capture small-scale, non-linear variability, and

---

30.10.04).

whether this would limit the skill of high-resolution atmosphere and ocean models.

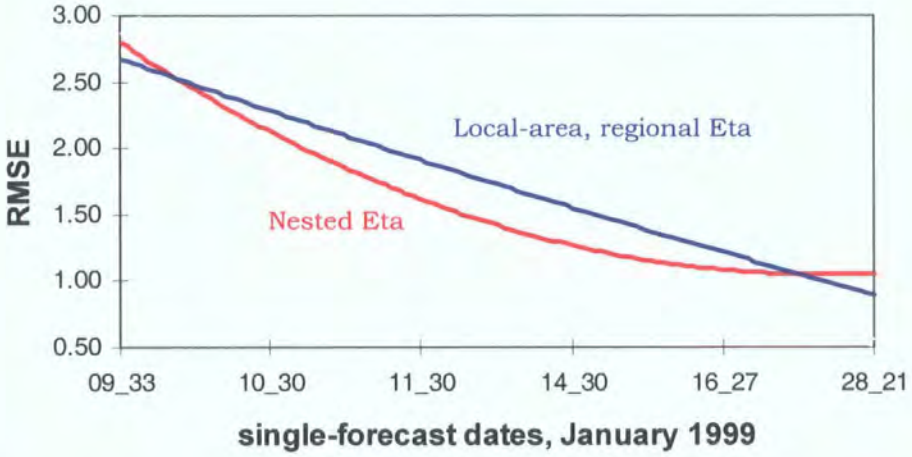

Figure 8.3. RMSE values for the predicted 10 m wind magnitude by the regional, local area Eta model (working at a resolution of 0.17° by 0.17°), and the nested Eta model (working at a resolution of 0.04° by 0.04°), against collocated measurements derived from the orbiting TMI sensor. X-axis relates to the forecasted date during January and nth hours in UT in the form dd_hr.

A fully objective study of this kind is very difficult to conduct as long as collocated observations at the same pixel resolution are not available. A feasibility study can be helpful to define the current limits of high-resolution modelling and to propose new Earth-observation missions to address this issue.

8.3.5. Closing the cycle to a fully-coupled ocean forecasting system.

With the provision of high spatio-temporal SST coverage by orbiting microwave sensors, coupled to the improved predictive capability of the POM model, the one-way coupling of the ocean forecasting system can now be transformed into a full, two-way coupled system. The final link is the provision of predicted SST fields by the POM model serving as the

initial surface boundary condition of the Eta model. The inclusion of the diurnal variability of the SST, linked to a 3-hourly updating frequency of the lower boundary condition of the POM model, can result in an accurate and extended medium- to longer-range prediction. However, coupling of atmosphere-ocean models requires a thorough understanding of the long-term dependence and coupling of small-scale atmospheric and ocean circulation and is a subject of future research.

8.3.6. Refined exploratory spatial data analysis for ocean forecasting systems.

Higher-resolution models need to be given a proper evaluation that measures well their predictive capabilities. When fine detail becomes one of the primary goals of a predictive model, new approaches need to be developed to characterise the observed and forecast fields. This thesis has shown how spatial analysis can provide users with more detailed information about the high-resolution forecasts and their quality.

This study recommends that verification of fine-scale modelling should rely more on entity-based techniques, pattern recognition, and exploratory spatial data analysis techniques. At the same time, computing environments for spatial data analysis are undergoing rapid change and are now able to address new theoretical questions leading to ever more sophisticated spatial analysis tools. This thesis showed the ease of geocoding modelled and observed data and the feasibility of analysing spatially the features of both forecasts and observation, and their relationships.

It is likely that the incorporation of spatial analysis as a standard routine for model verification will generate a demand for dedicated software tools, either in isolation, or in conjunction with existing GIS or statistical software. Based on the experience gained by this study, a number of recommendations are put forward in this respect. First, new

spatial analysis tools need to be modular, allowing the incorporation of reusable components to address the specific analytical requirements of numerical modelers. Secondly, new software tools will need to be able to read and manipulate spatial data which have different formats, independently whether they are obtained from satellite remote sensing platforms or numerical models. This is likely to be accomplished by specialised scripts that translate various formats into a common structure. Thirdly, the potential in terms of added functionality that could result from the fostering of a large community of developers in an "open source" context, should be taken into account.

REFERENCES.

Alvera-Azcarate, A., Barth, A., Ben Bouallegue, Z., Vandenbulke, L., Rixen, M., and Beckers, J.M., (2004), Wavelets in the forecast verification of an assimilation experiment in the Ligurian Sea. International Committee for the Scientific Exploration of the Mediterranean Sea, 37, p 81.

Anselin, L., (1999), Interactive techniques and Exploratory Spatial Data Analysis. Geographical Information Systems: principles, techniques, management and applications (Longley, P., Goodchild, M., Maguire, D., and Rhind D., eds.). Cambridge: Geoinformation International, 1999.

Antoine, J.Y., Derrien, M., Harang, L., Borgne, P., Le Gleau, H. and Le Goas, C., (1992), Errors at large satellite zenith angles on AVHRR derived sea surface temperatures. International. Journal of Remote Sensing, 13, 1797-1804.

Aqouris P., Stefanidies A., and Egenhofer M.J., (1997), I.Q. Image Query by sketch. Available at <http://www.spatial.maine.edu/~peggy/IQ.html>. Accessed on 30.10.04.

Aranuvachapun, S., and Maskell, S.J., (1997), A residual analysis method for quantitative comparison of spatial data from the Iceland-Faeroes front. Ocean Engineering, 24, 8, 721-741.

Arbelo, M., and Herrera, F., (1995), Comparison of total water vapour content obtained from TOVS-NOAA with radiosoundings data in Canary Islands zone. Atmospheric Sensing and Modelling II (Santer R.P., ed.), SPIE Proceedings Vol. 2582, 178-184, ISBN: 0-8194-1946-X.

Arbelo M., Hernandez-Leal P., Diaz J. P., Exposito F. J., and Herrera F., (2000), Efficiency of a global algorithm for retrieving SST from satellite data in a subtropical region. Adv. Space. Res., Vol. 25, No. 5, 1041-1044.

Atkinson P.M., and Curran P.J., (1995), Defining an optimal size of support for remote sensing investigations. IEEE Transactions on Geosciences and Remote Sensing, 33, 3, 768-776.

Atkinson P.M., and Lewis P (2000), Geostatistical classification for remote sensing: an introduction. Computers and Geosciences, 26, 361-371.

Atlas, R., Hoffman, R.N., Bloom, S.C., Jusem, J.C. and Ardizzone, J., (1996), A multilayer global surface wind velocity dataset using SSM/I wind observations. Bulletin of American Meteorological Society, 77(5) 869-882.

Barnier, B., (1998), Forcing the ocean. Ocean modelling and parameterisation (Chassignet E. P., and Verron, J. eds.), Proceedings of a NATO ASI, Les Houches, France, Jan 20-30, Dodrecht Kluwer, 451pp.

Barnier, B., Siefridt, L. and Marchesiello, P., (1996), Thermal forcing for a global ocean circulation model using a three-year climatology of ECMWF analysis. Journal of Marine Systems, 6, 363-380.

Barton I.J., (1995), Satellite-derived sea surface temperatures: Current status. Journal of Geophysical Research, 100, C5, 8777-8790.

Barton I.J, Prata A.J., and Cechet R.P., (1995), Validation of the ATSR in Australian water. Journal of Atmospheric Oceanic Technology, 12, 290-300.

Barton I.J., Zavody A.M., O'Brian M.D., Cutten D.R., Saunders R.W., and Llewellyn-Jones D.T., (1989), Theoretical algorithms for satellite-derived sea surface temperatures. Journal of Geophysical Research, 94, 3365-3375.

Bell M.J., Forbes R.M., and Hines A., (2000), Assessment of a Global Data Assimilation System for real-time operational ocean forecasting. Journal of Marine Systems, 25, 1-22.

Beljaars A.C.M., (2001), Ocean fluxes in the ECMWF model WCRP/SCOR Workshop on Intercomparison and Validation of Ocean-Atmosphere Flux Fields, Monday May 21 - Thursday May 24, 2001 Bolger Center, Potomac, MD (Metropolitan Washington, DC area).

Bentamy A., Grima N., Quilfen Y., Harscoat V., Maroni C., and Pouliquen S., (1997), An atlas of surface wind from ERS-1 scatterometer measurements 1991-1996, Janvier, Technical report DRO/OS, vol. 97-02, IFREMER BP 70, 29280 Plouzane, France.

Berger M., Camps A., Font J., Kerry Y., Miller J., Johannessen J., Boutin J., Drinkwater M.R., Skou N., Floury N., Rast M., Rebhan H., and Attema E., (2002), Measuring Ocean Salinity with ESA's SMOS Mission – Advancing the Science bulletin 111. Available at <http://esapub.esrin.esa.it/bulletin/bullet111/SMOS113-122.pdf.> Accessed on 30.10.04.

Black T.L., and Janjic Z.I., (1988), Preliminary forecast results from a step-mountain Eta coordinate regional model. Eighth Conference on Numerical Weather prediction, Baltimore, American Meteorology Society, 442-447.

Black T.L., and Mesinger F., (1989), Forecast performance of NMC's eta coordinate regional model, 12th Conf. on Weather Analysis and Forecasting, Monterey, CA, American Meteorology Society, 551-555.

Blumberg A.F., and Mellor G.L., (1987), A description of a three-dimensional coastal ocean circulation model, Heaps N.H., (ed.), Three-dimensional coastal ocean circulation models. Coastal Estuarine Science., Vol. 4, 1-16, AGU, Washington, DC.

Brasseur P., Beckers J.M., Brankart J.M., and Schoenauen R., (1996), Seasonal temperature and salinity fields in the Mediterranean Sea: Climatological analysis of a historical data set. Deep Sea Research, Part II, 43, 2, 159-192.

Brasseur P., Blayo E., and Verron J., (1996), Predictability experiments in the North Atlantic Ocean: Outcome of a quasi-geostrophic model with assimilation of TOPEX/POSEIDON altimeter data. Journal Geophysical Research, 101, C6, 14161-14173.

Brenner S., and Rosentraub Z., (2004), The influence of atmospheric pressure variations on the circulation in the Levantine basin, Intergovernmental Commission for thee Scientific Exploration of the Mediterranean Sea Conference, 37, p88.

Brown B., Takacs A., Mahoney J., and Fowler T., (2002), Summary of Workshop on Forecast Verification: Making Verification More Meaningful 30 July – 1 August 2002 at the National Center for Atmospheric Research (NCAR), Boulder, CO. Available at <http://www-ad.fsl.noaa.gov/fvb/publications/articles/summary_forecast_verif_2002.pdf>. Accessed on 30.10.04.

Brutsaert W., (1982), Evaporation into the Atmosphere: Theory, History and Applications (Reidel D., ed.), Hingham MA.

Burman, R.D., Jensen, M.E., and Allen, R.G. (1987), Thermodynamic factors in evapotranspiration. Procedures for Irrigation and Drainage

Special Conference (James, L.G., and English, M.J., eds.), ASCE, Portland, Ore.

Buzzi A., Fantini M., Malguzzi P., and Nerozzi F., (1994), Validation of a limited area model in cases of Mediterranean cyclogenesis: surface fields and precipitation scores. Meteorology and Atmospheric Physics, 53, 137-153.

Castellari S., Pinardi N., and Leaman K., (1998), A model study of air-sea interaction in the Mediterranean sea. Journal of Marine Systems, 18, 89-114.

Chai F., Xue H., Jiang M., and Thomas A., (1999), Coupled circulation and ecosystem model with coastal applications, Proceedings from the SIGMA Coordinate Ocean Model Users meeting '99. Bar Harbour, Maine, US, 20-22 September 1999.

Charnock H., (1994), Air-Sea exchanges and meridional fluxes. Ocean Processes in Climate Dynamics: Global and Mediterranean examples (Malanotte-Rizzoli and Robinson A.R., eds.), 1-27, Kluwer Academic Publishers.

Chassignet E. P., Bell M. J., Brasseur P., Evensen G., Griffies M., Hurlburt H. E., Leprovost C., Madec G., McClean J., Verrron J., Wallcraft A. J., (2004), The Modeling Component of Ocean Forecasting. The Global Ocean Data Assimilation Experiment Second Symposium 1-3 November, St Petersburg FL, USA

CLIVAR, (1996), Report of CLIVAR upper ocean panel - second session and joint workshop with CLIVAR NEG-1: Assessment of the Pacific Observing System for Analyses, Model-Testing and El Nino Forecasts, Villefranche-sur-Mer, 21-24 October 1996. Available at <http://www.clivar.com/publications/wg_reports/uop/uop_2.htm>. Accessed on 30.10.04.

Cobb M.A., Chung M.J., Foley III.H., Petry F.R., Shaw K.B., and Miller H.V., (1998), A rule-based approach for the conflation of attributed vector data, GeoInformatica: An International Journal on Advances of Computer Science for Geographical Information Systems, 2, 1, 7-37.

Coll C., Caselles V., Sobrino J.A., and Valor E., (1994), On the atmospheric dependence of the split-window equation for land surface temperature. International Journal on Remote Sensing, 15, 105-122.

Curran P.J., (1988), The semi-variogram in remote sensing: an introduction. Remote Sensing of Environment, 24, 3, 493-507.

D'Almeida G.A., (1986), A model for Saharan dust transport. Journal of Climate and Applied Meteorology, 25, 903-916.

D'Ortenzio F., Marullo S. and Santoleri R., (2000), Validation of AVHRR Pathfinder SST's over the Mediterranean Sea. Geophysical Research Letters, 27, 2, 241-244.

da Silva, A.M., Young C.C., Levitus S., (1994a), Atlas of Surface Marine Data 1994, Volume 1: Algorithms and Procedures, NOAA Atlas NESDIS 6. U.S. Department of Commerce, NOAA, NESDIS.

da Silva, A.M., Young C.C., Levitus S., (1994b), Atlas of Surface Marine Data 1994, Volume 2: Anomalies of Directly Observed Quantities. NOAA Atlas NESDIS 7. U.S. Department of Commerce, NOAA, NESDIS.

da Silva, A.M., Young C.C., Levitus S., (1994c), Atlas of Surface Marine Data 1994, Volume 3: Anomalies of Heat and Momentum Fluxes, NOAA Atlas NESDIS 8. U.S. Department of Commerce, NOAA, NESDIS.

da Silva, A.M., Young C.C., Levitus S., (1994d), Atlas of Surface Marine Data 1994, Volume 4: Anomalies of Fresh Water Fluxes, NOAA Atlas NESDIS 9. U.S. Department of Commerce, NOAA, NESDIS.

da Silva, A.M., Young C.C., Levitus S., (1994e), Atlas of Surface Marine Data 1994, Volume 5: Anomalies of Miscellaneous Derived Quantities, NOAA Atlas NESDIS 10. U.S. Department of Commerce, NOAA, NESDIS.

Daley R., (1991), Atmospheric Data Analysis, Cambridge Univ. Press, New York.

Darnell W.L., Staylor W.F., Ritchey N.A., Gupta S.K., and Wilber A.C., (1996), Surface radiation budget: A long term global dataset of shortwave and longwave fluxes. American Geophysical Union. Available at <http://www.agu.org/eos_elec/95206e.html>. Accessed on 30.10.04.

Day C., (2000), Two satellites observe details of ocean-atmosphere coupling. Physics Today, June 2000, 23-24.

De Mey P., Benkiran M., (2002), A multivariate reduced-order optimal interpolation method and its application to the Mediterranean basin-scale circulation. Ocean Forecasting, Conceptual basis and applications (Pinardi N. and Woods J.D., eds.), 472pp, Springer-Verlag, Berlin Heidelberg New York.

DeCosmo, J., Katsaros, K.B., Smith S.D., Anderson R.J., Oost W.A., Bumke K., and Chadwick H.M., (1996), Air-sea exchange of water vapour and sensible heat: The Humidity Exchange Over the Sea (HEXOS) results. Journal of Geophysical Research, 101, 12001-12016.

Dekic L., Zivkovic M., and Vasic R., (1997), Review of activities in regional weather prediction at the Federal Hydro meteorological

Institute of Yugoslavia. Proceedings of the Symposium on regional Weather Prediction on Parallel Computer Environments (Kallos G., Kotroni V. and Lagouvardas K., eds.), 59-64.

Donlon C.J., Minnett P.J., Gentemann C., Nightingale T.J., Barton I.J., Ward B., and Murray M.J., (2002), Toward Improved Validation of Satellite Sea Surface Skin Temperature Measurements for Climate Research. Journal of Climate, 15, 353-369.

Doswell C.A., (2000), On the use of models in meteorology. Available at <http://webserv.chatsystems.com/~doswell/forecasting/models.html>. Accessed on 30.10.04.

Drakopolous P.G., and Lascaratos A., (1997), Modeling the Mediterranean sea: climatological forcing. Journal of Marine Systems, 20, 157-173.

Dubayah R., Wood E.F., and Lavallee D., (1997), Multiscaling analysis in distributed modelling and remote sensing: an application using soil moisture. Scale in Remote Sensing and GIS (Quattrochi D.A., and Goodchild M.F., eds.). Lewis Publishers, 93-112.

Ellingson R.G., Yanuk D.J., Gruber A., (1989a), Effects of the choice of meteorological data on a radiation model simulation of the NOAA technique for estimating outgoing longwave radiation from satellite radiance observations. Journal of Climate and Applied Meteorology, 31, 761-765.

Ellingson R.G., Yanuk D.J., Lee H-T., Gruber A., (1989b), A technique for estimating outgoing longwave radiation from HIRS radiance observations. Journal of Atmospheric and Oceanic Technology, 6, 706-711.

Emery W.J., Yunyue Y., Gary A.W., Schluessel P., Reynolds R.W., (1994), Correcting infrared satellite estimates of sea surface

temperature for atmospheric water vapor attenuation. Journal of Geophysical Research, 99, C3, 5219-5236.

EuroGOOS (2004), available at <http://www.eurogoos.org/>. Accessed on 30.10.04.

EuroGOOS (2003), EuroGOOS Priorities. EG03.43. November 2003. p. 1

Ezer T., (2000), On the seasonal mixed-layer simulated by a basin-scale ocean model and the Mellor-Yamada turbulence scheme. Journal of Geophysical Research, 105, C7, 16843-16855.

Ezer T., and Mellow G.L., (1997), Data assimilation experiments in the Gulf stream region: Hew useful are satellite-derived data for nowcasting the subsurface fields? Journal of Atmospheric and Oceanic Technology, 14, 1379-1391.

Ferrier B., Lin Y., Parrish D., Pondeca M., Rogers E., Manikin G., Ek M., Hart M., DiMego G., Mitchell K., and Chuang H-Y., (2003), Changes to the NCEP Meso Eta analysis and forecast system: Modified cloud microphysics, assimilation of GOES cloud-top pressure, assimilation of NEXRAD 88D radial wind velocity data. Available at <http://wwwt.emc.ncep.noaa.gov/mmb/tpb.spring03/tpb.htm> Accessed on 30.10.04.

Fischer J., and Flemming N.C., (1999), Operational Oceanography: Data Requirements Survey. EuroGOOS Publication No. 12, February 1999 – EG99.04, 60pp.

Flemming N.C., (1995), Making the case for GOOS. Sea Technology, Special feature, 44-49.

Folland C.K., and Parker D.E., (1995), Correction of instrumental biases in historical sea surface temperature data. Quarterly Journal of the Royal Meteorology Society, 121, 319-367.

Francois C., and Ottle C., (1996), Atmospheric corrections in the Thermal Infrared: Global and Water Vapour Dependent Split-Winwod algorithms – Application to ATSR and AVHRR data. IEEE Transactions on Geoscience and Remote Sensing, 34, 2, 457-469.

Franklin R.B., and Mills A.L., (2003), Multi-scale variation in spatial heterogeneity for microbial community structure in an eastern Virginia agricultural field. FEMS Microbiology Ecology, 44, 3, 335-346.

Fritsch J.M., Houze J., *et al.,* (1998), Meeting summary: quantitative precipitation forecasts: report of the 8th prospectus development team, US Weather Research program. Bulletin of the American Meteorological Society, 8, 985-987.

Gascard, J.-C., (1978), Mediterranean deep water formation baroclinic instability and oceanic eddies. Oceanologica Acta, 1, 3, 315-330.

Gavart M., De Mey P., and Caniaux G., (1999), Assimilation of satellite altimeter data in a primitive-equation model of the Azores-Madeira region. Dynamics of the Atmosphere and Oceans, 29, 217-254.

Gemmill W.H., and Krasnopolsky V.M., (1998), Weather patterns over the ocean retrieved by neural network multi-parameter algorithm from SSM/I. Proceedings of 5th International Conference on Remote Sensing for Marine and Coastal Environment, October 5-7, 1998, San Diego, California.

Gemmill W.H., and Krasnopolsky V.M., (1999), The use of SSM/I data in operational marine analysis. Weather and Forecasting, 14, 5, 789-800.

Gentemann C.L., Wentz F.J., Mears C.A., and Smith D.K., (2004), *In situ* validation of Tropical Rainfall Measuring Mission microwave sea surface temperatures. Journal of Geophysical Research, 109, C04021.

Geshelin Y.S., and Dobson F.W., (1997), Comparative analysis of wind data sets from ERS-1 and NDBC buoys. Fourth International Conference on Remote Sensing for Marine and Coastal Environments, Orlando, Florida, 17-19 March, 1997.

GEWEX (1999), Summary of actions, recommendations and conclusions from the GEWEX radiation panel 1999 meeting (27-30 September 1999, New York City, New York, USA). Available at <http://www.wmo.ch/web/wcrp/documents/grp11draftrpt.html>. Accessed on 30.10.04.

Gill A.E., (1982), Atmosphere-Ocean Dynamics. Academic Press, San Diego, 662pp.

Glahn H.R., Murphy A.H., Wilson L.J., and Sensenius J.S., (1991), Lectures presented at the WMO training workshop on the interpretation of NWP products in terms of local weather phenomena and their verification. Wageningen, The Netherlands, 29 July – 9 August 1991, WMO/TD No. 421.

Gleckler, P.J. and Weare B.C., (1997), Uncertainties in global ocean surface heat flux climatologies derived from ship observations. Journal of Climate, 10, 2764-2781.

Goeber M., and Milton S.F., (2002), Verifying precipitation events forecast by the mesoscle model. NWP Gazette, March 2002, 9-11. Available at <www.metoffice.com/research/nwp/publications/nwp_gazette/mar02/verify.html>. Accessed on 30.10.04.

Gower, J.F.R., (1996), Intercalibration of wave and wind data from TOPEX/POSEIDON and moored buoys off the west coast of Canada. Journal of Geophysical Research, 101, C2, 3817 - 3829.

Graber H.C., Ebuchi N., Vakkayil R., Graber H.C., Ebuchi N., Vakkayil R., (1996), Evaluation of ERS-1 scatterometer winds with ocean buoy observations, 'Prospects for the 21st Century' Conference Proceedings. OCEANS 96 MTS/IEEE (Cat. No.96CH35967), 4 vol. (1564+vii+145), 1157-65 vol. 3.

Grassl H., (1976), The dependence of the measured cool skin of the ocean on wind stress and total heat flux. Boundary-Layer Meteorology, 10, 465-474.

Gruber A., Ellingson R.E., Ardanuy P., Weiss M., Yang S.K., and Oh S.N., (1994), A comparison of ERBE and AVHRR longwave flux estimation. Bulletin of American Meteorological Society, 75, 2115-2130.

Hagan D.E., (1989), A basic limitation of the split window method for SST retrievals when applied to a wide range of water vapour conditions. Geophysical Research Letters, 16(8), 815-817.

Hamad N., Millot C., and Taupier-Letage I., (2004), The surface circulation in the Eastern basin of the Mediterranean Sea. Intergovernmental Commission for the Scientific Exploration of the Mediterranean Sea Conference, 37, p. 106.

Haney L.R., (1971), Surface thermal boundary condition for ocean circulation models. Journal of Physical Oceanography, 1, 241-248.

Harris A.R., and Mason I.M., (1992), An extension to the split-window technique giving improved atmospheric correction and total water vapour. International Journal on Remote Sensing, 5, 881-892.

Hauser D., Branger H., Bouffies-Cloche S., Despiau S., Drennan W.M., Dupuis H., Durand P., Durrieu de Madron X., Estournel C., Eymard L., Flamant C., Graber H.C., Guerin C., Kahma K., Lachaud G., Lefevre J.M., Pelon J., Pettersson H., Piguet B., Queffeulou P., Taillez D., Tournadre J., and Weill A., (2003), The FETCH experiment: An overview. Journal of Geophysical Research, 108, C3, 8053, doi:10.1029/2001JC001202.

Hoke J.E., and Anthes R.A., (1976), The initialisation of numerical models by a dynamic initialisation technique. Monthly Weather Review, 104, 1551-1556.

Holdaway M.R., (1996), Spatial modelling and interpolation of monthly temperature using kriging, Climate Research, 6, 215-225.

Holland W.R., and Bryan F.O., (1994), Thermal forcing for a global ocean circulation model using a three-year climatology of ECMWF analysis. Journal of Marine Systems, 6, 363-380.

Holt A., (1999), Spatial Similarity and GIS: the grouping of spatial kinds. Presented at SIRC 99 – the 11th Annual Colloquium of the Spatial Information Research Centre, University of Otago, Dunedin, New Zealand, December 13-15, 1999.

Holt A., and Benwell G.L., (1997), Using spatial similarity for exploratory spatial data analysis: Some directions. The 2nd International Conference on GeoComputation, University of Otago, Dunedin, New Zealand, 279-288.

Holt, A., MacDonell, S.G., and Benwell G.L., (1998), Spatial Isomorphism. Department of Information Science Discussion Paper Series, University of Otago, New Zealand, March Number 98:8, 29pp.

Holt, A., MacDonell, S.G., and Benwell G.L., (1998), Assessing the Degree of Spatial Isomorphism for Exploratory Spatial Analysis. The Third International Conference on GeoComputation: Abstracts for paper presentations, Brooks, S.M., McDonnell, R., Longley, P. and Orford S., (eds.), University of Bristol, Bristol, England, 32pp.

Horton C., Clifford M., Schmitz J., and Kantha L.H., (1997), A real time oceanographic nowcast/forecast system for the Mediterranean Sea. Journal of Geophysical Research, 102, 123-125.

Huffman, G.J., Adler R.F., Arkin P., Chang A., Ferraro R., Gruber A., Janowiak J., McNab A., Rudolf B., and Schneider U., (1997), The Global Precipitation Climatology Project (GPCP) combined precipitation dataset. Bulletin of the American Meteorological Society, 78, 5-20.

Hunter G.J., Qiu J., and Goodchild M.F., (1999), Application of a new model of vector data uncertainty. Spatial Accuracy Assessment: Land Information Uncertainty in Natural Resources (Lowell K., and Jaton A., eds.). Chelsea, Michigan: Ann Arbor Press, 320, 203–208.

IOC (1998) "The GOOS 1998 Prospectus", IOC, UNESCO, Paris 168pp

Jain A.K., and Hoffmann R., (1988), Evidence-based recognition of 3D objects. IEEE Transactions on Pattern Analysis and Machine Learning, 10, 6, 783-801.

Janjic Z.I., (1984), Non-linear advection schemes and energy cascade on semi-staggered grids. Monthly Weather Review, 112, 1234-1245.

Janjic Z.I., (1990), The step-mountain coordinate: physical package. Monthly Weather Review, 118, 1429-1443.

Janjic Z.I., (1994), The step-mountain Eta coordinate model: further developments of the convection, viscous sublayer and turbulence closure schemes. Monthly Weather Review, 122, 927-945.

Janjic Z.I., (1996a), The surface parameterisation in the NCEP Eta model. Research Activities in Atmospheric and Oceanic Modelling. CAS/JSC Working Group on Numerical Experimentation, World Meteorological Organisation, 440pp.

Janjic Z.I., (1996b), The Mellor-Yamada level 2.5 turbulence closure scheme in the NCEP Eta model Preprints, 11th AMS Conference on Numerical Weather Prediction, Norfolk, VA, 19-23 August 1996.

Janjic, Z.I., Mesinger F., and Black T.L., (1995), The pressure advection term and additive splitting in split-explicit models. Quarterly Journal of the Royal Meteorological Society, 121, 953-957.

Jones C., Peterson P., and Gautier C., (1997), Satellite data estimation of ocean latent heat flux: a neural network approach. Available at <http://www.crseo.ucsb.edu/esrg/papers/LHF_ams.96/lhf_ams97.html>. Accessed on 01.11.04.

Jones C., Peterson P., and Gautier C., (1999), A new method for deriving ocean surface specific humidity and air temperature: An artificial neural network. Journal of Applied Meteorology, 38, 1229-1245.

Jones C., Peterson P., and Gautier C., (2003), Satellite Estimates of Air Temperature, Specific Humidity, Latent and Sensible Heat Fluxes over the Global Tropics, Technical Report, April 2003, Version 1.0, Institute for Computational Earth System Sciences, University of California, Santa Barbara, 40pp.

Jones E.K., and Roydhouse A., (1994), Spatial representations of Meteorological Data for intelligent retrieval. The sixth Annual Colloquium of the Spatial Research Centre, Proceedings. Benwelll G.L., and Sutherland N.C., (eds.), Dunedin, New Zealand, 45-58.

Josey S.A., (2001), A comparison of ECMWF, NCEP/NCAR and SOC surface heat fluxes with moored buoy measurements in the subduction region of the north-east Atlantic. Journal of Climate, 14, 8, 1780-1789.

Josey S.A., Kent E.C., and Taylor P.K., (1998), The Southampton Oceanography Centre (SOC) Ocean-Atmosphere Heat, Momentum and Freshwater Flux Atlas. Report No. 6, Southampton Oceanography Centre, Southampton, United Kingdom, 30pp+figs. Available at <http://www.soc.soton.ac.uk/JRD/MET/PDF/hadam3.pdf>. Accessed on 30.10.04.

Josey S.A., Kent E.C., and Taylor P.K., (1999), New insights into the ocean heat budget closure problem from analysis of the SOC air-sea flux climatology. Journal of Geophysical Research, 102, C13, 27,961-27,972.

Josey, S.A., Kent E.C., and Taylor P.K., (2002), On the Wind Stress Forcing of the Ocean in the SOC Climatology: Comparisons with the NCEP/NCAR, ECMWF, UWM/COADS and Hellerman and Rosenstein Datasets. Journal of Physical Oceanography, 32, 7, 1993-2019.

Josey, S., Pascal R., Taylor P., and Yelland M., (2003), A new formula for determining the atmospheric longwave flux at the ocean surface at mid-high latitudes. Journal of Geophysical Research, 108, C4, doi:10.1029/2002JC001418.

Justice C.O., Dugdale G., Townshend J.R.G., Narracott A.S., and Kumar M., (1991), Synergism between NOAA-AVHRR and Meteosat data for studying vegetation development in semi-arid West Africa. International Journal of Remote Sensing, 12, 6, 1349-1368.

Kallos G., Nickovic S., Papadopoulos A., Jovic D., Kakaliagou O., Misirlis N., Boukas L., Mimikou N., Sakellaridis G., Papageorgiou J., Anadranistakis E., and Manousakis M., (1997), The regional weather

forecasting system SKIRON: An overview. Proceedings of the Symposium on regional Weather Prediction on Parallel Computer Environments (Kallos G., Kotroni V., and Lagouvardas K., eds.), 109-122.

Kanamitsu M., (1989), Description of the NMC Global Data Assimilation and Forecast System. Weather and Forecasting, 4, 3, 335-342.

Kaufman Y.J., Tanre D., Gordon H.R., Nakajima T., Lenoble J., Frouin R., Grassl H., Herman B.M., King D.M., and Tiellet P.M., (1997), Passive remote sensing of tropospheric aerosol and atmospheric correction for the aerosol effect. Journal of Geophysical Research, 102, 16815-16830.

Komen, G.J., Cavaleri L., Donelan M., Hasselmann K., Hasselmann S., and Janssen P.A.E.M., (1994), Dynamics and Modelling of Ocean Waves. Cambridge University Press, 532pp.

Korres G., Lascaratos A., Nittis K., and Perivoliotis A. (1997), On the forced interannual variability of the Mediterranean Sea. Proceedings of the Symposium on regional Weather Prediction on Parallel Computer Environments (Kallos G., Kotroni V., and Lagouvardas K., eds.), 85-91.

Krasnopolsky V.M., and Gemmill W.H., (2001), Using QuikSCAT Wind Vectors in Data Assimilation System", Technical Note, OMB Contribution No. 209, NOAA/NCEP/EMC.

Kriebel K.T., (1996), Cloud detection using AVHRR data. Advances in the use of NOAA AVHRR Data for land application (G. D'Souza *et al.*, eds.), ECS, EEC, EAEC, Brussels and Luxembourg, 195-210.

Kummerrow C., Simpson J., Thiele O., Barnes W., Chang A.T.C, Stocker E., Adler R.F., Hou A., Kakar R., Wentz F., Ashcroft P., Kozu T., Hong T., Okamoto K., Iguchi T., Kuroiwa H., Im E., Haddad Z., Huffman G., Ferrier B., Olson W.S., Zipser E., Smith A.E., Wilheit T.T., North G.,

Krishnamurti T., and Nakamura K., (2000), The status of the Tropical Rainfall Measuring Mission (TRMM) after two years in orbit. Journal of Applied Meteorology, 39, 1965-1982.

Kuo Y.-H., Guo Y.-R., and Westwater E.R., (1993), Assimilation of precipitable water vapor into a mesoscale numerical model. Monthly Weather Review, 121, 1215-1238.

Laprise, R., Ravi Varma M., Denis B., Caya D., and Zawadzki I., (2000), Predictability in a nested limited-area-model. Monthly Weather Review, 128, 12, 4149-4154.

Large, W., and Pond S., (1981), Open ocean momentum flux measurements in moderate to strong winds. Journal of Physical Oceanography, 11, 324-336.

Large, W., and Pond S., (1982), Sensible and latent heat flux measurements over the ocean. Journal of Physical Oceanography, 12, 464-482.

Lascaratos A., and Nittis K., (1998), A high-resolution three-dimensional numerical study of intermediate water formation in the Levantine Sea. Journal of Geophysical Research, 103, 18497-18511.

Lasic L., (1990), Forecasts of AMEX tropical cyclones with step-mountain model. Australian Meteorological Magazine, 38, 207-216.

Lazic L., and Telenta B., (1988), UB/NMC Eta model (documentation). WMO/TMRP Technical Report, 40pp.

Legrand M., Cautenet G., and Buriez J.C., (1992), Thermal impact of Saharan Dust over Land. Part II: Application to Satellite IR Remote Sensing. Journal of Applied Meteorology, 31, 181- 193.

Lermusiaux P.F.J., and Robinson A.R., (2001), Features of dominant mesoscale variability, circulation patterns and dynamics in the Strait of Sicily. Deep-Sea Research, I, 48, 1953-1997.

Li X., Pichel W., Maturi E., Clemente-Colon P., and Sapper J., (2001), Deriving the operational non-linear multichannel sea surface temperature algorithm coefficients for NOAA-15 AVHRR/3. International Journal of Remote Sensing, 22, 4, 699-704.

Liebhold, A., Luzader E., Reardon R., Bullard A., Roberts A., Ravlin W., DeLost S., and Spears B., (1996), Use of a geographic information system to evaluate regional treatment effects in a gypsy moth (*Lepidoptera: Lymantriidae*) management program. Journal of Economic Entomology, 89:1192-1203.

Liu W.T., (1986), Statistical relation between monthly mean precipitable water and surface-level humidity over global oceans. Monthly Weather Review, 114, 1591-1602.

Liu W.T., (1988), Moisture ad latent heat-flux variabilities in the tropical Pacific derived from satellite data. Journal of Geophysical Research, 93, 6749-6760.

Liu W.T., and Niiler P.P., (1984), Determination of monthly mean humidity in the atmospheric surface layer over ocean from satellite data. Journal of Physical Oceanography, 14, 1452-1457.

Liu W.T., Katsaros K.B., and Businger J.A., (1979), Bulk parameterisation of air-sea exchanges of heat and water vapour including the molecular constraints at the interface. Journal of Atmospheric Science, 36, 1722-1735.

Liu L-J., and Rossini A.J., (1996), Use of kriging models to predict 12-hour mean ozone concentrations in metropolitan Toronto-a pilot study. Environment International, 22, 6, 677-692.

Llewellyn-Jones D.T., Minnett P.J., Saunders R.W., and Zavody A.M., (1984), Satellite multichannel infrared measurements of sea surface temperature of the NE Atlantic Ocean using AVHRR/2. Quarterly Journal of the Royal Meteorological Society, 110, 613-631.

Longley, P., and Batty, M., (eds.), (1996), Spatial Analysis: Modelling in a GIS Environment, Cambridge: GeoInformation International.

Manobianco J., Koch S., Karyampudi V.M., and Negri A.J., (1994), The impact of satellite-derived precipitation rates on numerical simulations of the ERICA IOP 4 cyclone. Monthly Weather Review, 122, 341-365.

Mathew K., Nagarani C.M., and Kirankumar A.S., (2001), Split-window and multi-angle methods of sea surface temperature determination: an anlysis. International Journal of Remote Sensing, 22, 16, 3237-3251.

May P.W., (1982), Climatological flux estimates in the Mediterranean Sea. I. Winds and wind stresses. NORDA Tech. Rep. 54, Naval Ocean Research and Development Activity, NSTL Station, Mississippi, 56pp.

May P.W., (1986), A brief explanation of Mediterranean heat and momentum flux calculations. Report of the Naval Oceanographic and Atmospheric Research Laboratory, Stennis Space Centre, Mississippi, USA.

May D., Stowe L., Hawkins J., and McClain E.P., (1992), A correction for Saharan dust effects on satellite sea surface temperature measurements. Journal of Geophysical Research, 97, 3611-3619.

McClain E.P., (1981), Multiple atmospheric window techniques for satellite-derived sea surface temperatures. Oceanography from Space (Gower J., ed.), Plenum, 73-85.

McClain E.P., Pichel W.G., and Walton C.C., (1985), Comparative performance of AVHRR-based multi-channel sea surface temperature. Journal of Geophysical Research, 90, 11587-11601.

McMillan L.M., (1975), Estimation of sea surface temperatures from two infrared window measurements with different absorptions. Journal of Geophysical Research, 80, 5113-5117.

McMillan L.M., and Crosby D.S., (1984), Theory and validation of the multiple window measurements with different absorption. Journal of Geophysical Research, 89, 655-661.

McMurdie L.A., and Katsaros K.B., (1996), Satellite derived integrated water vapour and rain intensity patterns: Indicators for rapid cyclogenesis. Weather Forecasting, 11, 230-245.

McPhaden, M.J., Busalacchi A.J., Cheney R., Donguy J-R., Gage K.S., Halpern D., Ji M., Julian P., Meyers G., Mitchum G.T., Niiler P.P., Picaut J., Reynolds R.W., Smith N., and Takeuchi K., (1998), The Tropical Ocean Global Atmosphere (TOGA) observing system: A decade of progress. Journal of Geophysical Research, 103, 14169-14240.

McWilliams, J.C., (1998), Oceanic general circulation models. Ocean Modelling and Parameterisation (Chassignet E., and Verron J., eds.), Kluwer Academic Publishers, Dordrecht, The Netherlands, 1-44.

Meissner T., Smith D., and Wentz F.J., (2001), A 10-year inter-comparison between collocated SSM/I oceanic surface wind speed retrievals and global analyses. Journal of Geophysical Research, 106, C6, 11731-11742.

Mellor G.L., and Yamada T., (1974), A hierarchy of turbulence closure models for planetary boundary layers. Atmospheric Science, 31, 1791-1806.

Mellor G.L., (1991), An equation of State for Numerical Models of Oceans and Estuaries. Journal of Atmospheric and Oceanic Technology, 8, 609-611.

Mellor G.L., (1998), Users guide for a three-dimensional primitive equation, numerical ocean model. Progress in Atmospheric and Oceanic Science, Princeton University, 41pp. Available at <http://www.aos.princeton.edu/WWWPUBLIC/htdocs.pom/>. Accessed on 30.10.04.

Mellor G.L., and Yamada T., (1982), Development of a turbulence closure model for geophysical fluid problems. Review of Geophysics and Space Physics, 20, 851-875.

Merchant C.J., (2003), Sea surface temperature – a dynamic field: Developments in research and operations. Proceedings of the 2003 Meteorological Satellite Data User's Conference, Weimar, Germany, September-October, 2003. Available at <www.met.ed.ac.uk/~chris/Publications/eumetsat2003_Merchant_CJ.pdf>. Accessed on 30.10.04.

Mesinger F. (1977) Forward-backward scheme, and its use in a limited area model. Contributions to Atmospheric Physics, 50, 200-210.

Mesinger F., (1984), A blocking technique for representation of mountain in atmospheric models. Rivista di Meteorologia Aeronautica, 44, 195-202.

Mesinger F., (1996), Improvements in quantitative precipitation forecasts with the Eta regional and mesoscale models at the National

Centers for Environmental Prediction: The 48-km upgrade. Bulletin of the American Meteorological Society, 77, 2637-2649.

Mesinger, F., (1997), Dynamics of limited-area models: formulation and numerical methods. Meteorology and Atmospheric Physics, 50, 47-60.

Mesinger F., and Black T.L., (1989), Verification tests of the Eta model, October-November 1988. NOAA/NWS/NMC Washington D.C. Office Notes 355, 47pp.

Mesinger F., Brill K., Chuang H-Y., DiMego G., and Rogers E., (2002), Limited Area Predictability: Can "Upscaling" also take place? Research Activities in Atmospheric and Oceanic Modelling, World Meteorological Organisation, 2002.

Mesinger F., Janjic Z.I., Nickovic S., Gavrilov D., and Deaven D.G., (1988), The step-mountain coordinate: model description and performance for cases of Alpine lee cyclogenesis and for a case of an Applachian redevelopment. Monthly Weather Review, 116, 1493-1518.

Millot C., (1991), Mesoscale and seasonal variability of the circulation in the western Mediterranean. Dynamics of the Atmosphere and the Oceans, 15, 179-214.

Minnett P.J., (1990), The regional optimisation of infrared measurements of sea surface temperature from space. Journal of Geophysical Research, 95, 13497-13510.

Minnett P.J., (1991), Consequences of sea surface temperature variability on the validation and applications of satellite measurements. Journal of Geophysical Research, 96, 18475-18489.

Monin A.S., and Obukhov A.M., (1954), Basic laws of turbulent mixing in the surface layer of the atmosphere. Tr. Akad Nauk SSSR, Geofiz. Inst. 24, 163-187.

Murphy A.H., (1997), Forecast Verification. Economic Value of Weather and Climate Forecasts (Katz W., and Murphy A.H., eds.), Eco. Cambridge University Press, 222pp.

Murphy A.H., and Daan H., (1985), Forecast evaluation. Probability, Statistics, and Decision Making in the Atmospheric Sciences (Murphy A.H., and Katz R.W. eds.), 379-437, Boulder , CO, Westview Press.

Murphy A.H., and Winkler R.L., (1987), A general framework for forecast verification. Monthly Weather Review, 115, 1330-1338.

Nittis K., Zervakis V., Perivoliotis L., Papadopolous A., and Chronis G., (2001), Operational monitoring and forecasting in the Aegean Sea: System limitations and forecasting skill evaluation. Marine Pollution Bulletin, 43, 7-12 154-163.

Oberhuber J.M., (1988), An atlas based on the COADS data set: the budgets of heat, buoyancy and turbulent kinetic energy at the surface of the global ocean. Max-Planck-Institut fur Meteorologie, Report No. 15.

Oh S.N., (1998), Estimation of earth OLR using a radiation model calculation and satellite radiance observations. Atmospheric Research, 49, 235-251.

Ohring G., Gruber A., and Ellingson R., (1984), Satellite determination of outgoing longwave radiation flux and infrared window radiance. Journal of Climate and Applied Meteorology, 23, 416-425.

Onken R., Robinson A.R., Lermusiaux P.F.J., Haley P.J., and Anderson L.A., (2003), Data-driven simulations of synoptic circulation and transports in the Tunisia-Sardinia-Sicily region. Journal of Geophysical Research, 108, C9, 8123-8136.

Orlic M., Beg Paklar G., Grbec B., Pasaric M., and Pasaric Z., (2004), A climatological simulation for the middle Adriatic coastal area. Intergovernmental Commission for the Exploration of the Mediterranean Sea Conference, 37, p129.

Ottle C., Outalha S., Francois C., and Le Maguer S., (1997), Estimation of total atmospheric water vapour content from split-window radiance measurements. Remote Sensing of the Environment, 61, 410-418.

Pacanowski R.C., Dixon K., and Rosati A., (1990), Readme file for GFDL-MOM 1.0, Geophysical. Fluid Dynamical Laboratory, Princeton, N. J.

Paccagnella T., Aptruno P., Cacciamani C., (1994), Operational quantitative precipitation forecasting at the regional meteorological Service of Emilia-Romagna Region (Northern Italy): The flood event in Piedmont occurred on November 1994". Proc. Atmospheric Physics and Dynamics in the Analysis and prognosis of precipitation fields, Rome, Nov., 298-307.

Papadopoulos A., Kallos G., Nickovic S., Jovic D., Dacic M., and Katsafados P., (1997), Sensitivity studies of the surface and radiation parameterisation schemes of the SKIRON system. Proceedings of the Symposium on regional Weather Prediction on Parallel Computer Environments (Kallos G., Kotroni V., and Lagouvardas K., eds.), 155-163.

Parrish D.F., and Derber J., (1992), The National Meteorological Centre's spectral statistical interpolation analysis system. Monthly Weather Review, 120, 1747-1763.

Petersen, R.A., and Stackpole J.D., (1989), Overview of the NMC Production Suite. Weather and Forecasting, 4, 313-322.

Pielke R. A., (2001), Further comments on "The differentiation between grid spacing and resolution and their application to numerical modeling". Bulletin of the American Meteorological Society, 82, 699-700.

Pinardi N., and Flemming N., (1998), The Mediterranean Forecasting System EuroGOOS. Publication No.11, November 1998 - EG98.52, 48pp.

Pinardi N., Korres G., Lascaratos A., Roussenov V., and Stanev E., (1997), Numerical simulation of the interannual variability of the Mediterranean Sea upper ocean circulation. Geophysical Research Letters, 24, 4, 425-428.

POEM (1992), General circulation of the eastern Mediterranean. Earth Science Review, 32, 285-308.

Prata A.J., Caselles V., Coll C., Sobrino J. and Ottle C., (1995), Thermal remote sensing of land surface temperature from satellite: current status and future prospects. Remote Sensing Review, 12, 175-224.

Price J.F., Weller R.A., and Pinkel R., (1986), Diurnal cycling: Observations and models of upper ocean response to diurnal heating, cooling, and wind mixing. Journal of Geophysical Research, 91, C7, 8411 - 8427.

Raicich F., (2004), Assessment of temperature and salinity sampling strategies in the Mediterranean Forecasting System. Intergovernmental Commission for the Scientific Exploration of the Mediterranean Sea, Conference, 37, p.137.

Rao C.R.N., (1992), Aerosol radiative corrections to the retrieval of sea surface temperatures from infrared radiances measured by AVHRR. International Journal of Remote Sensing, 13, 1757-1769.

Reis A.P., Sousa A.J., and Cardoso Fonseca E., (2003), Application of geostatistical methods in gold geochemical anomalies identification (Montemor-O-Novo, Portugal). Journal of Geochemical Exploration, 77, 1, 45-63.

Reynolds R.W., (1982), A monthly averaged climatology of sea surface temperature. NOAA Technical Report. NWS 31, Washington, DC, 33pp.

Reynolds R.W., (1993), Impact of Mount Pinatubo aerosols on satellite-derived sea surface temperatures. Journal of Climate, 6, 768-774.

Reynolds, R.W., (1999), Specific contributions to the observing system: sea surface temperatures. *Proceedings of the OCEANOBS99-Solicited Papers. OCEANOBS99 Conference,* 18-22 October 1999, St. Raphael France. Centre National d'Etudes Spatiales, Toulouse, France.

Reynolds, R.W., and Marisco, D.C., (1993), An improved real-time global sea surface temperature analysis. Journal of Climate, 6, 1, 114-119.

Richards, F., and Arkin P.A., (1981), On the relationship between satellite-observed cloud cover and precipitation. Monthly Weather Review, 5, 1081-1093.

Robinson A.R., and Golnaraghi M., (1994), Physical and dynamical oceanography of the Mediterranean Sea. Ocean Processes in Climate

Dynamics: Global and Mediterranean examples (Malanotte-Rizzoli P., and Robinson A.R., eds.), 255-306, Kluwer Academic Publishers.

Robinson A.R., Golnaraghi M., Leslie E.G., Artgeiani A., Hecht A., Lazzoni E., Michelato A., Sansone E., Theocharis A., Unluata U., (1991), Structure and variability of the Eastern Mediterranean general circulation. Dynamics of the Atmosphere and Oceans, 15, 215-240.

Robinson A.R., and Lermusiaux P.F.J., (2001), Data Assimilation in Models. Encyclopaedia of Ocean Sciences, Academic Press Ltd., London, 623-634.

Robinson A.R., Hecht A., Pinardi N., Bishop J., Leslie W.G., Rosentraub Y., Mariano A.J., and Brenner S., (1987), Small synoptic mesoscale eddies: The energetic variability of the eastern Levantine Basin. Nature, 327, 6118, 131-134.

Robinson, A.R., Theocharis A., Lascaratos A., and Leslie W.G., (2001), Mediterranean Sea Circulation. Encyclopaedia of Ocean Sciences, 1689-1706, Academic Press Ltd., London.

Robinson I.S., and Donlon C.J., (2000), Global measurement of sea surface temperature: Some new perspectives. Remote sensing of atmosphere and ocean from space: Models, instruments and techniques. 12pp. International summer schools on atmospheric and Oceanic sciences, ISSAOS, 2000, Italy 4-8th 2000.

Robinson I.S., Wells N.C., and Charnock H., (1984), The sea surface thermal boundary layer and its relevance to the measurement of sea surface temperature by airborne and spaceborne radiometers. International Journal of Remote Sensing, 5, 1, 19-45.

Rosati A., and Miyakoda K., (1988), A general circulation model for upper ocean simulation, Journal of Physical Oceanography, 18, 1601-1626.

Rogers E., Black T.L., Deaven D.G., DiMego G.J., Zhao Q., Baldwin M., Junker N.W., and Lin Y., (1996), Changes to the operational ``Early'' Eta analysis/forecast system at the National Centers for Environmental Prediction. Weather Forecasting, 11, 391-413.

Savitsky, B., & Anselin, L., (1997), Scale. Available at <http://www.ncgia.ucsb.edu/other/ucgis/research_priorities/paper6.html>. Accessed on 30.10.04.

Schaefer, J.T., (1990), The Critical Success Index as an indicator of warning skill. Weather and Forecasting, 5, 570-575.

Schluessel P., Emery W.J., Grassl H., and Mammen T., (1990), On the bulk skin temperature difference and its impact on satellite remote sensing of sea surface temperature. Journal of Geophysical Research, 95, 13341-13356.

Schluessel P., Schanz L., and Englisch G., (1995), Retrieval of latent heat flux and longwave irradiance at the sea surface from SSM/I and AVHRR measurements. Advances in Space Research, 16, 107-116.

Schluessel P., Shin H –Y., Emery W.J., and Grassl H., (1987), Comparison of satellite derived SST with *in situ* skin measurement. Journal of Geophysical Research, 92, 2859-2874.

Schott F., and Leaman K.D., (1991), Observations with moored acoustic Doppler current profiles in the convection regime of the Golfe du Lion. Journal of Geophysical Oceanography, 21, 558-574.

Schulz J., Meywerk J., Ewald S., and Schlussel P., (1997), Evaluation of satellite derived latent heat fluxes. Journal of Climate, 10, 2782-2795.

Schulz J., Schlussel P., and Grassl H., (1993), Water vapour in the atmospheric boundary layer over oceans from SSM/I measurements. International Journal on Remote Sensing, 14, 2773-2789.

SEAFLUX (1999) Rationale of the Ocean Surface Turbulent Flux Project. Available at <http://curry.eas.gatech.edu/SEAFLUX/rationale.html>. Accessed on 01.11.04.

Shenoi S.C., (1999), On the suitability of algorithm for the retrieval of SST from the north Indian Ocean using NOAA/AVHRR data. International Journal of Remote Sensing, 20, 11-29.

Siefridt L., Barnier B., Beranger K., and Roquet H., (1999), Evaluation of operational ECMWF surface heat fluxes: impact of parameterisation changes during 1986-1995. Journal of Marine Systems, 19, 1-3, 113 - 135.

Smagorinsky J., (1963), General circulation experiments with the primitive equations, I: The basic experiment. Monthly Weather Review, 91, 99-164.

Smith N., Blomley J.E. and Meyers G., (1991), A univariate statistical interpolation for subsurface thermal analyses in the tropical oceans. Progress in Oceanography, 28, 219-256.

Smith S.D., (1980), Wind stress and heat flux over the ocean in gale force winds. Journal of Physical Oceanography, 10, 709-726.

Smith S.D., (1988), Coefficients for sea surface wind stress, heat flux and wind profiles as a function of wind speed and temperature. Journal of Geophysical Research, 93, 15467-15472.

Smith S.D., (1989), Water vapour flux at the sea boundary. Boundary Layer Meteorology, 47, 277-283.

Sobrino J.A., Li L.Z., and Stoll M.P., (1993), Impact of the atmospheric transmittance and total water vapour content in the algorithms for estimating sea surface temperature. IEEE Transactions on Geoscience and Remote Sensing, 31, 5, 946-952.

Staniforth A., (2001), 50th Anniversary of NWP Commemorative Symposium. (Spekat A., ed.), European Meteor. Soc (Carl-Heinrich-nbecker-Weg 6-10, 12165 Berlin Germany), 185-200.

Steyn-Ross M.L., Steyn-Ross D.A., and Jelenak A., (1999), Comparison of atmospheric correction algorithms for deriving sea surface temperature from AVHRR. International Journal of Remote Sensing, 20, 18, 3515-3531.

Strong A.E., and McClain E.P., (1984), Improved ocean surface temperatures from space – Comparison with drifting buoys. Bulletin of the American Meteorological Society, 65, 138-142.

Takayama Y. and Takashima T., (1986), Aerosol optical thickness of yellow sand over the Yellow Sea derived from NOAA satellite data. Atmosphere and Environment, 20, 631-638.

Taylor P.K., (1982), Remote sensing of atmospheric water content and sea surface latent heat flux. Proceedings of the Annual Technical Conference on Remote Sensing and the Atmosphere, Reading, United Kingdom, Remote Sensing Society, 265-272.

Taylor P.K., (2000), Intercomparison and validation of ocean-atmosphere energy flux fields. Final Report of the Joint WCRP/SCOR Working Group on Air-Sea Fluxes (SCOR Working Group 110). 306pp.

Taylor P.K., and Yelland M.J., (2001), The dependence of sea surface roughness on the height and steepness of the waves. Journal of Physical Oceanography, 31, 2, 572 – 590.

Telenta, B., Music S., and Galdies C., (1998), A numerical study of Mediterranean sea responses on surface fluxes. International Conference On Coastal and Ocean Modelling, Valletta: 12 – 14 November. Available at <http://www.comnet.mt/issi/pastevnt/ocean.htm#topic> Accessed on 01.11.04.

Thiebux H.J., Kats B., Wang W., Burroughs L.D., (2001), The real-time, global sea surface temperature analysis: RTG_SST. Technical Procedures Bullettin, No. 477, National Weather Service, Office of Meteorology, NOAA.

Treitz P., (2001), Variogram analysis of high spatial resolution remote sensing data: An examination of boreal forecast ecosystems. International Journal of Remote Sensing, 22, 18, 3895-3900.

Tsintikidis D., and Zhang G.J., (1998), A numerical study on the coupling between sea surface temperature and surface evaporation. Journal of Geophysical Research, 103, D24, 31763-31774.

Turner S.J., O'Neill R.V., and Conley W., (1991), Pattern and scale: statistics for landscape ecology. Quantitative methods in landscape ecology (Turner S.J., and Gardner D., eds.),. Springer-Verlag, New York, 17-49.

Tufte E.R., (1983), The Visual Display of Quantitative Information. Cheshire, CT: Graphics Press.

Tziperman E., and Malanotte-Rizzoli P., (1991), The climatological seasonal circulation of the Mediterranean Sea. Journal of Marine Research, 49, 411-434.

Ulivieri C., Castronuovo M.M., Francioni R., and Cardillo A., (1994), A split-window algorithm for estimating land surface temperature from satellites. Advances in Space Research, 14, 3, 59-65.

Varma, H., (1999), Applying spatio/temporal concepts to correlative data analysis. Marine and Coastal Geographical Information Systems (Wright D.J., and Bartlett D.J. eds.), Dawn Wright and Taylor & Francis publishers.

Walton C.C., Pichel W.G., Sapper J.F., and May D.A., (1998), The development and operational application of non-linear algorithms for the measurement of sea surface temperatures with the NOAA polar-orbiting environmental satellites. Journal of Geophysical Research, 103, C12, 27999-28012.

Warner T.T., and Seaman N.L., (1990), A real-time, mesoscale numerical weather prediction system used for research, teaching, and public service at the Pennsylvania State University. Bulletin of the American Meteorological Society, 71, 792-805.

WCRP/GEWEX, (1996), Report of the eight session of the working group on radiative fluxes. WCRP Informal Report No. 13/1996, Killiney Bay, Dublin, Ireland, 22-26 July 1996.

Webster PJ, Clayson CA, Curry JA (1996), Clouds, radiation, and the diurnal cycle of sea surface temperature in the tropical western Pacific Ocean. Journal of Climate, 9, 1712-1730.

Weller, R.A. and Taylor P.K., (1998), A Strategy for Marine Meteorological and Air-Sea Flux Observation. Preprint volume: 3rd Symposium on Integrated Observing Systems, Dallas, Texas, January, 1999, American Meteorological Society.

Wells N.C., and King-Hele S., (1990), Parameterisation of tropical ocean heat flux. Quarterly Journal of the Royal Meteorological Society, 116, 1213-1224.

Wentz F.J., (1997), A well-calibrated ocean algorithm for special sensor microwave / imager. Journal of Geophysical Research, 102, 8703-8718.

Wentz F.J., Gentemann C., Smith D., and Chelton D., (2000), Satellite Measurements of Sea Surface Temperature through Clouds. Science, 288, 847-850.

Wentz F.J., and Meissner T., (1999), AMSR Ocean Algorithm, Version 2. RSS Tech. Report 121599A, Remote Sensing Systems, Santa Rosa, CA., 1999.

Wentz, F.J. and Spencer R.W., (1998), SSM/I rain retrievals within a unified all-weather ocean algorithm. Journal of the Atmospheric Sciences, 55, 1613 - 1627.

White, G.H. and da Silva A., (1999), A comparison of fluxes from the reanalyses with independent estimates. ECMWF Reanalysis Workshop, Reading, 23 - 27 August, 1999.

Woodruff, S.D., Diaz H.F., Elms J.D., and Worley S.J., (1998), COADS Release 2 Data and Metadata Enhancements for Improvements of Marine Surface Flux Fields. Phys. Chem. Earth, 23, 517-527.

Woodruff S.D., Lubcker S.J., Wolter K., Worley S.J., and Elms J.D., (1987), A comprehensive ocean-atmosphere data set. Bulletin of the American Meteorological Society, 68, 1239-1250,

WMO, (1993), International list of selected, supplementary and auxiliary ships. WMO Report No. 47, WMO, Geneva.

Wu P., and Haines K., (1996), Modeling the dispersal of Levantine Intermediate Waterand its role in the Mediterranean deep water formation. Journal of Geophysical Research, 101, 3261–3271.

Xie P., and Arkin P.A., (1997), Global Precipitation: A 17-year monthly analysis based on gauge observations, satellite estimates, and numerical model outputs. Bulletin of the American Meteorological Society, 78, 2539-2558.

Xue Y., Lawrence S.P., and Llewellyn-Jones D.T., (1997), Use of ATSR data to estimate surface fluxes over land and sea, In: Proc 3rd ERS Symposium on Space at the service of our environment, Italy, 17-21 March 1997.

Yu Y., and Barton I.J., (1994), A non-regression-coefficient method of sea surface temperature retrieval from space. International Journal of Remote Sensing, 15, 6, 1189-1206.

Yueh, S. H., West R., Wilson W.J., Li F.K., Njoku E.G., and Rahmat-Samii Y., (2001) Error sources and feasibility for microwave remote sensing of ocean surface salinity. IEEE Transactions on Geoscience and Remote Sensing, 39, 1049-1060.

Zavatarelli M., and Mellor G.L., (1995), A numerical study of the Mediterranean Sea circulation. Journal of Physical Oceanography, 25, 1384-1414.

Zavatarelli M., and Pinardi N., (1995) The Adriatic sea general circulation: modelling with the Princeton Ocean Model. Annales Geophysicae, 13 (suppl. 2).

Zecchetto S., and Cappa C., (2001), The spatial structure of the Mediterranean Sea winds revealed by ERS1 scatterometer. International Journal of Remote Sensing, 22, 1, 45-70.

Zhao, Q., and Carr F.H., (1997), A prognostic cloud scheme for operational NWP models. Monthly Weather Review, 125, 1931-1953.

Zodiatis G., Lardner R., Demirov E., Georgiou G. and Pinardi N., (2003), Cyprus coastal ocean forecasting and observing system. Building the European Capacity in Operational Oceanography, Elsevier Oceanography Series, 69, 36-45.

Zodiatis G., Lardner R., Lascaratos A., Georgiou G., Korres G. and Syrimis M., (2002a), High resolution nested model for the Cyprus and NE Levantine Basins, Eastern Mediterranean Sea: Implementation and Climatological Runs. Annales Geophysicae, 20, 1-16.

Zodiatis G., Lardner R., Demirov E., Georgiou G and Pinardi N., (2002b), The Cyprus coastal ocean forecasting system. 3rd EuroGOOS Conference, Athens, 3-6 December.

Zodiatis G., Lardner R., Lascaratos A., Georgiou G., Korres G. and Syrimis M., (2002c), Mediterranean Forecasting System: Submodel for the Cyprus and NE Levantine Basins, Intergovernmental Commission for the Scientific Exploration of the Mediterranean Sea Conference, 36, 90.

Appendix I

DATA PROCESSING AND REFORMATTING OF GEOPHYSICAL DATA DERIVED FROM THE TROPICAL MICROWAVE IMAGER.

Appendix I describes the computer codes used to calibrate the geophysical fields derived from the Tropical Microwave Imager. Following such processing, additional codes are used to convert the data in a number of different formats, including ascii x,y,z format (for statistical model verification), GrADS format (for 2-D visualisation), and software-specific formats, including ERMapper and ERDAS Imagine.

I.1 Data processing and reformatting of geophysical data derived from the Tropical Microwave Imager.

I.1.1. Data calibration, format and conversion of geophysical fields derived by the Tropical Microwave Imager into GrADS format.

The TMI-derived remotely sensed fields are converted into GrADS format data using *TMI2monthlyORB.f*. This formats the ascending and descending swaths using *TMI2centORB.ctl*.

```
c*******************************************************
c  Reading SSMI 'binary' data (www.ssmi.com)
c  and converting into GrADs;
c               by Pejanovic and Galdies
c               ICod 2000.
c*******************************************************
c*******************************************************
      parameter (IM=1440,JM=320)
      character *1 a1,aw(IM,JM),aw1(IM,JM)
      character *1 aw2(IM,JM),aw3(IM,JM),aw4(IM,JM),aw5(IM,JM)
        character *1 aw6(IM,JM)
      dimension id7(7),ar7(7)
      integer *2 i2
      character * 1 c1
      dimension r(im,jm)
      dimension r1(im,jm)
      dimension r2(im,jm)
      dimension r3(im,jm)
      dimension r4(im,jm)
        dimension r5(im,jm)
        dimension r6(im,jm)
      character * 100 fname
      equivalence ( a1,i2)
c     equivalence ( c1,iteroutside)
c     ----------------------------------------
      data id7 / 0,0,0,0,0,0,0/
      data ar7 / 0,1440,0.125,0.25,320,-39.875,0.25/
c     ----------------------------------------
      call getarg(1,fname)
```

```
      call getarg(2,c1)
      nb = index (fname,'  ') -1
      iteroutside = ichar(c1)-48
      print *,' iteroutside=',iteroutside
c     call system ('cp bdat/'//fname(1:nb)//'* .')
c     ---------------------------------------------
      read (fname(1:4),'(i4)') id7(1)
      read (fname(5:6),'(i2)') id7(2)
      read (fname(7:8),'(i2)') id7(3)
c     ---------------------------------------------
c     call system ('gzip -d '//fname(1:nb) )
c     ---------------------------------------------

      id7 ( 4) = 0
c     if ( index(fname,'am') .gt.0) id7(4) = 6
c     ---------------------------------------------
     open(10,file=fname(1:nb),form='unformatted',
     * status='old',access='direct',RECL=IM*JM)
c     ---------------------------------------------

      n= 0
c-------------------------------------
      do 500 iter=0,1
c-------------------------------------
c     id7(4) = iter
      n = iter*7
      if (iter.ne.iteroutside) goto 500

      read (10,rec=1+n) aw
      read (10,rec=2+n) aw1
      read (10,rec=3+n) aw2
      read (10,rec=4+n) aw3
      read (10,rec=5+n) aw4
         read (10,rec=6+n) aw5
         read (10,rec=7+n) aw6

      do j=1,JM
      do i=1, IM
      r (i,j) = ichar(aw(i,j))
      r1(i,j) = ichar(aw1(i,j))
      r2(i,j) = ichar(aw2(i,j))
      r3(i,j) = ichar(aw3(i,j))
      r4(i,j) = ichar(aw4(i,j))
         r5(i,j) = ichar(aw5(i,j))
         r6(i,j) = ichar(aw6(i,j))

c time
      if ( r (i,j).gt.250) then
          r (i,j) = -1
      else
          r(i,j) = r(i,j) * 6/ 60.
      endif
c SST
      if ( r1(i,j).gt.250) then
          r1(i,j) = -1
      else
          r1(i,j) = (r1(i,j) * 0.15  - 3.) + 273.16
      endif
c winds Z
```

```
      if ( r2(i,j).gt.250) then
         r2(i,j) = -1
         r2(i,j) =  0
      else
         r2(i,j) = r2(i,j) * 0.15
      endif

c winds W r
      if ( r3(i,j).gt.250) then
         r3(i,j) = -1
         r3(i,j) =  0
      else
         r3(i,j) = r3(i,j) * 0.15
      endif

c water vapour
      if ( r4(i,j).gt.250) then
         r4(i,j) = -1
         r4(i,j) =  0
      else
         r4(i,j) = r4(i,j) * 0.3
      endif

c cloud liquid water
      if ( r5(i,j).gt.250) then
         r5(i,j) = -1
         r5(i,j) =  0
      else
         r5(i,j) = r5(i,j) * 0.01
      endif

c rain
      if ( r6(i,j).gt.250) then
         r6(i,j) = -1
         r6(i,j) =  0
      else
         r6(i,j) = r6(i,j) * 0.1
      endif

c      r1(i,j) = ichar(aw1(i))
c      r2(i,j) = ichar(aw2(i))
      enddo
      enddo

      DUPE = 0

      print *,' id7=',id7
      print *,' ar7=',ar7
      print *,' IM,JM =',IM,JM
CGRADS!!!!!!!!!!!!!!!!!!!!!!!!!!!!!!!!!!!!!!!!!!!!!!!!!!!!!!!!!!!!!!!!!!!!!!!
        isat = 999
c-----------------------------------------------------------------
      CALL WGRADS (id7,9 ,0,0,ISAT,0,ar7,im,jm,1,0.,r ,DUPE)
      CALL WGRADS (id7,1 ,0,0,ISAT,0,ar7,im,jm,1,0.,r1,DUPE)
      CALL WGRADS (id7,2 ,0,0,ISAT,0,ar7,im,jm,1,0.,r2,DUPE)
      CALL WGRADS (id7,3 ,0,0,ISAT,0,ar7,im,jm,1,0.,r3,DUPE)
      CALL WGRADS (id7,4 ,0,0,ISAT,0,ar7,im,jm,1,0.,r4,DUPE)
        CALL WGRADS (id7,5 ,0,0,ISAT,0,ar7,im,jm,1,0.,r5,DUPE)
        CALL WGRADS (id7,6 ,0,0,ISAT,0,ar7,im,jm,1,0.,r6,DUPE)
```

```
c-------------------------------------------------------------
500    continue
c      call system ('rm '//fname(1:nb)//'*' )
       end
```

The *TMI2cent.ctl* file writes TMI-derived data into GrADS format using the following "*.ctl" file:

```
dset /usr/local/TMI/grads/tm2SEP.gdat
undef -1
title mqfull model
*xdef  1440 linear   0.125 0.25
*ydef   320 linear  -39.875 0.25
xdef  145 linear   0.125 0.25
ydef   41 linear  30.0 0.25
tdef 60 linear 00Z01sep1999 12hr
zdef 1 levels 1000
vars 7
time  0   9,1,0  Time
sst   0   1,1,0  Sea Surface Temperature
z     0   2,1,0  10m surface wind speed using 1GHz
w     0   3,1,0  10m surface wind speed using 37GHz
wv    0   4,1,0  water vapour
clw   0   5,1,0  cloud liquid water
p     0   6,1,0  precipitation rate
endvars
```

This dataset conists of twice daily sets of geophysical fields. The fields are visualized and their integrity noted together with the orbital overpass derived from the time t. Once suitable orbital swaths over the central Mediterranean sea are identified and selected, the following .csh script, is used to create a composite file (for example swath coverage during July and August) defining the right orbital passage (i.e. - either ascending [0] or descending [1]).

```
#/bin/csh

cp -f activectl.LST.monthlyORB activectl.LST

foreach dd (  22 23 24 25 26 27 28 29 30 31)
cp bdat/July/199907"$dd"TM.GZ  .
gzip -d 199907"$dd"TM.GZ  .
TMI2monthlyORB  199907"$dd"TM 0
rm -f 199907"$dd"TM
end

foreach dd (01)
cp bdat/August/199908"$dd"TM.GZ  .
gzip -d 199908"$dd"TM.GZ  .
TMI2monthlyORB 199908"$dd"TM 1
rm -f 199908"$dd"TM
end
```

```
foreach dd (02)
cp bdat/August/199908"$dd"TM.GZ .
gzip -d 199908"$dd"TM.GZ .
TMI2monthlyORB 199908"$dd"TM 0
rm -f 199908"$dd"TM
end

foreach dd (03)
cp bdat/August/199908"$dd"TM.GZ .
gzip -d 199908"$dd"TM.GZ .
TMI2monthlyORB 199908"$dd"TM 1
rm -f 199908"$dd"TM
end

foreach dd (04)
cp bdat/August/199908"$dd"TM.GZ .
gzip -d 199908"$dd"TM.GZ .
TMI2monthlyORB 199908"$dd"TM 0
rm -f 199908"$dd"TM
end

foreach dd (05)
cp bdat/August/199908"$dd"TM.GZ .
gzip -d 199908"$dd"TM.GZ .
TMI2monthlyORB 199908"$dd"TM 1
rm -f 199908"$dd"TM
end

foreach dd (06 07)
cp bdat/August/199908"$dd"TM.GZ .
gzip -d 199908"$dd"TM.GZ .
TMI2monthlyORB 199908"$dd"TM 0
rm -f 199908"$dd"TM
end
```

The resulting GrADS file containing TMI-derived SST with the right orbital elements is then made available for subsequent Eta and POM model initialization.

Appendix II

DESCRIPTION OF THE SURFACE LAYER PARAMETERISATION SCHEME AND IMPORTANT NUMERICAL CODES OF ETA ATMOSPHERIC MODEL

Appendix II is divided into three main sections. The first section includes a description of the Monin-Obukhov surface layer parameterisation scheme of the Eta model, which is fully treated and fine-tuned by the present model. Reference is made to this description in the main text of this thesis.

The second part of this Appendix describes a number of important numeric codes of the atmospheric model. The selection is done in view of their importance for model initialisation of the lateral and surface boundary conditions, for the calculation of surface air-sea fluxes, translation of predicted fields from model-grid to standard-grid format at standard pressure levels, formatting of predicted air-sea flux fields to drive an underlying ocean model, and conversion of forecasted fields into GrADS format and ascii xyz for visualisation and verification.

The third part of this Appendix describes the pre-, processing and post-processing stages of the local-area regional, and nested Eta model.

II.1 The Monin-Obukhov-based surface layer parameterisation scheme of the Eta model.

The physical package of the Eta model is based on several sophisticated parameterisation schemes. Vertical turbulent mixing between levels in the free atmosphere is performed by using mixing coefficients of the Mellor-Yamada 2.5 level turbulence (Mellor & Yamada 1974, 1982; Janjic, 1990).

Of particular importance to the numerical forecasting of the surface fluxes is the Monin-Obukhov based surface layer parameterisation scheme that provides the lower boundary conditions for the Level 2.5 turbulence model. This model assigns a logarithmic form to the profiles of the atmospheric variables as they approach the lower boundary. This log profile ends at some small, but finite height z_0 above the surface and the variable considered takes on its lower boundary value at this height. The assumption is that the values of the relevant variables in this thin layer of the air adjacent to the surface take on the surface values. This situation is schematically represented in figure II.1. The height z_0 is called the roughness height, and is associated with the roughness of the underlying surface. According to the similarity theory, the variation of z_0 can significantly affect the calculation of the air-sea fluxes.

The model extends the log curve beyond its range of validity (dashed line in figure II.1b to obtain an effective z_0 at the intersection of the extended log curve and the z-axis. Since the log curve defines the magnitude of the flux, the remaining problem is to define the effective z_0 as a function of the flow regime.

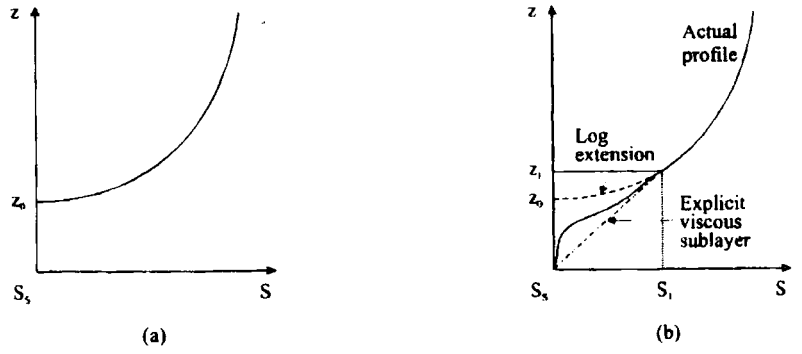

Fig II.1 (a) log profile ending, and (b) log profile with the viscous sublayer ending. (SOURCE: Kallos et. al., 1997).

The situation near the surface is rather complex (fig. II.1b). Within the thin layer near the surface, there is not enough space for turbulent eddies to develop, and instead molecular transports dominate this layer. This layer is often called the viscous layer. The work carried out by a number of investigators (e.g. Janjic, 1994) indicates that molecular processes can significantly affect the accuracy of the surface fluxes and consequently the evolution of the planetary boundary layer, such as for example, moist convection.

In the case of water surfaces (Janjic, 1994), the log curve is matched by a separate sublayer profile as to specify the height and the value of the considered variable at the matching point. By doing so, the lower boundary values for the turbulent layers would be defined. Following the surface renewal theory proposed by Liu *et. al.* (1979), Janjic (1994) makes the following relation for the values of the parameters at the two levels 0 and S:

$$\left.\begin{aligned} U_0 - U_S &= D_1\left[1-\exp\left(-\frac{zu_*}{D_1\nu}\right)\right]\left(\frac{F_U}{u_*}\right) \\ \theta_0 - \theta_S &= D_2\left[1-\exp\left(-\frac{zu_*}{D_2\chi}\right)\right]\left(\frac{F_\theta}{u_*}\right) \\ q_0 - q_S &= D_3\left[1-\exp\left(-\frac{zu_*}{D_3\lambda}\right)\right]\left(\frac{F_q}{u_*}\right) \end{aligned}\right\} \qquad (2.1)$$

Here the subscript S denotes the surface values; the subscript 0 (for the time being) indicates the values at a height z above the surface where the molecular diffusivities are dominant; D_1, D_2 and D_3 are parameters dependent on the Prandtl and Schmidt number and a constant; u_* is the frictional velocity; ν, χ and λ are the molecular diffusivities for momentum, heat and water vapour, respectively; and F_u, F_θ and F_q are the turbulent fluxes of momentum, heat and water vapour respectively above the viscous sublayer.

For a small argument ζ of the exponential functions in the equations above,

$$\frac{z_U u_*}{D_1 \nu} = \frac{z_\theta u_*}{D_2 \chi} = \frac{z_q u_*}{D_3 \lambda} = \zeta \tag{2.2}$$

$$1 - \exp(-\zeta) \approx \zeta \tag{2.3}$$

so that using these two equations, the above three equations can be approximated by:

$$\begin{aligned} U_0 - U_S &= \left(\frac{z_U}{\nu}\right) F_U \\ \theta_0 - \theta_S &= \left(\frac{z_\theta}{\chi}\right) F_\theta \\ q_0 - q_S &= \left(\frac{z_q}{\lambda}\right) F_q \end{aligned} \tag{2.4}$$

when, the heights z_u, z_θ and z_q are defined by (2.2), that is:

$$z_U = \frac{\zeta \nu D_1}{u_*} \qquad z_\theta = \frac{\zeta \chi D_2}{u_*} \qquad z_q = \frac{\zeta \lambda D_3}{u_*} \tag{2.5}$$

At this point, the following simplifying assumptions are made:

There are two distinct layers: (i) a thin viscous sublayer immediately above the surface, where the vertical transports are determined entirely by the molecular diffusion, and (ii) a turbulent layer above it, where the vertical transports are defined entirely by the turbulent fluxes.

The depths of the viscous sublayers for the respective physical variables are defined by the above three equations for a chosen fixed value of ζ.

With the definitions of the depths of the viscous sublayers 2.5, the values of the relevant physical quantities at the interfaces of the viscous and the turbulent layers are those denoted by the subscripts 0 in equations 2.4.

Using the bulk momentum and heat exchange coefficients K_{Msfc} and K_{Hsfc} respectively, the turbulent fluxes in the surface layer above the viscous sublayer are represented by:

$$\left.\begin{aligned} F_U &= \left(\frac{K_{Msfc}}{\Delta z_e}\right)(U_{lm} - U_0) \\ F_\theta &= \left(\frac{K_{Hsfc}}{\Delta z_e}\right)(\theta_{lm} - \theta_0) \\ F_q &= \left(\frac{K_{Hsfc}}{\Delta z_e}\right)(q_{lm} - q_0) \end{aligned}\right\} \qquad (2.6)$$

Here the subscript *lm* denotes the variables at the lowest model level, ΔZ_e is either the equivalent height of the lowest model level that takes into account the presence of the "dynamical turbulence layer" at the bottom of the surface layer or simply Z_{lm}-Z_0. In the shallow dynamical turbulence layer, the ratio of the height z and the Monin-Obukhov length scale (Monin & Obukhov, 1954) is small so that the logarithmic profiles are used.

Substituting equations 2.6 into 2.4, one obtains:

$$\left.\begin{aligned} \left(\frac{\nu}{z_U}\right)(U_0 - U_S) &= \left(\frac{K_{Msfc}}{\Delta z_e}\right)(U_{lm} - U_0) \\ \left(\frac{\chi}{z_\theta}\right)(\theta_0 - \vartheta_S) &= \left(\frac{K_{Hsfc}}{\Delta z_e}\right)(\theta_{lm} - \theta_0) \\ \left(\frac{\lambda}{z_q}\right)(q_0 - q_S) &= \left(\frac{K_{Hsfc}}{\Delta z_e}\right)(q_{lm} - q_0) \end{aligned}\right\} \qquad (2.7)$$

Note that equation 2.7 reflect the requirement for the continuity of the finite-difference fluxes across the interfaces between the two layers. Solving equation 2.7 for the variables with the subscript 0, one obtains:

$$
\left.
\begin{aligned}
U_0 &= \frac{U_S + \left[\frac{\left(K_{Msfc} z_U\right)}{\nu \Delta z_e}\right] U_{lm}}{1 + \left[\frac{\left(K_{Msfc} z_U\right)}{\nu \Delta z_e}\right]} \\
\theta_0 &= \frac{\theta_S + \left[\frac{\left(K_{Hsfc} z_\theta\right)}{\chi \Delta z_e}\right] \theta_{lm}}{1 + \left[\frac{\left(K_{Hsfc} z_\theta\right)}{\chi \Delta z_e}\right]} \\
q_0 &= \frac{q_S + \left[\frac{\left(K_{Hsfc} z_q\right)}{\lambda \Delta z_e}\right] q_{lm}}{1 + \left[\frac{\left(K_{Hsfc} z_q\right)}{\lambda \Delta z_e}\right]}
\end{aligned}
\right\} \qquad (2.8)
$$

Thus the required lower boundary conditions for the turbulent layer are expressed as weighted means of the values at the surface and at the lowest model level. Note that equation 2.8 together with equation 2.5 represent a closed system provided the parameters D_1, D_2, D_3 and ζ are known.

The viscous sublayer over the oceans is assumed to operate in three different regimes:

1. smooth and transitional,
2. rough, and
3. rough with spray.

Depending on the roughness Reynolds number:

$$
R_e = \frac{z_0 u_*}{\nu} \qquad (2.9)
$$

Here

$$z_0 = \frac{0.11\nu}{u_*} + \frac{0.018u_*^2}{g} \tag{2.10}$$

and

$$u_* = \left[\left(\frac{K_{Msfc}}{\Delta z_e}\right)\left(U_{lm} - U_0\right)\right]^{1/2} \tag{2.11}$$

Janjic (1994) gives the roughness length z_0 as a function of u_*. When the Reynolds number exceeds a prescribed value *Rr*, the flow ceases to be smooth and the rough regime is entered. In the rough regime the momentum is transported also by pressure forces on the roughness elements so that equation 2.11 looses validity. Consequently, the viscous sublayer for momentum is turned off. However, for heat and moisture, the viscous sublayer is still operating until the rough regime with spray is reached at a critical value Rr_S when the viscous sublayer collapses completely. In the rough regime, the breaking waves and the spray are assumed to provide much more efficient way of exchange of heat and moisture between the ocean and the air than can be accomplished by the molecular viscosity.

For the parameters D_1, D_2 and D_3, Liu *et al.* (1979) proposed the following relationship:

$$D_1 = MRr^{1/4} \tag{2.12}$$

$$D_2 = MRr^{1/4}\,\mathrm{Pr}^{1/2} \tag{2.13}$$

$$D_3 = MRr^{1/4}Sc^{1/2} \tag{2.14}$$

where Pr=v/x is the Prandtl number; Sc= v/λ is the Schmidt number and M is a constant, but different for different regimes. With these definitions, the new equation takes the form:

$$\left.\begin{aligned} z_U &= \frac{\zeta\nu}{u_*}\left[M\left(\frac{z_0 u_*}{\nu}\right)^{1/4}\right] \\ z_T &= \frac{\zeta\chi}{u_*}\left[M\left(\frac{z_0 u_*}{\nu}\right)^{1/4}\mathrm{Pr}^{1/2}\right] \\ z_q &= \frac{\zeta\lambda}{u_*}\left[M\left(\frac{z_0 u_*}{\nu}\right)^{1/4}Sc^{1/2}\right] \end{aligned}\right\} \qquad (2.15)$$

For the smooth regime a value of M close to 30 is used. When the flow ceases to be smooth a value of 10 has been suggested which best fits the data. These two values are also applied. At the present level of approximation, the Prandtl number and the Schmidt were assumed to be the same – i.e. Pr =Sc = 0.71 and the molecular viscosity for momentum is $1.5\text{x}10^{-5}$. The molecular diffusion coefficients for heat and moisture, χ and λ, are determined by ν, Pr and Sc.

The threshold velocities at which the transition between the different flow regimes occur are u^*_r=0.025m s^{-1} and u^*_s=0.70m s^{-1}. These values qualitatively agree in the order of magnitude with the laboratory measurements. The parameter that defines the depth of the viscous sublayer ζ, is given a default value of 0.35.

In the practical implementation within Eta model, u_* for the current time step is calculated by equation 2.11 using K_{MSfc} and U_0 from the previous time step. Thus obtained, u_* is then used by equation 2.10 to update z_0. With the depths z_u, z_t and z_q being calculated from the above equations, the lower boundary conditions for the surface layer U_0, θ_0 and q_0 can now be obtained by equation 2.8 using K_{Msfc} and K_{Hsfc} from the previous time step. However, in order to prevent the two-grid interval oscillation in time, the average values of U_0, θ_0 and q_0 from the present and the previous time steps are actually used.

II.2 Important numeric codes related to the atmospheric model.

II.2.1. Conversion of GRIB Files to GrADS format.

The *grb2grads.f* code called grib GDAS-derived SST file according to the day number "dd", extracted it and converted the data format into GrADS format according to the instructions defined by a specific "*.ctl" file as shown below:

```
#!/bin/csh
cp activectl.LST.monthly activectl.LST
foreach dd ( 22 23 24 25 26 27 28 29 30 31 )
cp July/"$dd"_07/* grib
grb2grads
end
exit
```

The "*.ctl" file writes the data according to the instructions below, and puts them in a "*.gdat" file:

```
dset /usr/local/GDAS/grads/gdasjul.gdat
undef  0
xdef 313 linear −10.0 0.1666667
ydef 112 linear  29.0 0.1666667
tdef 31 linear 00Z22jul1999 24hr
zdef 1 levels 1000
vars 1
sst   0   11,1,0  Sea Surface Temperature
endvars
```

	Regional Eta model	**Nested Eta model**
Center of domain:		
TLMOD	13.0°	17.5°
TPHOD	39.0°	34.5°
Domain parameters:		
West boundary	−23.3	−1.5
South boundary	−12.2	−1.375
Horizontal resolution:		
DLMD	1/6°	1/24°
DPHD	1/6°	1/24°
Time step (DTB):	75	18
Vertical number of layers:	32	24

Table II.1 Definition of domain of the atmospheric model setup. This information is coded in "all.inc" file.

The domain of Eta model is defined in the file *all.inc*

```
C-----------------------------------------------------------------
C    Center of domain :
                    P A R A M E T E R
   &(TLM0D=17.5,TPH0D=34.5)
C-----------------------------------------------------------------
C    Domain parameters
                    P A R A M E T E R
   &(WBD=-1.5,SBD=-1.375
   &,DLMD=1./24. ,DPHD=1./24. ,DTB=18.
   &,LM=24)
C-----------------------------------------------------------------
c LM=vertical number of layers -
```

The above script is for the nested Eta model.

The code *grb2.grads.f* converts grib files (such as the lateral boundary conditions of the regional Eta model, derived from the WAFS global model) into grads format for visualization:

```
c---------------------------
      parameter (im=69,jm=29,lm=11)
      dimension geop(im,jm,lm), temp(im,jm,lm), rh(im,jm,lm)
      dimension usl(im,jm,lm), vsl(im,jm,lm)
      dimension PSL (lm)
c---------------------------
      include 'tograds.inc'
      parameter (MXRECN=20000)
c---------------------------
      character * 8 Cdate8
c---------------------------
      character * 150 dirn
      character * 620 str
      character * 5 c5
      character * 2 c2
      dimension id7(7), ar7(7)
      dimension IPDS(120), IBMS(130), GDS(150)
      dimension ALL (120)
      dimension NPOS (MXRECN), VAL (400*200)
      data psl / 70.,100.,150.,200.,250.,300.,400.,500.,700.,850.,1000./

      call getarg (1, Cdate8)

      NCOUNT = 0
      print *,Cdate8
      read (Cdate8(1:2),'(i2)') id7(1)
      read (Cdate8(3:4),'(i2)') id7(2)
      read (Cdate8(5:6),'(i2)') id7(3)
      read (Cdate8(7:8),'(i2)') id7(4)
      RLEV = 0
      id7(5) = 0
      id7(6) = 0
      id7(7) = 0
      do k=1, MXRECN
```

```
      NPOS (k) = 0
      enddo
c     open (99,file='sst.datll',form='unformatted')
c     ---------------------------------------------
      call getctls (1, id7)
      call mklist (NF)
      if (NF.eq.0) call fmess('NF=0')
c     ---------------------------------------------
      open (12,file='L.out',status='old')
      call system ('rm S.out')
10     call clears (dirn)
      read (12,'(a)',end=99) dirn
c     ---------------------------------------------
      nb = index (dirn,'  ') - 1
      print *,dirn(1:nb)
c     ---------------------------------------------
      call system
     +('/usr/local/grads/bin/gribscan -gv -gd -ig '//dirn(1:nb)//' >> S.
     +out')
c     ---------------------------------------------
      goto 10
c     ---------------------------------------------
99     continue
      rewind  (12)
c     ---------------------------------------------
c     ---------------------------------------------
c     ---------------------------------------------
      open (25,file='S.out')
c     ---------------------------------------------
      IFILE = 0
c     ---------------------------------------------
20     call clears(str)
c     write (33,*) '*********************************'
      read (25,'(a)',end=88) str
c     ---------------------------------------------
      ips = 1
      call s2iass ( str, ips,'PDS #', IREC)
c     ---------------------------------------------
c ne file !
      if (IREC.eq.1) then
            IFILE = IFILE + 1
            call clears (dirn)
            read (12,'(a)') dirn
            NB = index (dirn,'  ') - 1
      print *,NB,' DIRN:',dirn(1:NB)
      endif
c     ---------------------------------------------
      call s2i ( str, ips, IGRID)
      call s2i ( str, ips, IPX)
      call s2i ( str, ips, ITL)
      call s2i ( str, ips, IL)
      call s2i ( str, ips, I61)
      call s2i ( str, ips, I62)
      call s2i ( str, ips, I63)
      call s2iass ( str, ips,'BMSFL', IBMDUM)
      call s2i    ( str, ips,       ID7(1))
      call s2i    ( str, ips,       ID7(2))
      call s2i    ( str, ips,       ID7(3))
      call s2i    ( str, ips,       ID7(4))
```

```
      call s2i   ( str, ips,       IBMDUM)
      call s2i   ( str, ips,       IBMDUM)
      call s2i   ( str, ips,       IP1   )
      call s2i   ( str, ips,       IP2   )
      call s2i   ( str, ips,       IACC  )
c     call s2i   ( str, ips,       IACC  )
      if ( IACC .ne. 10) then
            ID7(5) = IP2
            else
            ID7(5) = IP1
      endif
      call s2iass ( str, ips,'GDS ', IBMDUM )
      call s2i   ( str, ips,       NX)
      call s2i   ( str, ips,       NY)
      call s2r   ( str, ips,       WB)
      call s2r   ( str, ips,       EB)
      call s2r   ( str, ips,       DLM)
      call s2r   ( str, ips,       SB)
      call s2r   ( str, ips,       RNB)
      call s2r   ( str, ips,       DPH)

c     print *, IGRIDLL, NX, WB,EB,DLM
c     print *, IGRIDLL, Ny, SB,RNB,DPH
      IGRIDLL = 0
c gauss-case!
      if ( DLM.eq.937.0) then
            DLM = 0.9375
            DPH = DLM
            EB = -DLM
            IGRIDLL = -1
        endif
c-------------------------------------------------------
      IYREV = 0
      NSFLAG = 0
c thinned-case!
      if ( IGRID.ge.37.and.IGRID.le.44) IGRIDLL = -2
      if ( IGRIDLL.eq.-2) then
            NX = NY
            DLM = DPH
      ENDIF
c     ---------------------------------
      if ( EB.lt.WB) EB = EB + 360.
c     ---------------------------------
      if ( RNB.lt.SB) then
            HLP = SB
            SB = RNB
            RNB = HLP
            IYREV = 1
      endif
      if (SB.lt.0) NSFLAG = -1
c     ---------------------------------
      goto 1000
c     ---------------------------------
600   continue
c gaussian!

1000  c o n t i n u e
      ar7(1) = 0     ! warning!
      ar7(2) = NX
```

```
      ar7(3) = WB
      ar7(4) = DLM
      ar7(5) = NY
      ar7(6) = SB
      ar7(7) = DPH
c wafs
      RLEV =il
      if ( itl.ne.100) RLEV = 0
c     print *,NCTL, ip,itl,il,' ** ', id7,ar7
c     stop
c---------------------------------------
      do 33 J=1, NCTL
      NX0   = NX_CTL(J)
      NY0   = NY_CTL(J)
      NXNY   = NX_CTL(J)*NY_CTL(J)
      EBCTL  = X0_CTL(J) + (NX_CTL(j)-1)*XI_CTL(j)
      RNBCTL = Y0_CTL(J) + (NY_CTL(j)-1)*YI_CTL(j)
c-----------------------------------------------------------------
      if ( EB.le.X0_CTL(J)) goto 33
      if ( WB.ge.EBCTL) goto 33
      if ( RNB.le.Y0_CTL(J)) goto 33
      if ( SB.ge.RNBCTL) goto 33
c     print *,'ctl:',J, NX, NY, WB,SB,EB,RNB
c     print *,'ctl:',J, NX_CTL(j),NY_CTL(J), X0_CTL(j), Y0_CTL(j)
c    +         ,EBCTL, RNBCTL
34    continue
c-----------------------------------------------------------------
      call getrec(J,id7,RLEV,1,IPX,0,itl,il,NR1,NR2,NTP)
c-----------------------------------------------------------------
      if ( NR1.le.0) goto 33
c-----------------------------------------------------------------
c-----------------------------------------------------------------
      i9 = ar7(2)
      j9 = ar7(5)
c-----------------------------------------------------------------
      D = 0
      do 555 i=1, NR1
      ir1 = IREC1_CTL (i)
c     ir2 = IREC2_CTL (i)
      if( IR1.le.0) goto 555
c wgrib!
c-----------------------------------------------------------------
      if (ar7(1).ne.0.) then
            print *,' STOP - ONLY LL-grids are in use!'
            stop
      endif
      write (c5,'(i5)') IREC

      call system
     +('/usr/local/grads/bin/wgrib -v  '//dirn(1:nb)//' -d '//c5//' >1.0
     +')
      if (IGRIDLL.eq.-2) then
            call MW3FT33x(iret, NSFLAG, val)
      else if (IGRIDLL.ge.-1) then
            call readdump (IYREV, I9,J9,val)
      else
      print *, ' NO grid defining!'
      STOP
      endif
```

```
c     if ( iret.eq.-1) goto 555
      READ  (91+J,rec=ir1,err=777) (vall1(m),m=1,NXNY)
777   continue
      if ( IGRIDLL.eq.-1) then
      call llg2ll (omn,omx,ar7,0,J,i9,j9,val,D)
      else
      call ll2ll  (omn,omx,ar7,0,J,i9,j9,val,D)
      endif
      NPOS(ir1) = NPOS(ir1) + NPOI_CTL
      write (91+J,rec=ir1) (vall1(m),m=1,NXNY)
c-----------------------------------------------------------------
      IYY = ID7(1) - 1900
      NCOUNT =NCOUNT + 1
      write(*,67) J  ,IYY,(id7(m),m=2,5)
     + ,ipX , itl,il,ir1
     +, omn, omx
c     if (NCOUNT.gt.80) STOP
555   c o n t i n u e
c-----------------------------------------------------------------
67    format (' t=',i2,' f=',5i2,' p=',i3,  ' l=',i3,i3
     +,' r=',i4,' ou=',2f7.1)
c67   format (' t=',i2,i3,' f=',a13,' p=',i3,  ' l=',i3,i3
33    c o n t i n u e   ! new ctl!
c---------------------------------------
      goto 20
c---------------------------------------
88    continue
c---------------------------------------
      stop
c---------------------------------------
      do 205 ihr = 0, 60,6
      write (c2,'(i2)') ihr
      if (c2(1:1).eq.' ') c2(1:1) = '0'
      id7 (5) = ihr
      call RGRADS (id7, 07,100,0,im,jm,lm,psl, GEOP, NLRET)
      if ( NLRET.ne.LM) goto 205
      call RGRADS (id7, 11,100,0,im,jm,lm,psl, TEMP, NLRET)
      if ( NLRET.ne.LM) goto 205
      call RGRADS (id7, 52,100,0,im,jm,lm,psl, RH  , NLRET)
      if ( NLRET.ne.6) goto 205
      call RGRADS (id7, 33,100,0,im,jm,lm,psl, USL , NLRET)
      if ( NLRET.ne.LM) goto 205
      call RGRADS (id7, 34,100,0,im,jm,lm,psl, VSL , NLRET)
      if ( NLRET.ne.LM) goto 205
      print *,' .... Writing!'
c-----------
      open (55,file='../grads/wafs'//c2//'.dat',form='unformatted')
      write (55)  (id7(m),m=1,5),GEOP,USL, VSL, TEMP, RH
      close (55)
c-----------
c     writing!
205   continue
      end
c---------------------------
      subroutine mklist (NF)
      include 'tograds.inc'
c---------------------------
      character *150  str
      j1 = 1
```

```
      j2 = index (indset,' ') -1
      if ( j2.lt.j1) call fmess ('file name!')
      if (indset(j2:j2).ne.'/') then
            j2 = j2 +1
         indset(j2:j2)='/'
      endif
      print *,' indset=',indset(j1:j2)
      call system ('ls -l '//indset(j1:j2)//' > L.out')
      NF = 0
      open (12,file='L.out',status='old',err=299)
      open (22,file='L.out1',status='unknown')

10    call clears (str)
      read (12,'(a)',end=99) str
      if ( index(str,':').eq.0) goto 10
      NF = NF + 1
      i2 = 150
      do while (str(i2:i2).eq.' ')
      i2 = i2 - 1
      enddo
      i1 = i2
      do while (str(i1:i1).ne.' ')
      i1 = i1 - 1
      enddo
      write (22,'(a)') indset(j1:j2)//str(i1+1:i2)
      goto 10
99    continue
      close (12)
      close (22)
      call system('mv L.out1 L.out')
299   return
      end
```

The lateral boundary conditions for the regional area model are visualised using the script "*wafs.ctl*", with the following format:

```
dset /usr/local/ETA/ETA.1.a.test/grads/wafs.gdat
*indset /usr/local/ETA/ETA.1.a.test/input_grib
undef 9.999e+20
title AVN model
xdef  73  linear  -30.0 1.25
ydef  73   linear   0.0 1.25
tdef 9 linear 00Z28apr1999 6hr
zdef 10 levels 100 150 200 250 300 400 500 700 850 1000
vars 11
u10   0  33,105,10   Geopotential Height
v10   0  34,105,10   Geopotential Height
acp   0  61,  1, 0   Geopotential Height
t2    0  11,105, 2   Geopotential Height
rh2   0  52,105,2    Geopotential Height
seag  0   2,102,0    Geopotential Height
z    10   7,100  Geopotential Height
t    10  11,100  TEMP
u    10  33,100  U Winds
v    10  34,100  V Winds
rh   10  52,100  RH
endvars
```

II.2.2. Conversion of GrADS files into ascii xyz format.

The script *grads2xyz.f* converts GrADS-formatted data into ascii xyz. This data format facilitated data import into statistical software for model diagnostics and verification. The following is the *grads2xyz.f* script:

```
      include 'tograds.inc'
      parameter (NXNY=80000)
C-----------------------------------------------------------------------
c LL
      dimension VAR(NXNY), varh(NXNY)

      character *8 cdate8
      character *7 Cparm, Cpar, Clevt, Clev
      logical  run
      dimension  id7 (7)
      data id7 / 99,01,01,00,00,00,00/
c -------------------------------------------------------------
      wctln(1:1) = ' '
      print *,' ARGMENTS:yymmddss RDAYs'
      call getarg (1, Cdate8)
      call getarg (2, Cparm )
      call getarg (3, Cpar  )
      call getarg (4, Clevt )
      call getarg (5, clev  )
c     ---------------------------------
      call cdate2id7 ( cdate8,id7)
      read (Cpar ,*) IPAR
      read (Clevt,*) ILEVT
      read (Clev ,*) ILEV
      RLEV = ILEV
c     ---------------------------------
      print *,id7,' ** ',IPAR,ILEVT,ILEV
c     call RGRADS (id7, 7, 100,500, NXNY, 1, 1., 0.,varh , NLRET)
      call RGRADS (id7, IPAR,ILEVT,ILEV, NXNY, 1, 1, RLEV,VAR , NLRET)
      IM=RNX_CTL
      JM=RNY_CTL
      IMJM=IM*JM

c -------------------------------------------------------------
      print *,'IM,JM ',IM,JM,' IMxJM=',IM*JM,'   file size=',IM*JM*23
      call RGRADS (id7, IPAR,ILEVT,ILEV, IMJM, 1, 1, RLEV,VAR , NLRET)
      if(NLRET.eq.0) goto 1000

      nc = index(Cparm,' ') -1
      nl = index(Clev ,' ') -1
      open (50,file=
     +'../../XYZ/'//Cparm(1:nc)//'_'//Clev(1:nl)//'_'//Cdate8//'.xyz')
      n = 0
      tmin = 10000
      tmax = -10000
      do 50 j=1, JM
      rlat = RY0_CTL + (j-1)*RYI_CTL
      do 50 i=1, IM
      rlon = RX0_CTL + (i-1)*RXI_CTL
      n = n + 1
      if (VAR(n).ne.-999) then
```

```
      tmax= max(tmax,VAR(n))
      tmin= min(tmin,VAR(n))
      endif
      write ( 50,999) rlon, rlat,  VAR (n)
50    continue
      print *,' tmin - tmax: ',tmin,tmax
      stop
1000  continue
      print *,' No data avaiable!'
c
999   format(2f8.3,2x,f8.2)
c-----------------------------------------------------------
c
      end
```

II.2.3. Preparation of SST data from GrADS format to be ingested by the Eta model.

The subroutine *sst.f* prepares the sst file for the Eta model. For the case of remotely-sensed SST, this file reads the information embedded in GrADS file using the *WGRADS* command. This subroutine was included in the Eta package, but which was modified to accommodate the inclusion of TMI-derived SST into the model.

```
C     ********************************************************************
C     *                                                                  *
C     *  PROGRAM PREPARES THE SST DATA FROM GDAS and TMI DATA SET        *
C     *                                                                  *
C     ********************************************************************
C
C-----------------------------------------------------------------------
#include "large.inc"
#include "tmi.inc"
#include "tograds.inc"
C-----------------------------------------------------------------------
c                    P A R A M E T E R
c &(BOWEST=-180.,BOSOUT=-
90.,BOEAST=180.,BONORT=90.,DELON=1.,DELAT=1.
c    &,IME=(BOEAST-BOWEST)/DELON  ,JME=(BONORT-BOSOUT)/DELAT+1)
C-----------------------------------------------------------------------
      CHARACTER CARG1*2
      CHARACTER *8 cdate8
                              DIMENSION
     & COH(3,IMJM),INH(4,IMJM),JNH(4,IMJM)
     &,COV(3,IMJM),INV(4,IMJM),JNV(4,IMJM)

     &,WFB(IMJM),WFB1(IMJM1)

     &,SST(IMJM),SST2(IMT,JMT)

     &,WW(IME,JME)
     &,ALMD(IMJM),APHD(IMJM)
     &,PUS(IMJM1),PVS(IMJM1)
     &,TPUS(IMJM1),TPVS(IMJM1)
C
```

```
            DIMENSION
     & SSTF(IME,JME)
     +,id7(7)
C
      INCLUDE "../../decoding/src/decoding_nl.nml"
      INCLUDE "preproc_nl.nml"
C
C-----------------------------------------------------------------------
      OPEN (UNIT=11,FILE='../../namelists/name.list',FORM='FORMATTED')
      READ(11,DECODING_NL)
      READ(11,PREPROC_NL)
      CLOSE(11)
C--Check the command's input
      IF (IARGC().LT.1) THEN
c       print*,'Usage: climsst MONTH'
        print*,'Usage: sst YYMMDDHH'
        stop
      ELSE
      CALL GETARG (1,Cdate8)
      READ(CARG1,'(I2)')IMONTH
      END IF
C---- End command's input
C
      write(*,*)'IMJM,LDM,IMT,JMT,IM,JM,IMT,JMT'
      write(*,*) IMJM,LDM,IMT,JMT,IM,JM,IMT,JMT
      write(*,*)'IME*JME = ',IME*JME, IME,JME
C-----------------------------------------------------------------------
C
      CALL ECETA(COH,INH,JNH,COV,INV,JNV,CTPH0,STPH0,ALMD,APHD)
C
C-----------------------------------------------------------------------
      call cdate2id7 ( Cdate8,id7)
      wctln(1:1) = ' '
      idat(1) = id7(3)
      idat(2) = id7(2)
      idat(3) = id7(1)
      IHRST = id7(4)
      KDIM = IMJMLL*LDM
c -------------------------------------------------------------
      call datetohr(id7(3),id7(2),id7(1),id7(4),id7(5),IHRS)
      do 500 IHR = IHRS, IHRS - 10*24, -12
      call hrtodate
     + (IHR,id7(4),0,id7(3),id7(2),id7(1),id7(5))
      call RGRADS (id7, 1, 999,  0, IME, JME, 1, 0., WW , NLRET)
      if ( NLRET.ne.0) goto 410
500   continue
      print *,' No SST data avaiable'
      STOP
410   continue
      print *,' read sst:',WW
C
c     print *,' IMJM=',IMJM
c     print *,' WW  =', WW
                CALL BILINB(COH,INH,JNH,IMJM,IME,JME, WW, WFB)
                DO 411 IN=1,IMJM
 411              SST(IN)=WFB(IN)
C
      CALL CONH12(SST,SST2)
C
```

```
      ISST=47
      OPEN (UNIT=ISST,FILE=FN_SST
     &     ,STATUS='UNKNOWN',FORM='UNFORMATTED')
      WRITE (ISST) SST2
      PRINT*,' WRITE TO FILE: ',FN_SST
      CLOSE (ISST)
c     print *,'sst2=',sst2
C-----------------------------------------------------------------------
      STOP
      END
C
      SUBROUTINE BILINB(COB,INB,JNB,KB,IME,JME,WW,WFBC)
C     ***********************************************
C     *                                             *
C     * ROUTINE FOR BILINEAR INTERPOLATION        *
C     *                                             *
C     ***********************************************
C
          DIMENSION COB(3,KB),INB(4,KB),JNB(4,KB),WW(IME,JME),WFBC(KB)
C
C
          DO 10 K=1,KB
C
          I00=INB(1,K)
          I10=INB(2,K)
          I01=INB(3,K)
          I11=INB(4,K)
C
          J00=JNB(1,K)
          J10=JNB(2,K)
          J01=JNB(3,K)
          J11=JNB(4,K)
C
          P= COB(2,K)
          Q= COB(3,K)
          PQ=COB(1,K)
C
          Z=WW(I00,J00)+P*(WW(I10,J10)-WW(I00,J00))
     *                 +Q*(WW(I01,J01)-WW(I00,J00))
     *   +PQ*(WW(I00,J00)-WW(I10,J10)-WW(I01,J01)+WW(I11,J11))
C
 10       WFBC(K)=Z
          RETURN
          END
C
C&&&&&&&&&&&&&&&&&&&&&&&&&&&&&&&&&&&&&&&&&&&&&&&&&&&&&&&&&&&&&&&&
                    SUBROUTINE CONH12(H2,H3)
C     ***********************************************************************
C     *                                                                     *
C       * ROUTINE FOR REORDERING THIBUE-HEIGHT-POINT-1-DIMENSIONAL
*
C     * MATRICES FOR 2-DIMENSIONAL INDEXING                                 *
C     *                                                                     *
C     ***********************************************************************
#include "large.inc"
C-----------------------------------------------------------------------
                      D I M E N S I O N
     & H3   (IMT,JMT),H2   (IMJM)
C-----------------------------------------------------------------------
```

```
                    K=0
C-----------------------------------------------------------------------
          DO 100 J=1,JMT
        DO 110 I=1,IMT,2
     K=K+1
 110  H3(I,J)=H2(K)
C
     IF(J.EQ.JMT)          GO TO 100
C
        DO 120 I=2,IMT,2
     K=K+1
 120  H3(I,J)=H2(K)
C
 100         CONTINUE
C-----------------------------------------------------------------------
C-----------------------------------------------------------------------
                    RETURN
                    END
C&&&&&&&&&&&&&&&&&&&&&&&&&&&&&&&&&&&&&&&&&&&&&&&&&&&&&&&&&&&&&&&&&&&&&
     SUBROUTINE ECETA(COH,INH,JNH,COV,INV,JNV,CTPH0,STPH0,ALD,APD)
#include "tmi.inc"
#include "large.inc"
C                   #include "ecmwf.inc"
c                   P A R A M E T E R
c                                                        &(BOWEST=-180.,BOSOUT=-
90.,BOEAST=180.,BONORT=90.,DELON=1.,DELAT=1.
c    &,IME=(BOEAST-BOWEST)/DELON+1,JME=(BONORT-BOSOUT)/DELAT+1)
C
          D I M E N S I O N
    & COH(3,IMJM),INH(4,IMJM),JNH(4,IMJM)
    &,COV(3,IMJM),INV(4,IMJM),JNV(4,IMJM)
    &,ALD(IMJM),APD(IMJM)

          D I M E N S I O N
    & KHL0(JM),KVL0(JM),KHH0(JM),KVH0(JM)

       PRINT*,'IM=',IM,'JM=',JM,'IM=',IM,'JM=',JM
       PRINT*,'ECMWF DIMENSIONS IME,JME',IME,JME

C--------------- HIBU MODEL CONTS ---------------------------------
C
     DO 99 J=1,JM
C
     KHL0(J)=IM*(J-1)-(J-1)/2+1
     KVL0(J)=IM*(J-1)   - J/2+1
     KHH0(J)=IM* J      - J/2
 99  KVH0(J)=IM* J   -(J+1)/2
C
     ANBDC=BOSOUT+DELAT*(JME-1)
     EBDC=BOWEST+DELON*(IME-1)
C--------------- DEGREE TO RADIAN CONVERSION ----------------------
C--------------- HIBU
     WB=WBD*DTR
     SB=SBD*DTR
     TPH0=TPH0D*DTR
     TLM0=TLM0D*DTR
     CTPH0=COS(TPH0)
     STPH0=SIN(TPH0)
     DLM=DLMD*DTR
```

```
      DPH=DPHD*DTR
      TDLM=DLM+DLM
C---------- ECMWF
      WBC=BOWEST*DTR
      SBC=BOSOUT*DTR
      ANBC=ANBDC*DTR
      EBC=EBDC*DTR
      DLMC=DELON*DTR
      DPHC=DELAT*DTR
C---------- ENTRY TO THE HIBU I,J LOOP ----------
C           NEIGHBOUR ECMWF INDEX IDENTIFICATION
C           ECMWF DATA DEFINED IN LL SYSTEM
C-----------------------------------------------------------
C           HIBU HEIGHT PTS
C-----------------------------------------------------------
      TPH=SB-DPH
C
      DO 110 J=1,JM
C
      KHL=KHL0(J)
      KHH=KHH0(J)
C
      TPH=TPH+DPH
C
      DO 110 K=KHL,KHH
C
       TLM=WB+TDLM*(K-KHL)*MOD(J,2)+MOD(J+1,2)*(DLM+(K-KHL)*TDLM)
C---------- TLL TO LL CONVERSION ----------
      CALL  RTLL(TLM,TPH,TLM0D,DTR,CTPH0,STPH0,ALMD,APHD)
C----------CHECK IF HIBU PT IS OUT OF ECMWF DOMAIN ----------
      IF(ALMD .LT. BOWEST)     GO TO 200
      IF(APHD .GT. ANBDC)    GO TO 200
      IF(APHD .GE. BOSOUT)     GO TO 201
      IF(ALMD .LE. EBDC)     GO TO 200
      STOP
 201  IF(ALMD .GT. EBDC)     GO TO 200
C
      X=ALMD-BOWEST
      Y=APHD-BOSOUT
C
      INDEC=X/ DELON+1
      JNDEC=Y/ DELAT+1
C
      X=X-(INDEC-1)*DELON
      Y=Y-(JNDEC-1)*DELAT
C-----------------------------------------------------------
      COH(2,K)=X/ DELON
      COH(3,K)=Y/ DELAT
      COH(1,K)=COH(2,K)*COH(3,K)
C-----------------------------------------------------------
      INH(1,K)=INDEC
      INH(2,K)=INDEC+1
      INH(3,K)=INDEC
      INH(4,K)=INDEC+1
C
      JNH(1,K)=JNDEC
      JNH(2,K)=JNDEC
      JNH(3,K)=JNDEC+1
      JNH(4,K)=JNDEC+1
```

```
C
      GO TO 111
C
 200                PRINT        *,'HIBUPT        VISINE        K=',K,'JE        VAN
OBLASTI',APHD,ALMD,ANBDC,EBDC
      STOP
 111  CONTINUE
 110  CONTINUE
C-----------------------------------------------------------------
C                  WIND POINTS
C-----------------------------------------------------------------
C
      TPH=SB-DPH
C
      DO 210 J=1,JM
C
      KVL=KVL0(J)
      KVH=KVH0(J)
C
      TPH=TPH+DPH
      DO 210 K=KVL,KVH
C
       TLM=WB+DLM*MOD(J,2)+(K-KVL)*TDLM
C
C--------------------- TLL TO LL CONVERSION --------------------------
      CALL  RTLL(TLM,TPH,TLM0D,DTR,CTPH0,STPH0,ALMD,APHD)
C--------------------- CHECK IF HIBU PT IS OUT OF ECMWF DOMAIN --------
      IF(ALMD .LT. BOWEST)     GO TO 300
      IF(APHD .GT. ANBDC)    GO TO 300
      IF(APHD .GE. BOSOUT)     GO TO 301
      IF(ALMD .LE. EBDC)     GO TO 300
      STOP
 301  IF(ALMD .GT. EBDC)     GO TO 300
C
      ALD(K)=ALMD
      APD(K)=APHD
C
      X=ALMD-BOWEST
      Y=APHD-BOSOUT
C
      INDEC=X/ DELON+1
      JNDEC=Y/ DELAT+1
C
      X=X-(INDEC-1)*DELON
      Y=Y-(JNDEC-1)*DELAT
C-----------------------------------------------------------------
      COV(2,K)=X/ DELON
      COV(3,K)=Y/ DELAT
      COV(1,K)=COV(2,K)*COV(3,K)
C-----------------------------------------------------------------
      INV(1,K)=INDEC
      INV(2,K)=INDEC+1
      INV(3,K)=INDEC
      INV(4,K)=INDEC+1
C
      JNV(1,K)=JNDEC
      JNV(2,K)=JNDEC
      JNV(3,K)=JNDEC+1
      JNV(4,K)=JNDEC+1
```

```
C
      GO TO 210
C
 300                print          *,'HIBUPT'          BRZINE          K=',K,'JE          VAN
OBLASTI',APHD,ALMD,ANBDC,EBDC
 210  CONTINUE


      RETURN
      END
C-----------------------------------------------------------------------
      SUBROUTINE RTLL(TLM,TPH,TLM0D,DTR,CTPH0,STPH0,ALMD,APHD)
C
      STPH=SIN(TPH)
      CTPH=COS(TPH)
      CTLM=COS(TLM)
      STLM=SIN(TLM)
C
      APH=ASIN(STPH0*CTPH*CTLM+CTPH0*STPH)
      CPH=COS(APH)
C
      ALMD=TLM0D+ASIN(STLM*CTPH/CPH)/DTR
      APHD=APH/DTR
C
      RETURN
      END

      subroutine vfinit
      character*1 vc, vcscr(0:63)
      common/vform/vc(0:63)
      data vcscr/'0','1','2','3','4','5','6','7','8','9'
     +     ,'A','B','C','D','E','F','G','H','I','J'
     +     ,'K','L','M','N','O','P','Q','R','S','T'
     +     ,'U','V','W','X','Y','Z','a','b','c','d'
     +     ,'e','f','g','h','i','j','k','l','m','n'
     +     ,'o','p','q','r','s','t','u','v','w','x'
     +     ,'y','z','{','|'/

      do 10 n=0,63
        vc(n)=vcscr(n)
 10   continue

      return
      end

      subroutine vfirec(iunit,a,n,type)
      character*1 vc
      character*(*) type
      common/vform/vc(0:63)
      character line*80, cs*1
      dimension a(*)

      if(vc(0).ne.'0') call vfinit

      ich0=ichar('0')
      ich9=ichar('9')
      ichcz=ichar('Z')
      ichlz=ichar('z')
      ichca=ichar('A')
```

```
      ichla=ichar('a')

      read(iunit,10)nn,nbits,bias,fact
10    format(2i8,2e20.10)
      if(nn.ne.n) then
        print*,' Word count mismatch on vfirec record '
        print*,' Words on record - ',nn
        print*,' Words expected  - ',n
        stop 'vfirec'
      endif

      nvalline=(78*6)/nbits
      nchs=nbits/6
      do 20 i=1,n,nvalline
        read(iunit,'(a78)') line
        ic=0
        do 30 ii=i,i+nvalline-1
          isval=0
          if(ii.gt.n) go to 20
          do 40 iii=1,nchs
            ic=ic+1
            cs=line(ic:ic)
            ics=ichar(cs)
            if(ics.le.ich9)then
              nc=ics-ich0
            elseif(ics.le.ichcz) then
              nc=ics-ichca+10
            else
              nc=ics-ichla+36
            endif
            isval=intor(intlshft(nc,6*(nchs-iii)),isval)
40        continue
          a(ii)=isval
30      continue
20    continue

      facti=1./fact
      if(type.eq.'LIN') then
        do 48 i=1,n
          a(i)=a(i)*facti-bias
48      continue
      elseif(type.eq.'LOG') then
        scfct=2.**(nbits-1)
        do 55 i=1,n
          a(i)=sign(1.,a(i)-scfct)
     +          *(10.**(abs(20.*(a(i)/scfct-1.))-10.))
55      continue
      endif

      return
      end

      FUNCTION INTOR(IWORD1,IWORD2)
C
C     This function performs a bit-by-bit OR between IWORD1 and
C       IWORD2.
C
      INTOR=IOR(IWORD1,IWORD2)
      RETURN
```

```
      END
      FUNCTION INTLSHFT(IWORD,NSHFT)
C
C     This function shifts IWORD to the left NSHFT bits in a
C       circular manner.
C
      INTLSHFT=ISHFT(IWORD,NSHFT)
      RETURN
      END
```

II.2.4. Conversion of model predicted surface fluxes into GrADS format.

The surface geophysical fields, including the derived air-sea fluxes are calculated and converted into GrADS format for visualisation. The *SFC.ctl* contains the information necessary to write the predicted fields into GrADS format.

```
dset /usr/local/ETA/ETA.1.a.test/grads/SFC.gdat
*undef 1.e30
undef 0
title eta model
tdef 12 linear 00Z24jul1999 3hr
xdef 82 linear 15.8 0.041666
ydef 61 linear 33.24 0.041666
zdef 1 levels 1000
vars 33
smb   0  81,105,0   Sea Land Mask
sp    0  02,102,0   Sea Level Pressure
tp    0  61,105,0   Total Precipitation
ummf  0 125,105,10  U Momentum Flux
vmmf  0 126,105,10  V Momentum Flux
wtsurf 0 130,105,0  Total Heat Flux
swrad  0 117,105,0  Short Wave Radiation
ts    0  11,105,0   Surface Temperature
t2    0  11,105,2   2m Temperature
sfcl  0 121,105,0   Latent Heat Flux
sfcs  0 122,105,0   Sensible Heat Flux
akhl  0 131,105,0   Surface Mixing Coefficient (heat)
akml  0 132,105,0   Surface Mixing Coefficient (momentum)
u1    0  33,105,10  10 Meter U Wind
v1    0  34,105,10  10 Meter V Wind
uhl   0 133,105,10  Lowest Model Level U Wind (h points)
vhl   0 134,105,10  Lowest Model Level V Wind (h points)
uz0hl 0 136,105,0   U Wind at z0 (h points)
vz0hl 0 137,105,0   V Wind at z0 (h points)
ustr  0 135,105,0   Friction Velocity
z0l   0 138,105,0   z0
thz0l 0 139,105,0   Potential Temperature at z0
qz0l  0 140,105,0   Specific Humidity at z0
qfc   0 141,105,0   Moisture Flux
um    0 142,105,10  Lowest Model Level u Wind
vm    0 143,105,10  Lowest Model Level v Wind
czl   0 144,105,0   Cloudness M
czm   0 145,105,0   Cloudness L
cc    0  71,105,0   Cloudness
rlwi  0 205,105,0   Long wave radiation incoming
```

```
rswi   0 204,105,0   Short wave radiation incoming
rlwo   0 212,105,0   Long wave radiation outcoming
rswo   0 211,105,0   Short wave radiation outcoming
endvars
```

II.2.5. Preparation of predicted boundary conditions for the nested, high-resolution Eta model.

The subroutine that writes the predicted geopotential, specific humidity and wind components generated by the regional is *outnest.f.* The output files from this code is read by the nested model as its boundary conditions.

```
      SUBROUTINE OUTNEST
C     ******************************************************************
C     *                                                                *
C     * ROUTINE FOR WRITING DOWN GEOPOTENTIAL, SPECIFIC HUMIDITY
AND  *
C     * WIND COMPONENTS FOR NESTING PURPOSES                           *
C     *                                                                *
C     ******************************************************************
C-----------------------------------------------------------------------
C     INCLUDE/ SET PARAMETERS.
      INCLUDE "parmeta"
      INCLUDE "parm.tbl"
      INCLUDE "parmsoil"
C-----------------------------------------------------------------------
      PARAMETER (NSOIL=NSOLD)
      PARAMETER (LSLN=24)
                        P A R A M E T E R
     & (D50=.5E0,H1=1.E0,H2=2.E0,H4=4.E0,D00=0.E0
     &, H1000=1000.E0,H1M5=1.E-5,D125=.125E0
     &, H10000=10000.E0
     &, D608=0.608E0,D05=.05E0,D0065=0.0065E0,ROG=287.04E0/9.8E0
     &, OVERRC=1.75E0,AD05=OVERRC*D05,CFT0=OVERRC-H1,NRLX=15
     &, CAPA=0.28589641
     &, RGC=287.04E0,FFIS=1.E0/20000.E0,D61=.61E0,HSMTH=5000.)
C-----------------------------------------------------------------------
                        P A R A M E T E R
C***WARNING***IF LM.GT.16 THEN SET LDA=LM+9
     & (LDA=LM+9,LA=13)
C
                        P A R A M E T E R
     & (IMJM=IM*JM-JM/2,JMP1=JM+1,JAM=6+2*(JM-10),LB=2*IM+JM-3
     &, LM1=LM-1,LP1=LM+1,L3=LDA+LM+1,L4=LDA+2*LM+1,L7=L4+3
     &, LSCRCH=4*LM+1+LA+1
     &, IMT=2*IM-1)
C-----------------------------------------------------------------------
                      L O G I C A L
     & RUN,FIRST,RESTRT,SIGMA,STDRD,MESO,ONHOUR,NEST,PRINT_INIT
     &,PRINT_FIELDS, PRINT_GROUND
                        L O G I C A L
     & STDRD,OLDRD,SIGMA
C-----------------------------------------------------------------------
C
C     INCLUDE COMMON BLOCKS.
```

```
C
C-----------------------------------------------------------------------
      INCLUDE "CTLBLK"
      INCLUDE "LOOPS"
      INCLUDE "MASKS"
      INCLUDE "DYNAMD"
      INCLUDE "PHYS2"
      INCLUDE "MAPOT"
      INCLUDE "VRBLS"
      INCLUDE "PVRBLS"
      INCLUDE "BOCO"
      INCLUDE "INDX"
      INCLUDE "SOIL"
      INCLUDE "ACMRDS"
      INCLUDE "ACMRDL"
      INCLUDE "FOG"
      INCLUDE "CONTIN"
      INCLUDE "ACMPRE"
      INCLUDE "SRFDSP"
      INCLUDE "CLDWTR"
      INCLUDE "TCOEF"
      INCLUDE "FPREPC.COM"
C-----------------------------------------------------------------------
                        D I M E N S I O N
     & PBI   (IM,JM),PTI   (IM,JM)
     &,PTSL  (IM,JM),PFSL  (IM,JM),TSL   (IM,JM),FSL   (IM,JM)
     &,PSLP  (IM,JM),SLP   (IM,JM),SPRC  (IM,JM)
     &,ALP   (IM,JM,LP1),FI    (IM,JM,LP1)
     &,TTV(IM,JM),IMNT(IMJM,LM),JMNT(IMJM,LM),KMNTM(LM)
     &,GEOP  (IM,JM,LSLN),  TEMP  (IM,JM,LSLN),  SEAG  (IM,JM)
     &,USL   (IM,JM,LSLN),  VSL   (IM,JM,LSLN),  PDVP1 (IM,JM)
     &,PQSL  (IM,JM)   ,  QQSL  (IM,JM)   ,  SPHM  (IM,JM,LSLN)
C-----------------------------------------------------------------------
                        D I M E N S I O N
     & ZETA(LP1),PETA(IM,JM,LM)
C-----------------------------------------------------------------------
      DIMENSION SPLN(LSLN)
C-----------------------------------------------------------------------
      CHARACTER  CARG1*3
      CHARACTER  CDAT*3
C-----------------------------------------------------------------------
      CHARACTER*256 INFN,OUTFN
C-----------------------------------------------------------------------
                        D A T A
     & SPLN/
     &     10000.,15000.,20000.,25000.,30000.,35000.,
     &     40000.,45000.,50000.,55000.,60000.,65000.,
     &     70000.,73000.,77000.,82000.,85000.,87000.,
     &     90000.,92000.,94000.,96000.,98000.,100000./
C-----------------------------------------------------------------------
      INCLUDE "model2d_nl.nml"
C
      SIGMA=.FALSE.
      IHR=NTSD/TSPH+.5
C-----------------------------------------------------------------------
      WRITE(CDAT(1:3),'(I3.3)')IHR
Cekpatp
      print *,"IHR=",CDAT
```

```
C-----------------------------------------------------------------------
      OPEN (UNIT=11,FILE='../../namelists/name.list',FORM='FORMATTED')
      READ(11,MODEL2D_NL)
      CLOSE(11)
C-----------------------------------------------------------------------
      OUTFN=FN_NOUT(1:(INDEX(FN_NOUT,' '))-1)//CDAT//'.dat'
      print*,' Output file: ',OUTFN(1:INDEX(OUTFN,' '))
C-----------------------------------------------------------------------
      DO I=1,LM
        DETA(I)=ETA(I+1)-ETA(I)
        AETA(I)=0.5*(ETA(I+1)+ETA(I))
      END DO
C
C     CALCULATE THE I-INDEX EAST-WEST INCREMENTS
C
      DO J=1,JM
        IHE(J)=MOD(J+1,2)
        IHW(J)=IHE(J)-1
      ENDDO
C-------------INTERFACE GEOPOTENTIALS AND LN P VALUES-----------------
         DO 100 J=1,JM
            DO 100 I=1,IM
      PDSL(I,J)=RES(I,J)*PD(I,J)
      PBI(I,J)=PD(I,J)+PT
      FI(I,J,LP1)=FIS(I,J)
  100 ALP(I,J,LP1)=ALOG(PBI(I,J))
                        DO 110 IVI=1,LM
                        L=LP1-IVI
         DO 110 J=1,JM
         DO 110 I=1,IM
      PTI(I,J)=PDSL(I,J)*ETA(L)+PT
      FI(I,J,L)=HTM(I,J,L)*(Q(I,J,L)*D61+H1)*T(I,J,L)
     2      /(PBI(I,J)+PTI(I,J))*PDSL(I,J)*DETA(L)*RGC*H2+FI(I,J,L+1)
      peta(I,J,l)=(PBI(I,J)+PTI(I,J))*.5
      PBI(I,J)=PTI(I,J)
  110 ALP(I,J,L)=ALOG(PBI(I,J))
C-------------VRTCL INTRPLTION, STRTING BY THE UPPRMOST ST. PRESS. LVL.
                        DO 120 L=1,LSLN
C
                        ALSL(L) = LOG(SPLN(L))
                        TRF=H2*ALSL(L)
         DO 130 J=1,JM
         DO 130 I=1,IM
      LMA  =LMH(I,J)
      LMAP1=LMA+1
      PPDSL=PDSL(I,J)
      INTZO=0
               DO 140 IL=2,LMAP1
               IF((ALSL(L)-ALP(I,J,IL)).GT.D00) GO TO 140
               NL1=IL
               GO TO 150
  140             CONTINUE
      NL1=LMAP1
      INTZO=1
C
  150 IF((TRF-ALP(I,J,NL1)-ALP(I,J,NL1-1)).LE.D00)       NL1=NL1-1
C
      PNL1=PDSL(I,J)*ETA(NL1)+PT
C
```

```
      IF(NL1.EQ.1) THEN
        B=T(I,J,1)
        BQ=Q(I,J,1)
        FAC=H2*ALOG(PT+PDSL(I,J)*AETA(1))
        AHF=(T(I,J,2)-B)/(ALP(I,J,3)-ALP(I,J,1))
        AHFQ=(Q(I,J,2)-BQ)/(ALP(I,J,3)-ALP(I,J,1))
      ELSE IF(NL1.EQ.LMAP1) THEN
        B=T(I,J,LMA)
        BQ=Q(I,J,LMA)
        FAC=H2*ALOG(PT+PDSL(I,J)*AETA(LMA))
        AHF=(B-T(I,J,LMA-1))/(ALP(I,J,LMAP1)-ALP(I,J,LMA-1))
        AHFQ=(BQ-Q(I,J,LMA-1))/(ALP(I,J,LMAP1)-ALP(I,J,LMA-1))
      ELSE
        B=T(I,J,NL1)
        BQ=Q(I,J,NL1)
        FAC=H2*ALOG(PT+PDSL(I,J)*AETA(NL1))
        AHF=(B-T(I,J,NL1-1))/(ALP(I,J,NL1+1)-ALP(I,J,NL1-1))
        AHFQ=(BQ-Q(I,J,NL1-1))/(ALP(I,J,NL1+1)-ALP(I,J,NL1-1))
      END IF
C
      PTSL(I,J)=B+AHF*(TRF-FAC)
      PQSL(I,J)=BQ+AHFQ*(TRF-FAC)
      PFSL(I,J)=(PNL1-SPLN(L))/(SPLN(L)+PNL1)
     2     *((ALSL(L)+ALP(I,J,NL1)-FAC)*AHF+B)*RGC*H2
     3     +FI(I,J,NL1)
  130 CONTINUE
C-----------------SMOOTHING ABOVE HIGH TOPOGRAPHY----------------------
        DO 190 J=1,JM
        DO 190 I=1,IM
      FSL(I,J)=PFSL(I,J)
      QQSL(I,J)=PQSL(I,J)
  190 TSL(I,J)=PTSL(I,J)
C-------------------------------------------------------------------------
                        DO 410 KS=1,4
           DO 200 J=2,JM-1
        DO 200 I=2-mod(j+1,2),IM-1
      IF (FSL(I,J)-FIS(I,J).GT.10000.)       GO TO 200
      IF (FIS(I,J).GT.10000.)                GO TO 400
      IF (ABS(FIS(I+IHW(J),J-1)-FIS(I,J)).GT.HSMTH)  GO TO 400
      IF (ABS(FIS(I+IHE(J),J-1)-FIS(I,J)).GT.HSMTH)  GO TO 400
      IF (ABS(FIS(I+IHW(J),J+1)-FIS(I,J)).GT.HSMTH)  GO TO 400
      IF (ABS(FIS(I+IHE(J),J+1)-FIS(I,J)).GT.HSMTH)  GO TO 400
      IF (FSL(I+IHW(J),J-1)-FIS(I+IHW(J),J-1).LT.D00)     GO TO 400
      IF (FSL(I+IHE(J),J-1)-FIS(I+IHE(J),J-1).LT.D00)     GO TO 400
      IF (FSL(I,J  )-FIS(I,J  ).LT.D00)                   GO TO 400
      IF (FSL(I+IHW(J),J+1)-FIS(I+IHW(J),J+1).LT.D00)     GO TO 400
      IF (FSL(I+IHE(J),J+1)-FIS(I+IHE(J),J+1).LT.D00)     GO TO 400
                    GO TO 200
  400 FSL(I,J)=D125*(PFSL(I+IHW(J),J-1)+PFSL(I+IHE(J),J-1)
     1          +PFSL(I+IHW(J),J+1)+PFSL(I+IHE(J),J+1)
     2          +H4*PFSL(I,J))
      QQSL(I,J)=D125*(PQSL(I+IHW(J),J-1)+PQSL(I+IHE(J),J-1)
     1          +PQSL(I+IHW(J),J+1)+PQSL(I+IHE(J),J+1)
     2          +H4*PQSL(I,J))
      TSL(I,J)=D125*(PTSL(I+IHW(J),J-1)+PTSL(I+IHE(J),J-1)
     1          +PTSL(I+IHW(J),J+1)+PTSL(I+IHE(J),J+1)
     2          +H4*PTSL(I,J))
C-------------------------------------------------------------------------
  200 CONTINUE
```

```
        DO 410 J=1,JM
        DO 410 I=1,IM
      PFSL(I,J)=FSL(I,J)
      PQSL(I,J)=QQSL(I,J)
      PTSL(I,J)=TSL(I,J)
C-----------------------------------------------------------------------
      GEOP(I,J,L)=FSL(I,J)/ 9.8
      TEMP(I,J,L)=TSL(I,J)
      SPHM(I,J,L)=QQSL(I,J)
 410  CONTINUE
C-----------------------------------------------------------------------
C***
C***  CALCULATE AVERAGE PRESSURE DIFFERENCE BETWEEN ETA=1 AND
ETA=0
C***  AT VELOCITY POINTS (PDVP1) USING THE VALUES ALREADY KNOWN AT
C***  HEIGHT POINTS (PDSL).
C***
      DO 1800 J=2,JM-1
      DO 1800 I=2,IM-1
      PDVP1(I,J)=0.25E0*(PDSL(I,J)+PDSL(I+1,J)+PDSL(I,J+1)+PDSL(I,J-1))
 1800 CONTINUE
      DO 1810 I=1,IM-1
      PDVP1(I,1)=0.5E0*(PDSL(I,1)+PDSL(I+1,1))
      PDVP1(I,JM)=0.5E0*(PDSL(I,JM)+PDSL(I+1,JM))
 1810 CONTINUE
      DO 1820 J=1,JM-1
      PDVP1(1,J)=0.5E0*(PDSL(1,J)+PDSL(1,J+1))
      PDVP1(IM,J)=0.5E0*(PDSL(IM,J)+PDSL(IM,J+1))
 1820 CONTINUE
Cdule
      PDVP1(IM,JM)=0.
Cdule
C***
C***  INTERPOLATE WIND COMPONENTS FROM ETA TO PRESSURE.
C***
      DO 2900 J=1,JM
      DO 2900 I=1,IM
      LMB=LMV(I,J)
      DO 2100 IL=2,LMB
      PETAL=PT+PDVP1(I,J)*ETA(IL)
      PETAU=PT+PDVP1(I,J)*ETA(IL-1)
      ALPETL=ALOG(PETAL)
      ALPETU=ALOG(PETAU)
      ALPET2=SQRT(0.5E0*(ALPETL*ALPETL+ALPETU*ALPETU))
C***
C***  SEARCH FOR HIGHEST DASHED ETA SURFACE (NOT SUBMERGED) THAT
IS
C***  BELOW THE GIVEN STANDARD PRESSURE LEVEL.
C***
      IF(ALSL(L).LT.ALPET2.OR.IL.EQ.LMB)THEN
        NL1=IL-1
        GO TO 2150
      ENDIF
 2100 CONTINUE
 2150 ALPETL=ALPETU
      ULO=U(I,J,NL1)
      VLO=V(I,J,NL1)
      IF(NL1.GT.1)THEN
        PETAU=PT+PDVP1(I,J)*ETA(NL1-1)
```

```
      UHI=U(I,J,NL1-1)
      VHI=V(I,J,NL1-1)
    ELSE
      PETAU=PT
      UHI=ULO
      VHI=VLO
    ENDIF
    ALPETU=ALOG(PETAU)
    ALPET1=SQRT(0.5E0*(ALPETL*ALPETL+ALPETU*ALPETU))
    DIFALP=ALPET2-ALPET1
C***
C*** ALPET2 IS DASHED ETA SURFACE JUST BELOW STANDARD PRESSURE
LEVEL
C*** AND ALPET1 IS DASHED ETA SURFACE JUST ABOVE.
C*** NOTE THAT IF THE STANDARD PRESSURE SURFACE IS SUBMERGED,
THEN
C*** ALPET2 AND ALPET1 ARE THE LOWEST AND 2ND LOWEST DASHED ETA
C*** SURFACES ABOVE THE TOPOGRAPHY.
C***
csd     IF(NL1.GT.1)THEN
    IF(NL1.GT.1.and.DIFALP.ne.0.)THEN
      FACT=(ALPET2-ALSL(L))/(ALPET2-ALPET1)
    ELSE
      FACT=D00
    ENDIF
    USL(I,J,L)=ULO+(UHI-ULO)*FACT
    VSL(I,J,L)=VLO+(VHI-VLO)*FACT
 2900 CONTINUE
C

C
    DO 2999 J=2,JM-1
    DO 2999 I=2,IM-1
C
    IF(PD(I,J    )+PT.LT.SPLN(L).OR.PD(I-1,J )+PT.LT.SPLN(L).OR.
   &   PD(I,J+1)+PT.LT.SPLN(L).OR.PD(I,J-1)+PT.LT.SPLN(L)    ) THEN
    USL(I,J,L)=0.
    VSL(I,J,L)=0.
          END IF
 2999  CONTINUE
C-------------------------------------------------------------------
 120                  CONTINUE
C-------------------------------------------------------------------
C-------------SEA LEVEL PRESSURE-----------------------------------
C       HAVE SRDRD .FALSE. TO DO THE RELAXATION TEMPERATURE
REDUCTION
C       OR THE OLD ETA/SIGMA GRADINET (WEIGHTED FOR ETA) REDUCTION
C       HAVE OLDRD .TRUE. TO DO THE "OLD" (WEIGHTED) ETA REDUCTION
    STDRD=.FALSE.
    OLDRD=.FALSE.
    IF(SIGMA) STDRD=.TRUE.
C
    IF (.NOT.STDRD .AND. .NOT.OLDRD) GO TO 700
      DO 210 J=1,JM
      DO 210 I=1,IM
    IF(FIS(I,J).LT.H1)THEN
      PSLP(I,J)=PD(I,J)+PT
    ELSE
      LMA=LMH(I,J)
```

```
      ALPP1=ALOG(PDSL(I,J)*ETA(LMA+1)+PT)
        IF(OLDRD) THEN
      SLOP=(T(I,J,LMA)-T(I,J,LMA-1))
     1  /(ALPP1-ALOG(PDSL(I,J)*ETA(LMA-1)+PT))*H2
        ELSE
      SLOP=D0065*ROG*T(I,J,LMA)
        ENDIF
      IF(SLOP.LT.D50)THEN
        SLPP=ALPP1+FIS(I,J)/(RGC*T(I,J,LMA))
      ELSE
        TTT=-(ALOG(PDSL(I,J)*ETA(LMA)+PT)+ALPP1)*SLOP*D50+T(I,J,LMA)
        SLPP=(-TTT+SQRT(TTT*TTT+H2*SLOP
     1    *(FIS(I,J)/RGC+(TTT+D50*SLOP*ALPP1)*ALPP1)))/SLOP
      ENDIF
      PSLP(I,J)=EXP(SLPP)
     ENDIF
  210 CONTINUE
     IF(.NOT.SIGMA .AND. OLDRD)THEN
      DO 215 J=1,JM
      DO 215 I=1,IM
      FCFIS=FFIS*FIS(I,J)
      PSLP(I,J)=(PSLP(I,J)+(PDSL(I,J)+PT)*FCFIS)/(H1+FCFIS)
  215  CONTINUE
     ENDIF
      GO TO 715
C
C------- ETA SLP REDUCTION BASED ON RELAXATION TEMPERATURE ------------
C      FIND THE HIGHEST LAYER CONTAINING MOUNTAINS
  700                 DO 702 IVI=1,LM
                      L=LP1-IVI
        DO 701 J=1,JM
        DO 701 I=1,IM
      IF(HTM(I,J,L).EQ.D00) GO TO 702
  701    CONTINUE
                      LHMNT=L+1
                      GO TO 703
  702                 CONTINUE
C     NOW GATHER THE ADDRESSES OF ALL THE UNDERGROUND POINT
  703                 DO 705 L=LHMNT,LM
                      KMN=1
        DO 704 J=3,JM-2
        DO 704 I=2,IM-1
      IF(HTM(I,J,L).EQ.H1) GO TO 704
      IMNT(KMN,L)=I
      JMNT(KMN,L)=J
      KMN=KMN+1
  704    CONTINUE
                      KMNTM(L)=KMN-1
  705                 CONTINUE
C      AS THE FIRST GUESS, SET THE UNDERGROUND TEMPERATURE EQUAL
TO
C      THE VALUE GIVING PD/ETAS+PT AS SEA LEVEL PRESSURE
        KMM=KMNTM(LM)
        DO 706 KM=1,KMM  !!!POPRAVLJENO
      I=IMNT(KM,LM)
      J=JMNT(KM,LM)
      TGSS=FIS(I,J)/(RGC*ALOG((PDSL(I,J)+PT)/(PD(I,J)+PT)))
                      LMAP1=LMH(I,J)+1
                      DO 706 L=LMAP1,LM
```

```
 706    T(I,J,L)=TGSS
C   CREATE A TEMPORARY TV ARRAY, AND FOLLOW BY SEQUENTIAL
C   OVERRELAXATION, DOING NRLX PASSES
                    DO 711 L=LHMNT,LM
       DO 707 J=1,JM
       DO 707 I=1,IM
 707   TTV(I,J)=T(I,J,L)*(H1+D608*Q(I,J,L))
       KMM=KMNTM(L)
                    DO 711 N=1,NRLX
       DO 708 KM=1,KMM
     I=IMNT(KM,L)
     J=JMNT(KM,L)
 708   TTV(I,J)=AD05*(H4*(TTV(I+IHW(J),J-1)+TTV(I+IHE(J),J-1)
  1                +TTV(I+IHW(J),J+1)+TTV(I+IHE(J),J+1))
  2          +TTV(I-1,J)+TTV(I+1,J)+TTV(I,J+2)+TTV(I,J-2))
  3          -CFT0*TTV(I,J)
     IF(N.EQ.NRLX) THEN
       DO 710 KM=1,KMM
       I=IMNT(KM,L)
       J=JMNT(KM,L)
 710     T(I,J,L)=TTV(I,J)
     END IF
 711                CONTINUE
C      FINALLY, CALCULATE THE SEA LEVEL PRESSURE
       DO 712 J=1,JM
       DO 712 I=1,IM
 712   PSLP(I,J)=PD(I,J)+PT
       DO 714 KM=1,KMM
       I=IMNT(KM,LM)
       J=JMNT(KM,LM)
                    LMAP1=LMH(I,J)+1
                    SLPP=ALOG(PD(I,J)+PT)
                    DO 713 L=LMAP1,LM
 713  SLPP=SLPP+(DFL(L)-DFL(L+1))/(RGC*T(I,J,L))
 714  PSLP(I,J)=EXP(SLPP)
C
C-------------SMOOTH SEA LEVEL PRESSURE ------------------------------
 715     DO 220 J=1,JM
       DO 220 I=1,IM
 220  SLP(I,J)=PSLP(I,J)
C-------------------------------------------------------------------
        DO 460 KS=1,2
      DO 201 J=2,JM-1
      DO 201 I=2,IM-1
 201  SLP(I,J)=D125*(PSLP(I+IHW(J),J-1)+PSLP(I+IHE(J),J-1)
  1          +PSLP(I+IHW(J),J+1)+PSLP(I+IHE(J),J+1)
  2          +H4*PSLP(I,J))
C-------------------------------------------------------------------
      DO 460 J=1,JM
      DO 460 I=1,IM
   PSLP(I,J)=SLP(I,J)
   SEAG(I,J)=PSLP(I,J)*.01
 460  CONTINUE
C-------------------------------------------------------------------
C----------WRITING  SLP,H,T,U & V  FOR GRAPHICS ---------------------

   OPEN(UNIT=31,FILE=OUTFN
  &   ,STATUS='UNKNOWN',ACCESS='SEQUENTIAL',FORM='UNFORMATTED')
   WRITE(31)IDAT,IHRST,IHR,GEOP,SPHM,USL,VSL,SEAG
```

```
      CLOSE(31)

      WRITE (*,9807)IDAT,IHRST,IHR
 9807 FORMAT('Output : ',3(I2,'.'),' at ',I2,'UTC + ',I2,'h')
      print*,'*****************************'
C-----------------------------------------------------------------------
                        RETURN
                        END
```

II.2.6. Preparation of predicted surface fluxes to drive high resolution, POM model.

The atmospheric surface fields produced by the nested model are required to drive the ocean model. These fields are produced by the subroutine *flux.f*. A number of fields are calculated and written, including the surface latent and sensible heat flux, the surface moisture flux, the u- and v-components of the momentum flux, the surface incoming and outgoing short wave radiation flux, the surface incoming and outgoing longwave radiation flux, the cloud cover ratio, the lowest model level wind points, and the potential temperature at the lowest model level. Two sets of output files are written, the *surfce_pom* files and *GrADS* files using the information embedded in the *SFC.ctl* script.

```
PROGRAM FLUX
C-----------------------------------------------------------------------
C   Program for preparing atmospheric surface fields in LL grid
C-----------------------------------------------------------------------
#include "parmeta.inc"
#include "latlon.inc"
C-----------------------------------------------------------------------
                        P A R A M E T E R
     +(IMJM=IM*JM-JM/2,KNE=IM,KNW=IM-1,NINC=2*IM-1)
C
                        P A R A M E T E R
     & (PQ0=379.90516,A1=610.78,A2=17.2693882,A3=273.16,A4=35.86
     &, TRESH=.95E0)
C
                        D I M E N S I O N
     & IDAT(3)
     &,SEAG(IM,JM),U10(IM,JM),V10(IM,JM),ACPREC(IM,JM)
     &,CUPREC(IM,JM)
     &,T2M(IM,JM),TSURFCE(IM,JM),CCR(IM,JM,LM),CCRT(IM,JM)
     &,SSHFLX(IM,JM),SLHFLX(IM,JM),RSWIN(IM,JM)
     &,RSWOUT(IM,JM),RLWIN(IM,JM),RLWOUT(IM,JM),RFLUX(IM,JM)
     &,USTAR(IM,JM),ummflx(im,jm),vmmflx(im,jm),qlhflx(IM,JM)
     &,UHLM(IM,JM),VHLM(IM,JM),UZ0HC(IM,JM),VZ0HC(IM,JM)
     &,Z0(IM,JM),QZ0(IM,JM),THZ0(IM,JM),AKHS(IM,JM),AKMS(IM,JM)
     &,SM(IM,JM),CCZL(IM,JM),CCZM(IM,JM)
C
                        D I M E N S I O N
     & U10K(IMJM),V10K(IMJM)
     &,T2MK(IMJM),TSFCK(IMJM),SEAGK(IMJM),ACPRECK(IMJM)
     &,CCRTK(IMJM),RFLUXK(IMJM)
     &,SSHFLXK(IMJM),SLHFLXK(IMJM),USTARK(IMJM)
```

```
     &,ummflxk(imjm),vmmflxk(imjm),qlhflxk(imjm)
     &,Z0K(IMJM),AKHSK(IMJM),AKMSK(IMJM),SMK(IMJM)
     &,THZ0K(IMJM),QZ0K(IMJM),CCZLK(IMJM),CCZMK(IMJM)
     &,UZ0HK(IMJM),VZ0HK(IMJM),UHLMK(IMJM),VHLMK(IMJM)
     &,RLWINK(IMJM),RLWOUTK(IMJM),RSWINK(IMJM),RSWOUTK(IMJM)
C
     &,U1(IMLL,JMLL),V1(IMLL,JMLL)
     &,TM(IMLL,JMLL),T2(IMLL,JMLL),TS(IMLL,JMLL),SP(IMLL,JMLL)
     &,TP(IMLL,JMLL),RH(IMLL,JMLL),RF(IMLL,JMLL),SFCL(IMLL,JMLL)
     &,SFCS(IMLL,JMLL),CC(IMLL,JMLL),USTR(IMLL,JMLL)
     &,ummf(imll,jmll),vmmf(imll,jmll),CZL(imll,jmll)
     &,CZM(imll,jmll)
     &,WINSU(IMLL,JMLL),WINSV(IMLL,JMLL),WTSURF(IMLL,JMLL)
     &,SWRAD(IMLL,JMLL),qfc(imll,jmll),uhl(imll,jmll),vhl(imll,jmll)
     &,akhl(imll,jmll),akml(imll,jmll),z0l(imll,jmll)
     &,thz0l(imll,jmll),qz0l(imll,jmll)
     &,uz0hl(imll,jmll),vz0hl(imll,jmll)
     &,rlwi(imll,jmll),rlwo(imll,jmll),rswi(imll,jmll),rswo(imll,jmll)
     &,ALON(IMLL,JMLL),ALAT(IMLL,JMLL)
C
     &,SMB(IMLL,JMLL),SMBB(IMJMLL)
C
C-------------------------------------------------------------------------
     dimension id7(7), ar7(7),vrta(100)
c------------------------------
     CHARACTER  CARG1*3
     CHARACTER  CDAT*3
     CHARACTER  CDT*6
     CHARACTER  *8 CDATE8
     CHARACTER FFNAMES*256
C-------------------------------------------------------------------------
      INCLUDE "../../model/src/model2d_nl.nml"
C-------------------------------------------------------------------------
     BLN(P,Q,X1,X2,X3,X4)=X1+P*(X2-X1)+Q*(X3-X1)+P*Q*(X1-X2-X3+X4)
C-------------------------------------------------------------------------
     OPEN (UNIT=11,FILE='../../namelists/name.list',FORM='FORMATTED')
     READ(11,MODEL2D_NL)
     CLOSE(11)
C-------------------------------------------------------------------------
c     orv = 1.e+30
CPEJA 990226!!!!
      orv = 0
C-------------------------------------------------------------------------
     IF (IARGC().LE.0) THEN
          print*,' Usage: compass ihr'
     STOP
     ENDIF
C
     CALL GETARG(1,CARG1)
     READ(CARG1,'(I3)')IHR
     WRITE(CDAT(1:3),'(I3.3)')IHR
C
     print *,"IHR=",CDAT
C=================================================================
C
     FFNAMES=FN_SOUT(1:(INDEX(FN_SOUT,' '))-1)//CDAT//'.dat'
     print*,'im=',im,'jm=',jm,'imjm=',imjm
     print*,'imll=',imll,'jmll=',jmll,'imjmll=',imjmll
     print*,'wbdll=',wbdll,'sbdll=',sbdll
```

```
c-------------------------------------------------------
      OPEN(UNIT=33,
     &FILE='../../output/maskll_4km.dat',
     & STATUS='UNKNOWN',ACCESS='SEQUENTIAL',FORM='UNFORMATTED')
      READ(33)SMBB
      CLOSE(33)
c
C-------------------------------------------------------
C
      IF(MOD(IHR,3).eq.0)THEN
      OPEN(UNIT=31,FILE='../../output/msl'//CDAT//'.dat'
     &    ,STATUS='UNKNOWN',ACCESS='SEQUENTIAL',FORM='UNFORMATTED')
C---------------------------------
      READ (31)IDAT,IHRST,IHRR,SEAG
      print*,'IDAT=',IDAT
      print*,'IHRR=',IHRR
      CLOSE(31)
      ENDIF
c---------------------------------
C
      OPEN(UNIT=32,FILE=FFNAMES
     &
,STATUS='UNKNOWN',ACCESS='SEQUENTIAL',FORM='UNFORMATTED')
C-----------------------------------------------------------------------
C SSHFLX - surface sensible heat flux
C SLHFLX - surface  latent heat flux
C qlhflx - surface  moisture flux
C ummflx - u momentum flux
C vmmflx - v momentum flux
C RSWIN  - surface incoming short wave radiation flux
C RSWOUT - surface outcoming short wave radiation flux
C RLWIN  - surface incoming longwave radiation flux
C RLWOUT - surface outcoming longwave radiation flux
C CCR    - cloud cover ratio
C UHLM,VHLM - last model level winds (at H points)
C UZ0HC,VZ0HC - wind at Z0 in H points
C QZ0,THZ0 -  at Z0 in H points
C-----------------------------------------------------------------------
      READ (32)IDAT,IHRST,IHR
      READ (32)SSHFLX
      READ (32)SLHFLX
      READ (32)ummflx
      READ (32)vmmflx
      READ (32)qlhflx
      READ (32)RSWIN
      READ (32)RSWOUT
      READ (32)RLWIN
      READ (32)RLWOUT
      READ (32)T2M   !TSHLTR
      READ (32)TSURFCE
      READ (32)U10
      READ (32)V10
      READ (32)UHLM
      READ (32)VHLM
      READ (32)ACPREC
      READ (32)CUPREC
      READ (32)USTAR
      READ (32)Z0
      READ (32)UZ0HC
```

```
      READ (32)VZ0HC
      READ (32)QZ0
      READ (32)THZ0
      READ (32)AKHS
      READ (32)AKMS
      READ (32)SM
      READ (32)CCR
      READ (32)CCZL,CCZM
!!    READ (32)IDAT,IHRST,IHR,TLM0D,TPH0D,WBD,SBD,DLMD,DPHD,DTB,LM
      print*,'IHR=',IHR,FFNAMES
       CLOSE(32)
C=================================================================
      OPEN(UNIT=33,FILE='../../output/datum.dat'
     &    ,STATUS='UNKNOWN',ACCESS='SEQUENTIAL',FORM='UNFORMATTED')
      write(33)idat,ihrst,ihr
      close (33)
C=================================================================
      if (IHR.eq.0) then
      OPEN(UNIT=33,FILE='../../output/datum.YYMMDDHH'
     &    ,STATUS='UNKNOWN',ACCESS='SEQUENTIAL')
      write (CDATE8(1:2),'(I2.2)') idat(3)
      write (CDATE8(3:4),'(I2.2)') idat(2)
      write (CDATE8(5:6),'(I2.2)') idat(1)
      write (CDATE8(7:8),'(I2.2)') IHRST
      write(33, '(a)') CDATE8
      close (33)
      endif
C=================================================================
c-----conversion to 1dim indx
c-----------------------------------------------------------------
       k=0
       do j=1,jm
       do i=1,im - mod(j+1,2)
          k=k+1
c
       T2MK (K)=T2M (I,J)                !-273.15
       TSFCK(K)=TSURFCE (I,J)            !-273.15
       ACPRECK(K)=ACPREC(I,J)
       USTARK(K)=USTAR(I,J)
       CCZLK(K)=CCZL(I,J)
       CCZMK(K)=CCZM(I,J)
C
       ummflxk(k)=ummflx(i,j)
       vmmflxk(k)=vmmflx(i,j)
C
       U10K(k)=U10(i,j)
       V10K(k)=V10(i,j)
C
       SEAGK(K)=SEAG(I,J)
C
        enddo
       enddo
c-----------------------------------------------------------------
      DO I=1,IM
      DO J=1,JM
      RFLUX(I,J)=0.
      CCRT(I,J)=0.
C
      ENDDO
```

```
      ENDDO
      DO I=1,IM
      DO J=1,JM
      RFLUX(I,J)=RLWIN(I,J)-RLWOUT(I,J)+RSWIN(I,J)-RSWOUT(I,J)
      ENDDO
      ENDDO
C
C
      DO L=1,LM
      DO I=1,IM
      DO J=1,JM
      CCRT(I,J)=CCRT(I,J)+CCR(I,J,L)
      ENDDO
      ENDDO
      ENDDO
C-----------------------------------------
CGRADSGRADSGRADSGRADS
c------------------------
      ar7 (1) = 2.
      ar7 (2) = TLM0D
      ar7 (3) = WBD
      ar7 (4) = DLMD
      ar7 (5) = TPH0D
      ar7 (6) = SBD
      ar7 (7) = DPHD
c------------------------
      print *,im,jm,LSL,LSM
      id7 (1) = idat(3)
      id7 (2) = idat(2)
      id7 (3) = idat(1)
      id7 (4) = ihrst
      id7 (5) = ihr
      id7 (6) = 00
      id7 (7) = 00
      print *,' ar7:',ar7, id7
      D = 0.
c------------------------
      CALL WGRADS (id7, 02, 0, 0,102, 0,ar7,im,jm,1,0.,SEAG,D )
      CALL WGRADS (id7, 33,34, 1,105,10,ar7,im,jm,1,0.,u10, v10)
      CALL WGRADS(id7,122, 0,  0,105, 0, ar7,im,jm,1,0.,sshflx, D  )
      CALL WGRADS(id7,121, 0,  0,105, 0, ar7,im,jm,1,0.,slhflx, D  )
      CALL WGRADS(id7,125,126, 1,105,10, ar7,im,jm,1,0.,ummflx,vmmflx)
      CALL WGRADS (id7, 61, 0, 0,105, 0,ar7,im,jm,1,0.,ACPREC,D )
      CALL WGRADS (id7, 11, 0, 0,105, 0,ar7,im,jm,1,0.,TSURFCE,D)
      CALL WGRADS (id7, 11, 0, 0,105, 2,ar7,im,jm,1,0.,T2M,D )
c-----------------------------------------------------------------
      CALL WGRADS (id7,141, 0, 0,105, 0,ar7,im,jm,1,0.,qlhflx,D )
      CALL WGRADS (id7,117, 0, 0,105, 0,ar7,im,jm,1,0.,rflux ,D )
      CALL WGRADS (id7,138, 0, 0,105, 0,ar7,im,jm,1,0.,Z0 ,D )
      CALL WGRADS (id7,135, 0, 0,105, 0,ar7,im,jm,1,0.,ustar,D )
      CALL WGRADS (id7, 71, 0, 0,105, 0,ar7,im,jm,1,0.,ccrt,D )
      CALL WGRADS (id7,131, 0, 0,105, 0,ar7,im,jm,1,0.,akhs,D )
      CALL WGRADS (id7,132, 0, 0,105, 0,ar7,im,jm,1,0.,akms,D )
      CALL WGRADS (id7,139, 0, 0,105, 0,ar7,im,jm,1,0.,thz0,D )
      CALL WGRADS (id7,140, 0, 0,105, 0,ar7,im,jm,1,0.,qz0,D )
      CALL WGRADS (id7,133,134, 1,105,10,ar7,im,jm,1,0.,uhlm,vhlm)
      CALL WGRADS (id7,136,137,1,105, 0,ar7,im,jm,1,0.,uz0hc,vz0hc )
      CALL WGRADS (id7,142, 0, 0,105, 0,ar7,im,jm,1,0.,cczl,D )
      CALL WGRADS (id7,143, 0, 0,105, 0,ar7,im,jm,1,0.,cczm,D )
```

```
c--------------------
      CALL WGRADS (id7,204,  0,  0,105,  0,ar7,im,jm,1,0.,rswin ,D )
      CALL WGRADS (id7,211,  0,  0,105,  0,ar7,im,jm,1,0.,rswout,D )
      CALL WGRADS (id7,205,  0,  0,105,  0,ar7,im,jm,1,0.,rlwin ,D )
      CALL WGRADS (id7,212,  0,  0,105,  0,ar7,im,jm,1,0.,rlwout,D )
c--------------------
      print *,'ENDOFGRADSENDOFGRADSENDOFGRADS'
C-----------------------------------------------------------------------
       k=0
       do j=1,jm
       do i=1,im - mod(j+1,2)
C
           k=k+1
       RFLUXK(K)=RFLUX(I,J)
       RLWINK(K)=RLWIN(I,J)
       RSWINK(K)=RSWIN(I,J)
       RLWOUTK(K)=RLWOUT(I,J)
       RSWOUTK(K)=RSWOUT(I,J)
       SLHFLXK(K)=SLHFLX(I,J)
       SSHFLXK(K)=SSHFLX(I,J)
       qlhflxk(K)=qlhflx(I,J)
       CCRTK(K)=CCRT(I,J)
       Z0K(K)=Z0(I,J)
       UZ0HK(K)=UZ0HC(I,J)
       VZ0HK(K)=VZ0HC(I,J)
       QZ0K(K)=QZ0(I,J)
       THZ0K(K)=THZ0(I,J)
       AKHSK(K)=AKHS(I,J)
       AKMSK(K)=AKMS(I,J)
       SMK(K)=SM(I,J)
C
       enddo
       enddo
C=================================================================
C-----CALCULATION OF CONSTANTS
      PI=3.141592654
      DTR=PI/180.
      TPH0=TPH0D*DTR
      STPH0=SIN(TPH0)
      CTPH0=COS(TPH0)
C-----------------------------------------------------------------
          k=0
          DO J=1,JMLL
          DO I=1,IMLL
             k=k+1
           SMB(i,j)=SMBB(k)
              enddo
              enddo
C-----------------------------------------------------------------
           do j=1,jmll
          clat =sbdll+(j-1)*dphdll
           do i=1,imll
          clon =wbdll+(i-1)*dlmdll

C
       call  TLLC(clon,clat,TLM0D,DTR,CTPH0,STPH0,TLM,TPH)
C
       if ( tlm.lt.wbd+dlmd) goto 55
       if ( tlm.gt.-wbd-dlmd) goto 55
```

```
      if ( tph.lt.sbd+dphd) goto 55
      if ( tph.gt.-sbd-dphd) goto 55
C
      call  gcoef (tlm,tph, kh,ph,qh, kv,pv,qv)
C
 55     continue
c-----------------------------------
         KH1 = kh
       KH2 = kh + kne
       KH3 = kh + knw
       KH4 = kh + ninc
         KV1 = kv
       KV2 = kv + kne
       KV3 = kv + knw
       KV4 = kv + ninc
c-----------------------------------
       S1 = SMK(kh1)
       S2 = SMK(kh2)
       S3 = SMK(kh3)
       S4 = SMK(kh4)
          SL1 = 1 - S1
          SL2 = 1 - S2
          SL3 = 1 - S3
          SL4 = 1 - S4
c

c-----------------------------------
          if ( SMB(i,j).eq.1) then
          TS(i,j) = blu(0.,
     +    ph,qh,TSFCK(kh1)*S1,TSFCK(kh2)*S2,TSFCK(kh4)*S4,TSFCK(kh3)*S3)
          T2(i,j) = blu(0.,
     +    ph,qh,T2MK(kh1)*S1,T2MK(kh2)*S2,T2MK(kh4)*S4,T2MK(kh3)*S3)
          SFCL(i,j) = blu(0.,ph,qh,
     +
          SLHFLXK(kh1)*S1,SLHFLXK(kh2)*S2,SLHFLXK(kh4)*S4,SLHFLXK(kh3)*S
3)
          SFCS(i,j) = blu(0.,ph,qh,
     +
          SSHFLXK(kh1)*S1,SSHFLXK(kh2)*S2,SSHFLXK(kh4)*S4,SSHFLXK(kh3)*
S3)
          QFC (i,j) = blu(0.,ph,qh,
     +
          QLHFLXK(kh1)*S1,QLHFLXK(kh2)*S2,QLHFLXK(kh4)*S4,QLHFLXK(kh3)*
S3)
          UMMF (i,j) = blu(0.,ph,qh,
     +
          UMMFLXK(kh1)*S1,UMMFLXK(kh2)*S2,UMMFLXK(kh4)*S4,UMMFLXK(kh
3)*S3)
          VMMF (i,j) = blu(0.,ph,qh,
     +
          VMMFLXK(kh1)*S1,VMMFLXK(kh2)*S2,VMMFLXK(kh4)*S4,VMMFLXK(kh
3)*S3)
          U1 (i,j) = blu(0.,ph,qh,
     +    U10K(kh1)*S1,U10K(kh2)*S2,U10K(kh4)*S4,U10K(kh3)*S3)
          V1 (i,j) = blu(0.,ph,qh,
     +    V10K(kh1)*S1,V10K(kh2)*S2,V10K(kh4)*S4,V10K(kh3)*S3)
          RLWI (i,j) = blu(0.,ph,qh,
     +    RLWINK(kh1)*S1,RLWINK(kh2)*S2,RLWINK(kh4)*S4,RLWINK(kh3)*S3)
          RSWI (i,j) = blu(0.,ph,qh,
```

```
     +    RSWINK(kh1)*S1,RSWINK(kh2)*S2,RSWINK(kh4)*S4,RSWINK(kh3)*S3)
          RLWO (i,j) = blu(0.,ph,qh,
     +
          RLWOUTK(kh1)*S1,RLWOUTK(kh2)*S2,RLWOUTK(kh4)*S4,RLWOUTK(kh
    3)*S3)
          RSWO (i,j) = blu(0.,ph,qh,
     +
          RSWOUTK(kh1)*S1,RSWOUTK(kh2)*S2,RSWOUTK(kh4)*S4,RSWOUTK(kh
    3)*S3)
          else
          TS(i,j) = blu(0.,
       +ph,qh,TSFCK(kh1)*SL1,TSFCK(kh2)*SL2,TSFCK(kh4)*SL4,TSFCK(kh3)*SL3)
          T2(i,j) = blu(0.,
       +ph,qh,T2MK(kh1)*SL1,T2MK(kh2)*SL2,T2MK(kh4)*SL4,T2MK(kh3)*SL3)
          SFCL(i,j) = blu(0.,ph,qh,
       +SLHFLXK(kh1)*SL1,SLHFLXK(kh2)*SL2
       +              ,SLHFLXK(kh4)*SL4,SLHFLXK(kh3)*SL3)
          SFCS(i,j) = blu(0.,ph,qh,
       +SSHFLXK(kh1)*SL1,SSHFLXK(kh2)*SL2
       +              ,SSHFLXK(kh4)*SL4,SSHFLXK(kh3)*SL3)
          QFC (i,j) = blu(0.,ph,qh,
       +QLHFLXK(kh1)*SL1,QLHFLXK(kh2)*SL2,
       +                QLHFLXK(kh4)*SL4,QLHFLXK(kh3)*SL3)
          UMMF (i,j) = blu(0.,ph,qh,
       +UMMFLXK(kh1)*SL1,UMMFLXK(kh2)*SL2
       +              ,UMMFLXK(kh4)*SL4,UMMFLXK(kh3)*SL3)
          VMMF (i,j) = blu(0.,ph,qh,
       +VMMFLXK(kh1)*SL1,VMMFLXK(kh2)*SL2,
       +               VMMFLXK(kh4)*SL4,VMMFLXK(kh3)*SL3)
          U1 (i,j) = blu(0.,ph,qh,
       +U10K(kh1)*SL1,U10K(kh2)*SL2,U10K(kh4)*SL4,U10K(kh3)*SL3)
          V1 (i,j) = blu(0.,ph,qh,
       +V10K(kh1)*SL1,V10K(kh2)*SL2,V10K(kh4)*SL4,V10K(kh3)*SL3)
          RLWI (i,j) = blu(0.,ph,qh,
       +RLWINK(kh1)*SL1,RLWINK(kh2)*SL2,RLWINK(kh4)*SL4,RLWINK(kh3)*SL3)
          RSWI (i,j) = blu(0.,ph,qh,
       +RSWINK(kh1)*SL1,RSWINK(kh2)*SL2,RSWINK(kh4)*SL4,RSWINK(kh3)*SL3)
          RLWO (i,j) = blu(0.,ph,qh,
       +RLWOUTK(kh1)*SL1,RLWOUTK(kh2)*SL2,
       +               RLWOUTK(kh4)*SL4,RLWOUTK(kh3)*SL3)
          RSWO (i,j) = blu(0.,ph,qh,
       +RSWOUTK(kh1)*SL1,RSWOUTK(kh2)*SL2
       +              ,RSWOUTK(kh4)*SL4,RSWOUTK(kh3)*SL3)
        endif

          SP(i,j) = blu(SMK(kh),
       + ph,qh,SEAGK(kh1),SEAGK(kh2),SEAGK(kh4),SEAGK(kh3))
          TP(i,j) = 0.00001 + blu( 12345. ,
       + ph,qh,ACPRECK(kh1),ACPRECK(kh2),ACPRECK(kh4),ACPRECK(kh3))
          RF(i,j) = blu(SMK(kh),
       + ph,qh,RFLUXK(kh1),RFLUXK(kh2),RFLUXK(kh4),RFLUXK(kh3))
          CC(i,j) = blu(SMK(kh),
       + ph,qh,CCRTK(kh1),CCRTK(kh2),CCRTK(kh4),CCRTK(kh3))
          USTR(i,j) = blu(SMK(kh),
       + ph,qh,USTARK(kh1),USTARK(kh2),USTARK(kh4),USTARK(kh3))
          UHL(i,j) = blu(SMK(kh),
       + ph,qh,UHLMK(kh1),UHLMK(kh2),UHLMK(kh4),UHLMK(kh3))
          VHL(i,j) = blu(SMK(kh),
       + ph,qh,VHLMK(kh1),VHLMK(kh2),VHLMK(kh4),VHLMK(kh3))
```

```
        AKHL(i,j) = blu(SMK(kh),
     + ph,qh,AKHSK(kh1),AKHSK(kh2),AKHSK(kh4),AKHSK(kh3))
        AKML(i,j) = blu(SMK(kh),
     + ph,qh,AKMSK(kh1),AKMSK(kh2),AKMSK(kh4),AKMSK(kh3))
        Z0L(i,j) = blu(SMK(kh),
     + ph,qh,Z0K(kh1),Z0K(kh2),Z0K(kh4),Z0K(kh3))
      THZ0L(i,j) = blu(SMK(kh),
     + ph,qh,THZ0K(kh1),THZ0K(kh2),THZ0K(kh4),THZ0K(kh3))
      QZ0L(i,j) = blu(SMK(kh),
     + ph,qh,QZ0K(kh1),QZ0K(kh2),QZ0K(kh4),QZ0K(kh3))
      UZ0HL(i,j) = blu(SMK(kh),
     + ph,qh,UZ0HK(kh1),UZ0HK(kh2),UZ0HK(kh4),UZ0HK(kh3))
      VZ0HL(i,j) = blu(SMK(kh),
     + ph,qh,VZ0HK(kh1),VZ0HK(kh2),VZ0HK(kh4),VZ0HK(kh3))
        CZL(i,j) = blu(SMK(kh),
     + ph,qh,CCZLK(kh1),CCZLK(kh2),CCZLK(kh4),CCZLK(kh3))
        CZM(i,j) = blu(SMK(kh),
     + ph,qh,CCZMK(kh1),CCZMK(kh2),CCZMK(kh4),CCZMK(kh3))
c-----------------------------------
C
              enddo
              enddo
C=================================================================


         do j=1,jmll
        clat =sbdll+(j-1)*dphdll
         do i=1,imll
        clon =wbdll+(i-1)*dlmdll
C
      TPUS=U1(I,J)
      TPVS=V1(I,J)
C
     CALL RLTLW(CLON,CLAT,TPUS,TPVS,TLM0D,DTR,CTPH0,STPH0
    &           ,PUS,PVS)
C
      U1(i,j)=PUS
        V1(i,j)=PVS
C
C-----------------------------------------------------------
      TPUS=ummf(i,j)
      TPVS=vmmf(i,j)
C
     CALL RLTLW(CLON,CLAT,TPUS,TPVS,TLM0D,DTR,CTPH0,STPH0
    &           ,PUS,PVS)
      ummf(i,j)=PUS
        vmmf(i,j)=PVS
C
      TPUS=UHL(i,j)
      TPVS=VHL(i,j)
C
     CALL RLTLW(CLON,CLAT,TPUS,TPVS,TLM0D,DTR,CTPH0,STPH0
    &           ,PUS,PVS)
      UHL(i,j)=PUS
        VHL(i,j)=PVS
C
      TPUS=UZ0HL(i,j)
      TPVS=VZ0HL(i,j)
C
     CALL RLTLW(CLON,CLAT,TPUS,TPVS,TLM0D,DTR,CTPH0,STPH0
```

```
     &              ,PUS,PVS)
       UZ0HL(i,j)=PUS
          VZ0HL(i,j)=PVS
        enddo
        enddo
C=================================================================
C calculation of wind stress = rho*ustar**2
C direction of wind stress is the opposite of the rezultant wind
C=================================================================
      do j=1,jmll
      do i=1,imll
       DIR=WDIR(U1(i,j),V1(i,j))
          WINSU(I,J)=-ustr(i,j)**2*cos(dir)
          WINSV(I,J)=-ustr(i,j)**2*sin(dir)
C
C total latent and sensible heat flux
      WTSURF(i,j)=SFCL(i,j)+SFCS(i,j)+RLWI(i,j)
!     WTSURF(i,j)=SFCL(i,j)+SFCS(i,j)
C total short- and long-wave radiation
CCC    SWRAD(I,J)=RF(I,J)
      SWRAD(I,J)=RSWI(I,J)  !short wave radiation incoming flux
      enddo
      enddo
C
C=================================================================
C record of sea surface fields for POM model
C=================================================================
      WRITE(CDT(1:2),'(I2)')IDAT(1)
      WRITE(CDT(3:4),'(I2)')IDAT(2)
      WRITE(CDT(5:6),'(I2)')IDAT(3)
C
            do m=1,6
            if(CDT(m:m).eq.' ')CDT(m:m)='0'
            enddo
C-----------------------------------------------------------------------
      OPEN(UNIT=35,FILE='../../output/surfce_pom'//CDT//cdat//'.dat'
     &    ,STATUS='UNKNOWN',ACCESS='SEQUENTIAL',FORM='UNFORMATTED')
c
      WRITE(35)IDAT,IHRST,IHR
!    &,WTSURF,ummf,vmmf,SWRAD,qfc,tp,sp
     &,SFCL,SFCS,RLWI,RLWO,RSWI,RSWO,ummf,vmmf,qfc,tp,sp
      print*,'idat,ihrst,ihr=====',idat,' ',ihrst,' ',ihr
C-----------------------------------------------------------------
        k=0
        DO J=1,JMLL
        DO I=1,IMLL
           k=k+1
         SMB(i,j)=SMBB(k)
            enddo
            enddo
C=================================================================
        k=0
        DO J=1,JMLL
        DO I=1,IMLL
           k=k+1
         SMB(i,j)=SMBB(k)
            if (SMB(i,j).ne.1.)then
         smb(i,j)=orv
            endif
```

```
            enddo
            enddo
C=============================================================
 777     continue
C=============================================================
C Conversion fields into one dimension due to graphics
C-------------------------------------------------------------
C=============================================================
c-------------------------------------------------------------
      ar7 (1) = 0.
      ar7 (2) = IMll
      ar7 (3) = wbdll
      ar7 (4) = dlmdll
      ar7 (5) = JMll
      ar7 (6) = sbdll
      ar7 (7) = dphdll
      id7 (1) = idat(3)
      id7 (2) = idat(2)
      id7 (3) = idat(1)
      id7 (4) = IHRST! time start = ihrst
      id7 (5) = ihr
      id7 (6) = 00   ! minf
      id7 (7) = 00   ! secf
cgrads
C=============================================================
CGRADSGRADSGRADSGRADS
      DUPE = -9999
      print *,' GRADSGRADS!', id7(5),' lev:',vrta
c
      CALL WGRADS (id7,81 ,0,9,105,0,ar7,imll,jmll,1,0.,smb,DUPE)
      CALL WGRADS (id7,02 ,0,9,102,0,ar7,imll,jmll,1,0.,sp,DUPE)
      CALL WGRADS (id7,61 ,0,9,105,0,ar7,imll,jmll,1,0.,tp,DUPE)
      CALL WGRADS (id7,125,0,9,105,10,ar7,imll,jmll,1,0.,ummf, DUPE)
      CALL WGRADS (id7,126,0,9,105,10,ar7,imll,jmll,1,0.,vmmf,DUPE)
      CALL WGRADS (id7,130,0,9,105,0,ar7,imll,jmll,1,0.,wtsurf,DUPE)
      CALL WGRADS (id7,117,0,9,105,0,ar7,imll,jmll,1,0.,swrad,DUPE)
      CALL WGRADS (id7,11 ,0,9,105,0,ar7,imll,jmll,1,0.,ts,DUPE)
      CALL WGRADS (id7,11 ,0,9,105,2,ar7,imll,jmll,1,0.,t2,DUPE)
      CALL WGRADS (id7,121 ,0,9,105,0,ar7,imll,jmll,1,0.,sfcl,DUPE)
      CALL WGRADS (id7,122 ,0,9,105,0,ar7,imll,jmll,1,0.,sfcs,DUPE)
      CALL WGRADS (id7,131 ,0,9,105,0,ar7,imll,jmll,1,0.,akhl,DUPE)
      CALL WGRADS (id7,132 ,0,9,105,0,ar7,imll,jmll,1,0.,akml,DUPE)
      CALL WGRADS (id7, 33 ,0 ,9,105,10,ar7,imll,jmll,1,0.,u1,DUPE)
      CALL WGRADS (id7, 34 ,0 ,9,105,10,ar7,imll,jmll,1,0.,v1,DUPE)
      CALL WGRADS (id7,133 ,  0,9,105,10,ar7,imll,jmll,1,0.,uhl,DUPE)
      CALL WGRADS (id7,134 ,  0,9,105,10,ar7,imll,jmll,1,0.,vhl,DUPE)
      CALL WGRADS (id7,136,   0,9,105,0,ar7,imll,jmll,1,0.,uz0hl,DUPE)
      CALL WGRADS (id7,137,   0,9,105,0,ar7,imll,jmll,1,0.,vz0hl,DUPE)
      CALL WGRADS (id7,135 ,0,9,105,0,ar7,imll,jmll,1,0.,ustr,DUPE)
      CALL WGRADS (id7,138 ,0,9,105,0,ar7,imll,jmll,1,0.,z0l,DUPE)
      CALL WGRADS (id7,139 ,0,9,105,0,ar7,imll,jmll,1,0.,thz0l,DUPE)
      CALL WGRADS (id7,140 ,0,9,105,0,ar7,imll,jmll,1,0.,qz0l,DUPE)
      CALL WGRADS (id7,141 ,0,9,105,0,ar7,imll,jmll,1,0.,qfc,DUPE)
      CALL WGRADS (id7,142 ,  0,9,105,10,ar7,imll,jmll,1,0.,um,DUPE)
      CALL WGRADS (id7,143 ,  0,9,105,10,ar7,imll,jmll,1,0.,vm,DUPE)
      CALL WGRADS (id7,71  ,0,9,105,0,ar7,imll,jmll,1,0.,cc,DUPE)
      CALL WGRADS (id7,144 ,0,9,105,0,ar7,imll,jmll,1,0.,czl,DUPE)
      CALL WGRADS (id7,145 ,0,9,105,0,ar7,imll,jmll,1,0.,czm,DUPE)
      CALL WGRADS (id7,205 ,0,9,105,0,ar7,imll,jmll,1,0.,rlwi,DUPE)
```

```
      CALL WGRADS (id7,204 ,0,9,105,0,ar7,imll,jmll,1,0.,rswi,DUPE)
      CALL WGRADS (id7,211 ,0,9,105,0,ar7,imll,jmll,1,0.,rswo,DUPE)
      CALL WGRADS (id7,212 ,0,9,105,0,ar7,imll,jmll,1,0.,rlwo,DUPE)
      print *,' END_GRADSGRADS!', id7(5),' ar7:',ar7
CENDCGRADSGRADSGRADSEND
C=================================================================
c
                  STOP
                  END
C&&&&&&&&&&&&&&&&&&&&&&&&&&&&&&&&&&&&&&&&&&&&&&&&&&&&&&&&&&&&&&
      SUBROUTINE RTLL(TLM,TPH,TLM0D,DTR,CTPH0,STPH0,ALMD,APHD)
00028580
C                                                    00028590
      STPH=SIN(TPH)                                    00028600
      CTPH=COS(TPH)                                    00028610
      CTLM=COS(TLM)                                    00028620
      STLM=SIN(TLM)                                    00028630
C                                                    00028640
      APH=ASIN(STPH0*CTPH*CTLM+CTPH0*STPH)                    00028650
      CPH=COS(APH)                                     00028660
C                                                    00028670
      ALMD=TLM0D+ASIN(STLM*CTPH/CPH)/DTR                      00028680
      APHD=APH/DTR                                     00028690
C                                                    00028700
      RETURN                                           00028710
      END                                              00028720
C&&&&&&&&&&&&&&&&&&&&&&&&&&&&&&&&&&&&&&&&&&&&&&&&&&&&&&&&&&&&&&
      SUBROUTINE RLTLW(ALMD,APHD,TPUS,TPVS,TLM0D,DTR,CTPH0,STPH0
     &              ,PUS,PVS)
C&&&&&&&&&&&&&&&&&&&&&&&&&&&&&&&&&&&&&&&&&&&&&&&&&&&&&&&&&&&&&&
C
      RELM=(ALMD-TLM0D)*DTR
      SRLM=SIN(RELM)
      CRLM=COS(RELM)
C
      APH=APHD*DTR
      SPH=SIN(APH)
      CPH=COS(APH)
C
      CC=CPH*CRLM
      TPH=ASIN(CTPH0*SPH-STPH0*CC)
C
      RCTPH=1./COS(TPH)
      CRAY=STPH0*SRLM*RCTPH
      DRAY=(CTPH0*CPH+STPH0*SPH*CRLM)*RCTPH
      DC=DRAY*DRAY+CRAY*CRAY
      PUS=(DRAY*TPUS+CRAY*TPVS)/DC
      PVS=(DRAY*TPVS-CRAY*TPUS)/DC
C
      RETURN
      END
C&&&&&&&&&&&&&&&&&&&&&&&&&&&&&&&&&&&&&&&&&&&&&&&&&&&&&&&&&&&&&&
      SUBROUTINE CONV21(V2,V1B)
C     ****************************************************************
C     *                                                              *
C     * ROUTINE FOR REORDERING THIBUE-VELOCITY-POINT-3-DIMENSIONAL
*
C     * MATRICES FOR 2-DIMENSIONAL INDEXING                          *
C     *                                                              *
```

```
C     ****************************************************************
#include "largeOCT.inc"
C-----------------------------------------------------------------------
      D I M E N S I O N
     & V2    (IMT,JMT),V1B   (IMJM)
C-----------------------------------------------------------------------
c     DO 200 L=1,LM
      K=0
C-----------------------------------------------------------------------
      DO 100 J=1,JMT
      DO 110 I=2,IMT,2
      K=K+1
  110 V1B(K)=V2(I,J)
C
      IF(J.EQ.JMT)          GO TO 100
C
      DO 120 I=1,IMT,2
      K=K+1
  120 V1B(K)=V2(I,J)
C
  100         CONTINUE
C-----------------------------------------------------------------------
c 200                     CONTINUE
C-----------------------------------------------------------------------
      RETURN
      END
C&&&&&&&&&&&&&&&&&&&&&&&&&&&&&&&&&&&&&&&&&&&&&&&&&&&&&&&&&&&&&&&&&&&
                  SUBROUTINE CONH12(HI1,HI2)
C     ****************************************************************
C     *                                                              *
C     * ROUTINE FOR REORDERING THIBUE-HEIGHT-POINT-1-DIMENSIONAL
*
C     * MATRICES FOR 2-DIMENSIONAL INDEXING                          *
C     *                                                              *
C     ****************************************************************
#include "largeOCT.inc"
C-----------------------------------------------------------------------
                      D I M E N S I O N
     & HI2    (IM,JM),HI1    (IMJM)
C-----------------------------------------------------------------------
     K=0
          DO 100 J=1,JM
        DO 100 I=1,IM-1+MOD(J,2)
     K=K+1
  100 HI2(I,J)=HI1(K)
          DO 101 J=2,JM-1,2
  101 HI2(IM,J)=HI2(IM-1,J)
C-----------------------------------------------------------------------
                      RETURN
                      END
C&&&&&&&&&&&&&&&&&&&&&&&&&&&&&&&&&&&&&&&&&&&&&&&&&&&&&&&&&&&&&&&&&&&
                  SUBROUTINE CONV12(V1B,V2)
C     ****************************************************************
C     *                                                              *
C     * ROUTINE FOR REORDERING THIBUE-VELOCITY-POINT-1-DIMENSIONAL
*
C     * MATRICES FOR 2-DIMENSIONAL INDEXING                          *
C     *                                                              *
C     ****************************************************************
```

```
#include "largeOCT.inc"
C-----------------------------------------------------------------
                    D I M E N S I O N
   & V2    (IM,JM),V1B   (IMJM)
C-----------------------------------------------------------------
                    K=0
          DO 100 J=1,JM
        DO 100 I=1,IM-MOD(J,2)
     K=K+1
 100  V2(I,J)=V1B(K)
          DO 101 J=1,JM,2
 101  V2(IM,J)=V2(IM-1,J)
C-----------------------------------------------------------------
                    RETURN
                    END

C&&&&&&&&&&&&&&&&&&&&&&&&&&&&&&&&&&&&&&&&&&&&&&&&&&&&&&&&&&&&&&&&
                SUBROUTINE CONH21(H2,H1B)
C     ****************************************************************
C     *                                                              *
C     * ROUTINE FOR REORDERING THIBUE-HEIGHT-POINT-TWO-
DIMENSIONAL    *
C     * MATRICES FOR ONE-DIMENIONAL INDEXING                         *
C     *                                                              *
C     ****************************************************************
#include "largeOCT.inc"
C-----------------------------------------------------------------
                    D I M E N S I O N
   & H2    (IMT,JMT),H1B   (IMJM)
C-----------------------------------------------------------------
     K=0
          DO 100 J=1,JMT
        DO 110 I=1,IMT,2
     K=K+1
 110  H1B(K)=H2(I,J)
C
     IF(J.EQ.JMT)          GO TO 100
C
        DO 120 I=2,IMT,2
     K=K+1
 120  H1B(K)=H2(I,J)
C
 100         CONTINUE
C-----------------------------------------------------------------
                    RETURN
                    END
C&&&&&&&&&&&&&&&&&&&&&&&&&&&&&&&&&&&&&&&&&&&&&&&&&&&&&&&&&&&&&&&&
C=================================================================
     subroutine gcoef (tlm,tph, kh,ph,qh, kv,pv,qv)
C-----------------------------------------------------------------
#include "all.inc"
C-----------------------------------------------------------------
     parameter
    +( im= -wbd/ dlmd +1.5,jm=2*(-sbd/ dphd)+1.5, imjm=im*jm-jm/ 2
    +, im1 = im-1, rim1=im-1)
c
     X=(TLM-WBD)/ DLMD
     Y=(TPH-SBD)/ DPHD
     X1=0.5*( X+Y)
```

```
      Y1=0.5*(-X+Y)+RIM1
      I1=INT(X1)
      J1=INT(Y1)
        PH=X1-I1
        QH=Y1-J1
      JR=J1-IM1
      I2=I1-JR
      J2=I1+JR
        KH=J2*IM-J2/2+(I2+2)/2
C-----
      XV1=X1-.5
      YV1=Y1-.5
      I1=INT(XV1)
      J1=INT(YV1)
        PV=XV1-I1
        QV=YV1-J1
      JR=J1-IM1
      I2=I1-JR
      J2=I1+JR
        KV=(J2+1)*IM-(J2+1)/2+(I2+1)/2
C-----
       return
       end
C&&&&&&&&&&&&&&&&&&&&&&&&&&&&&&&&&&&&&&&&&&&&&&&&&&&&&&&&&&&&&&&
      SUBROUTINE TLLC(ALMD,APHD,TLM0D,DTR,CTPH0,STPH0,TLM,TPH)
C-----------------------------------------------------------------
      RELM=(ALMD-TLM0D)*DTR
      SRLM=SIN(RELM)
      CRLM=COS(RELM)
C
      APH=APHD*DTR
      SPH=SIN(APH)
      CPH=COS(APH)
C
      CC=CPH*CRLM
      ANUM=CPH*SRLM
      DENOM=CTPH0*CC+STPH0*SPH
C-----------------------------------------------------------------
      TLM=ATAN2(ANUM,DENOM)/DTR
      TPH=ASIN(CTPH0*SPH-STPH0*CC)/DTR
C-----------------------------------------------------------------
      RETURN
      END
c
c-----------------------------------------------------------------
c
C&&&&&&&&&&&&&&&&&&&&&&&&&&&&&&&&&&&&&&&&&&&&&&&&&&&&&&&&&&&&&&&
       FUNCTION WDIR(X,Y)
C-----------------------------------------------------------------
C      calculates wind direction (in degrees) from the (u,v) wind
C      components
C-----------------------------------------------------------------
       RDIR=270.-DIR(x,y)
       IF(RDIR.LT.0.)RDIR=RDIR+360.
       IF(RDIR.GE.360.)RDIR=RDIR-360.
       WDIR=RDIR
       RETURN
       END
C&&&&&&&&&&&&&&&&&&&&&&&&&&&&&&&&&&&&&&&&&&&&&&&&&&&&&&&&&&&&&&&
```

```
            SUBROUTINE VTOH (K,L,SPEED,DIR)
C-----------------------------------------------------------------------
C
C     Calculates H-point wind speed & direction by interpolating them
C     between neighbouring V-points
C
C     INPUT PARAMETERS:
C        K is a nuber of a desired gridpoint (H-point)
C          It should not lay at a domain boundary
C        L is a model level index
C
C     OUTPUT PARAMETERS:
C        SPEED is a wind speed
C        DIR is a wind direction (degrees)
C
C-----------------------------------------------------------------------
#include "parmeta.inc"
C-----------------------------------------------------------------------
                    P A R A M E T E R
   & (IMJM=IM*JM-JM/2, KHN=IM-1,KHS=-IM)
C-----------------------------------------------------------------------
                    C O M M O N / VRBLS/
   &  PD(IMJM),RES(IMJM),FIS(IMJM)
   &, U(IMJM,LM),V(IMJM,LM),T(IMJM,LM),Q(IMJM,LM)
C-----------------------------------------------------------------------
      UL=(U(K+KHS,L)+U(K-1,L)+U(K,L)+U(K+KHN,L))*0.25
      VL=(V(K+KHS,L)+V(K-1,L)+V(K,L)+V(K+KHN,L))*0.25
      SPEED=SQRT(UL**2+VL**2)
      DIR=WDIR(UL,VL)
      RETURN
      END

C&&&&&&&&&&&&&&&&&&&&&&&&&&&&&&&&&&&&&&&&&&&&&&&&&&&&&&&&&&&&&&&&&&&
                    FUNCTION DIR(X,Y)
C-----------------------------------------------------------------------
C     calculates vector direction (in degrees) from the (u,v) wind
C     components
C-----------------------------------------------------------------------
      IF(X.EQ.0.0)THEN
       IF(Y.GT.0.0)THEN
         DIR=90.
       ELSEIF(X.EQ.0.0)THEN
         DIR=0.
       ELSE
         DIR=270.
       ENDIF
      ELSE
       DIR=ATAN(Y/X)*180./3.14159
       IF(X.LT.0.0)THEN
         DIR=DIR+180.
       ENDIF
       IF(DIR.LT.0.0)THEN
         DIR=DIR+360.
       ENDIF
      ENDIF
      RETURN
      END
C-----------------------------------------
```

II.3. Setup and running of the local area (regional) and nested Eta atmospheric models.

The setup is divided into three stages: pre-processing, processing and post-processing.

II.3.1. Pre-processing stage.

II.3.1.1. Definition of model domains.

Two atmospheric models were setup: (1) a limited-area, Mediterranean-wide model and (2) a nested model within, localised over the Ionian basin.

The preprocessing stage for the atmospheric model started with the definition of the following settings (table 5.1):

- definition of central geographic points
- definition of west and south boundaries from central points
- definition of horizontal resolution in degrees
- definition of model time step
- definition of vertical resolution in terms of number of model layers

II.3.1.2. Preparation of constant input data.

Land topography was re-interpolated to the model grid points of the geographical domain and resolutions in both vertical and horizontal domain. The relevant topography datasets were obtained from USGS[1]. The re-interpolation of the land topography (*mount.13*) and sea-land mask file (*maskll30s*) files were created using *gt30mount.F* and *smaskll30s.F* respectively as provided in the Eta pre-processing source code. In the case of the nested model, the integration domain was entirely over water.

Soil texture information for the regional Eta model was created by re-interpolating the data to the regional model's grid points from the full FAOSOIL.DAT dataset obtained from NOAA[2]. Similarly, the vegetation cover for the regional model setup was derived from the full 10" by 10" vegetation dataset derived from the USGS/EROS database.

II.3.1.3. Definition of lateral and surface boundary conditions.

Daily World Area Forecast System (WAFS) data were used to initialise the lateral boundary conditions of the regional model. WAFS forecasts are primarily designed for aviation use and are produced by the

---

[1] *http://edcdaac.usgs.gov/gtopo30/gtopo30.html*
[2] *http://www.ngdc.noaa.gov/seg/eco/cdroms/gedii_a/datasets/a16/fao.htm*

aviation/medium-range forecast model at NCEP[3]. The data contains 1.25° by 1.25° latitude-longitude gridded forecasts of many meteorological parameters, including air temperature, u- and v-component wind, relative humidity and pressure at standard atmospheric levels. Forecasts of each of the meteorological parameters are available for up to 72 hours in advance of the time they are issued. These parameters are then used as 72-hour atmospheric "first-guess" fields for the numerical weather prediction community.

To reduce the size of the data files, data is made available in files covering one eight of the globe. Additionally, the data is stored in a highly compressed form known as GRIB which is a standard format for transmission of meteorological gridded data.

WAFS pertaining to octant grid 37 (I) were downloaded from the United States National Weather Service gateway ftp server. The necessary lateral and surface boundary conditions for all days during 1999 were downloaded and archived from NCEP as large-scale GRIB products with 6-hr time resolution. Daily WAFS forecasts are made available for 24 hours to the public and are substituted by forecasts of the subsequent day.

The retrieved forecasted WAFS data contained synoptic forecasted atmospheric conditions at 00, 06, 12, 18, 24, 30 and 36 hrs. The boundary field variables contained pressure at 11 mandatory levels (1000-70 mb), relative humidity at 1000-300 mb, vertical velocity at 850-300 mb, 1000 mb temperature, wind components, 2-m temperature and 10 m winds, precipitation, mean sea level pressure, and relative humidity. These variables are archived in standard grid binary (GRIB) format.

The Grid Analysis and Display System (GrADS) was used to display and convert gribbed data into an accessible 4-dimensional file format for eventual ingestion by the Eta model as defined by the date of model integration. The GrADS-formatted WAFS gribbed files included 11 variables:

u10	*0*	*33,*	*105, 10*	*Geopotential Height*
v10	*0*	*34,*	*105, 10*	*Geopotential Height*
acp	*0*	*61,*	*1, 0*	*Geopotential Height*
t2	*0*	*11,*	*105, 2*	*Geopotential Height*
rh2	*0*	*52,*	*105, 2*	*Geopotential Height*
seag	*0*	*2,*	*102, 0*	*Geopotential Height*
z	*10*	*7,*	*100*	*Geopotential Height*
t	*10*	*11,*	*100*	*TEMP*
u	*10*	*33,*	*100*	*U Winds*
v	*10*	*34,*	*100*	*V Winds*
rh	*10*	*52,*	*100*	*RH*

[3] *http://www.meted.ucar.edu/nwp/pcu2/avintro.htm (accessed on 01.11.04).*

where *u10(33)* and *v10(34)* are the 10-m vector winds, *acp(61)* is the accumulative precipitation with geopotential height, *t2(11,105,2)* is the air temperature at 2-m height from the surface, *rh2(52)* is the relative humidity with geopotential height, *seag(2)* is the air pressure with geopotential height, *z(7)* is 10-m vertical velocity, *t(11,100)* is the surface temperature, *u(34,100)* and *v(34,100)* are the vertical velocity with geopotential height, and *rh(10, 52)* is the 10-m relative humidity.

A fortran code *grb2grads.f* was written that called each successive 36-hour synoptic grib file and re-arranged it into pre-defined "*wafs.gdat*" file using a GrADS "*wafs.ctl*" script code. In this way, the WAFS gribbed data was formatted for subsequent display and ingestion by the regional Eta model as requested by the starting date string of the model integration.

The ingestion of the WAFS initial lateral boundary conditions by the model defined the inflow boundary points, while at outflow points, the velocity components tangential to the inflow boundary were extrapolated from the interior of the integration domain. The values of the second outermost row were blended with those along the boundary and those in the third row which were part of the true integration domain. The calculation of the value of variables for the boundaries h-points was carried out separately for the outer rows and columns and separately for the second outer rows and columns. Further details concerning the calculation in the outer, buffer and internal zone of the domain can be found in Kallos *et al.*, (1997).

II.3.1.4. Surface boundary conditions.

One of the operational systems of NCEP is the Global Data Assimilation System - (GDAS) which uses the spectral Medium Range Forecast model (MRF). Details of the GDAS are described by Kanamitsu (1989), and Parrish & Derber (1992). The GDAS is the final run in the series of NCEP operational model runs and includes late arriving conventional and satellite data (Petersen & Stackpole, 1989). It is run 4 times a day, i.e., at 00, 06, 12, and 18 UTC. Model output is for the analysis time and a 6-hour forecast, and consists of 1° latitude-longitude (360 by 181) grids in mandatory pressure levels. The data are written to the NOAA Information Center ftp server (nic.fb4.noaa.gov) in GRIdded Binary (GRIB) format. This set of forecasted synoptic data is made available for the numerical weather prediction community.

In total, GDAS makes available eighteen, 6-hour intervals meteo-oceanic output parameters[4] starting at 00hrs UT. Datasets containing surface temperature in Kelvin (Code U4) were extracted for the European domain area covering the period Jan 1st 1999 till December 31st 1999 and archived.

---

[4] *http://wwwt.emc.ncep.noaa.gov/gmb/gdas/ (accessed on 01.11.04).*

The Grid Analysis and Display System (GrADS) was used to convert gribbed data into an accessible 4-dimensional file format for eventual display and ingestion by the Eta models as defined by date of model integration.

The fortran code *grb2grads.f* calls each successive grib file pertaining to the specified date and time and re-arranging it into pre-defined 'gdas.gdat' file using a GrADS '*gdas.ctl*' script code. This code formatted GDAS-SST data (code 11) according to a matrix consisting of x- (313 grid points starting from -10°E) and y- (112 grid points starting from latitude 29°N) definition and interpolated on a 0.17° by 0.17° grid. Ingestion of this *'gdas"mon".gdat'* file by the Eta model was subsequently done during the pre-processing as defined by the starting 'date string' of the model integration:

```
      call cdate2id7 ( Cdate8,id7)
      wctln(1:1) = ' '
      idat(1) = id7(3)
      idat(2) = id7(2)
      idat(3) = id7(1)
      IHRST = id7(4)
      KDIM = IMJMLL*LDM
c -----------------------------------------------------------
      call datetohr(id7(3),id7(2),id7(1),id7(4),id7(5),IHRS)
      do 500 IHR = IHRS, IHRS - 10*24, -12
      call hrtodate
      + (IHR,id7(4),0,id7(3),id7(2),id7(1),id7(5))
      call RGRADS (id7, 1, 11,  0, IME, JME, 1, 0., WW , NLRET)
      if ( NLRET.ne.0) goto 410
500   continue
       print *,' No SST data avaiable'
      STOP
410   continue
      print *,' read sst:',WW
                        CALL
      BILINB(COH,INH,JNH,IMJM,IME,JME,WW,WFB)
```

The above set of instructions forms part of the sst.f file whereby it calls GDAS-SST according to user-defined date (datetohr) from the 'gdas"mon".gdat' data file. The subroutine RGRADS

```
call RGRADS (id7, 1, 11,  0, IME, JME, 1, 0., WW , NLRET)
```

browses the 'gdas.gdat' file until it finds the SST field with the specific code of 11 and defines the SST value as WW. The script then re-interpolates the 1° by 1° latitude-longitude grid SST onto the grid-points of the respective Eta model domain resolution.

II.3.1.5. Decoding, formatting and data interpolation.

After being initialised, the Eta model was executed for a 36-hour forecast period, with a 3-hourly output of atmospheric fields as defined by the *fcstdata* file:

```
$FCSTDATA
 TSTART=00.0,TEND=36.0,TCP=99.0,RESTRT=.FALSE.,SUBPOST=.FALSE.,
 NMAP=5,TSHDE=00.0,06.0,12.0,18.0,24.0,30.0,36.0,42.0,48.0,54.0,
         60.0,66.0,72.0,99.0,99.0,99.0,99.0,99.0,99.0,99.0,
 SPL=10000.,15000.,20000.,25000.,30000.,40000.,50000.,
    70000.,85000., 100000.,
 NPHS=4,NCNVC=2,NRADSH=1,NRADLH=1,
 TPREC=90.0,THEAT=90.0,TCLOD=90.0,
 TRDSW=1.0,TRDLW=1.0,TSRFC=1.0,
 HOUT=3., PRINT_INIT=.T.,
 PRINT_FIELDS=.F., PRFIELDS=25.,
 PRINT_GROUND=.F., PRGROUND=25.,
 PRINT_DUST=.T., PRDUST=3.,
 Z0contant=.T., FL_SLOPES=.F.,UPDATE_SM=.F.,
 PROUT=1.
 $END
```

where TSTART is the starting time of model integration in UT; TEND is the full forecasting period for each model run and HOUT defines the hourly output of forecasted fields. TSHDE defines time of initialisation of lateral boundary conditions of the model every 6 hours.

II.3.2. Processing stage.

The version of the Eta model used had the following characteristics:

- Dependent variables*: Temperature, horizontal wind components, surface pressure, specific humidity and turbulent kinetic energy. Prognostic soil and water models are incorporated.*
- Independent variables*: Longitude, Latitude, Eta coordinates, Time.*
- Basic equations*: primitive.*
- Diagnostic variables*: geopotential height and 'Eta vertical velocity'; precipitation, vertical velocity and turbulent exchange coefficients.*
- Integration domain*: regional and nested versions as defined by TLMOD and TPHOD.*
- Vertical coordinate*: Eta coordinate with step-like terrain representation.*

- Grid: *Arakawa E-grid on a transformed latitude/longitude grid centered at TLM0D and TPH0D.*

- Resolution: *According to values defined by DLMD and DPHD, with LM Eta levels in the vertical.*

- Time integration: *Split explicit adjustment scheme, Euler backward advection scheme; basic time step is DTB.*

Physical parameterisation schemes:

- Mellor-Yamada level 2 turbulence closure model for the ocean surface layer, which includes the viscous sublayer model.
- Fourth-order non-linear lateral diffusion.
- Modified Betts-Miller scheme for deep and shallow convection.
- GFDL radiation scheme.
- Ground surface processes and surface hydrology.
- Large-scale precipitation.
- Model-predicted cloud cover.
- Soil model.

II.3.2.1. Generation of mesoscale lateral boundary conditions for the nested Eta model.

The prognostic mesoscale output fields from the limited-area Eta model were used as the 36-hr lateral boundary conditions for the nested model. These fields were generated by the regional model using the code outnest.f [5], of which the main routine is:

```
C-----------------------------------------------------------------
     OPEN(UNIT=37,FILE=OUTFNN
    &    ,STATUS='unknown',ACCESS='SEQUENTIAL',FORM='UNFORMATTED')
     print*,' Output file for nesting: ',OUTFNN
      WRITE(37)IDAT,IHRST,IHR
    &,(((GP(I,J,K),I=1,IMLL),J=1,JMLL),K=LSL,1,-1)
    &,(((US(I,J,K),I=1,IMLL),J=1,JMLL),K=LSL,1,-1)
    &,(((VS(I,J,K),I=1,IMLL),J=1,JMLL),K=LSL,1,-1)
    &,(((SPH(I,J,K),I=1,IMLL),J=1,JMLL),K=LSL,1,-1)
      CLOSE(37)
C-----------------------------------------------------------------
```

[5] *Appendix II*

II.3.3. Post-processing stage.

II.3.3.1. Predicted met-ocean surface fluxes as surface boundary conditions for the ocean model.

Output fields were produced in binary format containing the full 36-hour, 3-hourly forecasted fields for latent and sensible heat fluxes, outgoing and incoming long- and short-wave radiation, u- and v-component of momentum flux, moisture heat flux, surface air temperature and surface pressure. These values were derived from calculations using the forecasted prognostic parameters produced by the model and converted from model levels to standard pressure levels and surface layers at 10 m and 2 m height above sea level.

```
OPEN(UNIT=35,FILE='../../output/surfce_pom'//CDT//cdat//'.dat'
  &
,STATUS='UNKNOWN',ACCESS='SEQUENTIAL',FORM='UNFORMATTED')
WRITE(35)IDAT,IHRST,IHR
&,SFCL,SFCS,RLWI,RLWO,RSWI,RSWO,ummf,vmmf,qfc,tp,sp
 print*,'idat,ihrst,ihr=====',idat,' ',ihrst,' ',ihr
```

II.3.3.2. Visualisation and preparation of gridded forecasted variables for statistical and spatial analysis.

The Linux-version of the GrADS was used to visualise model data during the post-processing stage.

A number of scripts were written to display graphics using GrADS' own scripting language. One main post-processing scripting file was prepared and used (SFC.ctl) to produce a GrADS-formatted SFC.gdat containing the predicted 4-dimensional geophysical variables. Using the GrADS terminal, these fields were displayed. Below is the list of relevant forecasted parameters produced by the limited-area Eta model:

- Total precipitation
- Total heat flux
- Sea surface temperature
- 2 m air-temperature
- Latent heat flux
- Sensible heat flux
- 10 m U wind
- 10 m V wind
- Moisture flux
- Total precipitable water vapour
- Cloud liquid water
- Incoming and outgoing longwave radiation

The script file initial information defined the structure of the Eta pre-projected model results (unstaggered). This included the spatial dimension of the variables, the number of model forecast times, the number of variables, etc. When these projected grids are opened into GrADS, bilinear interpolation constants are calculated and all data is displayed on an internal GrADS latitude and longitude grid defined by the *xdef* and *ydef* information in the data description ".ctl" file. The resolution defined in the script file in corresponds to the nested $1/24^{o}$ integration domain. The SFC.gdat was produced by relating the derived, forecasted fields to the ones defined in the *SFC.ctl* file.

II.3.3.3. Extraction of gridded ascii model results.

Following the generation of SFC.gdat file at the end of the model's 36-hr forecast, a set of gridded ascii XYZ files were produced for all relevant parameters at three-hourly intervals. These ascii files were generated in batch mode using an executable grads2xyz.f code as shown below (for the case of just three variables).

```
foreach hh (00 03 06 09 12 15 18 21 24 27 30 33 36)
grads2xyz 990722"$hh" u10 33 105 10
grads2xyz 990722"$hh" v10 34 105 10
grads2xyz 990722"$hh" ts 11 105 0
.....
end
```

In the case of the surface temperature ts, grads2xyz 990722"$hh" ts 11 105 0 called subroutine RGRADS in grads2xyz to read values from the '.gdat' file, such as IPAR, IMJM, ILEV and VAR:

```
call RGRADS (id7, IPAR,ILEVT,ILEV, IMJM, 1, 1, RLEV,VAR , NLRET)
```

where *IPAR* is the parameter code, *ILEV* and *RLEV* represent a particular standard pressure level, and *VAR* is the parameter value. The XYZ ascii file was then generated following the instruction:

```
write ( 50,999) rlon, rlat,  VAR (n)
```

which wrote the parameter value alongside with its X (rlon) and Y(rlat) coordinates. The value of X and Y were extracted from IMJM.

II.3.3.4. Automated model integration.

An example of script that integrates the Eta model using boundary conditions representing the 18th, 22nd and 24th January 1999.

```
#!/bin/csh
foreach dd ( 18 22 24 )
cd /usr/local/wafs
cp ../ETA/input_data/01/"$dd"/00/wafs* grib
rm -f /usr/local/wafs/grads/wafs.gdat
rm -f /usr/local/ETA/ETA.1.a.test/grads/wafs.gdat
```

```
cd /usr/local/wafs
grb2grads 9901"$dd"
cd grads
cp wafs.gdat  ../../ETA/ETA.1.a.test/grads
ll /usr/local/ETA/ETA.1.a.test/grads/*.gdat
**************************************************
cd /usr/local/ETA/ETA.1.a.test/output
rm -f decoding*
rm -f w_* s_* msl* preproc*
rm -f contam* p_* surf* v_*
rm -f ../input_grib/*
cd /usr/local/ETA/ETA.1.a.test/grads
rm -f SFC.gdat CSFC.gdat DUST.gdat
rm -f MS.gdat w10.gdat
cd /usr/local/ETA/ETA.1.a.test/preproc/exe
rm -f /usr/local/ETA/ETA.1.a.test/input_grib/*
#--------------
cp ../../../input_data/01/"$dd"/00/wafs* ../../input_grib
#--------------
ll ../../input_grib
cd /usr/local/ETA/ETA.1.a.test/preproc/exe
grb2grads 9901"$dd"
grads2anec 9901"$dd"
sst 9901"$dd"
#--------------
echo "xxxxxxxxxxxxxxxanecOCTsoil"
anecOCTsoil 000
echo "xxxxxxxxxxxxxxxptetaOCTsoil"
ptetaOCT    000
#--------------
#--------------
foreach hh ( 06 12 18 24 30 36 )
decodmiss $hh
echo "xxxxxxxxxxxxxxxanecOCTsoil"
anecOCTsoil $hh
echo "xxxxxxxxxxxxxxxptetaOCTsoil"
ptetaOCT    $hh
end
#--------------

echo "xxxxxxxxxxxxxxxconstOCTsoil"
constOCT_dustsoil
echo "xxxxxxxxxxxxxxxdstart     "
d_start
#--------------
echo "xxxxxxxxxxxxxxxdboco      "
foreach hh ( 1 2 3 4 5 6 )
dbocoOCT $hh
end
#--------------

#################
cd ../../rad_gfdl/exe
gfdlco2
#################
cd ../../model/exe
etaDUST.1
foreach hh ( 00 03 06 09 12 15 18 21 24 27 \
             30 33 36 )
```

```
outnew $hh
end
cd ../../postproc/exe
foreach hh ( 00 03 06 09 12 15 18 21 24 27 \
        30 33 36 )
compass $hh
end
#################
cd /usr/local/ETA/ETA.1.a.test/postproc/exe
rm -f ../../XYZ/*
cd ../../model/exe
foreach hh ( 00 03 06 09 12 15 18 21 24 27 \
        30 33 36 )
grads2xyz 9901"$dd""$hh" qload 202 1 0
end
cd ../../postproc/exe
foreach hh ( 00 03 06 09 12 15 18 21 24 27 \
        30 33 36 )
grads2xyz 9901"$dd""$hh" u10 33 105 10
grads2xyz 9901"$dd""$hh" v10 34 105 10
grads2xyz 9901"$dd""$hh" sshflx 122 105 0
grads2xyz 9901"$dd""$hh" slhflx 121 105 0
grads2xyz 9901"$dd""$hh" acprec 61 105 0
grads2xyz 9901"$dd""$hh" rflux 117 105 0
grads2xyz 9901"$dd""$hh" ccrt 71 105 0
grads2xyz 9901"$dd""$hh" uz0hc 136 105 0
grads2xyz 9901"$dd""$hh" vz0hc 137 105 0
grads2xyz 9901"$dd""$hh" rswin 204 105 0
grads2xyz 9901"$dd""$hh" rswout 211 105 0
grads2xyz 9901"$dd""$hh" rlwin 205 105 0
grads2xyz 9901"$dd""$hh" rlwout 212 105 0
grads2xyz 9901"$dd""$hh" ummflx 125 105 10
grads2xyz 9901"$dd""$hh" vmmflx 126 105 10
grads2xyz 9901"$dd""$hh" ts 11 105 0
grads2xyz 9901"$dd""$hh" t2 11 105 2
grads2xyz 9901"$dd""$hh" ustar 135 105 0
grads2xyz 9901"$dd""$hh" thz0 139 105 0
grads2xyz 9901"$dd""$hh" qhz0 140 105 0
grads2xyz 9901"$dd""$hh" ummf 125 105 10
grads2xyz 9901"$dd""$hh" vmmf 126 105 10
grads2xyz 9901"$dd""$hh" akhl 131 105 0
grads2xyz 9901"$dd""$hh" akml 132 105 0
grads2xyz 9901"$dd""$hh" qfc 141 105 0
end
**********************************
cd /usr/Results
mkdir 9901"$dd"
cd 9901"$dd"
mkdir gdat XYZ
cd XYZ
mkdir model
cd /usr/local/ETA/ETA.1.a.test/grads
cp * /usr/Results/9901"$dd"/gdat/
cd ../XYZ
cp * /usr/Results/9901"$dd"/XYZ/model/
end
exit
```

Appendix III

PREDICTION OF THE DUST AEROSOLS OVER THE AREA OF INTEREST.

Appendix III describes in brief, the setting up and execution of an Eta-based atmospheric dust model. Full description of this model is beyond the scope of this study. This model is used to forecast dust events over the model integration domain used for this study during the period 22 July - 6 August, which exactly corresponds to the integration run of the ocean model.

The scope of using this dust model is to simulate and provide information on the evolution of dust aerosols that would in turn affect the calibration of NOAA-14 infrared scenes derived from NOAA AVHRR. These scenes are used for model verification of the high-resolution SST forecasts generated by the ocean model.

Results showing the evolution of dust aerosols during a specified time period are included in this Appendix.

III.1. Setup of the atmospheric dust model.

The integration domain of the Eta model covered the region as shown in figure III.1. The domain settings were as follows:

```
C-----------------------------------------------------------------
C     Center of domain :
                    P A R A M E T E R
     &(TLM0D=15.,TPH0D=30.)
C-----------------------------------------------------------------
C     Domain parameters
                    P A R A M E T E R
     &(WBD=-25.,SBD=-10.0
     &,DLMD=1./12.,DPHD=1./12.,DTB=30.
     &,LM=24)
C-----------------------------------------------------------------
```

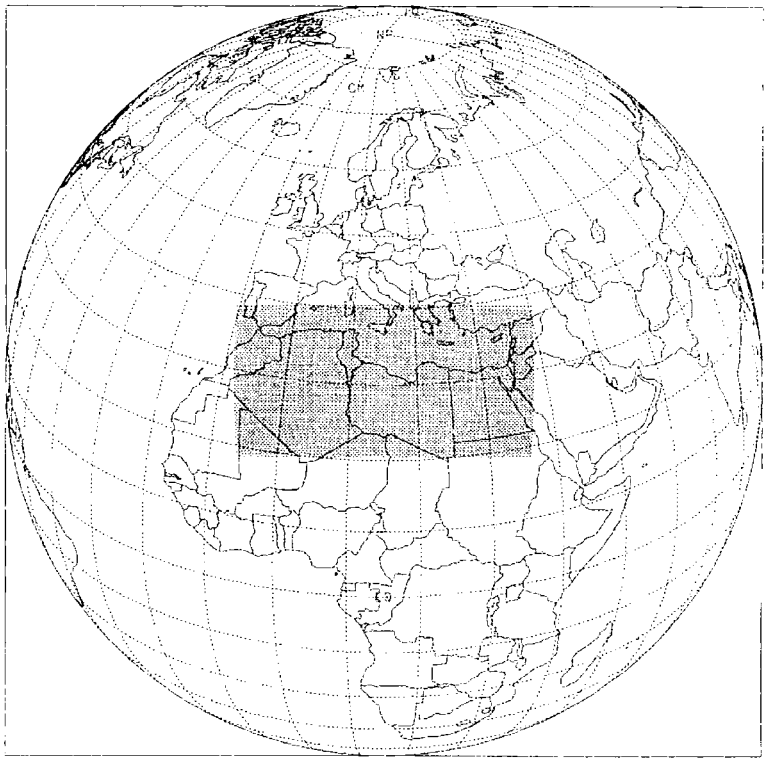

Figure III.1. Model integration domain of the atmospheric dust model.

III.2. Integration routine of the atmospheric dust model.

The script file used to run the dust model is as follows:

```
#!/bin/sh
#set -x
#####################################################################
IHRST=00
rm /usr/local/ETA/CAPEVERDE.1.a/output/decoding*llspl*
rm /usr/local/ETA/input_data/wafsc*
rm /usr/local/ETA/CAPEVERDE.1.a/grads/*.gdat
RUNHOME=/usr/local/ETA/CAPEVERDE.1.a
SCRIPTS=$RUNHOME/SCRIPTS
cd /usr/local/ETA/input_data/07/20/00
cp wafs* /usr/local/ETA/input_data
DATADIR=/usr/local/ETA/input_data
echo 'Running run12'
#####################################################################
#
```

```
day_of_month()
{
   case "$month" in
   02 | 2 )
     day=28
   ;;
   04 | 4 | 06 | 6 | 09 | 9 | 11 )
     day=30
   ;;
   01 | 03 | 05 | 07 | 08 | 10 | 12 | 1 | 3 | 5 | 7 | 8)
     day=31
   ;;
   esac
}
####################
day=`date '+ %d'`
month=`date '+ %m'`
month=`expr $month - 1`
month=`expr $month + 1`
year=`date '+ %y'`
day=`expr $day - 0`
####################
if [ $day -eq 0 ]; then
  month=`expr $month - 1`
  if [ $month -eq 2 ]; then
    day=28
  fi
####################
  if [ $month -eq 0 ]; then
   year=`expr $year - 1`
   month=12
  fi
day_of_month
####################
  year19=`expr $year + 2000`
  pyear=`expr $year19 / 4`
  pyear=`expr $pyear \* 4`
  if [ $pyear -eq $year19 ]; then
     if [ $month -eq 2 ]; then
        day=29
     fi
  fi
fi
#################################################################
hr=`date '+ %H'`
hr=`expr $hr `
echo 'hr=' $hr
####################
  if [ $hr -le 19 ]; then
day=`date '+ %d'`
day=`expr $day - 1`
#########
if [ $day -eq 0 ]; then
  month=`expr $month - 1`
  if [ $month -eq 2 ]; then
    day=28
  fi
####################
  if [ $month -eq 0 ]; then
```

```
    year=`expr $year - 1`
    month=12
  fi
day_of_month
####################
  year19=`expr $year + 2000`
  pyear=`expr $year19 / 4`
  pyear=`expr $pyear \* 4`
  if [ $pyear -eq $year19 ]; then
    if [ $month -eq 2 ]; then
       day=29
    fi
  fi
fi
#########
  fi
#################################################################
cd $DATADIR
################################################

if [ -s wafsc00  -a \
     -s wafsc06  -a \
     -s wafsc12 -a \
     -s wafsc18 -a \
     -s wafsc24 ];
then
  ls -l com.wafs*
  echo "All files are copied"
else
  echo "Not all files are copied !!!"
  cd $SCRIPTS
fi

day=20
month=7
year=99
carg=`printf "%.2d%.2d%.2d" $day $month $year`

#####################  before  arch ##########################
#echo before  arch : $IHRST 0
#cd $RUNHOME/archive/exe
#./arch_wafs $IHRST 0
#echo " after arch "
#####################  after arch ##########################

cd $RUNHOME/decoding/exe
pwd
./decodOCTlinux $carg $IHRST 00 $DATADIR/wafsc00
./decodOCTlinux $carg $IHRST 06 $DATADIR/wafsc06
./decodOCTlinux $carg $IHRST 12 $DATADIR/wafsc12
./decodOCTlinux $carg $IHRST 18 $DATADIR/wafsc18
./decodOCTlinux $carg $IHRST 24 $DATADIR/wafsc24

i=0
while test $i -le 12
do
   arg=`expr $i \* 6`
        ./decodmiss  $arg
   i=`expr $i + 1`
```

```
done

cd $RUNHOME/preproc/exe
i=0
while test $i -le 12
do
   arg=`expr $i \* 6`
   arg_dboco=$i

   echo "================ IHR = "$arg" ================"
   if test  $i -eq 0 ; then
      echo " climsst "
#            ./ncepsst
           ./climsst $month
   fi

   echo " anecOCTsoil \t" $arg
        ./anecOCTsoil     $arg

   echo " ptetaOCT \t" $arg
        ./ptetaOCT     $arg

   if test  $i -eq 0 ; then
      echo " constOCT_dustsoil \t"
           ./constOCT_dustsoil
      echo " d_start \t"
           ./d_start
   fi

    if test  $i -gt 0 ; then
        echo " dbocoOCT \t" $arg_dboco
             ./dbocoOCT     $arg_dboco
    fi

   i=`expr $i + 1`
done
#################
cd $RUNHOME/rad_gfdl/exe
./gfdlco2

#################
cd $RUNHOME/model/exe
*cp -f activectl.LST.Station activectl.LST
date
./etaDUST.1
date
echo "================ ETA finished successfuly ================"
#-------------------------------------------------------
cd /usr/local/ETA/CAPEVERDE.1.a/output
#mv decoding.llspl* Yesterday/.
#rm preproc*
#-------------------------------------------------------
date
#-------------------------------------------------------
carg1=`printf "%.2d%.2d%.2d%.2d" $year $month $day $IHRST`
 echo "carg1=$carg1"
date
#-------------------------------------------------------
cd $RUNHOME/model/exe
```

```
cp -f activectl.LST.outnew activectl.LST
./outnew 0
./outnew 3
./outnew 6
./outnew 9
./outnew 12
./outnew 15
./outnew 18
./outnew 21
./outnew 24
cd $RUNHOME/postproc/exe
./dust 0
./dust 3
./dust 6
./dust 9
./dust 12
./dust 15
./dust 18
./dust 21
./dust 24


date
exit
```

The *./dust* command calls a number of subroutines, including the one which converts the model dust fields into standard atmospheric pressure levels. This data is then converted into Grads format to be visualized using *dust.ctl* as shown below:

```
dset /usr/local/ETA/charlesdustETA.1.a/grads/MS.gdat
undef 1.e30
title eta model
xdef  619 linear -10.8 0.0833333
ydef  229 linear 17.5 0.0833333
tdef 12 linear 00Z20jul1999 3hr
zdef 1 levels 1000
vars 4
cload   0 203,  1,0  CLOAD
dload   0 204,  1,0  DLOAD
endvars
```

where dload is the dust load and cload is the concentration of the dust load.

Appendix IV

DESCRIPTION OF THE NUMERICAL PACKAGE AND IMPORTANT NUMERICAL CODES OF PRINCETON OCEAN MODEL

Appendix IV is divided into two main sections: the first one being a description of the numerical package of the Princeton Ocean Model.

The second part of this Appendix describes the pre-processing, processing and post-processing stages of the ocean model.

IV.1 The numerical package of the Princeton Ocean Model

The principal attributes of the Princeton Oceam Model (POM) are:

1. An embedded second moment turbulence closure sub-model to provide vertical mixing coefficients for accurate simulation of the surface and bottom mixed layers, assuming sufficient vertical resolution is provided.

2. A σ-coordinate system in that the vertical coordinate is scaled on the water column depth.

3. A horizontal grid using curvilinear orthogonal coordinates and an "Arakawa C" differencing scheme.

4. An explicit horizontal time differencing and an implicit vertical differencing. The latter eliminates time constraints for the vertical coordinate and permits the use of fine vertical resolution in the surface and bottom boundary layers.

5. A free surface and a split time step is included. The external mode portion of the model is two-dimensional and uses a short time step. The internal mode is three-dimensional and uses a long time step.

6. Complete hydrodynamics is implemented.

The σ-coordinate system is an important attribute in dealing with topographical variability such as that encountered over continental shelf breaks and slopes. Together with the turbulence sub-model, the model produces realistic bottom boundary layers which are important in coastal waters (Mellor, 1985). It has been found that the bottom boundary layers are important for deep water formation processes (Zavatarelli & Mellor, 1995, Baringer & Price, 1996) and possibly, for the maintenance of the baroclinicity of oceans basins (Mellor & Wang, 1996).

The POM model version used by this study had the following characteristics:

- *Dependent variables*: Potential temperature, salinity, velocity and surface elevation are prognostic variables.
- *Independent variables*: Longitude, Latitude, Sigma, Time.
- *Basic equations*: primitive.
- *Diagnostic variables*: Temperature, salinity, currents.
- *Integration domain*: 15.8°-19.1°E; 33.2° -35.8°N.
- *Vertical coordinate*: Bottom-following sigma coordinate system. The number of vertical levels in the water column is the same everywhere in the domain irrespective of the depth of the water column. It has 24 sigma levels in the vertical, which follow a logarithmic distribution near the surface in order to resolve the dynamics of the surface mixed layer.
- *Grid*: Arakawa E-grid (61 by 82 grid cells) on a transformed latitude/longitude grid centered at 17.5°E and 34.5°N.
- *Resolution:* 0.042° horizontally, with 24 sigma levels in the vertical.

The basic equations follow the sigma coordinate system (Blumberg & Mellor 1980, 1987). The basic equations (in horizontal Cartesian coordinates) are given in detail by Mellor (1998) in his *Users guide of the Princeton Ocean Model*[6].

IV.2 Important subroutines of the POM model.

The script *Comblk97.h* contains common block definitions, which is "include"d in each subroutine. No modifications were made to this script.

```
REAL KM,KH,KQ,L
c      INCLUDE 'IMJMKB'
       INCLUDE 'gridcom'
c     PARAMETER (IM=65,JM=49,KB=21)
C     PARAMETER (IM=100,JM=40,KB=15)
      PARAMETER (IMM1=IM-1,JMM1=JM-1,KBM1=KB-1)
      PARAMETER (IMM2=IM-2,JMM2=JM-2,KBM2=KB-2)
      PARAMETER (LIJ=IM*JM,LIJ2=LIJ*2,LIJK=LIJ*KB,LIJKM2=LIJ*KBM2)
      PARAMETER (LIJM1=IM*(JM-1),LIJKM1=LIJ*KBM1)
      COMMON/BLKCON/
```

[6] *http://www.pd.infn.it/AOD/immagini_models/POM_manual.pdf*

```
     1       IINT,IPRINT,DTE,DTI,TPRNI,UMOL,
     2       GRAV,TIME,RAMP,TBIAS,SBIAS,
     3       RFE,RFW,RFN,RFS
C---------- 1-D ARRAYS ------------------------------------
      COMMON/BLK1D/
     1   Z(KB),ZZ(KB),DZ(KB),DZZ(KB)
C---------- 2-D ARRAYS ------------------------------------
      COMMON/BLK2D/H(IM,JM),DX(IM,JM),DY(IM,JM),D(IM,JM),DT(IM,JM),
     1   ART(IM,JM),ARU(IM,JM),ARV(IM,JM),CBC(IM,JM),
     2   ALON(IM,JM),ALAT(IM,JM),
     3   DUM(IM,JM),DVM(IM,JM),FSM(IM,JM),COR(IM,JM),
     4   WUSURF(IM,JM),WVSURF(IM,JM),WUBOT(IM,JM),WVBOT(IM,JM),
     5   WTSURF(IM,JM),WSSURF(IM,JM),TPS(IM,JM),AAM2D(IM,JM),
     6   UAF(IM,JM),UA(IM,JM),UAB(IM,JM),VAF(IM,JM),VA(IM,JM),
     7   VAB(IM,JM),ELF(IM,JM),EL(IM,JM),ELB(IM,JM),PSI(IM,JM),
     8   ETF(IM,JM),ET(IM,JM),ETB(IM,JM),FLUXUA(IM,JM),FLUXVA(IM,JM),
     9   EGF(IM,JM),EGB(IM,JM)
C---------- 3-D ARRAYS ------------------------------------
      COMMON/BLK3D/
     1   A(IM,JM,KB),C(IM,JM,KB),EE(IM,JM,KB),GG(IM,JM,KB),
     1   UF(IM,JM,KB),VF(IM,JM,KB),
     2   KM(IM,JM,KB),KH(IM,JM,KB),KQ(IM,JM,KB),L(IM,JM,KB),
     3   Q2(IM,JM,KB),Q2B(IM,JM,KB),AAM(IM,JM,KB),
     4   Q2L(IM,JM,KB),Q2LB(IM,JM,KB),
     5   U(IM,JM,KB),UB(IM,JM,KB),W(IM,JM,KB),
     6   V(IM,JM,KB),VB(IM,JM,KB),
     7   T(IM,JM,KB),TB(IM,JM,KB),
     8   S(IM,JM,KB),SB(IM,JM,KB),
     9   RHO(IM,JM,KB),DTEF(IM,JM,KB),RMEAN(IM,JM,KB)
C---------- 1 AND 2-D BOUNDARY VALUE ARRAYS ----------------
      COMMON/BDRY/
     1   TBE(JM,KB),TBN(IM,KB),TBS(IM,KB),TBW(JM,KB),
     2   SBN(IM,KB),SBE(JM,KB),SBS(IM,KB),SBW(JM,KB),
     3   UBE(JM,KB),UBW(JM,KB),VBN(IM,KB),VBS(IM,KB),
     4   UABE(JM),UABW(JM),VABN(IM),VABS(IM),
     5   ELN(IM),ELE(JM),ELS(IM),ELW(JM)
```

A subroutine named *grid_oper.f* generates horizontal and vertical grids onto which the bottom topography is interpolated (using its embedded subroutine *BATH*). Tempertaure and salinity fields are also read and interpolated (using an embedded subroutine *TAND*). *grid_oper.f* writes grid and initial conditions for the model using its *WRITE(40)* subroutine. It needs paremeter fiels gridborder, gridcom and mapcom.

IV.3. Setup and running of the POM model.

IV.3.1. Pre-processing stage.

The main routine *grid_oper.f* was used to prepare the initial information described below in the correct grid format for the processing of the ocean model. The integration date and time was specified as follows: ./grid_oper DDMMYY.

IV.3.1.1. Definition of the ocean model domain.

This stage consisted of:

a) Setting-up of the ocean model;
b) Defining the model's lateral boundary conditions;
c) Defining the model's surface forcing fields.

The ocean model domain is identical to that of the nested Eta atmospheric model which starts from 15.8°E and 33.24°N (table IV.1). The grid consists of 82 grid points in the east-west direction, and 61 grid points in the north-south direction. The grid spacing in degrees is 0.042° with 24 sigma levels in the vertical. In order to resolve the mixed layer better, the vertical resolution of the model is highest in the upper 100 m. The domain area covering the experimental oceanic area is characterised by a maximum depth of 4000 m. The internal Rossby radius of deformation is 10-14 km for the eastern Mediterranean (Robinson *et al,* 1987), and since mesoscale eddies have a typical size few times larger than this radius, the model can resolve mesoscale and sub-mesoscale eddies.

Common pre-processing definitions were included in the *comblk97.h*[7].

	Ocean model
Domain parameters:	
West boundary (WBDLL)	15.8°E
South boundary (SBDLL)	33.24°N
East boundary (EBDLL)	19.17°E
North boundary (NBDLL)	35.74°N
Horizontal resolution:	
DLMD	1/24°
DPHD	1/24°

Table IV.1. Definition of integration domain of the ocean model. This information is coded in "latlon.inc" and "gridcom" file.

The script *latlon.inc* defines the geographical boundaries of the ocean model.

```
C-----------------------------------------------------------
C boundaries of the lat - lon area for 2deta outputs
C-----------------------------------------------------------
                PARAMETER
     +(wbdll=15.8, sbdll=33.24,dlmdll=1./24., dphdll=1./24.
     +,ebdll=19.175,mbdll= 35.74
     +,imll=(ebdll-wbdll)/dlmdll+1.5
     +, jmll=(mbdll-sbdll)/dphdll+1.5
     +,imjmll=imll*jmll)
C-----------------------------------------------------------
```

[7] *Section IV.2.*

The resolution and borders of the POM model is defined by the script *Gridcom*. It calculates the number of points of the integration domain of the ocean model.

```
C-----------------------------------------------------------------
C          resolution and borders of the POM model
C-----------------------------------------------------------------
C number of points of the integration domain for the POM model
C-----------------------------------------------------------------
C--rectangular integration domain--------
                  P A R A M E T E R
     $ (POMWE=15.80,POMES=19.175,POMSO=33.24,POMNO=35.74
     &,PDLO=1./24.,PDLA=1./24.
C*****************************************************************
C gridcom
C---------
     $,IM=(POMES-POMWE)/PDLO+1.5,JM=(POMNO-POMSO)/PDLA+1.5,KB=14)
c    &,im=120,jm=39,kb=14)
      PARAMETER (    ISKP=5    , JSKP=2      )
C*****************************************************************
```

The re-interpolation of land/sea mask was based on the model grid points in the horizontal and vertical dimension was done from the GTOPO30 original file[8]. The entire integration domain covered the sea surface.

The model bathymetry was re-interpolated to model grid points from a subset of the original US Navy Digital Bathymetric Base (with a nominal resolution of 0.083º by 0.083º) using bilinear interpolation.

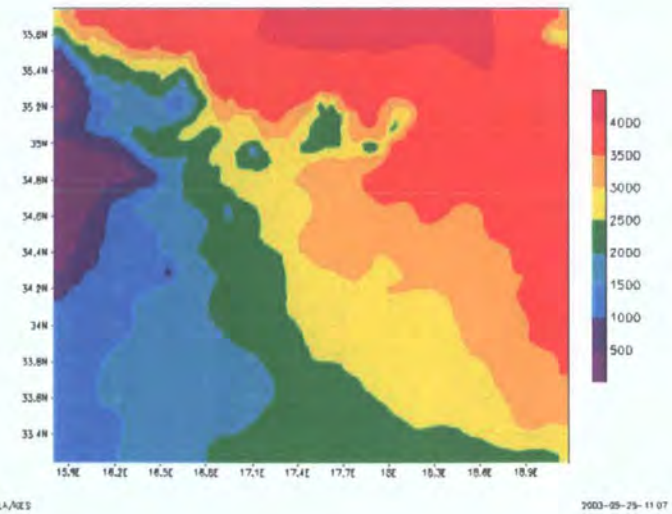

Figure IV.1. Ocean bathymetry over the integration model domain in meters.

[8] *http://edcdaac.usgs.gov/gtopo30/gtopo30.html (accessed on 01.11.04).*

IV.3.1.2. Definition of the lateral boundary conditions

The lateral boundary conditions consisted of seasonal temperature, salinity, and ocean currents (u- and v-components) at standard depth levels as archived in the Mediterranean Ocean Data Base - MODB MED4[9]. The dataset consists of >34,000 hydrographic stations in the Mediterranean Sea taken from the U.S. National Oceanographic data Center (NODC) and the Bureau des Donnees Oceanographiques (BNDO) historical data banks (Brasseur *et al.,* 1996).

For each season, initial fields at 36 depths levels were retrieved and read by the model and interpolated onto the 24-level σ-coordinate model sigma levels using the routine *ZTOSIG.* The MODB MED4 seasonal data sets with a horizontal resolution of 0.25°, were.

The extreme western and southern points for the retrieval of the seasonal data was defined as follows:

```
C western/south boundaries in MODB/med4
      wlon=-9.5 + smdb
      slat=30. + smdb
C-----------------------------------------------------------------
```

The selection of the summer lateral boundary conditions was done manually by selecting the data accordingly:

```
OPEN (UNIT=91,FILE=
&'/usr/local/ETA/input_data/modb/med4/summedoo.TEM'
&,STATUS='UNKNOWN',FORM='FORMATTED')
OPEN (UNIT=92,FILE=
&'//usr/local/ETA/input_data/modb/med4/summedoo.SAL'
&,STATUS='UNKNOWN',FORM='FORMATTED')
OPEN (UNIT=93,FILE=
&'/usr/local/ETA/input_data/modb/med4/summedoo.U'
&,STATUS='UNKNOWN',FORM='FORMATTED')
OPEN (UNIT=94,FILE=
&'/usr/local/ETA/input_data/modb/med4/summedoo.V'
&,STATUS='UNKNOWN',FORM='FORMATTED')
```

and reading the temperature TTB, salinity SSB, u- (UUB) and v- (VVB) component of the ocean currents:

```
C-----------------------temperature-----------------------------------
      CALL READMODB (91,TTB,IS,JS,KS)
      CLOSE (91)
C-----------------------salinity--------------------------------------
      CALL READMODB (92,SSB,IS,JS,KS)
      CLOSE (92)
```

[9] *http://modb.oce.ulg.ac.be/medmex/ss_st.html (accessed on 01.11.04).*

```
C----------------------u-current----------------------------------
      CALL READMODB (93,UUB,IS,JS,KS)
      CLOSE (93)
C----------------------v-current----------------------------------
      CALL READMODB (94,VVB,IS,JS,KS)
      CLOSE (94)
C-----------------------------------------------------------------
```

using the READMODB subroutine.

IV.3.1.3. Definition of the surface forcing fields.

The main routine *grid_oper.f*[10]routine was called in order to prepare the initial information described below in the correct grid format for the processing of the ocean model. The integration date and time was specified as follows: ./grid_oper DDMMYY.

The routine *grid_oper.f* accessed the archived surface fields[11] generated by the Eta model[12].

```
FILENAME=
&'../../../990722/COMPASS/surfce_pom'//CDT//cdat//'.dat'
OPEN(UNIT=35,FILE=FILENAME
     &
,STATUS='UNKNOWN',ACCESS='SEQUENTIAL',FORM='UNFORMATTED')
READ(35)IDAT,IHRST,IHR
&,sfcl,sfcs,rlwi,rlwo,rswi,rswo,ummf,vmmf,qflux,tprec,sfpr
print *,'+++cdat,ihrst,ihr========',idat,' ',ihrst,' ',ihr
```

where *sfcl* is the surface latent heat flux; *sfcs* is the surface sensible heat flux; *rlwi* is the incoming longwave radiation; *rlwo* is the outgoing longwave radiation, *rswi* is the incoming shortwave radiation; *rswo* is outgoing shortwave radiation; *ummf* and *vmmf* are the u- and v-components of the momentum flux; *qflux* is the net surface heat flux; *tprec* is the total precipitation and *sfpr* is the surface pressure.

Sea surface temperature data was read from a GrADS-formatted *.gdat file containing GDAS-derived SST data. This file was previously produced using the same *GDAS.ctl* file[13] using *grb2grads.f.* After visualising and checking the integrity of the data, the file was converted to binary format using *readgrads.f* code, which reads the GrADS-formatted SST data

```
call RGRADS (id7, 1, 11, 0, imll, jmll, 1, 0.,sst, NLRET)
```

---

[10] *Section IV.2.*

[11] *The relevant set of daily, 3-hourly surface fields were copied from archive to a new directory from which they were read and variables extracted to be interpreted on the model grid points.*

[12] *Appendix II; Section II.3.3.1.*

[13] *Appendix II; Section II.2.1.*

and produces date-specific binary file

```
open (unit=11,
    +file='/usr/local/Charles/POM/model/tmp/sst'//cdate8(1:6)//'12'
+,status='unknown',form='unformatted')
```

This data was then used to initialise and force the ocean model.

IV.3.1.4. Visualisation of initial lateral and surface boundary conditions.

The Linux-version of the Grid Analysis and Display System (GrADS) was used to visualise model data during the post-processing stage.

Scripts were written to display graphics using GrADS' own scripting language. One main post-processing scripting file was prepared and used (*WG.ctl*) to produce a GrADS-formatted WG.gdat containing the 4-dimensional initial geophysical variables[14]. Using the GrADS terminal, these fields were displayed.

The script file information defined the format and projection of the initial boundary conditions. This included the spatial dimension of the variables, the number of model forecast times, the number of vertical levels (14), the number of variables, etc. When these projected grids are opened into GrADS, bilinear interpolation constants are calculated and data was displayed on an internal GrADS latitude and longitude grid defined by the xdef and ydef information in the data description ".ctl" file.

The WG.gdat was produced by grid_oper.f by relating the initial fields to the ones defined in the WG.ctl file.

The initial boundary conditions of the POM model is visualised by converting the data into GrADS format. The script file to produce the GrADS-structured fields is *WG.ctl*

```
dset /usr/local/Charles/grads/WG.gdat
undef 0
title eta model
xdef 82 linear  15.8 0.041666
ydef 61 linear 33.24 0.041666
tdef 12 linear 12Z06aug1999 3hr
zdef 14 levels 1 2 3 4 5 6 7 8 9 10 11 12 13 14
vars 13
fsm  0  81,105,00  mask
h    0   7,105,00  Height
wts  0  129,105,00  Wusurf
wus  0  127,105,00  Wusurf
wvs  0  128,105,00  Wvsurf
```

[14] *i.e. u and v components of the ocean currents, salinity and temperture.*

```
swrp 0 204,105,00 rswinc
dum 0 205,105,00 ssalinfl
dvm 0 206,105,00 ssalinfltend
s10m 0 207,105,00 freshwater
t 14 11,107,00 TEMP
s 14 51,107,00 salt.
u 14 49,107,00 U current
v 14 50,107,00 V current
endvars
```

IV.3.2. Processing stage.

IV.3.2.1. Starting of POM model with zero velocity.

A hind-cast forecasting sequence was started on 1st July with zero velocity and continued for an additional 20 days. The initial climatological fields were obtained using the Mediterranean Ocean Data Base (MODB-MED4) Initial velocities were set to zero.

During this 21-day period, the 3-D oceanic fields were dynamically adjusted to a constant SST field derived from the TMI sensor on the 22nd of July 1999 at approximately 00UT to nudge the fields as much as possible to the oceanic-state of the 22nd July 1999.

Model integration was done using a batch script file. By defining a series of dates using the "foreach" command, dates and integration times and folder names for the output files were created[15].

Model integration started at 1200 hrs every integration day. This initiation time meant that the first 00-, 03-, 06-, and 09-hr Eta forecasted surface boundary conditions were discarded so that inaccurate flux values are not included. Such values may result from 'spin-up' errors produced during the initial stages of the Eta model integration. For this reason, the total forecasting period for the ocean model was 24 hours.

One main inclusion was made to the main program *pom97_oper.f* to dynamically initialise and propagate an imposed SST down to the vertical model prognostic fields. This information is introduced into the model in a 'pre-forecast' mode. First this pre-forecast nudging period *HNDG* was defined as the integration period during which the prognostic fields are re-adjusted and equilibrated according to the applied SST field.

```
HOUT=03.
HRST=48.
HNDG=12.  !06.  !24. !nudging period in hours
DTSURF=3.
ITSURF=DTSURF*3600/INT(DTI)
IHOUT=HOUT*3600/INT(DTI)
IRST=HRST*3600/INT(DTI)
```

[15] *Section IV.3.4.*

```
      INDG=HNDG*3600/INT(DTI)     !!!with sst-nudging and forcing
      IF(HNDG.eq.0.) INDG=1
      DAYS=1.+HNDG/24
      IEND=DAYS*24*3600/DTI
C=============================================================
      do i=1,im
      do j=1,jm
        frew(i,j)=0.
       enddo
       enddo
C=============================================================
      cnudg=5.E-5
```

The assigned value of HNDG was 06, 12 and 24.

Another important contributor to this pre-forecast initialisation was the inclusion of a variable nudging coefficient *cnudg* that modulated the degree of nudging.

The effect of initial SST introduced at the first sigma layer influenced that other fields at each model grid point such as:

(1) the horizontal velocities:

UF(I,J,1)=UF(I,J,1)-DTI***CNUDG***(UF(I,J,1)-**TSURF**(I,J))

where tsurf(i,j) is

TSURF(I,J)=SST(I,J)+ZZ(1)*H(I,J)*(T(I,J,2)-T(I,J,1))/((ZZ(2)-ZZ(1))*H(I,J))

cnudg is the nudging coefficient, **dti** is the internal mode time-step (s),

(2) the vertical temperature profile:

*T(I,J,K)=T(I,J,K)+.5*SMOTH*(UF(I,J,K)+TB(I,J,K)-2.*T(I,J,K))*

where SMOTH is a constant in time smoother to prevent solution splitting, and TSURF(I,J)=TB(I,J,1).

and (3) the turbulence kinetic energy:

Q2(I,J,K)=Q2(I,J,K)+.5*SMOTH*(UF(I,J,K)+Q2B(I,J,K)-2.*Q2(I,J,K))

where Q2 is twice the turbulence kinetic energy (m^2s^{-2}), and Q2(I,J,K)=Q2B(I,J,K)

At the end of every 24-hour integration time, a file called M_INIT or M_RESTRT were produced depending on whether the model started

from zero velocity (M_INIT)[16] or from a previously prepared ocean model run (M_RESTRT)[17].

In both cases, these files contained the necessary forecasted ocean fields that provided the initial 3-D conditions for the next 24-hr forecast. These fields included the momentum fluxes at the bottom, the vertical average of the horizontal kinematic viscosity, the vertical mean of horizontal velocities, the surface elevation, the sigma coordinate vertical velocity, the potential temperature, the density, the vertical diffusivity and the turbulence kinetic energy.

IV.3.3. Post-processing stage.

Post-processing included:

a) Visualisation and preparation of gridded forecasted variables for geo-statistical analysis.
b) Extraction of model results in gridded ascii format.

IV.3.3.1. Visualisation and preparation of gridded forecasted variables for model verification.

The Linux-version of the Grid Analysis and Display System (GrADS) was used to visualise model data during the post-processing stage.

A script was written to display the predicted 4-D geophysical variables using GrADS' own scripting language. Using the GrADS terminal, these fields were displayed. Below is the list of the relevant forecasted parameters produced by the ocean model, with a resolution equivalent to the nested, high-reolution Eta model.

- sea land mask
- Sea level Height
- Nudging period
- Sea Elevation
- U-component of surface momentum
- V-component of surface momentum
- Fresh water
- Temperature
- Salinity.
- U-component of current
- V-component of current

The *WZ.gdat* was produced by *pom97_oper.f* by relating the derived, forecasted fields to the ones defined in the *WZ.ctl* file.The forecasted

[16] *on 1st July 1999*
[17] *from 22nd July - 5th August 1999*

ocean model fields are converted into GrADS formatted data using *WZ.ctl.*

```
dset /usr/local/Charles/grads/WZ.gdat
undef 0
title eta model
xdef 82 linear 15.8 0.041666
ydef 61 linear 33.24 0.041666
tdef 13 linear 12Z06aug1999 03hr
zdef 1 levels 0
vars 12
fsm 0 81,105,00 mask
h 0 7,105,00 Height
tn 0 1007,105,00 Tnudg
el 0 77,105,00 Elevation
wts 0 121,105,00 Wusurf
wus 0 123,105,00 Wusurf
wvs 0 124,105,00 Wvsurf
frew 0 1049,105,00 Fresh water
t 18 11,160,00 TEMP
s 18 51,160,00 salt.
u 18 49,160,00 U current
v 18 50,160,00 V current
endvars
```

IV.3.3.2. Extraction of the model results into gridded ascii format.

Following the generation of the WZ.gdat file, a set of gridded ascii XYZ files were produced for all relevant parameters at three-hourly intervals. These ascii files were generated in batch mode using an executable *grads2xyz.f* code[18] as shown below (for the case of temperature) after the 'WZ.gdat' file is fully generated at the end of the model's 36-hr forecast.

```
foreach hh (00 03 06 09 12 15 18 21 24 27 30 33 36)
grads2xyz 990722"$hh" T 11 0 0
end
```

In the case of temperature T, *grads2xyz 990721"$hh" T 11 0 0* called subroutine RGRADS in *grads2xyz* to read values from the '*WZ.gdat*' file, such as IPAR, IMJM, ILEV and VAR:

```
call RGRADS (id7, IPAR,ILEVT,ILEV, IMJM, 1, 1, RLEV,VAR , NLRET)
```

where *IPAR* is the parameter code, *ILEV* and *RLEV* represent a particular standard pressure level, and *VAR* is the parameter value. The XYZ ascii file was then generated following the instruction:

```
write ( 50,999) rlon, rlat, VAR (n)
```

which wrote the parameter value alongside with its X (rlon) and Y(rlat) coordinates. The value of X and Y were extracted from IMJM.

[18] *Appendix II; Section II.2.2.*

IV.3.4. Automated model integration.

The automated POM batch script file for the running of the model between 22nd and 31st July 1999. The command *./readgrds* converts SST temperature into model-specific sigma levels. The executable file *./grid_oper* prepares the lateral boundary conditions of the model as read from the *m_restrt* file and used during the execution of the actual model run *./pom97_oper*. Following the model integration, the predicted model fields are converted into xyz ascii format for statistical analysis.

```
#!/bin/csh
#-------------------------------------------------------------
foreach dd ( 22 23 24 25 26 27 28 29 30 31 )
cd /usr/local/Charles/wrk/exe
  ./readgrds 9907"$dd"
cd /usr/local/Charles/POM/preproc/exe
  ./grid_oper "$dd"0799
cd /usr/local/Charles/POM/model/exe/
   ./pom97_oper
cd /usr/Results/TMI_POM_surfce/coeff_e04
mkdir "$dd"0799
cd /usr/local/Charles/grads
cp WZ.ctl WZ.gdat /usr/Results/TMI_POM_surfce/coeff_e04/"$dd"0799/
cd /usr/local/Charles/POM/model/tmp
cp m_restrt* /usr/Results/TMI_POM_surfce/coeff_e04/"$dd"0799/
rm sst*
rm -f /usr/local/Charles/XYZ/*
cd /usr/local/Charles/postproc/exe
foreach hh ( 00 03 06 09 12 15 18 21 24 27 \
        30 33 36 )
grads2xyz 9907"$dd""$hh" t 11 160 00
grads2xyz 9907"$dd""$hh" tn 1007 105 00
grads2xyz 9907"$dd""$hh" u 49 160 00
grads2xyz 9907"$dd""$hh" v 50 160 00
grads2xyz 9907"$dd""$hh" el 77 105 00
grads2xyz 9907"$dd""$hh" wts 121 105 00
grads2xyz 9907"$dd""$hh" wus 123 105 00
grads2xyz 9907"$dd""$hh" wvs 124 105 00
grads2xyz 9907"$dd""$hh" frew 1049 105 00
end
cd /usr/Results/TMI_POM_surfce/coeff_e04/"$dd"0799
mkdir XYZ
cd XYZ
mkdir model
cd /usr/local/Charles/XYZ/
cp * /usr/Results/TMI_POM_surfce/coeff_e04/"$dd"0799/XYZ/model/
end
exit
```

Appendix V

STATISTICAL RESULTS OF CHAPTER 4.

This Appendix includes the results of the statistical summary measures describing the accuracy of the synthesized database against independent climatological data.

	SOC climatology		Quasi-inst. calculation		BIAS
	mean	**stdev**	**mean**	**stdev**	
Jan	-116.60	2.06	**-72.51**	8.64	-44.09
Feb	-92.22	5.19	**-86.22**	11.36	-6.00
Mar	-78.28	1.63	-60.76	10.13	-17.52
Apr	-56.27	1.13	-69.41	10.03	13.14
May	-41.84	0.40	-59.28	11.15	17.44
Jun	-47.26	1.66	-62.32	11.01	15.06
July	-77.48	6.07	-65.13	9.83	-12.35
Aug	-88.29	4.37	-49.08	4.78	-39.21
Sept	-103.37	1.90	-75.94	11.17	-27.43
Oct	-117.58	4.44	-63.33	10.99	-54.25
Nov	-133.74	2.59	-99.79	18.91	-33.96
Dec	-136.31	4.15	-111.97	14.41	-24.34

Table V.1. Summary statistics for the monthly mean values of the latent heat flux (W m^{-2}) over the area of interest.

	SOC climatology		Quasi-inst. calculation		BIAS
	mean	**stdev**	**mean**	**stdev**	
Jan	-16.30	0.33	-13.55	1.57	-2.75
Feb	-10.48	1.62	-17.39	2.27	6.91
Mar	-6.08	0.27	-9.29	1.54	3.21
Apr	-0.95	0.28	2.08	0.30	-3.03
May	1.07	0.98	3.10	0.58	-2.03
Jun	0.40	0.46	3.15	0.41	-2.75
July	-1.93	0.59	3.29	0.50	-5.22
Aug	-2.72	0.58	0.71	0.07	-3.43
Sept	-4.80	0.17	-3.82	0.55	-0.98
Oct	-6.16	0.46	-6.76	1.17	0.60
Nov	-10.42	0.69	-13.75	2.50	3.33
Dec	-15.66	1.04	-19.11	2.41	3.46

Table V.2. Summary statistics for the monthly mean values for the sensible heat flux (W m^{-2}) over the area of interest.

	Min.	Max.	Mean.	Stdev.
Jan	-70.30	-66.30	-68.20	1.32
Feb	-68.20	-66.50	-67.09	0.50
Mar	-66.80	-63.90	-65.37	1.01
Apr	-65.20	-61.10	-62.88	1.27
May	-59.40	-57.50	-58.40	0.56
Jun	-58.60	-57.20	-57.79	0.48
July	-63.20	-59.80	-61.48	1.28
Aug	-61.00	-60.00	-60.16	0.62
Sept	-63.90	-63.90	-63.90	0.00
Oct	-64.90	-62.50	-63.79	0.84
Nov	-67.00	-64.10	-65.59	0.95
Dec	-69.30	-65.90	-67.92	1.05

Table V.3. Summary statistics of the monthly mean values for the outgoing longwave radiation (W m^{-2}) over the area of interest.

	SOC climatology		Quasi-inst. calculation		BIAS
	mean	**stdev**	**mean**	**stdev**	
Jan	7.89	0.15	5.60	0.90	2.29
Feb	7.52	0.21	6.92	1.15	0.60
Mar	7.20	0.19	4.58	1.22	2.62
Apr	6.66	0.05	5.11	0.97	1.55
May	5.73	0.11	3.33	1.11	2.41
Jun	5.08	0.08	3.92	0.94	1.16
July	5.07	0.26	4.45	0.99	0.62
Aug	4.73	0.12	2.68	0.58	2.05
Sept	4.93	0.13	4.35	1.04	0.58
Oct	6.01	0.10	4.44	1.13	1.57
Nov	7.16	0.13	7.71	1.59	-0.55
Dec	8.18	0.09	9.57	1.29	-1.39

Table V.4. Summary statistics of the monthly mean values for the wind magnitude (m s^{-1}) over the area of interest.

	SOC climatology		Quasi-inst. calculation		BIAS
	mean	stdev	mean	stdev	
Jan	16.14	0.29	15.74	3.09	0.40
Feb	15.40	0.25	15.72	0.33	-0.32
Mar	15.37	0.22	16.01	0.43	-0.64
Apr	16.39	0.23	16.49	0.60	-0.11
May	18.46	0.16	20.99	2.08	-2.53
Jun	21.77	0.13	23.54	0.68	-1.53
July	24.99	0.13	25.62	0.63	-0.63
Aug	26.30	0.13	26.93	1.25	-0.63
Sept	25.59	0.26	27.82	0.42	-2.23
Oct	23.57	0.20	25.22	0.38	-1.66
Nov	20.89	0.38	22.76	1.05	-1.87
Dec	18.06	0.37	19.35	0.75	-1.30

Table V.5. Summary statistics of the monthly mean values for SST (°C) over the area of interest.

	SOC climatology		Quasi-inst. calculation		BIAS
	mean	stdev	mean	stdev	
Jan	14.61	0.29	12.27	1.52	-2.00
Feb	14.29	0.40	13.15	0.97	-1.00
Mar	14.52	0.19	14.81	1.08	0.00
Apr	16.17	0.30	16.25	0.90	-0.48
May	18.54	0.27	20.21	0.50	-1.21
Jun	21.62	0.18	22.70	0.62	-1.08
July	24.43	0.15	25.18	1.24	-0.87
Aug	25.77	0.09	26.80	2.76	-0.25
Sept	24.66	0.26	27.39	0.48	0.00
Oct	22.52	0.33	24.32	1.40	0.00
Nov	19.88	0.51	21.61	1.00	-0.05
Dec	15.51	0.40	17.96	1.16	0.00

Table V.6. Summary statistics of the monthly mean values for the surface air temperature (°C) over the area of interest.

Date	Code		TB4	TB5	TB4-5	DELTAT4/DELTAT5	GAMMA	MEAN SWT	MAX SWT	MIN SWT	STDEV	MEAN NLSST	MAX NLSST	MIN NLSST	NLSST STDEV	NLSST-SWT
99_01_19	1908	B'	283.83	283.18	0.65	1.06	4.58	12.88	27.13	9.63	2.63	12.01	24.41	9.52	2.33	-0.87
		F	294.20	293.19	1.01	1.07	3.68	23.04	25.56	15.78	1.64	22.92	25.26	15.99	1.56	-0.12
		K	294.46	293.37	1.09	1.14	3.20	22.44	24.43	19.62	1.21	23.34	25.26	20.75	1.19	0.90
		O	293.48	292.41	1.07	1.10	3.79	22.62	25.75	16.90	1.45	22.33	25.26	17.09	1.35	-0.29
98_02_18	908	J	286.85	286.04	0.81	1.09	4.19	15.85	25.71	9.66	4.49	15.34	24.06	10.66	4.02	-0.51
	910	J	286.15	285.01	1.14	1.07	5.06	17.53	27.29	10.73	4.63	16.07	24.43	10.79	4.08	-1.46
		K	291.13	289.64	1.49	1.09	5.02	23.86	27.49	12.33	2.30	21.62	24.43	11.90	1.98	-2.24
		Q	291.39	290.02	1.37	1.09	3.53	20.49	23.10	18.30	0.79	21.58	24.18	19.72	0.75	1.09
		R	290.55	289.17	1.38	1.12	3.14	18.79	20.79	17.16	0.75	20.68	22.69	19.22	0.77	1.89
	922	J	285.65	284.80	0.85	1.12	4.33	14.81	25.26	9.48	4.41	15.16	24.06	11.04	3.74	0.36
98_02_19	8	A	280.28	279.80	0.48	0.91	3.36	7.40	10.15	0.19	0.62	8.41	9.18	2.60	0.50	0.98
		D	282.43	281.81	0.63	1.03	4.20	11.17	14.57	9.39	0.59	10.56	12.65	9.80	0.38	-0.61
		E	282.08	281.57	0.51	1.10	4.14	10.22	24.36	6.36	2.70	10.27	22.57	8.43	2.29	-0.01
		J	285.96	285.12	0.85	1.09	4.40	15.41	26.22	7.42	4.35	14.42	23.81	8.56	3.84	-0.98
		P	293.73	292.42	1.31	1.03	3.81	23.69	25.80	18.62	0.81	23.05	24.80	18.48	0.77	-0.65
	12	D	281.02	280.20	0.82	0.99	6.53	12.99	16.38	9.03	0.79	10.67	12.65	9.67	0.41	-2.36
		E	281.31	280.40	0.90	1.16	3.94	9.90	23.54	5.57	4.23	11.20	23.44	8.68	3.73	1.25
		I	282.32	281.37	0.95	1.12	4.19	11.63	22.83	8.78	2.41	12.07	21.95	10.17	2.03	0.45
		K	289.74	287.81	1.93	1.15	4.84	23.76	27.75	9.97	3.10	21.50	24.80	10.79	2.67	-2.26
		P	291.83	289.95	1.88	1.05	5.26	26.80	29.24	22.44	0.93	23.36	25.17	20.09	0.75	-3.44
		Q	290.04	288.28	1.76	1.04	4.49	22.69	25.49	18.19	0.83	21.34	23.68	18.10	0.74	-1.35
98_02_20	123	D	283.11	282.37	0.74	1.00	6.63	14.84	21.70	11.45	1.22	12.21	16.37	11.53	0.61	-3.09
		E	282.46	281.65	0.81	1.11	3.94	10.89	24.51	7.88	2.25	11.72	24.06	10.17	1.95	0.77
		I	284.51	283.65	0.86	1.07	4.33	13.91	20.85	10.53	1.21	13.65	19.22	12.15	0.95	-0.32
		J	286.11	285.08	1.03	1.08	5.01	16.99	28.21	11.20	4.73	15.53	24.92	11.28	4.03	-1.46

Table V.7a. Summary statistics for the derivation and accuracy assessment of the split-window algorithm as defined by Yu and Barton (1994) as per CoastWatch sector. (SWT = split-window technique according to the YB94 algorithm; NLSST = Nonlinear SST).

Date	Code		TB4	TB5	TB4-5	DELTAT4/DELTAT5	GAMMA	MEAN SWT	MAX SWT	MIN SWT	STDEV	MEAN NLSST	MAX NLSST	MIN NLSST	NLSST STDEV	NLSST-SWT
98_02_20	207	D	282.51	281.64	0.87	1.17	3.61	9.14	12.24	7.63	0.54	10.96	13.89	10.17	0.42	1.53
		E	282.34	281.57	0.77	1.09	4.50	11.95	26.04	8.55	2.66	10.79	23.31	8.68	2.31	-1.10
		I	284.20	283.28	0.92	1.06	4.54	14.16	20.87	11.60	1.30	12.77	18.48	11.04	1.15	-1.39
		J	285.79	284.81	0.98	1.08	4.42	15.74	27.06	6.81	4.50	14.50	24.68	7.94	4.10	-1.24
	211	A	280.14	279.53	0.61	0.92	3.25	7.31	8.50	5.21	0.39	9.25	9.92	8.43	0.29	1.89
		E	281.85	281.09	0.76	1.07	5.47	12.07	27.29	7.07	2.79	10.93	23.19	8.80	2.23	-1.14
		G	292.08	290.56	1.51	1.02	3.65	22.13	24.21	20.46	0.64	22.11	23.93	20.58	0.57	-0.02
		I	283.71	282.85	0.86	1.04	4.56	13.34	20.33	8.06	1.34	12.80	18.60	9.30	1.12	-0.54
		J	285.24	284.34	0.90	1.05	5.27	15.96	28.00	3.48	4.55	14.37	24.43	6.08	3.90	-1.60
		P	293.17	291.73	1.45	1.10	3.43	22.37	24.20	16.58	0.93	23.06	25.05	17.73	0.89	0.69
	222	D	282.71	282.00	0.71	0.95	4.55	11.95	16.39	9.21	0.86	11.61	14.51	10.54	0.54	-0.33
		E	282.62	281.87	0.75	1.08	4.30	11.64	25.24	7.98	2.58	11.71	23.44	10.17	2.19	-0.08
		I	284.54	283.75	0.79	1.07	4.38	13.71	19.13	10.03	1.09	13.58	17.98	12.03	0.84	-0.34
		J	285.97	285.11	0.86	1.06	5.42	16.72	27.95	10.76	4.64	15.00	24.18	11.04	3.94	-1.72
98_02_21	207	D	282.51	281.64	0.87	1.17	3.61	9.14	12.24	7.63	0.54	10.96	13.89	10.17	0.42	1.53
		E	282.34	281.57	0.77	1.09	4.50	11.95	26.04	8.55	2.66	10.79	23.31	8.68	2.31	-1.10
		I	284.20	283.28	0.92	1.06	4.54	14.16	20.87	11.60	1.30	12.77	18.48	11.04	1.15	-1.39
		J	285.79	284.81	0.98	1.08	4.42	15.74	27.06	6.81	4.50	14.50	24.68	7.94	4.10	-1.24
	211	A	280.14	279.53	0.61	0.92	3.25	7.31	8.50	5.21	0.39	9.25	9.92	8.43	0.29	1.89
		E	281.85	281.09	0.76	1.07	5.47	12.07	27.29	7.07	2.79	10.93	23.19	8.80	2.23	-1.14
		G	292.08	290.56	1.51	1.02	3.65	22.13	24.21	20.46	0.64	22.11	23.93	20.58	0.57	-0.02
		I	283.71	282.85	0.86	1.04	4.56	13.34	20.33	8.06	1.34	12.80	18.60	9.30	1.12	-0.54
		J	285.24	284.34	0.90	1.05	5.27	15.96	28.00	3.48	4.55	14.37	24.43	6.08	3.90	-1.60
		P	293.17	291.73	1.45	1.10	3.43	22.37	24.20	16.58	0.93	23.06	25.05	17.73	0.89	0.69
	222	D	282.71	282.00	0.71	0.95	4.55	11.95	16.39	9.21	0.86	11.61	14.51	10.54	0.54	-0.33
		E	282.62	281.87	0.75	1.08	4.30	11.64	25.24	7.98	2.58	11.71	23.44	10.17	2.19	-0.08
		I	284.54	283.75	0.79	1.07	4.38	13.71	19.13	10.03	1.09	13.58	17.98	12.03	0.84	-0.34
		J	285.97	285.11	0.86	1.06	5.42	16.72	27.95	10.76	4.64	15.00	24.18	11.04	3.94	-1.72

Table V.7b. Summary statistics for the derivation and accuracy assessment of the split-window algorithm as defined by Yu and Barton (1994) as per CoastWatch sector. (SWT = split-window technique according to the YB94 algorithm; NLSST = Nonlinear SST).

Date	Code		TB4	TB5	TB4-5	DELTAT4/DELTAT5	GAMMA	MEAN SWT	MAX SWT	MIN SWT	STDEV	MEAN NLSST	MAX NLSST	MIN NLSST	NLSST STDEV	NLSST-SWT
98_02_25	608	A	279.92	278.79	1.13	1.12	3.75	9.07	21.10	3.86	1.94	9.20	21.08	5.08	1.82	0.13
		D	281.91	280.87	1.04	0.99	6.21	14.61	17.55	9.11	1.10	11.00	12.28	9.92	0.35	-4.14
		E	281.38	280.21	1.16	1.12	4.20	11.45	25.09	7.15	2.77	10.80	23.81	9.05	2.61	-1.03
		I	284.17	283.14	1.03	1.03	5.28	15.67	21.30	11.58	1.52	13.16	18.48	10.29	1.41	-2.51
		J	285.72	284.51	1.21	1.07	4.54	16.64	25.43	8.69	4.07	15.21	23.19	8.93	3.90	-1.43
		O	289.44	288.10	1.34	1.08	3.02	17.56	21.93	10.25	2.56	19.25	23.93	11.90	2.67	1.69
		P	291.93	290.30	1.64	1.11	3.69	22.33	26.06	19.23	1.69	22.73	26.66	19.59	1.80	0.40
	611	A	280.84	280.04	0.80	1.06	4.32	9.94	23.00	7.05	1.94	9.96	21.20	8.43	1.66	0.01
		D	282.56	281.94	0.62	0.85	10.70	17.16	20.19	11.36	1.06	11.43	12.52	10.17	0.27	-5.73
		E	282.31	281.59	0.72	1.04	5.17	12.32	26.25	8.56	2.79	11.33	23.06	9.30	2.39	-0.99
		I	284.56	283.85	0.71	1.02	4.94	14.37	19.58	9.95	1.49	13.42	17.61	10.54	1.27	-0.95
		J	286.56	285.86	0.70	1.03	5.13	16.49	25.67	7.16	4.05	15.33	22.94	8.68	3.55	-1.16
		O	290.38	289.53	0.84	1.04	4.83	20.52	25.91	12.05	2.93	19.15	23.68	12.28	2.54	-1.37
		P	293.58	292.58	1.01	1.07	4.30	23.48	27.83	19.67	1.94	22.54	26.41	19.10	1.77	-0.94
		Q	294.31	293.11	1.21	1.00	4.93	26.07	29.08	20.18	1.18	23.73	26.16	18.23	1.02	-2.34
99_03_17	600	A	279.75	279.35	0.40	1.06	5.21	8.33	25.10	0.43	3.37	8.33	23.31	1.95	2.90	0.01
		B'	283.13	282.33	0.80	1.06	5.10	13.24	24.41	6.47	3.86	12.35	22.58	7.08	3.47	-0.89
		C	290.82	289.48	1.34	1.06	4.49	21.99	24.76	18.73	1.47	21.61	23.92	18.31	1.39	-0.38
		D	283.30	282.86	0.44	1.05	4.95	11.84	18.47	8.51	1.60	11.81	17.21	10.01	1.37	-0.05
		E	286.48	285.79	0.70	1.06	5.31	16.31	24.26	8.94	3.99	15.40	22.46	9.89	3.56	-0.93
		G	292.36	291.14	1.22	0.99	5.04	24.27	26.05	20.77	0.78	22.73	24.17	19.89	0.73	-1.57
		H	289.93	288.69	1.25	1.03	5.88	22.14	25.41	19.65	1.31	20.38	23.31	18.31	1.22	-1.79
		I	285.70	285.22	0.48	1.08	2.28	11.01	18.02	6.57	2.85	14.05	19.28	9.89	2.57	3.01
		J	288.30	287.63	0.67	1.06	4.94	17.72	24.64	9.81	3.78	17.20	23.43	10.37	3.38	-0.55
		K	292.04	291.11	0.93	1.07	4.60	21.97	24.89	16.15	1.65	21.55	24.29	16.60	1.53	-0.46
		L	293.17	292.06	1.11	1.01	4.08	22.98	24.20	19.76	0.56	23.18	24.41	20.26	0.55	0.16

Table V.7c. Summary statistics for the derivation and accuracy assessment of the split-window algorithm as defined by Yu and Barton (1994) as per CoastWatch sector. (SWT = split-window technique according to the YB94 algorithm; NLSST = Nonlinear SST).

Date	Code		TB4	TB5	TB4-5	DELTAT4/DELTAT5	GAMMA	MEAN SWT	MAX SWT	MIN SWT	STDEV	MEAN NLSST	MAX NLSST	MIN NLSST	NLSST STDEV	NLSST-SWT
99_03_17	600	M	291.20	290.02	1.19	1.02	3.77	20.70	22.61	17.87	0.79	21.41	23.31	19.04	0.74	0.67
Cont'd		N	289.45	288.21	1.24	0.93	8.76	26.96	32.53	24.22	0.98	19.86	22.09	17.21	0.76	-7.13
		O	290.81	290.01	0.80	1.06	4.08	19.69	23.22	12.67	1.19	19.85	23.56	13.67	1.06	0.13
		P	292.37	291.44	0.93	1.07	4.12	21.55	24.01	19.18	1.01	21.82	24.29	19.77	1.01	0.23
		Q	293.06	291.94	1.12	0.96	7.38	27.88	30.04	25.34	0.78	23.08	24.41	21.48	0.63	-4.85
		R	292.32	291.08	1.24	0.90	5.70	25.41	28.67	21.38	0.69	22.67	24.29	16.11	0.65	-2.78
		S	290.43	289.12	1.31	0.92	6.07	24.36	28.56	21.50	1.20	20.93	23.07	16.48	1.01	-3.47
		T	288.93	287.56	1.37	0.84	4.86	21.27	24.33	12.63	0.82	19.60	21.60	10.37	0.80	-1.70
	607	A	279.80	279.04	0.76	1.11	4.32	8.80	25.04	-2.62	3.87	8.56	23.43	1.95	3.39	-0.24
		A'	283.83	283.18	0.65	1.06	4.58	12.88	27.13	9.63	2.63	12.01	24.41	9.52	2.33	-0.87
		B'	282.99	281.94	1.06	1.10	4.25	12.87	23.43	6.80	3.77	12.12	22.09	7.08	3.37	-0.75
		C	290.82	289.13	1.69	1.08	3.47	20.84	23.17	15.38	1.38	21.36	23.80	15.62	1.47	0.52
		D	282.62	281.74	0.87	1.10	4.20	11.86	17.49	8.84	1.51	11.60	16.48	9.40	1.33	-0.26
		E	285.70	284.55	1.15	1.11	4.11	15.75	23.00	8.93	3.80	15.37	22.46	9.76	3.59	-0.45
		G	291.74	289.94	1.80	1.02	5.19	26.38	28.34	22.82	0.86	22.72	24.17	20.02	0.78	-3.65
		J	286.91	285.57	1.34	1.14	3.88	16.87	23.55	8.86	3.58	16.99	23.80	9.76	3.45	0.12
		K	290.69	288.96	1.73	1.14	3.49	20.82	23.35	15.43	1.65	21.75	24.53	16.23	1.71	0.92
		L	291.98	290.14	1.84	1.01	4.83	26.03	27.88	22.75	0.58	23.19	24.53	20.50	0.50	-2.84
		M	290.59	288.90	1.69	1.05	4.77	23.77	26.07	19.99	0.79	21.22	23.07	17.45	0.74	-2.55
		N	289.35	287.77	1.58	1.05	3.86	20.01	22.46	16.06	0.79	19.47	21.97	15.26	0.80	-0.55
		P	290.50	288.72	1.79	1.08	3.62	21.22	24.24	19.15	1.04	21.85	24.78	19.65	1.08	0.63
		Q	291.75	289.93	1.83	1.07	3.24	21.60	23.12	20.02	0.65	23.09	24.90	21.36	0.72	1.49
		R	291.20	289.39	1.80	0.97	4.40	24.06	26.23	11.97	1.03	22.25	24.41	11.59	1.09	-1.81
99_03_23	208	D	283.39	282.36	1.03	0.97	6.95	17.23	23.54	11.14	1.40	12.01	17.33	8.54	1.32	-5.22
		E	286.78	285.69	1.09	1.03	5.00	18.12	25.99	8.54	3.06	15.57	22.58	8.54	2.82	-2.55
		I	286.22	285.17	1.05	1.04	4.98	17.33	23.41	10.37	2.40	14.95	20.14	9.76	2.21	-2.38
		J	288.62	287.44	1.18	1.06	4.62	19.63	24.46	11.85	3.17	17.64	22.09	11.72	2.91	-2.00
		K	292.23	290.78	1.44	1.07	4.54	24.02	27.56	17.94	1.97	21.81	24.90	16.11	1.86	-2.21
		L	293.06	291.51	1.55	0.99	4.60	25.37	27.60	22.41	0.84	22.85	24.65	20.63	0.76	-2.52
		O	291.28	289.95	1.32	1.10	3.86	21.20	25.29	15.65	1.88	20.64	24.41	15.38	1.78	-0.56

Table V.7d. Summary statistics for the derivation and accuracy assessment of the split-window algorithm as defined by Yu and Barton (1994) as per CoastWatch sector. (SWT = split-window technique according to the YB94 algorithm; NLSST = Nonlinear SST).

Date	Code		TB4	TB5	TB4-5	DELTAT4/DELTAT5	GAMMA	MEAN SWT	MAX SWT	MIN SWT	STDEV	MEAN NLSST	MAX NLSST	MIN NLSST	NLSST STDEV	NLSST-SWT
99_03_29	808	A	281.06	280.23	0.83	1.06	4.55	10.60	26.94	6.09	3.35	9.56	24.29	7.32	3.08	-1.06
		D	284.30	283.51	0.78	1.05	4.63	14.00	17.66	9.35	1.15	12.72	15.87	10.01	0.94	-1.29
		E	287.81	286.81	1.00	1.06	4.74	18.37	26.89	11.22	3.53	14.66	20.99	9.76	2.85	-3.72
		G	292.00	290.29	1.71	0.92	5.28	26.63	29.31	23.52	0.72	22.53	24.65	20.02	0.62	-4.15
		H	289.67	287.81	1.86	1.02	3.43	20.04	22.46	11.20	1.30	20.52	22.82	11.72	1.36	0.44
		K	293.11	291.78	1.33	1.08	3.67	22.80	25.34	15.13	1.79	22.69	25.14	15.26	1.78	-0.16
		L	292.74	291.25	1.49	0.94	7.55	30.36	33.91	27.04	0.99	22.69	25.02	21.11	0.88	-7.71
		Q	292.87	291.12	1.74	0.95	5.52	27.95	31.28	24.98	1.16	23.39	25.75	21.11	1.01	-4.61
99_03_30	900	P	291.89	289.87	2.03	1.02	5.29	27.51	29.70	23.18	1.44	24.54	26.48	20.14	1.48	-2.96
		Q	290.60	288.45	2.16	1.00	2.29	17.32	19.45	15.85	0.89	23.72	26.36	21.60	1.18	6.40
98_03_14	307	A	279.65	278.05	1.61	1.04	5.48	14.13	27.06	1.44	3.17	9.73	22.57	1.86	3.01	-4.36
		B'	279.54	277.94	1.60	1.04	4.87	12.55	21.75	7.89	2.95	9.40	17.73	5.83	2.81	-3.15
		E	281.10	279.38	1.72	1.03	5.51	16.33	29.94	1.70	3.38	11.68	24.92	1.74	3.37	-4.58
		Q	291.43	289.31	2.12	1.03	5.39	27.81	31.56	23.29	2.12	23.67	27.16	19.59	2.12	-4.13
98_03_15	408	A	279.68	278.19	1.49	1.09	5.10	12.67	20.80	7.99	1.65	9.54	16.37	6.94	1.41	-3.13
		D	281.81	280.66	1.15	1.10	4.34	12.30	14.29	5.81	1.08	11.16	13.14	7.44	0.82	-1.22
		E	281.89	280.57	1.32	1.11	4.19	12.44	25.30	7.44	2.70	11.53	24.30	7.56	2.63	-0.90
		I	283.53	282.53	0.99	1.03	5.58	15.26	21.09	8.03	1.27	12.46	16.99	8.68	1.06	-2.82
		J	285.10	283.86	1.24	1.12	3.90	14.83	22.53	6.71	3.32	14.67	22.20	7.56	3.23	-0.16
		K	289.58	287.64	1.94	1.16	3.70	20.73	25.20	11.87	3.25	21.19	26.04	12.52	3.41	0.46
		O	288.44	287.07	1.37	1.13	4.02	18.81	26.23	12.07	2.53	18.32	25.54	12.40	2.46	-0.49
		P	289.49	287.88	1.62	1.12	2.90	17.86	22.67	14.94	1.26	20.11	25.79	16.86	1.42	2.25
		Q	290.54	288.59	1.95	1.21	3.24	20.34	23.49	16.86	2.10	22.30	26.04	18.60	2.42	1.97
99_04_14	400	A	287.90	287.32	0.57	1.04	6.17	17.41	27.26	8.11	3.70	16.34	24.78	11.23	3.21	-1.18
		B'	283.36	283.07	0.29	1.02	5.85	11.99	26.04	6.74	3.08	11.67	24.29	7.69	2.77	-0.36
		I	289.43	288.71	0.72	1.08	4.73	18.80	24.19	13.26	1.88	18.33	23.19	14.40	1.66	-0.51
		O	292.68	291.69	0.99	1.00	4.80	23.29	26.26	19.53	0.79	22.35	25.02	18.55	0.80	-1.03

Table V.7e. Summary statistics for the derivation and accuracy assessment of the split-window algorithm as defined by Yu and Barton (1994) as per CoastWatch sector. (SWT = split-window technique according to the YB94 algorithm; NLSST = Nonlinear SST).

Date	Code		TB4	TB5	TB4-5	DELTAT4/DELTAT5	GAMMA	MEAN SWT	MAX SWT	MIN SWT	STDEV	MEAN NLSST	MAX NLSST	MIN NLSST	NLSST STDEV	NLSST-SWT
98_04_13	308	A	283.12	282.27	0.85	1.05	4.38	12.62	17.64	3.71	2.14	11.67	16.12	6.70	1.89	-0.96
		A'	281.91	281.06	0.84	1.05	4.57	11.68	18.34	6.75	1.45	10.42	15.25	7.44	1.22	-1.26
		D	286.67	285.77	0.90	1.04	4.50	16.53	19.73	6.33	1.70	15.25	17.86	8.68	1.36	-1.38
		E	288.19	287.20	0.99	1.02	5.21	19.49	24.10	7.68	2.02	16.98	20.83	9.92	1.78	-2.56
		I	287.73	286.86	0.86	1.02	5.92	19.40	28.75	11.13	0.83	16.21	23.56	10.79	0.60	-3.19
		J	289.71	288.72	0.99	1.06	4.75	20.26	28.73	5.75	3.14	18.48	26.16	7.69	2.91	-1.77
		K	292.71	291.60	1.12	1.08	5.19	24.46	29.68	18.68	3.35	21.85	26.16	17.61	2.99	-2.61
98_05_16	607	A	286.06	285.22	0.84	1.21	3.57	13.95	25.75	8.64	2.90	14.86	26.66	11.28	2.74	0.83
		A'	285.18	284.57	0.61	1.21	3.10	11.80	16.23	8.80	1.63	13.62	17.98	11.04	1.53	1.82
		B'	282.44	282.08	0.36	0.96	4.37	10.60	14.92	8.40	0.65	10.55	13.76	8.93	0.43	-0.05
		C'	285.35	284.57	0.78	1.12	4.02	13.99	27.50	8.61	5.03	14.07	27.03	9.67	4.59	0.08
		D	288.67	287.29	1.38	1.14	3.84	18.87	20.52	15.98	0.61	18.74	20.21	16.49	0.54	-0.13
		E	288.03	286.55	1.48	1.20	3.45	17.11	25.62	11.46	3.83	18.21	27.16	13.64	4.00	0.99
		G	293.86	292.28	1.58	1.19	2.41	20.64	22.38	17.58	0.91	24.41	26.78	20.58	1.19	3.77
		H	292.56	291.35	1.21	1.23	3.02	20.24	24.11	18.63	1.20	21.97	26.16	20.34	1.30	1.72
		K	293.00	291.01	2.00	1.09	4.37	26.25	28.95	20.03	1.34	24.92	27.53	19.10	1.34	-1.34
		L	293.79	291.99	1.80	1.16	2.77	22.27	23.87	18.42	1.02	25.04	27.28	20.46	1.29	2.77
		M	291.82	290.66	1.16	1.01	4.82	23.20	28.31	21.54	0.77	21.16	25.42	20.09	0.60	-2.04
		N	291.96	290.87	1.09	1.03	3.28	20.26	21.81	18.39	0.54	21.06	22.57	18.97	0.53	0.80
		P	294.58	292.64	1.94	1.10	4.81	28.77	30.89	24.21	1.15	26.64	28.40	22.32	1.07	-2.14
		Q	294.11	292.36	1.75	1.16	2.94	22.90	24.59	20.54	0.85	25.40	27.53	22.57	1.03	2.50
		R	292.99	291.52	1.47	1.20	3.12	21.43	24.39	17.94	1.59	23.31	26.54	19.72	1.78	1.87
		S	291.41	290.29	1.12	0.93	4.27	21.93	23.06	18.58	0.39	20.66	21.58	17.73	0.28	-1.27

Table V.7f. Summary statistics for the derivation and accuracy assessment of the split-window algorithm as defined by Yu and Barton (1994) as per CoastWatch sector. (SWT = split-window technique according to the YB94 algorithm; NLSST = Nonlinear SST).

Date	Code		TB4	TB5	TB4-5	DELTAT4/DELTAT5	GAMMA	MEAN SWT	MAX SWT	MIN SWT	STDEV	MEAN NLSST	MAX NLSST	MIN NLSST	NLSST STDEV	NLSST-SWT
98_06_03	407	A	294.50	293.66	0.84	1.16	3.38	22.28	26.61	14.58	1.81	23.31	28.15	16.37	1.77	1.03
		A'	292.21	291.43	0.77	1.09	3.93	20.17	24.77	15.16	1.41	20.83	25.92	16.24	1.43	0.67
		B	294.67	292.90	1.78	1.21	2.26	21.10	22.97	17.54	1.51	25.79	28.40	20.83	2.06	4.70
		B'	291.61	290.37	1.24	1.29	2.57	17.94	22.81	14.31	2.40	21.30	27.40	17.48	2.84	3.37
		D	293.97	292.97	1.01	1.23	3.07	21.33	25.22	15.03	1.82	23.35	28.15	16.99	1.94	2.02
		E	295.23	294.12	1.10	1.49	1.94	19.29	21.25	14.54	1.00	24.75	27.78	18.48	1.47	5.47
		G	295.11	293.34	1.76	1.25	2.28	21.25	22.87	19.50	0.93	26.20	28.64	23.81	1.26	4.95
		I	295.75	294.44	1.32	1.24	2.50	22.44	23.72	19.63	0.67	26.33	27.78	22.94	0.62	3.72
		J	296.32	294.96	1.36	1.16	3.20	24.88	26.49	21.02	0.70	26.72	28.52	22.44	0.79	1.84
		M	295.23	293.27	1.97	1.23	2.06	21.02	22.42	19.51	0.84	26.84	28.89	24.43	1.22	5.82
98_08_23	507	A	292.86	290.37	2.49	0.78	3.37	24.80	27.41	22.90	0.52	25.87	28.64	23.68	0.64	1.07
		B	294.29	291.65	2.64	1.20	2.31	22.31	24.24	20.12	0.84	27.75	30.01	24.55	1.10	5.44
		B'	293.56	291.17	2.40	1.21	2.80	22.80	25.51	20.87	0.73	26.26	29.26	23.81	0.87	3.46
		C	295.03	292.14	2.90	0.84	12.61	25.17	26.26	23.53	0.38	26.26	29.26	23.81	0.87	0.87
		E	293.50	291.07	2.43	1.08	3.94	26.86	29.13	23.85	0.81	26.66	28.89	23.44	0.87	-0.19
		F	294.38	291.74	2.64	1.13	3.26	25.97	28.23	22.61	1.28	28.01	30.13	24.18	1.39	2.04
		G	294.85	291.93	2.92	0.77	-7.04	27.06	28.07	25.13	0.32	28.01	30.13	24.18	1.39	0.95
		H	294.67	291.95	2.73	0.72	5.14	33.40	36.17	30.94	0.63	28.14	29.76	25.92	0.46	-5.26
98_09_05	808	A	294.49	293.24	1.25	1.22	2.62	21.20	23.82	18.63	1.33	23.82	26.78	21.45	1.46	2.54
		A'	294.51	293.33	1.18	1.09	3.50	23.35	26.71	20.39	0.78	23.70	26.91	21.82	0.72	0.26
		B	295.66	293.94	1.73	1.07	2.57	23.25	25.37	18.47	1.34	26.26	29.26	20.71	1.60	3.01
		B'	294.98	293.39	1.59	1.35	2.40	21.24	24.41	18.06	1.38	25.20	29.14	21.33	1.77	3.96
		C'	295.66	293.85	1.81	1.29	2.49	22.68	25.10	20.53	1.43	26.52	29.51	23.93	1.82	3.84
		J	295.15	293.02	2.13	1.02	1.74	19.41	20.60	15.03	0.64	26.47	28.15	20.46	1.00	7.05
		K	296.62	294.47	2.14	0.96	3.34	27.69	29.46	24.62	0.89	28.19	29.88	25.05	0.96	0.49
		O	296.91	295.09	1.82	1.04	4.49	29.89	32.62	25.81	1.20	27.59	29.88	24.18	1.08	-2.30
		P	296.90	295.16	1.74	1.12	1.99	22.33	24.13	19.54	1.14	27.45	29.51	23.68	1.54	5.12
		Q	297.95	296.20	1.75	0.99	4.74	31.46	33.26	26.33	0.82	28.57	29.88	24.06	0.63	-2.89
		R	297.02	295.23	1.79	0.87	3.20	26.77	28.30	24.91	0.63	27.89	29.51	26.04	0.70	1.12
		S	296.03	294.14	1.89	1.01	10.19	39.10	39.96	35.92	0.79	27.14	29.14	25.17	0.65	-13.00

Table V.7g. Summary statistics for the derivation and accuracy assessment of the split-window algorithm as defined by Yu and Barton (1994) as per CoastWatch sector. (SWT = split-window technique according to the YB94 algorithm; NLSST = Nonlinear SST).

Date	Code		TB4	TB5	TB4-5	DELTAT4/DELTAT5	GAMMA	MEAN SWT	MAX SWT	MIN SWT	STDEV	MEAN NLSST	MAX NLSST	MIN NLSST	NLSST STDEV	NLSST-SWT
98_11_28	208	A	288.17	287.10	1.08	1.07	4.51	18.53	27.73	10.41	3.61	17.03	25.17	11.16	3.31	-1.51
		A'	285.85	284.75	1.11	0.97	3.97	15.97	17.74	11.56	0.71	14.65	16.24	11.28	0.65	-1.32
		B'	286.35	285.20	1.15	1.05	5.02	17.91	28.80	14.65	2.16	15.21	24.80	13.02	1.98	-2.70
		C	295.67	293.96	1.71	1.07	3.07	24.87	26.60	21.60	1.31	26.01	27.90	22.44	1.42	1.14
		D	289.31	288.31	1.00	1.05	3.26	17.36	22.21	9.09	1.67	18.07	22.82	11.28	1.60	0.69
		E	291.20	290.10	1.09	1.06	4.99	22.36	30.48	10.04	3.31	20.14	27.28	11.16	3.00	-2.22
		F	295.44	294.04	1.40	1.07	5.12	28.22	31.53	20.74	2.47	25.15	27.90	18.85	2.26	-3.08
		G	295.66	294.10	1.56	1.07	3.02	24.35	26.25	21.03	0.94	25.68	27.90	22.32	1.01	1.33
		H	293.46	292.02	1.44	1.00	8.02	31.50	36.62	28.17	1.21	23.06	26.04	22.07	0.64	-8.44
		I	290.99	289.84	1.16	1.07	3.99	20.75	25.59	9.48	2.41	20.18	24.80	11.16	2.27	-0.60
		J	293.25	292.01	1.24	1.09	4.20	23.64	28.59	4.58	3.06	22.68	27.53	7.32	2.89	-0.96
		K	295.97	294.50	1.48	1.09	3.41	25.37	27.30	22.10	1.04	25.94	27.78	22.69	1.06	0.57
		L	295.30	293.78	1.52	1.00	4.71	27.86	30.40	25.99	0.80	25.24	27.28	23.93	0.77	-2.62
		M	294.78	293.25	1.53	1.01	3.33	24.18	26.07	19.29	0.72	24.67	26.41	19.59	0.72	0.49
		N	293.46	292.15	1.31	1.06	3.42	22.34	24.41	21.37	0.51	22.84	24.68	21.95	0.45	0.50
		O	294.80	293.28	1.52	1.11	3.79	25.13	28.57	20.25	1.17	24.99	28.27	20.34	1.15	-0.14
		P	296.16	294.46	1.70	1.09	3.11	25.28	26.58	22.64	0.68	26.74	28.15	24.06	0.75	1.46
		Q	295.30	293.61	1.70	1.03	4.14	27.13	28.98	22.85	0.82	25.73	27.40	20.96	0.74	-1.40
99_11_07	100	A	291.85	290.82	1.03	1.10	4.39	21.78	27.13	15.72	2.05	21.32	26.00	16.72	1.88	-0.46
		B	294.62	293.26	1.37	1.12	3.68	24.20	25.99	20.61	0.98	24.92	26.24	21.48	0.94	0.72
		B'	293.38	292.01	1.37	1.05	3.77	22.96	25.91	17.11	1.55	24.92	26.24	21.48	0.94	1.96
		C	294.38	292.92	1.46	1.02	4.26	25.53	27.09	23.75	0.67	24.95	26.12	23.56	0.62	-0.59
		D	290.69	290.12	0.57	1.09	4.61	19.38	23.81	14.67	1.34	19.21	22.82	15.99	1.05	-0.17
		E	292.21	291.45	0.77	1.07	5.11	22.23	28.72	17.02	2.51	21.03	26.36	17.45	2.16	-1.21
		F	295.39	294.24	1.14	1.08	4.39	25.70	27.74	18.21	2.05	24.97	26.48	18.67	1.84	-0.74
		G	295.12	293.90	1.22	0.96	2.73	22.43	23.63	21.20	0.40	25.01	26.12	23.80	0.42	2.57
		I	291.67	291.12	0.55	1.06	4.97	20.66	26.68	16.58	2.23	20.15	25.39	17.57	1.84	-0.52
		J	294.48	293.73	0.75	1.05	5.99	25.53	29.47	17.40	2.89	23.26	26.12	17.21	2.44	-2.28

Table V.7h. Summary statistics for the derivation and accuracy assessment of the split-window algorithm as defined by Yu and Barton (1994) as per CoastWatch sector. (SWT = split-window technique according to the YB94 algorithm; NLSST = Nonlinear SST).

Date	Code		TB4	TB5	TB4-5	DELTAT4/DELTAT5	GAMMA	MEAN SWT	MAX SWT	MIN SWT	STDEV	MEAN NLSST	MAX NLSST	MIN NLSST	NLSST STDEV	NLSST-SWT
99_11_07	100	K	296.56	295.60	0.96	0.91	5.10	27.68	29.15	24.46	0.55	25.70	26.48	23.19	0.40	-1.98
Cont'd		L	296.05	295.02	1.03	1.07	3.88	25.13	26.70	22.87	0.72	25.36	26.36	23.56	0.56	0.22
		M	295.02	293.89	1.14	0.90	3.15	23.49	24.65	22.27	0.38	24.62	25.63	23.56	0.36	1.12
		O	295.96	295.34	0.62	1.01	6.05	26.39	29.08	21.37	1.31	24.54	26.24	20.63	1.14	-1.86
		P	296.76	296.02	0.74	1.05	4.35	25.76	27.37	23.41	0.78	25.57	26.48	23.80	0.62	-0.21
		Q	296.08	295.22	0.86	0.97	6.91	28.79	30.83	25.86	0.89	25.22	26.36	22.82	0.83	-3.57
	108	A	292.57	291.32	1.25	1.12	3.90	22.39	27.63	15.44	2.04	21.72	26.73	15.99	1.91	-0.69
		B	295.17	293.59	1.59	1.14	2.82	23.11	24.81	19.74	0.96	25.15	27.09	21.48	1.05	2.04
		D	290.40	289.34	1.06	1.12	3.53	19.03	23.34	16.66	1.22	19.16	23.19	17.21	1.14	0.13
		E	292.08	290.83	1.25	1.13	3.84	21.76	27.66	15.32	2.65	21.26	26.97	15.99	2.50	-0.50
		F	295.00	293.35	1.65	1.16	3.85	25.83	28.16	19.07	2.06	25.12	27.09	19.04	1.96	-0.73
		I	291.25	290.19	1.06	1.11	4.16	21.00	27.43	13.39	2.33	20.07	25.75	14.89	2.12	-0.95
		J	293.93	292.52	1.41	1.13	4.13	24.71	28.56	16.93	2.87	23.51	27.09	16.60	2.65	-1.22
		K	295.82	294.15	1.67	1.00	3.36	25.70	26.77	24.15	0.50	26.04	27.22	24.41	0.49	0.32
		L	295.33	293.61	1.72	1.10	3.03	24.30	25.55	22.36	0.59	25.58	26.85	23.56	0.62	1.26
		O	295.54	294.18	1.36	1.00	5.89	29.67	32.33	23.13	1.38	25.07	27.09	19.77	1.23	-4.61
		P	296.38	294.91	1.47	0.94	8.18	34.99	37.93	31.59	1.01	26.19	27.46	24.04	0.75	-8.83
		Q	295.84	294.43	1.41	1.06	3.45	25.40	27.12	22.66	0.81	25.46	27.09	22.94	0.82	0.04
		R	295.28	293.81	1.47	0.86	8.72	34.77	38.45	31.13	0.95	24.98	26.24	23.43	0.37	-9.81

Table V.7i. Summary statistics for the derivation and accuracy assessment of the split-window algorithm as defined by Yu and Barton (1994) as per CoastWatch sector. (SWT = split-window technique according to the YB94 algorithm; NLSST = Nonlinear SST).

Appendix VI

STATISTICAL RESULTS OF CHAPTER 5.

This Appendix includes the statistical summary measures of the Eta model verification against collocated observations.

	Eta forecasts		TMI observations		RMSE	BIAS
	mean	stdev	mean	stdev		
Jan	15.48	1.53	13.40	1.96	2.70	2.08
Feb	14.69	1.10	14.54	1.38	1.58	0.15
Mar	12.06	0.92	11.47	1.12	2.08	0.59
Apr	13.94	1.07	14.49	1.46	2.89	-0.56
May	19.66	1.07	21.34	1.09	2.05	-1.68
Jun	22.3	1.61	24.20	1.51	3.24	-1.72
July	24.82	1.89	26.48	2.66	4.28	-1.66
Aug	28.45	1.22	30.97	2.38	4.04	-2.52
Sept	30.31	1.98	32.31	2.12	1.45	-2.00
Oct	25.90	1.56	26.63	2.87	3.69	-0.73
Nov	23.48	1.75	21.94	2.03	3.00	1.54
Dec	15.95	1.20	15.00	1.59	2.73	0.95

Table VI.1 Summary statistics of the averaged, monthly predicted and observed integrated precipitable water vapour (mm) over the area of interest.

	Eta forecasts		TMI observations		RMSE	BIAS
	mean	stdev	mean	stdev		
Jan	0.17	0.15	0.03	0.01	0.19	0.15
Feb	0.05	0.04	0.04	0.01	0.08	0.01
Mar	0.04	0.06	0.03	0.02	0.06	0.01
Apr	0.03	0.08	0.02	0.00	0.05	0.01
May	0.04	0.06	0.02	0.01	0.06	0.02
Jun	0.02	0.02	0.01	0.01	0.03	0.01
July	0.01	0.02	0.01	0.01	0.03	-0.01
Aug	0.00	0.00	0.01	0.01	0.02	-0.01
Sept	0.05	0.03	0.02	0.01	0.07	0.02
Oct	0.06	0.08	0.03	0.01	0.08	0.03
Nov	0.11	0.10	0.04	0.02	0.15	0.07
Dec	0.13	0.18	0.03	0.01	0.19	0.10

Table VI.2 Summary statistics of the averaged, monthly predicted and observed integrated cloud liquid water vapour (mm) over the area of interest.

	Eta forecasts		TMI observations		RMSE	BIAS
	mean	stdev	mean	stdev		
Jan	7.23	2.21	5.86	3.18	1.75	1.37
Feb	7.68	2.24	6.92	3.16	1.52	0.76
Mar	6.11	1.80	4.58	1.85	1.82	1.53
Apr	5.50	1.22	5.47	1.79	0.24	0.03
May	3.64	2.97	3.40	1.88	0.34	0.07
Jun	5.43	2.70	3.92	1.64	0.89	1.51
July	5.05	1.17	4.45	1.54	1.29	0.60
Aug	4.40	0.66	2.68	1.02	1.28	1.72
Sept	5.44	1.99	5.00	2.44	1.47	0.44
Oct	5.11	0.96	4.44	1.15	1.62	0.67
Nov	7.22	2.15	8.19	2.54	1.98	-0.97
Dec	8.16	2.33	9.19	2.47	2.06	-1.04

Table VI.3. Summary statistics of the averaged, monthly predicted and observed wind magnitude (m s^{-1}) over the area of interest.

	NOAA Olwr total night	NOAA Olwr total day	Average NOAA	Average ETA	bias
Jan	228.56	235.20	231.88	400.63	168.76
Feb	231.86	240.35	236.10	394.39	158.28
Mar	235.73	241.34	238.53	395.34	156.81
Apr	237.39	245.43	241.41	397.65	156.24
May	251.16	257.68	254.42	414.81	160.40
Jun	265.20	272.20	268.70	433.09	164.38
Jul	279.25	286.73	282.99	451.36	168.37
Aug	281.74	288.40	285.07	462.99	177.92
Sep	269.26	269.60	269.43	465.48	196.05
Oct	260.86	264.40	262.63	450.72	188.09
Nov	224.34	229.64	226.99	438.86	211.87
Dec	227.83	231.09	229.46	415.02	185.56

Table VI.4. Summary statistics of the averaged, monthly predicted and observe outgoing longwave radiation (W m^{-2}) over the area of interest.

	Eta forecasts		observations		BIAS
	mean	stdev	mean	stdev	
Jan	15.45	0.77	14.27	1.52	1.18
Feb	13.45	0.68	14.15	0.97	-0.69
Mar	14.31	0.82	14.81	1.08	-0.50
Apr	15.99	0.71	16.73	0.90	-0.74
May	26.17	1.41	21.42	0.50	4.74
Jun	25.52	0.62	24.23	0.74	1.29
July	24.80	0.48	26.05	1.24	-1.25
Aug	29.00	0.88	27.05	2.76	1.95
Sept	26.03	0.69	27.39	0.48	-1.36
Oct	23.61	0.66	24.32	1.40	-0.71
Nov	20.45	0.79	21.65	1.00	-1.20
Dec	16.55	0.72	17.96	1.16	-1.41

Table VI.5. Summary statistics of the averaged, monthly predicted and observed surface air temperature (°C) over the area of interest.

	Eta forecasts		TMI observations		RMSE	BIAS
	mean	stdev	mean	stdev		
Jan	-17.18	4.18	-13.55	1.57	15.09	-3.62
Feb	-28.95	7.88	-17.39	2.27	16.93	-11.56
Mar	-16.27	5.00	-9.29	1.54	14.36	-6.98
Apr	-3.63	3.60	2.08	0.30	9.52	-5.71
May	-1.77	2.67	3.10	0.58	5.83	-4.87
Jun	-5.45	2.80	2.80	0.60	7.42	-6.20
July	-7.94	3.89	3.29	0.50	12.14	-11.22
Aug	-0.11	1.40	0.71	0.07	4.34	-0.81
Sept	-13.97	6.14	-3.77	0.55	13.45	-10.2
Oct	-13.96	4.37	-6.76	1.17	14.09	-7.20
Nov	-34.06	10.19	-13.22	2.5	30.87	-20.84
Dec	-40.09	9.59	-19.11	2.41	29.36	-20.98

Table VI.6. Summary statistics of the averaged, monthly predicted and observed sensible heat flux (W m^{-2}) over the area of interest.

	Eta forecasts		TMI observations		RMSE	BIAS
	mean	stdev	mean	stdev		
Jan	-89.44	18.20	-72.51	8.64	37.43	-16.93
Feb	-101.24	14.40	-86.22	11.36	31.8	-15.02
Mar	-74.35	14.32	-60.76	10.13	34.44	-13.59
Apr	-46.12	10.35	-69.41	10.03	28.70	23.28
May	-19.14	5.26	-59.28	11.15	41.77	40.15
Jun	-68.42	8.56	-61.82	10.14	42.12	-6.60
July	-89.27	23.20	-65.13	9.83	41.76	-24.14
Aug	-51.37	9.11	-48.82	4.78	37.95	-2.55
Sept	-123.28	36.47	-75.94	11.17	62.18	-47.34
Oct	-98.31	24.58	-63.33	10.99	53.35	-34.98
Nov	-168.29	36.63	-97.43	18.91	85.81	-70.87
Dec	-144.33	27.71	-107.93	14.41	62.37	-36.40

Table VI.7. Summary statistics of the averaged, monthly predicted and observed latent heat flux (W m^{-2}) over the area of interest.

Tables VI.8a – b represent the summary measures of the fine-tuning experiment of the viscous sublayer depth of the Mellor Yamada turbulence closure scheme of the Eta model.

Month	Forecast hr: observation	predicted wind speed ($m\ s^{-1}$)	Normalised RMSE Coefficient value			
			0.20	0.35	0.70	0.80
Jul	**0215_0212**	3.26	1.06	1.03	1.00	1.34
Jul	**0412_0400**	3.27	1.42	1.25	1.06	1.00
Oct	**2627_2712**	3.42	1.00	1.00	1.12	1.20
Oct	**1333_1412**	3.51	1.20	1.14	1.03	1.00
Oct	**1330_1400**	3.52	1.11	1.06	1.01	1.00
Sep	**0527_0600**	3.68	1.17	1.12	1.01	1.00
Jan	**1430_1512**	3.71	1.04	1.04	1.00	1.00
Sep	**0827_0912**	3.72	1.80	1.46	1.00	1.03
Nov	**1118_1112**	3.77	1.00	1.00	1.05	1.06
Sep	**0627_0700**	3.80	1.02	1.00	1.02	1.05
Jul	**0812_0812**	3.87	1.24	1.18	1.03	1.00
Mar	**0230_0312**	3.90	1.00	1.08	1.34	1.48
May	**0718_0700**	3.93	1.05	1.04	1.02	1.00
Jan	**1130_1200**	3.98	1.07	1.06	1.00	1.00
May	**2833_2912**	4.07	1.00	1.27	1.98	2.15
Aug	**0221_0200**	4.09	1.44	1.32	1.04	1.00
Aug	**0721_0700**	4.12	1.00	1.11	1.32	1.37
Jul	**2027_2100**	4.17	1.21	1.09	1.00	1.00
Aug	**0718_0712**	4.27	1.00	1.00	1.08	1.18
Jul	**1930_2012**	4.29	1.00	1.12	1.26	1.20
Sep	**2318_2300**	4.40	1.19	1.13	1.01	1.00
Apr	**1927_2000**	4.42	1.15	1.08	1.05	1.00
Mar	**2121_2112**	4.54	1.08	1.05	1.02	1.00
Nov	**2412_2412**	4.56	1.01	1.00	1.00	1.00
Mar	**0924_0900**	4.61	1.00	1.03	1.20	1.24
Jul	**0115_0112**	4.68	1.02	1.01	1.00	1.00
Oct	**1930_2012**	4.74	1.01	1.00	1.00	1.01
Sep	**0427_0500**	4.75	1.36	1.24	1.00	1.00
Aug	**1218_1212**	4.82	1.00	1.08	1.26	1.30
Oct	**2027_2100**	4.87	1.04	1.01	1.00	1.00
Aug	**0121_0100**	4.89	1.00	1.07	1.46	1.53
Apr	**0612_0612**	4.96	1.00	1.07	1.24	1.27

Table VI.8a. Normalised RMSE of predicted surface wind magnitude when the viscous sublayer depth varies from 0.20 to 0.80. The data is arranged according to the increasing predicted wind speed from 3.0 to 5.0 m s^{-1}.

Month	Forecast hr: observation	wind speed ($m\ s^{-1}$)	0.20	0.35	0.70	0.80
Jul	**2127_2200**	5.00	1.00	1.02	1.37	1.51
Sep	**2218_2200**	5.02	1.00	1.07	1.24	1.29
Apr	**1233_1312**	5.02	1.00	1.05	1.15	1.18
Mar	**0927_1012**	5.05	1.00	1.07	1.19	1.22
Apr	**1230_1300**	5.10	1.00	1.03	1.09	1.11
Mar	**2118_2100**	5.18	1.03	1.01	1.01	1.00
Aug	**1118_1112**	5.23	1.00	1.00	1.00	1.00
Nov	**1715_1712**	5.24	1.00	1.01	1.10	1.13
Nov	**2433_2500**	5.32	1.01	1.00	1.02	1.13
Mar	**1324_1312**	5.33	1.00	1.10	1.49	1.60
Mar	**2815_2800**	5.33	1.00	1.10	1.31	1.32
Nov	**1218_1212**	5.35	1.21	1.17	1.02	1.00
Sep	**2121_2112**	5.39	1.00	1.04	1.16	1.20
Apr	**2227_2312**	5.41	1.00	1.05	1.12	1.12
Jul	**1233_1312**	5.44	1.00	1.10	1.36	1.40
Apr	**0115_0112**	5.54	1.00	1.04	1.10	1.12
Oct	**1530_1600**	5.55	1.01	1.00	1.10	1.10
Apr	**0112_0100**	5.65	1.00	1.01	1.02	1.02
Jul	**1530_1600**	5.70	1.00	1.09	1.29	1.34
Jul	**2627_2712**	5.70	1.12	1.07	1.01	1.00
Oct	**1433_1512**	5.74	1.07	1.07	1.00	1.00
Jul	**2527_2612**	5.87	1.16	1.10	1.01	1.00
Aug	**0918_0912**	5.93	1.00	1.00	1.00	1.00
Oct	**1630_1700**	5.95	1.01	1.00	1.00	1.01
Jul	**0833_0900**	6.12	1.00	1.41	1.28	1.31
Mar	**2218_2200**	6.33	1.00	1.05	1.13	1.15
Sep	**1721_1700**	6.37	1.02	1.00	1.00	1.01
Oct	**2527_2612**	6.53	1.00	1.03	1.28	1.40
Nov	**1912_1900**	6.59	1.00	1.00	1.01	1.01
Jan	**1627_1700**	7.11	1.02	1.00	1.01	1.03
Nov	**1815_1812**	7.24	1.00	1.01	1.06	1.07
Apr	**1133_1212**	7.36	1.01	1.00	1.01	1.02
Nov	**0621_0612**	7.49	1.03	1.03	1.01	1.00
Jul	**1430_1500**	7.64	1.00	1.01	1.12	1.23
Jan	**0930_1000**	7.75	1.00	1.00	1.19	1.25
Jan	**0933_1012**	7.90	1.04	1.03	1.00	1.03
Jan	**1030_1100**	7.93	2.08	2.08	2.08	1.00
Nov	**0721_0712**	8.08	1.01	1.00	1.00	1.00
Nov	**1315_1300**	8.13	1.00	1.00	1.02	1.01
Mar	**2618_2612**	8.27	1.00	1.00	1.01	1.01
Mar	**0130_0212**	8.36	1.00	1.00	1.00	1.00
May	**0121_0100**	8.46	1.00	1.00	1.00	1.00
Apr	**0833_0900**	8.47	1.04	1.03	1.00	1.00
Nov	**0918_0900**	8.66	1.03	1.04	1.00	1.01
Nov	**0818_0800**	9.11	1.03	1.01	1.00	1.01
Sep	**2021_2012**	9.17	1.00	1.01	1.03	1.03
May	**1812_1800**	9.37	1.00	1.00	1.01	1.01
Jan	**2821_2800**	11.47	1.00	1.02	1.11	1.13

Table VI.8b. Normalised RMSE of predicted surface wind magnitude when the viscous sublayer depth varies from 0.20 to 0.80. The data is arranged according to the increasing predicted wind speed from 5.0 to 12 m s^{-1}.

Appendix VII

STATISTICAL RESULTS OF CHAPTER 7.

This Appendix includes the results of the accuracy of assessment of the data assimilation schemes used to improve the forecasting skill of the POM model.

Date		GDAS-SST + Reference air-sea fluxes FORECASTED SST (°C)				TMI-SST + Experimental air-sea fluxes FORECASTED SST (°C)				TMI maps (°C)
		mean	stdev	Bias	RMSE	mean	stdev	Bias	RMSE	mean
July	22	25.57	0.92	-0.67	1.10	25.58	0.92	-0.66	1.09	26.24
	23	25.75	0.92	-0.20	1.10	25.76	0.93	-0.18	1.10	25.95
	24	25.61	0.95	-0.68	1.21	25.68	0.94	-0.62	1.18	26.29
	25	25.46	1.12	-0.71	1.34	25.54	1.11	-0.63	1.29	26.17
	26	25.40	1.33	-0.77	1.56	25.47	1.31	-0.70	1.52	26.17
	27	25.40	1.50	-0.41	1.54	25.47	1.48	-0.35	1.53	25.81
	28	25.39	1.67	-0.43	1.70	25.45	1.68	-0.37	1.72	25.83
	29	25.13	2.02	-1.06	2.25	25.18	2.05	-1.00	2.26	26.19
	30	24.79	2.27	-1.41	2.64	24.91	2.26	-1.29	2.59	26.20
	31	24.65	2.37	-1.88	3.04	24.80	2.36	-1.73	2.97	26.53
August	1	24.69	2.42	-2.45	3.45	24.81	2.43	-2.32	3.38	27.13
	2	24.78	2.46	-2.21	3.30	24.89	2.46	-2.10	3.24	26.99
	3	24.84	2.46	-2.20	3.30	24.93	2.43	-2.10	3.22	27.03
	4	24.83	2.45	-1.83	3.06	24.93	2.44	-1.73	2.99	26.66
	5	24.90	2.49	-1.89	3.14	24.98	2.48	-1.81	3.09	26.79

Table VII.1. Basic statistical and model performance measures when no data assimilation scheme is active throughout the entire model integration period. The mean value shown represents the average value for the entire predicted/observed SST field.

Nudging period τ	Date	GDAS-TMI + ref. air-sea fluxes FORECASTED SST (°C)				TMI-SST + exp. air-sea fluxes FORECASTED SST (°C)				TMI SST (°C)
		mean	stdev	bias	RMSE	mean	stdev	bias	RMSE	mean
	22	26.79	0.55	0.55	0.83	26.75	0.65	0.51	0.90	26.24
	23	26.31	0.47	0.36	0.78	26.09	0.68	0.14	0.88	25.95
	24	26.59	0.35	0.29	0.56	26.00	0.78	-0.30	1.04	26.29
	25	26.34	0.39	0.17	0.59	26.45	0.79	0.28	0.66	26.17
	26	26.60	0.35	0.42	0.72	26.13	0.56	-0.05	0.66	26.17
06	27	26.59	0.35	0.78	1.02	26.30	0.77	0.48	0.76	25.81
	28	26.67	0.35	0.84	1.07	25.79	0.64	-0.03	0.57	25.83
	29	26.38	0.37	0.19	0.52	25.97	0.71	-0.22	0.69	26.19
	30	26.51	0.36	0.31	0.60	26.30	0.60	0.10	0.65	26.20
	31	26.38	0.38	-0.15	0.60	26.31	0.63	-0.22	0.59	26.53
	1	26.37	0.37	-0.76	0.90	26.73	0.63	-0.41	0.74	27.13
	2	26.50	0.37	-0.49	0.80	27.39	0.62	0.40	0.90	26.99
	3	26.69	0.37	0.03	0.42	27.21	0.65	0.56	0.84	26.29
	4	26.70	0.36	0.04	0.43	27.22	0.64	0.56	0.84	26.66
	5	26.72	0.35	-0.05	0.35	26.52	0.56	-0.27	0.67	26.79
	22	26.80	0.56	0.55	0.84	26.75	0.65	0.51	0.91	26.24
	23	26.32	0.47	0.38	0.79	26.10	0.67	0.15	0.89	25.95
	24	26.57	0.36	0.28	0.57	25.99	0.80	-0.31	1.06	26.29
	25	26.33	0.40	0.16	0.58	26.47	0.81	0.30	0.68	26.17
	26	26.65	0.37	0.47	0.79	26.15	0.56	-0.02	0.69	26.17
12	27	26.57	0.35	0.76	1.00	26.30	0.79	0.48	0.78	25.81
	28	26.71	0.37	0.89	1.12	25.82	0.65	-0.01	0.58	25.83
	29	26.34	0.39	0.16	0.52	25.94	0.74	-0.24	0.71	26.19
	30	26.57	0.37	0.37	0.67	26.35	0.60	0.15	0.68	26.20
	31	26.33	0.41	-0.20	0.62	26.28	0.65	-0.25	0.62	26.53
	1	26.44	0.38	-0.70	0.86	26.77	0.66	-0.36	0.75	27.13
	2	26.45	0.39	-0.54	0.82	27.36	0.63	0.37	0.89	26.99
	3	26.41	0.38	-0.63	0.75	26.87	0.81	-0.16	0.87	27.03
	4	26.69	0.38	0.03	0.45	27.22	0.65	0.56	0.85	26.66
	5	26.73	0.36	-0.06	0.35	26.51	0.56	-0.28	0.68	26.79
	22	26.80	0.53	0.56	0.82	26.76	0.63	0.51	0.89	26.24
	23	26.30	0.48	0.35	0.78	26.08	0.68	0.13	0.89	25.95
	24	26.58	0.37	0.29	0.58	25.98	0.80	-0.31	1.07	26.29
	25	26.36	0.42	0.19	0.62	26.48	0.81	0.31	0.70	26.17
	26	26.60	0.39	0.43	0.76	26.11	0.58	-0.06	0.69	26.17
24	27	26.57	0.39	0.76	1.01	26.29	0.81	0.48	0.79	25.81
	28	26.71	0.41	0.89	1.13	25.79	0.64	-0.03	0.59	25.83
	29	26.35	0.42	0.17	0.54	25.96	0.75	-0.23	0.71	26.19
	30	26.55	0.42	0.35	0.66	26.32	0.63	0.12	0.68	26.20
	31	26.34	0.44	-0.19	0.65	26.29	0.66	-0.24	0.64	26.53
	1	26.40	0.43	-0.73	0.90	26.75	0.67	-0.39	0.75	27.13
	2	26.46	0.43	-0.53	0.83	27.37	0.70	0.38	0.93	26.99
	3	26.40	0.43	-0.63	0.78	26.87	0.85	-0.16	0.90	27.03
	4	26.67	0.46	0.01	0.52	27.20	0.68	0.54	0.86	26.66
	5	26.73	0.46	-0.05	0.44	26.51	0.59	-0.28	0.71	26.79

Table VII.2. Basic statistical and model performance measures when Newtonian relaxation was used with a variable nudging period.

Nudging period τ	Date	GDAS-TMI + ref. air-sea fluxes FORECASTED SST (°C)				TMI-SST + exp. air-sea fluxes FORECASTED SST (°C)				TMI SST (°C)
		mean	stdev	bias	RMSE	mean	stdev	bias	RMSE	mean
	22	26.79	0.55	0.55	0.84	26.75	0.65	0.50	0.90	26.24
	23	26.13	0.65	0.18	0.80	25.98	0.89	0.03	1.03	25.95
	24	26.48	0.78	0.19	0.87	25.85	1.04	-0.44	1.29	26.29
	25	26.04	0.98	-0.13	1.10	26.32	1.17	0.15	1.07	26.17
	26	26.54	1.13	0.37	1.23	25.86	1.21	-0.31	1.36	26.17
06	27	26.40	1.14	0.59	1.41	26.29	1.40	0.47	1.36	25.81
	28	26.64	1.17	0.81	1.51	25.62	1.28	-0.21	1.34	25.83
	29	26.15	1.21	-0.04	1.28	25.92	1.31	-0.26	1.26	26.19
	30	26.51	1.15	0.31	1.23	26.18	1.21	-0.02	1.24	26.20
	31	26.16	1.20	-0.37	1.33	26.13	1.34	-0.40	1.35	26.53
	1	26.32	1.19	-0.81	1.47	26.60	1.32	-0.53	1.42	27.13
	2	26.27	1.21	-0.72	1.49	27.23	1.28	0.24	1.40	26.99
	3	25.61	0.95	-0.68	1.21	25.68	0.94	-0.62	1.18	26.29
	4	26.54	1.19	-0.12	1.22	27.14	1.32	0.48	1.40	26.66
	5	26.56	1.24	-0.23	1.26	26.27	1.34	-0.52	1.47	26.79
	22	26.79	0.58	0.54	0.85	26.74	0.67	0.50	0.91	26.24
	23	26.08	0.69	0.13	0.81	25.93	0.91	-0.02	1.04	25.95
	24	26.46	0.87	0.16	0.96	25.82	1.06	-0.47	1.33	26.29
	25	26.10	1.01	-0.07	1.10	26.39	1.26	0.22	1.14	26.17
	26	26.65	1.05	0.48	1.21	25.99	1.15	-0.19	1.28	26.17
12	27	26.38	1.06	0.57	1.33	26.26	1.32	0.45	1.27	25.81
	28	26.69	1.11	0.86	1.51	25.66	1.21	-0.16	1.27	25.83
	29	26.19	1.17	0.00	1.25	25.92	1.30	-0.27	1.27	26.19
	30	26.50	1.15	0.30	1.23	26.20	1.20	0.01	1.25	26.20
	31	26.16	1.20	-0.37	1.32	26.15	1.33	-0.38	1.32	26.53
	1	26.33	1.20	-0.81	1.48	26.59	1.31	-0.54	1.42	27.13
	2	26.31	1.22	-0.68	1.47	27.23	1.33	0.24	1.42	26.99
	3	26.28	1.26	-0.75	1.48	26.66	1.50	-0.38	1.56	27.03
	4	26.53	1.25	-0.13	1.28	27.14	1.34	0.48	1.42	26.66
	5	26.63	1.25	-0.15	1.26	26.28	1.35	-0.50	1.48	26.79
	22	26.76	0.57	0.51	0.82	26.71	0.67	0.47	0.90	26.24
	23	26.03	0.75	0.08	0.87	25.87	0.96	-0.08	1.10	25.95
	24	26.56	0.91	0.27	0.98	25.92	1.02	-0.37	1.24	26.29
	25	26.24	0.93	0.07	1.01	26.49	1.16	0.32	1.07	26.17
	26	26.56	0.99	0.38	1.13	25.94	1.06	-0.23	1.20	26.17
24	27	26.50	1.03	0.69	1.35	26.30	1.25	0.48	1.21	25.81
	28	26.63	1.10	0.80	1.47	25.66	1.17	-0.17	1.19	25.83
	29	26.21	1.16	0.03	1.22	25.91	1.25	-0.27	1.24	26.19
	30	26.47	1.14	0.27	1.21	26.18	1.19	-0.02	1.21	26.20
	31	26.23	1.15	-0.30	1.26	26.16	1.28	-0.37	1.28	26.53
	1	26.31	1.15	-0.82	1.45	26.63	1.25	-0.50	1.35	27.13
	2	26.36	1.17	-0.63	1.39	27.24	1.28	0.25	1.37	26.99
	3	26.24	1.18	-0.79	1.43	26.73	1.48	-0.30	1.54	27.03
	4	26.59	1.18	-0.07	1.21	27.13	1.35	0.47	1.43	26.66
	5	26.61	1.23	-0.18	1.24	26.37	1.37	-0.42	1.45	26.79

Table VII.3. Basic statistical and model performance measures when data assimilation scheme 2 is active throughout the entire model integration period. Coefficient value: $5x10^{-3}$ with variable pre-forecast nudging period.

Nudging period τ	Date	GDAS-TMI + ref. air-sea fluxes FORECASTED SST (°C)				TMI-SST + exp. air-sea fluxes FORECASTED SST (°C)				TMI SST (°C)
		mean	stdev	bias	RMSE	mean	stdev	bias	RMSE	mean
	22	26.79	0.54	0.54	0.82	26.74	0.64	0.50	0.89	26.24
	23	26.15	0.63	0.20	0.79	26.00	0.86	0.06	1.01	25.95
	24	26.52	0.73	0.22	0.83	25.88	1.02	-0.42	1.27	26.29
	25	26.07	0.92	-0.10	1.04	26.35	1.13	0.19	1.03	26.17
	26	26.47	1.16	0.29	1.24	25.77	1.21	-0.40	1.38	26.17
	27	26.37	1.24	0.55	1.48	26.25	1.49	0.43	1.43	25.81
	28	26.65	1.23	0.82	1.57	25.65	1.34	-0.17	1.40	25.83
06	29	26.15	1.26	-0.04	1.32	25.93	1.36	-0.25	1.32	26.19
	30	26.50	1.19	0.30	1.26	26.15	1.24	-0.05	1.27	26.20
	31	26.23	1.21	-0.30	1.32	26.18	1.34	-0.35	1.33	26.53
	1	26.30	1.17	-0.83	1.46	26.60	1.28	-0.54	1.40	27.13
	2	26.31	1.18	-0.68	1.45	27.27	1.28	0.28	1.39	26.99
	3	26.31	1.18	-0.72	1.41	26.61	1.47	-0.42	1.56	27.03
	4	26.56	1.17	-0.10	1.21	27.19	1.28	0.53	1.37	26.66
	5	26.57	1.21	-0.22	1.23	26.27	1.34	-0.52	1.47	26.79
	22	26.79	0.57	0.55	0.85	26.74	0.67	0.50	0.91	26.24
	23	26.11	0.67	0.16	0.80	25.97	0.89	0.02	1.03	25.95
	24	26.46	0.84	0.17	0.93	25.83	1.06	-0.47	1.33	26.29
	25	26.04	1.04	-0.13	1.14	26.33	1.26	0.16	1.15	26.17
	26	26.63	1.13	0.46	1.28	25.95	1.21	-0.23	1.34	26.17
	27	26.40	1.16	0.59	1.42	26.27	1.39	0.45	1.34	25.81
	28	26.64	1.19	0.82	1.55	25.65	1.26	-0.18	1.31	25.83
12	29	26.18	1.23	0.00	1.30	25.93	1.33	-0.26	1.30	26.19
	30	26.50	1.20	0.30	1.28	26.20	1.27	0.00	1.31	26.20
	31	26.19	1.23	-0.34	1.33	26.14	1.37	-0.40	1.36	26.53
	1	26.30	1.22	-0.83	1.51	26.61	1.33	-0.52	1.45	27.13
	2	26.30	1.22	-0.69	1.45	27.23	1.35	0.24	1.45	26.99
	3	26.29	1.24	-0.74	1.46	26.65	1.54	-0.38	1.60	27.03
	4	26.54	1.25	-0.12	1.28	27.14	1.37	0.48	1.44	26.66
	5	26.58	1.27	-0.21	1.29	26.31	1.38	-0.48	1.50	26.79
	22	26.77	0.56	0.53	0.83	26.73	0.66	0.48	0.90	26.24
	23	26.04	0.74	0.09	0.85	25.88	0.95	-0.07	1.08	25.95
	24	26.52	0.94	0.23	1.01	25.87	1.04	-0.42	1.27	26.29
	25	26.23	0.99	0.06	1.07	26.48	1.22	0.31	1.12	26.17
	26	26.57	1.03	0.40	1.18	25.94	1.12	-0.23	1.25	26.17
	27	26.46	1.05	0.65	1.36	26.29	1.28	0.48	1.23	25.81
	28	26.65	1.11	0.82	1.49	25.63	1.19	-0.19	1.22	25.83
24	29	26.22	1.18	0.03	1.23	25.93	1.27	-0.26	1.25	26.19
	30	26.47	1.15	0.27	1.22	26.16	1.22	-0.04	1.24	26.20
	31	26.20	1.17	-0.34	1.29	26.19	1.30	-0.34	1.29	26.53
	1	26.34	1.18	-0.80	1.45	26.60	1.29	-0.53	1.40	27.13
	2	26.31	1.19	-0.68	1.44	27.28	1.30	0.29	1.41	26.99
	3	26.31	1.22	-0.73	1.43	26.73	1.47	-0.30	1.52	27.03
	4	26.58	1.23	-0.09	1.26	27.12	1.33	0.45	1.40	26.66
	5	26.59	1.27	-0.20	1.29	26.34	1.36	-0.45	1.46	26.79

Table VII.4 Basic statistical and model performance measures when data assimilation scheme 2 is active throughout the entire model integration period. Coefficient value: $5x10^{-4}$ with variable pre-forecast nudging period.

Nudging period τ	Date	GDAS-TMI + ref. air-sea fluxes FORECASTED SST (°C)				TMI-SST + exp. air-sea fluxes FORECASTED SST (°C)				TMI SST (°C)
		mean	stdev	bias	RMSE	mean	stdev	bias	RMSE	mean
	22	25.80	0.78	-0.45	0.88	25.79	0.78	-0.45	0.88	26.24
	23	26.10	0.73	0.16	0.95	26.07	0.73	0.12	0.94	25.95
	24	26.11	0.74	-0.19	0.81	25.98	0.77	-0.31	0.89	26.29
	25	25.98	0.92	-0.19	0.97	25.94	0.94	-0.23	0.98	26.17
	26	25.95	1.02	-0.23	1.15	25.88	1.06	-0.29	1.18	26.17
	27	26.00	1.11	0.18	1.16	25.87	1.18	0.06	1.17	25.81
	28	26.04	1.25	0.22	1.29	25.79	1.32	-0.03	1.30	25.83
06	29	25.85	1.48	-0.33	1.53	25.57	1.55	-0.62	1.66	26.19
	30	25.55	1.74	-0.65	1.87	25.30	1.81	-0.90	2.02	26.20
	31	25.37	1.95	-1.16	2.33	25.22	1.91	-1.31	2.36	26.53
	1	25.37	2.01	-1.77	2.69	25.35	1.95	-1.78	2.65	27.13
	2	25.45	2.04	-1.54	2.59	25.64	1.98	-1.35	2.41	26.99
	3	25.51	2.06	-1.52	2.57	25.78	2.03	-1.25	2.40	27.03
	4	25.59	2.09	-1.07	2.37	25.85	2.11	-0.81	2.30	26.66
	5	25.71	2.14	-1.08	2.40	25.83	2.14	-0.96	2.37	26.79
	22	25.73	0.82	-0.52	0.94	25.73	0.81	-0.52	0.94	26.24
	23	26.01	0.77	0.06	0.96	25.99	0.78	0.04	0.96	25.95
	24	25.99	0.78	-0.31	0.88	25.92	0.79	-0.38	0.93	26.29
	25	25.87	0.97	-0.30	1.03	25.86	0.98	-0.31	1.04	26.17
	26	25.84	1.09	-0.34	1.23	25.81	1.11	-0.37	1.25	26.17
	27	25.89	1.17	0.08	1.19	25.81	1.22	0.00	1.22	25.81
	28	25.94	1.28	0.12	1.29	25.78	1.34	-0.05	1.32	25.83
12	29	25.80	1.48	-0.38	1.55	25.60	1.55	-0.58	1.66	26.19
	30	25.51	1.72	-0.69	1.85	25.30	1.77	-0.90	1.98	26.20
	31	25.31	1.87	-1.22	2.28	25.18	1.87	-1.35	2.34	26.53
	1	25.22	1.96	-1.91	2.75	25.20	1.94	-1.93	2.75	27.13
	2	25.24	2.02	-1.75	2.69	25.37	1.98	-1.62	2.56	26.99
	3	25.28	2.06	-1.75	2.71	25.46	2.04	-1.57	2.58	27.03
	4	25.34	2.08	-1.32	2.48	25.53	2.09	-1.13	2.40	26.66
	5	25.48	2.08	-1.31	2.46	25.56	2.11	-1.23	2.45	26.79
	22	25.87	0.75	-0.38	0.82	25.86	0.74	-0.39	0.82	26.24
	23	26.20	0.69	0.25	0.93	26.15	0.69	0.20	0.92	25.95
	24	26.22	0.70	-0.07	0.75	26.05	0.75	-0.24	0.85	26.29
	25	26.08	0.87	-0.09	0.91	26.03	0.90	-0.14	0.91	26.17
	26	26.05	0.96	-0.12	1.08	25.96	1.02	-0.22	1.11	26.17
	27	26.10	1.05	0.28	1.13	25.93	1.14	0.12	1.12	25.81
	28	26.14	1.22	0.32	1.30	25.81	1.29	-0.02	1.28	25.83
24	29	25.90	1.47	-0.29	1.52	25.54	1.55	-0.65	1.66	26.19
	30	25.59	1.76	-0.61	1.88	25.30	1.84	-0.90	2.05	26.20
	31	25.42	2.03	-1.11	2.38	25.26	1.96	-1.27	2.37	26.53
	1	25.51	2.06	-1.63	2.63	25.49	1.95	-1.64	2.55	27.13
	2	25.65	2.05	-1.34	2.49	25.91	1.98	-1.08	2.27	26.99
	3	25.74	2.06	-1.29	2.44	26.10	2.01	-0.94	2.22	27.03
	4	25.85	2.10	-0.82	2.26	26.18	2.13	-0.49	2.20	26.66
	5	25.94	2.19	-0.85	2.35	26.11	2.18	-0.68	2.29	26.79

Table VII.6. Basic statistical and model performance measures when data assimilation scheme 2 is active throughout the entire model integration period. Coefficient value: $5x10^{-6}$ with variable pre-forecast nudging period.

Nudging period τ	Date	GDAS-TMI + ref. air-sea fluxes FORECASTED SST (°C)				TMI-SST + exp. air-sea fluxes FORECASTED SST (°C)				TMI SST (°C)
		mean	stdev	bias	RMSE	mean	stdev	bias	RMSE	mean
	22	26.09	0.53	-0.15	0.54	26.08	0.52	-0.17	0.56	26.24
	23	26.37	0.51	0.42	0.85	26.26	0.53	0.31	0.81	25.95
	24	26.36	0.54	0.07	0.59	26.00	0.67	-0.29	0.83	26.29
	25	26.19	0.69	0.02	0.75	26.10	0.74	-0.07	0.71	26.17
	26	26.19	0.75	0.01	0.90	26.00	0.86	-0.17	0.91	26.17
	27	26.20	0.93	0.39	1.11	25.92	1.02	0.10	0.99	25.81
	28	26.17	1.19	0.35	1.35	25.64	1.25	-0.19	1.27	25.83
06	29	25.90	1.50	-0.29	1.50	25.41	1.51	-0.77	1.63	26.19
	30	25.80	1.69	-0.40	1.77	25.54	1.63	-0.66	1.76	26.20
	31	25.94	1.72	-0.59	1.86	25.83	1.62	-0.70	1.77	26.53
	1	26.11	1.67	-1.03	1.98	26.22	1.67	-0.92	1.91	27.13
	2	26.19	1.69	-0.80	1.90	26.67	1.72	-0.32	1.75	26.99
	3	26.09	1.75	-0.94	2.00	26.60	1.84	-0.43	1.89	27.03
	4	26.16	1.79	-0.50	1.89	26.62	1.86	-0.04	1.88	26.66
	5	26.27	1.80	-0.51	1.86	26.41	1.88	-0.38	1.92	26.79
	22	26.39	0.42	0.15	0.48	26.36	0.45	0.12	0.53	26.24
	23	26.42	0.54	0.48	0.87	26.30	0.58	0.35	0.85	25.95
	24	26.39	0.56	0.10	0.65	25.90	0.76	-0.39	1.01	26.29
	25	26.17	0.76	0.00	0.85	26.21	0.80	0.04	0.74	26.17
	26	26.22	0.95	0.05	1.05	25.96	0.99	-0.22	1.02	26.17
	27	26.20	1.22	0.39	1.37	25.85	1.33	0.03	1.30	25.81
	28	26.31	1.46	0.48	1.65	25.60	1.52	-0.23	1.54	25.83
12	29	26.16	1.58	-0.03	1.57	25.72	1.56	-0.46	1.59	26.19
	30	26.26	1.51	0.06	1.53	26.04	1.47	-0.15	1.46	26.20
	31	26.23	1.53	-0.30	1.61	26.13	1.52	-0.40	1.57	26.53
	1	26.19	1.58	-0.95	1.87	26.38	1.61	-0.76	1.77	27.13
	2	26.25	1.60	-0.74	1.80	26.98	1.60	-0.01	1.64	26.99
	3	26.18	1.60	-0.85	1.82	26.70	1.74	-0.34	1.78	27.03
	4	26.37	1.57	-0.30	1.62	26.87	1.65	0.21	1.67	26.66
	5	26.53	1.54	-0.26	1.56	26.45	1.64	-0.34	1.69	26.79
	22	26.67	0.46	0.42	0.68	26.63	0.55	0.38	0.75	26.24
	23	26.28	0.59	0.34	0.81	26.14	0.74	0.19	0.91	25.95
	24	26.40	0.75	0.10	0.85	25.81	0.94	-0.48	1.23	26.29
	25	26.11	1.02	-0.06	1.11	26.27	1.13	0.10	1.05	26.17
	26	26.31	1.29	0.13	1.36	25.84	1.29	-0.34	1.38	26.17
	27	26.43	1.41	0.62	1.62	26.13	1.53	0.32	1.49	25.81
	28	26.56	1.45	0.74	1.71	25.75	1.45	-0.08	1.45	25.83
24	29	26.22	1.45	0.03	1.48	25.81	1.44	-0.37	1.46	26.19
	30	26.37	1.41	0.17	1.46	26.15	1.41	-0.04	1.42	26.20
	31	26.24	1.40	-0.29	1.47	26.16	1.45	-0.37	1.47	26.53
	1	26.27	1.40	-0.86	1.67	26.54	1.45	-0.60	1.57	27.13
	2	26.30	1.40	-0.69	1.62	27.19	1.52	0.20	1.58	26.99
	3	26.28	1.44	-0.76	1.64	26.71	1.62	-0.33	1.67	27.03
	4	26.53	1.45	-0.13	1.48	27.03	1.55	0.37	1.60	26.66
	5	26.55	1.50	-0.24	1.51	26.45	1.53	-0.34	1.59	26.79

Table VII.5. Basic statistical and model performance measures when data assimilation scheme 2 is active throughout the entire model integration period. Coefficient value: $5x10^{-5}$ with variable pre-forecast nudging period.